# Rapid Bounds on Electrostatic Energies Using Diagonal Approximations of Boundary-integral Equations

**J. P. Bardhan**

Rush University Medical Center, USA

**Abstract**— Life as we know it depends critically on electrostatic interactions within and between biological molecules such as proteins. One simple, but surprisingly effective, model for studying these interactions treats a biomolecule of interest as a dielectric continuum of homogeneous low permittivity with some embedded distribution of charges, and the aqueous solvent around it as another homogeneous dielectric with higher permittivity. This gives rise to a mixed-dielectric Poisson problem, widely studied in the mathematics and electromagnetics communities. In this paper we describe some simple analytical approximations to a boundary-integral equation formulation of the mixed-dielectric problem. Remarkably, the approximations (which we call BIBEE, for boundary-integral-based electrostatics estimation) give provable upper and lower bounds for the actual electrostatic energy. Because BIBEE methods preserve interactions between components of the charge distribution, they may represent one approach to rapidly approximate the Green's function for the geometry of interest.

## 1. INTRODUCTION

Virtually all biological molecules perform their functions in aqueous solutions — that is, surrounded by water molecules and a mixture of ions and small molecules, the presence of which profoundly impact biomolecular structure and function [1]. Although all-atom molecular dynamics (MD) simulations of biomolecules in explicit solvent are the highest-resolution calculations feasible on a day-to-day basis, unfortunately the majority of computational effort is spent on the solvent molecules rather than the biomolecule of interest. To improve efficiency, alternative methods have been developed to capture the average influence of the solvent on a biomolecule [2, 3], and can be hundreds to thousands of times faster. Implicit-solvent models often (but not always [4]) separate the average solute-solvent energetics into polar and nonpolar components. The polar component, which is the focus of this paper, models the electrostatic interactions between the biomolecule and the solvent, and the nonpolar component captures remaining aspects such as the energy of forming a solvent-free cavity for the molecular volume, and surface-tension effects [3].

The electrostatic interactions between a molecule and surrounding water are frequently modeled using a continuum dielectric framework, in which the solvent is assumed to be a homogeneous dielectric with permittivity approximately that of bulk water, and the molecule is assumed to be a low-dielectric body containing some distribution of charge. This mixed-dielectric Poisson problem has been studied in numerous areas of mathematical physics, particularly in electromagnetics [5, 6]; in this paper, we do not address the nonlinear Poisson-Boltzmann equation [7], or its linearized form, which are commonly used to account for the effects of mobile ions in solution. Given that linear continuum theory is an extreme oversimplification at the molecular scale, neglecting phenomena like dielectric saturation [8, 9] and the molecular nature of the solvent, the success of continuum models, in a variety of contexts, has been surprising [8, 10]. The existence of well-validated numerical software [11–13] has also helped to make continuum electrostatic theory a popular and widely accepted tool for studying molecular structure and function.

Despite the popularity of continuum methods, computational costs have remained a significant bottleneck in spite of rapid growth in CPU power and the development of powerful numerical algorithms. Although any one simulation may require only a minute to an hour, many types of theoretical studies require hundreds to thousands of simulations. For example, some approaches to computational molecular design assess the contribution of each chemical group (such as amino acid side chains or the chemical groups that make up the protein backbone) to the binding affinity between molecules; each such chemical group then requires its own simulation [14]. To make these and other large-scale calculations tractable, many groups have described heuristics capable of estimating electrostatic energies with much less computational effort [15, 16]. The generalized-Born (GB) method [15] is among the most popular of these simplified approaches [17, 18], and has been extensively tested against accurate simulations [19]. Nevertheless, the essentially empirical nature of these methods and the numerous reports of its shortcomings motivate much work to improve

the physical and mathematical rigor of computationally efficient methods to approximate energies within the continuum electrostatic model (e.g., [20]).

In this paper, we describe a widely used boundary-integral equation (BIE) formulation of the problem and present simple approximations, which we call BIBEE (boundary-integral-based electrostatics estimation) methods [21], that make numerical simulation almost trivial. The original BIE is widely known in electrostatics [5], and it is the author's hope that the electromagnetics community will be able to recognize characteristics of the BIBEE method and contribute to further advances in molecular simulation. In BIBEE, one replaces the dense boundary-integral operator of the BIE with a chosen diagonal operator. One choice for the diagonal gives a provable upper bound for the reaction energy induced by the molecular charge distribution [22]; this method is called BIBEE by the Coulomb-field approximation (BIBEE/CFA). A different choice for approximating the integral equation gives a provable lower bound and is called BIBEE/LB. A third choice, called BIBEE by preconditioning (BIBEE/P) because its numerical implementation is identical to a diagonal preconditioner for BEM solution of the integral equation, gives an effective (but not yet proven) lower bound, much closer to the actual energy than BIBEE/LB.

The next section presents the theoretical background for the BIBEE approach and Section 3 presents the BIBEE approximations themselves. Computational results in Section 4 illustrate how BIBEE approximations compare to full numerical solution and to a simple GB model. A brief discussion in Section 5 concludes the paper.

## 2. BACKGROUND

### 2.1. Boundary-integral Equation Formulation of the Mixed-dielectric Problem

Figure 1 is an illustration of the problem of interest [5, 23, 24]. Two dielectric regions, labeled $I$ and $II$, with dielectric constants $\epsilon_I$ and $\epsilon_{II}$, are separated by a boundary $\Omega$. A distribution of fixed charges exists in region $I$, and in this paper it is assumed to be a set of $n_c$ point charges, the $i$th of which is located at $r_i$ and has value $q_i$. These charges polarize the solvent, which in turn creates a *reaction potential* in the molecule, which gives rise to what is known as the *reaction-field energy*. In region $I$, the electrostatic potential satisfies the Poisson equation

$$\nabla^2\varphi(r) = -\sum_{i=1}^{n_c} q_i\delta(r - r_i) \tag{1}$$

where $\delta(r)$ is the Dirac delta function, and in region $II$ the potential satisfies the Laplace equation $\nabla^2\varphi_{II}(r) = 0$. At the boundary the potential and the normal displacement field are continuous [25].

Having assumed linear response, the $n_c$-length vector of potentials at the charge locations can be expressed as $\varphi^{\mathrm{reac}} = Lq$ and the reaction-field energy can be expressed as the quadratic expression $\frac{1}{2}q^TLq$, where $q$ is the $n_c$-length vector of the charge values and $L$ is called the reaction-potential matrix, because the matrix entry $L_{i,j}$ represents the reaction potential that a $+1e$ charge at $r_j$ induces at $r_i$. From reciprocity it is clear that $L$ is symmetric, and in addition for $\epsilon_I < \epsilon_{II}$ it can be shown that $L$ is negative definite. Note that eigenvectors of $L$ that correspond to distinct eigenvalues represent charge distributions that do not interact via solvent polarization (although they do interact Coulombically) [21].
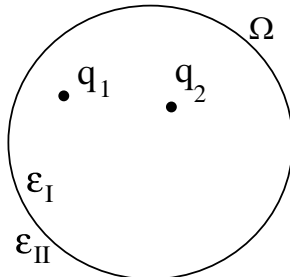


Figure 1: The mixed-dielectric Poisson problem.

Straightforward application of Gauss's law [5] leads to the second-kind boundary-integral equa-

tion

$$\left(1 - \frac{\epsilon_I}{\epsilon_{II}}\right)\left(\frac{\partial}{\partial n(r)}\sum_{i=1}^{n_c}\frac{q_i}{4\pi||r - r_i||} + \frac{\partial}{\partial n(r)}\int_\Omega \frac{\sigma(r')}{4\pi||r - r'||}dA'\right) = \sigma(r), \tag{2}$$

where $\sigma(r)$ represents the layer of surface charge induced on $\Omega$ and $n(r)$ is the outward normal at $r \in \Omega$ (pointing into region $II$ from region $I$). After accounting for the singular nature of the boundary integral at $r = r'$, we may re-write Eq. (2) as

$$\sigma(r) + \hat{\epsilon}\!\!\fint \frac{\partial}{\partial n(r)}\frac{\sigma(r')}{4\pi||r - r'||}dA' = -\hat{\epsilon}\sum_i \frac{\partial}{\partial n(r)}\frac{q_i}{4\pi||r - r_i||} \tag{3}$$

where the notation $\fint$ denotes the principal value of the integral [26] and $\hat{\epsilon} = \frac{2(\epsilon_I - \epsilon_{II})}{\epsilon_I + \epsilon_{II}}$. After solving Eq. (3), the reaction potential at a point $r$ in the molecule is simply the Coulomb potential induced by $\sigma$:

$$\varphi^{\text{reac}}(r) = \frac{1}{\epsilon_I}\int_\Omega \frac{\sigma(r')}{4\pi||r - r'||}dA'. \tag{4}$$

In operator notation Eq. (3) can be written as $(\mathcal{I} + \hat{\epsilon}\mathcal{D}^*)\sigma = -\hat{\epsilon}\mathcal{B}q$ and Eq. (4) as $\varphi^{\text{reac}} = \mathcal{C}\sigma$.

## 2.2. Numerical Solution of Boundary-integral Equations

To solve Eq. (3) numerically using the boundary-element method (BEM), one discretizes $\Omega$ into a set of $n_p$ boundary elements and then defines a set of compactly supported basis functions $\chi_i(r)$ on the boundary elements so as to represent $\sigma(r)$ approximately as the weighted sum $\sigma(r) = \sum_{i=1} x_i\chi_i(r)$ where the weights $x_i$ are unknown. In the present work, we approximate $\Omega$ as a set of planar triangles, and define basis functions such that $\chi_i(r) = 1$ on boundary element $i$ and 0 otherwise. Finally, one enforces a set of $n_p$ independent linear constraints on the weights so that the integral equation is satisfied as closely as possible [26]. Regardless of the choice of constraints (one has some freedom to choose), this process generates the square matrix equation

$$Ax = Bq, \tag{5}$$

where the $n_p$-by-$n_p$ matrix $A$ is the discretized form of the operator $(\mathcal{I} + \hat{\epsilon}\mathcal{D}^*)$ and the $n_p$-by-$n_c$ matrix $B$ represents the discretization of $\hat{\epsilon}\mathcal{B}$. In many BEM simulations, one forces the integral equation to be satisfied exactly at the centers (centroids) of the boundary elements; this is known as centroid collocation [6, 26]. However, as noted by Tausch and White [6], this type of constraint leads to inaccurate results for the electric-field integral operator in Eq. (3), and it is preferable to use a method known as *qualocation* instead [6, 27–29]. Writing the discretized form of the Coulomb integral operator $\mathcal{C}$ as $C$, which maps the $n_p$-length vector $x$ to the $n_c$-length $\varphi^{\text{reac}}$, one can write the reaction-potential matrix as $L = CA^{-1}B$.

The matrices $A$, $B$, and $C$ are all dense, which precludes the use of Gaussian elimination for all but the smallest problems. Instead, one computes sparsified representations of the matrices using algorithms such as the fast multipole method (FMM) [30, 31], pre-corrected FFT [32], or FFTSVD [33], which allow the matrices to be applied to vectors using only linear time and memory. The linear system in Eq. (5) is then solved approximately using Krylov-subspace iterative methods like GMRES [34], in which one repeatedly applies $A$ to $Bq$ to generate a vector space from which an suitable approximation to the solution is found. A *preconditioner* matrix $P$ can be employed so that the linear system $PAx = PBq$ yields an acceptable approximate solution $x$ in fewer iterations than would be required to solve the original linear system.

## 2.3. Generalized-born Methods For Estimating Electrostatic Energies

The reaction energy for a sphere of radius $R$ with a central charge $q$ is known as the *Born energy* $E^{\text{Born}}$,

$$E^{\text{Born}} = \frac{1}{8\pi}\left(\frac{1}{\epsilon_{II}} - \frac{1}{\epsilon_I}\right)\frac{q_i^2}{R_i} \tag{6}$$

where $R_i$, called the Born radius for the ion, is clearly a measure of the degree to which the high dielectric can approach the point charge. Still et al. suggested the generalized-Born (GB) model that employs *effective* Born radii for molecules [15]. For an atom $i$ in the given molecule, one sets $q_i = 1$ and the rest to zero, calculates the resulting reaction energy $E_i$, and then substitutes $E_i$

into the left-hand side of Eq. (6) to solve for a radius $R_i$. The reaction-potential matrix entries are then according to

$$L_{i,j}^{\text{GB}} = \frac{1}{8\pi} \left( \frac{1}{\epsilon_{II}} - \frac{1}{\epsilon_I} \right) \frac{1}{\sqrt{r_{ij}^2 + R_i R_j \exp(-r_{ij}^2/4R_i R_j)}}, \tag{7}$$

so that the self-term entries $L_{i,i}^{\text{GB}}$ recover the original self-energy $E_i$ in the limit as $r_{ij} \to 0$, and for large distances one recovers the difference in Coulomb energies between the same charges interacting in the different dielectrics. The empirical interpolation formula of Eq. (7) is the core equation of Generalized-Born (GB) methods and works surprisingly well to predict reaction energies [15, 19, 35, 36].

Of course, calculating $L^{\text{GB}}$ in such a way requires simulating the electrostatics problem $n_c$ times, whereas the total energy could be computed in only one simulation, and thus would offer no time savings at all. Instead, the charges' self-energies are estimated using rapidly computed approximate methods, and then the radii are trivially calculated from Eq. (6). The history of GB methods centers predominantly, but not entirely [37], around finding efficient means to estimate these individual self-energies so that GB reaction energies agree with known analytical results or full numerical simulation [17, 18].

Most approaches to computing a charge's self energy begin with what is called the *Coulomb-field approximation* (CFA) [35], in which one integrates the energy density of the bare Coulomb-field in the molecule (omitting the volume interior to the atom itself):

$$R_i^{-1} \propto \int_V \frac{(r'-r_i)^T n(r')}{||r'-r_i||^4} dV'. \tag{8}$$

Converting Eq. (8) to surface-integral form [16] reveals a direct connection between the CFA and the boundary-integral equation of Eq. (3): the surface-Generalized-Born (SGB)/CFA entails neglecting the integral operator in Eq. (2). In earlier work this was justified by the approximation's exactness for the sphere with central charge [16] and considered to be a consequence of spherical symmetry.

## 3. BIBEE APPROXIMATIONS

### 3.1. BIBEE/CFA: A Provable Upper Bound

The SGB/CFA method calculates each charge's self energy by approximating the induced surface charge via

$$\left( 1 - \frac{\hat{\epsilon}}{2} \right) \sigma^{\text{CFA}} = -\hat{\epsilon} \mathcal{B} q \tag{9}$$

where again $q_i = 1$, $q_j = 0 \; \forall i \neq j$. The second term on the left-hand side arises from the neglect of the integral operator in Eq. (2) — one assumes that all the eigenvalues of $\mathcal{D}^*$ in Eq. (3) are the same extremal eigenvalue associated with the constant normal electric field on the boundary [22]. The crux of the BIBEE/CFA method is to use the same diagonal approximation as in Eq. (9) but with all of the actual charges, rather than just one, so that $\sigma^{\text{CFA}}$ includes contributions from all charges. The BIBEE/CFA reaction energy is then calculated the same way as in the actual boundary-integral equation approach, i.e., via Eq. (4). BIBEE/CFA is therefore the straightforward extension of the SGB approach to multiple charges, and it appears to be the boundary-integral formulation of the variational Coulomb-field approximation method [38].

The proof that BIBEE/CFA reaction energy is an upper bound to the actual reaction energy proceeds in two main stages [22]. In the first, one re-writes $\mathcal{C}$ in terms of $\mathcal{B}$, and exploits the fact that the normal electric field operator $\mathcal{D}^*$ is similar to a Hermitian operator $\mathcal{H}$ (see [39]), so that the reaction energy can be expressed as a sum over the modes of $\mathcal{H}$:

$$E^{\text{reaction}} = \hat{\epsilon}^{-1} \sum_i \left( 1 - 2\lambda_i^{\mathcal{D}} \right)^{-1} \left( 1 + \hat{\epsilon}\lambda_i^{\mathcal{D}} \right)^{-1} x_i^2 \tag{10}$$

where $x_i$ represents the projection of $\mathcal{B}q$ onto the $i$th eigenvector of $\mathcal{H}$. It is well known [26] that $\lambda_i^{\mathcal{D}} \in [-1/2, +1/2)$. In the proof's second stage, the original operator $(1 + \hat{\epsilon}\mathcal{D}^*)$ is replaced by

$(1 - \hat{\epsilon}/2)$ and subjected to the same decomposition by modes to obtain

$$E^{CFA} = \hat{\epsilon}^{-1} \sum_i \left(1 - 2\lambda_i^{\mathcal{D}}\right)^{-1} \left(1 - \frac{\hat{\epsilon}}{2}\right)^{-1} x_i^2. \tag{11}$$

It is then easy to show that each term of the sum in Eq. (11) is greater than the corresponding term in Eq. (10); the full details of the proof are provided elsewhere [22].

### 3.2. BIBEE/LB and BIBEE/P: Lower Bounds

Other diagonal operators can be chosen to give alternative approximations. The BIBEE/LB approximation solves

$$(\mathcal{I} + \frac{\hat{\epsilon}}{2})\sigma^{\mathrm{LB}} = -\hat{\epsilon}\mathcal{B}q, \tag{12}$$

thus exploiting the other extremal eigenvalue of $\mathcal{D}^*$; this can be proven to give a general lower bound for the electrostatic energy [22]. The BIBEE/P approximation arises from

$$\mathcal{I}\sigma^{\mathrm{P}} = -\hat{\epsilon}\mathcal{B}q, \tag{13}$$

and gives a provable lower bound to the reaction energy for geometries in which $\mathcal{D}^*$ is known to not possess positive eigenvalues, for instance spheres and prolate spheroids [40]. It is not yet understood why BIBEE/P seems to provide a lower bound for a wide variety of surfaces [22], given that it is known that for some shapes, including oblate spheroids [41], $\mathcal{D}^*$ can be proven to possess eigenvalues arbitrarily close to $+1/2$.

### 3.3. Numerical Implementation

As described previously, the reaction-potential matrix can be written as $L = CA^{-1}B$ where $B$ maps the vector of charges to the normal electric field at the boundary, $A$ is the BEM matrix, and $C$ maps the induced surface charge $\sigma$ to the reaction potentials at the charge locations. Numerical computations using BIBEE simply employ different diagonal matrices in place of $A$, where the diagonal entries are the discretized operators in Eqs. (9), (12), and (13). A MATLAB implementation of BIBEE is freely available online [42].

## 4. RESULTS

All of the numerical simulations performed in this section employed an interior dielectric constant $\epsilon_I = 4$ and exterior dielectric constant $\epsilon_{II} = 80$. All surfaces were discretized using MSMS [43], and all BEM operators were compressed using FFTSVD [33, 44]. Results for the BIBEE/LB approximation are not plotted because the bound is so loose that other results are obscured [22].

### 4.1. Charges in a Sphere

The simplest possible case is a single charge in a sphere; we use a sphere of radius 20 Å as a model for a small protein. Figure 2(a) contains plots of the reaction energy of a single $+1e$ charge as a function of the charge's distance from the sphere center. As explained previously, the SGB/CFA and BIBEE/CFA theories should give identical results for the single-charge case. In Figure 2(a), the numerical results for these theories are slightly different because SGB/CFA energies are calculated by direct numerical integration over the discretized surface [45], whereas the BIBEE/CFA calculations are based on the BEM approach described above. As is well known [37, 46], the CFA is inaccurate for the single charge problem as the charge approaches the sphere surface. Figure 2(b) are plots of the reaction energy of an ion pair in a sphere, as a function of the pair's distance from the sphere center. The ion pair is composed of two charges, one $+1e$ and one $-1e$, separated by 3 Å, with the line segment between them pointing radially outward from the sphere center. The CFA approaches are increasingly inaccurate as the ion pair nears the surface, but the BIBEE/P approxiation exhibits excellent accuracy throughout; in general, BIBEE/P is most accurate at approximating energies that arise from charge distributions that generate highly localized electric fields on the dielectric boundary [21]. It is also significant that the BIBEE/CFA answers are substantially more accurate near the surface than the SGB/CFA answers. Because each ion taken in isolation would have the two CFA theories agree perfectly (as demonstrated by the results in Figure 2(a)), the BIBEE/CFA improvement must be due to the inclusion of the actual physics of interaction between the ions, by accounting for their mutual induction of surface charge even in the Coulomb-field approximation. The inadequacy of the heuristic Still interpolation formula
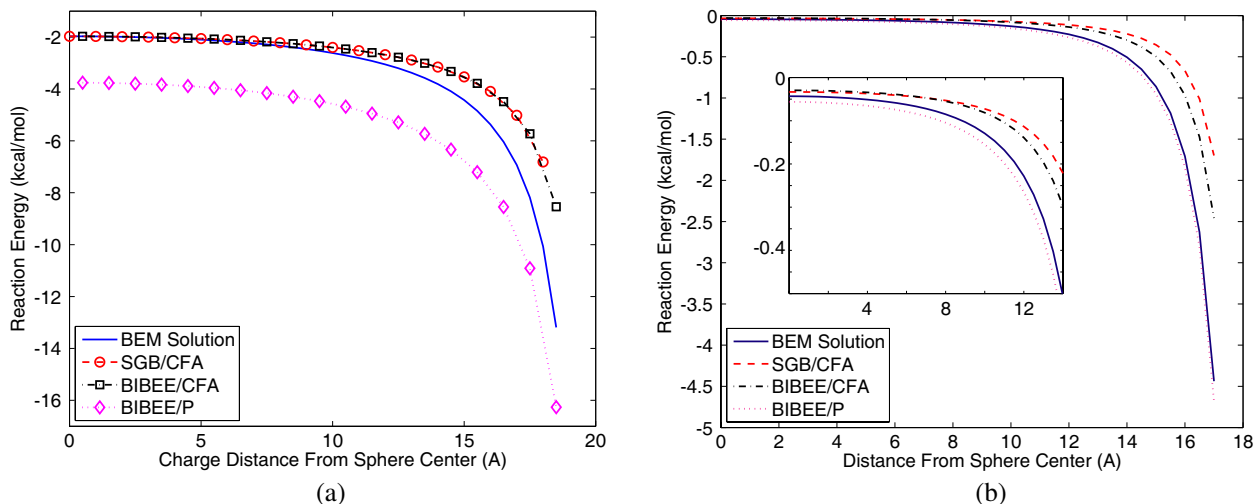
Figure 2: The accuracy of approximate electrostatic models for charges in a sphere. All energies are in kcal/mol. Reaction energies have been computed by BEM solution of Eq. (3), surface-Generalized Born/Coulomb-field approximation (SGB/CFA) theory, and BIBEE approximations. (a) The reaction energy of a single $+1e$ charge in a sphere of radius $20\,\text{Å}$, as a function of the charge's distance from the sphere center. (b) The reaction energy of two charges of opposite sign, $+1e$ and $-1e$, separated by $3\,\text{Å}$, in a sphere of radius $20\,\text{Å}$, such that the charge locations and the sphere center are collinear. The distance is measured from the sphere center to the midpoint between the charges.

for calculating reaction energies in these cases has motivated the development of improved GB methods (see, e.g., [20, 37, 46]).

## 4.2. Electrostatics in a Realistic Small Molecule

Most molecules have highly irregular shapes. To illustrate that BIBEE approaches perform well for nonspherical shapes, we use a small molecule, the 22-atom alanine dipeptide [47] and calculate the full $L$ matrices using BEM, SGB/CFA, and BIBEE/CFA and BIBEE/P. Figure 3(a) contains plots of the magnitudes of the eigenvalues of the computed matrices, sorted in increasing order; physically, all eigenvalues should all be negative, but the final eigenvalues of the SGB/CFA matrix appear to be increasing in magnitude because they are positive (nonphysical). Note that the BIBEE methods exhibit opposite regimes for good accuracy: BIBEE/CFA is most accurate for large-magnitude eigenvalues, whereas BIBEE/P is most accurate for smaller eigenvalues. This behavior suggests that it may be possible to find a physically-motivated, charge-distribution-dependent scheme to interpolate between the two estimates. Figures 3(b) and (c) are pseudocolor plots of the magnitudes of the projections of the eigenvectors of the CFA-based matrices $L^{\text{SGB}}$ and $L^{\text{BIBEE}}$ onto the eigenvectors of $L^{\text{BEM}}$, i.e., the cell $(i, j)$ in Figure 3(b) represents the magnitude of $V_i^{\text{BEM, T}} V_i^{\text{SGB}}$. Figure 3(c) appears more "diagonal" than Figure 3(b) because the BIBEE approach more accurately preserves the charge distributions that do not interact via solvent polarization [21]. This example also serves to demonstrate the computational advantages of BIBEE. The total time to compute the BEM matrix was 5.73 seconds, whereas only 0.44 seconds were needed to compute each BIBEE matrix. Comparable performance advantages, showing that BIBEE is at least an order of magnitude faster than BEM, and within a factor of two or three slower than SGB/CFA, were found in [21] for a tripeptide example and for a protein-inhibitor example.

## 4.3. Interactions between Charges in Two Spheres

We now turn to an example in which one of the conditions of the original proof [22] does not hold: the case of multiple, disconnected, low-permittivity regions. This multiple-region problem could model a situation in which ones wishes to study interactions between multiple bodies that are not in physical contact, such as the interactions between ions, or how two molecules approach each other before binding. Figure 4(a) contains plots of reaction energies for a pair of spheres $1\,\text{Å}$ in radius, each with a central $+1e$ charge, as a function of the separation between them. Similar results are obtained for charges of opposite sign, and for larger spheres containing random charge distributions (results not shown). Figure 4(b) plots the CFA methods' deviations from BEM simulation. Importantly, BIBEE/CFA appears to continue to offer an upper bound; BIBEE/P and
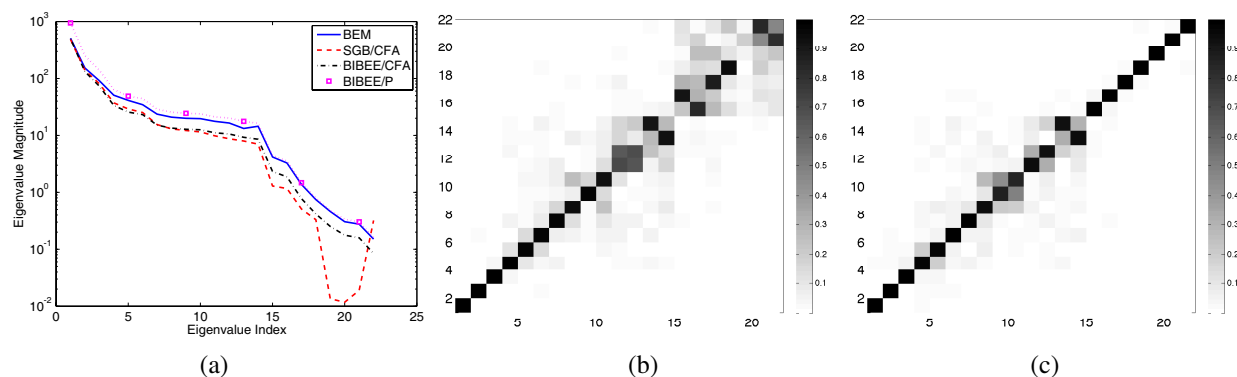
Figure 3: A comparison of the reaction-potential matrices computed using BEM, SGB/CFA, and BIBEE methods. (a) The eigenvalue magnitudes. The eigenvalues have been sorted in increasing order, and should all be negative; the final SGB/CFA eigenvalues are small and positive, which is why the magnitudes appear to increase. (b) The magnitudes of the projections of the SGB/CFA eigenvectors onto the BEM eigenvectors. (c) The magnitudes of the projections of the BIBEE/CFA eigenvectors onto the BEM eigenvectors. It can be seen that the BIBEE/CFA eigenvectors are well aligned with those from BEM across the entire spectrum.
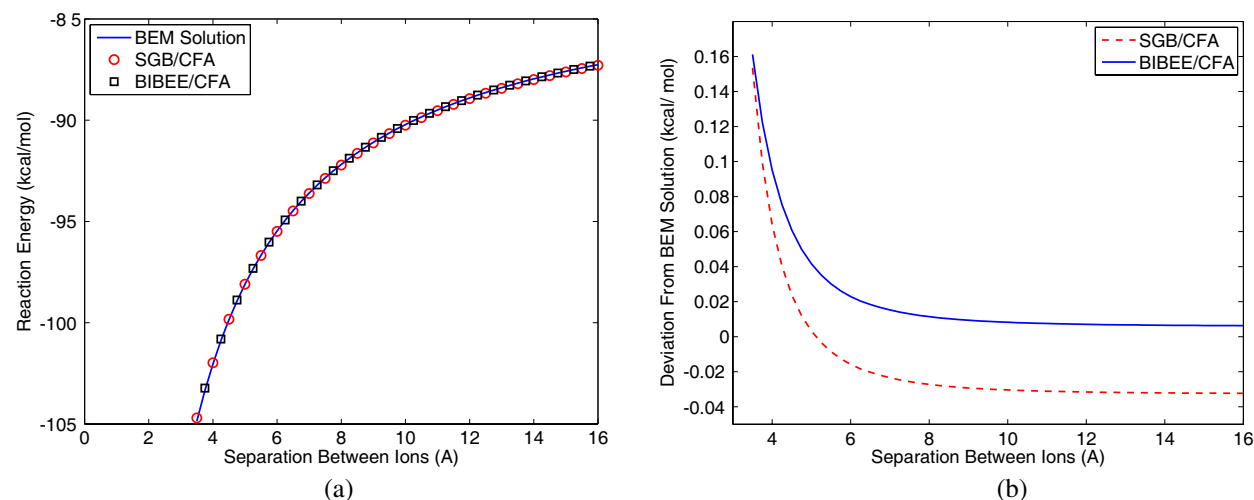


Figure 4: The reaction energy of two spheres with $+1e$ charges inside, as a function of the spheres' separation; both spheres are of radius $1\,\text{Å}$. All energies are in kcal/mol. (a) The reaction energies. (b) The deviations of the SGB/CFA and BIBEE/CFA estimates from the BEM solution.

BIBEE/LB appear to offer lower bounds as well (data not shown).

One expects the reasonably good agreement between the CFA-based methods and fully detailed numerical solution of the problem that is observed in Figure 4(a), given that the dominant contribution to the reaction energy arises from the spheres' individual reaction energies. However, the deviations of the CFA-based estimates from the actual BEM results is illustrative of the difference between SGB/CFA and BIBEE/CFA methods (Figure 4(b)). Although in the present example these deviations are small enough to be essentially insignificant as a practical matter (i.e., the energies are so small as to rarely be of importance in studying the function of biological systems), they point again to the improved physical model in BIBEE that employs the CFA using all charges simultaneously.

## 5. DISCUSSION

This article has described the performance of diagonal approximations to a boundary-integral equation widely used to study electrostatic interactions in mixed dielectrics [5]. This boundary-integral equation is a valuable tool for studying the structure and function of proteins and other biological molecules by modeling both the molecule of interest and the aqueous solvent as dielectric continua, and assuming that the molecule contains some distribution of charge [23, 24]. By replacing the

dense integral operator with a diagonal one (what we call the boundary-integral-based electrostatics estimation, or BIBEE, method), one eliminates the computationally expensive solution of the mixed-dielectric problem and obtains instead a rapidly computed approximation. The choice of diagonal approximation allows one to obtain provable upper and lower bounds to the actual electrostatic energy. Pairwise interactions are remarkably well preserved even in this approximation of the integral operator. We hope that the computational and theoretical electromagnetics communities, which have long history and extensive experience with the theory and practice of boundary-integral equations, may recognize these approximation or similarities they may have to other techniques, and thereby stimulate future advances in modeling molecular interactions. To support this goal, a simple MATLAB implementation of BIBEE is freely available online [42].

The BIBEE/CFA approximation appears to be the boundary-integral form of the variational Coulomb-field approximation (CFA) described by Borgis et al. [38], although a more detailed comparison remains to be performed. One advantage of the boundary-integral analysis is that it allowed direct identification that the CFA exploits the extremal eigenvalue of the electric-field integral operator, immediately giving theoretical support to the BIBEE/P and BIBEE/LB methods [21, 22]. We acknowledge that for reasons of space, we have only compared BIBEE methods to the simplest formulation of the Generalized-Born model, SGB/CFA [16], without using any of the sophisticated correction factors that have been described in the literature [16, 46, 48]; earlier work on BIBEE compared results to the recent GBMV (Generalized Born with Molecular Volume) method [48]. Hopefully, the BIE analysis that clarified the CFA can offer similar support for these new GB methods.

Numerous questions remain for future investigation. It is still not known whether the effective lower bound offered by BIBEE/P is actually a provable lower bound, or if there are conditions under which its apparent bounding properties may be proven. Also, as the last example illustrated, it appears that BIBEE/CFA continues to offer an upper bound for multiple disconnected low-dielectric regions; a proof of this would be a valuable contribution. Finally, in earlier work [22] a simple and purely empirical interpolation between BIBEE/CFA and BIBEE/P was tested and found to give excellent agreement with BEM results for a small peptide. A mathematically justified interpolant, perhaps based on the work of Onufriev and collaborators [20], could obviate the need for much more expensive simulations without the need to resort to largely heuristic approaches like GB. Other extensions for biomolecular electrostatics are also of interest, including problems with more than two dielectric constants and problems in which sources exist in regions with different dielectric constants. The latter, for example, would allow BIBEE to rigorously accelerate Monte Carlo simulations for understanding how ion-channel proteins in cell membranes can selectively pass one kind of ion (e.g., sodium) but not others [49].

## ACKNOWLEDGMENT

## REFERENCES

1. Sharp, K. A. and B. Honig, "Electrostatic interactions in macromolecules: Theory and applications," *Annual Review of Biophysics and Biophysical Chemistry*, Vol. 19, 301–332, 1990.

2. Roux, B. and T. Simonson, "Implicit solvent models," *Biophysical Chemistry*, Vol. 78, 1–20, 1999.

3. Baker, N. A., "Improving implicit solvent simulations: A Poisson-centric view," *Current Opinions in Structural Biology*, Vol. 15, 137–143, 2005.

4. Vitalis, A. and R. V. Pappu, "ABSINTH: A new continuum solvation model for simulations of polypeptides in aqueous solutions," *Journal of Computational Chemistry*, Vol. 30, 673–700, 2009.

5. Rush, S., A. H. Turner, and A. H. Cherin, "Computer solution for time-invariant electric fields," *Journal of Applied Physics*, Vol. 37, No. 6, 2211–2217, 1966.

6. Tausch, J., J. Wang, and J. White, "Improved integral formulations for fast 3-D method-of-moment solvers," *IEEE Transactions on Computer-Aided Design of Integrated Circuits and Systems*, Vol. 20, No. 12, 1398–1405, 2001.

7. Sharp, K. A. and B. Honig, "Calculating total electrostatic energies with the nonlinear Poisson-Boltzmann equation," *Journal of Physical Chemistry*, Vol. 94, No. 19, 7684–7692, 1990.

8. Rick, S. W. and B. J. Berne, "The aqueous solvation of water: A comparison of continuum methods with molecular dynamics," *Journal of the American Chemical Society*, Vol. 116, 3949–3954, 1994.

9. Gong, H. and K. F. Freed, "Langevin-Debye model for nonlinear electrostatic screening of solvated ions," *Physical Review Letters*, Vol. 102, 057603, 2009.

10. Jean-Charles, A., A. Nicholls, K. Sharp, B. Honig, A. Tempczyk, T. F. Hendrickson, and W. C. Still, "Electrostatic contributions to solvation energies: Comparison of free energy perturbation and continuum calculations," *Journal of the American Chemical Society*, Vol. 113, 1454–1455, 1991.

11. Gilson, M. K., A. Rashin, R. Fine, and B. Honig, "On the calculation of electrostatic interactions in proteins," *Journal of Molecular Biology*, Vol. 184, 503–516, 1985.

12. Rocchia, W., S. Sridharan, A. Nicholls, E. Alexov, A. Chiabrera, and B. Honig, "Rapid grid-based construction of the molecular surface and the use of induced surface charge to calculate reaction field energies: Applications to the molecular systems and geometric objects," *Journal of Computational Chemistry*, Vol. 23, 128–137, 2002.

13. Baker, N. A., D. Sept, M. J. Holst, and J. A. McCammon, "Electrostatics of nanosystems: Application to microtubules and the ribosome," *Proceedings of the National Academy of Sciences of the USA*, Vol. 98, 10037–10041, 2001.

14. Lee, L.-P. and B. Tidor, "Barstar is electrostatically optimized for tight-binding to barnase," *Nature Structural Biology*, Vol. 8, 73–76, 2001.

15. Still, W. C., A. Tempczyk, R. C. Hawley, and T. F. Hendrickson, "Semianalytical treatment of solvation for molecular mechanics and dynamics," *Journal of the American Chemical Society*, Vol. 112, No. 16, 6127–6129, 1990.

16. Ghosh, A., C. S. Rapp, and R. A. Friesner, "Generalized Born model based on a surface integral formulation," *Journal of Physical Chemistry B*, Vol. 102, 10983–10990, 1998.

17. Bashford, D. and D. A. Case, "Generalized Born models of macromolecular solvation effects," *Annual Review of Physical Chemistry*, Vol. 51, 129–152, 2000.

18. Feig, M. and C. L. Brooks III, "Recent advances in the development and application of implicit solvent models in biomolecule simulations," *Current Opinions in Structural Biology*, Vol. 14, 217–224, 2004.

19. Feig, M., A. Onufriev, M. S. Lee, W. Im, D. A. Case, and C. L. Brooks III, "Performance comparison of generalized Born and Poisson methods in the calculation of electrostatic solvation energies for protein structures," *Journal of Computational Chemistry*, Vol. 25, 265–284, 2004.

20. Sigalov, G., A. Fenley, and A. Onufriev, "Analytical electrostatics for biomolecules: Beyond the generalized Born approximation," *Journal of Chemical Physics*, Vol. 124, 124902, 2006.

21. Bardhan, J. P., "Interpreting the Coulomb-field approximation for Generalized-Born electrostatics using boundary-integral equation theory," *Journal of Chemical Physics*, Vol. 129, 144105, 2008.

22. Bardhan, J. P., M. G. Knepley, and M. Anitescu, "Bounding the electrostatic free energies associated with linear continuum models of molecular solvation," *Journal of Chemical Physics*, Vol. 130, 104108, 2009.

23. Miertus, S., E. Scrocco, and J. Tomasi, "Electrostatic interactions of a solute with a continuum — A direct utilization of *ab initio* molecular potentials for the prevision of solvent effects," *Chemical Physics*, Vol. 55, No. 1, 117–129, 1981.

24. Shaw, P. B., "Theory of the Poisson Green's-function for discontinuous dielectric media with an application to protein biophysics," *Physical Review A*, Vol. 32, No. 4, 2476–2487, 1985.

25. Jackson, J. D., *Classical Electrodynamics*, 3rd Edition, Wiley, 1998.

26. Atkinson, K. E., *The Numerical Solution of Integral Equations of the Second Kind*, Cambridge University Press, 1997.

27. Altman, M. D., J. P. Bardhan, J. K. White, and B. Tidor, "An efficient and accurate surface formulation for biomolecule electrostatics in non-ionic solution," *Engineering in Medicine and Biology Conference (EMBC)*, 2005.

28. Bardhan, J. P., "Numerical solution of boundary-integral equations for molecular electrostatics," *Journal of Chemical Physics*, Vol. 130, 094102, 2009.

29. Bardhan, J. P., R. S. Eisenberg, and D. Gillespie, "Discretization of the induced-charge boundary integral equation," *Physical Review E*, Vol. 80, 011906, 2009.

30. Greengard, L., *The Rapid Evaluation of Potential Fields in Particle Systems*, MIT Press, 1988.

31. Nabors, K. and J. White, "FASTCAP: A multipole accelerated 3-D capacitance extraction program," *IEEE Transactions on Computer-Aided Design of Integrated Circuits and Systems*, Vol. 10, No. 10, 1447–1459, 1991.

32. Phillips, J. R. and J. K. White, "A precorrected-FFT method for electrostatic analysis of complicated 3-D structures," *IEEE Transactions on Computer-Aided Design of Integrated Circuits and Systems*, Vol. 16, No. 10, 1059–1072, 1997.

33. Altman, M. D., J. P. Bardhan, B. Tidor, and J. K. White, "FFTSVD: A fast multiscale boundary-element method solver suitable for BioMEMS and biomolecule simulation," *IEEE Transactions on Computer-Aided Design of Integrated Circuits and Systems*, Vol. 25, 274–284, 2006.

34. Saad, Y. and M. Schultz, "GMRES: A generalized minimal residual algorithm for solving nonsymmetric linear systems," *SIAM Journal of Scientific and Statistical Computing*, Vol. 7, 856–869, 1986.

35. Qiu, D., P. S. Shenkin, F. P. Hollinger, and W. C. Still, "The GB/SA continuum model for solvation. A fast analytical method for the calculation of approximate Born radii," *Journal of Physical Chemistry A*, Vol. 101, No. 16, 3005–3014, 1997.

36. Onufriev, A., D. A. Case, and D. Bashford, "Effective Born radii in the generalized Born approximation: The importance of being perfect," *Journal of Computational Chemistry*, Vol. 23, 1297–1304, 2002.

37. Fedichev, P. O., E. G. Getmantsev, and L. I. Men'shikov, "Fast surface based electrostatics for biomolecules modeling," 2009.

38. Borgis, D., N. Lévy, and M. Marchi, "Computing the electrostatic free-energy of complex molecules: the variational Coulomb field approximation," *Journal of Chemical Physics*, Vol. 119, No. 6, 3516–3528, 2003.

39. Ahner, J. F., V. V. Dyakin, V. Ya. Raevskii, and St. Ritter, "Spectral properties of operators of the theory of harmonic potential," *Mathematical Notes*, Vol. 59, No. 1, 3–11, 1996.

40. Ahner, J. F. and R. F. Arenstorf, "On the eigenvalues of the electrostatic integral operator," *Journal of Mathematical Analysis and Applications*, Vol. 117, 187–197, 1986.

41. Ahner, J. F., V. V. Dyakin, and V. Y. Raevskii, "New spectral results for the electrostatic integral operator," *Journal of Mathematical Analysis and Applications*, Vol. 185, 391–402, 1994.

42. http://bitbucket.org/jbardhan/bibee-demo/.

43. Sanner, M., A. J. Olson, and J. C. Spehner, "Reduced surface: An efficient way to compute molecular surfaces," *Biopolymers*, Vol. 38, 305–320, 1996.

44. Altman, M. D., J. P. Bardhan, J. K. White, and B. Tidor, "Accurate solution of multi-region continuum electrostatic problems using the linearized Poisson-Boltzmann equation and curved boundary elements," *Journal of Computational Chemistry*, Vol. 30, 132–153, 2009.

45. Bardhan, J. P., M. D. Altman, J. K. White, and B. Tidor, "Numerical integration techniques for curved-panel discretizations of molecule–solvent interfaces," *Journal of Chemical Physics*, Vol. 127, 014701, 2007.

46. Grycuk, T., "Deficiency of the Coulomb-field approximation in the generalized Born model: An improved formula for Born radii evaluation," *Journal of Chemical Physics*, Vol. 119, No. 9, 4817–4826, 2003.

47. Scarsdale, J. N., C. Van Alsenoy, V. J. Klimkowski, L. Schafer, and F. A. Momany, "Ab initio studies of molecular geometries. 27. Optimized molecular structures and conformational analysis of $N^\alpha$-$N$-methylalaninamide and comparison with peptide crystal data and empirical calculations," *Journal of the American Chemical Society*, Vol. 105, 3438–3445, 1983.

48. Lee, M. S., F. R. Salsbury, and C. L. Brooks III, "Novel generalized Born methods," *Journal of Chemical Physics*, Vol. 116, No. 24, 10606–10604, 2002.

49. Boda, D., W. Nonner, M. Valiskó, D. Henderson, B. Eisenberg, and D. Gillespie, "Steric selectivity in Na channels arising from protein polarization and mobile side chains," *Biophysical Journal*, Vol. 93, 1960–1980, 2007.

# ISAR Simulations of Complex Objects and Verification with Measurements at TUBITAK MRC

**Uğur Saynak**[1], **Alper Çolak**[1], **Harun Cetinkaya**[2], **Mustafa Tekbas**[2], **I. Hakki Tayyar**[1,3],
**Deniz Bölükbas**[1], **Caner Ozdemir**[1,4], **and Alexey Vertiy**[2]

[1]Information Technologies Institute (ITI), TÜBİTAK MRC, Gebze, Kocaeli, Turkey
[2]Material Institute, International Laboratory for High Technology (ILHT)
TUBITAK-MRC, Gebze, Kocaeli, Turkey
[3]GYTE, Dept. of Electronics Engineering, Gebze, Kocaeli
[4]Mersin University, Dept. of Electrical-Electronics Engineering, Mersin, Turkey

**Abstract**— In this paper, ISAR images of a scaled model target have been demonstrated for the simulated and measurement data at TUBITAK-MRC facilities. The simulation was carried out with a high frequency electromagnetic simulator that can predict electromagnetic scattering from large and complex bodies. The measurement radar cross section data were collected by an ISAR experimental setup with 100 GHz anechoic chamber. All measurements have been supplied by sub-THz vector network analyzer. The millimeter (mm) wave band set-up used for ISAR test-case is presented. For validation, the scaled model of an airplane target has been selected. The two-dimensional ISAR measurements have been performed around the center frequency of 90 GHz. The comparison of the simulated ISAR image of the CAD model of the target and the measured ISAR image of the scaled model provides a good match.

## 1. INTRODUCTION

Two-dimensional (2D) inverse synthetic aperture radar (ISAR) imaging is a powerful tool in analyzing the electromagnetic scattering from targets such that it can be used for identification and classification of different targets [1]. Recently, there has been an increasing interest for ISAR research in Marmara Research Center (MRC) and The National Research Institute of Electronics and Cryptology (UEKAE) of Scientific and Technological Research Council of Turkey (TUBITAK).

Recent radar cross section (RCS) studies at TUBITAK-MRC has yielded development of a high frequency electromagnetic field estimator code that can predict scattering from complex and large objects with good fidelity [1]. The EM simulation of the scaled model target is performed with this code that is based on the shooting and bouncing ray (SBR) technique [2] and can also estimate and add the diffracted field contributions to the total scattered field. ISAR measurements were made in a special RCS measurement room with anechoic chamber working up to 100 GHz. Measurement system, used in these measurements, consists of Network Analyzer, master computer, turn table, transmitter and receiver antennas, working in quasi-monostatic condition,. In addition, it should be defined that network analyzer and turn table controls are fully automated with the master computer. Scattered electric field from the target located on the turn table was measured for a selected frequency bandwidth at each angular position.

In this study, a scaled model target has been selected to test the effectiveness of the measurement system by comparing the ISAR images of the measured and the simulated data from the target.

## 2. REVIEW OF ISAR IMAGING

Inverse Synthetic Aperture Radar (ISAR) is a very convenient and effective imaging technique for detecting and diagnosing targets [2, 3]. The traditional 2D ISAR image is constructed by collecting the scattered field for various frequencies and aspects. The following inversion integral should be carried out to be able to display the monostatic ISAR image of the target for the small angle and small bandwidth approximations:

$$ISAR(x,y) = \int_{f_1}^{f_2} \int_{\phi_1}^{\phi_2} E^S(f,\phi) \cdot e^{-j\frac{4\pi fc}{c}\phi \cdot y} d(\phi) \cdot d(f) \tag{1}$$

Here, $E^S$ is the complex backscattered electric field, $f_c$ is the center frequency of the radar. The backscattered field is collected as 2D data ranging from $f_1$ to $f_2$ for different frequencies and from $\phi_1$ to $\phi_2$ for different angles. It is a common practice to use small-angle small bandwidth

approximation while collecting the backscattered data from the target. The ISAR image of the target can be obtained in a much faster manner by the help of 2D inverse fast Fourier transform (IFFT) operation as given below

$$ISAR(x, y) = IFFT_2\left\{E^S(f, \phi)\right\} \tag{2}$$

The detailed derivation of ISAR imaging can be found in [3] and will not be repeated here.

## 3. HIGH FREQUENCY ELECTROMAGNETIC SIMULATOR

The simulation of the scattering from a target is carried out by a high frequency electromagnetic simulator that can predict scattered electric field from large and complex structured at L-band and beyond [1]. This code is based on physical optics (PO) and the shooting and bouncing ray (SBR) approximations [2]. First, millions of rays are shot from the radar towards the target; rays are bounced and traced by the laws of geometric optics. The electromagnetic field is also traced while the ray bouncing on the hit points on the target. At the last hit point, the PO-based current distribution is found via

$$\vec{J}_s = 2\vec{E}(x_N, y_N, z_N) \times \hat{n} \tag{3}$$

Here, $\vec{E}(x_N, y_N, z_N)$ is the incident electric field at the last hit point and $\hat{n}$ is the surface's unit vector of the target at the last hit point. Then, the PO based far-field radiation integral is carried out towards the radar to find the contribution of this particular ray to the total scattered field as

$$\vec{E}^S = \frac{jk\eta \cdot e^{-jkr}}{4\pi r} \cdot \iint_{S_A} \vec{J}_S \cdot e^{-j\vec{k}\cdot\vec{r}_N} \cdot \vec{ds} \tag{4}$$

where $\vec{r}_N$ is the displacement vector from the last hit point towards to radar and $S_A$ is the area on which the $\vec{J}_S$ exists. Furthermore, diffraction fields from the edges of the target is also added to the total field to have a more reliable calculation, For this purpose, Incremental Length Diffraction Coefficient (ILDC) method specially tailored to physical theory of diffraction (PTD) has been utilized to calculate the diffracted field contribution from the edges of the target.

## 4. ISAR MEASUREMENT SYSTEM

While the simulated ISAR images of the CAD model of the target (see Figure 1(a)) were obtained after post processing the backscattered electric field data obtained by our PO-SBR based electro-magnetic simulator, the measurement from the manufactured version of the model (see Figure 1(b)) were obtained by our RCS measurement room at TUBITAK-MRC facilities. We have designed and constructed anechoic chamber that can measure frequencies up to 100 GHz. The measurement setup (see Figure 2) composes of sub-THz vector network analyzer (ELMIKA S4403), master computer, turn table, transmitter and receiver antennas (ELMIKA WR-10) to be work in quasi-monostatic condition.

First, a calibration measurement is carried out by the help of a sphere that has a diameter of 60 mm. Since the radar cross section (RCS) behavior of the sphere is known analytically and is independent of angle, it acts as a good calibration object. Then, the measurement is performed for different look-angles by the help of the turn table that has an angular sensitivity of 0.1. For each look-angle, the frequency is also varied by the help of the vector network analyzer that uses the stepped frequency waveform.



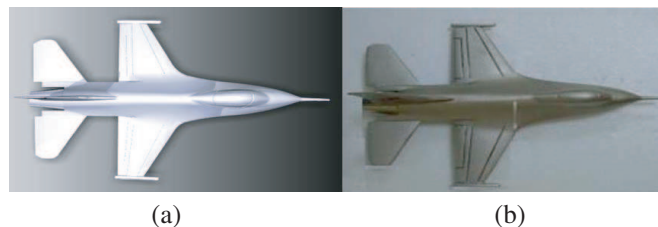(a)                                             (b)

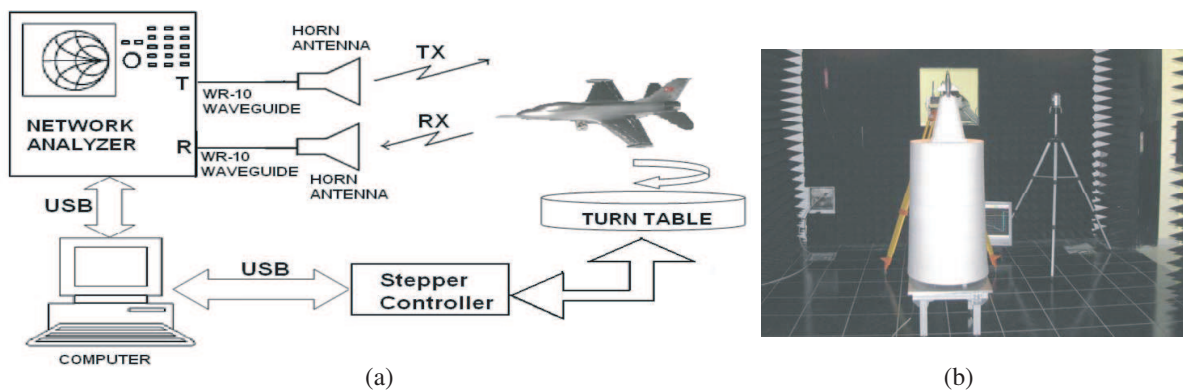Figure 1: (a) CAD model of a fighter target. (b) Picture of the manufactured fighter target.

Figure 2: (a) The block diagram of our ISAR measurement system. (b) A scene from the measurement set-up.
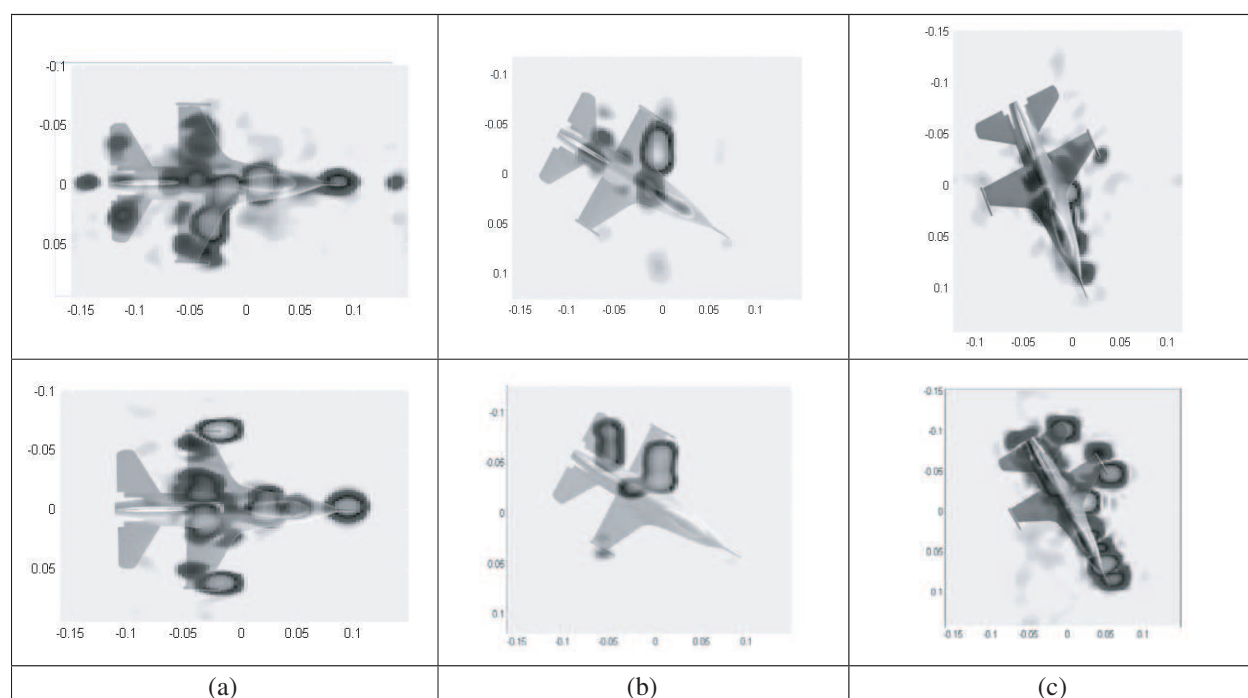


Figure 3: Measurement and simulation results for central look-angle of (a) 0°, (b) 30°, (c) 60°.

## 5. MEASUREMENT AND SIMULATION RESULTS

Three different measurements were performed for different arrangements of a same target which is the scaled model of a fighter (see Figure 2). In the first measurement, the model is positioned horizontally and the backscattered electric field data is collected from the nose of the target with an azimuthal angular variation from $-7.4°$ to $6.9°$ measured for 32 discrete points. The frequency is varied from 87.14 GHz to 98.39 GHz with 25 stepped frequencies. In the second experiment, the model is positional vertically but the center of the look angle is set to 30° in the azimuth. The frequency bandwidth is chosen to be 14.4 GHz around the center frequency of 93.3 GHz with 25 discrete frequency points. The angular bandwidth is selected as 9.8° with 32 discrete angles. Finally, in the third experiment, the target is again positioned flat but with an azimuth angle of 60°. The measurement was conducted around the center frequency of 92.7654 GHz with the bandwidth of 11.25 GHz for a total of 25 different stepped frequencies. The two-dimensional (2D) backscattered field data were collected by changing the angular positions of the target between 55.1° and 64.0° with 32 equally spaced discrete angles.

The simulated ISAR images were obtained by numerically calculating the electric field for the three different experimental cases listed above by simulating the CAD model of the target in

Figure 2(a). The measured ISAR images of these three experiments were also obtained by applying the ISAR imaging procedure to the measured data. Figure 3 shows the comparison of the simulated and measured ISAR images for different experimental set-ups; namely when the radar's axis makes an angle of 0°, 30° and 60° with the fighter's nose, respectively. As obvious from the images, the good match between the simulated ISAR images of the CAD file and the measured ISAR images of the scaled model have been attained. The scattering centers shown in the simulated ISAR images can also be detected in the measured ones as well.

## 6. CONCLUSION

In this paper, we have presented the recent ISAR simulation and measurement studies that were conducted at TUBITAK-MRC facilities. The electromagnetic simulation is carried out by a PO-SBR based high frequency estimator that was also developed at TUBITAK-MRC. A special compact-range measurement room is designed and constructed for this research. After collecting the 2D measured electric field data, the comparative ISAR images were obtained for the simulated and the measured data. Visual comparison of these images clearly indicates the success of both the simulator and the measurement system.

**REFERENCES**

1. Saynak, U., A. Çolak, Y. Avcıbası, D. Bölükbas, İ. H. Tayyar, and C. Özdemir, "2-D ISAR imaging of complex objects using shooting-bouncing ray (SBR) and physical theory of diffraction (PTD) techniques," *V. Intern. Workshop on Electromagn. Wave Scattering*, 9.7–9.14, Antalya, Oct. 22–25, 2008.
2. Bhalla, R. and H. Ling, "Image domain ray tube integration formula for the shooting and bouncing ray technique," *Radio Science*, Vol. 30, No. 5, 1435–1446, 1995.
3. Özdemir, C., *Syntetic Aperture Radar*, Editor: K. Chang, *Encyclopedia of RF and Microwave Engineering*, Wiley Interscience, 5067–5080, 2005.
4. Ling, H., R. C. Chou, and S. W. Lee, "Shooting and bouncing rays: Calculating the RCS of an arbitrary shaped cavity," *IEEE Tran. on Antennas and Prop.*, Vol. 37, No. 2, 1989.

# Investigating Energetic and Impedance Relations of Microwave Transmission Line Filled with Dielectric Material

**Attila Gollei, A. Magyar, and M. Gerzson**

Department of Electrical Engineering and Information Systems, Faculty of Information Technology
University of Pannonia, Hungary

**Abstract**— During microwave treatment, microwave energy is transferred to a material sample placed in an applicator of given geometric parameters. As a result of the energy transfer, the sample absorbs energy from the microwave field depending on its dielectric properties. The degree of energy absorption is directly proportional to the dielectric loss and proportional to the square root of the dielectric constant. The temperature of the sample continuously increases due to the energy transfer and the dielectric properties of the sample also change with the rising temperature. Although the microwave energy supply is constant, time and temperature dependent energy impedance and dielectric relations are developed. A part of them is measurable, but the other part of them can not be directly measured, they can only be computed from the previously measured ones. In a closed model which contains the parameters of the sample and the waveguide, the continuously changing parameters can be determined in relation of the temperature. These parameters are as follows: Attenuation of the transmission line, temporal change of the sample temperature, dielectric properties of the sample, loss factor of the sample, penetration depth, impedance of the transmission line, standing wave ratio reflection factor. The above parameters can be modeled as a function of the sample's temperature or as a function of time.

## 1. INTRODUCTION

During the microwave treatment, energy is being transferred to a sample of given geometry being in the transmission line. As a result, the temperature of the sample continuously rises and its dielectric properties also change [1]. From the generator's viewpoint the value of terminating impedance represented by the transmission line changes accordingly. For the microwave generator the transmission line acts as an impedance terminator whose value depends on the wavelength and on the geometric properties of the transmission line [2]. The impedance of transmission line also depends on the dielectric properties of the material which are either partially or fully filling the transmission line. Since the temperature of the sample changes due to the energy impact, the value of the impedance terminator represented by parameters the transmission line also changes together with the sample properties. During the energy impact the varying dielectric properties of the sample change the axial distribution of the microwave energy in the transmission line, therefore the amount of energy absorbed in the sample also changes.

Because of the constant microwave energy input, temperature dependent energy-, impedance-, and dielectric conditions are developed. Some of them (e.g., temperature, dielectric property) are measurable others can only be determined by computation [3]. By constructing a model containing the parameters of the transmission line and the sample placed in the transmission line, it is possible to determine the continuously varying parameters during the heating. The model of the transmission line is built based on the following aspects and relations.

## 2. THE MODEL

If the microwave transmission line filled with sample, which has nonzero loss factor is considered as a variable impedance connected to the microwave generator, then the energy conditions developed in the transmission line can be analyzed as follows.

The power leaving the generator enters and propagates in the transmission line as a wave. The medium in the transmission line — according to its dielectric properties — modifies the portrait of lines of force, and takes energy from the electromagnetic field. The electromagnetic wave reflected from the shortcut at the end of the transmission line leaves the line towards the generator. The ratio of forwarding and reflected waves is the standing wave ratio and it depends first of all on the dielectric loss of the medium filling the transmission line. The standing wave ratio is infinity in the ideal case (there is no sample, i.e., loss in the transmission line) if the transmission line is closed with the wave impedance of the line. Since the standing wave ratio is given as the ratio of

forwarding and reflected waves, it is greater than one if the transmission line has loss, and it equals to the ratio of powers entering and leaving the transmission line.

That is, knowing the standing wave ratio $r$, and the generator power $P_M$, it is possible to determine the power entering the transmission line. Since the medium's (sample's) dielectric parameters are functions of the temperature, it is necessary to appear the temperature dependence in the formulae explicitly. Denoting the microwave power entering the transmission line by $P_A$ and the generator's power by $P_M$, the following formula holds:

$$P_A(T) = \frac{1}{r(T)} P_M \tag{1}$$

A part of this power will dissipate and heat up the sample placed inside the transmission line. The amount of power absorbed in the sample depends on the sample's dielectric properties: It is directly proportional to the dielectric loss and inversely proportional to the square root of the dielectric constant. The coefficient 0.5126 is an experimental value [4].

$$P_D(T) = 0.5126 \frac{\varepsilon''(T)}{\sqrt{\varepsilon'(T)}} P_A(T) \tag{2}$$

The temperature dependence of the dielectric parameters is respected in the above formula. The power absorbed in the sample increases its temperature, the degree of warming depends on the specific heat $(C_p)$ and the density $(\rho)$ of the sample. A sample having greater specific heat or density warms slower. The change of temperature is given as follows,

$$\frac{dT}{dt} = K \frac{1}{C_p \rho} P_D(T) \tag{3}$$

where $K$ is a coefficient regarding the volume of the sample, its unit is $1/\text{cm}^3$. The formula gives the speed of temperature change; on the other hand, the integral of the formula with respect to time gives the value of the temperature in the sample as a function of time. The temperature dependence of the dielectric parameters $(\varepsilon', \varepsilon'')$ of the sample can be measured with a microwave dielectrometer [9], thus it is possible to define the relationships $\varepsilon'(T)$ and $\varepsilon''(T)$ regarding to the specific sample material by fitting polynomials on the resulted data.

The impedance of the transmission line is a function of its geometric parameters and the dielectric properties of the sample. The characteristic wave impedance $Z_{0t}$ of the transmission line depends on the size of the transmission line sizes (in two dimensions) and the wavelength $(\lambda_g)$ of the electromagnetic wave propagates inside according to the following formula,

$$Z_{0t} = \frac{2Z_{0l}b}{a\sqrt{1 - \left(\frac{\lambda_g}{2a}\right)^2}} = 754 \frac{4.4}{9.4\sqrt{1 - \left(\frac{12.24}{18.8}\right)^2}} = 465\,\Omega \tag{4}$$

where $Z_{0l}$ is the open air wave impedance of the air $(377\,\Omega)$, is the electromagnetic wavelength, $a$ and $b$ are the dimensions of the transmission line $(9.4\,\text{cm}, 4.4\,\text{cm})$, respectively. Note that $Z_{0t}$ is independent of the sample properties and depends only on the transmission line geometry and wavelength. From $Z_{0t}$ and the dielectric loss it is possible to calculate the overall impedance (of the transmission line and the sample) as a function of temperature [5]:

$$Z_T(T) = \frac{Z_{0t}}{\sqrt{\varepsilon'(T)}} \left(1 - \frac{3}{8}(\text{tg}\delta(T))^2 + j\frac{1}{2}\text{tg}\delta(T)\right) \tag{5}$$

From the overall impedance and the wave impedance one can determine the reflection coefficient of the transmission line:

$$|\Gamma(T)| = \frac{Z_T(T) - Z_{0t}}{Z_T(T) + Z_{0t}} \tag{6}$$

Afterwards, it is possible to express the standing wave ratio.

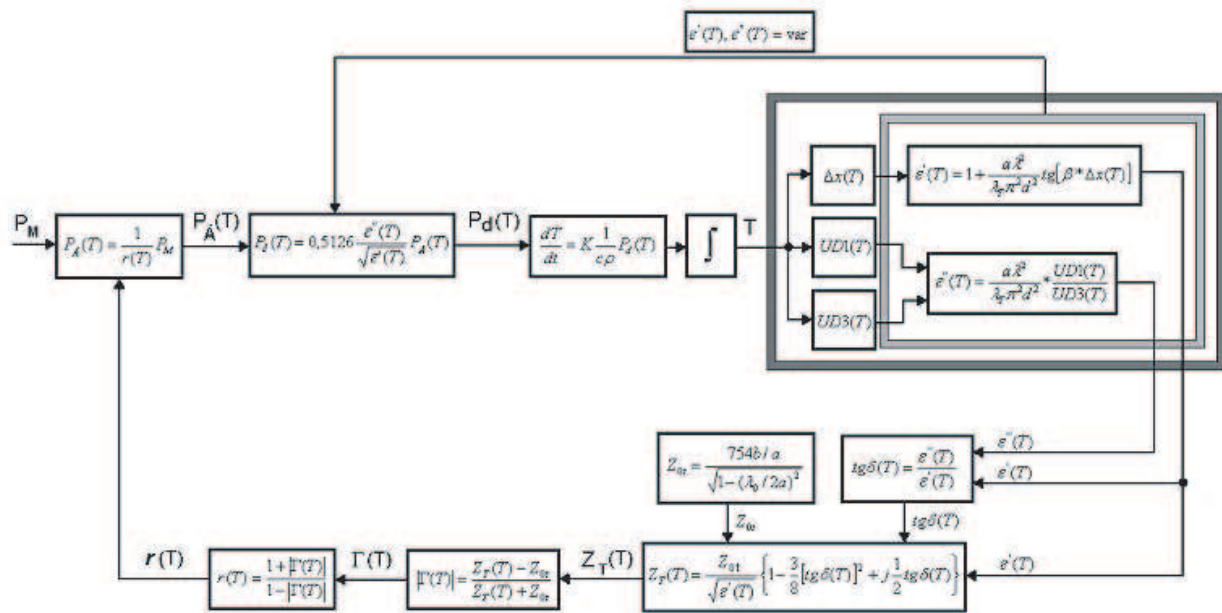$$r(T) = \frac{1 + |\Gamma(T)|}{1 - |\Gamma(T)|} \tag{7}$$

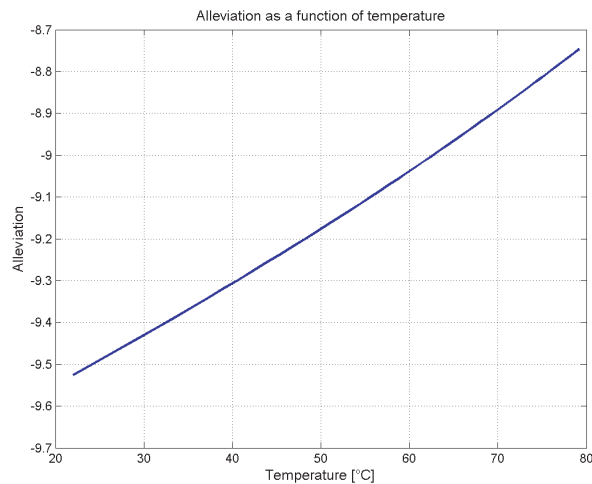Figure 1: Model for calculate of parameters of the waveguide.
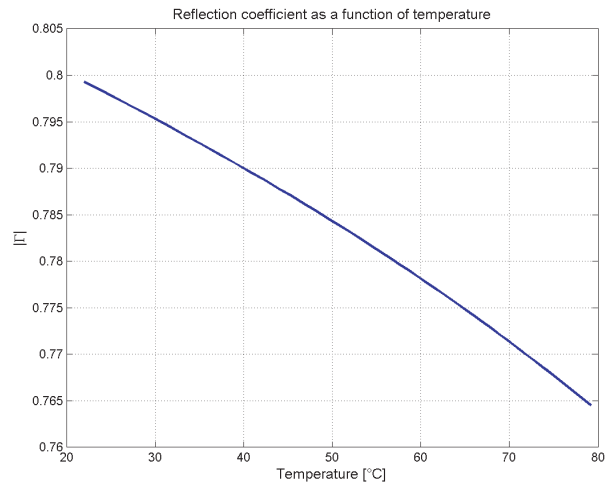


Figure 2: Computed values of alleviation.

Figure 3: Computed values of reflection coefficient.

From the standing wave ratio it is possible to give the power entering the transmission line knowing the generator power, as it was mentioned before. Now, it is possible to build a model from the above equations, which has the following input parameters: Microwave generator power, density of the sample, specific heat of the sample, sample specific dielectric characteristics as a function of temperature, transmission line and wavelength parameters.

The outputs of the model are the temperature dependence of the power and the impedance conditions developed in the transmission line. The model structure can be seen in Fig. 1. The formulae used for computing the dielectric properties of the sample are inside the wide-lined frame, the fitted polynomials of the dielectric properties can be substituted here.

The model structure has been implemented in MatLab® environment. First the pure water has been investigated. The temperature dependence of dielectric values of water is described by Eqs. (8) [6]:

$$\varepsilon'(T) = 87 - 0.36T \quad \varepsilon''(T) = 283/T - 1.17 \tag{8}$$

Some computed parameters for the pure water can be seen in Figs. 2, 3, 4 and 5.

If the theoretical relationships of the temperature dependence of dielectric parameters are not available a microwave dielectrometer can be used to establish the necessary equations [7]. As an
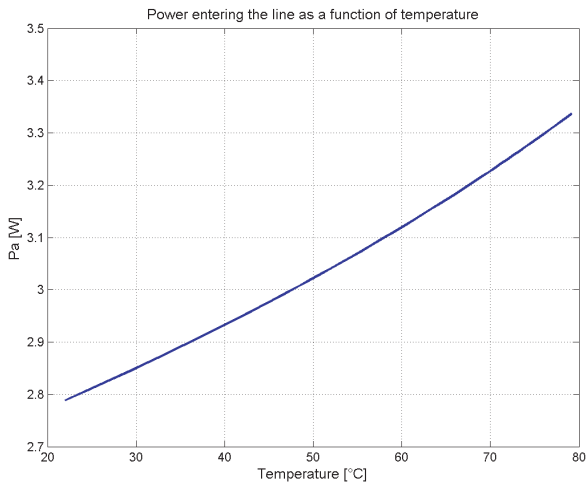
Figure 4: Computed values of entering power.
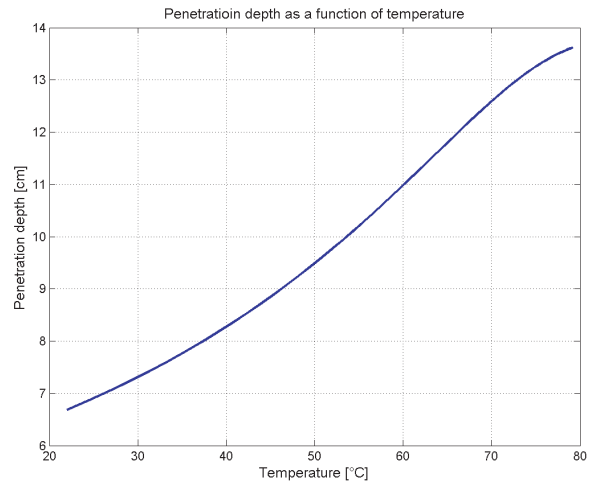


Figure 5: Computed values of penetration depth.
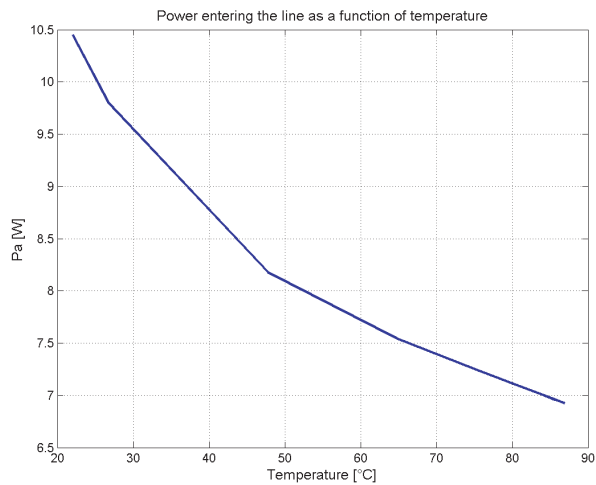


Figure 6: Computed values of entering power using ethanol as a sample.
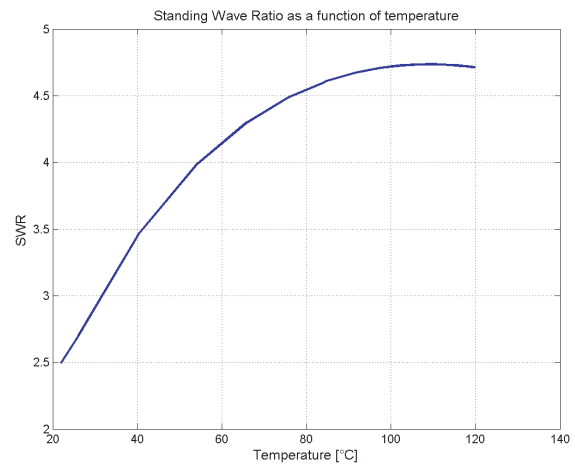


Figure 7: Computed values of standing wave ratio using glycerol as a sample.

example the temperature dependence of dielectric parameters have been defined in case of ethanol and glycerol using this method and the resulted relationships have been substituted into the model described above. Some calculated values in case of ethanol and glycerol can be seen in the Figs. 6 and 7.

## 3. CONCLUSION

A numerical simulation method is developed for the determination of directly unmeasurable dielectric properties. The model needs the temperature dependences of dielectric parameters $\varepsilon'$ and $\varepsilon''$ which relationships can be determined experimentally. The resulted model is suitable for the description of system having rectangular shaped waveguide. The simulation was performed in MatLab® Simulink® environment. As a result of the simulation the temperature dependence of the power and the impedance conditions developed in the transmission line can be determined either as a function of temperature or as a function of time. The simulation could be improved by more precise determination of dielectric parameters $\varepsilon'$ and $\varepsilon''$. The results could be used both for the design of new methods and for optimizing processes in drying technology.

## ACKNOWLEDGMENT

**REFERENCES**

1. Knoerzer, K., M. Regier, and H. Schubert, "A computational model for calculating temperature distributions in microwave food applications," *Innovative Food Science and Emerging Technologies*, Vol. 9, 374–384, 2008.
2. Zhu, J., A. V. Kuznetsov, and K. P. Sandeep, "Mathematical modeling of continuous flow microwave heating of liquids," *International Journal of Thermal Sciences,* Vol. 46, 328–341, 2007.
3. Johns, P. B., "Simulation of electromagnetic wave interactions by transmission-line modelling (TLM)," *Wave Motion*, Vol. 10, No. 6, 597–610, 1998.
4. MacDowell, J. F., "Microwave heating of nepheline glass-ceramics," *Am. Ceram. Soc. Bull.*, Vol. 63, 282–286, 1984.
5. Almássy, Gy, Mikrohullámú kézikönyv; Műszaki Könyvkiadó, Budapest, 1973.
6. Kegel, K., Villamos Hotechnikai Kézikönyv, Muszaki Könyvkiadó, Budapest, 1978.
7. Göllei, et al., "Apparatus and method to measure dielectric properties ($\varepsilon'$ and $\varepsilon''$) of ionic liquids," *Rev. Sci. Instrum.*, Vol. 80, 044703, 2009.

# Electromagnetic Field Analysis in Permanent Magnet Retarder Based on Finite Element Method

**L. Z. Ye**, **D. S. Li**, **B. F. Jiao**, and **Y. Z. Wang**

School of Mechanical Engineering and Applied Electronics Technology
Beijing University of Technology, China

**Abstract**— Eddy current retarder for vehicle generates a large number of heats when it works continuously, and it leads to serious decline in braking torque. This paper proposes a novel permanent magnet retarder (PMR) for vehicle, whose cooling system is connecting with engine cooling-water. A 3-dimensional finite element model is developed to model the electromagnetic behavior of permanent magnet retarder under constant speed operation. Magnetic field and eddy current field in PMR are numerically solved by finite element method. By accounting for non-linear permeability of rotor and weaken effect in magnetic field generated by eddy current magnetic field, the calculation accuracy of air-gap magnetic field is enhanced. Experiment shows that temperature of retarder is below 150°C, and the braking torque keep hard characteristic curve. The calculated air-gap magnetic flux density is fairly good agreement with measured one.

## 1. INTRODUCTION

As the rapid development of modern automotive technology, the safety of vehicle driving is more urgent requirements than the vehicle dynamics and comfort. Auxiliary braking device for vehicle can consume parts of motion energy before main brake system works, and improve the safety performance of vehicles effectively. At present, auxiliary braking device includes eddy current retarder, hydraulic retarder and permanent magnet retarder and so on [1–4]. Permanent Magnet Retarder (PMR) is a new type of auxiliary braking device in recent years, and has more advantages than other devices, such as energy-saving and environmental protection.

At 1990s, Japanese successfully developed a new type of auxiliary braking device (PMR) which produce magnetic source using NdFeB permanent magnet. PMR is a revolutionary technology which has light weight, simple structure and easy-install. Domestic and foreign scholars have in-depth studied from the structure to the theory, but these PMR structures have the disadvantages of small braking torque and high price. Traditional PMR is made by the stator, rotor and permanent magnet. Its structure is shown in Figure 1. The rotor cuts the stator magnetic field lines generated by permanent magnet, so the rotor produces eddy current. The interaction between eddy current and the stator magnetic field prevents the rotor from rotation. A large number of heat generated eddy current within the rotor. The heat spread into the atmosphere by forced convection air-cooling. The same to eddy current retarder, PMR braking torque will occur hot recession at 5 minute. Braking torque will be decreased by 50% or more in severe, and thus PMR has not been a large-scale promotion [5–7].

In order to overcome the above-mentioned shortcomings of the traditional PMR, water-cooling PMR is designed which has a good cooling effect. The paper designs a kind of water-cooling PMR (Figure 2). Its rotor is permanent magnet, and water-cooling heat conduction replaces air-cooling forced convection. The heats disperse through the engine cooling system generated by braking. Since the engine is idle state when retarder works generally, heat load of the system will not be greatly aggravated.

## 2. MATHEMATICAL MODEL

### 2.1. Electromagnetic Equations

When water-cooling PMR works, the magnetic line generated by permanent magnet will form loop in the rotor, air gap and stator. The stator cuts magnetic line, and generated eddy currents in the stator radial surface. The interaction between eddy currents magnetic field and permanent magnetic field bring braking to the rotor.

On the cylindrical coordinates $(r, z)$ plane, retarder model is cyclical symmetry around the $Z$-axis and $\theta$ is rotation angle. The two-dimensional geometric shapes of PMR $\theta/360$ is shown in Figure 1. Rotor inner diameter is $R_1$ and its thickness $h_1$. Permanent magnet external diameter is $R_2$, and its width is $w$. The gap of permanent magnet and stator is $g$. The stator thickness is $h_2$.

Because of the eddy current in the stator, complex magnetic vector potential and using standardized methods is introduced, and electromagnetic field equation is:

$$\nabla \times v\nabla \times \mathbf{A} + j\omega\sigma\mathbf{A} - \mathbf{J}_s = 0 \tag{1}$$

where $v$ and $\sigma$, respectively is retarder stator reluctance rate and electrical conductivity, $\mathbf{J}_s$ is current density. There is no eddy current in the permanent magnet, so the equation as follows:

$$\text{rot}(v_0\text{rot}\mathbf{A}) = v_0\text{rot}\mathbf{M} \tag{2}$$

where $\mathbf{M}$ is magnetization vector, and $v_0$ is the vacuum magneto-resistance ratio. Using quasi-three-dimensional method, $\mathbf{A}$ and $\mathbf{J}_s$ expressed as:

$$\mathbf{A} = [\mathbf{A}_r(r,z)i_r + j\mathbf{A}_\theta(r,z)i_\theta + \mathbf{A}_z(r,z)i_z]\, e^{jp\theta} \tag{3}$$
$$\mathbf{J}_s = [\mathbf{J}_r(r,z)i_r + j\mathbf{J}_\theta(r,z)i_\theta + \mathbf{J}_z(r,z)i_z]\, e^{jp\theta} \tag{4}$$

where, $p$ is the number of permanent magnet. Combination of the above Equations (1)–(4), the magnetic flux density vector in the rotor as follows:

$$\mathbf{B} = \left[ j\left(\frac{p}{r}\mathbf{A}_z - \frac{\partial\mathbf{A}_\theta}{\partial z}\right)i_r + \left(\frac{\partial\mathbf{A}_r}{\partial z} - \frac{\partial\mathbf{A}_z}{\partial r}\right)i_\theta + j\left(\frac{1}{r}\frac{\partial(r\mathbf{A}_\theta)}{\partial r} - \frac{p}{r}\mathbf{A}_r\right)i_z \right] e^{jp\theta} \tag{5}$$

The equation gets the rotor electromagnetic field distribution of PMR.

### 2.2. Braking Torque

Braking torque is the interaction result of eddy currents and magnetic field inside the stator. Its intensity depends on stator resistance ratio and eddy current density. When electromagnetic field is solved in PMR, the eddy current losses per unit volume in stator are as follows:

$$\Delta P = \rho J^2 \tag{6}$$

where, $\rho$ is the rotor resistance, then the consumed power is:

$$P = \sum_{e=1}^{e_0} \int_{\Omega_e} \rho J^2 d\Omega \tag{7}$$
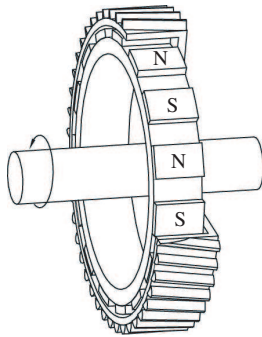


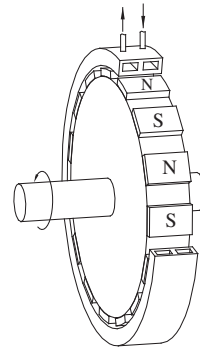Figure 1: The structure of air-cooling PMR.
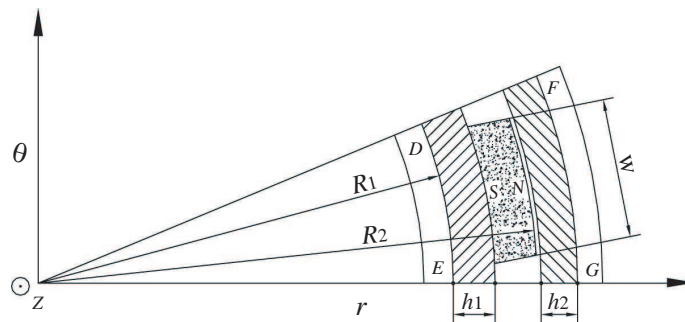


Figure 2: The structure of water-cooling PMR.



Figure 3: Permanent magnet retarder analysis model.

where, $P_r$ is the stator power consumption, $e_0$ is split nodes, $\Omega$ is the solution region. So PMR braking torque is:

$$T = \frac{P}{\omega} \qquad (8)$$

### 2.3. Numerical Simulation

To reduce the model size and effectively save computing resources, it is established PMR 1/32 model according to periodic boundary and face conditions of symmetry. Stator and rotor material are 20CrMo and permanent magnet is NdFeB N38SH. Detailed size parameters are shown in Table 1.

Table 1: PMR size parameters.

| project | size | project | size |
|---|---|---|---|
| Rotation degree $\theta/$ deg | 22.5 | Permanent magnet depth $d/$mm | 15 |
| Rotor radius $R_1/$mm | 140 | Permanent magnet length $L/$mm | 75 |
| Rotor depth $h_1/$mm | 14 | Gap $g/$mm | 1 |
| Permanent magnet width $w/$mm | 50 | Stator depth $h_2/$mm | 14 |

JMAG-Studio is electromagnetic field analysis software, which developed by Japan Research Institute (JRI). JMAG-Studio can solve electromagnetic field problem about a variety of electrical and electromagnetic equipment. In this paper, numerical simulation solves eddy current magnetic field using JMAG-Studio8.4 in PMR. Through modeling, material properties, boundary conditions and solving, eddy current field distribution is derived by post-processing, as is shown in Figure 4.

Figure 5 is flux density distribution on stator at 1000 r/min. Compared with the static status, the direction of magnetic flux density vector change, and there exist axial component in the inner surface of the stator, Because of the interaction of magnetic field between eddy-current and permanent magnet.

### 3. EXPERIMENTS

### 3.1. Experiments System and Devices

PMR test system is shown in Figure 6. The retarder imposed loads through the eddy current effects. The torque signals from sensor and from LCD will be transmitted to PLC through RS232. PLC control the stepper motor to change loads through the appropriate algorithm, which receives the torque command and compares them. Permanent magnet retarder photos are shown in Figure 7. The tube is used to deliver cooling water.
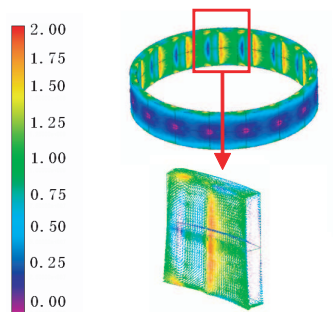


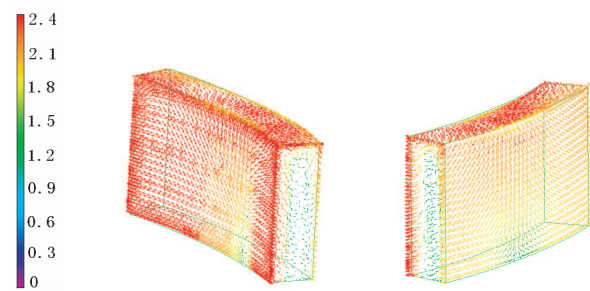Figure 4: Stator eddy currents distribution at 3000 r/min (unit $10^8$ A/m$^2$).

Figure 5: Flux density distribution on stator (units T).

### 3.2. Experiments Result

Experiment shows that temperature of retarder is below 150°C, and water-cooling PMR has a good cooling effect. Digital Tesla meter measure the flux density of working air gap at PMR stationary. The experiment parameters of Tesla meter are as follows: Measuring range: $0 \sim 2$ T; the highest resolution: 0.1 mT; Accuracy: (25 mT $\sim$ 1.5 T) within $\leq \pm 1\%$ (of reading) $\pm 0.1\%$ (full scale). Figure 8 is the calculated and measured flux density curves of the working air gap at PMR stationary, and the error of calculated and measurement values is less than 5%. Figure 9 compares
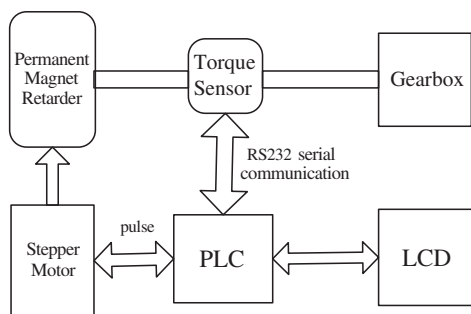
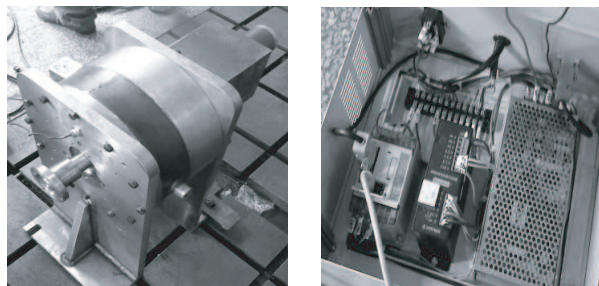Figure 6: PMR test system.



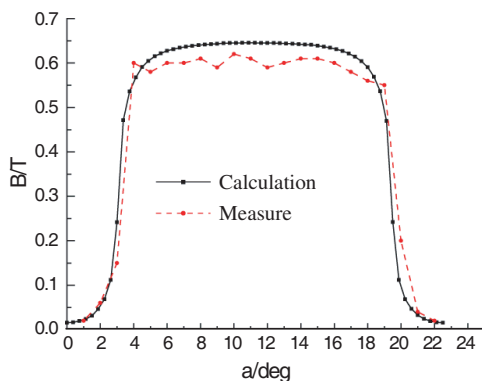Figure 7: Permanent magnet retarder photos.
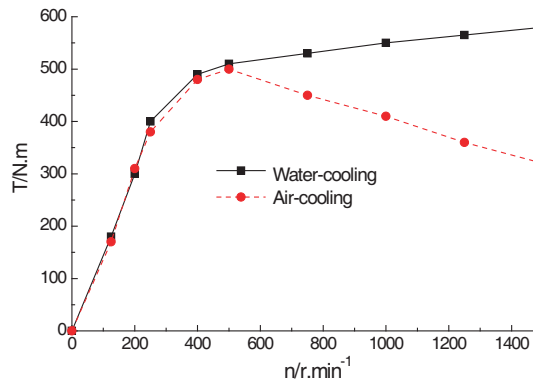


Figure 8: Flux densities in the air gap.



Figure 9: Braking torque curve.

the air-cooling PMR braking torque curves with water-cooling, and water-cooling braking torque keep hard characteristic curve.

## 4. CONCLUSION

The paper introduces a kind of water-cooling PMR, which overcomes the heat recession short-comings of the traditional PMR. Using quasi-three-dimensional meth and introducing complex magnetic vector potential **A**, it is analyzed that dynamic eddy current field in PMR. We can gain some conclusion from the analysis and discussion:

(1) Retarder dynamic eddy current field is described using complex magnetic vector potential method. Through impose boundary conditions and finite element mesh, magnetic and eddy current field distribution are derived.

(2) The error of calculated and measurement flux density values at PMR working air gap stationary is less than 5%.

(3) The working temperature of water-cooling PMR is below 150°C, and the braking torque keep hard characteristic curve.

### REFERENCES

1. Ye, L., D. Li, Z. Y. Lu, and Q. Guo, "Study on a novel permanent magnet retarder for vehicles," *PIERS Proceedings*, 531–535, Hangzhou, China, March 24–28, 2008.

2. Hu, Q. X. and R. He, "Working principle and usage of vehicle-used permanent-magnet type retarder Design," *Computation Research*, Vol. 3, 22–25, 2005.

3. Zhu, N. and Y. H. Wang, "Light type permanent magnet retarder for vehicle," *Bus Technology and Research*, Vol. 24, No. 4, 19–20, 2002.

4. He, R., *Auxiliary Braking Equipment for Vehicle*, Chemical Industry Press, Beijing, 2005.

5. Wang, B. L., *Electromagnetism and Electro-instrument Design Base*, National Defense Industry Press, Beijing, 1989.

6. Takahashi, N., M. Natsumeda, and K. Muramatsu, "Optimization of permanent magnet type of retarder using 3D finite element method and direct search method," *IEEE Transactions on Magnetics*, Vol. 34, No. 5, 2996–2999, 1998.

7. Bigeon, J. and J. C. Sabonnadiere, "Finite element analysis of an electromagnetic brake," *IEEE Transactions on Magnetics*, Vol. 19, No. 6, 2632–2634, 1983.

# Simulation of 3D Laser Imaging

**Gerard Berginc and Michel Jouffroy**

THALES, 2 avenue Gay Lussac, 78995 Elancourt Cedex, France

**Abstract**— This paper addresses modeling of new optical non-conventional imaging with laser systems. Laser systems use a light source, such as a laser (burst illumination laser technique), that can be controlled by the user and tailored for specific applications. The use of an active illuminator boosts the signal-to-noise ratio while relaxing the sensitivity requirements in the receiver. The availability of near infrared lasers and near infrared focal plane arrays can make laser systems practical and cost efficient. The eye-safe property of wavelengths around 1.5 m is perfectly suited to laser imagery applications. Laser systems provide high-resolution day and night imaging. Optical non-conventional imaging explores the advantages of laser imaging to form a three-dimensional image of the scene. 3D laser imaging can be used for three-dimensional medical imaging, topography, surveillance, robotic vision because of ability to detect and recognize objects hidden behind porous occluders, such as foliage or camouflage. In this paper, we present a 3D laser imaging simulation of a large scale scene. For the inversion method, we use a cone-beam algorithm, which is a convolution-backprojection algorithm deduced from the Radon transform.

## 1. INTRODUCTION

In this paper, we describe a simulation of 3D laser imaging. The first step of the simulation process is the generation of a scene of interest which consists of many types of objects: trees, vehicles. The vehicles are often hidden by other objects. A CAD model of the scene is generated. The second step contains the simulation of the receiver, the transmitter and the optics system. For the receiver, we can simulate the response of the different types of detectors we can use: detector response function, noise sources. The third step is the modeling of the electromagnetic scattering from the different objects of the scene. The physics based model, we present in this paper, is designed to provide accurate results but to also include all of the electromagnetic interaction mechanisms. The surfaces of the different vehicles or hard targets are considered as randomly rough surfaces and we compute the laser signature (laser cross-section) of the vehicles. To model the laser interaction with the randomly rough surfaces, we use the second-order Small-Slope Approximation method [1, 2]. Because the problem, we consider in this paper, is three-dimensional, all the scattering coefficients (coherent and incoherent components of the electromagnetic field) are functions of the azimuth angles, and the cross-polarized terms do not vanish. We define, in this case, the Mueller matrix, which gives all the combinations of the polarization states of the scattered electromagnetic waves. The randomly rough surfaces of the complex object are characterized by electromagnetic parameters (permittivity...) and roughness parameters (standard deviation of rough surface height and autocorrelation function). Our model addresses also transparent structures. Buildings and trees are modeled by polarized reflectance applied to the different facets generated by the CAD model. The fourth step contains the absorption and scattering of the laser wave by the components of the atmosphere, the simulation of the atmospheric turbulence effects: scintillation, beam spreading, beam wandering. The last step of the simulation contains the development of three-dimensional reconstruction algorithm to obtain a high-resolved three-dimensional image. This computer model can help predict 3D imaging performance and it is used to develop reconstruction algorithms.

## 2. THREE-DIMENSIONAL TOMOGRAPHIC RECONSTRUCTION

Our technique is based upon a 3D tomographic reconstruction. The scenario is the following: the observed target is illuminated by a laser source deployed on any land or airborne vehicle. The target is viewed through a dense scattering foliage. The configuration is monostatic and the focal plane array collects 2D laser image depending on the target/platform angle of view. The laser images are related to the intensity scattered by the target illuminated by the laser source. Then the obtained image sequence is processed by a tomographic algorithm allowing to transform the 2D laser images sequence in a 3D reconstructed volume. Input data are conventional 2D intensity laser images taken in a plane containing the platform trajectory and a fixed point in the scene. The 3D reconstruction for the set of images of the considered scenario is carried out by using a Radon transform: the filtered back-projection. Using the Fourier Slice Theorem, we can express

the object function $f(x, y)$ as a function of the parallel projections $P_\theta(t)$ and the impulse response $h(t, \theta)$ of a filter with which the projection must be processed:

$$f(x, y) = \int_0^\pi \int_{-t_m}^{+t_m} P_\theta(t) h(x \cos(\theta) + y \sin(\theta) - t) \, dt d\theta \tag{1}$$

This formula can be extended in three dimensions assuming that the third dimension is consisting on a set of 2D parallel reconstructions along a perpendicular axis. The practical algorithm is the following:

- Images acquisition of the optronic scene: the platform and a point in the scene have to belong to a plane and the distance between the platform and the target remains almost constant. If not the case, we must recalculate the different images to have the same optical magnification.
- Read-out of the complete image sequence.
- Weighting of the pixels as a function of the gap to the image center.
- Convolution of the weighted pixels with the smoothing filter response (low-pass type).
- Back-projection of every pixel upon the reconstruction grid.

## 3. RECONSTRUCTION OF CONCEALED VEHICLES: GROUND/GROUND CASE

In this section, a simulated scene reconstruction is achieved to evaluate the contribution of the 3D tomography on the target identification process. First, we simulate a complete scene containing a hidden vehicle behind bushes. Top view of the scene is presented in Fig. 1 with the corresponding occultation rate of the vehicle by the foliage in ground-ground configuration.

Figure 2 exhibits two pictures extracted from the simulated sequence in the visible domain. The first one corresponds to a minimum occultation rate of the sequence (about 30%) and the second
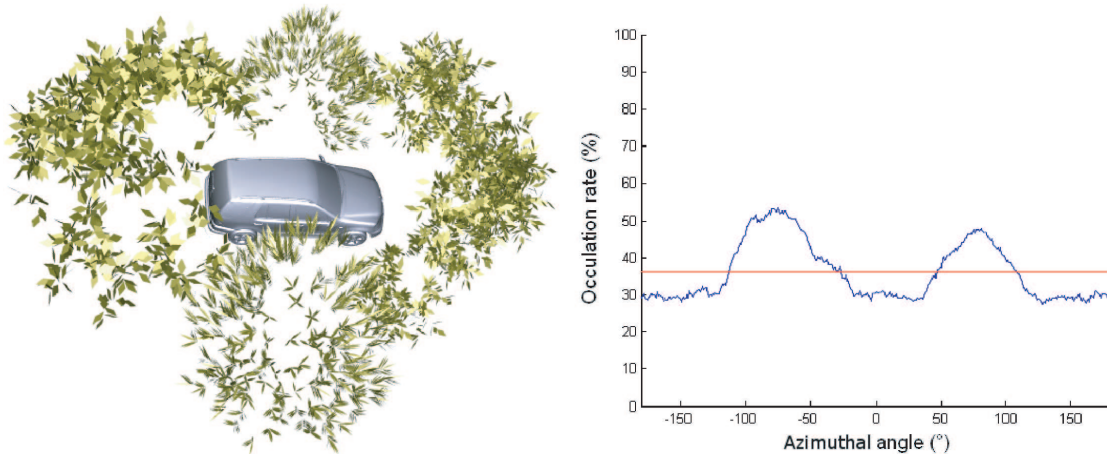


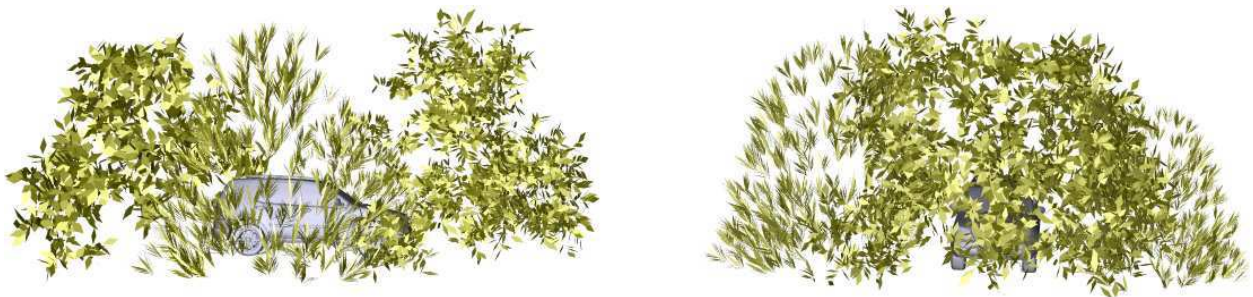Figure 1: Top view of the CAD scene and occultation rate of the vehicle.
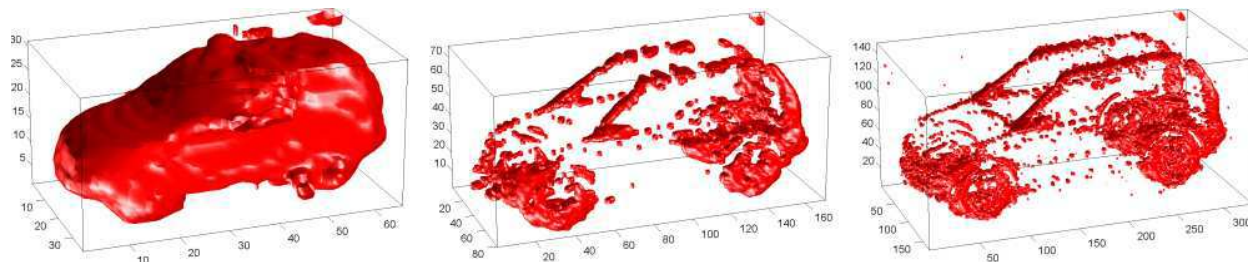


Figure 2: Two types of simulated foliage.

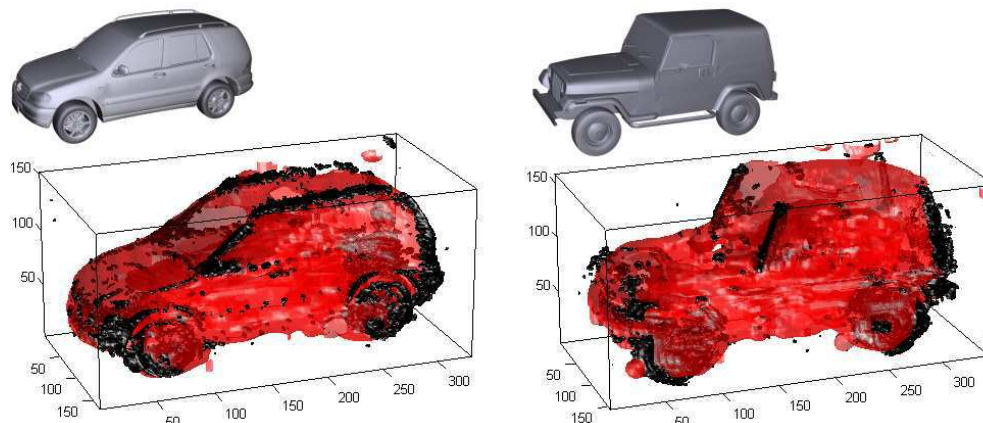Figure 3: Reconstructed targets for three resolutions.



Figure 4: Aggregation of the low resolution reconstruction and the high resolution reconstruction for two hidden targets (scenario of the Fig. 1).

one to a maximum occultation (about 50%) picture. For these conditions, the average occultation rate is about 36% between this two values. Military nets have a typical occultation rate of 40 to 50% but the net structure is smaller than the foliage used in our CAD model and the structure of a camouflage net is more easily taken into account by a reconstruction algorithm.

Intensity pictures are taken every degree for a complete revolution. Center of rotation is supposed to be well-known. In this configuration, there is only one acquisition scenario if we assume that the laser system (laser and receiver) and the target remains in the same plane during the recording sequence. For the wavelength used: 1.54 m, the typical reflectance of the foliage is about 0.25. The transmittance has the same magnitude order, therefore we can assume that the backscattering contribution comes from the reflectance coefficient. BRDF data used for the simulation take into account the relatively low reflectance of the foliage. The rest of the vehicle is assumed to be metallic. The aim of the simulation is double: we want firstly to estimate the robustness of the reconstruction algorithm in case of relatively strong camouflage, and secondly the resolution of the reconstruction. Three volume resolutions have been studied: 80, 180 and 350 pixels; the reconstructed volumes have been computed with the full resolution of the sensor and the reconstructed vehicles are shown in Fig. 3.

For the lower resolution we can notice that we can reconstruct the target envelope. For the higher resolution, we obtain a kind of wireframe structure. Using this wireframe structure allows visualization of the underlying 3D target. Surface structures can be added automatically after aggregation of the low resolution reconstruction as shown in the Fig. 4. This process allows a good identification of the target (Fig. 4).

## 4. RECONSTRUCTION OF CONCEALED VEHICLES: AIR/GROUND CASE

The Fig. 5 represents the CAD model of the air-ground scenario and the occultation rate depending on the zenithal angle. The rate varies from 30% to 55% with a mean value of 43%.

For this case, we use a resolution of 120 pixels. We obtain the 3D reconstruction of the right side of the Fig. 5. We want now to increase the signal-to-noise ratio for each collected 2D image. To do that, we apply a discrete wavelet transform to the original image, we obtain a denoised 2D

laser image. The original image is then low-pass filtered to produce a mask. We multiply these two images to obtain the final image in the upper-right of the Fig. 6. We can compare this final image to the original 2D image. The final image contains more information. Then we can reconstruct the volume with the set of processed images, we obtain the 3D image of the vehicle in Fig. 6.

We present another technique of 3D reconstruction for a high rate of occultation (Fig. 7). The rate of occultation vary from 45% to 70% with a mean value of 60%. We obtain a wireframe structure for the 3D reconstruction. With the wireframe structure, we can extract plane surfaces from three projections onto the sides of the bounding box. The set of the points situated inside these projections belongs to the planar structure. In Fig. 8, we have the original wireframe structure, the three projections and the aggregation of the wireframe structure and the planar structure.
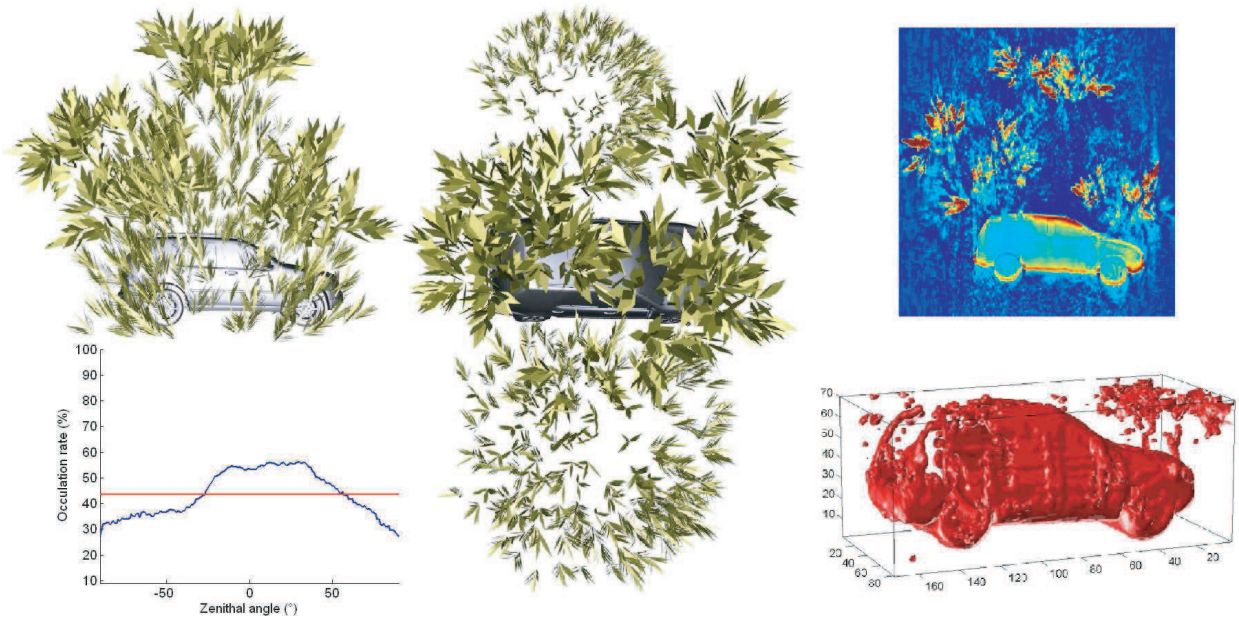


Figure 5: CAD model and occultation rate for a air-ground scenario.
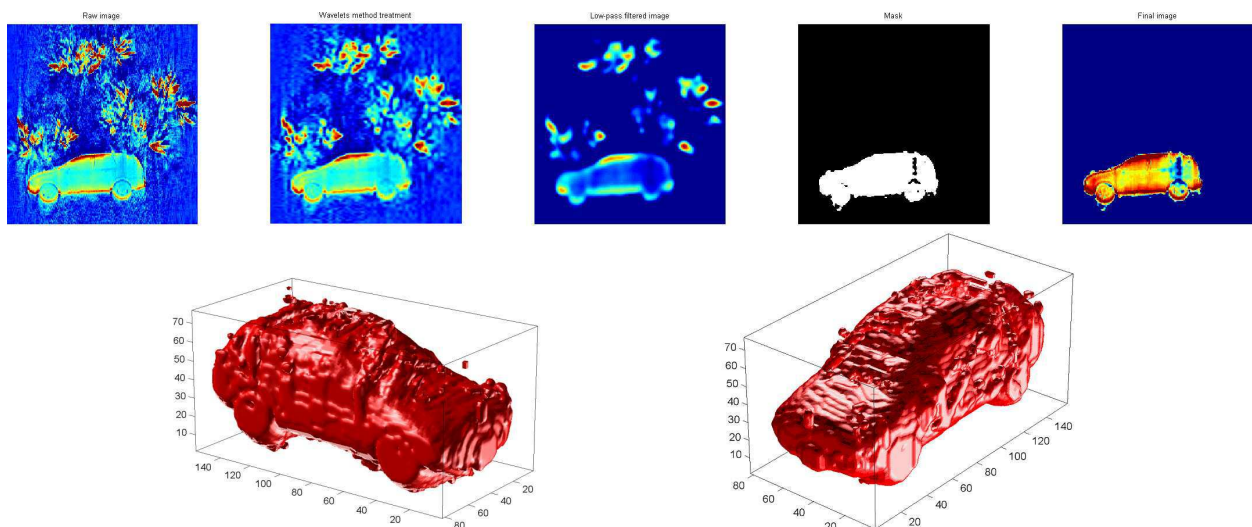


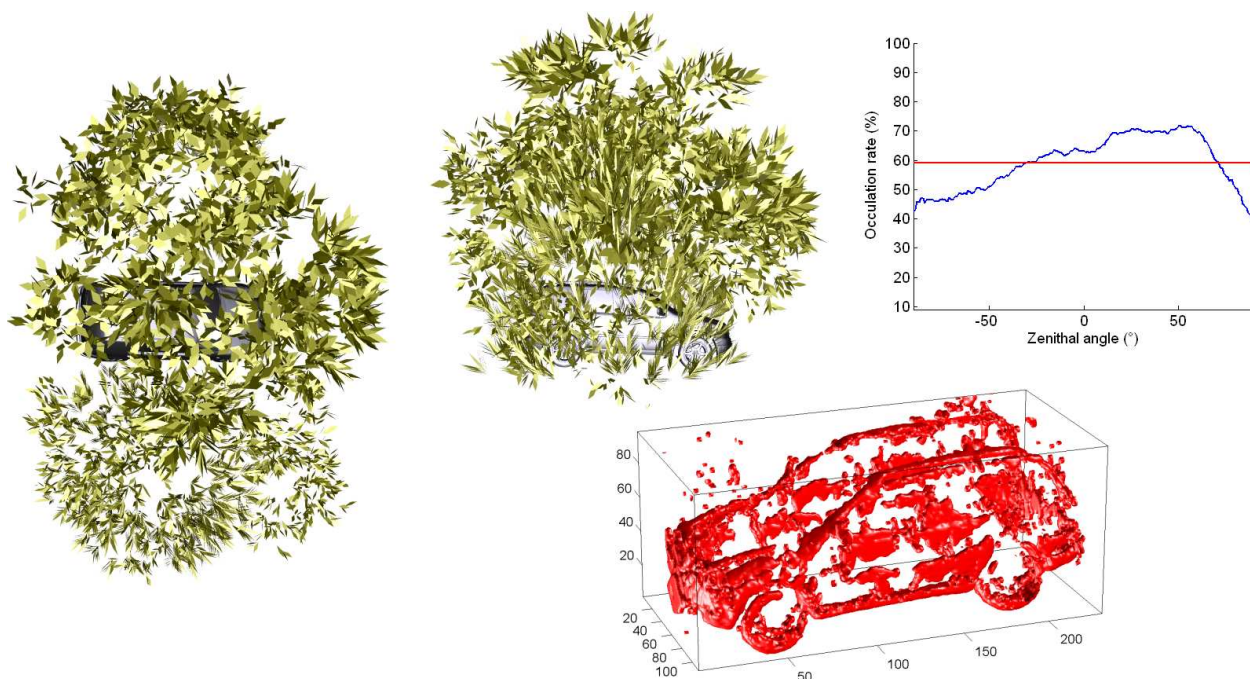Figure 6: Processed images and reconstruction.

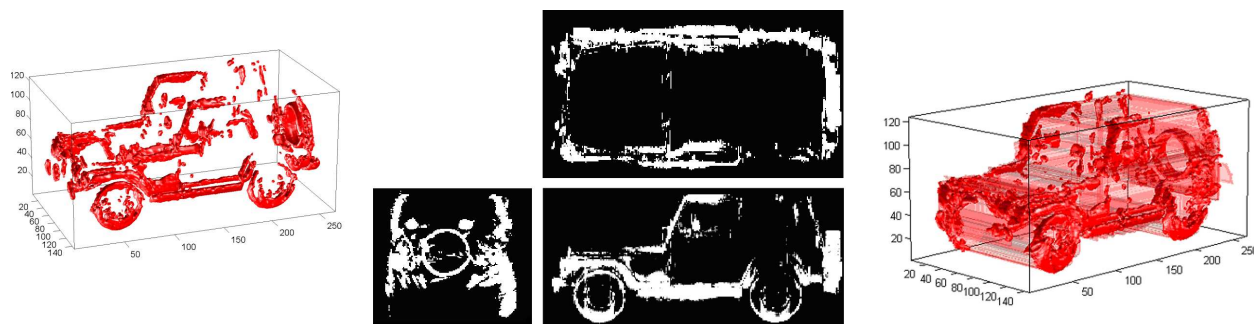Figure 7: Target reconstruction for a high reconstruction rate.



Figure 8: Wireframe structure, planar structure and aggregation.

## 5. CONCLUSION

In this paper, we have presented a simulation of a 3D laser imaging for objects hidden behind porous occluders as dense foliage. Because any view of the scene contains rays hitting the surface of the object, we proposed a tomographic algorithm to reconstruct the object of interest. We have tested the robustness of the algorithm in the cases of high rate of occultation.

## REFERENCES

[1] Voronovich, A. G., "Small-slope approximation for electromagnetic wave scattering at a rough interface of two dielectric half-spaces waves," *Random Media*, Vol. 4, 337–367, 1994.

[2] Berginc, G., "Small-slope approximation method: A further study of vector wave scattering from twodimensional surfaces and comparison with experimental data," *Progress In Electromagnetics Research*, PIER 37, 251–287, Y. Zhang and T. M. Grzegorczyk (Ed.), EMW publishing Cambridge, Massachusetts, USA, 2002.

# Studying the Effects of Wind Farms on a Terrain to the Scattered Field by Utilizing the ISAR Concept

**Deniz Bölükbas**[1], **Uğur Saynak**[1], **Alper Çolak**[1], **I. Hakki Tayyar**[1, 2], **and Caner Özdemir**[1, 3]

[1]Information Technologies Institute (ITI), TÜBITAK MRC, Gebze, Kocaeli, Turkey
[2]Department of Electronics Engineering, GYTE, Gebze, Kocaeli, Turkey
[3]Department of Electrical-Electronics Engineering, Mersin University, Mersin, Turkey

**Abstract**— In this paper, the radar cross section (RCS) values of the wind turbines (WTs) are simulated and presented depending on the material of the blades and the tower, if they are metal, concrete, fiberglass or radar absorbing material (RAM) coated. The two dimensional (2D) inverse synthetic aperture radar (ISAR) images of a wind farm are formed by using a total of five WTs. A terrain data is adopted from a Digital Terrain Elevation Data (DTED) map and used in the analysis. The polarization effects of the incident field are observed clearly at the scattered field. To analyze the effects of the terrain, different terrain specifications are used such as soil, sea or concrete. All 2D ISAR images are constructed by the help of a Shooting and Bouncing Ray based simulator that can predict the scattered and the diffracted fields from complex bodies at high frequencies.

## 1. INTRODUCTION

There has been a growing public and private sector interest on wind turbines (WTs) for generating electrical power in a more economical way. Beside the many advantages of wind energy, the WTs have their own drawbacks that must be taken into account when planning a wind farm site. The turbines are physically large structures, typically 70 meters in height or more. Therefore, they are in the coverage of the radar even at long ranges in most cases. Furthermore, the WTs consist of rotating blades whose directions and the rotation speeds are dependent on the wind direction and supplied power. It is clear that the rotating large blades will generate the Doppler effect such that the radar echo appears as a moving target on the radar operator's screen. In addition, a large number of WTs are generally constructed on a very limited field in most wind farms; therefore, the adverse impacts to the radar echo become even much worse.

There are a number of studies in the literature that pay attention to the analysis the impacts of a WT on radar parameters including but not limited to radar cross section (RCS) analysis from a WT. However, it is clear that such an analysis will not be adequate to understand the full scattering phenomena from a wind farm that have many WTs. Moreover, the strong electromagnetic interaction between the terrain and the other WTs must also be taken into account.

## 2. RCS OF A WIND TURBINE AND ISAR IMAGE CONSTRUCTION

As known well, the only parameter at the radar equation belongs to the target is the RCS. To examine the adverse impacts of WT on radar, the RCS of these large structures should be analyzed. To calculate the RCS of the target when the wavelength is much shorter than the target's dimensions, generally high frequency approximations such as geometric optics (GO), physical optics (PO), the shooting and bouncing ray (SBR) are used. The SBR is known to be a powerful high frequency electromagnetic (EM) simulation technique for the estimation of EM scattering from large and complex bodies [1, 2]. In SBR, the multiple-scattered field terms can also be calculated as well as the single-bounce term. Rays are shot from the transmitter towards the target and are traced according to the laws of geometrical optics. The PO contribution is calculated from the first hit point of each ray. On the other hand, a ray-tube integration is performed for the last hit point. PO contribution to the scattered field can be written as:

$$\mathbf{E}_{po}^{s}(r, \theta, \phi) = \frac{jk_0 z}{4\pi r} e_0^{jk_0 r} \iint_S \left( \hat{k}_s \times \hat{k}_s \times \mathbf{J}(r') \right) e^{jk_0 \hat{k}_s \cdot r'} ds' \tag{1}$$

where $\mathbf{J}(r')$ is the current density calculated as defined below.

$$\mathbf{J} \approx \begin{cases} 2\hat{\mathbf{n}} \times \mathbf{H}_i & \text{illuminated} \\ 0 & \text{shadowed} \end{cases} \tag{2}$$

In the above equation, $\hat{\mathbf{n}}$ is the surface normal of the illuminated part of the target, $k_0$ is the wave number of the free space, $\hat{k}_s$ is the unit vector directed from origin to observation point and $Z$ is the characteristic impedance of the surrounding medium. To find the contribution of each ray to the total scattered field, we calculate the far field contribution of the first and the last hit points for each ray before leaving the target as described [3]. It should be noted that PO method does not include the multi-bouncing effects since the multi-reflection phenomena does not taken into account.

For a more reliable result, edge effects may also be added to the scattered field calculation. At high frequencies, the diffracted field computation is performed by physical theory of diffraction based ILDC (Incremental Length Diffraction Coefficient) method to calculate a diffraction contribution for incident wave at the vicinity of an edge. The final equation for the diffracted field is obtained as

$$\mathbf{E}_d = \frac{e^{-jks}}{4\pi s} dl \left[ (D_m - D'_\perp) (\mathbf{E}_i \cdot \hat{\mathbf{e}}_{\perp,i}) \hat{\mathbf{e}}_{\perp,s} - \left( D_e - D'_\parallel \right)' \frac{\sin\beta}{\sin\beta'} (\mathbf{E}_i \cdot \hat{\mathbf{e}}_{\parallel,i}) \hat{\mathbf{e}}_{\parallel,s} \right.$$
$$\left. - \left( D_{em} \sin\beta' - D'_x \right) \frac{\sin\beta}{\sin\beta'} (\mathbf{E}_i \cdot \hat{\mathbf{e}}_{\perp,i}) \hat{\mathbf{e}}_{\parallel,s} \right] \tag{3}$$

where $\mathbf{E}_i$ is the incident electric field strength and the parameters $\hat{\mathbf{e}}$, $\beta$, $\beta'$, and $D$ are defined in [4]. Finally, we can get the 2-D ISAR image by using the following formulation defined in [5]:

$$\text{ISAR}(x,y) = \int_{-\infty}^{\infty} \int_{-\infty}^{\infty} E^s(k,\phi) \cdot e^{j2kx} \cdot e^{j2k\phi y} \cdot d(k) \cdot d(k_c\phi) \tag{4}$$

## 3. RCS CALCULATION

To evaluate the RCS values of different types of WTs, three WT's (WT-1, WT-2 and WT-3) whose CAD (computer aided design) models are shown in Figure 1 were used during the analysis. The CAD models of these turbines consist of triangular facets. The effects of multiple bounces and diffraction are investigated by analyzing perfectly conducting WT-1 with PO, SBR and SBR augmented with ILDC methods. The RCS analyses are performed at $f = 6\,\text{GHz}$ while the elevation angle is $1°$ $(\theta = 89°)$ for vertical polarization. As it can be seen from the Figure 2, multiple reflections are not that effective when the WT is assumed to be at free space and when the elevation
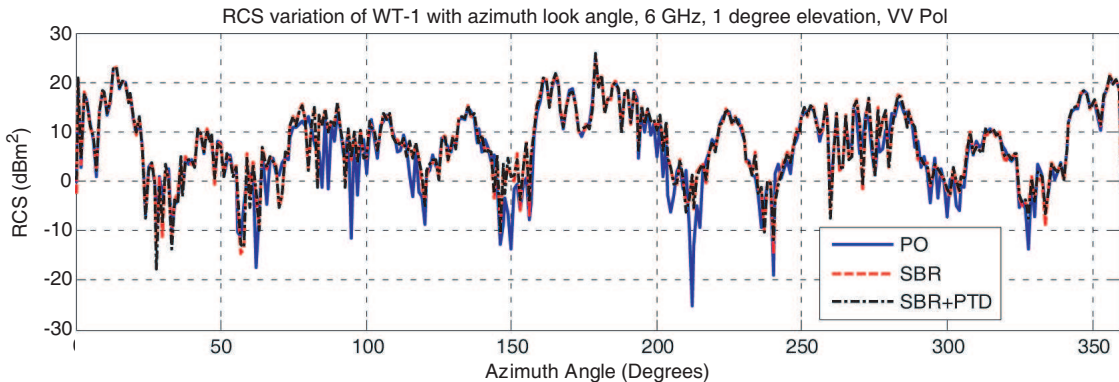


Figure 1: WT-1, WT-2 and WT-3 models.



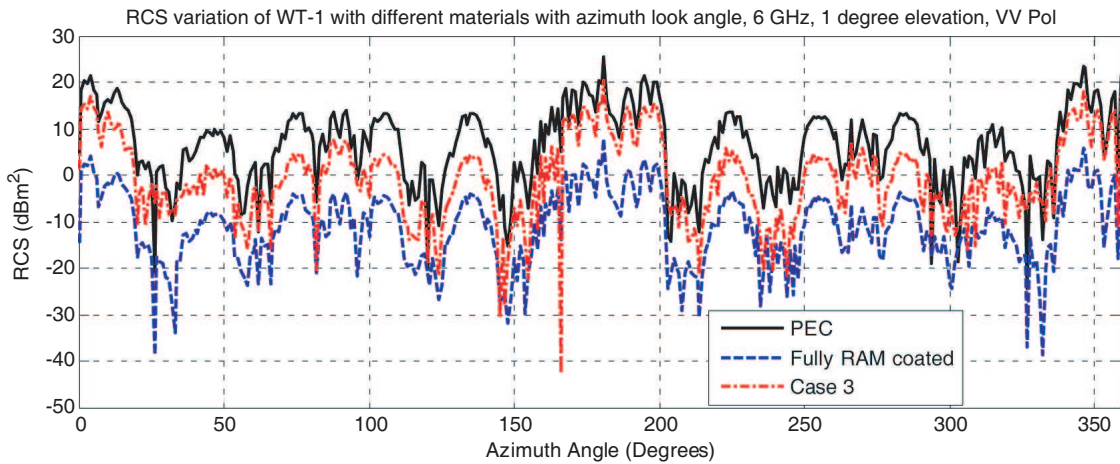Figure 2: The RCS variation of WT-1 with calculation method.

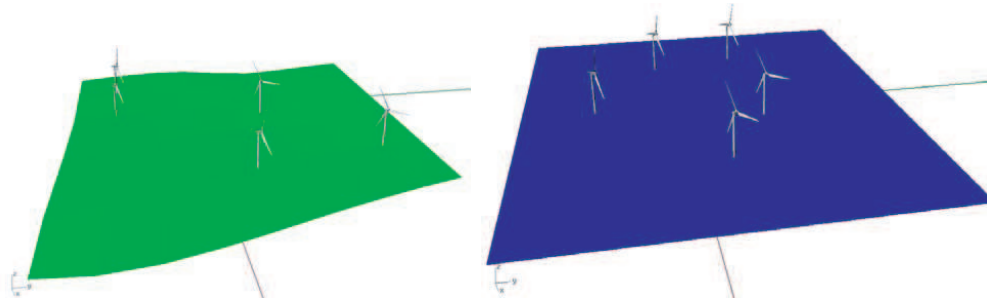Figure 3: RCS variation of WT-1 with different material application.



Figure 4: (a) The model of wind farm located on a terrain. (b) An off-shore wind farm model.

angle is $1°$. Also it should be noted that the contribution of the diffraction is negligible when compared to the effect of multiple bounces. The angular variation of RCS may be quite high on the azimuth plane (such as $10\,\mathrm{dBm}^2$ when the elevation angle is $1°$).

One of the well known mitigation method to reduce the adverse effects of a WT to radar, can be done by lowering its RCS value. For this purpose, the RCS variation with respect to the material type of the WT body is analyzed. The RCS of a PEC WT is compared to the fully RAM coated WT (Case 2). At this analysis the relative permittivity and relative permeability of RAM is selected to be $\varepsilon_r = 4.0 - j1.0$ and $\mu_r = 2.0 - j1.0$, respectively. The thickness of the RAM material is taken as $2\,\mathrm{cm}$. Another comparison performed with the PEC constructed WT and with a realistic WT model in which the tower is made up with concrete and the blades are made up with fiber glass (Case 3). For Case 3, the relative permittivity of the fiber glass and the concrete is selected to be $\varepsilon_r = 3.9$ and $\varepsilon_r = 4.5 - j0.05$ respectively. Both materials relative permeability are $\mu_r = 1$. The analysis are performed at $f = 6\,\mathrm{GHz}$ while the elevation angle is $1°$ $(\theta = 89°)$ for vertical polarization. The result of this analysis is given at Figure 3. It's observed that the RAM coating is more successful when compared with the Case 3 in the sense of reducing the RCS.

## 4. THE EFFECTS OF TERRAIN ON THE SCATTERED EM FIELD

As explained above, the free space RCS of a WT may not be adequate to fully analyze the scattering phenomena. The multi-reflection effects from the terrain and from the other WTs should be considered as well. In this section, the presence of more than one WT with terrain is considered and corresponding ISAR images are presented. For this analysis, a wind farm is formed with five WTs using WT-3 model. A terrain data is adopted from a DTED map and the ISAR image is constructed for this wind farm can be seen at Figure 4(a). The dimension of the terrain is $38\,\mathrm{m} \times 34\,\mathrm{m}$ and the relative permittivity is $\varepsilon_r = 23.3 - j0.5$ while the relative permeability is $\mu_r = 1.0$ which characterizes typical soil characteristics. This RCS analysis is performed for vertical polarization at $f = 6\,\mathrm{GHz}$ the elevation angle is $5°$ $(\theta = 85°)$ and the azimuth angle is $45°$. The spatial resolution is $0.7\,\mathrm{m}$ and the analysis is performed by SBR so the multi-bounce effects are also included during EM
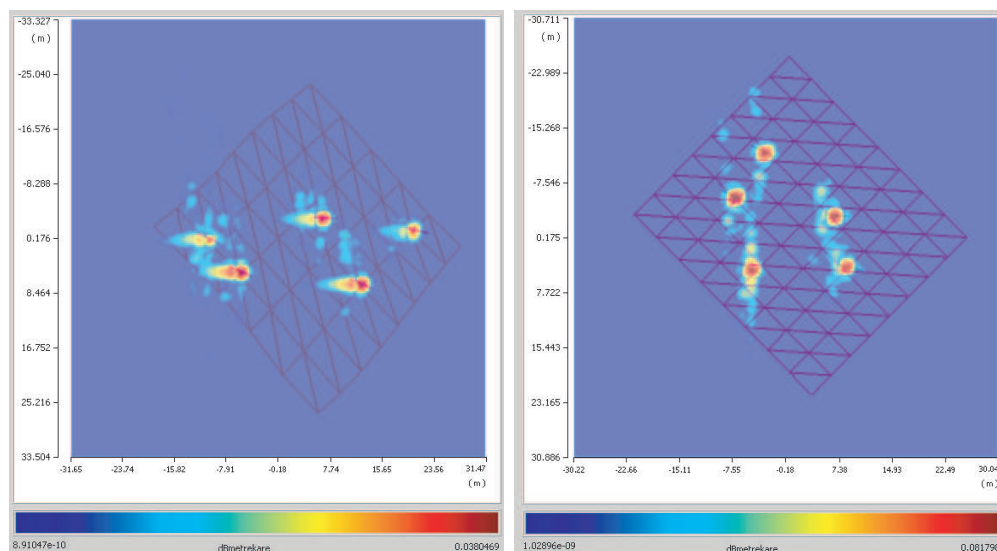
Figure 5: (a) The ISAR image of a wind farm located on a terrain. (b) The ISAR image of an off-shore wind farm.

calculation. The WTs are selected as the RAM coated whose parameters are given at Section 3. After the EM scattering calculation via SBR-based simulator code, ISAR image of the scene is constructed as it can be seen at Figure 5(a).

As the second analysis, an off shore wind farm is modeled as demonstrated at Figure 4(b). The WTs are modeled with WT-3 and assumed to be PEC constructed. The maximum dimension of the sea in the scene is $35\,\mathrm{m} \times 31\,\mathrm{m}$ and the sea surface is also assumed to be PEC. This analysis is performed for vertical polarization for $f = 6\,\mathrm{GHz}$, the elevation angle is $5°$ ($\theta = 85°$) and the azimuth angle is $45°$. The spatial resolution is $0.7\,\mathrm{m}$. The EM scattered field simulation of the scene was carried out by our SBR-based estimator. Corresponding ISAR image can be seen at Figure 5(b). It is clearly observed that the terrain characteristic varies the scattered field and should be taken into account for impact analysis on radar. As stated at Section 3, the multi-bounce effects are not that significant when the RCS calculation is considered in free space. However, these effects are clearly detected when the ISAR analysis is employed.

## 5. CONCLUSION

At this paper, the scattering behavior of a wind turbine and a wind farm on a field is analyzed. It is observed that free space RCS is not sufficient to fully understand the scattering phenomena from a wind farm that consists of many WTs. The electromagnetic interaction between the terrain and the other WTs also gives significant contribution to the total RCS. For a complete radar impact analysis of the wind farms, these effects should be considered as well.

**REFERENCES**

1. Ling, H., R. C. Chou, and S. W. Lee, "Shooting and bouncing rays: Calculating the RCS of an arbitrary shaped cavity," *IEEE Tran. on Antennas and Prop.*, Vol. 37, No. 2, 1989.
2. Bhalla, R. and H. Ling, "Image domain ray tube integration formula for the shooting and bouncing ray technique," *Radio Science*, Vol. 30, No. 5, 1435–1446, 1995.
3. Michaeli, A., "Equivalent edge currents for arbitrary aspects of observation," *IEEE Tran. on Antennas and Prop.*, Vol. 32, No. 3, 1984.
4. Özdemir, C., "Syntetic aperture radar," *Encyclopedia of RF and Microwave Engineering*, 5067–5080, K. Chang, Ed., Wiley Interscience, 2005.

# FDTD Analysis in a PCB Stripline Structure

**E. Y. S. Lutif**[1], **M. R. F. Gontijo**[1], **A. J. F. Orlando**[1], **and A. C. C. Migliano**[1, 2]

[1]Aerospace Technological Institute (ITA), CTA, Brazil
[2]Advanced Study Institute (IEAv), CTA, Brazil

**Abstract**— An FDTD analyses is reported in changes in the permittivity and permeability and also in the dimensions in a PCB stripline structure of stripline-dielectric-ground plane as the dielectric thickness are fixed and these distributions of electromagnetic waves are described graphically. Extensive computation is performed in the spectral domain and the sample shows sensitivity in the work area in the PCB stripline structure. An electromagnetic wave is formatted of the type TEM $12.0 \times 0.64\,\text{mm}^2$. The derivation of $\varepsilon_r$ and $\mu_r$ as a function of $S_{11}$ and $S_{21}$ is included, as well a practical design for a stripline sample holder.

The exact knowledge of material permittivity $\varepsilon^*$ and permeability $\mu^*$ is essential in the study of physical phenomena which govern interactions between electromagnetic waves and matter. The accurate electromagnetic analysis of discontinuities in a stripline device, used for the broad band measurement of complex permittivity and permeability of materials, is presented.

In this paper, we will first describe the electromagnetic analysis of the stripline treated by the FDTD software approach then we will focus our attention on the study of the cell discontinuities based on the transmission line methods. We will analyses two $w/h$ relations 0.86 and 1.3 and two materials permittivity. The sample shows two works areas between 5.7 GHz–6.7 GHz for the relation $w/h = 0.86$ and 6.7 GHz–7.4 GHz for the relation $w/h = 1.3$ for air permittivity. The work area increased for the relation $w/h = 1.3$ when we use the dielectric material with permittivity 3. In particular, there were resonant-like peaks at 13–15 GHz in both permittivity analyzed.

## 1. INTRODUCTION

FDTD can solve models with arbitrary geometries comprised of dielectric materials. FDTD is a computer simulation technique with which an arbitrary space is meshed with small cells ($\Delta x\,\Delta y\,\Delta z$ : $\Delta x$, $\Delta y$, $\Delta z < \lambda/10$) and the electromagnetic field and current are calculated in the space by solving Maxwell's equations in each cell at each time step of $\Delta t$ ($< \lambda/10c$). The critical dimensions for the stripline chamber are as follows: ground plane separation 3 mm and 2 mm, center conductor width 2.6 mm. Both the ground planes and the center conductor are made of a beryllium copper alloy for rigidity, while the housing is made of aluminum with approximate inside dimensions of $12\,\text{mm} \times 10\,\text{mm} \times 0.64\,\text{mm}$. Remcom's XFDTD was employed for this FDTD simulation work and all the simulated results were taken as in the steady state.

An obvious limitation of the numerically rigorous techniques, however, is their ability to solve large problems that place a heavy burden on the CPU memory and time. Due to the gradual increase of the computer resources numerous approaches have been made by researchers to solve very large electromagnetic problems using rigorous techniques, e.g., FDTD, methods of moments, finite element (FE) method.

## 2. THEORY

The broad band electromagnetic characterization of isotropic materials requires knowing two independent complex parameters as a function of frequency. The accessible parameters are here the reflection and transmission coefficients calculated using FDTD with the sample under test. The complex relative permittivity and permeability are given below

$$\varepsilon_r = \varepsilon_r' - j\varepsilon_r''$$
$$\mu_r = \mu_r' - j\mu_r''$$

The stripline has characteristic impedance of $Z_0$ which when loaded with the sample material becomes $Z$, where

$$Z = Z_0\sqrt{\frac{\mu_r}{\varepsilon_r}} \tag{1}$$

In the unloaded regions, the propagation constant is $k = k_0\sqrt{\mu_0\varepsilon_0}$, while in the loaded region, the propagation constant is generally complex and is designated by $k$, where

$$k = k_0\sqrt{\mu_r\varepsilon_r} \tag{2}$$

At the plane boundaries, there are complex reflection coefficients $R$ and $-R$, respectively, where

$$R = \frac{Z - Z_0}{Z + Z_0} \tag{3}$$

Using (1), Equations (2) and (3) may be solved simultaneously to yield the desired parameters

$$\varepsilon_r = \frac{k}{k_0}\left(\frac{1 - R}{1 + R}\right) \tag{4}$$

$$\mu_r = \frac{k}{k_0}\left(\frac{1 + R}{1 - R}\right) \tag{5}$$

FDTD is used to solve Maxwell's equations for arbitrary model spaces. Indeed, FDTD allows us to solve models that would be difficult or impossible with analytical methods. FDTD is a direct time-domain solution to Maxwell's curl equations [1], which are given here below.

$$\frac{\partial \overline{E}}{\partial t} = \frac{1}{\varepsilon}\nabla \times \overline{H} - \frac{1}{\varepsilon}\left(\overline{J}_{source} + \sigma\overline{E}\right) \tag{6}$$

$$\frac{\partial \overline{H}}{\partial t} = -\frac{1}{\mu}\nabla \times \overline{E} - \frac{1}{\mu}\left(\overline{M}_{source} + \sigma^*\overline{H}\right) \tag{7}$$

In the FDTD scheme, Maxwell's curl equations are first scalarized into their $x$, $y$, and $z$ field components. Then, centered finite difference expressions are used to approximate the spatial and time derivatives. Below is the resulting $x$-directed $H$ field equation; the other 5 field components are similar.

$$\frac{Hx_{i,j,k}^{n+1/2}}{\Delta t} = \frac{1}{\mu}\left[\frac{Ey_{i,j,k-1/2}^n - Ey_{i,j,k-1/2}^n}{\Delta z} - \frac{Ez_{i,j+1/2,k}^n - Ez_{i,j-1/2,k}^n}{\Delta y} - \left(M_{source} + \sigma^* Hx_{i,j,k}^{n-1/2}\right)\right] \tag{8}$$

This method was first introduced in the original FDTD paper by Kane Yee [2]. In particular, he introduced the next important FDTD concept known as the Yee Space Grid.

The key features of the Yee Space Grid relate to the staggering of the $E$ and $H$ fields. The $E$ and $H$ field are staggered to one another with respect to time by one half of the time step. $E$ and $H$ centered in space such that each $E$ field component is surrounded by 4 $H$ field components and vice versa.

**Figures and Tables:** The $S$-parameters were analyzed and XFDTD was employed for this FDTD simulation work and all the simulated results were taken as in the steady state. The values of the $S$-parameters are in decibels (dB) as a function of frequency (GHz). The conversion of the decibels values in percent are given in the logarithmic formula, according to the Equation (9). The Table 1 shows some values in decibels calculated from the Equation (9).

$$A(\%) = (1 - 10^{-\text{dB}/10}) * 100 \tag{9}$$

Table 1: Values of $S$-parameter in dB converted in percent [3].

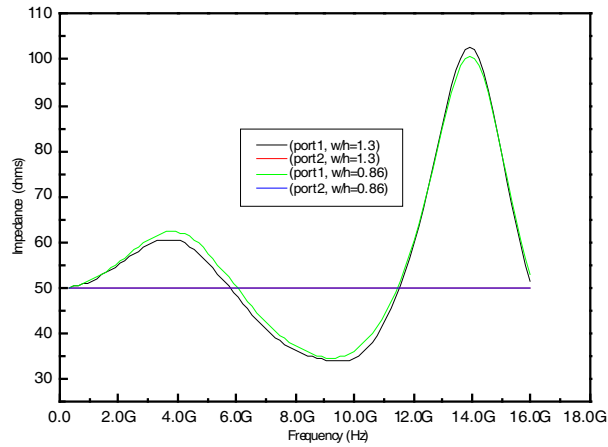| $S$-parameters (dB) | $S$-parameters (%) |
|---|---|
| 0 | 0 |
| $-3$ | 50 |
| $-10$ | 90 |
| $-20$ | 99 |
| $-30$ | 99.9 |
| $-40$ | 99.99 |

Figure 1: Impedance as a function of frequency when the test device is loaded with a dielectric $\varepsilon_r = 1$, length = 12 mm.
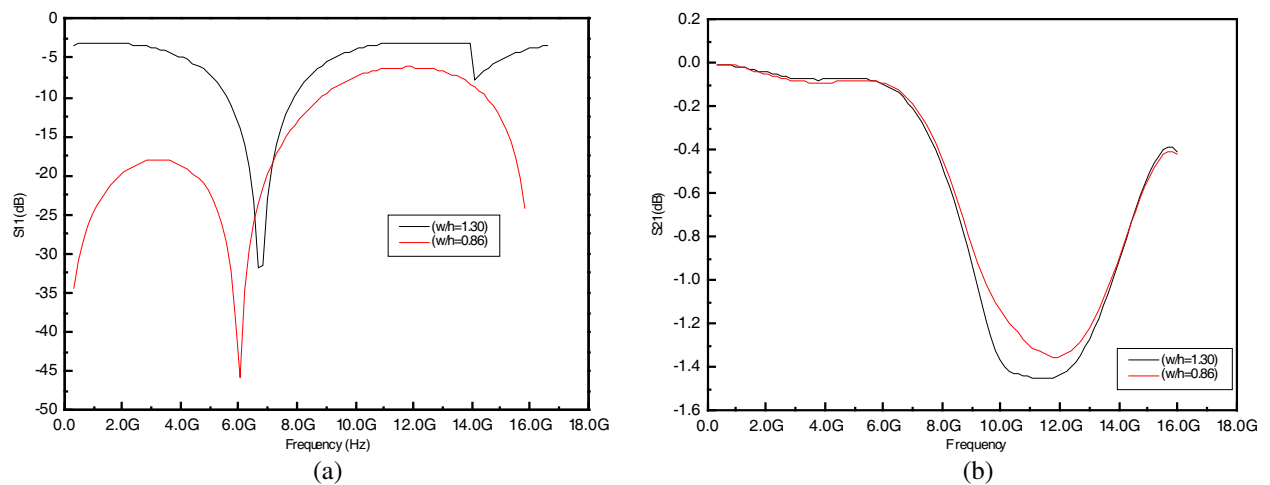


Figure 2: Dimensional resonance in the simulation of the reflection and transmission coefficient as a function of frequency when the test device is loaded with a dielectric $\varepsilon_r = 1$, length = 12 mm. (a) Reflection modulus. (b) Transmission modulus.
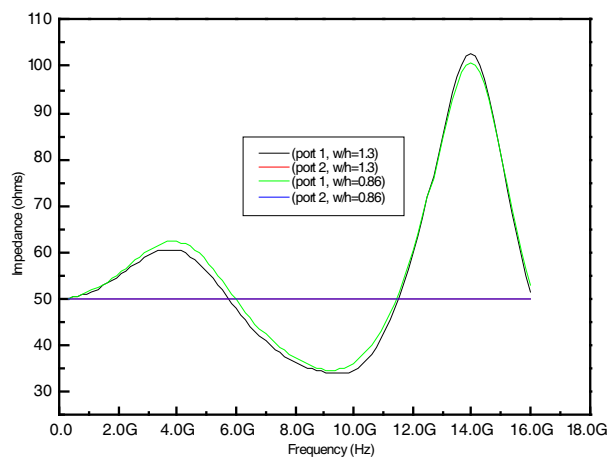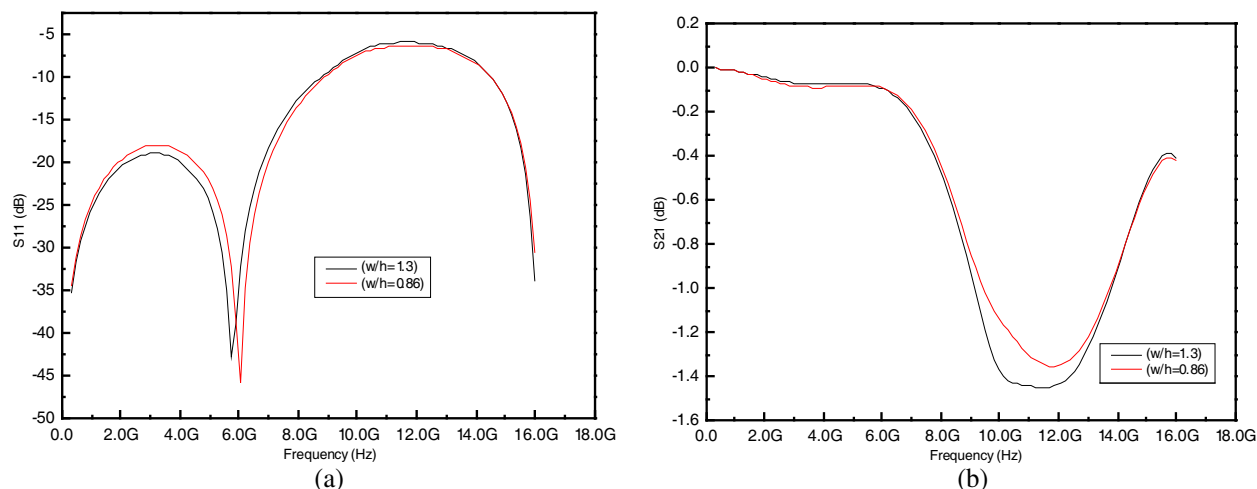


Figure 3: Impedance as a function of frequency when the test device is loaded with a dielectric $\varepsilon_r = 3$, length = 12 mm.

Figure 4: Dimensional resonance in the simulation of the reflection and transmission coefficient as a function of frequency when the test device is loaded with a dielectric $\varepsilon_r = 3$, length $= 12\,\text{mm}$. (a) Reflection modulus. (b) Transmission modulus.

## 3. NUMERICAL RESULTS

In order to know the influence of the permittivity and permeability on the $S$-parameters of the stripline cell and the domain of validity of the transmission-line theory previously used, we have simulated $S$-parameters using FDTD. The Figs. 1–4 show the results obtained for four discontinuities using the stripline structure described bellow. We have chosen dielectric materials with well-known properties and a relative permittivity which is constant in the exploited frequency band.

## 4. CONCLUSIONS

This work analyzed general phenomena of the reflection and transmission as a function of frequency taken placed by a general PCB stripline structure. The exact numerical value for the stripline and the spatial range of the electric field can be changed with any variation of the stripline frequency. The simulations show sensitivity with changes in the PCB stripline structure and also in the dielectric materials. Therefore, one must be input the specific numerical values for all variables above for FDTD simulation to obtain quantitative values for the frequency and fields of interest. We can also see in Figs. 1 and 3 that the sample is like a filter between $13\,\text{GHz}$ and $15\,\text{GHz}$.

### ACKNOWLEDGMENT

### REFERENCES

1. Jackson, J. D., *Classical Electrodynamics*, John Wiley & Sons, Inc., New York, 1999.
2. Kane, Y., "Numerical solution of initial boundary value problems involving Maxwell's equations in isotropic media," *IEEE Transactions on Antennas and Propagation*, Vol. 14, No. 3, 802–807, May 1966.
3. Lee, S. M., *International Encyclopedia of Composites*, Vol. 6, VHC Publishers, New York, 1991.

# Magnetic Field Distribution of a Novel Variable Inductor Based on Orthogonal Magnetization

**Zhengrong Jiang[1], Zhengxi Li[1], and Jianye Chen[2]**

[1]Department of Electrical & Mechanical Engineering, North China University of Technology
Beijing 100144, China
[2]Department of Electrical Engineering, Tsinghua University, Beijing 100084, China

**Abstract**— A computation method for the magnetic field distribution of a novel variable inductor based on orthogonal magnetization is presented. The inductor includes two windings, one is an ac winding for exciting ac field, another is a dc winding for creating dc bias field, the latter is perpendicular to the former. The vector combination results in a semi-rotating field in the core and make the hysteresis "shearing". This feature makes the variable inductor safely and have linearly characteristic in case application on HVDC. The effect on material magnetic characteristic caused by orthogonal bias field is explained and the field distribution is computed, the calculated results are consistent with the experimental data well.

## 1. INTRODUCTION

With the development of HVDC transmission, a greater demand for high quality variable inductor is expected. The safety and linearity are essential to the application of voltage variation, VAR compensator, harmonic filtering and DC-AC converter. Several magnetic devices for variable inductor have been presented [1]. However, the harmonics of the output current can not be neglected.

In this paper, we present an approach to control the permeability of an inductor core made of toroidal grain oriented Fe-Si laminations. This approach is based on the vectorial magnetization response of the core under two orthogonal field components. The vectorial sum results in a semi-rotating field in the inductor core. This method brings about many good virtues. Details of the inductor under consideration, its analytical aspects, numerical simulations and control characteristic are given in the following sections.

## 2. INDUCTOR STRUCTURE AND MAGNETIZATION MECHINISM

The novel variable inductor consist of a vacant winding and a toroidal core winding, the former is the main coil and connected with AC exciting current, the latter is placed in the former and connected with DC control current.

Due to the two windings orthogonal orientation, there is no inductance voltage in the DC control winding, hence the DC control element is safe even if under a high voltage application.

As for the oriented Fe-Si lamination core, it is subjected to two direction magnetic fields, one is the shifting $\vec{H}(t)$ in the axis direction (often as easy axis of Fe-Si silicon sheet) creating by AC current, another is circumaxile $H_\perp$ which derives from DC current. It is perpendicular to the $\vec{H}(t)$, thus a semi-rotating field is created in the Fe-Si core.

Conventionally the magnetic properties of material are analysed assuming that the directions of $B$ and $H$ are parallel. However, under the orthogonal fields the magnetic properties of the oriented lamination core are related by tensor permeability since $B$ vector is not parallel to $H$ vector in the core and permeability depend on magnetic flux density [2], the effective core permeability $\mu$ can be described phenomenally by a complex permeability $\mu = \mu' - j\mu''$, the permeability tensor consists of an anisotropic matrix involving the permeabilities $\mu_x$ and $\mu_y$ and a rotating matrix, which describes the perpendicular component $H_\perp$ by shifting $\vec{H}(t)$ with an angle $\alpha$ in space. The relationship of $B$, $H$ and permeability $\mu$ can be described as

$$\vec{B} = \begin{pmatrix} \cos\alpha & \sin\alpha \\ -\sin\alpha & \cos\alpha \end{pmatrix} \cdot \begin{pmatrix} \mu_x & 0 \\ 0 & \mu_y \end{pmatrix} \cdot \vec{H} = \vec{\vec{\mu}} \cdot \vec{H} \tag{1}$$

where, $\alpha$ is the loss angle and $\alpha = \arc(\vec{H}) - \arc(\vec{B})$.

As for the rotating matrix, the diagonal terms represent for alternating flux permeability tensors and the off-diagonal terms denotes the rotational ones [3]. When the phase difference between $B$

and $H$ caused by rotational hysteresis is considered the permeability tensor becomes the full tensor as follows:

$$\begin{pmatrix} B_x \\ B_y \end{pmatrix} = \begin{bmatrix} \mu_{xx} & \mu_{xy} \\ \mu_{yx} & \mu_{yy} \end{bmatrix} \begin{pmatrix} H_x \\ H_y \end{pmatrix} \tag{2}$$

The two-dimensional governing equation including two dimensional magnetic property is written as follow:

$$\frac{\partial}{\partial x}\left(v_{yy}\frac{\partial A}{\partial x}\right) + \frac{\partial}{\partial y}\left(v_{xx}\frac{\partial A}{\partial y}\right) - \frac{\partial}{\partial x}\left(v_{yx}\frac{\partial A}{\partial y}\right) - \frac{\partial}{\partial y}\left(v_{xy}\frac{\partial A}{\partial x}\right) = -J_0 - J_m \tag{3}$$

where, $A$ is the magnetic vector potential, $v$ is the reluctivity tensor, $J_0$ is the current density and $J_m$ is the equivalent magnetizing current density.

The non-linear Equation (3) is solved using the Newton-Raphson method and the field distribution of flux in the grain oriented lamination core can be calculated.

## 3. B-H HYSTERESIS AND FIELD DISTRIBUTION

Figure 2 shows the hysteresis loops of the grain-oriented lamination core under the various DC bias currents. The measurements are performed under dc and ac field simultaneously. It is clearly apparent that the orthogonal bias field (dc field) changed the hysteresis behavior of the magnetic material, the $B$-$H$ loops shows a "shearing" with increasing dc current. The magnetization at maximum applied field, the remanence and the coercivity all decreased with increasing orthogonal bias field. Whence the orthogonal bias field alters the inductance of the device.

Figure 3 shows the finite model of the grain oriented core. The circumcolumnar arrows denote the ac exciting current, the dc control current is divided into four sections toroidally. Figure 4 shows the flux distribution.

According to Neel's phase theory [4], the hysteretic magnetization curve is dependent on the direction of the applied field relative to the easy axis. Looking at above $B$-$H$ measurement results, the $B$-$H$ loop became less slope with increasing dc bias current. it is realized that the orthogonal dc bias field affects the magnetization process by enhancing the anisotropy of the grain oriented laminations and gives rise to a decrease in effective inductance of the device. The role of dc bias field is like a "magnetic valve" on the path to control the flux. It can be seen from Figure 4.
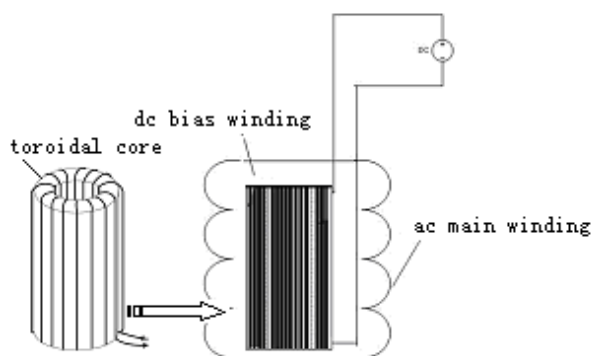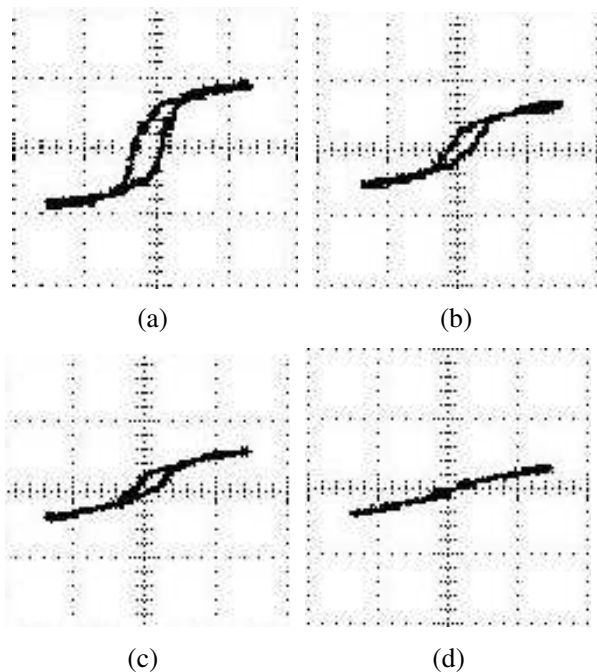


Figure 1: Inductor based on orthogonal magnetization.



(a)          (b)

(c)          (d)

Figure 2: $B$-$H$ loop with various dc bias current (a)0 A, (b) 1 A, (c) 2 A, (d) 3 A.
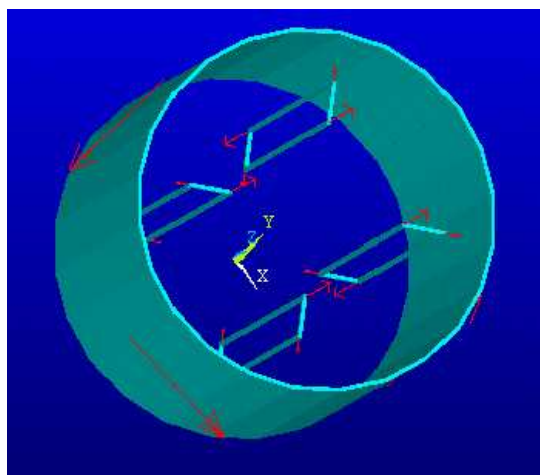
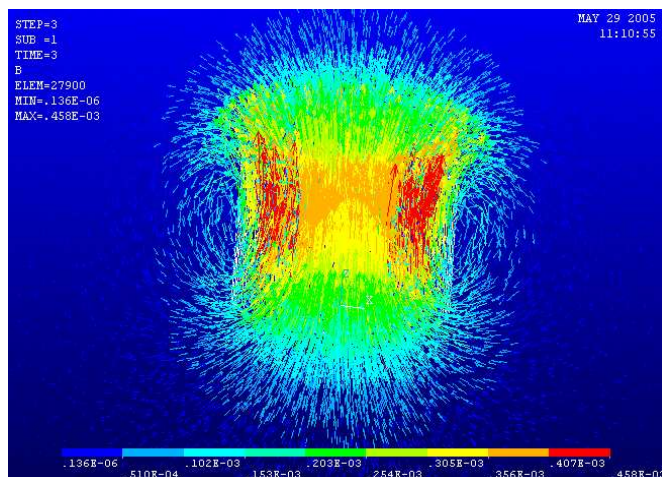Figure 3: Loading current density in finite element model.
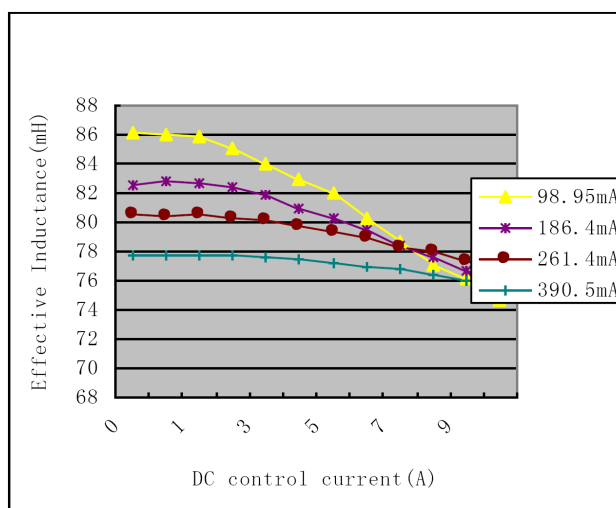


Figure 4: Flux distribution of grain-oriented core.



Figure 5: Control characteristic.

## 4. CONTROL CHARACTERISTIC

Under various main ac currents from 98.95 mA to 390.5 mA, the inductor is subject to series dc control currents from 0 A to 10 A respectively. Write down the voltages and currents of the inductor accordingly, then the efficient inductance can be given as:

$$L = \frac{\dot{U}}{2\pi f \cdot \dot{I}} \, (\text{mH}) \tag{4}$$

The following is the control characteristic curve.

From the control characteristic, we found that the control ability of DC current to the main inductance decrease with the main current increasing, it is because that when the field caused by the main current is much larger than the dc bias MMF, the domain wall rotation is prevailing subject to ac exciting field and the dc bias field has no significant effect on the overall effective inductance any more.

## 5. CONCLUSION

The permeability of magnetic materials can be changed by applying a orthogonal dc magnetic field which is oriented perpendicular to the main flux direction, in this way the inductance of the main coil can be controlled. This method has the effect of lowering the permeability by adding anisotropic of the magnetic material without affecting the linearity of the magnetizing process [5]. Due to

maintaining magnetization linearity no additional harmonics are produced on the application of HVDC.

**REFERENCES**

1. Cho, G. C., G. H. Jung, N. S. Choi, and G. H. Cho, "Analysis and controller design of static var compensator using three-level GTOinverter," *IEEE Trans. Power Electron.*, Vol. 11, 57–65, 1996.

2. Enokizono, M., K. Yuki, and S. Kawano, "An improved magnetic field analysis in oriented steel sheet by finite element method considering tensor reluctivity," *IEEE Transactions on Magnetics*, Vol. 31, No. 3, May 1995.

3. Enkinono, M. and K. Yuki, "An improved magnetic field analysis in oriented steel sheet by finite element method considering tensor reluctivity," *Proceedings ofthe 6th CEFC, P3C04*, 1994.

4. Fiorillo, F. and L. R. Dupre, "Comprehensive model of magnetization curve, hysteresis loops, and losses in any direction in grain-oriented Fe-Si," *IEEE Transactions on Magnetics*, Vol. 38, No. 3, May 2002.

5. Jiang, Z. R. and J. Y. Chen, "Semi-core variable inductor based on DC excitation field," *Automation of Electric Power Systems*, Vol. 31, No. 5, Mar. 10, 2007.

# Polarimetric UHF Calibration for SETHI

**H. Oriot[1], C. Coulombeix[1], and P. Dubois-Fernandez[2]**

[1]ONERA, Chemin de la Hunière, F-91761 Palaiseau cedex, France
[2]ONERA, Base aérienne 701, 13661 Salon AIR, France

**Abstract**— The SETHI sensor from ONERA is an airborne radar equipped with different bands (UHF-VHF, L, X) on a Falcon 20. The UHF-VHF band is fully polarimetric and can operate between 225 MHz up to 460 MHz. In August 2009, this system was used in French Guiana for the TROPISAR experiment. Data were acquired from 0° incidence angle up to 65° incidence angle and a swath of about 6000 m. The antenna pattern being quite large, this configuration induced a secondary reflection of the incident wave with the wing leading to an antenna pattern deformation (in intensity, phase and frequency). This paper explains the calibration procedure that was performed on the data. First the crosstalk is estimated and removed, then, the antenna pattern is compensated.

## 1. INTRODUCTION

The SETHI sensor from ONERA (Figure 1) is an airborne radar equipped with different bands (UHF-VHF, L, X) on a Falcon XX [1]. The UHF-VHF band is fully polarimetric and can operate between 225 MHz up to 460 MHz. In August 2009, this system was used in French Guiana for the TROPISAR experiment. This experiment was conducted to provide ESA and CNES with measurements of temporal coherence at P- and L-band over tropical forests for time intervals compatible with spaceborne missions (typically 20–30 days). In this paper we present the methodology used to calibrate the UHF data.

Data were acquired from 0° incidence angle up to 65° incidence angle and a swath of about 6000 m. The UHF antenna is located under the left wing of the Falcon 20. For this experiment, it was pointing with an incident angle of 45° and the bandwidth used was from 335 MHz up to 460 MHz.

The antenna pattern being quite large, this configuration induced a secondary reflection of the incident wave with the wing leading to an antenna pattern deformation (in intensity, phase and frequency). This paper explains the calibration procedure that was performed on the data. First the cross-talk is estimated and removed, then, the antenna pattern is compensated.

## 2. PROCESSING

The full polarimetric data were processed using the ONERA SAR processor [2]. This processor uses a modified version of the RMA algorithm. Data were processed with a 1 m meter resolution in range and 1.5 m resolution in azimuth.

The analysis of the four channels show some defaults:

- $Hv$ and $Vh$ appear to be unbalanced.



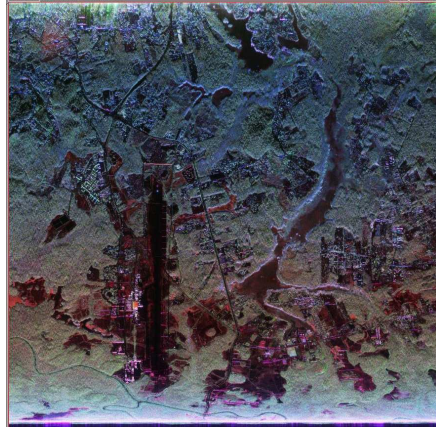Figure 1: Falcon XX equipped with the ONERA Sethi system.

Figure 2: Color composite of the calibration test-site (Rochambeau airport, French Guiana). $Hh$ channel appears in red, $Hv$, in green, $Vv$ in blue. The aircraft is flying from the left-bottom of the image to the right bottom of the image.

- Radiometry varies across the swath and these variations differ from one channel to the other (this variation can be observed on Figure 2: the main color of the image varies with range which indicates that the radiometric variations are different from channel to channel).
- The polarimetric phase $Hh$-$Vv$ is also affected.

The data acquisition geometry is suspected to be responsible for this behavior: The pod is located under the wing and the antenna pattern is large so a secondary reflection of the incident wave with the wing leads to an antenna pattern deformation (in intensity, phase and frequency). This deformation has to be compensated by the calibration procedure. This procedure is divided into two steps: the first one aims at removing the cross-talk that can be observed on the images; the second one aims at improving the radiometric and phase calibration of the four channels.

## 3. CALIBRATION PROCEDURE

### 3.1. Crosstalk Removal

The crosstalk removal procedure was inspired by the Quegan's polarimetric calibration procedure described in [3]. S. Quegan models the cross-talk by a Transmission and Reception matrices.

$$\begin{bmatrix} Sm_{Hh} & Sm_{Vh} \\ Sm_{Hv} & Sm_{Vv} \end{bmatrix} = \begin{bmatrix} R_{Hh} & R_{Vh} \\ R_{Hv} & R_{Vv} \end{bmatrix} \begin{bmatrix} S_{Hh} & S_{Vh} \\ S_{Hv} & S_{Vv} \end{bmatrix} \begin{bmatrix} T_{Hh} & T_{Vh} \\ T_{Hv} & T_{Vv} \end{bmatrix} =>$$

$$\begin{bmatrix} Sm_{Hh} & Sm_{Vh} \\ Sm_{Hv} & Sm_{Vv} \end{bmatrix} = \begin{bmatrix} 1 & \frac{w}{k} \\ u & \frac{1}{k} \end{bmatrix} \begin{bmatrix} S_{Hh} & S_{Vh} \\ S_{Hv} & S_{Vv} \end{bmatrix} \begin{bmatrix} \alpha k & \alpha kz \\ v & 1 \end{bmatrix}$$

$$\text{with} \quad \alpha = \frac{R_{Hh}}{R_{Vv}}\frac{T_{Vv}}{T_{Hh}}, \quad k = \frac{R_{Vv}}{R_{Hh}}$$

where $S_{mij}$ stands for the measured signal for the polarization channel $ij$, $S_{ij}$ the polarized signal on the ground, $R_{ij}$, reception matrix $T_{ij}$ Transmission matrix.

The $R$ and $T$ matrix coefficients are rewritten as a set of parameters $(u, v, w, z, \alpha, k)$. The complete set of parameters can be found in [3].

Under the hypothesis that the co-polar and cross-polar channels are uncorrelated over natural clutter (under the assumption of reflection symmetry), and that the $Hv$ channel and $Vh$ channel are equal (if one neglects the noise level). The covariance matrix $\langle S^* \cdot S \rangle$ can be written as:

$$\langle S^* \cdot S \rangle = \left\langle \begin{bmatrix} S_{Hh}^* \\ S_{Hv}^* \\ S_{Vv}^* \\ S_{Vv}^* \end{bmatrix} \cdot \begin{bmatrix} S_{Hh} & S_{Hv} & S_{Vh} & S_{Vv} \end{bmatrix} \right\rangle = \begin{bmatrix} \sigma_{Hh-Hh} & 0 & 0 & \sigma_{Hh-Vv} \\ 0 & \sigma_{Hv-Hv} & \sigma_{Hv-Vh} & 0 \\ 0 & \sigma_{Hv-Vh} & \sigma_{Vh-Vh} & 0 \\ \sigma_{Hh-Vv}^* & 0 & 0 & \sigma_{Vv-Vv} \end{bmatrix}$$

S. Quegan shows that the parameters $(u, v, w, z, \alpha)$ only depend on $\langle Sm^* \cdot Sm \rangle$. Therefore, they can be computed from the polarimetric covariance matrix estimated form the data.

In this experiment, we modified the Quegan's methodology by (1) removing the geometrical cross-talk due to attitude variation of the plane over the flight (2) estimating the Quegan's parameters both in range and frequency.

Figure 3 shows an example of the $\alpha$ parameter estimated over frequencies (vertical axis) and range (horizontal axis) on our data. This figure shows the dependency of the parameter with both range and frequency.

Figure 4 is a plot of the $v$ parameter according to the incidence angle before removing the aircraft attitude (left figure) and after removing the aircraft attitude. The different curves correspond to different acquisitions and attitude conditions. The $v$ parameters differ if the aircraft attitude is not removed whereas, they display the same behavior when the attitude is compensated.

### 3.2. Image Quality Improvement

The secondary bounce of the wave on the wing results in an antenna pattern deformation. This deformation depends on (1) the frequency, (2) the incidence angle of wave and (3) the polarization state. In order to remove this effect, we used the corner reflectors that have been placed across the swath on the calibration area. 5 corner reflectors were installed and several acquisitions were gathered using different flight configurations so that we have the frequency response of the corner reflectors for 11 incidences. By measuring the frequency response of each corner reflector on the images and interpolating these frequency responses in between, the residual radar transfer function was estimated and removed from the different channels.

### 4. RESULTS

In order to assess the quality of the calibration we used several measurements:

- we verified that the ratio $Hv/Vh$ was equal to 1 in intensity and 0 in phase.
- we measured the system noise by computing the $\langle Hv \cdot Hv^* \rangle$-$\langle Hv \cdot Vh^* \rangle$. This measurement should only be noise and should not depend on the nature of the ground. It is very useful measurement to assess the quality of the cross-talk removal. Results are shown on Figure
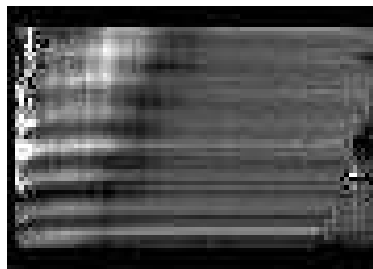


Figure 3: Quegan's parameter $\alpha$ estimated for different range and different frequencies on the TROPISAR data.
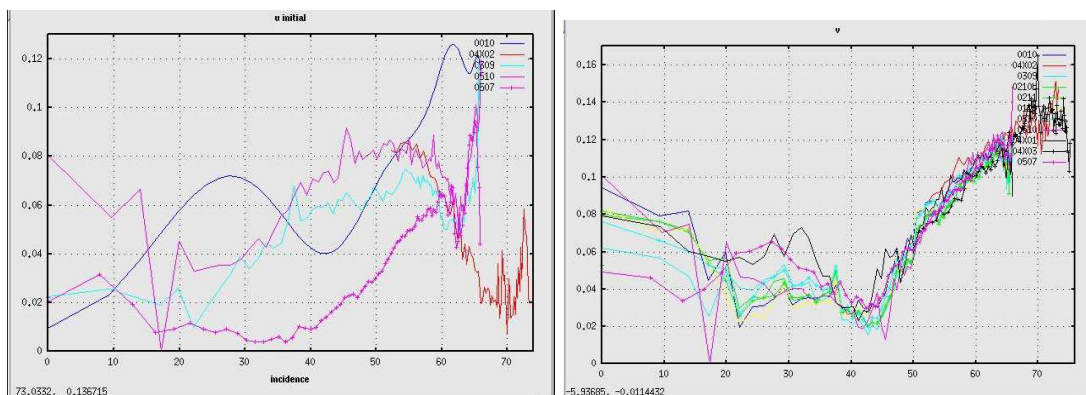


Figure 4: Quegan's parameter $v$ estimated over range before aircraft-attitude compensation (left image) and after aircraft-attitude compensation (right images). The different curves correspond to different data with different aircraft attitudes.

5. The left image corresponds to the noise image before cross-talk removal, the right image corresponds to the one after noise removal. The ground is less visible on the right image than on the left image showing that the cross-talk removal procedure was effective.

- We measured the radar cross section of the different corner reflectors across the swath to verify that the radiometry was correctly calibrated. Results are presenting in Table 1.

The final color composite after calibration is presented in Figure 6. The radiometric artifacts that were observed on Figure 2 have disappeared.

Table 1: Radar cross section of 3 corner reflectors placed across the swath for the different polarization states.

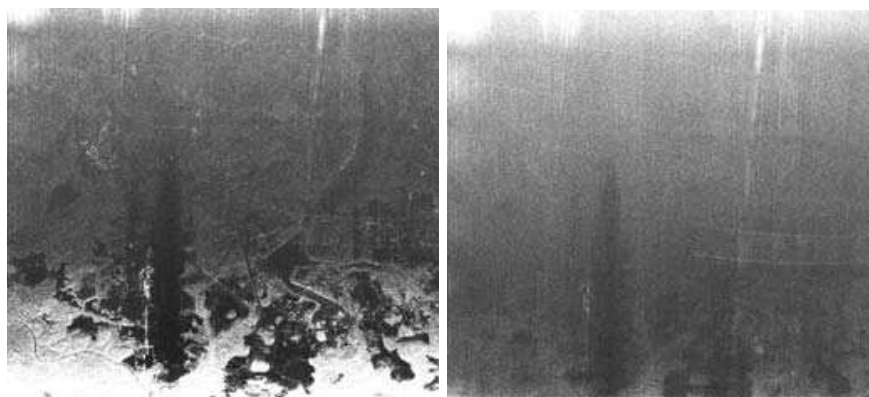| Polarization | Corner reflector #1 | Corner reflector #2 | Corner reflector #3 |
|:---:|:---:|:---:|:---:|
| $Vv$ | $22.6 \, \mathrm{dBm}^2$ | $23 \, \mathrm{dBm}^2$ | $23 \, \mathrm{dBm}^2$ |
| $Vh$ | $0.5 \, \mathrm{dBm}^2$ | $3.9 \, \mathrm{dBm}^2$ | $3.5 \, \mathrm{dBm}^2$ |
| $Hv$ | $0.7 \, \mathrm{dBm}^2$ | $3.8 \, \mathrm{dBm}^2$ | $3.5 \, \mathrm{dBm}^2$ |
| $Hh$ | $22.10 \, \mathrm{dBm}^2$ | $22.8 \, \mathrm{dBm}^2$ | $22.8 \, \mathrm{dBm}^2$ |



Figure 5: Noise image computed using the cross-polarized channels before (left image) and after (right image) cross-talk removal.
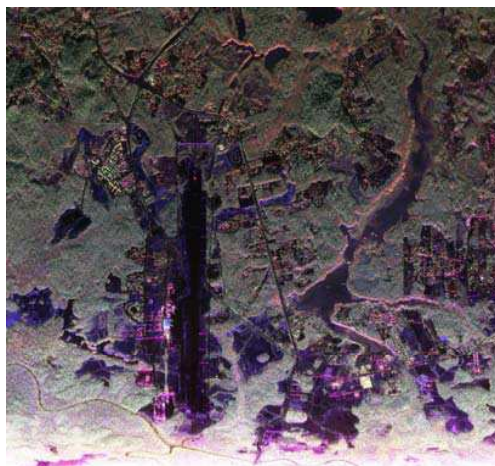


Figure 6: Color composite of the calibration test-site (Rochambeau airport, French Guiana) after calibration (right). $Hh$ channel appears in red, $Hv$, in green, $Vv$ in blue. The aircraft is flying from the left-bottom of the image to the right bottom of the image.

## 5. CONCLUSION

In this paper, a calibration procedure for large band UHF full polarimetric data was developed. This procedure is based on a modified version of the Quegan's algorithm and the estimation/correction of a the residual radar transfer function across the swath, which was found to depend on range due to a secondary bounce of the incident wave on the aircraft wing.

## REFERENCES

1. Bonin, G. and P. Dreuillet, "The airborne SAR-system: SETHI — Airborne microwave remote sensing imaging system," *Proceedings of EUSAR*, 2008.
2. Cantalloube, H. and P. Dubois-Fernandez, "Airborne X-band SAR imaging with 10 cm resolution: technical challenge and preliminary results," *IEE Proc. Radar Sonar Navig.*, Vol. 153, No. 2, April 2006.
3. Quegan, S., "A unified algorithm for phase and cross-talk calibration of polarimetric data – Theory and observations," *IEEE Trans. Geosci. Remote Sensing*, Vol. 32, 89–99, 1994.

# Towards a Polarimetric SAR Processor for Airborne Sensor

**H. M. J. Cantalloube[1], B. Fromentin-Denoziere[1], and C. E. Nahum[2]**

[1]ONERA (Office National d'Études et Recherches Aérospatiales), Palaiseau, France
[2]DGA (Direction Génŕale pour l'Armement), Bagneux, France

**Abstract**— True polarimetric SAR imaging with an airborne radar is difficult due to carrier fluctuations in attitude during acquisition that modify the polarisation axes through the integration time. Even worse, at lower frequency, the wide antenna pattern (and wide angle of integration) results in an interaction between the radiated waves and the surrounding aircraft cell, causing a significant deviation of the illumination pattern from the "centre of phase" (point-like) model, and yielding non linear effective polarisation off-axis.

Here are described improvements in frequency domain SAR processing that should allow to include time-varying factor in the azimuth integration thus compensating for antenna pattern beyond the centre of phase hypothesis. This factor can be complex (already implemented today) and even a complex matrix (work in progress) thus allowing true polarimetric SAR image synthesis.

An example is given with SETHI, the airborne Radar developed at ONERA for which a UHF/VHF (two linear polarised) antenna is attached in a pod under a Falcon 20 jet aircraft wing. The far field radiation including both the antenna itself and the aircraft cell interactions has been modelled by finite elements, and the resulting illumination field (during the effective integration time) for one of the linear polarised channel can be simulated. From this simulation, we can evaluate the backscattering matrix error made by ignoring the aircraft attitude motion and depolarisation (i.e., simple channel calibration and per channel SAR image synthesis) or by including only rotation of the polarisation axes for compensating attitude changes.

## 1. INTRODUCTION

As ONERA recently added an UHF/VHF (222 to 470 MHz) component to its airborne SAR system Sethi (which replaces the former RAMSES system), investigations were conducted in order to determine the most appropriate location and design of the antenna inside the two pods under the carrier aircraft wings (a Falcon 20). The proposed antenna is made of two dipole pairs (for polarimetric measurements) with a cylindrical reflector on its back, either positioned in the front of the pod partially beyond the leading edge of the wing, or positionned just below the wing. A set of angles of incidence was also considered (for the trade-offs between left-right ambiguities and the reflections on the wing surface).

Due to the proximity of the wing and the large wavelength, the antenna pattern is highly distorted compared to that of the naked antenna. Furthermore, as we wish azimuth resolutions similar to attainable range resolution (60 cm), a wide integration angle (around 32 degrees) is required. Finite elements modelling of the antenna including the surrounding aircraft with the program ELSEM3D allowed to compute the far field radiation of the antenna in various candidate operating positions. Simulations showed that the "centre of phase" approximation does not hold to the accuracy required by SAR processing in any case.

However, the forward antenna position was discarded because the phase variation along azimuth angle (mainly due to strong reflections on the tilted leading edge) is strongly frequency dependent, while this effect is mostly confined to the elevation angle in the central antenna position. Since the integration for SAR image synthesis is mostly along the azimuth angle, a strong frequency dependency would have made the focusing during the synthesis more difficult and more sensitive to the unavoidable modelling error of the pattern computation.

The phase variation with squint during integration must be corrected for (in a similar manner to motion compensation) and is more or less comparable to a complex value for the antenna pattern. This algorithmic improvement, decisive even in focusing non polarimetric SAR image synthesis will be described below.

Finite elements modelling also showed that the radiated waves from each of the two antenna feeds could not be approximated as a linear polarised light with axis in the direction of the excited antenna axis, but a small but significant cross-polarisation component (i.e., elliptically polarisation) was also radiated.

Previously, polarimetric images were obtained by computing 16 single look complex images (combined later into the 4 polarimetric single look complex images). Each image is computed for one transmit and one receive antenna ports and during the azimuth integration, its signal was multiplied by the cosine or sinus of the angle between the antenna axes and the terrain vertical. This angle varies during integration due to both attitude fluctuations and motion nonlinearities of the aircraft trajectory. Due to the difficulty of including this time-varying factor in the frequency domain processor, this polarimetric processing was done in time domain (2-stage factored, but still slow compared to frequency domain processing). The new frequency domain algorithm allows this type of processing, but the elliptical component would require to synthesise simultaneously the 4 channel images, and, instead of a scalar complex antenna pattern, apply a complex polarisation restauration matrix. Design of such a processor will be sketched at the end of the paper.

## 2. ANTENNA PATTERN MODELLING AND DEPOLARISATION SIMULATION

Antenna patterns (Fig. 1) obtained by a mesh of the aircraft and the antenna with the rear position at 45 degree incidence (the configuration eventually used for acquisitions) show strong variations in elevation angle, but slow variations in azimuth (though the variation in phase should be compensated for). At the lower end of the bandwidth, the strong reflection on the wing causes a near blind spot slightly above antenna axis and a strong over-Nadir transmission. This results in a strong left-right ambiguity that triggers the investigation in progress on more grazing (or even upwards)
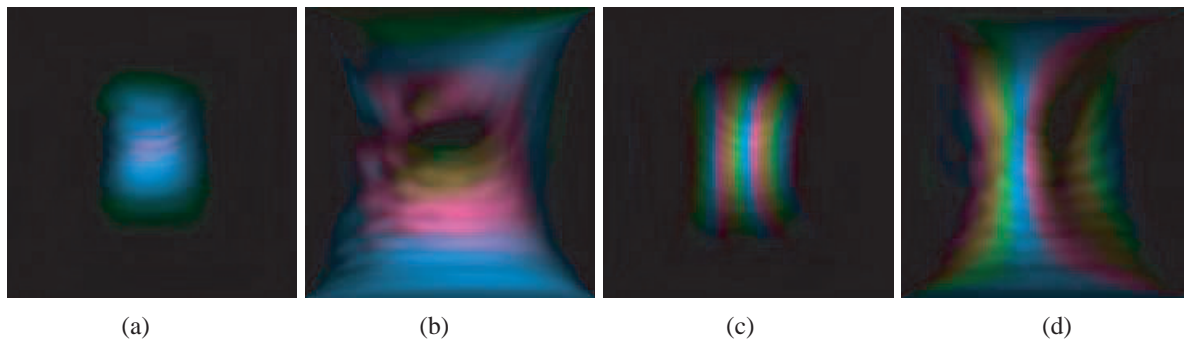


(a)                    (b)                    (c)                    (d)

Figure 1: Antenna pattern with aircraft interaction at 460 MHz (a) and 222 MHz (b) $V$ polar channel, phase is colour-coded. antenna axis (45 degree incidence) is at the middle, elevation angle is vertical axis, horizon is at 25% from the top edge and Nadir is at 25% from the bottom edge. Patterns at the right are the corresponding radiation with the antenna in the forward position inside the pod, showing the strong phase variation with azimuth and its frequency dependency.
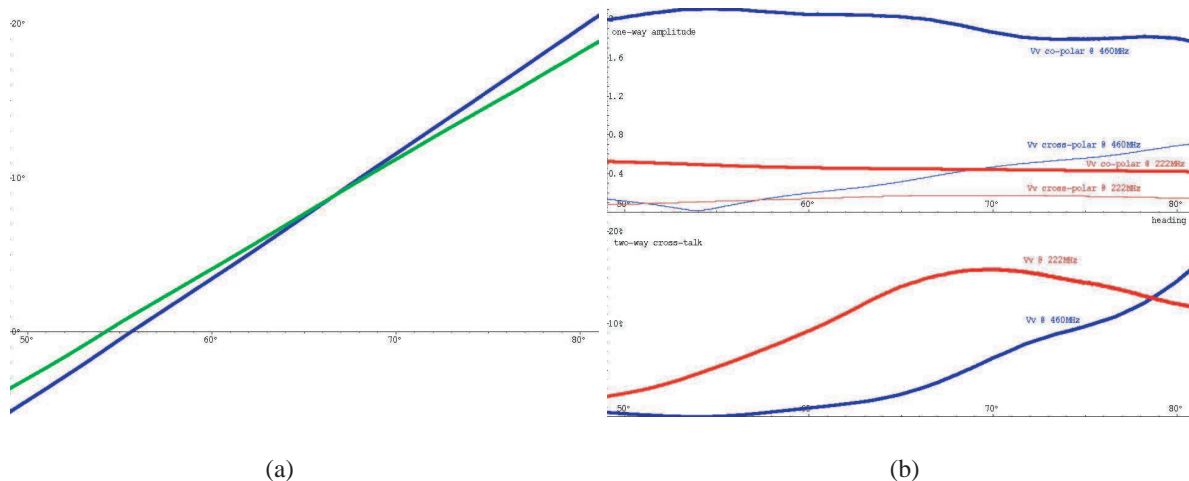


(a)                                              (b)

Figure 2: Angle between the antenna axes (blue = $H$, green = $V$) and the ground relative horizontal and vertical directions towards one of the corner reflectors during the 32-integration around the zero-Doppler direction of the acquisition of Fig. 6. (a). Amplitude of the inter channel contamination (crosstalk, blue = highest frequency, red = lowest frequency) due to both attitude and elliptical polarisation of effective radiation (b).

angle steering of the antenna in order to use the wing as a reflector for the antenna.

The low accuracy of the polarimetric quality of the SAR images synthesised from the raw sensor channel signals can be assessed by computing, with a real acquisition trajectory, the rotation during integration of the sensor axes relative to the ground and by adding the contribution of the elliptical (cross-polarisation) component of the far field radiation of the antenna with its surrounding aircraft body (Fig. 2). It should be emphasised that a cross-talk $Hh$ to $Vv$ of 10% on average is far from negligible and that the $Vv$ component is also contaminated with the one-way cross-talk by the $Hv$ target response (generally some 3 dB below direct polarisation response). Cross-polar contamination are even worse because the one-way cross-talk applies on the stronger direct polarisation response.



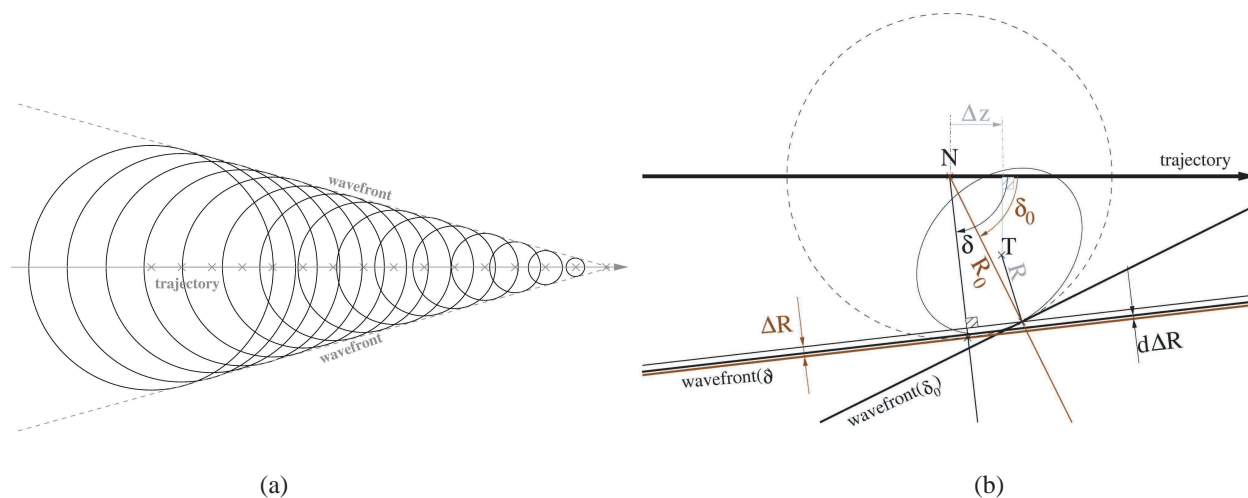(a)                                                                              (b)

Figure 3: Principle for the frequency domain processing, the signal component for a given bandwidth and Doppler frequency for perfect linear uniform acquisition corresponds to a single space frequency of the image in cylindrical or slant-range coordinate (a). If the trajectory deviates from linear uniform, the 0th and 1st order motion compensation is made by range migration $R - R_0$ and azimuth migration $\Delta Z$, while higher order compensation requires to locally alter the "nominal processing phase" $\Delta R$ function of the squint angle $\delta$ by the "quadratic phase" $d\Delta R$ (b).

## 3. PRESENT FREQUENCY DOMAIN SAR PROCESSOR

Frequency domain processing is based on the fact that for perfect linear uniform monostatic acquisition, a point in the 2D signal spectrum can be mapped (the map is called "stolt interpolation") to a point of the 2D focused image spectrum. Fig. 3(a) illustrates this by representing a wavefront of a nonzero Doppler pure frequency signal radiated at half the light velocity (thus making equivalent the two-ways propagation to a single-way one). However, for an airborne acquisition, the unavoidable trajectory irregularities must be compensated for. The motion compensation ("mocomp" for short) involves range and azimuth migration i.e., time domain resampling of the signal, which are intrinsically a wide-band process for low order mocomp and, for higher order mocomp, a "quadratic phase" local correction (Fig. 3(b)) so called because it is roughly a quadratic function of the difference between the local and nominal squint angles $\delta - \delta_0$. Since this compensation depends both of range azimuth and $\delta$ it must be performed in range-Doppler domain as a phase correction and is thus narrow-band in nature. In our processor (Fig. 4) the quadratic phase is compensated for by small azimuth sub-blocks, and in fact the average quadratic phase on the full bloc is compensated for during the nominal processing (in frequency domain, thus wide-band), and only the local deviations of the quadratic phase are compensated in the range-Doppler domain (Fig. 5). Note that in Fig. 3 the motion compensation is unrealistically emphasised (the true trajectory deviates by half of the nominal range from the nominal trajectory) and in Fig. 5 an ultra wide band type of aperture is depicted (it is typical of the processing of the CARABAS system of the Swedish FOI).

In this processor design, it was easy to include an antenna pattern phase (as an addition to the mocomp quadratic phase) and focus SAR images acquired with our new antenna (Fig. 6).
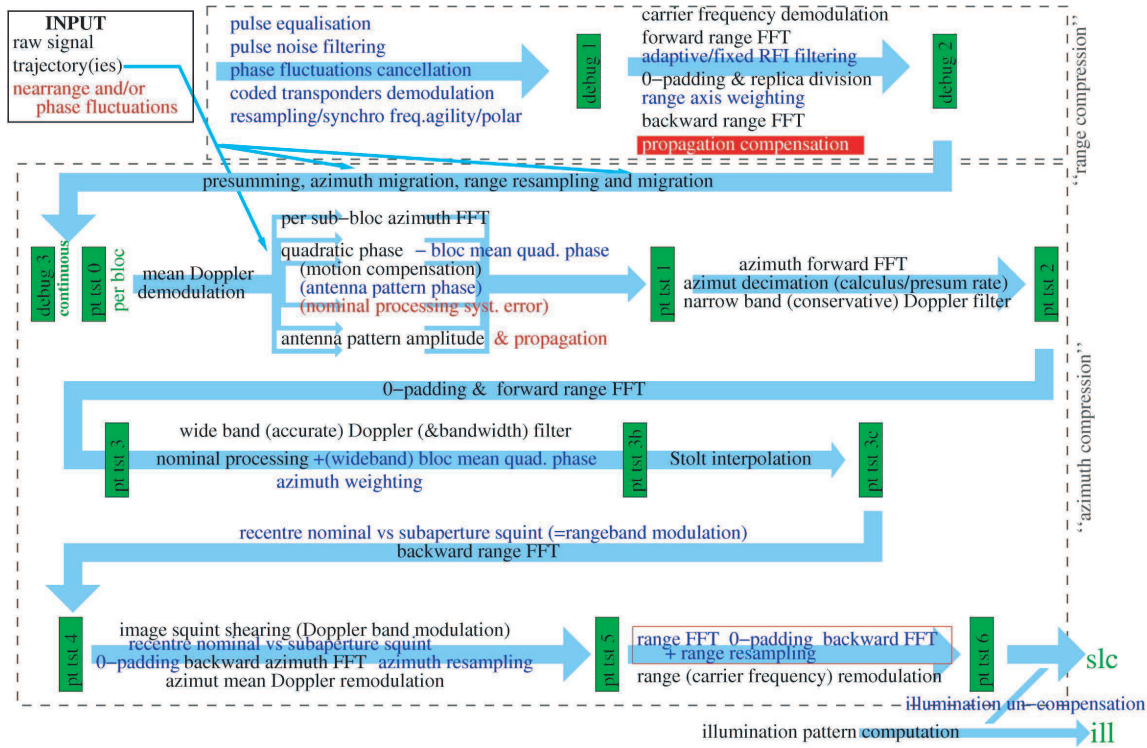
Figure 4: Synoptic of the frequency domain SAR processor (present state). Black indicates mandatory steps, (red mandatory steps for bistatic case, and red background forbidden steps for bistatic case). Blue indicates optional steps, and green outputs (green background test/debug output points).
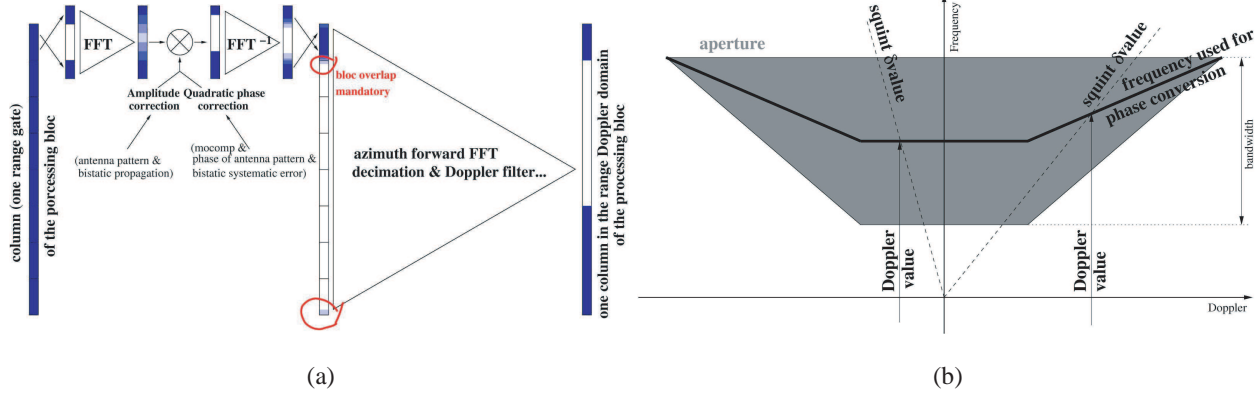


(a)                                     (b)

Figure 5: Detail of the sub-block compensation of the quadratic phase (a). Frequency within the bandwidth and squint (wavefront) angle used for compensating the quadratic phase, emphasising the narrow band approximation (b).

## 4. TOWARDS A TRUE POLARIMETRIC SAR PROCESSOR FOR AIRBORNE ACQUISITIONS

A truly polarimetric frequency domain SAR processor can be derived from the above described design. The idea is to run simultaneously 4 instances of the processor (one for each polarisation channel). The image grid must be the same for all channels, hence there should be a trajectory offset at the azimuth migration stage for compensating for the time separation because in our system each polarisation channel (both transmit and receive at UHF/VHF, only transmit at high frequency bands) are acquired on successive radar pulses. At the stage where quadratic phase is compensated for, the four range Doppler terms for the raw sensor polar channels $Hh$, $Hv$, $Vh$ and $Vv$ (upper case is the transmit feed, lower case is the receive port) must be corrected by a $2 \times 2$ complex matrix coordinate change to yield the polarimetric channel corrected to local (from the
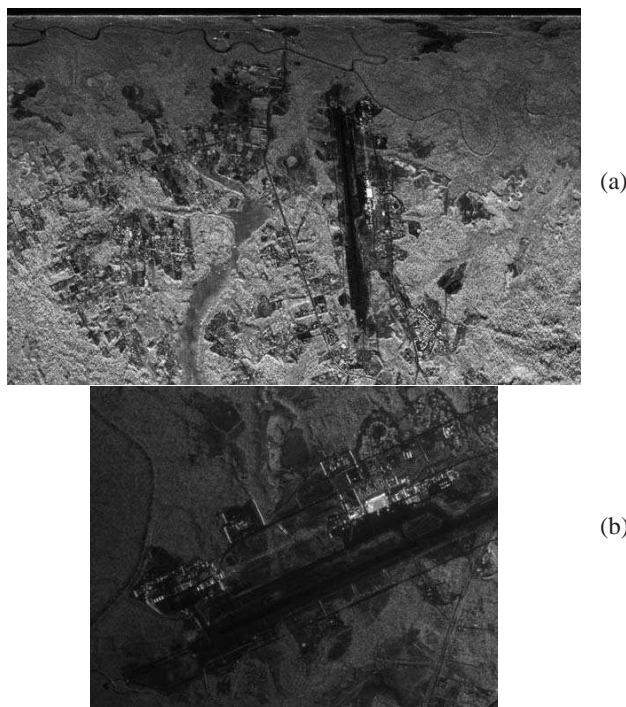
Figure 6: P-band (400–460 MHz) single look image, $V$ polar channel, with 8 degree squint angle, computed using frequency domain processing. Aircraft is flying from right to left on top of the image (left side imaging). Observe the strong Nadir reflection on the ground and the dim backscatter of the vegetation cover just above it (it is interrupted above the dark area corresponding to free water with low vegetation). Scene is the French Guyana airport located in Amazon rain forest (a). Detail of geocoded 5-look image, $V$ polar channel, computed using frequency domain processing. Bright echoes along the road South-East from the runway are calibrating corner reflectors and the airport VOR (radio navigation) antenna (b).

ground viewpoint) $H$ and $V$ directions.

$$\left[ \begin{array}{cc} Hh_{loc} & Hv_{loc} \\ Vh_{loc} & Vv_{loc} \end{array} \right] = A^T \left[ \begin{array}{cc} Hh & Hv \\ Vh & Vv \end{array} \right] A, \text{ with } A = \left( \left[ \begin{array}{c} \hat{H}_{loc} \\ \hat{V}_{loc} \end{array} \right] \left[ \begin{array}{cc} \vec{E}_H & \vec{E}_V \end{array} \right] \right)^{-1}$$

where $\vec{E}_H$ is the complex electrical field components radiated from feed $H$ and $\hat{H}_{loc}$ the unit vector of the horizontal direction at the aim point on the ground. Once this restauration is done, each instance of the SAR processor goes on with the signal corresponding to a ground relative linear polarisation basis.

## 5. CONCLUSIONS AND PERSPECTIVES

The SAR processor described above is yet to be implemented, but the work is in progress for a simpler (but less efficient) 16-pass version and comparison between full images obtained from the raw sensor polarimetry channels and obtained with corrected ground polarisation axes should be available at the time of conference.

However, the simple point computation of the polarisation channels contamination through the wide integration angle required at low frequency already demonstrated that the airborne polarimetric SAR image computed by merely calibrating the sensor (even in the accurate way described in [1]) may produce single digit accuracy for direct polarisation and irrelevant data for cross polarisation. Due to the high sensitivity of some polarimetric parameters derived from the scattering matrix, even in less critical conditions (narrower integration and antenna pattern) the careful compensation of aircraft attitude and antenna depolarising is mandatory for polarimetric airborne SAR imaging.

## REFERENCES

1. Cantalloube, H. M. J., É. Colin, V. Giroux, L. Pastore, et al., "Polarimetric repeat-pass interferometric airborne UHFSAR data acquisition and calibration," *Proceeding of PolInSAR Conference*, Frascati, Italy, January 17–21, 2005.

# Polarimetric SAR Image Classification Using Radial Basis Function Neural Network

**Turker Ince**

Izmir University of Economics, Izmir, Turkey

**Abstract**— This paper presents a robust radial basis function (RBF) network based classifier for polarimetric synthetic aperture radar (SAR) images. The proposed feature extraction process utilizes the covariance matrix, the gray level co-occurrence matrix (GLCM) based texture features, and the backscattering power (Span) combined with the $H/\alpha/A$ decomposition, which are projected onto a lower dimensional feature space using principal component analysis. For the classifier training two popular techniques are explored: conventional backpropagation (BP) and particle swarm optimization (PSO). By using both polarimetric covariance matrix and decomposition based pixel values and textural information (contrast, correlation, energy, and homogeneity) in the feature set, classification accuracy is improved. An experimental study is performed using the fully polarimetric San Francisco Bay and Flevoland data sets acquired by the NASA/Jet Propulsion Laboratory Airborne SAR (AIRSAR) at L-band to evaluate the performance of the proposed classifier. Classification results (in terms of confusion matrix, overall accuracy and classification map) compared with competing state of the art algorithms demonstrate the effectiveness of the proposed RBF network classifier.

## 1. INTRODUCTION

Image and data classification techniques play an important role in the automatic analysis and interpretation of remote sensing data. Particularly polarimetric synthetic aperture radar (SAR) data poses a challenging problem in this field due to complexity of measured information from its multiple polarimetric channels. Recently, the number of applications which use data provided by the SAR systems having fully polarimetric capability have been increasing. Over the past decade, there has been extensive research in the area of the segmentation and classification of polarimetric SAR data. In the literature, the classification algorithms for polarimetric SAR can be divided into three main classes: 1) classification based on physical scattering mechanisms inherent in data [1, 2], 2) classification based on statistical characteristics of data [3, 4] and 3) classification based on image processing techniques [5, 6]. Additionally, there has been several works using some combinations of the above classification approaches [3, 1]. While these approaches to the polarimetric SAR classification problem can be based on either supervised or unsupervised methods, their performance and suitability usually depend on applications and the availability of ground truth.

As one of the earlier algorithms, Kong et al. [7] derived a distance measure based on the complex Gaussian distribution and used it for maximum-likelihood (ML) classification of single-look complex polarimetric SAR data. For multilook data represented in covariance or coherency matrices, Lee et al. [3] proposed a new unsupervised classification method based on combination of polarimetric target decomposition (specifically the Cloude and Pottier decomposition [8]) and the maximum likelihood classifier using the complex Wishart distribution. The unsupervised Wishart classifier has an iterative procedure based on the well-known *K-means* algorithm, and has become a preferred benchmark algorithm due to its computational efficiency and generally good performance. However, this classifier still has some significant drawbacks since it entirely relies on *K-means* for actual clustering, such as it may converge to local optima, the number of clusters should be fixed *a priori*, its performance is sensitive to the initialization and its convergence depends on several parameters. Recently, a two-stage unsupervised clustering based on the EM algorithm [9] is presented for classification of polarimetric SAR images. The EM algorithm estimates parameters of the probability distribution functions which represent the elements of a 9-dimensional feature vector, consisting of six magnitudes and three angles of a coherency matrix. In [6], a new wavelet-based texture image segmentation algorithm is successfully applied to unsupervised SAR image segmentation problem. More recently, neural network based approaches [10, 11] for classification of polarimetric synthetic aperture radar data have been shown to outperform other aforementioned well-known techniques. Compared with other approaches, neural network classifiers have the advantage of adaptability to the data without making *a priori* assumption of a particular probability model or distribution. However, their performance depends on the network structure, training data, initialization and

parameters. In this study, the RBF neural network classifier is chosen due to its robustness, faster learning capability compared with other feedforward networks, and superior performance with simpler network architectures. The performance of the proposed RBF network classifier is evaluated using the fully polarimetric San Francisco Bay and Flevoland data sets acquired by the NASA/Jet Propulsion Laboratory Airborne SAR (AIRSAR) at L-band. The classification results (in terms of confusion matrix, overall accuracy and classification map) are compared with competing state of the art classifiers.

## 2. POLARIMETRIC SAR DATA PROCESSING

Polarimetric radars measure the complex scattering matrix $S$ produced by a target under study with the objective to infer its physical properties. Assuming linear horizontal and vertical polarizations for transmitting and receiving, $S$ can be expressed as

$$S = \begin{bmatrix} S_{hh} & S_{hv} \\ S_{vh} & S_{vv} \end{bmatrix} \tag{1}$$

Reciprocity theorem applies in a monostatic system configuration, $S_{hv} = S_{vh}$. For coherent scatterers only, the decompositions of the measured scattering matrix $S$ can be employed to characterize the scattering mechanisms of such targets. Alternatively, the second order polarimetric descriptors of the $3 \times 3$ average polarimetric covariance $\langle [C_3] \rangle$ and the coherency $\langle [T_3] \rangle$ matrices can be employed to extract physical information from the observed scattering process. The elements of the covariance matrix can be written in terms of three unique polarimetric components of complex scattering matrix:

$$\begin{array}{ll} C_{11} = S_{hh}S_{hh}^*, & C_{21} = S_{hh}^* S_{hv} \\ C_{22} = S_{hv}S_{hv}^*, & C_{32} = S_{hv}^* S_{vv} \\ C_{33} = S_{vv}S_{vv}^*, & C_{31} = S_{hh}^* S_{vv} \end{array} \tag{2}$$

For single-look processed polarimetric SAR data, the three polarimetric components ($HH$, $HV$, and $VV$) has a multivariate complex Gaussian distribution and the complex covariance matrix form has a complex Wishart distribution [13]. Due to presence of speckle noise and random vector scattering from surface or volume, polarimetric SAR data are often multi-look processed by averaging $n$ neighboring pixels.

Cloude-Pottier decomposition [8] is based on eigenanalysis of the polarimetric coherency matrix, $\langle [T] \rangle$:

$$\langle T \rangle = \lambda_1 e_1 e_1^{*T} + \lambda_2 e_2 e_2^{*T} + \lambda_3 e_3 e_3^{*T} \tag{3}$$

where $\lambda_1 > \lambda_2 > \lambda_3 \geq 0$ are real eigenvalues and the corresponding orthonormal eigenvectors $e_i$ (representing three scattering mechanisms) are

$$e_i = e^{i\phi_i} \left[ \cos \alpha_i, \ \sin \alpha_i \cos \beta_i e^{i\delta_i}, \ \sin \alpha_i \sin \beta_i e^{i\gamma_i} \right]^T. \tag{4}$$

Cloude and Pottier defined entropy $H$ and average of alpha angle, $\bar{\alpha}$ for analysis of the physical information related to the scattering characteristics of a medium:

$$H = -\sum_{i=1}^{3} p_i \log_3 p_i \quad \text{where} \quad p_i = \frac{\lambda_i}{\sum_{i=1}^{3} \lambda_i}. \tag{5}$$

$$\bar{\alpha} = \sum_{i=1}^{3} p_i \alpha_i \tag{6}$$

For a multi-look coherency matrix, the entropy, $0 \leq H \leq 1$, represents the randomness of a scattering medium between isotropic scattering ($H = 0$) and fully random scattering ($H = 1$), while the average alpha angle can be related to target average scattering mechanisms from single-bounce (or surface) scattering ($\bar{\alpha} \approx 0$) to dipole (or volume) scattering ($\bar{\alpha} \approx \pi/4$) to double-bounce scattering ($\bar{\alpha} \approx \pi/2$). Due to basis invariance of the target decomposition, $H$ and $\alpha$ are roll invariant

hence they do not depend on orientation of target about the radar line of sight. Additionally, information about target's total backscattered power can be determined by the *span* as

$$span = \sum_{i=1}^{3} \lambda_i \qquad (7)$$

$H$, $\bar{\alpha}$, and span calculated by the above noncoherent target decomposition method have been widely used as the main polarimetric features of a scatterer in many target classification schemes.

## 3. FEATURE EXTRACTION

The proposed feature extraction process utilizes the complete covariance matrix information, the gray level co-occurrence matrix (GLCM) based texture features, and the backscattering power (*span*) combined with the $H/\alpha/A$ decomposition [8]. As suggested by the previous studies [14, 10] appropriate texture measures for SAR imagery based on the gray level co-occurrence probabilities are included in the feature set to improve its discrimination power and classification accuracy. In this study, *contrast*, *correlation*, *energy*, and *homogeneity* features are extracted from normalized GLCMs which are calculated using interpixel distance of 2 and averaging over four possible orientation settings ($\theta = 0°$, $45°$, $90°$, $135°$).

To reduce the dimensionality (and redundancy) of input feature space, the principal components transform is applied and the most principal components (in this paper, ten principal components are selected) are then selected as features.

## 4. RBF NEURAL NETWORKS

An artificial neural network (ANN) consists of a set of connected processing units, usually called neurons or nodes. ANNs can be described as directed graphs, where each node performs some activation function to its inputs and then gives the result forward to be the input of some other neurons until the output neurons are reached. ANNs can be divided into feedforward and recurrent networks according to their connectivity. In a recurrent ANN there can be backward loops in the network structure, while in feedforward ANNs such loops are not allowed. A popular type of feedforward ANN is the radial basis function (RBF) network [15], which has always two layers in addition to the passive input layer: a hidden layer of RBF units and a linear output layer. Only the output layer has connection weights and biases. The activation function of the kth RBF unit is defined as,

$$y_k = \varphi \left( \frac{\|X - \mu_k\|}{\sigma_k^2} \right), \qquad (8)$$

where $\varphi$ is a radial basis function or, in other words, a strictly positive radially symmetric function, which has a unique maximum at $N$-dimensional center $\mu_k$ and whose value drops rapidly close to zero away from the center. $\sigma_k$ is the width of the peak around the center $\mu_k$. The activation function gets noteworthy values only when the distance between the $N$-dimensional input $X$ and the center $\mu_k$, $\|X - \mu_k\|$ is smaller than the width $\sigma_k$. The most commonly used activation function in RBF networks is the Gaussian basis function defined as

$$y_k = \exp \left( -\frac{\|X - \mu_k\|^2}{2\sigma_k^2} \right), \qquad (9)$$

where $\mu_k$ and $\sigma_k$ are the mean and standard deviation, respectively, and $\|.\|$ denotes the Euclidean norm. More detailed information about RBF networks can be obtained from [15] and [16].

In this study, two distinct training methods for RBF network classifiers, the traditional backpropagation (BP) and particle swarm optimization (PSO) are investigated. For the BP algorithm, RPROP enhancement is used when training RBF networks. The main difference in RPROP is that it modifies the update-values for each parameter according to the sequence of signs of partial derivatives. This only leads to a faster convergence, while the problems of a hill-climbing algorithm are not solved. Further details about BP and RPROP can be found in [17] and [18], respectively. For PSO-based training, the proposed approach is to apply multi-dimensional particle swarm optimization (MD PSO) [19] based dynamic clustering to determine the optimal number of Gaussian neurons with their correct parameters (centroids and variances). Afterwards, BP can conveniently be used to compute the remaining network parameters, weights ($w$) and bias ($\theta$) of the each output layer neuron.

## 5. EXPERIMENTAL RESULTS

The NASA/Jet Propulsion Laboratory Airborne SAR (AIRSAR) L-band data of the San Francisco Bay and Flevoland are used for performance evaluation of the proposed RBF network classifier. The original four-look fully polarimetric SAR data of the San Francisco Bay, having a dimension of $900 \times 1024$ pixels, provides good coverage of both natural (sea, mountains, forests, etc.) and man-made targets (buildings, streets, parks, golf course, etc.) with a more complex inner structure. In this study, the sub-area with size $600 \times 600$ is extracted and used for the purpose of comparing the classification results with the Wishart [3] and the NN-based [10] classifiers. The aerial photographs for this area which can be used as ground-truth are provided by the TerraServer Web site [20]. In this study, the speckle filter suggested by Lee et al. [21] is employed with $5 \times 5$ window to preserve the texture information as recommended.

The same training and testing areas for three classes, the sea (15810, 6723 pixels respectively), urban areas (9362, 6800), and the vegetated zones (5064, 6534) which are manually selected in an earlier study [10] are also used for training and testing of the proposed classifier in this study. The confusion matrix of the proposed method on the training and testing areas are given in Table 1. The classification accuracy values are averaged over 10 independent runs. From the results, the main drawback of the proposed method is the separation of vegetated zones from urban areas. Compared to two other competing techniques, the proposed method is able to differentiate better the uniform areas corresponding to main classes of scattering such as the ocean, vegetation, and building areas. In Table 2, the overall accuracies in training and testing areas for the proposed RBF classifier trained using the BP and PSO algorithms and two competing methods, the Wishart Maximum Likelihood (WML) classifier [3] and the NN-based classifier [10], are compared. The proposed RBF classifier trained by the global PSO algorithm is superior to the WML and NN-based methods with higher accuracies in both training (99.5%) and testing (99.0%) areas. The classification map of the whole image produced by the proposed classifier is shown in Fig. 1.

The overall classification results of the proposed RBF classifiers and two competing methods, the wavelet-based [22] and NN-based [10] classifiers, for the Flevoland dataset (an agricultural area in the Netherlands) are also given in Table 3.

Table 1: Summary table of pixel-by-pixel classification results of the proposed RBF-PSO method for the training and testing data of San Francisco Bay.

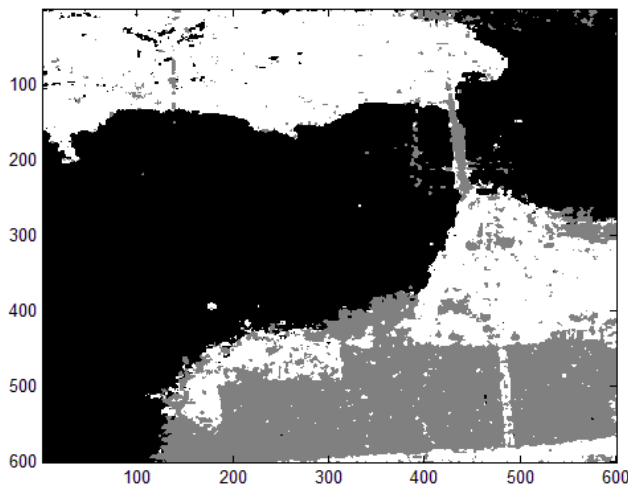|  | Training data | | | Test data | | |
|---|---|---|---|---|---|---|
|  | **Sea** | **Urb** | **Veg** | **Sea** | **Urb** | **Veg** |
| **Sea** | 14264 | 4 | 0 | 6804 | 0 | 0 |
| **Urb** | 11 | 9422 | 22 | 10 | 6927 | 23 |
| **Veg** | 10 | 87 | 4496 | 21 | 162 | 6786 |



Figure 1: The classification results of the proposed RBFPSO technique on the extracted $600 \times 600$ sub-image of San Francisco Bay (black denotes sea, gray urban areas, white vegetated zones).

Table 2: Overall performance comparison (in percent) for San Francisco Bay dataset.

| Method | Training Area | Testing Area |
|---|---|---|
| RBF-BP | 97.87 | 95.70 |
| WML [3] | 97.23 | 96.16 |
| NN [10] | 99.42 | 98.64 |
| **RBF-PSO** | **99.50** | **99.0** |

Table 3: Overall performance comparison (in percent) for Flevoland dataset.

| Method | Training Area | Testing Area |
|---|---|---|
| Wavelet-based [22] | - | 88.28 |
| RBF-BP | 95.14 | 92.07 |
| NN [10] | **98.62** | 92.87 |
| **RBF-PSO** | 97.30 | **95.51** |

## 6. CONCLUSIONS

In this paper, the RBF network classifier for classification of polarimetric SAR data has been proposed. Two different learning algorithms, the backpropagation and particle swarm optimization, were applied for the proposed classifier training. The promising results were obtained for the San Francisco Bay and Flevoland datasets and compared to competing state of the art classifiers. More experiments using larger real data sets will be done for further validation.

**REFERENCES**

1. Pottier, E. and J. S. Lee, "Unsupervised classification scheme of POLSAR images based on the complex Wishart distribution and the $H/A/\alpha$-Polarimetric decomposition theorem," *Proc. of the 3rd EUSAR 2000 Conf.*, May 2000.
2. Van Zyl, J. J., "Unsupervised classification of scattering mechanisms using radar polarimetry data," *IEEE Trans. Geosci. Remote Sensing*, Vol. 27, 36–45, Jan. 1989.
3. Lee, J. S., M. R. Grunes, T. Ainsworth, L.-J. Du, D. Schuler, and S. R. Cloude, "Unsupervised classification using polarimetric decomposition and the complex Wishart classifier," *IEEE Trans. Geosci. Remote Sens.*, Vol. 37, No. 5, 2249–2257, Sep. 1999.
4. Wu, Y., K. Ji, W. Yu, and Y. Su, "Region-based classification of polarimetric SAR images using Wishart MRF," *IEEE Geosci. Rem. Sens. Lett.*, Vol. 5, No. 4, 668–672, 2008.
5. Tan, C. P., K. S. Lim, and H. T. Ewe, "Image processing in polarimetric SAR images using a hybrid entropy decomposition and maximum likelihood (EDML)," *Proc. Int. Symposium on Image and Signal Processing and Analysis (ISPA)*, 418–422, Sep. 2007.
6. Ye, Z. and C.-C. Lu, "Wavelet-based unsupervised SAR image segmentation using hidden markov tree models," *Proc. of the 16th International Conference on Pattern Recognition (ICPR'02)*, Vol. 2, 20729, 2002.
7. Kong, J. A., A. A. Swartz, H. A. Yueh, L. M. Novak, and R. T. Shin, "Identification of terrain cover using the optimum polarimetric classifier," *Journal of Electromagnetic Waves and Applications*, Vol. 2, No. 2, 171–194, 1988.
8. Cloude, S. R. and E. Pottier, "An entropy based classification scheme for land applications of polarimetric SAR," *IEEE Trans. Geosci. Remote Sensing*, Vol. 35, 68–78, Jan. 1997.
9. Khan, K. U., J. Yang, and W. Zhang, "Unsupervised classification of polarimetric SAR images by EM algorithm," *IEICE Transactions on Communications*, Vol. 90, No. 12, 3632–3642, 2007.
10. Zhang, Y. D., L.-N. Wu, and G. Wei, "A new classifier for polarimetric SAR images," *Progress In Electromagnetics Research*, PIER 94, 83–104, 2009.
11. Yang, S. Y., M. Wang, and L. C. Jiao, "Radar target recognition using contourlet packet transform and neural network approach," *Signal Processing*, Vol. 89, No. 4, 394–409, 2009.
12. Kiranyaz, S., T. Ince, A. Yildirim, and M. Gabbouj, "Fractional particle swarm optimization in multi-dimensional search space," *IEEE Transactions on Systems, Man, and Cybernetics — Part B*, Vol. 40, No. 2, 298–319, 2010.
13. Lee, J. S., M. R. Grunes, and R. Kwok, "Classification of multi-look polarimetric SAR imagery based on complex Wishart distribution," *Int. J. Rem. Sens.*, Vol. 15, No. 11, 2299–2311, 1994.
14. Clausi, D. A., "An analysis of co-occurrance texture statistics as a function of grey level quantization," *Canadian J. Remote Sensing*, Vol. 28, No. 1, 45–62, 2002.
15. Poggio, T. and F. Girosi, "A theory of networks for approximation and learning," *A. I. Memo*, No. 1140, M.I.T. A.I Lab, 1989.
16. Haykin, S., *Neural Networks: A Comprehensive Foundation*, Prentice Hall, USA, Jun. 1998.

17. Chauvin, Y. and D. E. Rumelhart, *Back Propagation: Theory, Architectures, and Applications*, Lawrence Erlbaum Associates Publishers, UK, 1995.

18. Riedmiller, M. and H. Braun, "A direct adaptive method for faster backpropagation learning: The RPROP algorithm," *Proc. of the IEEE International Conference on Neural Networks*, 586–591, 1993.

19. Kiranyaz, S., T. Ince, A. Yildirim, and M. Gabbouj, "Evolutionary artificial neural networks by multi-dimensional particle swarm optimization," *Neural Networks*, Vol. 22, No. 10, 1448–1462, 2009.

20. U.S. Geological Survey Images, [Online], Available: http://terraserver-usa.com.

21. Lee, J. S., M. R. Grunes, and G. de Grandi, "Polarimetric SAR speckle filtering and its implications for classification," *IEEE Trans. Geosci. Remote Sensing*, Vol. 37, No. 5, 2363–2373, 1999.

22. Fukuda, S. and H. Hirosawa, "A wavelet-based texture feature set applied to classification of multifrequency polarimetric SAR images," *IEEE Trans. on Geoscience and Remote Sensing*, Vol. 37, No. 5, 2282–2286, 1999.

# A Fully Polarimetric Borehole Radar Based Numerical Modeling: Fully Polarimetric Response to Synthetic Natural Fractures

**J. G. Zhao[1, 2] and M. Sato[3]**

[1]State Keylab of Petroleum Resource & Prospecting
China University of Petroleum, Beijing, China
[2]Keylab of Geophysical Prospecting, CNPC, China
[3]Center for Northeast Asian Studies, Tohoku University, Japan

**Abstract**— A fully polarimetric borehole radar system with four combinations of dipole and cylindrical slot antennas was developed to acquire fully polarimetric data sets in drilled boreholes. To better under the fully polarimetric response to subsurface fractures with different roughness, in this study, synthetic fractures with different roughness are generated on a computer via fractal theory based simulation techniques. Quantitative assessment for the roughness of synthetic fractures is possible by use of three main parameters: the fractal dimension, the rms roughness at a reference length, and a length scale describing the degree of mismatch between the two fracture surfaces, allowing future detailed study of mechanical and transport properties of fractures and fully polarimetric radar response on them. Next, a 3D sub-grid FDTD numerical simulation is used to synthesize fully polarimetric data sets with synthetic fractures as primary reflectors. Based on the synthetic data sets, it is possible to relatively quantitatively evaluate the applicability of different radar polarimetry analysis approaches to physical characterization of subsurface fractures.

## 1. INTRODUCTION

A fully polarimetric borehole radar system with four combinations of dipole and cylindrical slot antennas was developed to acquire fully polarimetric data sets in drilled boreholes. Using this radar system, we carried out single-hole and cross-hole measurements in the Mirror Lake watershed in Grafton County, New Hampshire, USA. Also, we have proposed a case-specific antenna characteristic compensation algorithm, which enables accurately quantitative determination of scattering matrix $[S]$ for further polarimetric analysis. Radar polarimetry techniques with fully polarimetric borehole radar datasets provide the possibility to separate scattering contributions of different nature for physical properties recognition of subsurface fractures. As a result, The system in conjunction with a methodology of radar polarimetry analysis, proposed in previous research [1], has proved to be a potential tool for physical characterization and classification of subsurface fractures.

Despite of such progress, current polarimetric research on subsurface targets, such as subsurface fractures, is restricted to qualitative analysis. This motivates us to explore more quantitative approaches to characterize the fractures in real world environmental engineering projects by using fully polarimetric borehole radar signal properties. To achieve this goal, in this work, we utilize a procedure of computer numerical modeling to systematically investigate fully polarimetric radar response to fractures with different conditions. First, synthetic fractures with different roughness are generated on a computer via fractal theory based simulation techniques. Quantitative assessment for the roughness of synthetic fractures is possible by use of three main parameters: the fractal dimension, the rms roughness at a reference length, and a length scale describing the degree of mismatch between the two fracture surfaces, allowing future detailed study of mechanical and transport properties of fractures and fully polarimetric radar response on them. Next, a FDTD numerical simulation is used to synthesize fully polarimetric data sets with synthetic fractures as primary reflectors. Based on the synthetic data sets, it is possible to relatively quantitatively evaluate the applicability of different radar polarimetry analysis approaches to physical characterization of subsurface fractures.

## 2. FULLY POLARIMETRIC BOREHOLE RADAR

The fully polarimetric borehole radar is a stepped-frequency system based on a network analyzer (VNA). An advantage of the usage of VNA is that it can generate broadband frequencies without changing any components. Figure 1(a) shows the diagram of this system. In general, electric and magnetic disturbance exists during a measurement. To avoid this, an analog optical link system is utilized for signal transmission between a VNA on the ground surface and a radar system sonde

in the subsurface instead of coaxial cables. We employ a downlink system, which consists of a R/O (R: RF signal; O: Optical signal) and a O/R converters to transfer the electromagnetic source energy from a VNA transmitting port into subsurface, whereas a uplink system with a O/R and a R/O converters is utilized for the signal transmission from subsurface to ground surface. Thus, in the measurement, the RF output of a VNA is converted to optical signal and then transmitted to the downhole sonde. Afterwards, the optical signal from the VNA is converted to RF signal, amplified by a power amplifier and lastly fed to the transmitting antenna. Similarly, the received radar signal is amplified by a built-in amplifier firstly, and converted to optical signal in the receiver sonde, finally acquired by the VNA. Compared with the prototype. (Sato et al. 1999), the newly developed fully polarimetric borehole radar system uses two receivers to obtain interferometric data sets. Therefore, a switch system, shown in Figure 1(a), is needed to construct a signal transmission path for only one receiver at the same time. The study on radar inteferometry with the system is the other important issue, and is not involved in this paper.

The antenna deployment for polarimetric data sets collection with combinations of dipole and axial slot antennas is as shown in Figure 1(b). Dipole antenna radiates vertical ($V$) electrical field, on the contrary, axial slot antenna can be approximated as a vertical magnetic dipole in a vertical borehole to radiate horizontal ($H$) electrical field. Figure 1(c) shows a downhole sonde used to deploy antenna system, and with a custom-built 1000-m winch optical cable, the maximum depth of measurement can reach 1000-m with the radar system. Previously, 100 m is the maximum measurement depth limited by the length of commercial optical fibers.

The fully polarimetric borehole radar enables us to obtain the polarimetry response of subsurface targets surrounding a borehole. This kind of information is quite valuable since radar polarimetry gives the information such as size, shape, orientation or subsurface condition of radar targets [2]. The change of the polarization state is described by a scattering matrix depending on shape or properties of the scatter. Equation (1) gives the classical scattering matrix as:

$$
\begin{pmatrix} E_H^S \\ E_V^S \end{pmatrix} = \begin{pmatrix} S_{HH} & S_{HV} \\ S_{VH} & S_{VV} \end{pmatrix} \begin{pmatrix} E_H^i \\ E_V^i \end{pmatrix}
\tag{1}
$$

where $V$ and $H$ mean vertical and horizontal polarization, $i$ and $s$ represent a incident and scattered field, respectively. The final purpose of single-hole fully polarimetric radar system is to extract the



(a) Measurement configuration    (b) Antenna combinations

(c) Antenna deployment with a sonde connected to a 1000-m winch cable
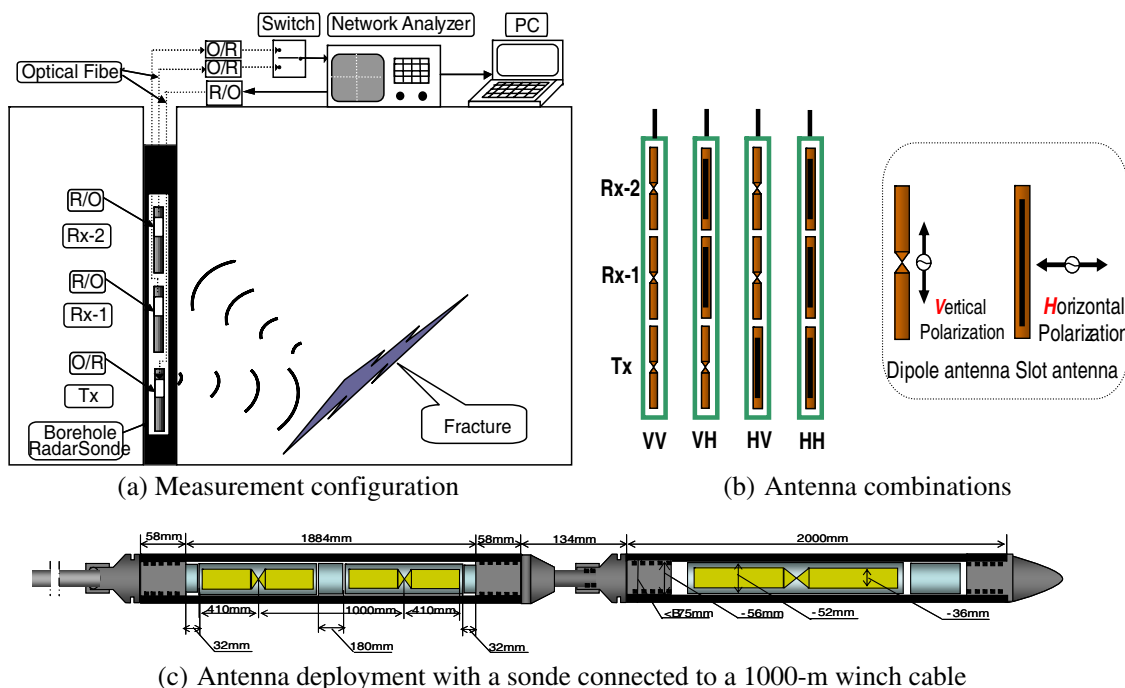
Figure 1: Fully polarimetric borehole radar system: (a) Measurement configuration, (b) Antenna combinations for polarimetric data collection, and (c) Antenna deployment with a sonde connected to a 1000-m winch cable.

scattering matrix:

$$\begin{pmatrix} S_{HH} & S_{HV} \\ S_{VH} & S_{VV} \end{pmatrix} \tag{2}$$

## 3. NUMERICAL SIMULATION

Stephen R. Brown proposed a simple mathematical model for numerically creating a rough fracture [3]. According to the mathematical model, rough-walled fractures can be described by only three main parameters: the fractal dimension, the rms roughness at a reference length scale, and a length scale describing the degree of mismatch between the two fracture surfaces. By computing power spectral densities of various natural rock surfaces, they found that there is remarkable similarity among these surfaces. Profiles of these widely different fracture surfaces have decreasing power law power spectra of the form

$$G(f) = c \cdot k^{-\alpha} \tag{3}$$

where $k$ is the wavenumber. The exponent $\alpha$ has a fairly limited range (typically between 2 and 3). The power spectrum (the roughness) can thus be described to first approximation by two parameters: (1) the exponent in the power law $\alpha$ and (2) the proportionality constant $C$. Thus, the fractal dimension of the surface, $D$, can be described as

$$D = (5 - \alpha)/2 \tag{4}$$

For natural fracture surfaces, $D$ tends to fall approximately in the range $2 \leq D \leq 2.5$, with small values representing smoother surfaces. According to the method, we chose $\alpha = 2.4$ to synthesize two fractures with $c = 1000$, and $c = 2000$, respectively, as shown in Figure 2.



(a) Upper fracture ($c=1000$)         (b) Lower fracture ($c=1000$)         (c) Fracture description ($c=1000$)
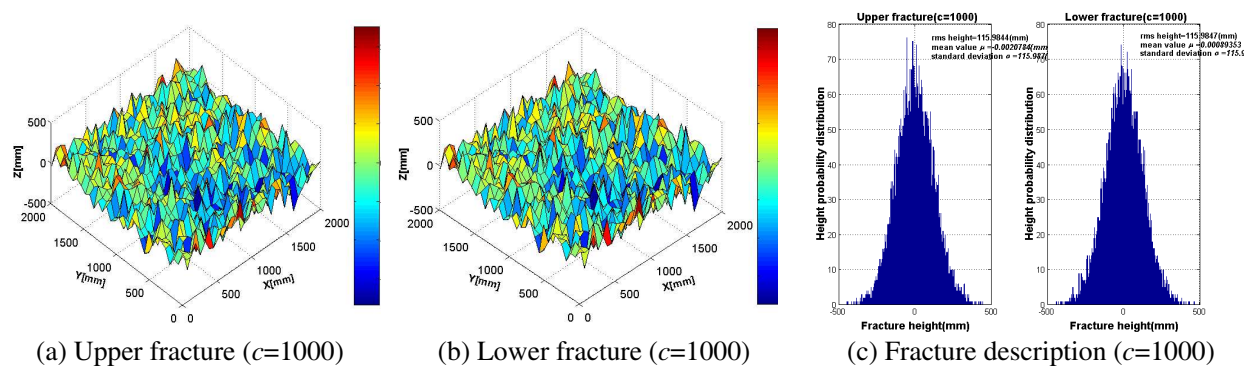
Figure 2: Synthetic rough-walled fractures. Fracture 1: (a) Upper fracture ($c = 1000$), (b) Lower fracture ($c = 1000$), and (c) Fracture description ($c = 1000$).
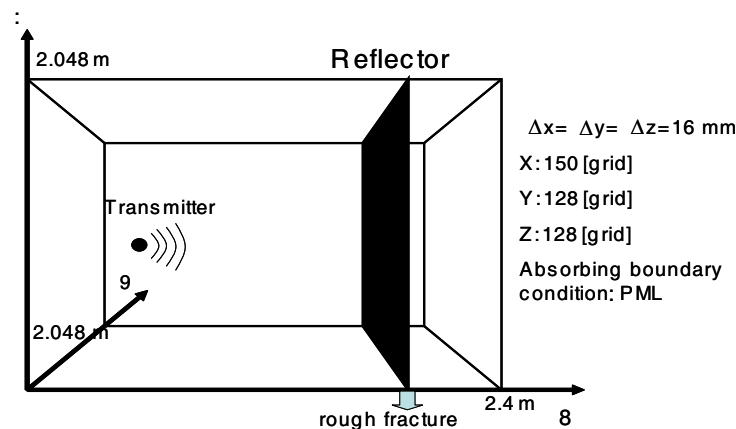


Figure 3: 3-D sub-grid FDTD simulation model. One synthetic fracture through the above described method is loaded at the position of arrow.

Next, a FDTD numerical simulation is used to synthesize fully polarimetric data sets with one synthetic fracture as a primary reflector. Figure 4 shows the EM wavefield snapshot of the fully polarimetric response to the synthetic fracture. Further radar polarimetry analysis based on the synthetic fully polarimetric data sets is possible.



(a) *VV* component

(b) *VH* component

(c) *HV* component

(d) *HH* component
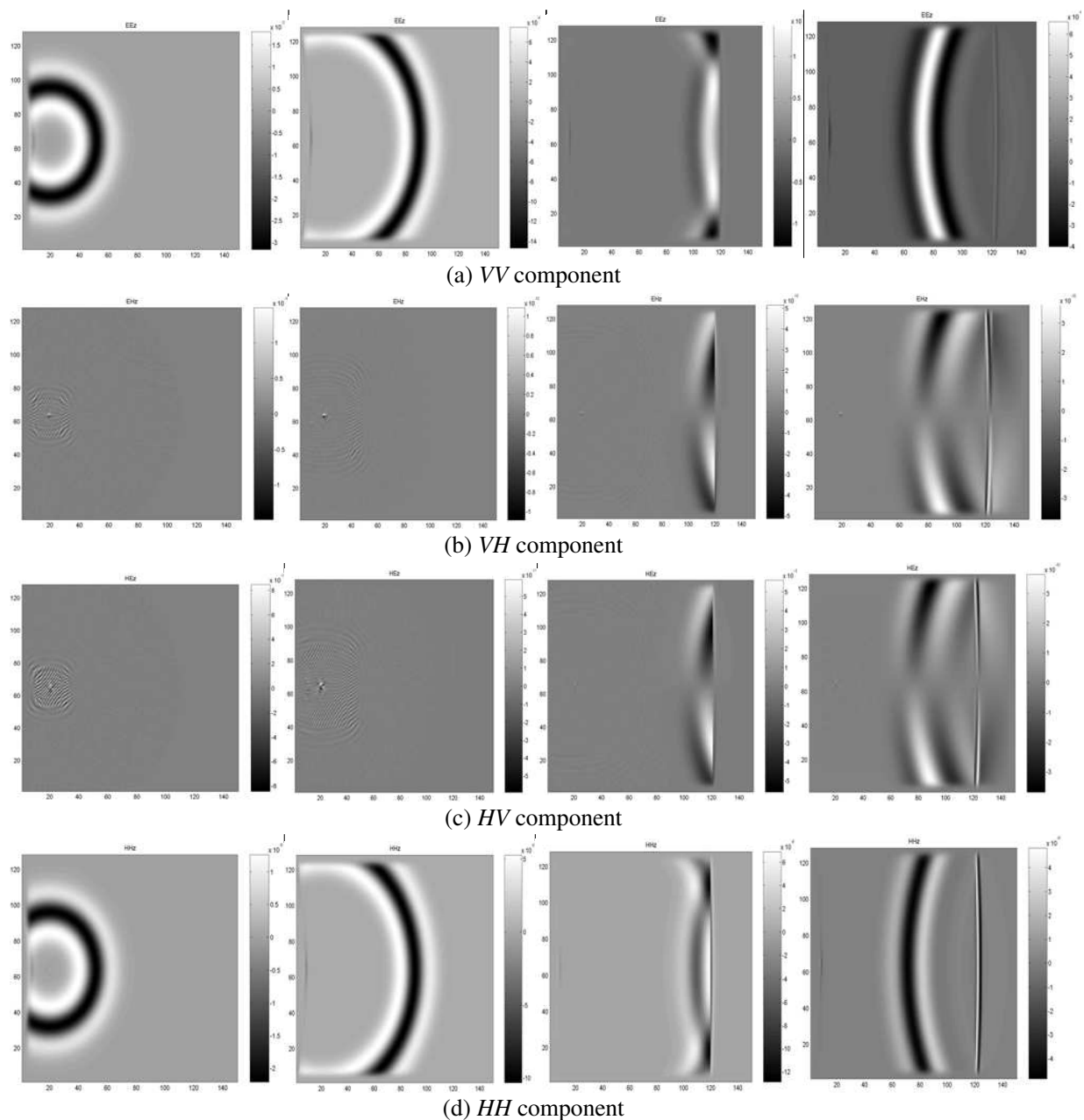
Figure 4: EM wavefield snapshot of the fully polarimetric response to one synthetic rough fracture.

## 4. CONCLUSIONS

We conclude that synthetic fully polarimetric data sets through computer forward modeling allows us to quantitatively investigate polarimetric scattering mechanism from synthetic natural subsurface fractures with known roughness parameters. The simulation research is conducive to practical field data processing and interpretation.

## ACKNOWLEDGMENT

**REFERENCES**

1. Zhao, J. G., "Radar polarimetry analysis applied to single-hole fully polarimetric borehole radar," *IEEE Trans. Geosci. Remote Sens.*, Vol. 44, No. 12, 3547–3554, 2006.
2. Cloude, S. R. and E. Pottier, "A review of target decomposition theorems in radar polarimetry," *IEEE Trans. Geosci. Remote Sens.*, Vol. 34, No. 2, 498–518, 1996.
3. Stephen, R. B., "Simple mathematical model of a rough fracture," *Journal of Geophysical Research*, Vol. 100, No. B4, 5941–5952, 1995.

# A New Method of Near-field Three Dimensional Synthetic Aperture Radar Imaging

**Nan-Jing Li[1], Chu-Feng Hu[1], Yong-Xin Zhao[2], and Jianjun Wei[3]**

[1]National Key Laboratory of UAV Specialty Technique
Northwestern Polytechnic University, Xi'an, China
[2]The 46th Middle School of Xi'an, Shaanxi, China
[3]Shaanxi Qiangde Technology Co., Ltd., Shaanxi, China

**Abstract**— A new fully three-dimensional (3-D) microwave image reconstruction algorithm is presented, which based on echo data of stepped-frequency sweeping radar system. The algorithm is not restricted by far field as the traditional imaging algorithm. By synthetic aperture processing for radar data, the high resolution of the image can be achieved. The algorithm belong to a new three dimensional back-projected method, which can hold good accuracy of interpolation, 3-D image of target can be achieved through fast Fourier transform and integrating after interpolation. The imaging results from simulation and experiment were presented. These results show that the algorithm is correct, 3-D image reconstruction based on this back-projected method can provide a microwave 3-D image with high resolutions effectively.

## 1. INTRODUCTION

Inverse synthetic aperture radar (ISAR) based on rotator mode is a well-known imaging technique that has shown the ability to analysis and diagnosis the scattering characteristics of objectives. An image with high resolution 2-D spatial distribution can be obtained by precise imaging algorithm. There are many imaging arithmetic applied to reconstruct the two dimensional image [1–6], and the back-projected (BP) algorithm with processing at time-domain is the most accurate method for rotator mode [3]. According the idea of 2-D BP, if the rotator can be moved along azimuthal angle and pitch angle respectivelyBP method can also be extended to image in three dimension. In this paper, the BP algorithm of three dimension is analyzed in details. Simulated and experimental results by the new algorithm show that the distribution of image is consistent with the actual location and amplitude of targets.

## 2. IMAGING MODEL OF 3-D BP ALGORITHM

The imaging measurement system in an anecho chamber is shown in Fig. 1. Two adjacent antennas are set on two tripods with height equal to the top of rotator. One of them is used for transmitting microwave signals, the echoes are received by another antenna. The low RCS support can rotate along azimuthal angle and pitch angle respectively. All measured data include amplitude and phase of different frequency can be saved in the network analyzer. Azimuthal angle $\varphi$ and pitch angle $\theta$ are shown in Fig. 2, the distance between antennas and rotary center is constant $R_0$, the coordinate $x$-$y$-$z$ is fixed on target circum rotating around the center of rotator.

The relation between spherical coordinate and Descartes coordinate is given as following:

$$R = x \cos\varphi \cos\theta + y \sin\varphi \cos\theta + z \sin\theta \tag{1}$$

The stepped-frequency signals are transmitted for gaining wideband frequency-domain response, and when the rotator arrives at a certain angle, the received signal can be expressed:

$$E_s(f, \varphi, \theta) = \int\limits_z \int\limits_y \int\limits_x g(x, y, z) \exp\left(-j\frac{4\pi}{\lambda}R\right) dx\,dy\,dz \tag{2}$$

where, $g(x, y, z)$ is three dimension distribution of scattering centre, it also can be regarded as the image of target, so it's not only the function of target coordinate $(x, y, z)$, but also the function of transmitted frequency $f$ and target azimuthal angle $\varphi$ and pitch angle $\theta$. After scaling, Fourier transform is taken on formula (3), then

$$\hat{g}(x, y, z) = C \cdot \int\limits_{\theta_{\min}}^{\theta_{\max}} \int\limits_{\varphi_{\min}}^{\varphi_{\max}} \int\limits_{f_{\min}}^{f_{\max}} E_s(f, \varphi, \theta) \exp[j(4\pi f/c) \cdot R]f^2 \sin\theta\,df\,d\phi\,d\theta \tag{3}$$
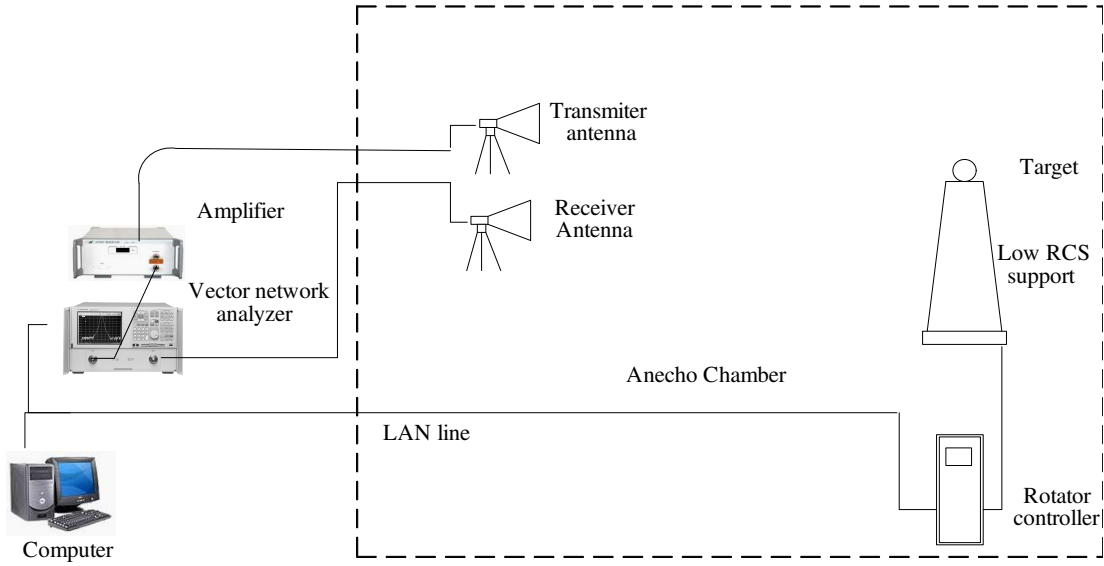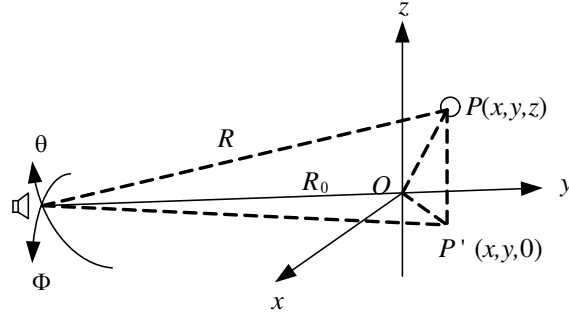
Figure 1: Imaging measurement system.



Figure 2: The rotate model of imaging measurement system.

$C$ is a constant, $c$ is the speed of light. For the limited sample of frequency-domain and angle data, the reconstructed image $\hat{g}(x, y, z)$ is a estimate of original image $g(x, y, z)$. Equation (5) is the mathematical expression of three dimension imaging for rotary object.

A FFT can be processed firstly along frequency to Equation (4):

$$P(x, y, z, \varphi, \theta) = \int_{f_{\min}}^{f_{\max}} E_s(f, \varphi, \theta) f^2 \sin \theta df \tag{4}$$

$$\hat{g}(x, y, z) = C \cdot \int_{\theta_{\min}}^{\theta_{\max}} \int_{\varphi_{\min}}^{\varphi_{\max}} \hat{P}(x, y, z, \varphi, \theta) d\varphi d\theta \tag{5}$$

$\hat{P}(x, y, \varphi, \theta)$ is the result after linear interpolation to $P(x, y, z, \varphi, \theta)$, after two procedures of integrating to $\varphi$ and $\theta$, the 3-D image $\hat{g}(x, y, z)$ can be calculated.

In the case of planar scanning, if every sampling point can be corrected a corresponding complex factor, all the sampling data can be equivalent as data from spherical scanning, as Fig. 3.

We can calculate the complex factor from Fig. 4, scanner moved from point A to point B straightlysampling the echo data with the same interval, the center of target is O, the distance between O and line AB is $R_0$, the distance between O and A is $R_n$, before using BP method, all echo data of scanner are required to correct to the curved line CD, with the amplitude and phase changing as following:

$$E_C/E_A = R_n^2/R_0^2, quad \Phi_C - \Phi_A = -4\pi (R_0 - R_n)/\lambda \tag{6}$$

So the corresponding complex factor is $R_n^2/R_0^2 e^{j4\pi(R_n - R_0)/\lambda}$.

## 3. RESULT OF SIMULATION AND EXPERIMENT

The simulated model as Fig. 5, two spheres which the location are $(0, 0, -0.1)$ and $(0, 0, 1.5)$ respectively, their amplitude equal 1. The distance between radar and rotate center O is 5 m, sweep frequency band is 33–35 GHz, the range of azimuthal angle $\varphi$ is $-3 \sim 3$ degree, and pitch angle $\theta$ is $87 \sim 93$ degree. The 3-D BP image result is shown in Fig. 6, the amplitude and position is very consistent with the gived model.

The experiment system as Fig. 7, in an anecho chamber, the distance between antenna scanner
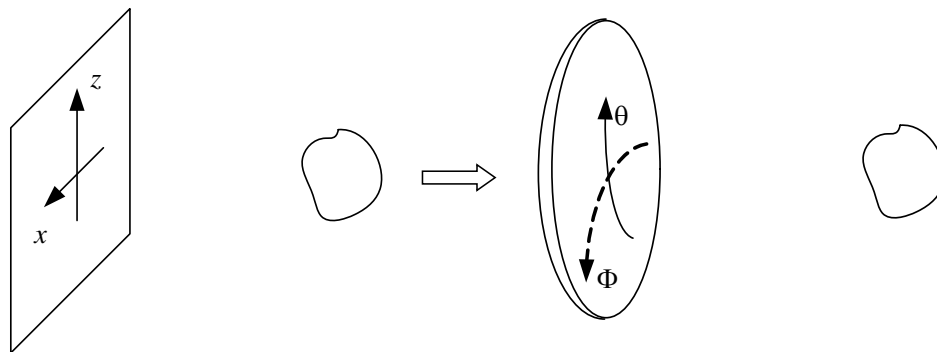


Figure 3: Planar scanning can be corrected as spherical scanning.
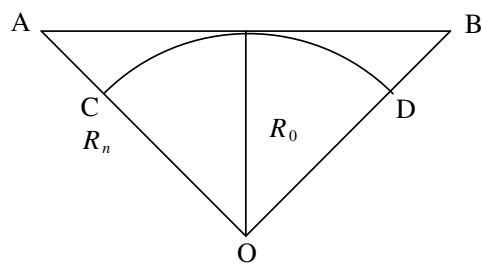


Figure 4: The relation between signals and space.
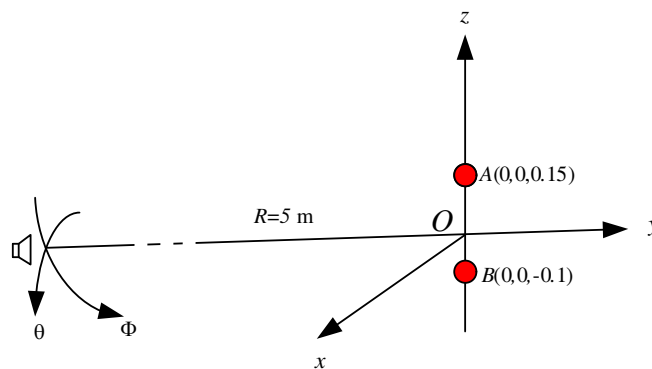


Figure 5: The simulation model of two spheres.
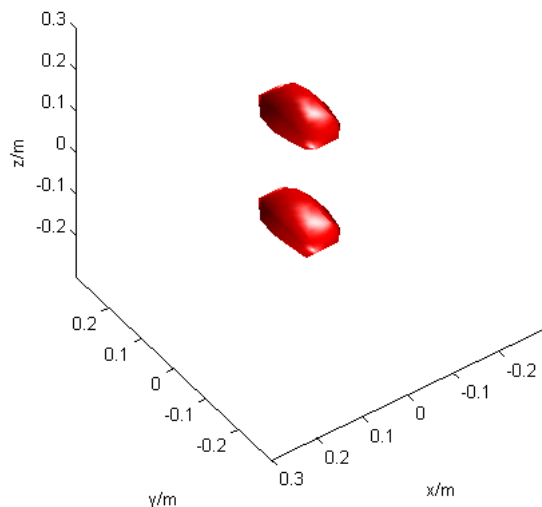


Figure 6: 3-D BP image result.



Figure 7: The photo of Planar scanning imaging system.

and center of target is $2\,\mathrm{m}$, The span of frequency is $8\,\mathrm{GHz} \sim 12\,\mathrm{GHz}$, and the scanning range is $1\,\mathrm{m} \times 1\,\mathrm{m}$, interval distance is $0.02\,\mathrm{m}$. A foam structure includes five metal spheres as DUT as Fig. 8. From the result as Fig. 9 the image is very consistent with the target, the boundary of every sphere is slippery.



Figure 8: A foam include spheres as DUT.
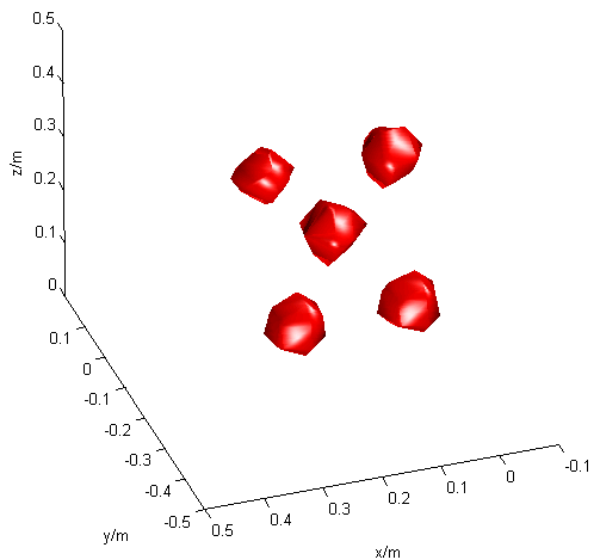


Figure 9: 3-D image of DUT.

## 4. CONCLUSION

Imaging results from simulation and experiment were presented. These results show that the 3-D back-projected algorithm for image reconstruction can produce an effective microwave 3-D image with high resolutions, the algorithm can be applied to diagnose complex 3-D spatial target.

## ACKNOWLEDGMENT

## REFERENCES

1. Anyong, Q., "Electromagnetic imaging of two-dimensional perfectly conducting cylinders with transverse electric scattered field," *IEEE Transactions on Antennas and Propagation*, Vol. 50, No. 12, 1786–1793, 2002.
2. Odendaal, J. W., "Radar cross section measurements using near-field radar imaging," *IEEE Transaction on Instrument and Measurement*, Vol. 45, No. 6, 948–954, 1996.
3. Uetas, A. B., "Spherical wave near-field imaging and radar cross section measurement," *IEEE Transaction on Antennas and Propagation*, Vol. 46, No. 5, 730–735, 1998.
4. Burns, J. W., "Enhanced resolution 2-d image formation using the reweighted minimum norm method," *Proc. AMTA*, 206–211, Oct. 1999.
5. Mensa, D. L., *High Resolution Radar Imaging*, Artech House, Norwood, MA, 1991.
6. Li, H. J., "Imaging interpretation and prediction in microwave diversity imaging," *IEEE Transaction on Geoscience Remote Sensing*, Vol. 27, No.1, 25–30, 1994.

# Wide Band Radar with Detecting and Tracing Corona Arc around Any High Speed and Anti Radar Aircraft

**Milad Johnny and Maryam Johnny**

Iran University of Science and Technology, Narmak, Tehran, Iran

**Abstract**— As we know, radar is an electromagnetic system for detecting and tracing any target. The base of this machine is to transfer some electromagnetic waveforms (like a square wave with sinusoidal modulator) and to analyze its echoes. Simple radar consists of a transmitter and receiver antenna and an electromagnetic detector. Transmitter antenna generates and emits electromagnetic waves. Some parts of these transmitted signals reflected from the body of target scatter and therefore; the receiver can detect the target and its features such as velocity and position of it.

In this paper, we are suggesting a new system that can detect any flying object without transmitting any electromagnetic wave. It can detect the object by analyzing the received signals that are generated by corona arc. It can be a revolution in the new radar systems and their usual and military application. At the end of the article, we briefly discuss the detecting and tracing the corona signals.

## 1. INTRODUCTION

If we consider the body of an aircraft flying in the air, we can consider the air as a cloth that touches the surface of an aircraft and releases its charges on the body of aircraft [3]. The aircraft body consists of a lot of small surface fractions that the charges are stored on them. In other words, as uncharged precipitation particles strike the aircraft, they acquire a positive charge, leaving an equal and opposite (negative) charge on the aircraft and raising its potential (negatively) to tens or hundreds of thousands of volts [4, 5]. Charging occurs both on the metal structure of the aircraft and on dielectric surfaces such as the windshield. Dielectric surfaces can thus become charged with respect to the airframe [6, 7].

This stored voltage on the surface of aircraft can cause a lot of problems in its radio systems and in some cases makes it explode. Therefore, some discharging needles are used on the body of the aircraft, these needles cause the air to be ionized and discharge the aircraft. The escape of these ionized charges from the point of needle can generate electromagnetic waves. Our aim is to analyze these waves in frequency domain. But before it, we should calculate electric field around the point of a needle. To simplify our model, we assume that a plane with zero potential is perpendicular to a point of a needle and in general, we make its distance tend from needle to infinite (because the aircraft is in the altitude that needle dimension is much smaller than this distance). To calculate electrical field, we consider the point of needle as a hyperbolic with asymptote angle of $\gamma$ (see Figure 1) and with the below form of potential in asymptote coordinate, we can write [1, 2]:

$$V = A + B \ln \left( \cot an \right) (\theta/2) \tag{1}$$

By applying boundary condition in $\theta = \theta_1$ and $\theta = 0$, we conclude that:

$$\theta = \frac{\pi}{2} \rightarrow v = 0$$
$$\theta = \theta_1 \rightarrow v = v = \text{needle potential}$$
$$V = U \frac{\ln \cot (\theta/2)}{\ln \cot (\theta_1/2)} \tag{2}$$

Therefore, electrical field of a needle and a zero potential plane is converted to a one-dimensional electric field, it means that $V$ only is the function of $\theta$ and for $\theta = \text{cte}$ we have hyperbolas plans with the same potential and electrical field lines are ones that for which $\eta = \text{cte}$ and they are like ellipses. And as we know voltage gradient in hyperbolic coordinate is:

$$\text{grad } V = \frac{L}{a\sqrt{\sinh^2 \eta + \sin^2 \theta}} + \left( a_n \frac{\partial v}{\partial \eta} + a_\theta \frac{\partial v}{\partial \theta} \right) + \frac{a_\psi}{a \sinh \eta \sin \theta} \frac{\partial v}{\partial \psi} \tag{3}$$

$$|E| = \frac{U}{a\sqrt{\sinh^2 \eta + \sin^2 \theta} \sin \theta \ln \cot (\theta_1/2)} \tag{4}$$
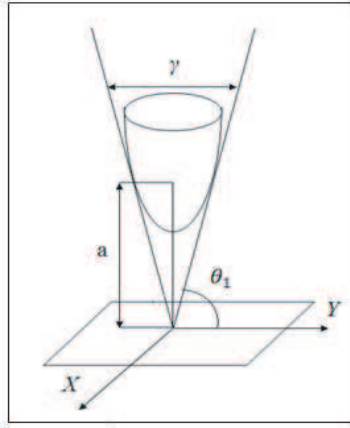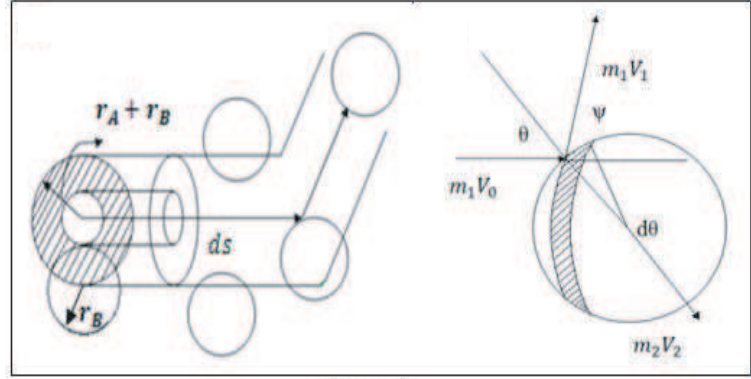
Figure 1.



(a)                                          (b)

Figure 2.

In hyperbolic coordinate:

$$\begin{cases} u^1 = \eta & 0 \le \eta < \infty, & x = a \sinh \eta \cos \theta \cos y \\ u^2 = \theta & 0 \le \theta < \pi, & y = a \sinh \eta \sin \theta \sin y \\ u^3 = \psi & 0 \le \psi < 2\pi, & z = a \cosh \eta \cos \theta \end{cases} \tag{5}$$

As we know, a molecule after colliding with another molecule travels through a free path until it collides with another molecule. The length of the free path is completely coincidental, but we can consider its average. When there is an electric field in an ionized gas, it can give rise to acceleration of charge particles. These charge particles continue their accelerating movement before they collide with other particles. The longer the path is, the particles get more and more energy. And this kinetic energy may get to the extent that after colliding with another molecule produces other ions. The thermal agitation of molecules by collisions can be considered as constant and even velocity, whereas the motion of charged particles in the presence of electric field is an accelerating motion. The motion of charged particle is an irregular and zigzag one but the resultant of all these movements is in the direction of electric field and generally charged particles travel with average velocity that we call it repulsing velocity. In addition, it can be calculated by the bellow relation [1, 2]:

$$V_e = bE \tag{6}$$

where $V_b$ the average velocity and $b$ is called particle motion that is the function of the dimension of the particles and molecules that they move through and the number of molecules in the unit of volume, pressure, and temperature if we pinpoint the problem we can show it in this way. Particle (**A**) with radius $r_A$ moves through a gas with molecule (**B**) with radius $r_B$. The path of particle **A** is shown in Figure 2 the collision of **A** and **B** occurs in area $(r_A + r_B)^2$ that appears when the particles collide with each other, their centers of mass are situated in an area that is called the area of collision and it is shown in the hachured area in Figure 2. In the path shown, the probability of collision of two particles is:

$$a_s dp = ds n_B \tag{7}$$

where $n_B$ in the formula is the volume density. On other hand, if we can consider $\lambda_m$ as an average free path, the probability of the collision in the length of $ds$ is:

$$dp = \frac{ds}{\lambda_m} \tag{8}$$

Therefore, the average free path is given as:

$$n = \frac{P}{KT} \tag{9}$$

$$\lambda_m = \frac{1}{a_s} \frac{KT}{p} \tag{10}$$

As we know, area of collision for small particles such as electrons is approximated $\pi r_B^2$ and for ions $4\pi r_B^2$.

$$\lambda_{me} \approx \frac{1}{\pi r B^2} \frac{KT}{p} \tag{11}$$

$$\lambda_{m1} \approx \frac{1}{4\pi r_B^2} \frac{KT}{p} \tag{12}$$

In addition, the average time between two collisions is:

$$t_m = \frac{\lambda_m}{V_m} \tag{13}$$

For a particle, which is, accelerating under the influence of a external force, the distance paved by this particle is calculated by the following equation:

$$S = \frac{1}{2}at^2 = \frac{eE}{2m}t_m^2 \rightarrow V_e = \frac{eE}{2m}\tau_m \rightarrow= \left(\frac{e\lambda_m}{2mV_m}\right) \tag{14}$$

Because of high ions mass, they exchange less energy in collisions, in fact, they play very less important role in ionization and their collisions can be considered completely elastic.

Consider two particles, where masses are $m_1$, $m_2$ (see Figure 2(b)) by applying Newton classic laws:

$$m_1v_0 - m_1v_1 \cos\psi = m_2v_2 \cos\theta_1 \tag{15}$$

$$m_1v_1 \sin\psi = m_2v_2 \sin\theta \tag{16}$$

$$\frac{1}{2}m_1v_0^2 - \frac{1}{2}m_1v_1^2 = \frac{1}{2}m_2v_2^2 \tag{17}$$

$$-m_1v_1 \cos\psi = m_2v_2 \cos\theta - m_1v_0 \tag{18}$$

$$\rightarrow v_2 = \frac{2mv_0}{m_1 + m_2} \times \cos\theta \tag{19}$$

$$\xrightarrow{18,19} \frac{\Delta w}{w} = \frac{4m_1m_2 \cos^2\theta}{(m_1 + m_2)^2} \tag{20}$$

Therefore, probability of collision between two particles in angle of $\theta$ can be calculated by the following formula:

$$P(\theta)\,d\theta = \frac{2\pi(r_1 + r_2)^2 \sin\theta \cos\theta\,d\theta}{\pi(r_1 + r_2)^2} = \sin 2\theta\,d\theta \tag{21}$$

By analyzing the path of a charged particle with a computer, electromagnetic spectrum of this particle can be plotted. To achieve the mentioned aim we consider a charge particle that is affected by external electric field and along its path, it can be collided by other particles. To simplify our problem, we consume that other particles have the same mass and they have no charges (because charged particles in external electric field have the same direction and magnitude velocity and they repel each other; therefore, most of collisions occur between charged and uncharged particles) see Figure 3.

Consider that a charged particle moving along $x$ axis and its velocity is the function of time and has a sinusoidal form the electromagnetic wave that this particle produces has also sinusoidal form. Therefore, the main harmonics of the particle's motion are the main harmonics of its electromagnetic waves and vice versa.

By considering collision as a random process and energy handover between collisions from 37th equation, we can conclude that, the particle velocity at the time between collisions has two forms:

1) Increasing speed in direction of $y$-axis (see Figure 3).
2) Constant speed in other directions ($x$-$z$).

By computer analysis of the electromagnetic noise of this phenomenon, we plot these three charts in $E = 100000\,\text{V/m}$ and after 1000 collisions (see Figures 4(a), 4(b), 4(c), 4(d)).

Figure 3.



(a)             (b)

(c)             (d)
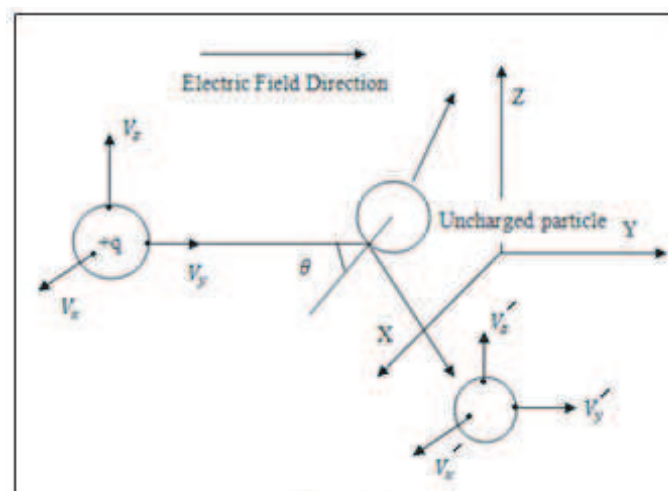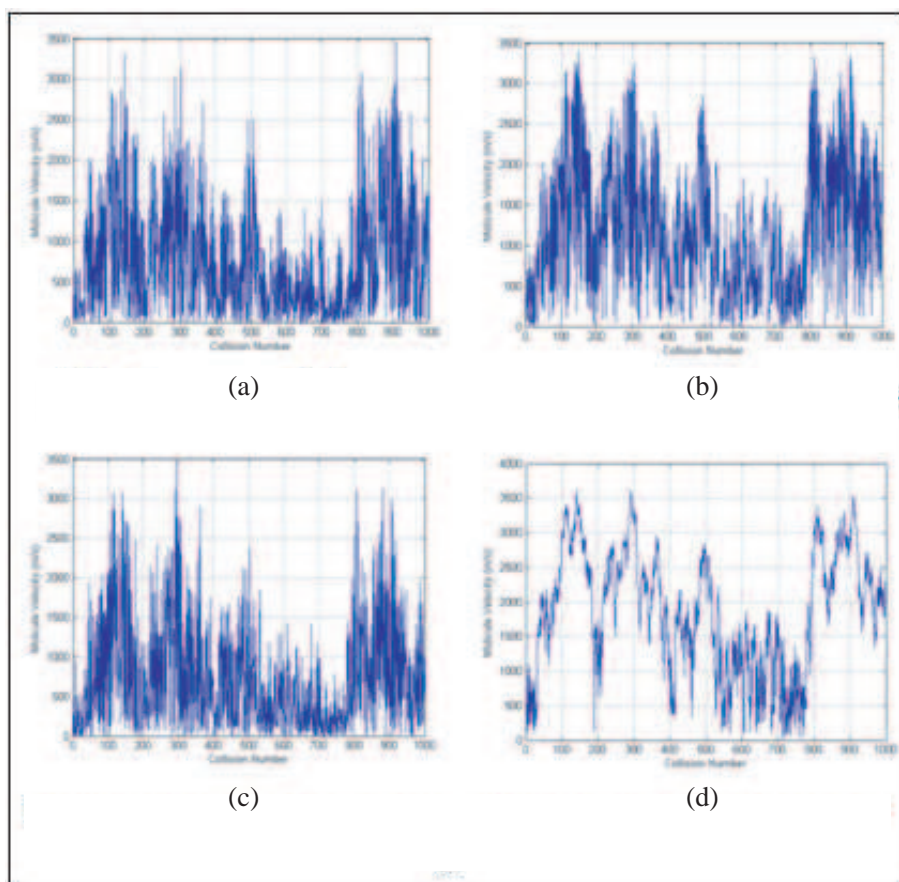
Figure 4. (a) $V_y$ velocity in terms of collision. (b) $V_x$ velocity in terms of collision number. (c) $V_z$ velocity in terms of collision number. (d) Total velocity in terms of collision number.

As mentioned before in Equation (18), we calculate electric field around a needle and each point around it has different electric field and therefore generate different electromagnetic wave spectrum, by adding up all spectrums of these points we can calculate generated frequency spectrum of a needle. If we assume that around a needle we have a lot of small dipole antennas, which are directed to the direction of electric field around a needle, we can estimate $E$ plan pattern of a needle (see Figure 5).

This is a corona noise spectrum which all aircraft generated by discharging, Furthermore any airplane during connecting to its base generates electromagnetic wave that for our system can be
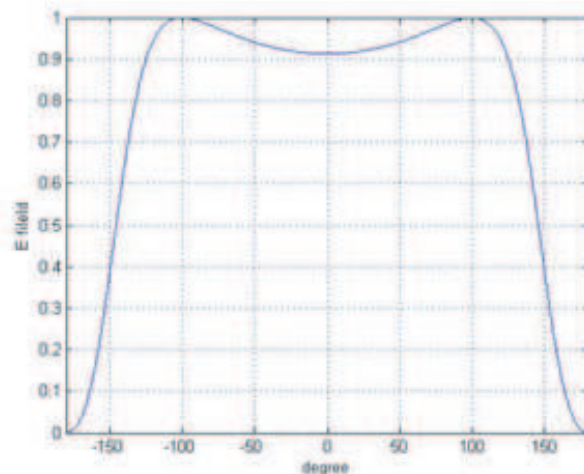
Figure 5. The pattern of electric field plan.



(a)     (b)
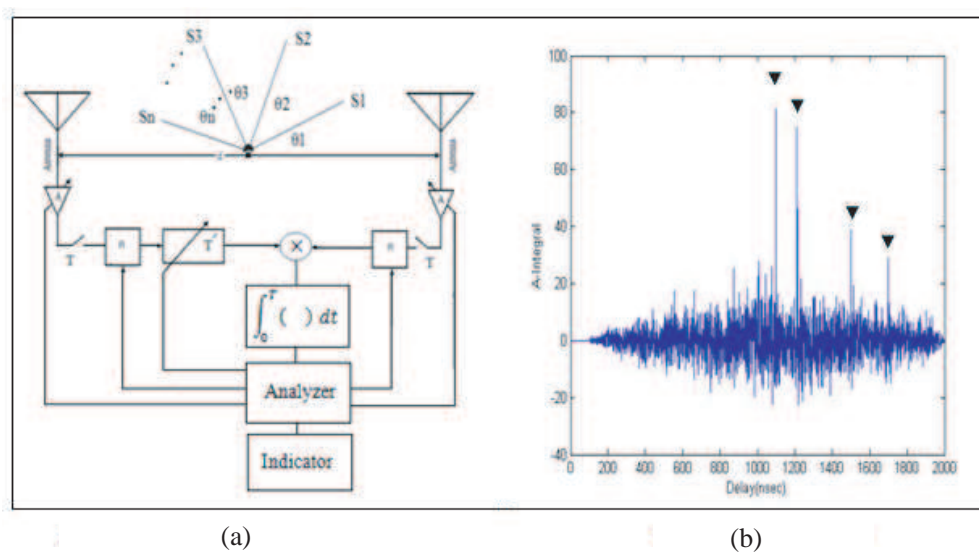
Figure 6. (a) DOA Estimator block diagram. (b) Output of integrator.

considered as an electromagnetic sign or a clue as soon as we detect and trace it. However, how we can do this. This problem can be solved by designing a new directional filter that can analyze and separate any signals which have different direction regardless of their frequency overlaps.

**DOA Estimation:** Here, we discuss a DOA method that can separate signals which overlap each other but their receiving directions are different (this method only detect directions and cannot say what this signal is). In addition to detecting and tracing flying objects it can be used for voice imaging that has a lot of applications (see Figure 6(a)). This system consists of (in 2D application) two receiver antennas (in 3D application we apply four receiver antennas with two delay blocks) that receive and amplify signals. In second receiver antenna (**B**) signal is delayed and multiplied by signal which is obtained from receiver antenna (**A**) then they enter the analyzer system that controls delays and computes the direction of signals which have different directions. In other words it can separate signals $\{S_1, S_2, S_3, \ldots, S_n\}$ which have frequency overlaps and different reception directions (these signals have zero average over the time of $T$).

To simplify our problem, we consider $n$ signals which are in 2D plane and our goal is to find out the signals and their directions. These signals enter the first high gain LNA from the first antenna at the same time these signals with some delays are received by second high gain LNA these delays are calculated by the following equation:

$$td_n = \frac{d\cos(\theta n)}{c} \tag{22}$$

Therefore, the signals, which are received after the key for the first receiver, have the following form.

$$A[x_1(t)(U(t) - U(t - T)) + x_2(t)(U(t) - U(t - T)) + \ldots + x_n(t)(U(t) - U(t - T))] \tag{23}$$

By considering Equation (23) the signals, which are received after the key for the second receiver, have the following form.

$$X_1(t) = A[x_1(t-t_1)(U(t) - U(t-T)) + x_2(t-t_2)(U(t) - U(t-T)) + \ldots + x_n(t-t_n)(U(t) - U(t-T))] \tag{24}$$

These signals are recorded in $R$ block and they can be simultaneously played again by the command of **Analyzer**. But in the second signal path we have a delay block. Therefore, after this block the Equation (24) changes into the following form:

$$X_2(t) = A\big(U\big(t - T'\big) - U\big(t - T' - T\big)\big)\big[x_1\big(t - t_1 - T'\big) + x_2\big(t - t_2 - T'\big) + \ldots + x_n\big(t - t_n - T'\big)\big] \tag{25}$$

The signals, which are input to integral block yield the following form:

$$(42, 41) \rightarrow X_{out} = X_1(t)X_2(t) \tag{26}$$

Something which is input to analyzer is:

$$\int_0^T X_1(t)X_2(t)dt = \int_{T'}^T X_1(t)X_2(t)dt \tag{27}$$

By applying the second antenna signals with different time delays, we can achieve some integrals. By plotting, the result of integral in term of $T'$, we can achieve a curve like Figure 6(b).

## 2. CONCLUSION

In this paper, we discuss the electric field that an aircraft's discharging needle can generate. We proved that, any electric field in ionized gas could produce corona noise that its properties were the function of electric field and the molecules velocity. High magnitude of electric field can bring into being higher frequency noise. This noise and some electromagnetic waves that an aircraft or other flying object produces can be used as a sign for tracing it, at the end we shortly discuss a direction filter that is able to distinguish the signals which are received in different angles.

### REFERENCES

1. Cheng, D. K., *Field and Wave Electromagnetic*, 1992.
2. Mohseni, M., *High Voltage Engineering*, Tehran University, Tehran, 1995.
3. Nanevicz, J. E., "Static charging and its effects on avionic systems," *IEEE Transaction on Electromagnetic Compatibility*, Vol. 24, No. 2, 203–208, May 1982.
4. Tanner, R. L. and J. E. Nanevicz, "Precipitation charging and corona-generated interference in aircraft," *Tech. Rep.*, No. 73, Stanford Research-Institute, Menlo Park, CA, 1961.
5. Tanner, R. L. and J. E. Nanevicz, "An analysis of corona-generated interference in aircraft," *Proc. IEEE*, Vol. 52, No. 1, 44–52, Jan. 1964.
6. Tanner, R. L. and J. E. Nanevicz, "Radio noise generated on aircraft surfaces," Final Report, Stanford Research Institute, Menlo Park, CA, 1956.
7. Nanevicz, J. E. and E. F. Vance, "Studies of supersonic vehicle electrification," *1970 Lightning and Static Electricity Conf. Proceedings*, 73–88, San Diego, 1971.

# Matrix Calculation and Compensation of Multiple CFO Interferences in the OFDMA Uplink Communication System

**Heung-Gyoon Ryu**

Department of Electronic Engineering, Chungbuk National University, CheongJu 361-763, Korea

**Abstract**— Like other OFDM-based systems, OFDMA system is very sensitive to frequency synchronization errors, especially in the uplink channel where many mobile users have individually different CFOs (Carrier Frequency Offset). When many different CFOs exist, the orthogonality between the subcarriers will be lost so that ICI (Inter Carrier Interference) as well as MAI (Multi-Access Interference) will be generated to disturb the received signal. Therefore, the system BER performance will be seriously degraded. Thus, research on the suppression to the interference caused by many different CFOs is of great importance. In this paper, we firstly analyze the interferences, including ICI and MAI, caused by multiple CFOs in the uplink channel of OFDMA system. Next, the suppression method based on block type pilots is proposed to overcome this interference simultaneously. From the simulation results, it can be seen that the multiple CFOs will make serious degradation to the system performance. However, by the proposed suppression processing method, the system performance can be significantly improved.

## 1. INTRODUCTION

OFDM (Orthogonal Frequency division multiplexing) has been widely used in digital communication system to achieve very high data rate. Combined with frequency division multiple access technique, OFDMA is proposed as a multiple access scheme. The OFDMA system inherits the advantages of OFDM, and has been widely used in wireless communication system [1]. However, similar to other OFDM based systems, OFDMA system is sensitive to CFO. In OFDMA uplink communication, the received signal is the sum of multiple signals coming from different users, each of which experiences a different CFO mainly due to oscillator instability and Doppler shift [2]. These CFOs among users destroy the orthogonality among subcarriers, thus, not only ICI but also MAI will be generated to disturb the received signal. Then the system performance will be seriously degraded.

Synchronization between users is different in uplink communication. Conventional CFO correction methods, such as [3], which are used in the downlink, are designed for signal user system, and therefore are unable to correct the multiple CFOs in the uplink. To overcome this problem, many previous works has been proposed to estimate [2, 4–6] or suppress the CFO effects [7–13]. These synchronization methods can be classified as two groups. The first is called feedback method, which exploits a downlink control channel to transmit the estimated CFO information obtained by the BS (Base Station), to each user, and each user can then correct the CFOs by adjusting the carrier frequency. However, this method will increase the transmission overhead and possibly cause outdated estimation in time-varying scenario. An alternative is to achieve synchronization via signal processing at the uplink receiver without the help of a control channel, such as [7–13]. In [7], a filtering method was proposed. And in [8–10], SIC (Successive Interference Cancellation) as well as PIC (Parallel Interference Cancellation) methods were raised. Inverse matrix methods were discussed in [11–13]. However, the methods in [8–12] need perfect CFO estimation, which is impossible in practical system, and the residual CFO will also degrade system performance.

In this paper, firstly, we analyze the interferences caused by multiple CFOs in OFDMA uplink system. From the analysis, we express the received signal in matrix form. If we can obtain these components in the interference matrix, we can reconstruct the interference matrix and the influence of multiple CFOs can be easily suppressed. Next, a joint suppression method based on block type pilots is proposed. From the pilot block, we can estimate the components in the interference matrix. Then, making suppression to the interferences caused by multiple CFOs is feasible. Finally, the suppression method is simulated and the results are shown. Comparing the simulation results, we can draw the conclusion that multiple CFOs will make great degradation to the system performance, but after making suppression processing, the system can achieve better performance.

## 2. OFDMA UPLINK SYSTEM MODEL

Figure 1 shows the OFDMA uplink system block diagram. In the OFDMA uplink system, all subcarriers are divided into several sets, and each user exploits one set of subcarriers to simultaneously
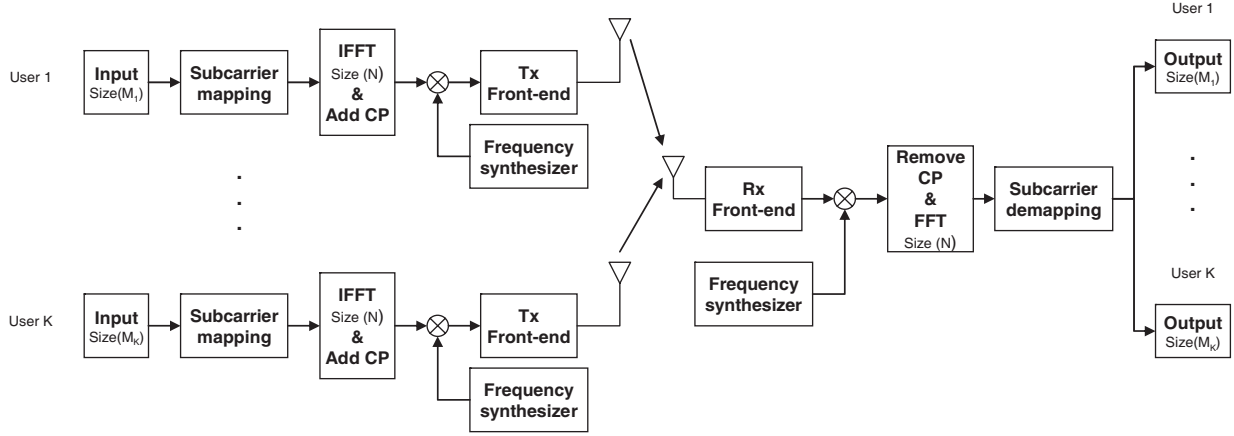
Figure 1: OFDMA uplink system block diagram.

transmit OFDM symbols.

We consider an OFDMA uplink system in which total available subcarrier number is $N$ and $K$ users communicate with the base station. We suppose the subcarrier set assigned to the $k$th user is $S^k$, the subcarrier number of set $S^k$ is $M_k$ and $\mathbf{D}_k = [d_0^k, d_1^k, d_2^k, \ldots, d_{Mk-1}^k]^T$ is the transmitted data of the $k$th user. Then, $\cup_{k=1}^{K-1} S^k = \{0, 1, 2, \ldots, N-1\}$ and $S^i \cap S^j = \phi$, for $i \neq j$.

After subcarrier mapping, the data on $k$th user can be shown as $\mathbf{X}^k = \mathbf{\Theta}^k \cdot \mathbf{D}_k$, where $\mathbf{\Theta}^k$ is the subcarrier mapping matrix with the size of $N \times M_k$. And the component in $\mathbf{\Theta}^k$ satisfy the following demand, if the $j$th data in $\mathbf{D}_k$ transmitted on the $i$th subcarrier, $\Theta_{ij}^k = 1$, otherwise $\Theta_{ij}^k = 0$. Then after $N$-IFFT, the transmitted signal can be shown as

$$s^k(n) = \sum_{l=0}^{N-1} X_l^k \cdot e^{j2\pi nl/N} = \sum_{l=0}^{N-1} X_l^k \cdot p_{n,l}, \tag{1}$$

and a cyclic prefix is inserted in the transmitted signal to overcome the influence of ISI.

Here we consider each user experience a frequency selective channel with the impulse response $h^k(n)$, then the received signal at the base station is

$$r(n) = \sum_{k=0}^{K-1} \left[ s^k(n) \otimes h^k(n) + v^k(n) \right], \tag{2}$$

where $v^k(n)$ is the AWGN noise on the $k$th user.

All users are assumed to be synchronized in the time domain. Then after $N$-FFT, the output of the $i$th subcarrier can be written as

$$Y_i = \frac{1}{N} \sum_{n=0}^{N-1} r(n) \cdot e^{-j2\pi ni/N}. \tag{3}$$

After frequency domain equalizer and subcarrier demapping, the transmitted data of each user can be recovered.

## 3. MULTIPLE CFO AND INTERFERENCE CANCELLATION

We suppose the CFO of the $k$th user is $\Delta f_k$, the, at the receiver, the received signal can be written as

$$r(n) = \sum_{k=0}^{K-1} \left\{ \left[ s^k(n) \cdot e^{j2\pi \Delta f_k n} \right] \otimes h^k(n) + v^k(n) \right\}. \tag{4}$$

Performing FFT, the obtained symbol is

$$Y_i = \frac{1}{N} \sum_{n=0}^{N-1} r(n) \cdot e^{-j2\pi ni/N}$$

$$= \frac{1}{N} \sum_{n=0}^{N-1} \sum_{k=0}^{K-1} X_i^k H_i^k \cdot e^{j2\pi \Delta f_k n} + \frac{1}{N} \sum_{n=0}^{N-1} \sum_{k=0}^{K-1} \sum_{\substack{l=0, \\ l \neq i}}^{N-1} X_l^k H_l^k \cdot e^{j2\pi n(l-i)/N} \cdot e^{j2\pi \Delta f_k n} + V_i \quad (5)$$

where $H_l^k$ is the frequency domain channel response.

According to the subcarrier mapping method, one subcarrier can only be assigned to one user. Thus, among the $K X_i^k$, only one $X_i^k$ is the the transmitted data, and the other $X_i^k$ are zero. We suppose this $X_i^k$ belongs to the $k$th user. Then, $Y_i$ can be written as

$$Y_i = \frac{1}{N} \sum_{n=0}^{N-1} X_i^{k'} H_i^{k'} e^{\frac{j2\pi n \varepsilon_{k'}}{N}} + \frac{1}{N} \sum_{n=0}^{N-1} \sum_{\substack{l=0, \\ l \neq i}}^{N-1} X_l^{k'} H_l^{k'} e^{\frac{j2\pi n[(l-i)+\varepsilon_{k'}]}{N}}$$

$$+ \frac{1}{N} \sum_{n=0}^{N-1} \sum_{\substack{k=0, \\ k \neq k'}}^{K-1} \sum_{\substack{l=0, \\ l \neq i}}^{N-1} X_l^k H_l^k e^{\frac{j2\pi n[(l-i)+\varepsilon_k]}{N}} + V_i$$

$$= \underbrace{X_i^{k'} H_i^{k'} \cdot I_0^{k'}}_{I} + \underbrace{\sum_{\substack{l=0, \\ l \neq i}}^{N-1} X_l^{k'} H_l^{k'} \cdot I_{l-i}^{k'}}_{II} + \underbrace{\sum_{\substack{k=0, \\ k \neq k'}}^{K-1} \sum_{\substack{l=0, \\ l \neq i}}^{N-1} X_l^k H_l^k \cdot I_{l-i}^k}_{III} + \underbrace{V_i}_{IV} \quad (6)$$

where $\varepsilon_k$ is the normalized CFO and

$$I_L^k = \frac{1}{N} \sum_{n=0}^{N-1} e^{j2\pi n[L+\varepsilon_{k'}]/N} \quad (7)$$

is the interference coefficient.

From (6), we can see that the received signal is comprised of 4 components. Component $I$ corresponds to the original data of the $k$th user transmitted on the $i$th subcarrier, component $II$ corresponds to ICI caused by the other data of the $k$th user transmitted on the other subcarrier, component $III$ corresponds to the MAI caused by the data of the other users, and component $IV$ corresponds to the AWGN noise.

From the above analysis, we can see that the multiple CFOs not only generate ICI but also MAI. Thus, the received signal will be seriously distorted and the system performance will be degraded. In order to improve system performance, we have to make suppression to these interferences.

In this part, we propose a suppression method which based on block type pilots. From the received pilot block, we can estimate all information of the interferences caused by the multiple CFO, and then making suppression to these interferences is feasible and system performance can be improved.

As described above, when multiple CFOs exist in the uplink communication, the received signal at the base station can be expressed as (6). Then we change (6) into matrix expressed form as

$$\mathbf{Y} = \mathbf{I} \cdot \mathbf{X} + \mathbf{V}, \quad (8)$$

where $\mathbf{X} = \sum_{k=1}^{K} \mathbf{X}^k = [D_0, D_1, \ldots, D_{N-1}]^T$ is the data vector transmitted on the communication band, $D_i$ denotes the data of the $k$th user transmitted on the $i$th subcarrier, $\mathbf{V}$ is the AWGN noise

vector and

$$
\mathbf{I} = \begin{bmatrix}
I_0^k & I_1^k & I_2^k & \cdots & I_{N-1}^k \\
I_{-1}^k & I_0^k & I_1^k & \cdots & I_{N-2}^k \\
I_{-2}^k & I_{-1}^k & I_0^k & \cdots & I_{N-3}^k \\
\cdots & \cdots & \cdots & \cdots & \cdots \\
I_1^k & I_2^k & I_3^k & \cdots & I_0^k
\end{bmatrix} \tag{9}
$$

is the interference matrix. The superscript of $I_L^k$ is related with the user's index. Form example, if the $i$th subcarrier is assigned to the $k'$th user to transmit data, the superscripts of the components in the $i$th column of interference matrix should be set as $k'$. From (7), we can see that

$$
I_{-L}^k = \frac{1}{N} \sum_{n=0}^{N-1} e^{j2\pi n[-L+\varepsilon_{k'}]/N} = \frac{1}{N} \sum_{n=0}^{N-1} e^{j2\pi n[N-L+\varepsilon_{k'}]/N} = I_{N-L}^k \tag{10}
$$

Thus the interference can be rewritten as

$$
\mathbf{I} = \begin{bmatrix}
I_0^k & I_1^k & I_2^k & \cdots & I_{N-1}^k \\
I_{N-1}^k & I_0^k & I_1^k & \cdots & I_{N-2}^k \\
I_{N-2}^k & I_{N-1}^k & I_0^k & \cdots & I_{N-3}^k \\
\cdots & \cdots & \cdots & \cdots & \cdots \\
I_1^k & I_2^k & I_3^k & \cdots & I_0^k
\end{bmatrix}. \tag{11}
$$

From the above formula, we can see that the interference matrix is comprised of $K \times N$ different components. However, the rank of (8) is $N$, so it is impossible to get these $K \times N$ components directly.

Then in one OFDM symbol, only one pilot block from one user will arrive at the base station. Therefore, estimating the components is feasible.

The first OFDM symbol arrived at the base station is the first user's pilot block. Because the other users haven't communicate with the base station, we can get $\mathbf{X}=\mathbf{X^1}$ and $I_L^k = 0$, $(k \neq 1)$. Rewrite (8) as

$$
\mathbf{Y} = \mathbf{I} \cdot \mathbf{X} = \mathbf{X'} \cdot \mathbf{I^1} = \begin{bmatrix}
X_0^1 & X_1^1 & \cdots & X_{N-1}^1 \\
X_1^1 & X_2^1 & \cdots & X_0^1 \\
\cdots & \cdots & \cdots & \cdots \\
X_{N-1}^1 & X_0^1 & \cdots & X_{N-2}^1
\end{bmatrix} \cdot \begin{bmatrix}
I_0^1 \\
I_{10}^1 \\
\cdots \\
I_{N-1}^1
\end{bmatrix}, \tag{12}
$$

where $\mathbf{I^1} = [I_0^1, I_1^1, \ldots, I_{N-1}^1]^T$ is the components which related with the first user in the interference matrix. Then $\mathbf{I^1}$ can be obtained by the inverse matrix as

$$
\mathbf{I^1} = \mathbf{X'^{-1}} \cdot \mathbf{Y}. \tag{13}
$$

Then, we update the interference matrix with $\mathbf{I^1}$, and in the following OFDM symbols, if the other users don't communicate with the base station, the interference in the received signal can be suppressed as

$$
Y_{\text{suppressed}} = I^{-1} \cdot Y = X + I^{-1} \cdot N. \tag{14}
$$

We assume the second user start to communicate with the base station after several OFDM symbols. Thus, $\mathbf{X} = \mathbf{X^1} + \mathbf{X^2}$ and $I_L^k = 0$, $(k \neq 1, 2)$.

To get the interference components related with the second user, firstly, we get the received data of the first user by subcarrier demapping and suppress the interference (ICI) as (14). Secondly, the suppressed signal is detected and the transmitted frequency domain data of the first user is reconstructed from the detection result. Thirdly, we calculate the MAI from the first user by using the reconstructed data and (8). Finally, the interference vector of the second user $\mathbf{I^2}$ can be estimated by the processing which is same with estimating the interference vector of the first user. Then we can update the interference matrix with $\mathbf{I^2}$ and suppress the interference as (14).

To obtain more accurate estimation results, the above processing can be replaced with iteration process.
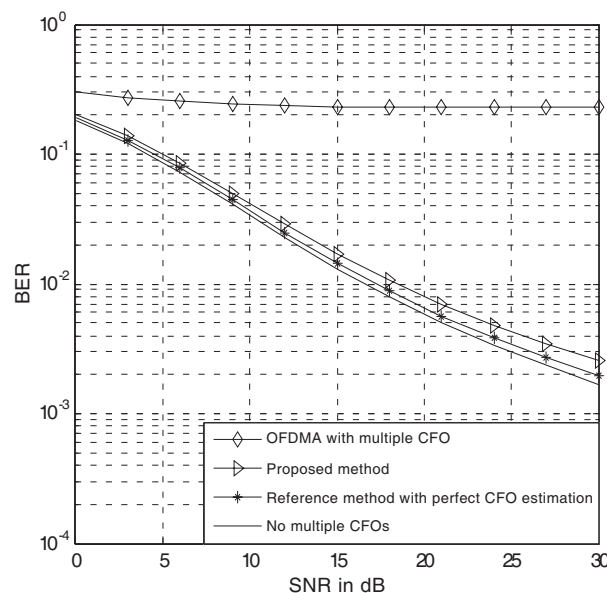
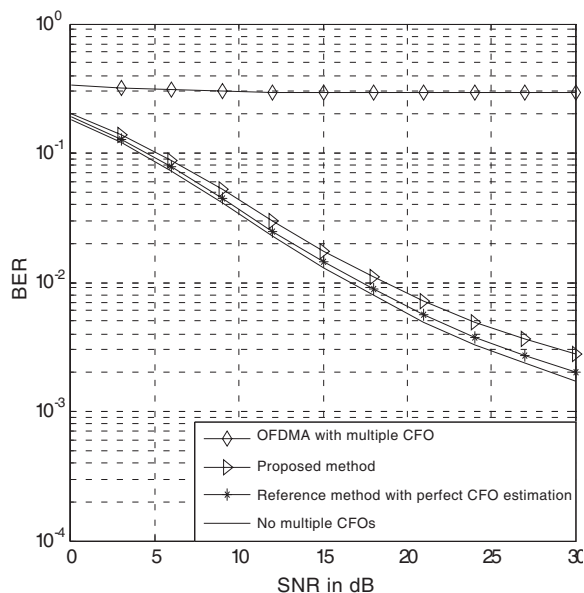Figure 2: BER in multipath channel (interleaved mapping).



Figure 3: BER in multipath channel (localized mapping).

## 4. SIMULATION RESULTS AND DISCUSSION

Simulation Parameters are as follows. Modulation scheme is 16 QAM. Number of subcarriers ($N$) is 512. Number of users ($K$) is 4. Subcarrier Spacing is 10.94 kHz. Subcarrier mapping method is Localized and Interleaved method. CP length is 32. Frame size is 6. Channel model is AWGN and 802.16 SUI channel model. We assume that the normalized frequency offset of each user is a random value uniformly distributed in $[-0.1, 0.1]$, and the CFO doesn't change in one frame's time. Then we can get the following simulation results.

The channel model used here is the 802.16 SUI-5 channel model, which is modeled as a tapped-delay ling with 3 non-uniform delay traps. The channel gain of each tap is $[0, -5, -10]$ dB and the delay of each tap is $[0, 4, 10]$ μs respectively. Fig. 2 shows the BER performance of interleaved subcarrier mapping OFDMA and Fig. 3 shows the BER performance of localized subcarrier mapping OFDMA. Comparing the simulation results, we can see that the proposed suppression method works well. Compared with interleaved subcarrier mapping method, localized subcarrier mapping is more robust to MAI, thus, the algorithm work better in the localized subcarrier mapping OFDMA system.

## 5. CONCLUSION

In this paper, we have analyzed the interferences generated from multiple CFOs in OFDMA uplink communication system. According to the analysis results, we can see that the received signal will be seriously distorted and the system performance will be degraded. Also, we can see that the interference matrix is comprised of $K \times N$ different components. However, the rank of the received signal function is $N$, so it is impossible to get these $K \times N$ components directly. Thus we suppose all users start to communicate with the base station at different time and propose a novel suppression method which is based on block type pilots. Through the received pilot block, we can estimate all components in the interference matrix. Then by reconstructing the interference matrix from the estimation result, we can make suppression to the interference generated from the multiple CFOs easily and finally improve system performance. Simulation results show that the joint suppression algorithm works well in frequency selective fading channel.

**REFERENCES**

1. Institute of Electrical and Electronics Engineers, "IEEE Standard for Local and metropolitan area networks, Part16: Air interface for fixed and mobile broadband wireless access systems, Amendment 2: Physical and medium access control layers for combined fixed and mobile operation in licensed bands," *IEEE Std 802.16e-2005*, Feb. 2006.

2. Morelli, M., "Timing and frequency synchronization for the uplink of an OFDMA system," *IEEE Transactions on Communications*, Vol. 52, No. 2, 296–306, Feb. 2004.

3. Van De Beek, J. J., P. O. Borjesson, M. L. Boucheret, D. Landstrom, J. M. Arenas, P. Odling, C. Ostberg, M. Wahlqvist, and S. K. Wilson, "A time and frequency synchronization scheme for multiuser OFDM," *IEEE Journal on Selected Areas in Communications*, Vol. 17, No. 11, 1900–1914, Nov. 1999.

4. Na, Y. and H. Minn, "Line search based iterative joint estimation of channels and frequency offsets for uplink OFDMA systems," *IEEE Globecom'06*, 1–5, Nov. 2006.

5. Movahedian, M., Y. Ma, and R. Tafazolli, "An MUI resilient approach for blind CFO estimation in OFDMA uplink," *IEEE 19th International Symposium on PIMRC*, 1–5, Sep. 2008.

6. Cao, Z., U. Tureli, and Y.-D. Yao, "Deterministic multiuser carrier-frequency offset estimation for interleaved OFDMA uplink," *IEEE Transactions on Communications*, Vol. 52, No. 9, 1585–1594, Sep. 2004.

7. Dai, X., "Carrier frequency offset estimation and correction for OFDMA uplink," *IET Communications*, Vol. 1, No. 2, 273–281, Apr. 2007.

8. Fantacci, R., D. Marabissi, and S. Papini, "Multiuser interference cancellation receivers for OFDMA uplink communications with carrier frequency offset," *IEEE Globecom'04*, Vol. 5, 2808–2812, Nov. 2004.

9. Manohar, S., D. Sreedhar, V. Tikiya, and A. Chockalingam, "Cancellation of multiuser interference due to carrier frequency offsets in uplink OFDMA," *IEEE Transactions on Wireless Communications*, Vol. 6, No. 7, 2560–2571, Jul. 2007.

10. Nguyen, H. C., E. De Carvalho, and R. Prasad, "Multi-user interference cancellation scheme(s) for muliple carrier frequency offset compensation in uplink OFDMA," *IEEE 17th International Symposium on PIMRC*, 1–5, Sep. 2006.

11. Cao, Z., U. Tureli, Y.-D. Yao, and P. Honan, "Frequency synchronization for generalized OFDMA uplink," *IEEE Globecom'04*, Vol. 2, 1071–1075, Nov. 29–Dec. 3, 2004.

12. Yucek, T. and H. Arslan, "Carrier frequency offset compensation with successive cancellation in uplink OFDMA systems," *IEEE Transactions on Wireless Communications*, Vol. 6, No. 10, 3546–3551, Oct. 2007.

13. Sun, P. and L. Zhang, "A novel pilot aided joint carrier frequency offset estimation and compensation for OFDMA uplink systems," *IEEE VTC Spring*, 963–967, May 2008.

14. Erceg, V., K. V. S. Hari, M. S. Smith, D. S. Baum, et al., "Channel models for fixed wireless applications," Contribution IEEE 802.16.3c-01/29r1, Feb. 2001.

15. Goldsmith, A., *Wireless Communications*, Stanford University, 2004.

# Threshold Power-based Radiation Pattern Measurement of Passive UHF RFID Tags

**Leena Ukkonen and Lauri Sydänheimo**

Department of Electronics, Rauma Research Unit, Tampere University of Technology, Finland

**Abstract**— This paper is concentrated on explaining threshold power-based radiation pattern measurement of passive ultra-high frequency (UHF) radio frequency identification (RFID) tags. This measurement technique is wireless and the tag is measured in active state, i.e., in operation with the microchip. Information about the radiation pattern of an RFID tag is important in analyzing the strongest operation directions of the tag both in air and attached to identified objects. In this paper we present examples of measured radiation patterns of a passive UHF RFID tag.

## 1. INTRODUCTION

Measuring the radiation pattern of passive ultra-high frequency (UHF) radio frequency identification (RFID) tags is challenging due to the special characteristics of RFID systems. Traditional antenna measurements where cables and matching circuits are attached to antennas are not recommendable because attaching cables affects the properties of tag antennas. In addition, these kinds of measurements do not give proper information about the functioning of the tag. Therefore, novel and contactless radiation pattern measurement systems have been proposed to be used in RFID tag antenna radiation pattern measurement [1–3]. In this paper, we will measure tag's radiation pattern with threshold-power based method in active mode, i.e., when the tag is characterized in operation with the microchip.

Radiation pattern measurement of RFID tags is important in characterization of tag functioning. Similarly as the traditional antenna radiation pattern measurement, it gives information about the best radiation directions of the tag. More importantly, radiation pattern of a tag can be measured when the tag has been attached to the identified object. This way the effect of the identified material on the radiation pattern of the tag can be verified.

Figure 1 presents the components of a passive UHF RFID system. The operation abilities of passive UHF RFID systems depend mainly on two fundamental operational principles of passive UHF tags [3]:

1. The capability of the tag for wireless energy collection from the reader, i.e., tag's energy harvesting. This depends on the impedance matching between the tag's antenna and the microchip and the microchip's sensitivity. The energy harvesting information provides factors that define a minimum transmission power level for the reader unit to turn the tag on over a certain reading distance, i.e., tag's threshold power.

2. The strength and clarity of desired backscattered signal from the tag, i.e., the radar cross section (RCS) properties of the tag.
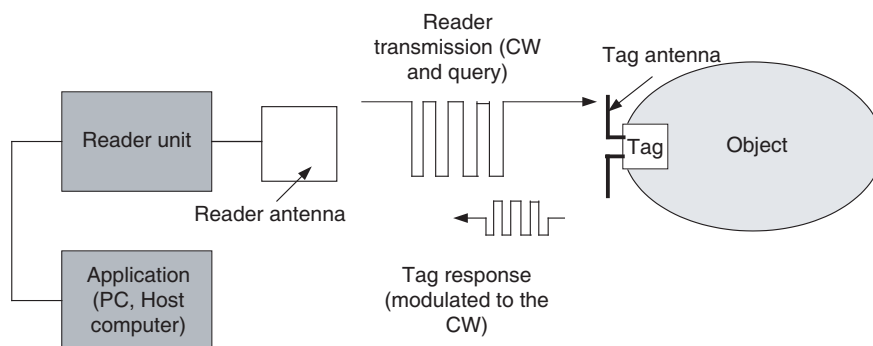


Figure 1: Components of a passive UHF RFID system.

First operational principle describes the quality of forward communication link whereas the second one defines the properties of the reverse link. In addition to the tag's backscattering properties, the reader unit's receiver sensitivity is a strong defining factor in the reverse link.

The radiation pattern of an RFID tag can be measured based on these two fundamental operational principles analyzing the forward and reverse communication links [3]. In practice, the forward link limits the read range of passive UHF RFID systems. Therefore, in this paper we concentrate on threshold-power based radiation pattern measurement of passive UHF RFID tags. Threshold power-based technique is demonstrated in measuring $E$ and $H$ plane radiation patterns of an RFID tag in air and on a package containing metallic cans.

## 2. THRESHOLD POWER AND FORWARD LINK OF THE RFID SYSTEM

As stated in Introduction, threshold power of an RFID tag can be defined as the minimum transmission power required to activate the tag and to receive a response to ID query at a certain frequency and distance from the transmitter antenna. Introduction chapter also states that the forward link communication typically limits the read range of passive UHF RFID systems. This statement can be analyzed with the following measurement results and RFID system characteristics.

Typical sensitivity of an RFID microchip can nowadays be around $-14$ dBm [4]. Sensitivity of the receiver of the reader unit can be around $-80$ dBm [5]. We measured the threshold power level and backscattered power of a typical, dipole-type tag [6] at 4 m measurement distance and we got the following results: 22 dBm for threshold power and $-50$ dBm for backscattered power. In the case of the used measurement set up, 27 dBm is the maximum allowed transmitted power. From these results we can see that at the 4 m measurement distance, there is a 5 dB safety margin in the forward link whereas in the reverse link there is a 30 dB safety margin. This shows that the forward link runs out of transmitted power first when the measurement distance is further increased and therefore the forward link limits the achievable read range of passive UHF RFID systems.

## 3. DEFINING THE RADIATION PATTERN BASED ON THRESHOLD POWER MEASUREMENTS

Normalization of RFID tag radiation patterns differs from the process used in conventional antenna measurements where the maximum power is used as a reference power level [7]. In the case of threshold power-based measurement, the results cannot be normalized to the maximum threshold power because it presents the worst result. The results have to be normalized and plotted as a function of angle using the minimum threshold power and the following calculation technique.

When the received power is defined to be the sensitivity of the microchip, the Friis transmission formula [8] can be presented as

$$P_{IC,th} = G_{TX} G_{tag} L \left( \frac{\lambda}{4\pi R} \right)^2 P_{t,th} \tag{1}$$

where $P_{IC,th}$ is the sensitivity of the microchip, $G_{TX}$ is the gain of the transmitter antenna, $G_{tag}$ is the gain of the tag antenna, $L$ is attenuation factor including cable loss, polarization loss etc., and $P_{t,th}$ is transmitted threshold power.

In the above equation, only $P_{t,th}$ and $G_{tag}$ are functions of an angle. Other factors remain constant and can be expressed with $K$. Based on these definitions, $G_{tag}$ can be defined as

$$G_{tag} = \frac{P_{IC,th}}{G_{TX} L \left( \dfrac{\lambda}{4\pi R} \right)^2 P_{t,th}} = K \frac{1}{P_{t,th}} \tag{2}$$

For normalizing the tag's gain the minimum threshold power, $P_{th,\min}$, should be used as a reference power value. Normalized gain of the tag can then be written as

$$G_{tag,\, norm.} = \frac{(K/P_{t,th})}{(K/P_{th,\min})} = \frac{P_{th,\min}}{P_{t,th}} \tag{3}$$

$$G_{tag,\, norm.}\,(dB) = P_{th,\min}\,(dBm) - P_{t,th}\,(dBm) \tag{4}$$

## 4. MEASUREMENT SET-UP

Tagformance measurement system [9] was used in the threshold power measurements carried out for this study. Tagformance system allows power ramping at a defined frequency and thereby threshold power analysis. The core operations of this system are performed with vector signal

analyzer. Measurements were carried out in a compact measurement cabinet, inside of which is presented in Figure 2. Measurement distance was 0.45 m and measurement frequency was 866 MHz, which is the UHF RFID band center frequency in Europe. Gain of the transmitter and receiver antenna in the measurement system was 8.5 dBi.

Figure 3 presents the measured commercial dipole-type tag [10] on a Styrofoam (in-air measurement) and Figure 2 mounted on a package of metallic cans. The purpose of this measurement was to study the effect of metallic material in the vicinity of the tag on its radiation pattern. There was an approximately 5–7 mm air gap between the tag and the metallic cans, which is sufficient to enable operation of a dipole tag in the vicinity of metallic surface [11].

## 5. MEASUREMENT RESULTS

Figure 4 presents the measured radiation patterns in air (Free-space) and on the six-pack of metallic cans. The results show that in air both the $E$ and $H$ plane radiation patterns of the measured tag are symmetrical and in agreement with the expected dipole antenna radiation pattern. However, when the dipole-type tag is attached to the six-pack of metallic cans, changes can be seen in the radiation pattern. Figure 4 shows that there is distortion in the $E$ plane radiation pattern due to reflections of the electromagnetic wave from the metallic surface. In addition, the shape of the $H$ plane pattern has changed from the in-air omnidirectional pattern to a directive pattern with a back lobe. This is also due to the reflections of the electromagnetic wave from the metallic surface.



Figure 2: Measurement cabinet and the measured tag on six-pack of cans.
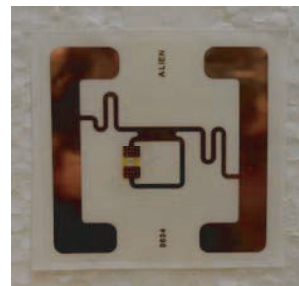


Figure 3: The measured tag [10].
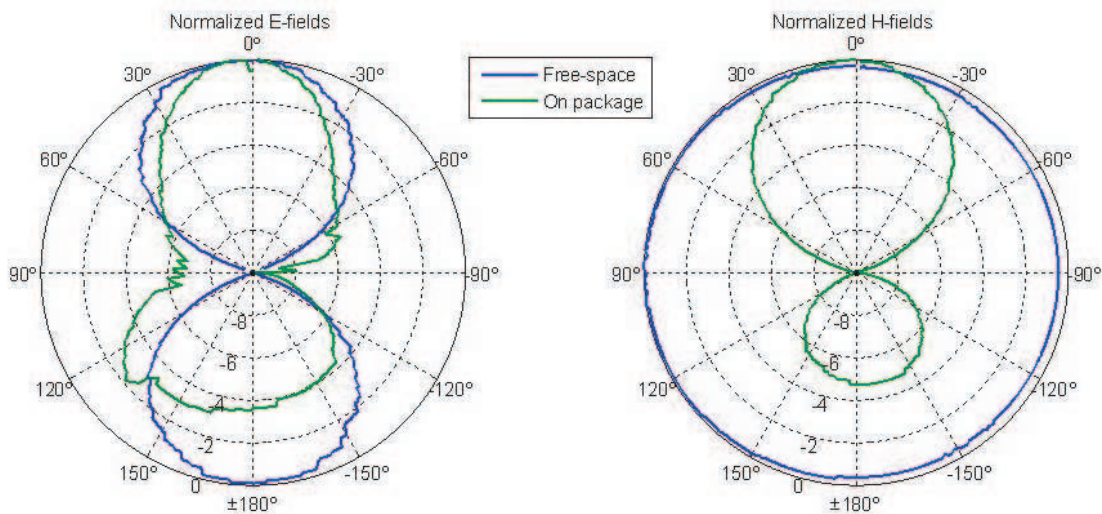


Figure 4: Measured $E$ and $H$ plane radiation patterns in air (free-space) and on six-pack of metallic cans.

## 6. CONCLUSION

In this paper, we present a threshold power-based radiation pattern measurement technique for passive UHF RFID tags. This measurement method is contactless, which means that no extra

cables need to be attached to the tag antenna. The tag is measured wirelessly in active mode, i.e., in operation with the microchip. Forward and reverse links of an RFID system are analyzed and a calculation technique for the radiation pattern is presented. This technique is based on Friis transmission equation and normalization with minimum threshold power level. Measured radiation pattern of a commercial RFID tag is presented and the effects of metallic material on the shape of the radiation pattern are analyzed.

**REFERENCES**

1. Ritamäki, M., A. Ruhanen, V. Kukko, J. Miettinen, and L. H. Turner, "Contactless radiation pattern measurement method for UHF RFID transponders," *IEE Electronics Letters*, Vol. 41, No. 13, June 2005.
2. Lao, R.-R., W.-T. Shay, J. C. Hsu, and J.-H. Tarng, "Optically modulated scatterer technique for radiation pattern measurement of small antennas and RFID tags," *IEEE Antennas and Wireless Propagation Letters*, Vol. 8, 76–79, April 2009.
3. Ukkonen, L. and L. Sydänheimo, "Radiation pattern measurement of passive UHF RFID tags," *Proc. Antenna Measurement Techniques Association 31st Annual Symposium*, 369–374, Salt Lake City, UT, USA, November 1–6, 2009.
4. Alien Technology, *Higgs 2 Datasheet*, online: www.alientechnology.com/docs/products/DS_H2.-pdf, last accessed, February 4, 2010.
5. Wang, J., B. Chi, X. Sun, T. Gao, C. Zhang, and Z. Wang, "System design considerations of highly-integrated UHF RFID reader transceiver RF front end," *Proc. ICSICT 9th International Conference on Solid State and Integrated Circuit Technology*, 1560–1563, October 2008.
6. Alien Technology, *Squiggle Tag Datasheet*, online: http://www.alientechnology.com/docs/products/DS_ALN_9540_Squiggle.pdf, last accessed, February 4, 2010.
7. Balanis, C. A., *Antenna Theory and Design*, 2nd Edition, John Wiley & Sons, 1997.
8. Saunders, S. R., *Antennas and Propagation for Wireless Communication Systems*, John Wiley & Sons, 1999.
9. Voyantic, *Tagformance Product Overview*, online: http://www.voyantic.com, last accessed, February 4, 2010.
10. Alien Technology, 2×2 *Tag Datasheet*, online: http://www.alientechnology.com/docs/products/DS_ALN-9634.pdf, last accessed, February 4, 2010.
11. Raumonen, P., L. Sydänheimo, L. Ukkonen, M. Keskilammi, and M. Kivikoski, "Folded dipole antenna near metal plate," *Proc. IEEE Antennas and Propagation Society International Symposium*, Vol. 1, 848–851, June 2003.

# Energy Efficient Fuzzy Logic Based Intelligent Wireless Sensor Network

**Malay Ranjan Tripathy**[1], **Kunal Gaur**[2], **Sonam Sharma**[3], **and G. S. Virdi**[1]

[1]Department of Electronics and Communication Engineering
Jind Institute of Engineering and Technology (JIET), Jind, Haryana, India
[2]Department of Electrical and Electronics Engineering
Jind Institute of Engineering and Technology (JIET), Jind, Haryana, India
[3]Department of Information Technology, Jind Institute of Engineering and Technology (JIET)
Jind, Haryana, India

**Abstract**— An intelligent wireless sensor network (WSN) is used in this paper to monitor the environment of interest. Each Sensor node is empowered by Fuzzy Logic system for environment monitoring, so that a sensor is in sleep mode when there is no data to transmit. It conserves energy when the node is not transmitting or receiving any tokens. By using Petri net modeling and HPSim Network Simulator, the behavior of Hybrid network topology is studied so as to make the system energy efficient and have property of liveness, soundness, without any deadlock state during execution.

## 1. INTRODUCTION

Rapid growth of wireless sensor network (WSN) [1–3] is becoming possible because of the availability of recent advanced technologies in the areas of sensors, VLSI, Micro-electromechanical systems (MEMS), computations and wireless communication systems. In WSN, a large number of low cost specially distributed sensor nodes [4] with real time embedded systems based on limited computation, energy and memory resources are used to monitor the environment of interest. To make these sensor networks intelligent enough a control mechanism like fuzzy logic based control system [5] is being used widely for many WSN applications. Fuzzy logic is basically the extension of dual logic (crisp logic) that includes the intermediate value between absolutely true and absolutely false. It improves the accuracy in taking a decision about a system that has vague information. It has the efficiency to solve the system uncertainties when mathematical models fail to describe the system. Due to its numerous applications fuzzy logic based WSN is a topic of prime interest to many researchers.

Sensor nodes in general powered by small batteries that is hard to replace or recharge. Therefore energy constraint is a major challenge for wide and remote applications [6, 7]. In a typical wireless enabled sensor system energy consumption occurs in three domains: Sensing, data processing and communication. During sensing the least possible of energy is consumed by the sensing circuits. In this paper we propose to use fuzzy logic control mechanism to activate rest of the sensing circuits (i.e., data processing and communication) only when the event of interest in the environment is available. So that WSN empowered by fuzzy logic control mechanism will work as an intelligent and power efficient sensing network.

In this paper, Fuzzy logic system (FLS) for energy efficient WSN is described in the Section 2. Hybrid network topology for energy efficient WSN is discussed in the Section 3. Section 4 is outlined on the results and discussions. The conclusion is made in the Section 5.

## 2. FUZZY LOGIC SYSTEM FOR ENERGY EFFICIENT WSN

Fuzzy logic is derived from fuzzy set theory dealing with reasoning that is approximate rather than precisely deduced from classical predicate logic. Fuzzy logic based system performs its work with the help of four steps denoted as fuzzifier, fuzzy inference machine, rule base and defuzzifier. A typical FLS is shown in Figure 1.

In fuzzy logic world we express numeric data into word language known as linguistic variable. The values of Linguistic variables are words or sentences in a natural or artificial language, providing a means of systematic manipulation of vague and imprecise concepts. For an example, the linguistic variable for input data of forest environment temperature is taken as "Normal (N), Less Hot (LH), Hot (H), Too Hot (TH) and Excessive Hot (EH)" and linguistic variable for output data of forest fire status is taken as "Normal (N) [0–0.25], Smoke (S) [0.23–0.30], Fire (F) [0.28–4.0], Blaze (B)
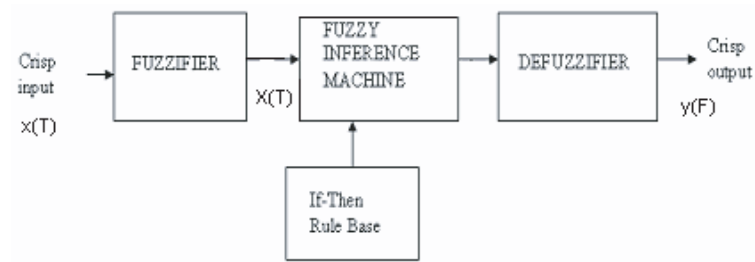
Figure 1: Fuzzy logic system (FLS) for fire monitoring.
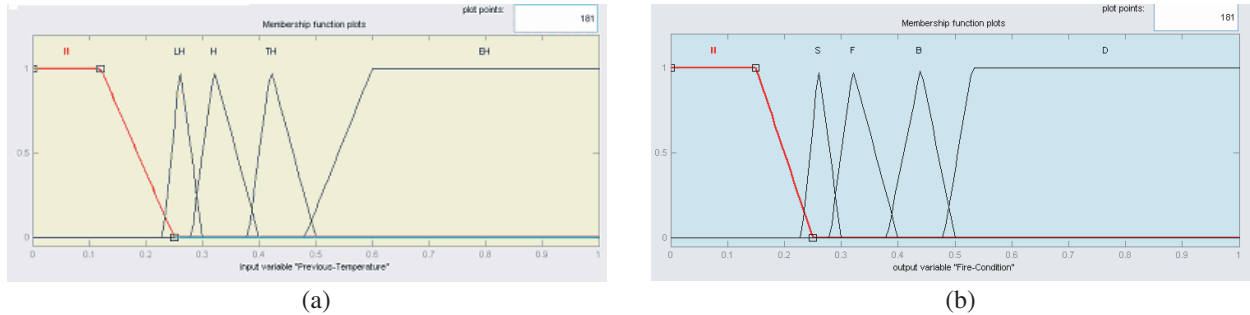


|         (a)         |         (b)         |

Figure 2: (a) Membership function of input variable (previous and current temperature). (b) Membership function for fire condition.

[0.38–0.5] and Dangerous (D) [0.48–1.0]". This linguistic input can be expressed directly by a fuzzy system with the help of membership function. The member ship functions for input and output variables are shown in Figures 2(a) & (b) below. In this paper, 16 rules are considered to analyze forest fire conditions depending on expert knowledge.

With the help of these rules the inference engine infers the result by computing each rules corresponding to a given input data. Here, we have considered Mamdani model, according to which the output generated by the inference engine is a fuzzy set. It is then converted into crisp set by the help of centroid type defuzzifier.

## 3. HYBRID NETWORK TOPOLOGY FOR ENERGY EFFICIENT WSN

The proposed scheme is the combination of hierarchical and cluster based network [8]. In Cluster-based schemes, the network is divided into groups of nodes, which saves energy and increase the network lifetime by utilizing concept of sleep mode so that only the nodes with data to be sent are awake. Within each cluster group one node is selected to be a cluster-head (leader node). The leader node receives data from its group members, combine them and send them to its master node. Figure 3 shows the view of the proposed four-layered scheme in WSN. Leader node handles communication issues between nodes within the cluster and master node. Master node manages cluster leaders and sending sensed information to the end users.

Data centric approach helps in energy saving of node, where users can query from master node for any sensed information instead of querying any individual node [9]. Leader node allots Time Division Multiple Access (TDMA) slots to every node in its cluster, which provide a schedule of sleep and communication that is based on the number of nodes in the group. Nodes can send data during the slots allotted to them and sleep otherwise. In mesh topology, the order in which tokens received may not be the same as they were send because every data packet take different route to reach the destination, so it may be the case that data packet '2' reach earlier than packet '1', which can be avoided using tree based approach. In this case, (mesh topology) data is sent to neighboring node just because it is close to the active node, which is not relevant at all. Therefore, instead of sending data to other nodes, data should be sent to the leader node directly, so that energy consumption of other nodes can be reduced, as they do not need to get active for the data, which is not meant for them.
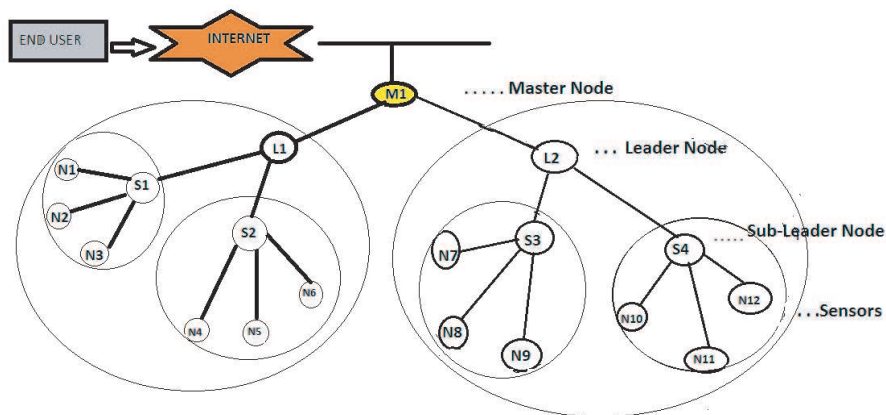
Figure 3: Four-layered scheme in WSN.

Table 1: Rules for forest fire status monitoring.

| Sr. No | Previous us Temp | Current Temp | Forest Fire Status |
|--------|------------------|--------------|--------------------|
| 1  | N  | LH | S |
| 2  | N  | H  | F |
| 3  | N  | TH | B |
| 4  | N  | EH | D |
| 5  | LH | H  | S |
| 6  | LH | TH | F |
| 7  | LH | EH | D |
| 8  | H  | TH | F |
| 9  | H  | EH | D |
| 10 | EH | TH | F |
| 11 | EH | LH | N |
| 12 | TH | H  | S |
| 13 | TH | LH | N |
| 14 | TH | N  | N |
| 15 | H  | N  | N |
| 16 | LH | H  | N |

## 4. RESULTS AND DISCUSSION

### 4.1. Fuzzy Logic Based Sensor Node

The simulated results of a knowledge based WSN used for the fire detection are carried out by the help of fuzzy logic toolbox of MATLAB and some of them are shown in Figures 4(a) & (b). From above figures we can clearly define the fire condition at different temperature situations. For Figure 4(a), if we compare with Table 1 then it can be seen that the previous temperature lies in EH (app. 50°C) range and current temp also lies in EH (app. 50°C) range. In this case the fire condition can be considered as dangerous. Therefore, it is necessary to take action as soon as possible. From Figure 4(b) it is inferred that the previous temp is H (app. 30°C) and current temp is TH (app. 37°C), i.e., in one minute the temp is increased by 7°C. So it can be considered as the situation like fire. From these figures we can find out that FLS has an ability to distinguish between a normal condition and fire condition very efficiently and accurately. This helps in controlling the communication and processing systems of WSN to switch into either active or sleep mode. Thus by applying fuzzy logic we can save the power as well as life of battery used for WSN node.
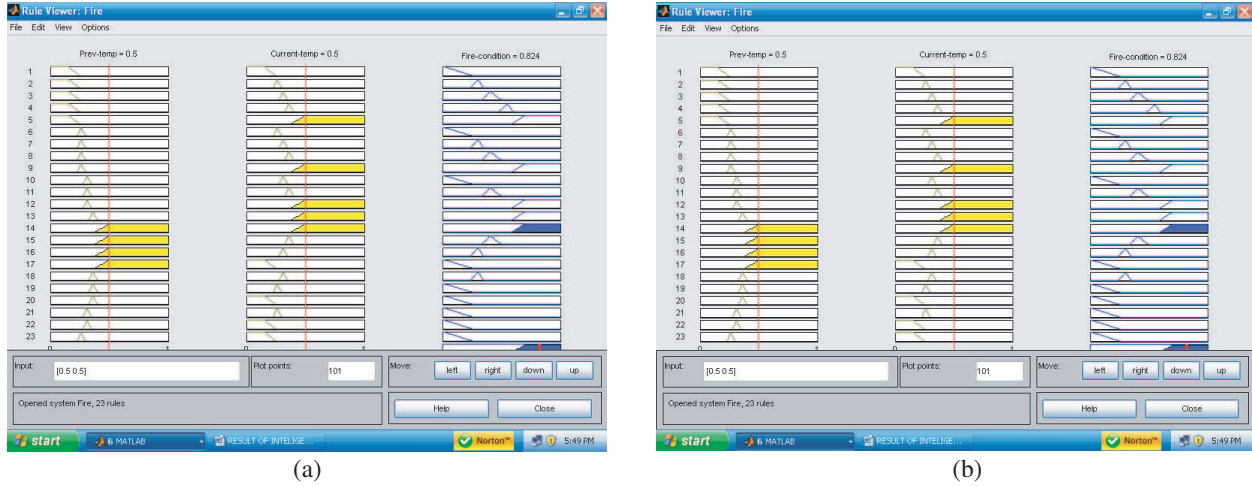
Figure 4: (a) Fire condition (Dangerous) when previous temp is EH and current temp is EH. (b) Fire condition (Fire) when previous temp is H and current temp is TH.

## 4.2. Petri Net Algorithm Based Hybrid WSN

A Petri net (known as place/transition) is a mathematical modeling language for distributed system [8]. By using this model and simulation tool like HPSim, we can analyze, verify relationship among actors and can test for any deadlock state. However, if we compare Figures 3 and 5 it is difficult to understand the behavior of both the topologies. Since model is based on Petri net's algorithm, it inherit the property of liveness, soundness, and boundedness.
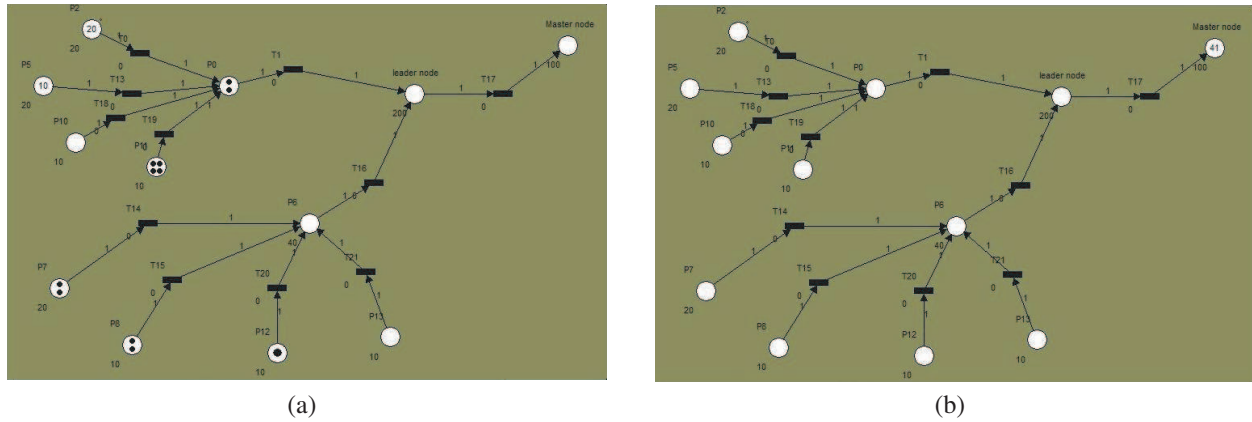


Figure 5: (a) Before firing. (b) After firing.

The Figure 5(a) shows the initial state of scheme. Here, p0 and p6 represent sub-leader nodes. They have small group of nodes such as p2, p5, p10 and p11 under p0 and p7, p8, p12 and p13 under p6. Each node is empowered by fuzzy logic control system. In the presence of event these nodes become active and start communicating data to corresponding sub-leaders. However, it is seen that in the presence of event at node p2, which has 20 tokens to send, in other case the node p10 has nothing to send that means the p10 in the state of sleep mode. In this network we have 12 places, 11 transitions and a total of 41 tokens to send to master node. After firing (as shown in Figure 5(b)), it is seen that all the tokens are successfully transferred to master node. This shows, there is no deadlock state during execution of the scheme.

## 5. CONCLUSION

In this paper, we apply FLS to save battery life and to have an efficient, robust and cost effective sensing network to monitor the event of interest. The wireless sensor network is used for remote applications. We have seen that fuzzy logic system helps efficiently to decide the situation of ON/OFF state for active/sleep mode of the processing and communication parts of the sensor

node. Petri net modeling and HPSim simulator is used for a hybrid network topology. It is seen that the network system is energy efficient and have property of liveness, soundness, without any deadlock state during execution.

**REFERENCES**

1. Akyildiz, I. F., W. Su, Y. Sankarasubramaniam, and E. Cayirci, "Wireless sensor networks: A survey," *Computer Networks*, Vol. 38, No. 4, 393–422, March 2002.
2. Zhang, Q. and Y. Zhang, "Cross layer design for QoS supporting multi hop wireless network," *Proceeding of the IEEE*, Vol. 96, No. 1, 64–76, 2008.
3. Zhang, J., P. V. Orlik, Z. Sahinoglu, A. F. Molisun, and P. Kinney, "UWB system for wireless sensor network," *Proceeding of the IEEE*, Vol. 97, No. 2, 313–331, 2009.
4. Jain, E. and Q. Liang, "Sensor placement and lifetime of wireless sensor networks: Theory and performance analysis," *Sensor Network Operations*, S. Phoha, T. F. LaPorta, and C. Griffin, Eds., Wiley, New York, 2005.
5. Mendel, J. M., "Fuzzy logic systems for engineering: A tutorial," *Proceeding of the IEEE*, Vol. 83, No. 3, 345–377, March 1995.
6. Shu, H., Q. Liang, and J. Gao, "Wireless sensor network lifetime analysis using interval type-2 fuzzy logic systems," *IEEE Transaction on Fuzzy Systems*, Vol. 16, No. 2, 416–427, April 2008.
7. Estrin, D. and R. Govindan, "Next century challenges; scalable coordination in sensor networks," *Mobicon'99*, 263–270, Seattle, WA, August 1999.
8. Kim, S. Y., O. Guzide, and S. Cook, "Towards an optimal network topology in wireless sensor networks," *SUJUR*, Vol. 1, 2009.
9. Yupho, D. and K. Joseph, "The effect of physical topology on wireless sensor network lifetime," *J. of Networks*, Vol. 2, No. 5, 14–23, September 2007.

# Rain Fade Modelling Using Hidden Markov Model for Tropical Area

**Baso Maruddani**[1,2], **Adit Kurniawan**[2], **Sugihartono**[2], **and Achmad Munir**[2]

[1]Electrical Engineering Department, State University of Jakarta
Jl. Rawamangun Muka, Jakarta 13220, Indonesia
[2]Radio Telecommunication and Microwave Laboratory
School of Electrical Engineering and Informatics, ITB
Jl. Ganesha 10, Bandung, West Java 40132, Indonesia

**Abstract**— This research is aimed to model the channel fading due to rain, especially rain fading in the tropical area, to know the characteristic of the channel mainly the attenuation. Hidden Markov Model (HMM) was used for generate the rain rate model. HMM parameters such as initial matrix, transition matrix, output symbol and emission matrix are obtained from measurement. CDF is used to evaluate the generated rain rate model and there is no significant different between measured rain rate and generated rain rate model. HMM most probable state path value is 0.9512 which means the similarity between measurement and simulation is 95.12%.

## 1. INTRODUCTION

Nowadays, demand for broadband services increases rapidly. Millimeter wave communication system is one of the infrastructures which can be used for application of broadband multimedia. However, the use of frequency above 10 GHz creates a problem, that is, increasing the frequency will increase rain attenuation. Rainfall rate is one of the dominant factors that govern the level of rain attenuation in wireless propagation of communication system. As a tropical country, Indonesia has higher rain rate than other non-tropical country. Communication system using millimeter wave need special attention in order to mitigate the received signal level and quality degradation that caused by rain. If Indonesia wants to use Ka-band frequency, it has to know deeper about rain attenuation characteristics to develop Ka-band communication systems.

Several studies related to channel modeling and rain attenuation mitigation have been carried out in non-tropical regions. For fading channel modeling, one approach used is to use a Markov process. Markov process is an appropriate technique to model the stochastic random process because it can take into account a variety of errors in the channel. Many experimental results show that the hidden Markov model (HMM) can be used to model the errors in digital communications systems in fading channels. In addition, many efficient statistical algorithms to adjust the fading channel model using HMM with measured data and to predict various forms of stochastic processes by using HMM. The use of HMM to model the Rayleigh fading channel is relatively simple but with high accuracy to calculate various parameters on the channel fading which is generally more difficult if done with other approaches [1–3]. Research on Ka-band in Indonesia is still relatively small. In [4, 5] conducted research to model the millimeter wave channel frequency by considering the effect of rain on the attenuation experienced by the millimeter waves.

From the [8], the rain can be divided into 2 groups, i.e., stratiform and convective rain. Characteristics of each type of rains give a different effect on the propagation and signal attenuation in the wireless communications systems which using a Ka-band frequency. Rain duration, rain area and rainfall rate each time determine the quality of the signal received at the receiver. The distribution events of these factors are needed in order to know the attenuation characteristics of Ka-band frequency signal and how to make a rain fading mitigation techniques.

## 2. MARKOV MODEL

Markov model is a model that related to a series of events which result of an experiment only depends on the events that immediately preceded it, and do not depend on the sequence of events before the other before. If a particular occurrence of a series of experiments depending on the number of possible events, the series of experiments is called a stochastic process. The process is said Infinity (Finite), when all possible events that can occur, Infinity. Further below is notation required for mathematical of Markov models decision-making:

Markov model has been applied to propagation channel modeling. There are three types of Markov Model which are Multi-state Markov Model, Hidden Markov Model and Non-stationer Markov Model. Markov methods are generally appropriate to use a hidden Markov model (HMM) [7].
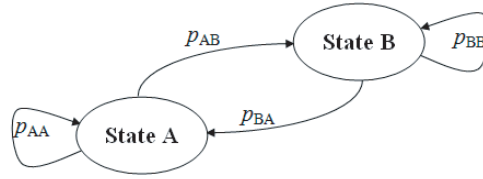
Figure 1: State diagram for Markov model.

Table 1: Types of clouds that cause rain.

| *Stratiform* | *Convective* | |
| --- | --- | --- |
|  |  |  |
| • Rain period is long enough<br>• Rain area is wide enough<br>• Rainfall rate is less than 25 mm/h | • Short time rain period<br>• Rain area is narrow enough<br>• Rainfall rate is more than 25 mm/h | • Short time rain period<br>• Rain area is narrow enough<br>• Rainfall rate is more than 25 mm/h<br>• Accompanied by lightning and storms |

The joint probability of final state with assumption the state space $S = \{1, 2, \ldots, \mu\}$, the final state $s_t$ and the received sequence $b_1^t = (b_1, b_2, \ldots, b_t)$ conditioned upon the initial state $s_0$ and the transmitted sequence $a_1^t$ is

$$Pr\left\{b_1^t, s_t | a_1^t, s_0\right\} = \sum_{s_1^{t-1}} \prod_{i=1}^{t} Pr\{b_i, s_i | a_i, s_{i-1}\} \tag{1}$$

Assume $P(b_t, a_t)$ is the conditional matrix probability (MP) of the output symbol $b_t$ given the input symbol $a_t$, is a matrix wth $i$-$j$-element $Pr\{b_t, s_t = j | a_t, s_{t-1} = i\}$, then $P(b_1^t, a_1^t)$ is the conditional matrix probability (MP) of the output symbol $b_1^t$ given the input symbol $a_1^t$. $P(b_1^t, a_1^t)$ is given by:

$$P\{b_1^t | a_1^t\} = P\{b_1, a_1\}P\{b_2, a_2\}P\{b_3, a_3\} \ldots P\{b_t, a_t\} = \prod_{i=1}^{t} P\{b_i | a_i\} \tag{2}$$

The conditional probability $Pr(b_1^t | a_1^t, s_0)$ of receiving $b_1^t$ given the initial state $s_0$ and the input sequence $a_1^t$ is the sum over $s_t$ of $Pr(b_1^t, s_t | a_1^t, s_0)$ is $p\{b_1^t | a_1^t\} = P\{b_1^t | a_1^t\}1$, where $1 = [111\ldots1]'$ and $P(b_1^t | a_1^t)$ is a matrix column whose elements are the probabilities $Pr(b_1^t | a_1^t, s_0)$.

Therefore, a FSC can be described as $\{S, A, B, \pi, P\{a\}\}$, where $S$ is the channel state space, $A$ is its input alphabet, $B$ is its output alphabet, $\pi$ is the initial state probability vector, and the conditional MP $P\{a\}$ whose elements are the probabilities $Pr\{a, j | i\}$ of transferring from the channel state $i$ to state $j$ and producing the output symbol $a$. The channel states are not directly observable (hidden). The observed symbol sequence is a probabilistic function of the hidden states, and the symbol conditional probability (given a sequence of states) depends only on the previous state and the current state. If this conditional probability depends only on the current state, i.e., $Pr\{a, i | j\} = Pr\{a | j\}$, then the autonomous FSC is called a discrete hidden Markov model (HMM).

A HMM is, therefore, a doubly stochastic process with an underlying stochastic process that is not observable, but can be observed through another set of stochastic processes that produce the sequence of observed symbols. In general, a HMM is described as $\{S, A, \pi, P, F\}$, where $S$ is the set of its hidden states, $A$ is the set of its observations, $\pi$ is the state initial probability vector, $P$ is the state transition probability matrix, and the state observation probability matrix, $F$, gives the probability of observing a symbol $a \in A$ in any state $s \in S$. If the underlying Markov chain is stationary, and the matrix $P$ is regular, then the state initial probability vector can be found as a solution to the system

$$\pi P = \pi \quad \pi 1 = 1 \tag{3}$$

Therefore, a stationary HMM can be defined by the collection of the MPs $P\{a\}$ only, since the initial state probability vector can be determined as a unique solution to (3).

## 3. MEASUREMENTS AND RESULT

This research measured rainfall rate for one year with assumption that the rain cycle repeated annually. Rainfall measurements using a rain gauge 0.2 mm placed in an open area so that the rainfall measurements obtained valid. The rain gauge that use in this research is recording the rain when the rainfall happens. Therefore, the rain gauge data is the rainfall accumulation in certain period to achieve 0.2 mm water from rain. To modify the rain gauge data to the rainfall rate in minutes, the assumption is the rainfall rate is same in certain period to achieve 0.2 mm. Fig. 2 shows the assumption and explanation. The assumption is used to get the rain fall events every minute in a year that can be seen in Fig. 3.
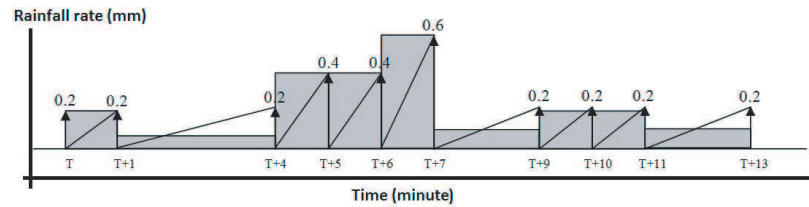


Figure 2: Rain gauge data to rainfall rate in minute modified assumption.
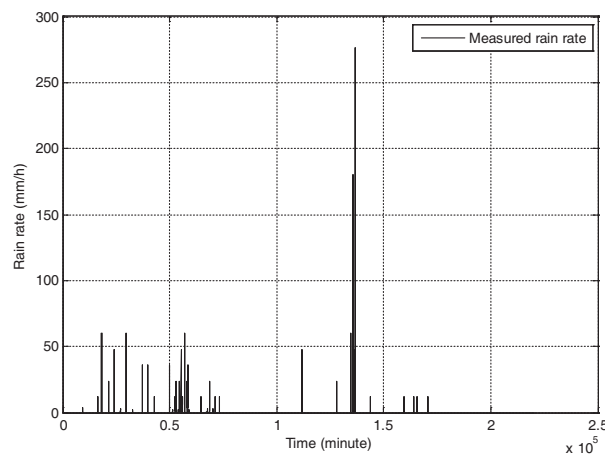


Figure 3: Every-minute-rain-rate in a year.
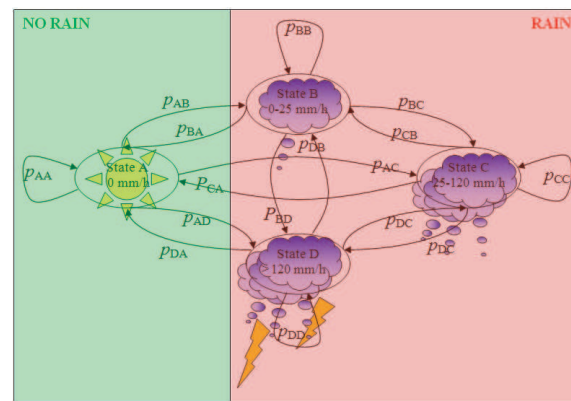
Figure 4: State diagram for modeling rainfall rate in tropical area.

## 4. CHANNEL MODELLING

From the minutely-rain-events data and types of rain clouds, this research divided into four state of Markov model, which every state has their own characteristics. State 1 is the state where rainfall events are considered to be 0 mm/h or no rain events. State 2 is an event where there is a stratiform cloud that makes rainfall rate is 0 to 25 mm/hour.

State 3 is the state where it is assumed that there is a convective cloud which produces rainfall with intensity more than 25 mm/hour. In this state considered that there is no lightning/thunder. The upper limit of rainfall rate in this state is 120 mm/hour. State 4 is the last state where it is assumed that in this state that there are convective clouds, but in this state, considered that there are also lightning/thunder and rainfall rate that produced is greater than 120 mm/hour. The rain rate above 120 mm/hour are generally only occurs in tropical regions, where the incidence and rain rate are higher than the non-tropical regions. Fig. 4 shows the diagram state of Markov model for this research.

Minutely-rain-events data is used to determine HMM parameter such as the initial matrix, the transition matrix, the output symbol and emission matrix. Here are the initial matrix, the matrix of transition, set the output symbol and emission matrix that obtained from measured rainfall. The output symbol is a rain rate in mm/h unit. This symbol is emission every minute to get rainfall

rate sequence.

Initial matrix

$$[0.974682280319535 \quad 0.0235793391430646 \quad 0.00164760348583878 \quad 9.07770515613653e\text{-}05]$$

Transition matrix

$$\begin{bmatrix} 0.999813729096912 & 0.000107105769275546 & 7.91651338123600e\text{-}05 & 0 \\ 0.00654475457170356 & 0.986333012512031 & 0.00692974013474495 & 0.000192492781520693 \\ 0.0165289256198347 & 0.132231404958678 & 0.84848484848449 & 0.00275482093663912 \\ 0 & 0 & 0.100000000000000 & 0.900000000000000 \end{bmatrix}$$

| 0 | 0.146341 | 0.307692 | 0.6 | 1.714286 | 72 |
|---|---|---|---|---|---|
| 0.021779 | 0.157895 | 0.342857 | 0.631579 | 2 | 84 |
| 0.028103 | 0.166667 | 0.352941 | 0.666667 | 2.4 | 96 |
| 0.047809 | 0.181818 | 0.375 | 0.705882 | 3 | 120 |
| 0.051064 | 0.184615 | 0.413793 | 0.75 | 3.428571 | 132 |
| 0.089552 | 0.193548 | 0.428571 | 0.8 | 4 | 144 |
| 0.099174 | 0.20339 | 0.444444 | 0.857143 | 6 | 168 |
| 0.10084 | 0.222222 | 0.461538 | 0.923077 | 8 | 180 |
| 0.110092 | 0.235294 | 0.48 | 1 | 12 | 228 |
| 0.113208 | 0.255319 | 0.5 | 1.090909 | 24 | 240 |
| 0.12 | 0.26087 | 0.521739 | 1.2 | 36 | 252 |
| 0.125 | 0.27907 | 0.545455 | 1.333333 | 48 | 264 |
| 0.134831 | 0.3 | 0.571429 | 1.5 | 60 | 276 |

EmissionMatrix

```
1     0        0        0        0        0        0        0        0        0        0        0        0
0     0.10035  0.07776  0.04571  0.04298  0.02440  0.02204  0.02167  0.01985  0.01930  0.01821  0.01767  0.01639  ....
0     0        0        0        0        0        0        0        0        0        0        0        0
0     0        0        0        0        0        0        0        0        0        0        0        0

      0        0        0        0        0        0        0        0        0        0        0        0
....  0.01512  0.01402  0.01311  0.01202  0.01184  0.01147  0.01093  0.01002  0.00947  0.00874  0.00838  0.00783  0.01457
      0        0        0        0        0        0        0        0        0        0        0        0
      0        0        0        0        0        0        0        0        0        0        0        0

      0        0        0        0        0        0        0        0        0        0        0        0
      0.007102531 0.01293 0.00619 0.00583 0.01056 0.0051 0.0049 0.00965 0.00455 0.00437 0        0.012012 0.0076  ....
      0        0        0        0        0        0        0        0        0        0        0        0
      0        0        0        0        0        0        0        0        0        0        0        0

      0        0        0        0        0        0        0        0        0        0        0        0
      0.00728  0.01056  0.00346  0.00929  0.00911  0.01366  0.00546  0.01202  0.01329  0.01038  0.01111  0.01839  0.02477
....  0        0        0        0        0        0        0        0        0        0        0        0
      0        0        0        0        0        0        0        0        0        0        0        0

      0        0        0        0        0        0        0        0        0        0        0        0
      0.02295  0.02768  0.02295  0.01402  0.00127  0.0173   0.02094  0.00109  0.03296  0.02094  0        0        0
....  0        0        0        0        0        0        0        0        0        0        0.52703  0.21621  0.14865 ....
      0        0        0        0        0        0        0        0        0        0        0        0

      0        0        0        0        0        0        0        0        0        0        0        0     0
      0        0        0        0        0        0        0        0        0        0        0        0     0
....  0.01351  0.02703  0.05405  0.01351  0        0        0        0        0        0        0        0     0
      0        0        0        0        0.07692  0.23077  0.07692  0.07692  0.07692  0.15385  0.07692  0.15385  0.07692
```



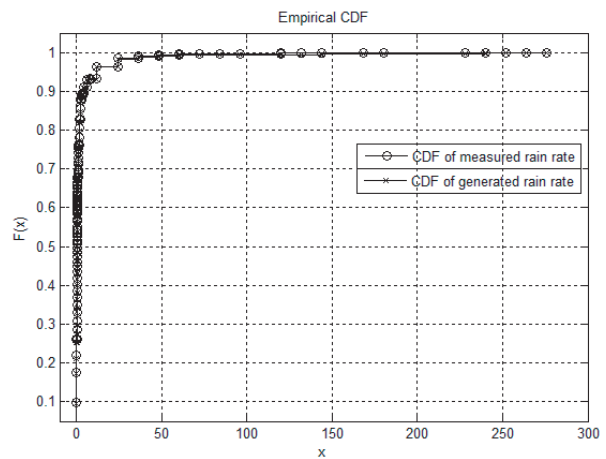Figure 5: Generated rain rate.



Figure 6: CDF of measured and generated rain rate.

## 5. SIMULATION RESULT

Simulation was done after HMM parameter was known. HMM parameter s used to generate rain rate sequence every minute. From the generated rain rate, there are some rain rates which more than 120 mm/h. This rain rate is one of the characteristics for tropical area. Fig. 5 shows the simulation result for generated rain rate.

To know the simulation validity, this generated rain rate is compared to measured rain rate using their CDF. From the Fig. 6, there is no significant different between CDF of measured rain rate with CDF of generated rain rate, which means that the distribution of minutely-rain-rate is same. Not only CDF, but also HMM most probable state path can show its similarity. HMM most probable state path value is 0.9512 which means the similarity between measurement and simulation is 95.12%.

From the generated rain rate and general rain rate formula, the rain fade can be shown. Simulation shows that higher rain rate gives higher attenuation. Fig. 7 shows the rain fade model. The characteristic of rain fade gives clue how to make the rain fade mitigation technique. One of the mitigation techniques that can be implemented is power control. The power control used is evaluated every minute because the information about attenuation is gathered every minute.
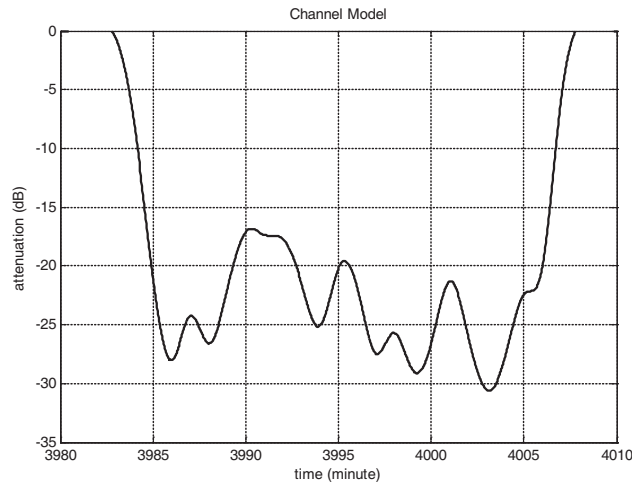


Figure 7: Rain fade model.

## 6. CONCLUSION

Telecommunication using millimeter wave i.e., Ka-band is the answer to problem that face by broadband communication. Increasing the frequency will make greater bandwidth available, but will increase rain attenuation. Rain attenuation makes imperfect communication. In tropical area that has higher rain rate than non-tropical area is one of problem if Ka-band use in tropical area. One of the solutions is make the mitigation technique based on characteristic of rainfall rate in tropical area. Markov model is a method to model the rain rate and rain fading based o their characteristic. This research gives information about rain rate events at tropical area and rain fade model that has is 95.12% similarity with the measurement result.

## REFERENCES

1. Lin, H. P., M. J. Tseng, and D. B. Lin, "Modeling fading properties for mobile satellite link channels using markov model approaches," *Antennas and Propagation Society International Symposium IEEE*, Vol. 4, No. 22–27, 192–195, June 2003.
2. Hsieh, J. C., H. P. Lin, and C. Yang, "A two-level, multi-state Markov model for satellite propagation channels," *53rd IEEE Vehicular Technology Conference*, Vol. 4, 3005–3009, 2001.
3. Paulson, K. S. and C. J. Gibbins, "Rain models for the prediction of fade durations at millimetre wavelengths," *Proc. IEE Microwaves, Antennas and Propagation*, Vol. 147, 431–436, Dec. 2000.
4. Mauludiyanto, A., G. Hendrantoro, and P. Hutajulu, "Simulation of tropical rain attenuation for evaluation of millimeter-wave wireless network," *Proc. 5th IFIP International Conference on Wireless and Optical Communications Networks*, 1–5, May 5–7, 2008.
5. Yadnya, M. S., A. Mauludiyanto, and G. Hendrantoro, "Statistical of rain rates for wireless channel communication in surabaya," *Proc. 5th IFIP International Conference on Wireless and Optical Communications Networks*, 1–5, May 5–7, 2008.
6. Kandella, P., "Studi perencanaan satelit broadband nasional menggunakan Ka-band," School of Electrical Engineering and Informatics, Bandung Institute of Technology, 2008.
7. Khan, A. A., "Iterative decoding and channel estimation hidden markov fading channels," Faculty of the Virginia Polytechnic Institute and State University, May 2000.
8. Ihwan, A., "Estimasi curah hujan beberapa kota di indonesia menggunakan data MT-SAT Kanal inframerah (IR1)," Geophysics and Meteorological Department, Bandung Institute of Technology, 2007.

# Power Control and Diversity Performance Analysis in CDMA Systems

**Baso Maruddani[1,2] and Adit Kurniawan[2]**

[1]Electrical Engineering Department, State University of Jakarta, Indonesia
[2]School of Electrical Engineering and Informatics, Bandung Institute of Technology, Indonesia

**Abstract**— In wireless communications systems, fading can degrade a system's performance. In this paper, the problem that will be observed is the increase of system's performance when the antenna diversity techniques combined with power control in CDMA communication system to overcome fading. This research simulates the performance of the system, which power control algorithm is fixed step algorithm and combination of diversity is selective diversity combining. The simulation results show that combined power control and antenna diversity gives more performance improvement than using power control only. In the cases where the user of Doppler frequency is greater than 1/10 of the power control rate value, performance improvement also occurred, but the BER curves of $\mathbf{E}_b/\mathbf{I}_0$ tend toward the direction of the channel fading characteristics.

## 1. INTRODUCTION

CDMA as a wireless communication technique has some unique features such as high spectrum efficiency, soft hand-off, low transmit power, and multipath mitigation. A system design description for CDMA applied to digital cellular radio communications is described in [1], where a multiple pseudonoise (PN) receiver is employed to demodulate the received signals.

The main problem in CDMA is multiple access interference because all users use the same frequency at the same time and the PN code is not orthogonal. The distance between base station and mobile station also affects the signal strength received by the base station. Users that were located closer to the base station will be more dominating than the user who is relatively further. This problem can be overcome by power control by the process so that the average received power at base station is same for each user.

Power control to mitigate Rayleigh fading in CDMA system has been studied in [2]. And evaluation about CDMA performance using diversity technique is shown in [3]. The purpose of this research is to determine the performance improvement for system when use combined power control and diversity technique on the receiver using 2-branch and 3-branch antenna.

In this research the problem that will be observed is the increase of system's performance when diversity techniques combined with power control to overcome the deep and shallow fading that experienced by signals. The idea is the received signal that experience fading is overcome by diversity technique then power control works to make fading shallower.

The simulation in this research using fixed step power control algorithm combined with selective diversity algorithm. This paper will evaluate the performance about combined power control and diversity technique with 2-branch antenna and with 3-branch antenna.

## 2. POWER CONTROL AND CHANNEL MODEL IN CDMA

Power control in CDMA can be classified into several categories. According to the algorithm used, power control can be divided into open-loop power control, and closed-loop power control.

### 2.1. Open Loop Power Control

Near-far effect is a problem that occurs because the distance of each mobile station to base station is not the same. Signals from each mobile station will experience different propagation attenuation, depends on the distance between the mobile station to base station. Open-loop power control is designed to ensure that the amount of power received from each user at the base station will be the same (on average). In open-loop algorithm, the mobile station can calculate the required transmit power by using the estimated downlink signal (not required feedback information). This is because the large scale propagation attenuation is reciprocal on the uplink and downlink channels.

To overcome the problems of near-far effect is simply to say that the mobile station is located far from the base station should transmit a signal with greater power than mobile stations that are

closer to the base station. Signals sent by the mobile station must have the power of [1]:

$$P_t = -P_r + P_{off} + P_p \tag{1}$$

with:
     $P_t$ (dBm) = power to be emitted MS,
     $P_r$ (dBm) = received power at the MS,
     $P_{off}$ (dB) = parameter offset power,
     $P_p$ (dB) = power parameter adjustment

## 2.2. Closed Loop Power Control

Closed-loop power control aims to eliminate signal fluctuation due to small scale propagation attenuation. Unlike the large scale propagation attenuation, small-scale propagation attenuation on the uplink and downlink do not have any correlation. Therefore, to control the uplink fading on the uplink channel, the base station must estimate the information and then give the feedback to the mobile stations, so the mobile stations can adjust the power emitted in accordance with feedback information. To obtain the uplink channel information, the base station can estimate the SIR. However, in CDMA system, power control based on SIR is preferable than power control based on received signal level because in CDMA is interference limited [1].

Power Control based on the SIR is more preferable because SIR value shows BER value. Especially in uplink channel, power control based on SIR has ability to respond the change of interference on base station for each user[4].
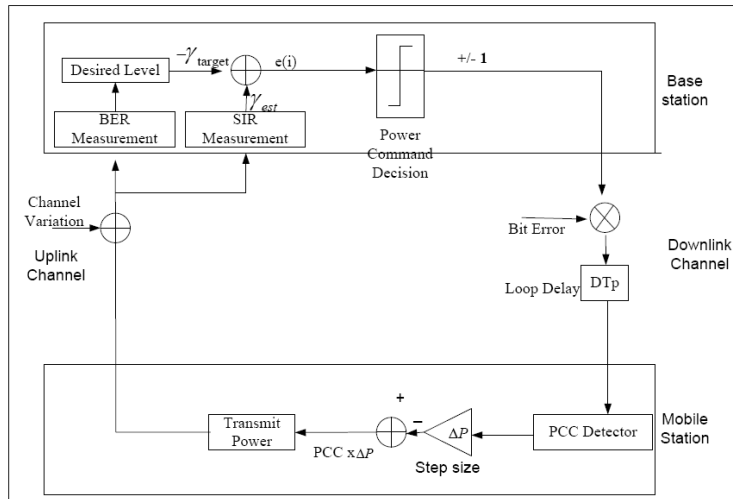


Figure 1. Closed-loop power control model [1].

## 2.3. Channel Model

Generally, the wireless channel can be modeled as a superposition of several paths with different amplitudes and time delays which can be expressed as:

$$h(t) = \sum_{l=0}^{L-1} \beta_l \delta(t - \tau_l) e^{j\theta_l} \tag{2}$$

where $\beta_l$ is the magnitude of the $l-$th path impulse response at time $\tau_l$, $\delta(t - \tau_l)$ is an impulse at $t = \tau_l$, and $\theta_l$ is the phase shift of the $l$-th path. If the transmitted baseband signal of the user is expressed as:

$$x(t) = \sqrt{2P}bs(t) \tag{3}$$

where $2P$ is the transmitted power, $b$ is the transmitted symbol and $s(t)$ is the binary waveform, then the received signal can be expressed as:

$$r(t) = x(t) * h(t) = h(t) = \sum_{l=0}^{L-1} \sqrt{2P}b\beta_l s(t - \tau_l) e^{j\theta_l} \tag{4}$$

The received signal in (4) may experience fluctuations due to constructive and destructive interference from $L$ paths and also will suffer from time spreading due to different arrival time instants of $L$ paths. When all signal paths have approximately the same time delay, the effect of delay spread is not significant and the channel can be said as a frequency nonselective or flat fading, known as a Rayleigh fading channel.

## 3. DIVERSITY TECHNIQUE

Diversity is one technique to exploit the same information from several independent and uncorrelated signal paths than can be resolved and combined by the diversity receiver. If the received paths are correlated, no diversity gain can be attained. Generally, there are three diversity techniques; time diversity, frequency diversity and space diversity. In time diversity, a signal path came with the same information but arrived at a different time slot, then signals are combined. Arrival time difference between signal paths with the other signals is uncorrelated, so the benefits from the use of diversity can be obtained. In frequency diversity, frequency diversity gained obtained from a signal path that came to bring the same information but using different frequencies carrier, and then signal are combined. The separation of several different carrier frequencies must exceed the bandwidth of the channel. In space or antenna diversity, several signal paths bearing the same information that come from different antennas are combined. The separation between one antenna and another must exceed the coherence distance of the channel.

In our simulation, we choose to use antenna diversity to evaluate the performance of CDMA system when it is combined with power control. We will consider reception diversity at the base station because we will use this technique in conjunction with power control on the uplink.
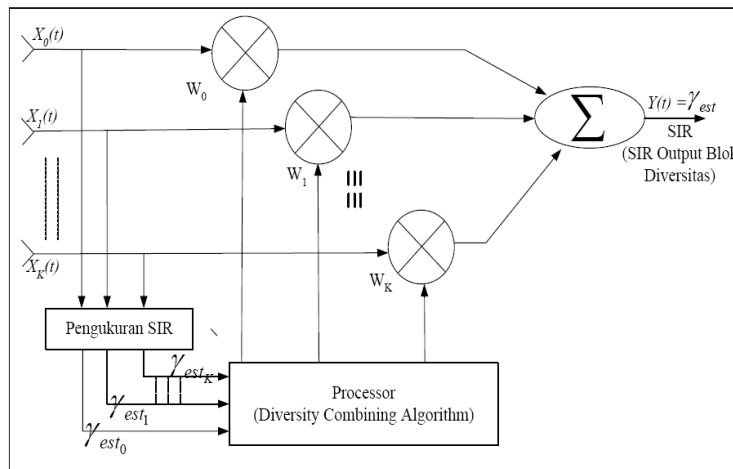


Figure 2. Simple model for antenna diversity.

Diversity combining in Fig. 2 can be selective diversity when the weight factor $w_s$ is selected to the strongest signal $x_s(t)$, equal gain diversity when the weight factor $w_1$, $w_2$, ... are set to unity, or maximal ratio combining when the weight factor $w$ is set proportional to the value of SIR.

To investigate the effect of diversity techniques on power control, we repeat our power control simulation, but now we consider diversity channels at the base station. We simulate selective diversity combining (SDC) algorithm with 2-elements antenna array and 3-elements antenna array. With its simple algorithm, SDC is enough to alleviate the deep fade that experienced by signal. SDC select only the strongest signal in its branch. We considered using 2-branch and 3-branch antenna to see how significant this method to improve the performance compared with no diversity. Our previous work just compares system with no diversity and system with 2-branch antenna diversity [5].

## 4. SIMULATION AND RESULT

In this simulation, the assumption is the problems of near-far effect and shadowing already overcome by open-loop power control so that the average received signal level by the mobile station is constant. Open-loop power control algorithm is overcome the fluctuations caused by Rayleigh distributed flat fading only. For closed loop power control, the process is based on SIR measurement on the base

station. This research uses some parameter for simulation. The parameters that used can be seen on Table 1 and the simulation result for fading channel can be seen on Fig. 3.

Figure 3(a) show the fading channel for Doppler frequency is 16.67 Hz and Fig. 3(b) shows the fading channel for Doppler frequency 116.67. Doppler frequency depends on user's velocity.

Simulation result for SIR can be seen on Fig. 4. For controlled SIR value that controlled by power control only can be seen on Fig. 4(a). The variation between the highest SIR value and the lowest SIR value is still wide. But when power control combined with diversity, the variation SIR is getting narrowed. Controlled SIR value for 2-branch antenna and 3-branch antenna diversity can be seen on Fig. 4(b) and Fig. 4(c) respectively.

Simulation result for diversity block can be seen on Fig. 5. This figure shows that selective diversity combining algorithm works successfully to overcome fading, which this algorithm select the strongest signal in each branch for each time slot. Fig. 5(a) shows the diversity block for 2-branch antenna and Fig. 5(b) shows the diversity block for 3-branch antenna.

Based on parameter simulation, we will investigate user which moves with velocity 10 km/h and 70 km/h. For user with velocity is 10 km/h, the simulation result can be seen in Fig. 6.

Figure 6 shows that using 3-antenna diversity can improve performance better than using 2-antenna diversity or not using diversity. It's because 3-antenna diversity is more efficient to eliminate deep fades. But the performance improves significantly from 1-antenna (not using diversity) to 2-antenna diversity compared than from 2-antenna diversity to 3-antenna diversity. To achieve BER of $10^{-3}$, the required $E_b/I_0$ for 3-antenna diversity system is 5 dB higher than for AWGN channel. To achieve BER of $10^{-3}$, the required $E_b/I_0$ for 2-antenna diversity system is 5.5 dB higher than for AWGN channel. And to achieve BER of $10^{-3}$, the required $E_b/I_0$ for no diversity system

Table 1. Simulation parameter.

| Parameter | Symbol | Value |
|---|---|---|
| Carrier frequency | $f_c$ | 1.8 GHz |
| Number of user | $K$ | 10 user |
| Vehicle's speed | $v$ | 10, 40, and 70 km/h |
| Doppler frequencies | $f_d$ | 17, 67, and 117 Hz |
| Symbol rate for QPSK | $R_s$ | 60 ksps |
| Chip rate | $R_c$ | 3,84 Mcps |
| Power control period | $T_p$ | 0,667 ms |
| Processing gain | $M$ | 64 |
| Number of symbol/time slot | $B$ | 40 |



(a)  (b)
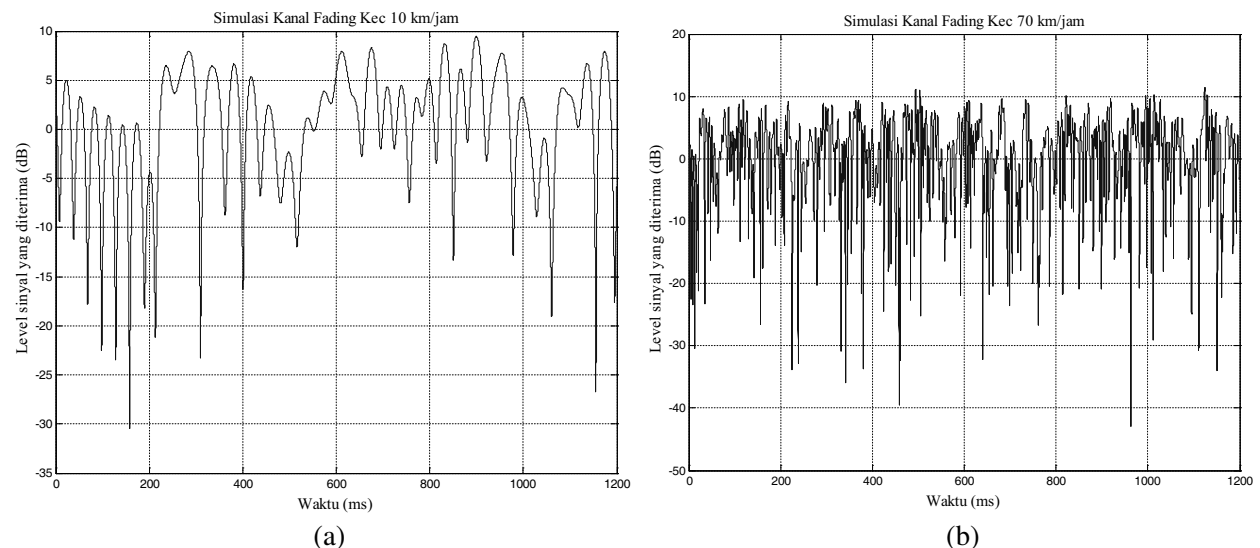
Figure 3. Fading channel simulation.
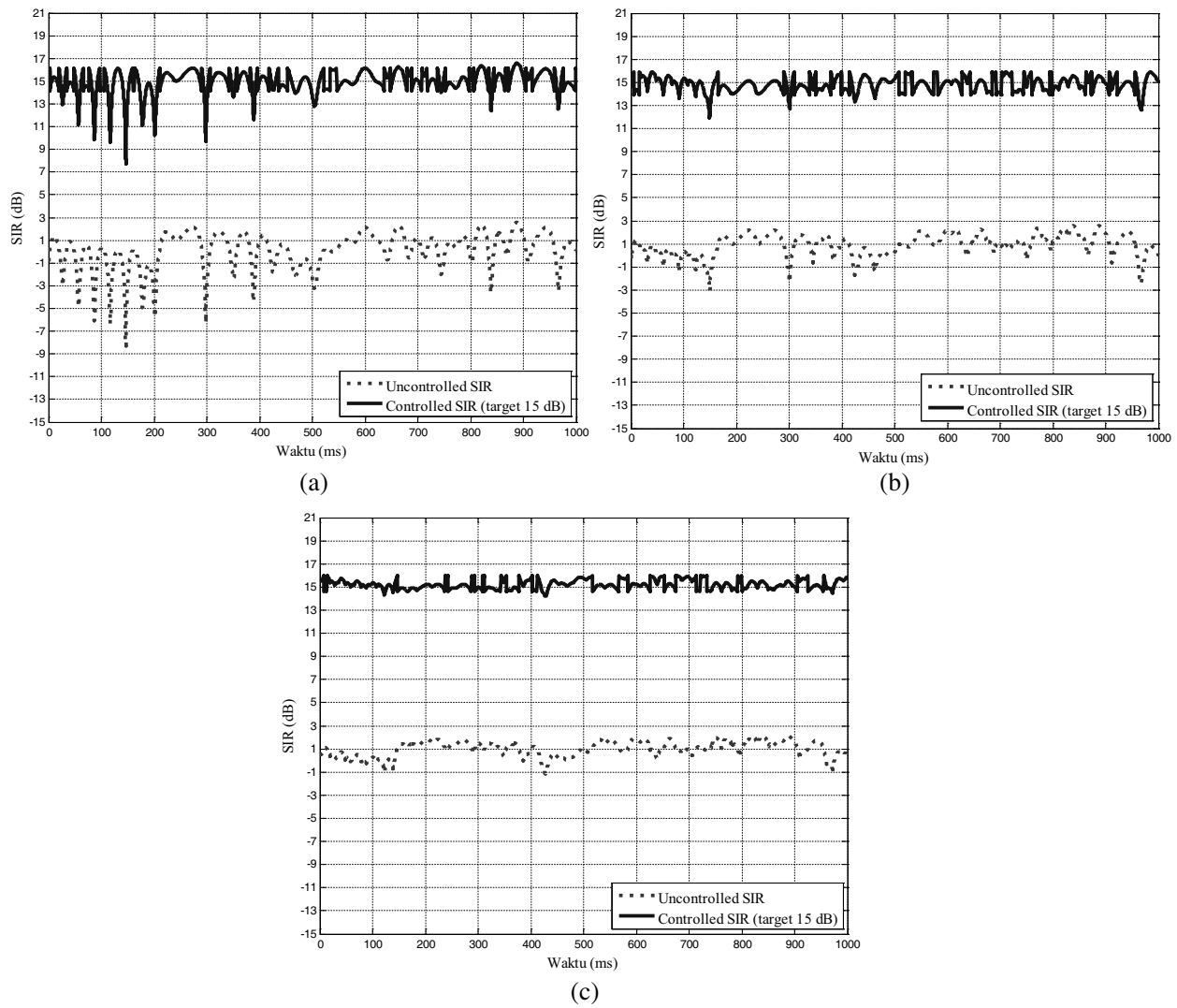
Figure 4. Controlled SIR simulation.
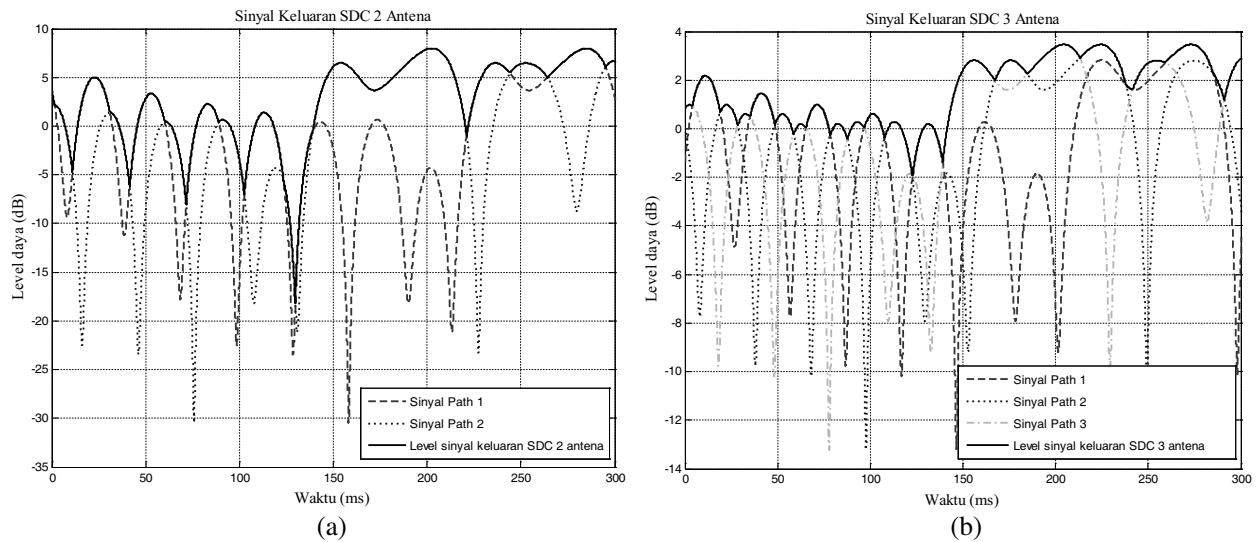


Figure 5. Diversity block output.
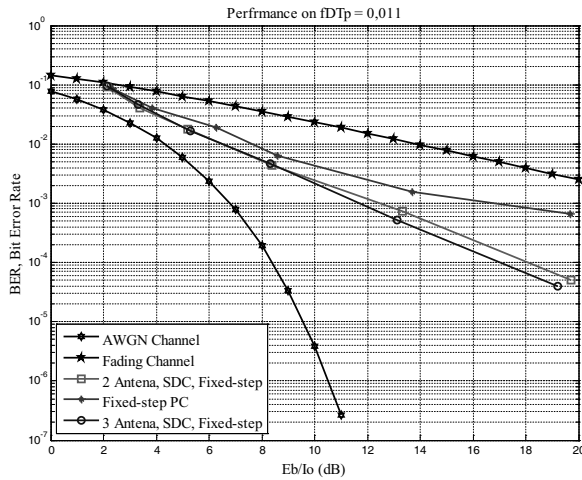
Figure 6. BER Performance with $fDTp = 0.011$.        Figure 7. BER Performance with $fDTp = 0.078$.
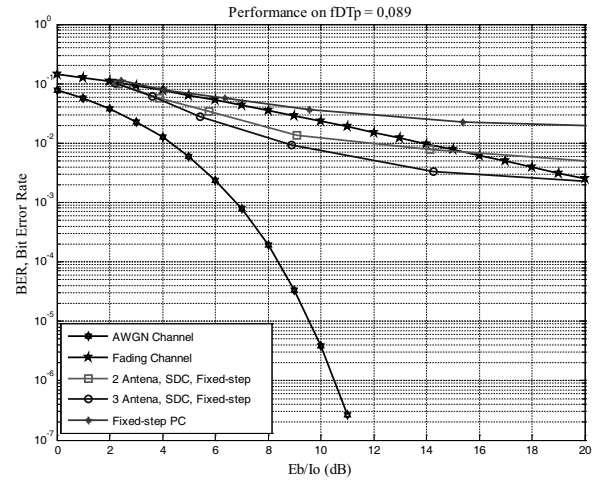
is 10.2 dB higher than for AWGN channel. User with velocity 10 km/h, the experienced fading is slow fading. It makes the power control and antenna diversity is enough to handle the fading and improve the performance.

For user with velocity is 70 km/h, the simulation result can be seen in Fig. 7. User with velocity 70 km/h experienced fast fading. In fast fading, diversity technique can eliminates deep fades but power control cannot works perfectly because power control rate is too slow relative to the fading rate. From figure, power control seems unable to improve the fading channel performance. However, improvement can be seen when it combined with diversity technique.

## 5. CONCLUSION

Under ideal conditions, power control can turn the fading channel into an AWGN channel performance. Power control can improve the BER performance of slow fading channel. In fast fading channel, power control failed to combat multipath fading. Diversity technique, on the other hand, also can improve the performance.

From our simulation, in slow fading condition, using diversity can improves the performance significantly and using 3-antenna diversity at receiver gives performance better than 2-antenna diversity.

### REFERENCES

1. Kurniawan, A., *Predictive Power Control in CDMA Systems*, Institute for Telecommunications Research, University of South Australia, 2003.
2. Salmasi, A. and K. Gilhousen, "On the system design aspects of code division multiple access (CDMA) applied to digital cellular and personal communications networks," *Proc. 41th IEEE VTC Conf.*, 57–62, 1991.
3. Kurniawan, A., "Power control to combat rayleigh fading in wireless mobile communications systems," *Proceedings of APT Workshop on MCMT 2002*, Jakarta, October 2002.
4. Naghian, S., M. Rintamaki, and R. Baghaie, "Dynamic step size power control in UMTS," *Proc. of the 13th. IEEE International Symposium on Personal, Indoor and Mobile Radio Communications*, Vol. 4, 1606–1610, 2002.
5. Kurniawan, A. and B. Maruddani, "Performance evaluation of the combined power control and antenna diversity in CDMA systems," *Proceeding ICEEI 2007*, Bandung, Indonesia, June 2007.

# A Novel Power Controller of Wireless Sensor Network Node Circuit for Energy Saving

**Shi-Sheng Jin**[1], **Wei-Wei Cheng**[2], **Shun Yuan**[1], **Jun-Yong Wang**[1], **and Jue Li**[1]

[1]Guizhou Meteorological Information Center, Guiyang, Guizhou 550002, China
[2]Institute of Microelectronics and Optoelectronics, Zhejiang University
Hangzhou, Zhejiang 310027, China

**Abstract**— A novel power controller of wireless sensor network node circuit for energy saving are designed, fabricated and tested. It adopts TDMA mode to control the power parts of all the circuit module of the wireless sensor network node, and utilizes the low frequency signal to awake the monitoring circuit to enable the power controller to work, then the controller circuit makes decision to shift the status of the sensor node and manages the distributing power modules to reduce the power consumption.

## 1. INTRODUCTION

A novel power controller of wireless sensor network node circuit for energy saving are designed, fabricated and tested. In fact, autonomous sensors play a very important role in the environmental, structural, and medical fields [1–3]. The use of this kind of systems can be expanded for several applications, for example in implantable devices inside the human body where it is impossible to use wires [4–6]. Furthermore, they enable measurements in harsh or hermetic environments, such as under extreme heat, cold, humidity or corrosive conditions. The use of batteries as a power supply for these devices represents one solution, but the size, and sometimes the cost and unwanted maintenance burdens of replacement are important drawbacks [7–10].

In this paper, a novel power controller of wireless sensor network node circuit for energy saving are discussed. Their general architectures are presented. Power sensing strategies, communication techniques and power management are analyzed, and it gives an extensive application for the wireless sensor node which includes transmitting channel and receiving channel.

## 2. THEORY AND SOLUTION

Reduction in size and power consumption of consumer electronics has opened up many opportunities for low power wireless sensor networks. One of the major challenges is in supporting battery operated devices as the number of nodes in a network grows [11, 12]. The two main alternatives are to utilize higher energy density sources of stored energy, or to generate power at the node from local forms of energy [13, 14]. And in this paper, to get the reduction in power consumption, the adopted circuit consists of wakeup circuit, logic control switch circuit, several power switch arrays and power controller.

This paper mentions the state-of-the art technology in the field of both energy storage and energy harvesting for sensor nodes. The options discussed for energy storage include communication mode, waking method, decision strategy to enable the work of power controller, distributing power management by the power controller and so on.

## 3. CIRCUITS AND WORKING PROCESSING

On account of the advantages above, a novel power controller of wireless sensor network node circuit for energy saving is designed, which is shown in Fig. 1. There is only transmitting channel of communication, and the wakeup circuit only receiving the low frequency signal to accumulate the energy and without the function to demodulating the information of the low frequency signal.

It consists of LF antenna (low frequency antenna), RF antenna (radio frequency antenna), wakeup circuit, logic control switch, battery which is composed of three power supply modules, power switch array which is composed of three power array modules, duplexer, monitor circuit which is composed of detector, filter and comparator, radio frequency transmitting circuit which is composed of PA (power amplifier), gain amplifier and modulator, DSP (digital signal processing), and data sampling circuit which is composed of A/D (analogue to digital converter) and sensor.

In Fig. 1, the wakeup block is a passive circuit to get the signal to store the energy which is enough to finish the waking works. After being waked up, the logic control switch block enables

the PSA1 and power controller work, and the latter controls the logic control switch and gives the power supply to the monitor. Then the monitor receives the radio frequency signal which is a TDMA signal and detects it to a low frequency pulse signal and sends it to comparator to create a sign, according to this sign, the logic control switch block and power controller block make a decision to enable the data sampling block and radio frequency transmitting circuit block by turn on the PSA2 and PSA3. In the whole process, there is no power consumption of the sensor node if the receiving data is invalid and the system works only powered by the coupling energy.
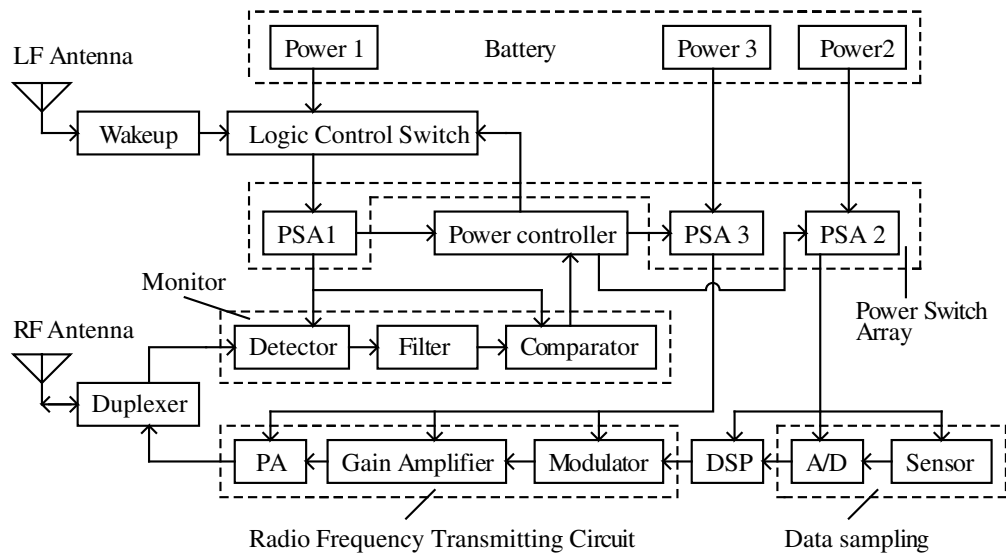


Figure 1: Wireless sensor circuit (only transmitting channel).
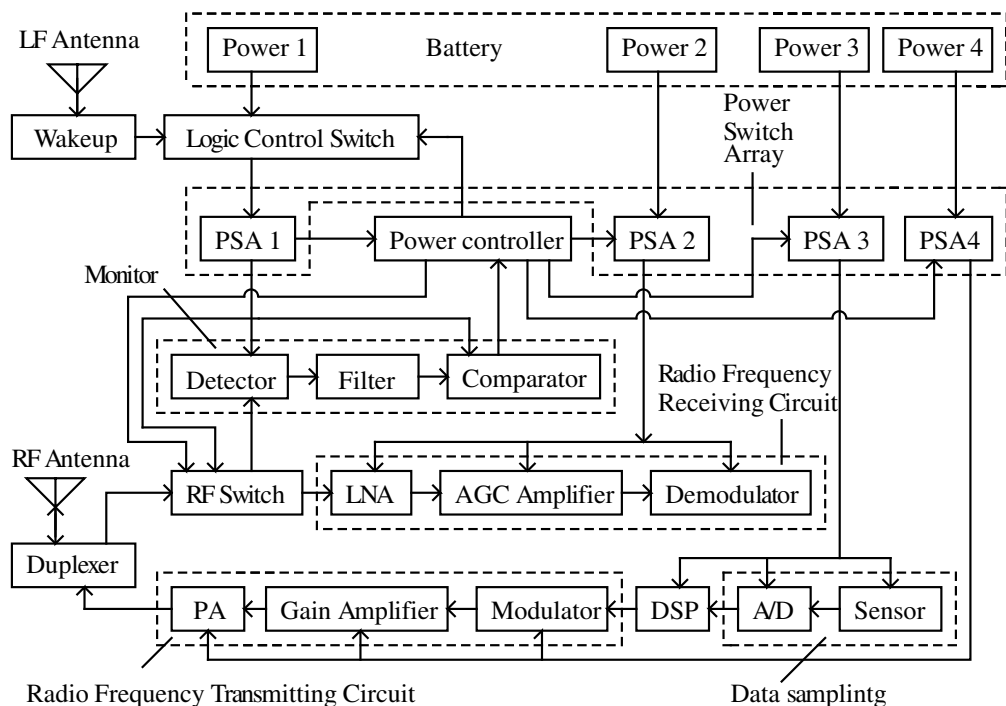


Figure 2: Wireless sensor circuit for extensive applications (transmitting channel and receiving channel).
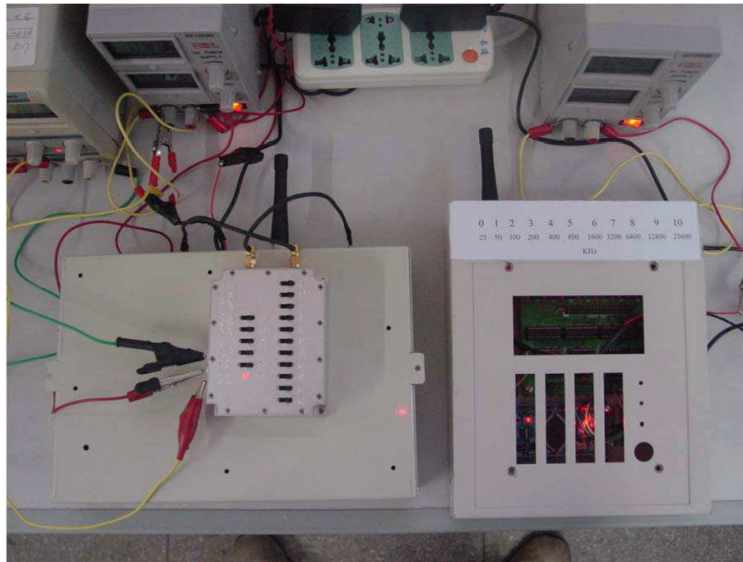
Figure 3: Wireless sensor circuit and receiver system photo.

## 4. EXTENSIVE CIRCUITS

We develop the extensive applications of the novel power controller of wireless sensor network node circuit for energy saving based the above circuit, shown in Fig. 2. There are two channels for communication, transmitting channel and receiving channel.

It consists of LF antenna (low frequency antenna), RF antenna (radio frequency antenna), wakeup circuit, logic control switch, battery which is composed of four power supply modules, power switch array which is composed of four power array modules, duplexer, RF switch (radio frequency switch), monitor circuit which is composed of detector, filter and comparator, radio frequency receiving circuit which is composed of LNA (low noise amplifier), AGC amplifier (automatic gain control amplifier) and demodulator, radio frequency transmitting circuit which is composed of PA (power amplifier), gain amplifier and modulator, DSP (digital signal processing), and data sampling circuit which is composed of A/D (analogue to digital converter) and sensor. And Fig. 3 is the photo of the above circuit system.

## 5. CONCLUSION

The wakeup circuit, logic control switch circuit, several power switch arrays and power controller constitute the whole low power controlling. The passive wakeup circuit decreases the coupling time and makes it more accurate by adjusting the parameters of the key component of it, and increases the coupling energy to get less coupling time; the TDMA mode is to avoid data communication conflict and data missing; and the logic control switch circuit is very important to the power controller by make the most reasonable time to enable its work. After testing of the whole system in the Fig. 3, all the above techniques make the power consumption reduce and realize that the power consumption is zero when the data to the wireless sensor node is invalid.

## REFERENCES

1. Akyildiz, I. F., et al., "Wireless mesh networks: A survey," *Computer Networks-the International Journal of Computer and Telecommunications Networking*, Vol. 47, 445–487, Mar. 2005.
2. Anastasi, G., et al., "Energy conservation in wireless sensor networks: A survey," *Ad Hoc Networks*, Vol. 7, 537–568, May 2009.
3. Baronti, P., et al., "Wireless sensor networks: A survey on the state of the art and the 802.15.4 and ZigBee standards," *Computer Communications*, Vol. 30, 1655–1695, May 2007.
4. Buratti, C., et al., "An overview on wireless sensor networks technology and evolution," *Sensors*, Vol. 9, 6869–6896, Sep. 2009.
5. Huang, G. Q., et al., "Wireless manufacturing: A literature review, recent developments, and case studies," *International Journal of Computer Integrated Manufacturing*, Vol. 22, 579–594, Jul. 2009.

6. Joshi, C. V., et al., "A review of the challenges in the implementation of next-generation ZigBee networking," *Iete Technical Review*, Vol. 25, 161–167, Jul.–Aug. 2008.

7. Knight, C., et al., "Energy options for wireless sensor nodes," *Sensors*, Vol. 8, 8037–8066, Dec. 2008.

8. Lopez, T. S., et al., "Integrating wireless sensors and RFID tags into energy-efficient and dynamic context networks," *Computer Journal*, Vol. 52, 240–267, 2009.

9. Oweis, R. and M. Minarik, "Design, simulation and realization of a dual-mode oscillator with distributed RC structure," *Radioengineering Radioengineering*, Vol. 8, 17–21, 1999.

10. Rhee, I. K., et al., "Clock synchronization in wireless sensor networks: An overview," *Sensors*, Vol. 9, 56–85, Jan. 2009.

11. Sardini, E. and M. Serpelloni, "Passive and self-powered autonomous sensors for remote measurements," *Sensors*, Vol. 9, 943–960, Feb. 2009.

12. Willig, A., "Recent and emerging topics in wireless industrial communications: A selection," *IEEE Transactions on Industrial Informatics*, Vol. 4, 102–124, May 2008.

13. Xiao, R. Y. and G. Z. Wu, "A survey on routing in wireless sensor networks," *Progress in Natural Science*, Vol. 17, 261–269, Mar. 2007.

14. Yick, J., et al., "Wireless sensor network survey," *Computer Networks*, Vol. 52, 2292–2330, Aug. 2008.

# A UHF and HF RFID Integration System for Access Control Application

**Wei He**, **Yinlong Huang**, and **Weihua Sun**

Anti-counterfeit Information Department, The Third Research Institute of MPS, China

**Abstract**— In this paper, a novel RFID (Radio Frequency Identification) application integration system for UHF (ultra high frequency) and HF (high frequency) operation is presented. This system is at UHF and HF band operation, and consists of UHF reader, CP (circular polarization) antenna, HF reader, HF loop antenna, control computer, LED touching display, affiliated video camera, fingerprint identification fixture etc. In this design, UHF reader complies with standard of ISO 18000-6B, 6C and HF reader complies with standard of ISO 15693. Designing this system make it a suitable candidate for RFID application in access control for some importance meetings and sporting contests etc.

## 1. INTRODUCTION

At the current moment, RFID is of a great practical interest for various fields of industry, trade and transport services ([1–4]) such as electronic toll collection, tracking containers, asset identification, retail item management, access control, remote monitoring, vehicle security and etc. Especially, the demands for long range identification by access control and manufacturers supply chain management have raised the frequency for RFID from HF into UHF and microwave frequency.

A typical RFID system includes RFID readers and RFID tags. Each RFID tag has the unique identifier, saying unique ID, and is attached to some object. A user reads the unique ID of an RFID tag with his RFID readers. That enables the user to identify the object provided with the RFID tag. The unique ID of an RFID tag can be related to some useful information. In RFID application in access control for some importance meetings, one of the important information is the location information and the identity information of the participants with the RFID tag. From the unique ID, the location information and the identity information of the participants concerning the RFID tag, the participants is identified and judged when he enters into the meeting.

In access control of some importance meetings or conference, it is always required to have both short and long range identification. Generally, HF RFID has identification distance within 0.8 m, and UHF RFID has most long identification distance is 10 m. So, HF RFID and UHF RFID are always used for short and long range object identification respectively. In this study, an integration system at UHF and HF operation for RFID application in access control for some importance meetings and sporting contests is presented.

## 2. SYSTEM MODELING DESIGNING

Figure 1 is the UHF and HF RFID integration system. It is mainly consists of UHF reader, UHF antenna, HF reader, HF loop antenna, control computer and LED touching display screen and affiliated video camera, fingerprint identification fixture. In this system, UHF antenna is circular polarization and operates at 900–930 MHz band. HF loop antenna operates at 13.56 MHz. UHF reader complies with standard of ISO 18000-6B, 6C and HF reader complies with standard of ISO 15693. Video camera is used to take photograph for those who are walking past this system. Fingerprint identification fixture is used to validate the participants' identity in company with HF RFID. Because HF RFID has short identification distance and UHF RFID has long identification distance, in company with the monitor function of video camera and fingerprint identification fixture, this RFID application integration system can well meet the requirements of short and long range exact identification for RFID application in access control for some importance meetings and sporting contests etc.

## 3. ANALYSIS OF THE UHF RFID PERFORMANCES OF THE SYSTEM

The presented UHF and HF RFID integration system has two working mode. One is short range identification mode and the other is long range identification mode. When the system works at long range identification mode, the UHF reader, UHF antenna, control computer and LED touching display screen and affiliated video camera are working. It has about 10 m identification distance. UHF antenna is circular polarization and has approximately semi-spherical coverage area radiation
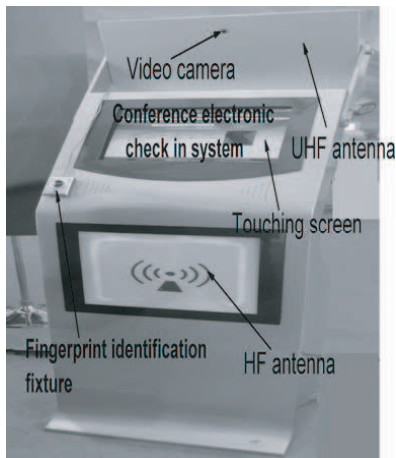
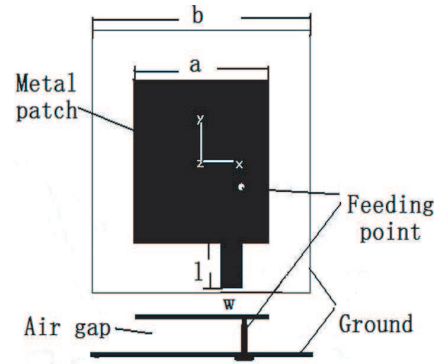Figure 1: The UHF and HF RFID integration system.



Figure 2: The schematics of the CP antenna element.

patterns, with more than 8 dBi gains and less than 2 dB axial ratio at 900–930 MHz band. Using this UHF RFID structure can guarantee the RFID system being reliably readable. RFID application in access control for some importance meetings, the participant with a tag can be oriented arbitrary with respect to reader antennas and, therefore, can be readable in any position within the range of readable distance. At the same time, the information of the unique ID of an RFID tag being related to the location and the identity information of the participants and the photograph of the participants from video camera can be gotten in time on the spot. The unique ID of the participants is exclusive corresponding with his photograph stored in database in advance. By contrasting the photograph of the participants from video camera instantly on the spot and the photograph of the same participants stored in database in advance, we can validate the participants' real identity and prevent the misfeasor from entering the meeting. This UHF RFID system can well meet the requirements RFID location tracing applications in a long distance in the scene of meeting.

Figure 2 is the UHF CP antenna element. In combination with the technique of air gap, approximately diagonal feeding of square patch and phase modulating, the antenna element exhibits a broad-band characteristic and circular polarization. In Fig. 2, $a = 128$ mm, $b = 200$ mm, $l = 36$ mm, $w = 21.5$ mm. The $l$ is phase modulating line. The air gap substrate is used to obtain a particular broad-band characteristic. Approximately diagonal feeding in combination with phase modulating $l$ make the fundamental resonant frequency of the square patch to be split into two resonant modes with 90 phase difference. With such an arrangement, CP operation of antenna can be obtained. In Fig. 2, phase modulating $l$ design can make the antenna to operate on left-hand CP (LHCP) mode. In the RFID system, the antenna is covered by the radome as shown in Fig. 1 and can achieve an approximately semi-spherical coverage area, which guarantee the RFID system being reliably readable in the most coverage area.

Figure 3 shows the simulated and the measured return loss of the CP antenna element. The measured results show satisfactory agreement with the simulation data. It can be seen that distinct resonance modes at 873–968 MHz are excited with good impedance matching. The simulated impedance bandwidths, assuming a limit of $-15$ dB return loss, are about 895–962 MHz (about 7.2%). The measured impedance bandwidths, assuming a limit of $-15$ dB return loss, are about 891–939 MHz (about 5.2%). These can well meet the bandwidths of our UHF RFID 900–930 MHz band.

Figure 4 shows the simulated radiation patterns of the CP antenna element in $E$-plane ($x$-$z$ plane) and $H$-plane ($y$-$z$ plane) at 920 MHz respectively. The antenna has good characteristic of directional beam in the $x$-$z$ plane and in the $y$-$z$ plane. The simulated 3-dB beam width in the $x$-$z$ and $y$-$z$ planes are 68.7° and 66° respectively as shown in Fig. 4. Modeling of such antennas, with simplicity in designing and feeding, can well achieve an approximately semi-spherical coverage area. Peak antenna gains for two operating bands have been determined by simulated as 8.45 dBi at 920 MHz and 8.5 dBi at 925 MHz respectively.
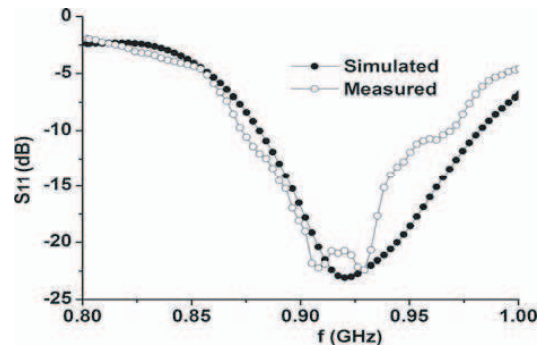
Figure 3: The measured and simulated return loss for the CP antenna element.



(a)

(b)
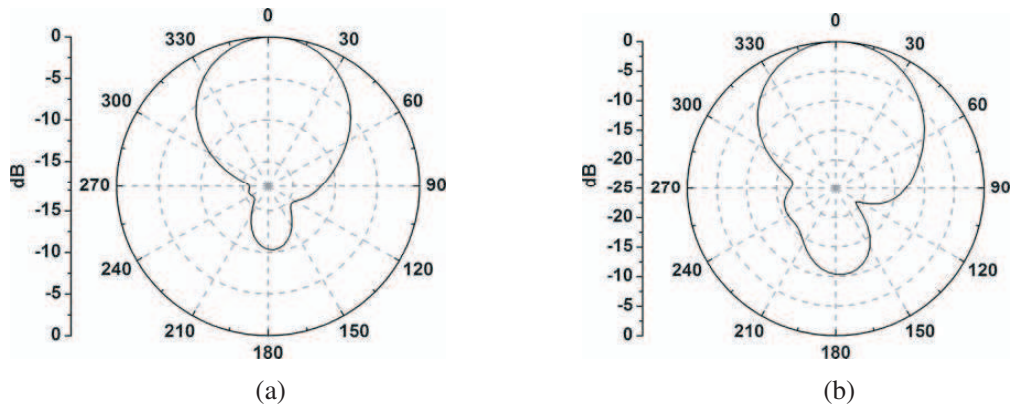
Figure 4: The radiation patterns at 920 MHz for the CP antenna element. (a) $E$-plane ($x$-$z$ plane), (b) $H$-plane ($y$-$z$ plane).

## 4. ANALYSIS OF THE HF RFID PERFORMANCES OF THE SYSTEM

When the system works at short range identification mode, the HF reader, HF antenna, control computer, LED touching display screen, affiliated video camera and the fingerprint identification fixture are working. Because the HF RFID has characteristic of short identification distance, it can be combine with the fingerprint identification fixture to attain exact identical validating for the participants. The fingerprint information of the participants can be collected in advance. During RFID application in access control for some importance meetings, the unique ID of an RFID tag is related to the unique identity information, photograph and the fingerprint information of the participant. When the participants entering into meeting scene, the participants is required to put his appointed fingerprint on the fingerprint identification fixture, if the fingerprint information of the participants being collected on the spot is not identical to the former information, the control computer will give an alarm. This HF RFID system can well meet the requirements of strict security in RFID access control for some importance meetings.
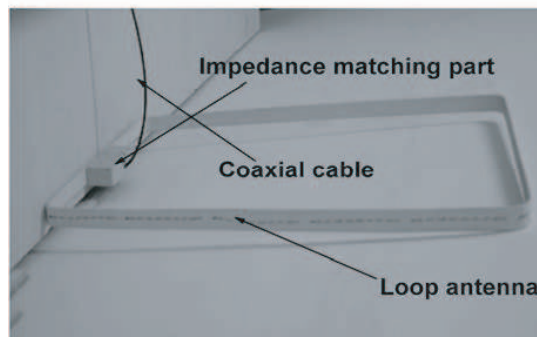


Figure 5: The photograph of the HF loop antenna.

Figure 4 is the photograph of HF loop antenna. The loop antenna is connected to HF reader by impedance matching part and coaxial cable. Because the loop antenna appears inductive impedance and HF reader appears $50\,\Omega$ impedance, so the impedance matching part which appears $50\,\Omega$ resistance and capacitive impedance is designed to match the impedance of the HF loop antenna and the HF reader. Thus the HF RFID system has good power transmitting from signal source to antenna. This HF RFID system has effective identification range of $0.8\,\mathrm{m}$ distance and $25\,\mathrm{cm} \times 25\,\mathrm{cm}$ area.

## 5. CONCLUSION

In this study, a RFID application integration system at UHF and HF operation is presented. This integration system can be used for short and long range object identification respectively. The UHF RFID can well meet the requirements of location tracing applications in a long distance in the scene of meeting and the HF RFID can well meet the requirements of strict security in access control for some importance meetings.

REFERENCES
1. Tuttle, J. R., "Traditional and emerging technologies and applications in the radio frequency identification (RFID) industry," *IEEE Radio Frequency Integrated Circuits (RFIC) Symposium*, 5–8, Jun. 8–11, 1997.
2. Pala, Z. and N. Inanc, "Smart parking applications using RFID technology," *RFID Eurasia*, 1–3, Sep. 5–6, 2007.
3. Qiu, J., B. Sun, and Q. You, "Study on RFID antenna for railway vehicle identification," *IEEE 6th International Conference on ITS Telecommunications Proceedings*, 237–240, 2006.
4. Marrocco, G., "RFID antennas for the UHF remote monitoring of human subjects," *IEEE Transactions on Antennas and Propagation*, Vol. 55, No. 6, 1862–1870, Jun. 2007.

# Fast Integral Equation Solution Techniques for Planar-3D Structures in Multilayered Media

**Thomas Vaupel**

Fraunhofer Institute for High Frequency Physics and Radar Techniques FHR
Wachtberg, Germany

**Abstract**— In this contribution, a hybrid space/spectral domain integral equation approach is presented for the characterization of quasi-3D structures in multilayered media. The vertical conductors for the quasi-3D components like vias, through holes, airbridges, finite dielectric regions etc. can cross an arbitrary number of dielectric layers with arbitrary vertical discretization. The electrodynamic behavior of the vertical currents is incorporated by extended spectral domain Green's functions derived by analytical integrations over the vertical direction and by a summation over the Cartesian wavenumbers which must be computed only once and stored in a database. For short lateral distances, the couplings are computed with a subtraction technique based on asymptotic representations of the extended Green's functions, whereas for larger distances and for group coupling computations in context with fast matrix vector product evaluations, adaptive integration path deformations with extended Laguerre quadrature methods are applied. For the solution of the linear systems of equations, a GMRES solver was implemented together with a diakoptic preconditioner based on the group decomposition of larger structures, combined with a reversed Cuthill McKee reordering applied to the submatrix pattern of the system matrix. With all these techniques, the analysis of complex quasi-3D structures can be carried out with the same performance than pure planar microstrip and/or slotline structures.

## 1. INTRODUCTION

For the analysis and design process of (M)MIC structures and printed antenna systems, electromagnetic simulators based on the Method of Moments (MoM) combined with the Green's function of the multilayered environment are widely used due to their high accuracy and good modeling capabilities which have been accomplished over the last years. For the incorporation of quasi 3D components within microstrip/stripline and/or slotline/aperture components, spatial domain techniques with mixed potential formulations and the discrete complex image method are used for solving such structures [1–3] showing typically a very good numerical performance for planar metallizations. However, for quasi-3D elements the numerical effort is often significantly increasing using these techniques since the performance may strongly depend on the required number of complex images and problems occur with large source to observation point distances.

In our approach volume currents with vertical direction are employed for the modeling of vertical interconnects, via- or throuh holes, coaxial feedings as well as finite dielectric regions, where arbitrary vertical discretizations in combination with arbitrary crossings of layer interfaces are possible. For the interactions of the vertical currents under each other and with the planar components, extended Green's functions are derived by analytical space domain integrations of the pertinent Green's functions over the vertical direction. After sampling the Cartesian wavenumber plane, all Green's functions are computed and stored at the selected sampling points in a database. In case of crossings of vertical basis functions over several dielectric layers, a further summation over the wavenumber plane is employed. With this database technique, the characterization of complex Planar-3D structures with large vertical extensions (e.g., LTCC structures) or electromagnetic bandgap (EBG) structures with a large number of vias is possible using enhanced spectral domain techniques [5] in the same way and with the same high performance than pure planar microstrip and/or slotline structures. For the computation of couplings with small lateral distances of the basis functions, an asymptotic subtraction technique for drastical convergence acceleration of the reaction integrals is used [4]. For larger distances, an adapted integration path deformation is used leading as well to a fast convergence of the integrals. For large structures, a group decomposition is made combined with diagonalized translation operators on the Cartesian wavenumber plane [6].

## 2. FORMULATION

For the self and mutual coupling of vertical currents, the pertinent Green's function component can be advantageously formulated by

$$
\begin{aligned}
G_{Jzz}^{E,TM,z<z',i\leq j} &= -\frac{1}{2\omega\varepsilon_i}\frac{k_x^2+k_y^2}{k_{zi}}\frac{e^{-jk_{zi}z'}+\hat{\Gamma}_i^{TM}e^{-jk_{zi}(2d_{i-1}-z')}}{1-\Gamma_i^{TM}\hat{\Gamma}_i^{TM}e^{-2jk_{zi}(d_{i-1}-d_i)}}\\
&\quad\cdot T_{i,j}^{TM,\,\text{mod}}\left[e^{jk_{zj}z}+\Gamma_j^{TM}e^{jk_{zj}(2d_j-z)}\right]-\frac{1}{j\omega\varepsilon_i}\delta(z-z'),
\end{aligned}
\tag{1}
$$

here for observation points below the source points. For the transmission factor from an upper to a lower dielectric layer, the compact formulation not depending on $z$ and $z'$ reads:

$$
T_{i,j}^{TM,\,\text{mod}}(k_\rho) = \frac{1}{2^{j-i}}e^{-j\sum_{n=i}^{j-1}(k_{zn+1}-k_{zn})d_n}\prod_{n=i}^{j-1}[\varepsilon(+)_{n+1}^n+\Gamma_n^{TM}\varepsilon(-)_{n+1}^n]
\tag{2}
$$

Figure 1, left shows a vertical electric current within two dielectric layers, (here schematically scetched as a line current). The actual basis functions have a rectangular cross-section in the $x$-$y$ plane, leading to the volume current description

$$
\vec{f}_{vm}(x,y,z) = \text{rect}\left(\frac{x-x_m}{w_{xm}/2}\right)\text{rect}\left(\frac{y-y_m}{w_{ym}/2}\right)\text{rect}\left(\frac{z-\Delta z/2-z_{vi1}}{\Delta z/2}\right)\vec{e}_z
\tag{3}
$$

with $w_{xm}$, $w_{xm}$ the lateral dimensions and $\Delta z$ the height of the basis function. For the later computation of the self-coupling of this current, the following integral (assuming a constant current distribution over the length) is formulated:

$$
\begin{aligned}
I(z,d_2\leq z\leq d_1) &= \int_{z_{v1}}^{z}G_{jzz}^{E,TM,z\geq z',i=j=2}(z,z')\,dz'+\int_{z}^{d_1}G_{jzz}^{E,TM,z<z',i=j=2}(z,z')\,dz'\\
&\quad+\int_{d_1}^{z_{v2}}G_{jzz}^{E,TM,z<z',i=1,j=2}(z,z')\,dz'
\end{aligned}
\tag{4}
$$

This integral is relevant for the computation of the $E_z$-component of the electric field within the lower layer with permittivity $\varepsilon_2$. For the first and second integral in Eq. (4), the $\delta$-function in Eq. (1) is relevant which results in the contribution $-1/j\omega\varepsilon_2$. Furthermore a $z$-independent term $j(k_x^2+k_y^2)/(k_{z2}^2\omega\varepsilon_2)$ occurs, which can be combined with the $-1/j\omega\varepsilon_2$ term to $jk_2^2/(\omega\varepsilon_2 k_{z2}^2)$ decaying with $\sim 1/(k_x^2+k_y^2)$ using the condition $k_x^2+k_y^2+k_{z2}^2=k_2^2$.

After the integration over the source coordinates $z'$ in Eq. (4), the integration over the observation coordinates $z$ must be performed. For this goal, a vertical current basis function is decomposed into several segments, if it crosses through several layers. Accordingly a vertical current segment is defined to be restricted to one layer of the multilayered environment. Thus the current in Fig. 1, left is decomposed into two segments whereas the vertical currents in the general coupling situation
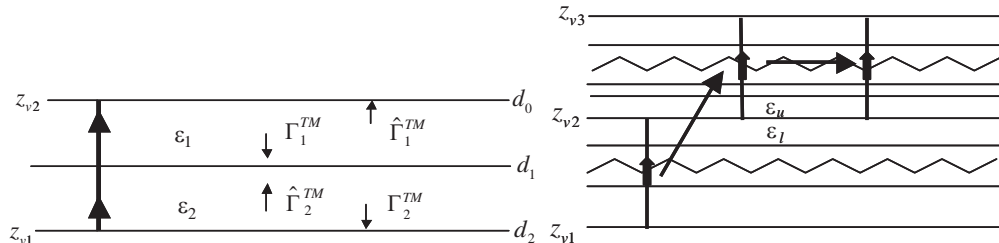


Figure 1: left: Vertical current crossing a dielectric interface. Right: General coupling situation of vertical currents in a multilayer environment.

sketched in Fig. 1, right are decomposed into an arbitrary number of segments depending on the number of crossed layers. The extended Green's function which is necessary for the self or mutual coupling computation between segments on the same level is denoted with $Intvvii(k_x, k_y, z_{i1}, z_{i2})$. It is derived e.g., for the self coupling of the lower segment in Fig. 1, left by the integration $\int_{d_2}^{d_1} I(z, d_2 \le z \le d_1)dz$. The analytical result is very extensive thus only the mathematical structure is given here by

$$Intvvii(k_x, k_y, z_{i1}, z_{i2}) = \frac{jk_i^2}{k_{zi}^2 \omega \varepsilon_i}(z_{i2} - z_{i1}) - \frac{k_x^2 + k_y^2}{2\omega\varepsilon_i k_{zi}^3 (1 - \Gamma_i^{TM}\hat{\Gamma}_i^{TM} e^{-2jk_{zi}(d_{i-1}-d_i)})}$$

$$\cdot (2 + \sum_{n=1}^{9} V_n e^{-j(a_n k_{zi}+b_n k_{zj})}) \tag{5}$$

illustrating the extended Green's function for the mutual coupling of vertical current segments (or self coupling of one segment) extending over the same vertical region from $z_{i1}$ to $z_{i2}$ within a layer of permittivity $\varepsilon_i$. The coefficients $a_n$ and $b_n$ depend on the layer interface coordinates as well as $z_{i1}$ and $z_{i2}$. If the vertical current basis functions extent over several layers, the extended overall Green's function is derived as for example the couplings of vertical currents basis functions (self or mutual couplings) between $z_{vi1}$ and $z_{vi2}$ (source region) as well as $z_{vj1}$ and $z_{vj2}$ (test or observation region) by the summation:

$$IG_{VV}(k_x, k_y, z_{vi1}, z_{vi2}, z_{vj1}, z_{vj2}) = \sum_{i=1}^{isegiq}\sum_{j=1}^{isegia} Intvvlu/ul(z_{i1}, z_{i2}, z_{j1}, z_{j2}, k_x, k_y)$$

$$+ \sum_{i=1}^{isegiq} Intvii(z_{i1}, z_{i2}, k_x, k_y) \tag{6}$$

Here $isegiq$ denotes the number of segments of the source region and $isegia$ the number of segments of the test region, the expression $Intvvlu/ul$ denotes the use of the function $Intvvlu$ in case of the coupling of an upper to a lower segment and $Intvvul$ in case of a coupling from a lower to an upper segment (without vertical overlapping). The mathematical structure of $Intvvul$ and $Intvvlu$ is similar as Eq. (5).

In case of mutual couplings of basis functions without overlapping in vertical direction, only the first summation with the $Intvvlu/ul$-functions in Eq. (6) is relevant. Further extended Green's functions are computed for the interactions of vertical currents with planar basis function of electric (microstrip structures) and magnetic surface currents (slot structures) with similar but less extensive expressions than Eqs. (5) and (6). The effort for the computation of all these extended Green's functions is always negligible.

After evaluating all necessary components of the extended Green's function, the overall couplings are computed by

$$V_{nm} = \int_{k_x}\int_{k_y} [\vec{IG}(k_x, k_y, z_{vi1}, \ldots, z_{vj2}) - \vec{IG}^{Asy}(k_x, k_y, z_{vi1}, \ldots, z_{vj2})]$$

$$\cdot \vec{F}_m(k_x, k_y.z_{vi1}) \cdot \vec{F}_n^*(k_x, k_y, z_{ji1})\, dk_x\, dk_y + V_{nm}^{Asy} \tag{7}$$

in the case of couplings with overlapping or small distance between the basis functions ($< \lambda/4$). Here $\vec{IG}$ is the tensor containing the extended Green's functions like Eq. (6) and the $\vec{F}_{m,n}(k_x, k_y.z_m)$ are the spectral domain representations of the basis functions.

The $\vec{IG}^{Asy}$ are asymptotic representations of the $\vec{IG}$-functions for large wavenumbers $\sqrt{k_x^2 + k_y^2} = k_\rho \to \infty$. The subtraction of the $\vec{IG}^{Asy}$ in Eq. (7) typically leads to a strong exponential decay of the integrands with a corresponding fast convergence of the numerical integration.

The asymptotic representations for couplings with only planar basis functions can be found in [4].

The derivation of the corresponding asymptotic representations becomes significantly more complicated, if basis functions for vertical currents according to Eq. (3) are involved. As an example we consider the derivation for couplings between vertical basis functions. First we consider the case of a mutual coupling between the lower basis function and the upper basis functions in Fig. 1, right having the common plane $z_{v2}$. A careful analysis of the limit values of $Intvvlu$ and $Intvvul$ for large $k_\rho$ using the asymptotic transmission factors $T_{u,l}^{Asy}$ and $\hat{T}_{l,u}^{Asy}$ finally leads to:

$$Intvvlu^{Asy} = \frac{-j}{2\omega k_\rho \varepsilon_u} \cdot \underbrace{\frac{2\varepsilon_u}{\varepsilon_l + \varepsilon_u}}_{=T_{u,l}^{Asy}},$$

$$Intvvul^{Asy} = \frac{-j}{2\omega k_\rho \varepsilon_l} \cdot \underbrace{\frac{2\varepsilon_l}{\varepsilon_u + \varepsilon_l}}_{=\hat{T}_{l,u}^{Asy}} \Rightarrow Intvvlu^{Asy} = Intvvul^{Asy} = \frac{-j}{\omega k_\rho(\varepsilon_u + \varepsilon_l)}. \tag{8}$$

with $\varepsilon_u$, $\varepsilon_l$ see Fig. 1, left. i.e., the asymptotic representations are the same for both coupling directions as it is expected in context with the reciprocity theorem. For self- or mutual couplings between vertical current segments on the same level within a layer of permittivity $\varepsilon_i$ it can be derived:

$$IG_{VV}^{Asy} = \frac{j}{2\omega\varepsilon_i k_\rho}(2 - \Gamma_i^{Asy} - \hat{\Gamma}_i^{Asy}) \tag{9}$$

where the asymptotic reflection factors

$$\Gamma_i^{TM,Asy} = \frac{\varepsilon_{i+1} - \varepsilon_i}{\varepsilon_{i+1} + \varepsilon_i}, \quad \hat{\Gamma}_i^{TM,Asy} = \frac{\varepsilon_{i-1} - \varepsilon_i}{\varepsilon_{i-1} + \varepsilon_i} \tag{10}$$

must be only considered, if the lower and/or upper ending of the segment falls together with the corresponding layer interface of the assigned reflection factor. Otherwise the asymptotic reflection factor is set to zero. If we compute the complete extended asymptotic Green's function for vertical basis functions extending from $z_{v1}$ to $z_{v2}$ as in Fig. 1, left, it can be written according to Eq. (6) and Eqs. (8)–(10):

$$IG_{VV}^{Asy}(z_{v1}, z_{v2}) = Intvii^{Asy}(d_2, d_1) + Intvii^{Asy}(d_1, d_0) + Intvvlu^{Asy}(d_1, d_0, d_2, d_1)$$

$$+ Intvvul^{Asy}(d_2, d_1, d_1, d_0) = \frac{j}{2\omega\varepsilon_2 k_\rho}(2 - \hat{\Gamma}_2^{Asy} - \Gamma_2^{Asy}) + \frac{j}{2\omega\varepsilon_1 k_\rho}(2 - \Gamma_1^{Asy} - \hat{\Gamma}_1^{Asy})$$

$$- \frac{j}{2\omega\varepsilon_1 k_\rho}\frac{2\varepsilon_1}{\varepsilon_2 + \varepsilon_1} - \frac{j}{2\omega\varepsilon_2 k_\rho}\frac{2\varepsilon_2}{\varepsilon_2 + \varepsilon_1} = \frac{j}{2\omega k_\rho}\left(\frac{1}{\varepsilon_1} + \frac{1}{\varepsilon_2} - \frac{\hat{\Gamma}_1^{Asy}}{\varepsilon_1} - \frac{\Gamma_2^{Asy}}{\varepsilon_1}\right) \tag{11}$$

due to the fact that $\hat{\Gamma}_2^{Asy} = -\Gamma_1^{Asy} = (\varepsilon_1 - \varepsilon_2)/(\varepsilon_1 + \varepsilon_2)$. It can be quickly seen that Eq. (11) converts to Eq. (9) for the case $\varepsilon_2 = \varepsilon_1$.

If this analysis is done for a vertical current basis function crossing an arbitrary number of layers, it can be found that Eq. (11) is still valid for this general case if $\varepsilon_1$ is replaced by the permittivity at the upper ending of the vertical current and $\varepsilon_2$ with the permittivity at the lower ending because the contributions of all the other layers in between are compensating each other.

The $V_{nm}^{Asy}$ in Eq. (7) are integral representations formulated in polar coordinates containing the $\overleftrightarrow{IG}^{Asy}$ and the $\vec{F}_{m,n}(k_x, k_y.z_m)$. These integrals can be completely evaluated analytically [4], thus, Eq. (7) is evaluated for all applied basis functions with the same high efficiency and accuracy.

In the case of couplings with larger separations of the basis functions and for group coupling computations in context with fast iterative solvers, partly adaptive integration path deformations are used for the $k_x$ or the $k_y$ wavenumber, depending on the lateral separation of the basis functions or the groups. If we e.g., look at the coupling computation between the observation and source groups $g_l$ and $g_{l'}$ during a fast matrix vector product evaluation $\vec{b} = Z_{far} \cdot \vec{I}$ we get (see also [6]):

$$b_{n,ll'} \approx \sum_{k_{xi}} \sum_{k_{yi}} w_{kxi} w_{kyi} F_{ln}^*(k_{xi}, k_{yi}) \cdot \overleftrightarrow{T}_{ll'}(k_{xi}, k_{yi}, z_{vi1}, \ldots, z_{vj2}) \cdot \vec{J}_{l'}(k_{xi}, k_{yi}),$$

$$\text{with } \vec{J}_{l'}(k_{xi}, k_{yi}) = \sum_{m \in g_{l'}} I_m \vec{F}_{l'm}(k_{xi}, k_{yi}), \tag{12}$$

introducing the translation operators $\overleftrightarrow{T}_{ll'}(k_{xi}, k_{yi}, z_{vi1}, \ldots, z_{vj2}) = I\overleftrightarrow{G}(k_x, k_y, z_{vi1}, \ldots, z_{vj2})e^{jk_x(x_l - x_{l'})}$ $e^{jk_y(y_l - y_{l'})}$ containing the extended Green's functions and $(x_l, y_l)$, $(x_{l'}, y_{l'})$ the center points of the groups $g_l$ and $g_{l'}$, respectively and $w_{kxi}, w_{kyi}$ suited integration weights. The spectral currents $\vec{J}_{l'}(k_{xi}, k_{yi})$ are created during the aggregation step given in Eq. (12) as well. In the case, that $|x_l - x_{l'}| > |y_l - y_{l'}|$ is valid, the last integration path for $k_x$ is chosen by $k_x(t) = \pm k_i - jt, t \geq 0$, whereas $k_y$ remains real, what leads to an exponential decay of the term $e^{jk_x(x_l - x_{l'})}$ within the translation operators. In the case $|x_l - x_{l'}| < |y_l - y_{l'}|$ the same is done vice versa for the wavenumbers with an exponential decay for $e^{jk_y(y_l - y_{l'})}$, always guaranteeing a fast convergence of the numerical integration in Eq. (12). However, if the groups contain different levels of volume and/or surface currents, the integration in Eq. (12) must be performed in several steps using the pertinent (extended) Green's functions between the pertinent current levels.

## 3. APPLICATION

As an example of a larger structure with many vias, two patch antennas with an electromagnetic bandgap structure (EBG) between the antennas was investigated, already outlined in [7]. In Fig. 2, left, the structure is given with the two antennas and the EBG structure consisting of 56 quadratical patches (size 3 mm, gap width 0.5 mm) with vias to the ground all mounted on a grounded dielectric slab with $\varepsilon_r = 10.2$ and thickness 1.92 mm. The used meshing also shown leads to 5008 unknowns. The structure was decomposed into 30 groups. Using the standard MoM, the time for the matrix fill was about 60 sec. (AMD 3 GHz PC) and the linear system solution time amounts to 74 sec. per frequeny step. However, the time for a matrix redundancy analysis amounts to 140 sec which must be done only once for all frequency steps. The results show nearly the same matching behavior with an antenna resonance at 5.8 GHz. With the EBG, the mutual coupling is reduced up to ca. 6 dB around the resonance. The effect of the EBG is smaller than outlined in [7]. However, some geometrical parameters like the feeding points of the antennas and exact substrate thickness are not exactly known. Maybe due to this, the antenna length had to be increased from 6.8 to 7.4 mm to get a resonance at 5.8 GHz. Further examples and the detailed behavior of the fast solver are given in the oral presentation.
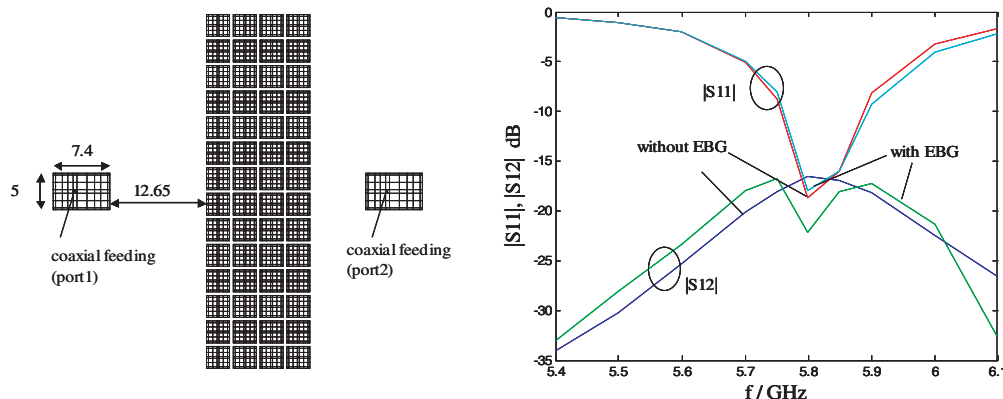


Figure 2: Investigation of patch antennas with an EBG-mushroom structure to reduce the mutual coupling. Dimensions in mm.

## 4. CONCLUSION

In this study, a MoM approach for the characterization of quasi-3D structures in a multilayered environment has been presented which is based on extended spectral domain Green's functions created by analytical integrations in context with the vertical volume basis functions used for the modeling of the vertical interconnects or finite dielectric regions of the quasi-3D components. Although an arbitrary discretization can be applied for the vertical currents which can furthermore cross an arbitrary number of dielectric layers, the characterization of such quasi-3D structures can be accomplished with the same performance as pure planar structures. At the moment, the new approach is tested with regard to fast matrix-vector multiplication strategies in a similar way as it is done in fast multipole methods in free space.

**REFERENCES**

1. Onal, T., M. I. Aksun, et al., "A rigorous and efficient analysis of 3D printed circuits: Vertical conductors arbitrarily distributed in multilayer environment," *IEEE Trans. on Antennas and Propagations*, Vol. 55, No. 12, 3726–3729, Dec. 2007.

2. Tang, W.-H. and S. D. Gedney, "An efficient application of the discrete complex image method for Quasi-3-D microwave circuits in layered media," *IEEE Trans. on Microwave Theory and Techniques*, Vol. 55, No. 8, 1723–1729, Aug. 2007.

3. Grzegorczyk, T. M. and J. Mosig, "Full-wave analysis of antennas containing horizontal and vertical metallizations embedded in planar multilayered media," *IEEE Trans. on Antennas and Propagations*, Vol. 51, No. 11, 3047–3054, Nov. 2003.

4. Vaupel, T. and V. Hansen, "Electrodynamic analysis of combined microstrip and coplanar/slotline structures with 3-D components based on a surface/volume integral-equation approach," *IEEE Trans. on Microwave Theory and Techniques*, Vol. 47, No. 9, 1788–1800, Sep. 1999.

5. Vaupel, T., T. F. Eibert, and V. Hansen, "Spectral domain analysis of large (M)MIC-structures using novel quadrature methods," *Int. Journal of Num. Modelling: Electronic Networks, Devices and Fields*, 23–38, Jan./Feb. 2005.

6. Vaupel, T., "A fast spectral domain solver for the characterization of larger microwave structures in multilayered environments," *ACES Journal*, Vol. 24, No. 5, 493–503, Oct. 2009.

7. Yang, F. and Y. Rahmat-Samii, "Microstrip antennas integrated with electromagnetic bandgap (EBG) structures: A low mutual coupling design for array applications," *IEEE Trans. on Antennas and Propagations*, Vol. 51, No. 10, 2936–2946, Oct. 2003.

# Staggered Grid Pseudo-spectral Time-domain Method for Light Scattering Analysis

**Y. Ohmura and Y. Okamura**

Graduate School of Engineering Science, Osaka University, Japan

**Abstract**— A pseudo-spectral time-domain (PSTD) method has been widely used for light scattering in a random medium because of its efficiency to compute electromagnetic fields in a large scale structure. However, artifacts appear when simulating a small particle scattering problem with the PSTD method. The particle size must be large enough compared to a cell size to reduce the appearance of the artifacts. In this paper, we propose a staggered grid PSTD method to overcome this problem. Being different from the PSTD method reported so far, electric and magnetic fields are sampled on a Yee's lattice. We found that the artifacts are caused by neglecting a Nyquist spatial frequency component in spatial differentiation and can be eliminated by using the staggered grid.

## 1. INTRODUCTION

A pseudo-spectral time-domain (PSTD) method is one of the numerical methods to solve the Maxwell's equations [1, 2]. The PSTD method is excellent in an accuracy and a size of analytical space compared with a FDTD method. In particular we can calculate electromagnetic wave transport with micrometers of wavelength in millimeters of scale. The light scattering property of random media is analyzed by directly with the method [3]. This approach gives the understanding of phenomena that can't be described with transport theory, such as wave localization [4]. However, the particle size must be large enough compared to a cell size, that leads to difficulty to compute electromagnetics in a larger random medium. In the traditional PSTD method, both electric and magnetic fields are sampled at the same point but we suggest to sample them on a Yee's lattice [5] to reduce the restriction on the particle size.

## 2. A PSEUDO-SPECTRAL TIME-DOMAIN METHOD

We consider the following Maxwell's equation with no charges and currents. In this paper we assume a 2-dimensional transverse magnetic mode propagating in an $x$-$y$ plane.

$$\frac{\partial}{\partial t}E_z = \frac{1}{\varepsilon}\frac{\partial}{\partial x}H_y - \frac{1}{\varepsilon}\frac{\partial}{\partial y}H_x \tag{1}$$

$$\frac{\partial}{\partial t}H_x = -\frac{1}{\mu}\frac{\partial}{\partial y}E_z \tag{2}$$

$$\frac{\partial}{\partial t}H_y = \frac{1}{\mu}\frac{\partial}{\partial x}E_z \tag{3}$$

where $\varepsilon$ is a permittivity and $\mu$ is a permeability. In the PSTD method, spatial differentiation is calculated using the Fourier transformation, and temporal differentiation is replaced by the mid-point differentiation. Dividing finite analytical space into $n_x \times n_y$ cells (each size is $\Delta x \times \Delta y$), the discretized fields are calculated as follows.

$$E_{z,l,m}^{n+1} = E_{z,l,m}^{n} + \frac{\Delta t}{\varepsilon_{l,m}}\left[\mathcal{F}^{-1}jk_x\mathcal{F}H_y\right]_{l,m}^{n+\frac{1}{2}} - \frac{\Delta t}{\varepsilon_{l,m}}\left[\mathcal{F}^{-1}jk_y\mathcal{F}H_x\right]_{l,m}^{n+\frac{1}{2}} \tag{4}$$

$$H_{x,l,m}^{n+\frac{3}{2}} = H_{x,l,m}^{n+\frac{1}{2}} - \frac{\Delta t}{\mu_{l,m}}\left[\mathcal{F}^{-1}jk_y\mathcal{F}E_z\right]_{l,m}^{n+1} \tag{5}$$

$$H_{y,l,m}^{n+\frac{3}{2}} = H_{y,l,m}^{n+\frac{1}{2}} + \frac{\Delta t}{\mu_{l,m}}\left[\mathcal{F}^{-1}jk_x\mathcal{F}E_z\right]_{l,m}^{n+1} \tag{6}$$

$$k_x = \begin{cases} 2\pi l'/n_x\Delta x & (l' < n_x/2) \\ 2\pi(l' - n_x)/n_x\Delta x & (n_x/2 \le l' < n_x) \end{cases} \tag{7}$$

$$k_y = \begin{cases} 2\pi m'/n_y\Delta x & (m' < n_y/2) \\ 2\pi(m' - n_y)/n_y\Delta x & (n_y/2 \le m' < n_y) \end{cases} \tag{8}$$

where subscripts $l$ and $m$ are indexes specifying sampling points, $\mathcal{F}$ is the Fourier transformation, $l'$ and $m'$ are indexes in spatial frequency, superscript $n$ is time step index, $n + \frac{1}{2}$ means time shift by $\frac{1}{2}\Delta t$. In this equation, $\mathcal{F}^{-1}jk_x\mathcal{F}E_z$ corresponds to spatial differentiation. Differentiation contains imaginary part, whose spatial frequency is $\pi/\Delta x$ and is eliminated. That causes an error in second order derivative of $E_z$, which causes artifacts in the electromagnetic analysis. To hold the Nyquist frequency component and eliminate this error, we introduce a staggered grid PSTD method. In this method, fields are calculated as follows.

$$E_{z,l,m}^{n+1} = E_{z,l,m}^n + \frac{\Delta t}{\varepsilon_{l,m}}\left[\mathcal{F}^{-1}jk_x e^{jk_x\Delta x/2}\mathcal{F}H_y\right]_{l,m}^{n+\frac{1}{2}} - \frac{\Delta t}{\varepsilon_{l,m}}\left[\mathcal{F}^{-1}jk_y e^{jk_y\Delta y/2}\mathcal{F}H_x\right]_{l,m}^{n+\frac{1}{2}} \tag{9}$$

$$H_{x,l,m+\frac{1}{2}}^{n+\frac{3}{2}} = H_{x,l,m+\frac{1}{2}}^{n+\frac{1}{2}} - \frac{\Delta t}{\mu_{l,m}}\left[\mathcal{F}^{-1}jk_y e^{-jk_y\Delta y/2}\mathcal{F}E_z\right]_{l,m+\frac{1}{2}}^{n+1} \tag{10}$$

$$H_{y,l+\frac{1}{2},m}^{n+\frac{3}{2}} = H_{y,l+\frac{1}{2},m}^{n+\frac{1}{2}} + \frac{\Delta t}{\mu_{l,m}}\left[\mathcal{F}^{-1}jk_x e^{-jk_x\Delta x/2}\mathcal{F}E_z\right]_{l+\frac{1}{2},m}^{n+1} \tag{11}$$

In the traditional PSTD (colocate grid PSTD), both electric and magnetic fields are sampled at the same point in each cell, but in the staggered grid PSTD, electric and magnetic fields are sampled on the Yee's lattice. In this method, $\mathcal{F}^{-1}jk_x e^{-jk_x\Delta x/2}\mathcal{F}E_z$ corresponds to spatial differentiation, adding operation of shift in space to the colocate grid PSTD. Figure 1 shows the computed second order derivatives for an impulse field. In the second order derivative, the artifact appears with the colocate grid PSTD, on the other hand, it is eliminated with the staggered grid PSTD.

## 3. COMPARISON BETWEEN COLOCATE GRID PSTD AND STAGGERED GRID PSTD

To demonstrate the staggered grid PSTD method, we calculate electromagnetic wave scattering by a small particle. Figure 2 shows a configuration of scattering by the small particle. The cell size is $0.1\,\mu m \times 0.1\,\mu m$. $S$ is an incident pulse plane wave with the center wavelength of $660\,nm$. P is a particle with the dimension of $0.1\,\mu m \times 0.1\,\mu m$ and the permittivity of $4\varepsilon_0$, where $\varepsilon_0$ is the permittivity in vacuum. Berenger's PML is used as an absorbing boundary. Figure 3 shows field distributions by the colocate grid PSTD method at each time. An incident wave goes from left to right, and after the incident wave goes over a particle, a scattered wave and artifacts are generated.
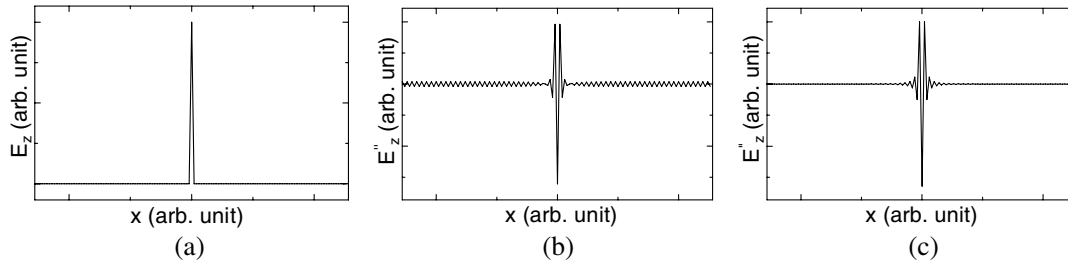


Figure 1: Derivatives of field. (a) Original field, (b) second order derivative calculated with the colocate grid PSTD, (c) second order derivative calculated with the staggered grid PSTD.
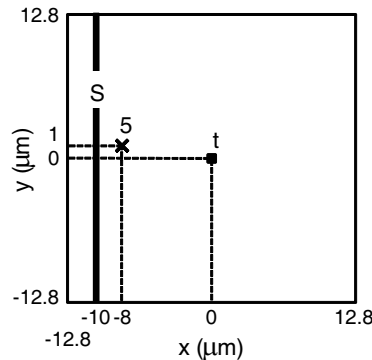


Figure 2: Configuration to demonstrate the staggered grid PSTD method.
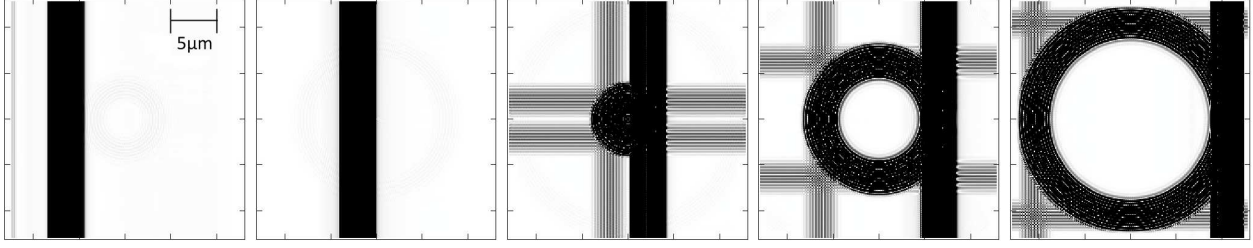
Figure 3: Spatial distribution of $|E_z|$ field at every 14 fs.
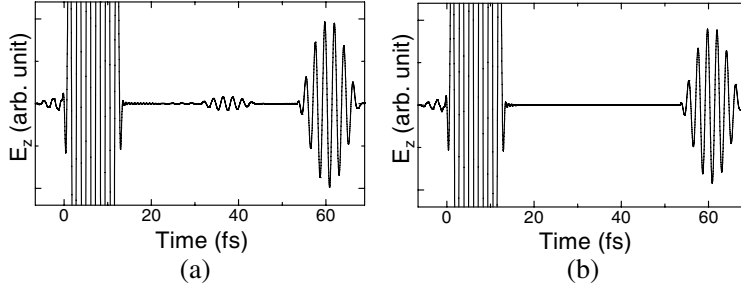


Figure 4: Electric field at point D in Figure 2. (a) Colocate grid PSTD and (b) Staggered grid PSTD.
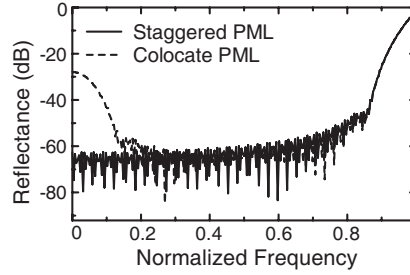


Figure 5: PML reflectance for the frequency. Frequency is normalized by $c/2\Delta x$.

Scattered wave roundly extends, and the artifact waves go straight with each wavefront. Figure 4 shows an electric field at the observation point D in Figure 2 with the colocate grid and staggered grid PSTD methods. An incident wave and a scattered wave are confirmed to be at around 10 fs and 60 fs for both cases, respectively. An artifact appears at around 40 fs for the colocate grid PSTD method; on the other hand it disappears for the staggered grid PSTD method.

## 4. A PERFECT MATCHED LAYER FOR STAGGERED GRID PSTD

To prevent the wrap around effect, the Berenger's perfect matched layer (PML) [6] is set at the edge of the analytical space. In the PML, electric and magnetic fields are calculated as follows.

$$E_{zx,l,m}^{n+1} = \frac{2\varepsilon - \sigma_{x,l}\Delta t}{2\varepsilon + \sigma_{x,l}\Delta t} E_{zx,l,m}^n + \frac{2\Delta t}{2\varepsilon + \sigma_{x,l}\Delta t} \left[ \mathcal{F}^{-1} jk_x e^{jk_x\Delta x/2} \mathcal{F}H_y \right]_{l,m}^{n+\frac{1}{2}} \tag{12}$$

$$E_{zy,l,m}^{n+1} = \frac{2\varepsilon - \sigma_{y,m}\Delta t}{2\varepsilon + \sigma_{y,m}\Delta t} E_{zy,l,m}^n - \frac{2\Delta t}{2\varepsilon + \sigma_{y,m}\Delta t} \left[ \mathcal{F}^{-1} jk_y e^{jk_y\Delta y/2} \mathcal{F}H_x \right]_{l,m}^{n+\frac{1}{2}} \tag{13}$$

$$H_{x,l,m+\frac{1}{2}}^{n+\frac{3}{2}} = \frac{2\mu - \sigma_{y,m+\frac{1}{2}}^*\Delta t}{2\mu + \sigma_{y,m+\frac{1}{2}}^*\Delta t} H_{x,l,m+\frac{1}{2}}^{n+\frac{1}{2}} - \frac{2\Delta t}{2\mu + \sigma_{y,m+\frac{1}{2}}^*\Delta t} \left[ \mathcal{F}^{-1} jk_y e^{-jk_y\Delta y/2} \mathcal{F}E_z \right]_{l,m+\frac{1}{2}}^{n+1} \tag{14}$$

$$H_{y,l+\frac{1}{2},m}^{n+\frac{3}{2}} = \frac{2\mu - \sigma_{x,l+\frac{1}{2}}^*\Delta t}{2\mu + \sigma_{x,l+\frac{1}{2}}^*\Delta t} H_{y,l+\frac{1}{2},m}^{n+\frac{1}{2}} + \frac{2\Delta t}{2\mu + \sigma_{x,l+\frac{1}{2}}^*\Delta t} \left[ \mathcal{F}^{-1} jk_x e^{-jk_x\Delta x/2} \mathcal{F}E_z \right]_{l+\frac{1}{2},m}^{n+1} \tag{15}$$

where $E_z = E_{zx} + E_{zy}$, $\sigma_x$ and $\sigma_y$ are electric conductivities and $\sigma_x^*$ and $\sigma_y^*$ are magnetic conductivities. At the same point, the relations of $\sigma_x/\varepsilon_0 = \sigma_x^*/\mu_0$ and $\sigma_y/\varepsilon_0 = \sigma_y^*/\mu_0$ must be satisfied for

the PML. In staggered grid PSTD, these values are sampled alternatively. This sampling leads to prevention of reflection in a low frequency region. Figure 5 shows the reflectance for the frequency, when electric and magnetic conductivity are sampled alternatively (stagged PML) and at same point (colocate PML). This figure shows that reflectance in low frequency region is large using the PML same as colocate grid PSTD. The result indicates that the waves with wavelength near 2 cells cannot be employed because of large reflectance due to PML.

## 5. CONCLUSION

We have proposed a staggered grid PSTD method. Electric and magnetic fields are sampled on a Yee's lattice. The artifacts are caused by removing a Nyquist frequency component in spatial differentiation and can be eliminated by using the staggered grid. We are now working on simulating the wave propagation in a multi-scattering system.

## ACKNOWLEDGMENT

## REFERENCES

1. Liu, Q. H., "The PSTD algorithm: A time-domain method requiring only two cells per wavelength," *Microwave and Optical Technology Letters*, Vol. 15, No. 3, 158–165, 1997.
2. Okamura, Y., "PSTD method for transient electromagnetics and its application to optical waveguide analysis," *The Review of Laser Engineering*, Vol.36, No.10, 621–627, 2008.
3. Tseng, S. H., Y. L. Kim, A. Taflove, D. Maitland, V. Backman, and J. T. Walsh, Jr., "Simulation of enhanced backscattering of light by numerically solving Maxwell's equations without heuristic approximations," *Optics Express*, Vol. 13, No. 10, 3666–3672, 2005.
4. Sheng, P., *Introduction to Wave Scattering, Localization, and Mesoscopic Phenomena*, Academic Press, New York, 1995.
5. Kunz, K. S. and R. J. Luebbers, *The Finite Difference Time Domain Method for Electromagnetics*, CRC Press, New York, 1993.
6. Berenger, J. P., "A perfectly matched layer for the absorption of electromagnetic waves," *Journal of Computational Physics*, Vol. 144, No. 2, October 1994.

# Application of Alternating Direction Implicit (ADI) Algorithm to Staggered-grid PSTD Modeling of Electromagnetic Waves

**Zijian Liu**[1], **Lanbo Liu**[1, 2], **and Benjamin Barrowes**[2]

[1]Department of Biomedical Engineering, University of Connecticut, Storrs, CT 06269-2037, USA
[2]USACE Engineering Research and Development Center
Cold Regions Research and Engineering Laboratory, Hanover, NH 03755, USA

**Abstract**— By applying the fast Fourier transform (FFT) and inverse transform to represent the spatial derivatives, the pseudo-spectral time-domain (PSTD) method has achieved a spatial grid of only two points per wavelength while maintaining a high accuracy. Its computational speed can be further accelerated by applying alternating-direction implicit (ADI), which makes PSTD works even when the time step exceeds the maximum time step allowed under the Courant-Friedrich-Levy (CFL) condition. However, due to the unsuitability of FFT on non-continuou condition, conventional ADI-PSTD turns to be unstable in media with high property contrast. We have expanded current ADI-PSTD into staggered-grid ADI-PSTD. After applying the staggered-grid approach into our algorithm by shifting the spatial derivatives halfway between 2 adjacent nodes, the stability of the differentiation operators is enhanced. We will discuss the staggered-grid ADI-PSTD method in detail and apply it to the simulation of a half-space model. The analysis and discussion of the results show its advantages and further potential.

## 1. INTRODUCTION

It is well known that pseudo-spectral time-domain (PSTD) method has been successfully used in various cases of electromagnetic (EM) field simulation. By applying the fast Fourier transform (FFT) and inverse transform to represent the spatial derivatives, PSTD has achieved a spatial girding of only two points per wavelength while maintaining a high accuracy as conventional finite-difference time domain (FDTD) method does, which requires 20–30 points per wavelength during computation. Nevertheless similar to FDTD, the computation speed of PSTD is also limited by the Courant-Friedrich-Levy (CFL) condition, which sets an upper bound for the size of the time steps. Recently, alternating-direction implicit (ADI) method has been successfully developed to overcome this obstacle. Applying ADI to the FDTD method can efficiently enhance the stability and convergence of the calculation, even when the time step exceeds the maximum time step allowed under the CFL condition. However this approach seems to be not effective when ADI is applied to PSTD on highly inhomogeneous media. Due to the property of spatial Fourier transform, which requires the field to be continuous within the entire spatial domain, errors appear when the fields are non-uniform [1].

In order to seek the clue for the problem mentioned above, in the paper the author intends to use staggered grid scheme instead of the original spatial differential formation in PSTD, which was first proposed by Yee [2] and now widely applied in EM modeling for maintaining high accuracy and stability in FDTD approach. It has long been proved that the application of staggered grid scheme has always been robust in FDTD computation. This encouraged several researchers [3, 4] considered about the possibility of combining ADI with PSTD. From the research of L. Liu. etc. [5], staggered-grid ADI-PSTD was applied to model a Ground Penetrating Radar system and the result clearly demonstrated that using a staggered grid in the PSTD scheme made the time marching more stable and suppressed numerical dispersion for models with large contrast in material properties. Based on this the author mainly discusses the application of ADI on staggered-grid PSTD modeling. In this paper, ADI-PSTD algorithms is firstly set up associated with stretched coordinate perfect matched layer (SC-PML) [6] for EM modeling with 2D transverse magnetic (TMz) mode. Staggered-grid scheme is then included to replace the conventional spatial formulation used in PSTD. Finally a half-space model including air and earth are set up to testify the stability of staggered-grid ADI-PSTD developed.

## 2. THE SPLIT-STEP ADI FORMULATION FOR TMZ MODE MAXWELL'S EQUATIONS WITH SC-PML

Without considering electric conductivity, combined with the SC-PML technique as the absorption boundary condition, the 3-D Maxwell's equations can be written as Equations (1a) and (1b), where

$\varepsilon$ and $\mu$ denote dielectric permittivity and magnetic permeability separately. Both $a^{(\eta)}$ and $\omega^{(\eta)}$ are general stretch coordinate factors. In which $a^{(\eta)}$, the scaling factor, is set to be constant 1 in this paper. $\omega^{(\eta)}$, which represents the energy loss in PML, is set to be 0 in the computational domain and increased exponentially in the absorption boundary [7]. Under 3-D condition, (1a) and (1b) consist twelve equations, since $H = H^{(x)} + H^{(y)} + H^{(z)}$, $E = E^{(x)} + E^{(y)} + E^{(z)}$, and each components can be divided into two sub-components perpendicular to axis $\eta$. For 2D TMz mode, Equation (1) can be transformed as four split-field Equations (2a)–(2d).

$$a_\eta \mu \frac{\partial H^{(\eta)}}{\partial t} + \mu \omega_\eta H^{(\eta)} = -\frac{\partial}{\partial \eta} \left( \hat{\eta} \times E \right) \tag{1a}$$

$$a_\eta \varepsilon \frac{\partial E^{(\eta)}}{\partial t} + \varepsilon \omega_\eta E^{(\eta)} = \frac{\partial}{\partial \eta} \left( \hat{\eta} \times H \right) \tag{1b}$$

$$\mu \frac{\partial H_y^{(x)}}{\partial t} + \mu \omega_x H_y^{(x)} = \frac{\partial E_z}{\partial x} \tag{2a}$$

$$\varepsilon \frac{\partial E_z^{(x)}}{\partial t} + \varepsilon \omega_x E_z^{(x)} = \frac{\partial H_y}{\partial x} \tag{2b}$$

$$\mu \frac{\partial H_x^{(y)}}{\partial t} + \mu \omega_y H_x^{(y)} = -\frac{\partial E_z}{\partial y} \tag{2c}$$

$$\varepsilon \frac{\partial E_z^{(y)}}{\partial t} + \varepsilon \omega_y E_z^{(y)} = -\frac{\partial H_x}{\partial y} \tag{2d}$$

Need to note that Equation (2) are coincident with the split-step formulation, a widely used scheme to achieve ADI-PSTD in further step, which was first introduced by Lee and Fornberg [8]. In split-step method, Maxwell's equations are divided into sub-problems with spatial differential on different direction. Each sub-problem can be further written into three pairs of mutually uncoupled 1-D equations. By doing this, one intact time-step marching is divided into several sub-stages; each sub-stage only contains independent 1-D problem. Research from Zhao and Liu [9] indicates that the implicit formulation for split-step method can guarantee unconditionally stability for PSTD computation in uniform media. It is obvious that every equation in (2) is a 1-D problem. (2a) and (2b), which is updated in $X$ direction, is gathered to be the first sub-problem marching from sub-step $n \to n + 1/2$. In the same way, (2c)–(2d) is set to be the second sub-problem marching from sub-step $n + 1/2 \to n + 1$. When Equations (2a)–(2d) are written in an implicit form and by using discretization, they become split-step ADI formulation as (3):

Sub-step $n \to n + 1/2$:

$$\frac{E_z^{(x)}(n+1/2) - E_z^{(x)}(n)}{\Delta t/2} + \frac{\omega_x}{2} \left[ E_z^{(x)}(n+1/2) + E_z^{(x)}(n) \right] = \frac{1}{2\varepsilon} \frac{\partial}{\partial x} H_y^{(x)}(n+1/2) \tag{3a}$$

$$\frac{H_y^{(x)}(n+1/2) - H_y^{(x)}(n)}{\Delta t/2} + \frac{\omega_x}{2} \left[ H_y^{(x)}(n+1/2) + H_y^{(x)}(n) \right] = \frac{1}{2\mu} \frac{\partial}{\partial x} \left[ E_z^{(x)}(n+1/2) + E_z^{(y)}(n) \right] \tag{3b}$$

Sub-step $n + 1/2 \to n + 1$:

$$\frac{E_z^{(y)}(n+1) - E_z^{(y)}(n+1/2)}{\Delta t/2} + \frac{\omega_y}{2} \left[ E_z^{(y)}(n+1) + E_z^{(y)}(n+1/2) \right] = -\frac{1}{2\varepsilon} \frac{\partial}{\partial y} H_x^{(y)}(n+1) \tag{3c}$$

$$\frac{H_x^{(y)}(n+1) - H_x^{(y)}(n+1/2)}{\Delta t/2} + \frac{\omega_y}{2} \left[ H_x^{(y)}(n+1) + H_x^{(y)}(n+1/2) \right] = -\frac{1}{2\mu} \frac{\partial}{\partial y} \left[ E_z^{(y)}(n+1) + E_z^{(x)}(n+1/2) \right] \tag{3d}$$

Among the above equations, since $E_z^{(x)}(n+1/2)$ and $E_z^{(y)}(n+1)$ appears at both sides of (3a) and (3c) respectively as synchronous variables, (3a) and (3c) can not be used for direct computation. To solve this problem, (3a') is derived from (3a) and (3b) by eliminating $E_z^{(x)}(n + 1/2)$ and (3c')

leads from (3c) and (3d) by eliminating $E_z^{(y)}(n+1)$.

$$E_z^{(x)}(n+1/2) - \frac{\Delta t^2}{\mu\varepsilon(4+\omega_x\Delta t)^2}\frac{\partial^2}{\partial x^2}E_z^{(x)}(n+1/2) = \frac{4-\omega_x\Delta t}{4+\omega_x\Delta t}E_z^{(x)}(n)$$

$$+\frac{\Delta t^2}{\mu\varepsilon(4+\omega_x\Delta t)^2}\frac{\partial^2}{\partial x^2}E_z^{(y)}(n) + \frac{\Delta t(4-\omega_x\Delta t)}{\varepsilon(4+\omega_x\Delta t)^2}\frac{\partial}{\partial x}H_y^{(x)}(n) \tag{3a'}$$

$$E_z^{(y)}(n+1) - \frac{\Delta t^2}{\mu\varepsilon(4+\omega_y\Delta t)^2}\frac{\partial^2}{\partial y^2}E_z^{(y)}(n+1) = \frac{4-\omega_y\Delta t}{4+\omega_y\Delta t}E_z^{(y)}(n+1/2)$$

$$+\frac{\Delta t^2}{\mu\varepsilon(4+\omega_y\Delta t)^2}\frac{\partial^2}{\partial y^2}E_z^{(x)}(n+1/2) - \frac{\Delta t(4-\omega_y\Delta t)}{\varepsilon(4+\omega_y\Delta t)^2}\frac{\partial}{\partial x}H_x^{(y)}(n+1/2) \tag{3c'}$$

## 3. STAGGERED GRID ADI-PSTD ALGORITHM

In conventional PSTD methods, people use fast-Fourier-transform (FFT) and inverse FFT together rather than finite differences to solve the problem with spatial differentiation shown in Equation (3). Mathematically, differentiation formulation in time domain can be transformed as direct multiplication by wave number in frequency domain. By using this property, the conventional method to solve spatial derivative on function $f$ in certain direction $\eta$ can be calculated in the way as (4) and (5), where $k_\eta$ is the spatial wave number.

$$\frac{\partial f}{\partial \eta} = iFFT_\eta\left(ik_\eta FFT_\eta(f)\right) \tag{4}$$

The spatial derivative computation method in (4) can be further described in Figure 1a, where a 1-D relationship between $E_z$ and $H_y$ is taken to represent a general condition in PSTD calculation. Vertical axis and horizontal axis denote time stepping in time domain and location of field components in spatial domain separately. Figure 1(a) clearly shows that by using (4) in PSTD algorithm, all field components of f are co-located at the same points or nodes without moving. This doesn't coincide with Yee's theory [2], so the principle of spatial staggered grid was introduced here to modify the original spatial method.
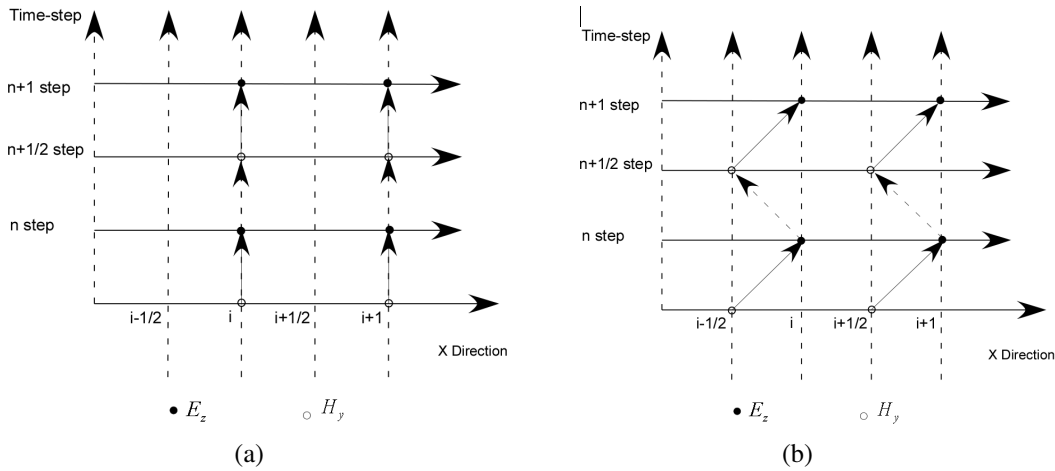


Figure 1: The relationship between space and time-stepping for non-staggered grid spatial derivative method (a) and staggered grid spatial derivative method (b) in a 1-D example applied to the EM fields.

In staggered-grid scheme, the spatial derivatives of either electric or magnetic field are shifted halfway between 2 nodes to meet with the structure of Yee's grid. As Figure 1(b) shows, the spatial derivative of the electric field $E_z$ is shifted forward with the distance of $\Delta x/2$ in $X$ direction to match the location of the magnetic components. And the direction of spatial derivative of $H_y$ is set to be shifted backward to $E_z$ again. In staggered-grid derivative scheme, forward-shifted derivative and backward-shifted derivative must be set alternatively to ensure the stability of time stepping marching in "zigzag" way as Figure 1(b) shows. In real case, if the direction of spatial derivative on

electric field is set to be forward, then the corresponding magnetic field must be set to be backward, and vise versa.

Based on the property of Fourier transform, the conventional spatial derivative method used in PSTD approach can be replaced with staggered-grid scheme as:

$$\frac{\partial f}{\partial \eta} = iFFT_\eta \left[ ik_\eta e^{ik_\eta \left( \pm \frac{\Delta x}{2} \right)} FFT_\eta(f) \right] \tag{5}$$

In which $\pm \Delta x/2$ relates both forward and backward staggered-grid spatial derivative in one formulation. Let

$$\begin{aligned} FD_\eta &= ik_\eta e^{ik_\eta \left( \frac{\Delta x}{2} \right)} \\ BD_\eta &= ik_\eta e^{ik_\eta \left( -\frac{\Delta x}{2} \right)} \end{aligned} \qquad \eta = x, y, z \tag{6}$$

After combined with (3), the formulation of staggered grid ADI-PSTD algorithms can be expressed in (7) as:

Sub-step $n \to n + 1/2$:

$$E_z^{(x)}(n+1/2) = iFFT_x \left\{ \frac{FFT_x \left[ \begin{array}{l} \frac{4-\omega_x \Delta t}{4+\omega_x \Delta t} E_z^{(x)}(n) + \frac{\Delta t^2}{\mu\varepsilon(4+\omega_x \Delta t)^2} iFFT_x \left( FD_x^2 FFT_x(E_z^{(y)}(n)) \right) \\ + \frac{\Delta t(4-\omega_x \Delta t)}{\varepsilon(4+\omega_x \Delta t)^2} \frac{\partial}{\partial x} H_y^{(x)}(n) \end{array} \right]}{1 - \frac{\Delta t^2}{\mu\varepsilon(4+\omega_x \Delta t)^2} FD_x BD_x} \right\} \tag{7a}$$

$$H_y^{(x)}(n+1/2) = \frac{4-\omega_x \Delta t}{4+\omega_x \Delta t} H_y^{(x)}(n) + \frac{\Delta t}{\mu(4+\omega_x \Delta t)} iFFT_x \left\{ BD_x FFT_x \left[ E_z^{(x)}(n+1/2) + E_z^{(y)}(n) \right] \right\} \tag{7b}$$

Sub-step $n + 1/2 \to n + 1$:

$$E_z^{(y)}(n+1) = iFFT_y \left\{ \frac{FFT_y \left[ \begin{array}{l} \frac{4-\omega_y \Delta t}{4+\omega_y \Delta t} E_z^{(y)}(n+1/2) + \frac{\Delta t^2}{\mu\varepsilon(4+\omega_y \Delta t)^2} iFFT_y \\ \left( FD_y^2 FFT_y(E_z^{(x)}(n+1/2)) \right) \\ - \frac{\Delta t(4-\omega_y \Delta t)}{\varepsilon(4+\omega_y \Delta t)^2} \frac{\partial}{\partial y} H_x^{(y)}(n+1/2) \end{array} \right]}{1 - \frac{\Delta t^2}{\mu\varepsilon(4+\omega_y \Delta t)^2} FD_y BD_y} \right\} \tag{7c}$$

$$\begin{aligned} H_x^{(y)}(n+1) = &\frac{4-\omega_y \Delta t}{4+\omega_y \Delta t} H_x^{(y)}(n+1/2) \\ &- \frac{\Delta t}{\mu(4+\omega_y \Delta t)} iFFT_y \left\{ BD_y FFT_y \left[ E_z^{(y)}(n+1) + E_z^{(x)}(n+1/2) \right] \right\} \end{aligned} \tag{7d}$$

## 4. NUMERICAL EXAMPLE

The stability of staggered-grid method on ADI-PSTD can be testified by the following numerical realization. A half space computational domain containing both air and earth, surrounded with SC-PML, is taken to be $76.8\,\mathrm{m} \times 76.8\,\mathrm{m}$ ($256 \times 256$ cells). In this simulation the time function of electrical dipole source is set to be Ricker wavelet function with the central frequency of $200\,\mathrm{MHz}$. Five transducers are used to record electrical field information. Their related detail information in computational domain is shown in Figure 2.

In numerical computation, based on CFL condition, the time step is around $\Delta t = 0.5\,\mathrm{ns}$, close to upper bound for conventional PSTD methods. But for ADI-PSTD methods, different time steps of $1\times$, $4\times$, and $8\times \Delta t$ are still working when applied in same computational domain. Figure 3 shows the computation results of ADI-PSTD by using both non-staggered grid approach and staggered grid approach when time step equal to different times of CFL limitation (CFLN). The advantage of using staggered-grid approach on ADI-PSTD can be observed in two aspects. Firstly, using staggered grid method greatly suppresses numerical dispersion appears at the beginning of the timeline. In non-staggered grid PSTD, this error is obvious in the record of receiver No. 2, which
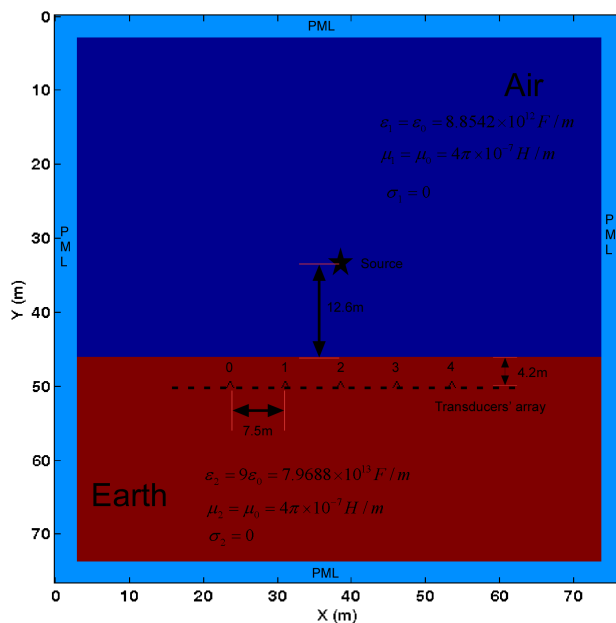
Figure 2: Setup of the half-space computational domain. Electrical dipole source is located above the earth to simulate the antenna. EM wave prorogates from the antenna, penetrates the ground, and is received by the receiver array inside the earth.
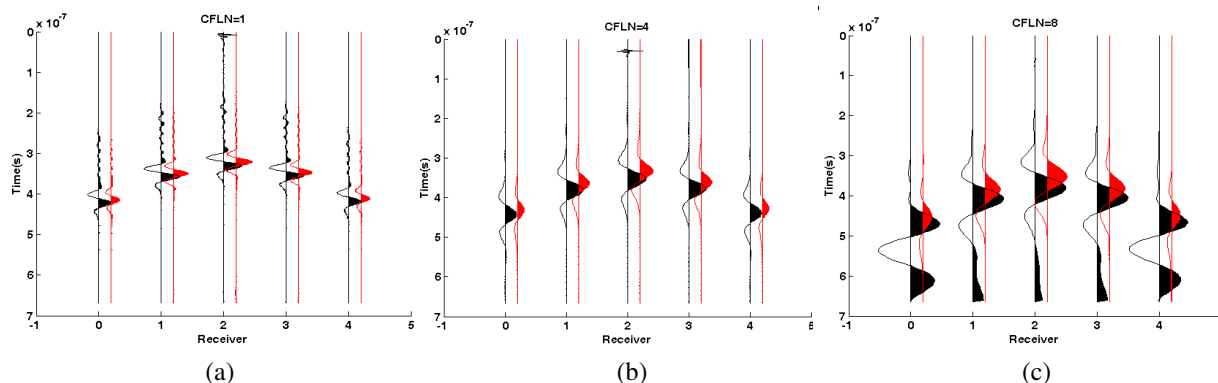


Figure 3: Computation results of ADI-PSTD by using both non-staggered grid approach (black) and staggered grid approach (red) when the time step reaches $1\times$ (a), $4\times$ (b), and $8\times$ (c) of the Courant limit $\Delta t$. The locations of the receivers are the central 5 of them as shown in Figure 2.

locates on the symmetry axis of computational domain (See Figure 2). These errors diminished after staggered grid approach is applied. On the other hand the accuracy of the computation result by using staggered-grid approach can be better preserved than using non-staggered grid approach in ADI-PSTD. This advantage becomes distinct when the time step increases to be far larger than CFL limitation. In Figure 3(c), the shape of Ricker's wavelet is still intact in the result of staggered-grid ADI-PSTD even time step reach to $8 \times \Delta t$ ($CFLN = 8$). This turns to be far better than the result of using non-staggered-grid scheme which induces serious distortion.

## 5. CONCLUSIONS

Combined with split-step ADI scheme, staggered-grid approach, and the SC-PML as the absorption boundary condition with conventional PSTD, the staggered-grid ADI-PSTD is derived in this paper. It is illustrated by an example in the TMz mode and applied in a half space computational domain as the test run. The result shows that with the staggered-grid ADI-PSTD algorithm the time marching is stable when the time step is 8 times of the Courant limit. It has great potential for both reducing numerical dispersion and preservation on the accuracy of the computation result when time step goes far larger than the CFL condition.

**REFERENCES**

1. Zheng, F., "Novel unconditionally stable finite-difference time-domain method for electromagnetic and microwave modeling," PhD dissertation, Dalhousie University, 2001.
2. Yee, K. S., "Numerical solution of initial boundary problems involving Maxwell's equations in isotropic media," *IEEE Trans. Antennas Propag.*, Vol. 14, 302–307, 1966.
3. Fornberg, B., "High-order-finite -difference and the pseudospectral method on staggered-grids," *SIAM J. Num. Anal.*, Vol. 27, 904–918, 1990.
4. Witte, D. C., "The pseudospectral method for simulating wave propagation," PhD dissertation, Columbia University, 1989.
5. Liu, L., "Staggered-grid pseudospectral time domain (PSTD) method using real fourier transform for 2.5D electromagnetic wave propagation," *PIERS Proceedings*, 1238–124, Hangzhou, China3, March 24–28, 2008.
6. Chew, W. C. and W. H. Weddon., "A 3-D perfectly matched medium from modified Maxwell's equations with stretched coordinates," *Micro. Opt. Tech. Lett.*, Vol. 7, No. 13, 599–604, 1994.
7. Zhu, L., L. Liu, J. W. Lane, Jr., and F. D. Day-Lewis, "Numerical simulation of EM wave propagation with a split-step alternating direction implicit FDTD method," *11th International Conference on Ground Penetrating Radar*, Columbus Ohio, USA, June 19–22, 2006.
8. Lee, J., and B. Fornberg, "A split step approach for the 3-D Maxwell's equations," *Journal of Computational and Applied Mathematics*, Vol. 158, 485–505, 2003.
9. Zhao, G. and Q. Liu, "The unconditionally stable pseudospectraltime-domain (PSTD) method," *IEEE Microwave and Wireless Components Letters*, Vol. 13, No. 11, November 2003.

# Discussion of Reverberation Chamber Uniformity Using Neural-network Method

**Li Zhang[1], Yong Qi[2], and Guizhen Lu[1]**

[1]Communication University of China, Beijing 100024, China
[2]China Radio International, Beijing 100040, China

**Abstract**— In this paper, a new method is applied to discuss the uniformity of a reverberation chamber. The calibration of reverberation chamber uniformity is a tedious task and the examination of field uniformity requires a great number of computing. Here a neural-network method is presented to analyze the uniformity. According to some of the evaluation data got by GEMS, the network is trained on both GRNN method and BP method, then the obtained neural network is used to predict the rest of data, which are used to analyze uniformity.

## 1. INTRODUCTION

A reverberation chamber is a large shielded cavity formed by highly conductive walls equipped with metal stirrers. These stirrers vary the electromagnetic boundary conditions to change the electromagnetic field distribution and thus provide a statistically isotropic and uniform field environment for the duration of EMI measurement and testing [1–3]. The use of reverberation chambers and TEM waveguides, such as strip lines and TEM-cells, has been discussed in IEC/SC77B (a subcommittee of the International Special Committee on Radio Interference) as methods that are alternative or independent to anechoic chambers [4–7].

The reverberation chamber has been employed for more and more electromagnetic testing, such as radiated emission test, radiated susceptibility test and shielding test. The equipment under test (EUT) is placed under the test volume within the chamber and its performance is monitored while the stirrers are rotated in discrete steps. The evaluation of the field uniformity in a reverberation chamber is not the same with the calibration procedure defined by the IEC standard for an anechoic chamber [8].

While the stirrers are rotated, the field uniformity in the test volume is statistically evaluated from the distribution of the maximum electric field strengths at each point location, which is chosen to place a dipole antenna [8]. Both the number of steps of stirrers during one complete rotation, and the number of test points affect the statistically field uniformity. On the basis of these steps the standard deviation will be calculated, which is required to be within a given limit-3 dB. It is a tedious task and the examination of field uniformity demands a great number of computing.

In this paper, two neural-network methods are presented to give aids, including the generalized regression neural network (GRNN) and the back-propagation (BP) network. 24 test points are chosen to simulate the $E$-field within the chamber using GEMS. According to these evaluation data, 20 points are picked up to train the network. After the training process, the network is applied to predict the $E$-field of the left 4 points based on the point position. The different results got by the two networks will be compared, and the error analysis will be performed.

## 2. METHODOLOGY

### 2.1. The Architecture of GRNN

The GRNN is a feed-forward network which is some kind of the radial basis function (RBF) network. It is divided into three layers: an input layer, an output layer which is also called a linear layer and a hidden layer which is also called a radial basis layer. The network structure in GRNN is shown in Fig. 1, where **X** is the input vector and **Y** is the output vector.
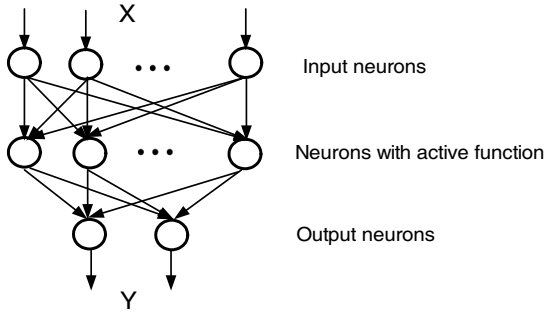
Figure 1: Network structure of GRNN.
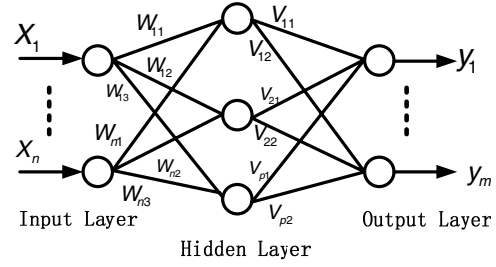


Figure 2: BP neural network diagram.

GRNN can be formulated as

$$y(x) = \frac{\sum\limits_{i=1}^{n} y_i \exp(-d_i^2/2\sigma^2)}{\sum\limits_{i=1}^{n} \exp(-d_i^2/2\sigma^2)} \tag{1}$$

$$d_i^2 = |x - x_i|^2 \tag{2}$$

$$W_i = \exp\left(-\frac{d_i^2}{2\sigma^2}\right) \tag{3}$$

where $y(x)$ is the output of the estimator, $x_i$ is the training sample and is used as the mean of a normal distribution, and $x$ is the predicted value. $d_i$ is the Euclidean distance between $x$ and $x_i$. $N$ is the number of the training samples. $W_i$ is Gaussian kernel function. The spread factor or standard deviation $\sigma_i$ is a critical consideration in the effectiveness of GRNN. As the spread factor becomes larger, the radial basis function's slope becomes smoother, and several neurons can respond to an input vector. If the spread is quite small, the radial basis function is very steep, so that the neuron with the weight vector, closest to the input, will have a much larger output than other neurons.

### 2.2. The Principle of BP Network

BP network algorithm is on the basis of error back-propagation, and it is used in practice for its good nonlinear mapping capability. It is a kind of multi-layer feed forward neural network based on BP algorithm, which consists of input layer, implied layer and output layer. A 3-layer neural network is taken as an example [9]. The diagram is shown as Fig. 2.

$W_{ij}$ is the weight from input unit to implied unit, the appropriate initialization method is to take the weights as very small evenly distributed random numbers between 0 and 1. $V_{ij}$ is the weight from hidden unit to output unit, $y_j$ is the output.

Proper train of BP neural network is needed to enable BP neural network to predict precisely. The weight values, the transfer function and the train function should be selected carefully.

### 3. FDTD SIMULATION

The simulation is carried out with an electromagnetic simulation software — GEMS. It is developed based on parallel conformal FDTD method and can be used to simulate the extremely large problems using the computer cluster at a relatively high parallel efficiency.

The chamber which is made to be analyzed is 1.1 meters long, 0.7 meters wide, and 0.6 meters high, whose lowest using frequency (LUF) is 762 MHz. The working frequency is set between 1 GHz and 2.5 GHz. Fig. 3 shows the model of the reverberation chamber in GEMS.

The separation distance must be greater than $\lambda/4$ for the lowest test frequency. In this chamber the minimum distance is 7.5 cm, so we choose the distance as 10 cm for the reliable results.

The field uniformity of this chamber should be verified before it is used to perform tests at operational frequency range. In this simulation 24 points are picked up, locating at peaks of three different test volumes. The tuners' step is defined at 5°, resulting in 72 values during one complete rotation. The average field strength ($\bar{E}_{x,y,z}$) for each axis of the test point is selected. According to IEC 61000-4-21, the field within the chamber is considered as uniform if the standard deviation is
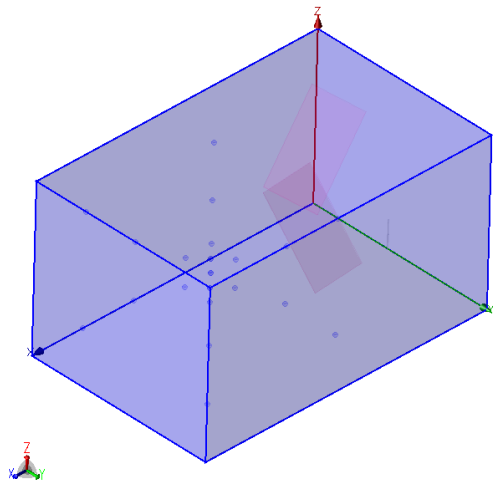
Figure 3: Simulation model.
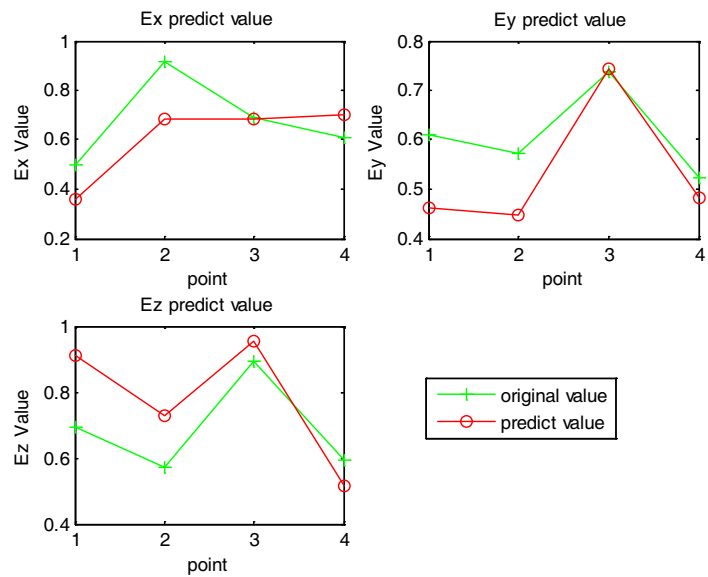


Figure 4: E-field strength predication.
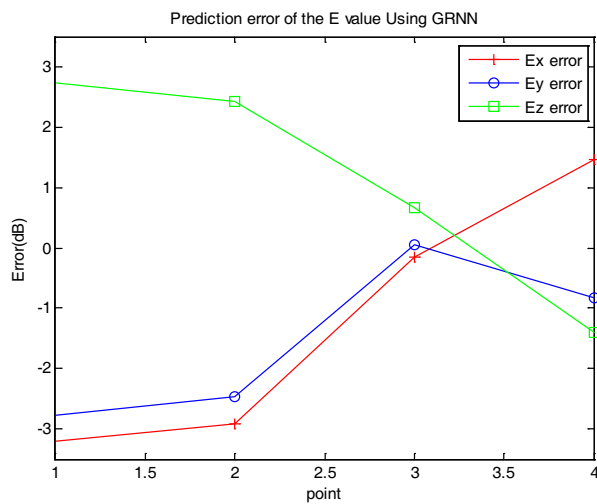


Figure 5: E-field strength predication error.
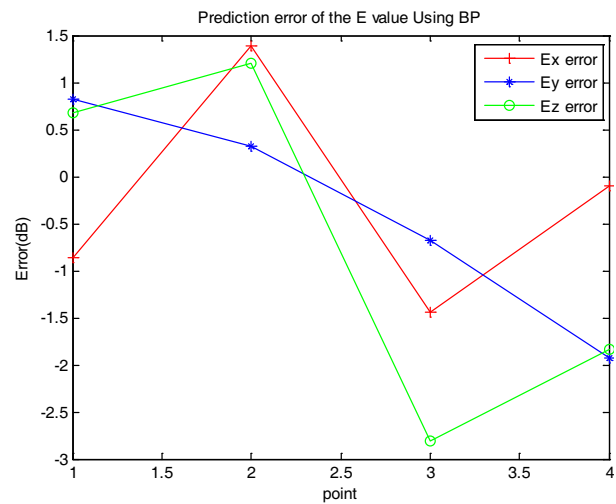


Figure 6: E-field strength predication error at 2 GHz.

within 3 dB above 400 MHz. Basing on these evaluation data GRNN and BP network are utilized to try to reduce the amount of calculation.

## 4. RESULTS AND CONCULSION

### 4.1. GRNN Prediction

For the purpose of the convergence of the network and the predication accuracy, the E-field strength values should be normalized. The spread factor $\sigma$ is defined as 0.01. Fig. 4 shows the predication results, and Fig. 5 shows the error.

### 4.2. BP Network Prediction

In BP network the transfer function and the train function are selected as logarithmic function and gradient function. Fig. 6 shows the prediction error.

The BP network prediction errors are all under 3 dB. Comparing with BP network, GRNN only has spread factor to adjust. It can be determined that BP network is more available. This conclusion infers that we can take advantage of this neural-network method to study the reverberation chamber uniformity.

**REFERENCES**

1. Lehman, T. H., "A statistical theory of electromagnetic fields on complex cavities," *Interaction Note Series, Note 494*, May 1993.
2. Hill, D. A., "Plane wave integral representation for fields in reverberation chamber," *IEEE Transactions on Electromagn. Compatibility*, Vol. 40, 209–217, August 1998.
3. Freyer, G. J., T. H. Lehman, J. M. Ladbury, G. H. Koepke, and M. O. Hatfield, "Verification of fields applied to an EUT in a reverberation chamber using statistical theory," *IEEE International Symposium on Electromagn. Compatibility*, Vol. 1, 34–38, August 1998.
4. "Electromagnetic compatibility (EMC) — Part-4-21: Testing and measurement techniques — Reverberation chamber test methods," IEC61000-4-21, 2003.
5. CISPR Publication 16-1, "Reverberation chamber for total radiated power measurement," 1996.
6. Harima, K. and Y. Yamanaka, "Evaluation of $E$-field uniformity for radiated immunity testing in a reverberation chamber," *IEEE*, 2001.
7. Huang, Y. S. and Y. F. Lin, "Freight prediction based on BP neural network improved by chaos artificial fish-swarm algorithm," *International Conference on Computer Science and Software Engineering*, Vol. 5, 1287–1290, 2008.

# Application of EH4 in the 102 Ore Belt in Shihu Gold Deposit of Western Hebei, China

**Xiaoming Fu[1], Tagen Dai[1], and Chaozhuang Xi[2]**

[1]School of Geosciences and Environmental Engineering, Central South University
Changsha, Hunan 410083, China
[2]Hunan Jinxin Gold Group Co., Ltd., Changsha, Hunan 410015, China

**Abstract**— Shihu gold deposit is under the administrative divisions of Chenzhuang town Lingshou Country Hebei Province. The authors have reached the conclusion that the gold ore bearing horizon is Tuanpokou Formation of Archean Fuping Group, the Mapeng rock mass is I-type granite. EH4 is widely used in solid minerals, especially in finding concealed ore deposit. In this paper, the author adopted EH4 method to make a synthetic study on 102 ore belt in Shihu gold deposit in Hebei. The result showed that the geophysical method was quite useful in the exploration of concealed ore deposit.

## 1. INTRODUCTION

Shihu gold deposit is under the administrative divisions of Chenzhuang town Lingshou Country Hebei Province. And it is located 66 km to the west-north of Lingshou Country. The mining geographic coordinates are: Longitude $114°03'15'' \sim 114°04'21''$ and Latitude $38°39'04'' \sim 38°40'19''$. The mining area is $4.1 \, \text{km}^2$.

Mining Ore formation is gneiss of Tuanpokou Formation of Archean Fuping Group, lithology is mainly a set of biotite plagioclase gneiss, plagioclase amphibolites, amphibole-plagioclase gneiss, with fibrolite K-feldspar leucoleptite and marble, that composed of senior metamorphic rocks. Most researchers believe that Tuanpokou group is the formation of gold ore source region layer, their views are consistent.

Mine is located in the NW wing of chenzhuang syncline, the overall structural outline for the east of the anticline pitching, structure and near-SN-, NW and EW to the fracture (fracture) structure. Structure acting mainly folds, fracture. Major fold structure withTulingdonggou anticline, Shihu syncline, Yankou reverse anticline syncline and Xionggou syncline. The former two larger scales, laid the structure of the main frame of mine. Major faults, nearly SN-, NW to, NE direction and NNW. Nearly SN-trending faults within the mining area is very developed, often in a certain direction for the change, generally expressed as the swinging to the NNE or NNW. Nearly SN-trending faults are mostly direct and guide mine ore, ore-hosting structure, at Shihu gold deposits are mainly 24, 28, 101, 102, 115, and 116, such as fault belt.

Mining Magmatic rocks are several varieties Yanshanian intrusion the Mapeng rock and granodiorite porphyry, quartz diorite porphyry rock, etc. dyke. Rock mining area is located in the northwest, north along the NNE Beiye-Mapeng-Yangjiazhuang deep faults and intrusion, space was rock strains-like, with the Fuping Group strata penetrated into contact, contact with extraversion.

With the gold mineralization is closely related to the mine wall rock alteration the type of very extensive, mainly silicification, pyrite, sericite, sericite rock-oriented, K-feldspar-oriented, green mud Petrochemical and local carbonate, kaolin-based and so on.

In general, the conductivity of gold-bearing quartz veins showed high resistance response. In this area of quartz vein-type gold deposits there were virtually fracture zones within the fracture zones due to strong water-rich, it showed low resistance response, and therefore show low resistance response to fracture broken belt. This choice of EH4 to predict an extension of the deep veins trend 102 ore belt.

## 2. FIELD WORK METHOD AND TECHNOLOGY OF EH-4 SYSTEM

1. Choice of operating frequency: The gneiss, with resistivity more than $1000 \, \Omega \cdot \text{m}$, was the main bedrock in this project area. In order to meet the design requirement, we chose 10 Hz, the lowest operating frequency while detecting. Three frequency groups like the second, the third and the fourth were in our choice, ranging from 10 Hz to 99 kHz.

2. Arrangement of observation points: The geophysical section line of survey area in Shihu gold deposit was located by our study team. We adopted GPS position and fix distance with measuring wire.

3. Systematic inspection: The parallel test was carried out the day before we began. It was required that the two magnetic bar parallel on the ground, $2 \sim 3$ m apart. The two electric dipole were arranged parallel, and be vertical to the bar. We observed the time series signal of electric field and magnetic field channels to make sure if it works properly.

## 3. DATA PROCESSING METHOD

The time series collected in field were pretreated firstly, and then changed to FFT. The imaginary and real component, and the phase data were obtained though it. The one-dimensional BOSTICK inversion was performed to transform from frequency to depth. Based on one-dimensional inversion, the two-dimensional electromagnetic was imaged fast and automatically by the two-dimensional imaging software used abroad.

The data obtained by inversion was done Kringing griddling in the $XZ$ plane. Meeting the actual situation of electrical anisotropy, $X$-axis and $Y$-axis were to taken anisotropy method to search radius.

## 4. WORKLOAD COMPLETED AND QUALITY ASSEMENT

Only 5 representative profiles were arranged this time because of high investigation cost. They were Line 100, Line 105, Line 111, Line 117 and Line 125 respectively. The workload completed was list in Table 1 in details.

The profile layout obeyed the following three principles. Firstly, it can basically reflect deep extension in the production midcourse of 102 ore belt. Secondly, it can reflect the extension of the all section of the ore belt roughly. Thirdly, it was favorable for verifying with pitting and drilling in near future. Base on these principles, the Line 100, Line 105, Line 111, Line 117 and Line 125 were layout.

## 5. ANOMALY INTERPRETATION

### 5.1. Anomaly Interpretation of Line 100

The weathered surface layer of Line 100 about 100–150 m thick, showed low resistivity layer, the low resistivity layer thickness along the survey line changed little, only some changes near the mountain peak. West of the Line from the measured elevation of 300 meters to the east elevation of 400 meters in position resistivity contour-intensive, electrical changes, be assumed that this layer of bits may be weathered parent rock layer and the interface. $F_1$ (fault 1) structure in the shallow (elevation 400 meters or more) tend to a more steep, while in the deep is more moderate, and north and north-west to the development of obvious. From the electrical point of view section of the east elevation of the distribution of 0–350 m of the rock mass had local low-impedance body, a smaller scale may be caused by $F_1$. The west side of the deep section (elevation $-100$ m) has a low resistivity body, is to the deep extension of $F_1$ is caused by other reasons, need to be further identified.

### 5.2. Anomaly Interpretation of Line 105

Compared with Line 100 are similar, but also showed two-story structure. $F_1$ construct develop a steeper and has extended to the deep trends; shallow layer of low resistivity along the profile developed only in the peak of its thickness is relatively large; profile east elevation of $-100$ m to 350 m of rock between the existences of localized low resistivity body. In the elevation of $-100$ m has a low resistivity anomaly, combined with Line 100 and Line 111 to see if it has a gradual trend of pinch-out. Interface, with its parent rock regolith watched roughly about 350 meters in elevation.

Table 1: The workload table of survey in 102 ore belt in Shihu gold deposit.

| Survey-Line Number | Points Number | Dot Pitch (m) | Polar Distance (m) | Profile Length (m) |
|---|---|---|---|---|
| Line 100 Section | **26** | **20** | **20** | **500** |
| Line 105 Section | **26** | **20** | **20** | **500** |
| Line 111 Section | **26** | **20** | **20** | **500** |
| Line 117 Section | **26** | **20** | **20** | **500** |
| Line 125 Section | **26** | **20** | **20** | **500** |
| Total observation points | **130** | | | |

### 5.3. Anomaly Interpretation of Line 111

$F_1$ tectonic shift in the profile of the east 180 meters, but the cutting depth significantly increased at elevation of 100 meters or deeper. Cross-section of 40 meters of another development of a structure $F_2$ (fault 2), it is almost parallel with the development of $F_1$, but the shallow depth of cut to the elevation of 300 meters, presumed to be $F_1$'s secondary structure. Deep rock is more complete, Line 100, 105 and the west side of 117 the deep low resistivity body did not see in the test line. Shallow layer of low resistivity survey lines evenly distributed throughout the thickness of about 250 meters. Regolith watched their parent rock interface, roughly between 300 to 400 meters elevation.

### 5.4. Anomaly Interpretation of Line 117

$F_1$ structure developed in the cross-section of 120 meters, the shallow (above 600 m elevation) than steep, deep gentler. Larger cutting depth to the elevation of 300 meters or so, from the electrical point of view there are further north and north-west to the development of deep lines and measuring elevation of 100 meters west of the low resistivity body may be linked. Development of a 70 m section $F_2$ construct, but also broadly in line with $F_1$ parallel to the cutting depth of more lines, with Line 111 to see if it should also be the $F_1$ secondary structure. Profile of the west side of the deep (elevation 100 meters) in front of low resistivity body occurs in the test line again, with Line 100, 105 of difference is that its location has been uplifted. The survey line measured relative to the north line of the low resistivity layer is relatively thin surface layer of about 100 meters thick.

### 5.5. Anomaly Interpretation of Line 125

Compared to other measurements of the low resistance layer of thin lines, less than 50 meters. $F_1$ in the profile of the 100 meters, cutting to the elevation of 300 meters. The west side of the deep survey line (elevation 0 meters) also has a relatively low resistivity body exists but not as well as Line 117 clear. The east of measuring line (100 m east) deep rock is basically more complete.

## 6. CONCLUSION

It was the second time to apply EH-4 electrical conductivity imaging system, and take high-frequency magneto telluric sounding method in deep part ore prediction for the mining area in Shihu gold deposit. It was identified that distribution and extension of the deep structure in 102 ore belt, and pointed out the favorable ore-forming parts. Then quantitative imputation for its depth was made.

From the entire surveyed area, $F_1$ construct the main structure, cutting mostly in the elevation of 300 meters depth, only Line 100, 111 more deeper. Its west side there is a secondary structure $F_2$, cutting depth shallower. The thickness of the surface low resistivity layer thick in northern, southern thinner. Relatively high resistance of rock deep integrity. Measuring line the west side of the deep low resistivity almost every local body of the existence of low resistivity body size from north to south there is a gradual trend towards smaller, its location there is a gradual uplift trend. Its causes need to be further identified.

From the $F_1$ position, the resistivity changes and the shape contours of view, measuring low resistance line of the west side of the deep body region that is Line 100 and 105 elevation of $-100$ m, Line 117 elevation of 100 meters, Line 125 elevation of 0 meters. Measuring Line 100 elevation of 100 meters and 250 meters west elevation of 200–300 m survey line is relatively low resistance of the body, Line 117's 150 meters at 150 meters elevation relative low resistance of the body, Line 117's 120 meters of the relatively low elevation of 200 meters body resistance favorable areas for possible mineralization.

### REFERENCES

1. Zhang, Y. X., S. L. Chen, and S. L. Peng, "Study on the gold ore structural controlling over TS ore-field, Lingshou, Hebei province," *Geotectonical et Metallogenia*, Vol. 20, No. 1, 71–80, 1996.
2. Chen, G. D., "China metallogenic geotectonic map," Central South University of Technology Press, Changsha, 1999.
3. Yang, D. F. and G. S. Li, "Study on the ore-forming conditions and genesis of Tuling and Shihu gold deposit in the Taihang mountain region," *Journal of Changchun University of Earth Science*, Vol. 21, No. 1, 47–53, 1991.

4. Xi, C. Z., T. G. Dai, and W. Liu, "Geological-geochemical characteristics of the Shihu gold deposit in western Hebei Province," *ACTA Geoscientica Sinica*, Vol. 29, No. 4, 451–458, Aug. 2008.

5. Xi, C. Z., T. G. Dai, W. Liu, and H. J. Zhang, "Petrogeochemical characteristics of the intrusive bodies of Mapeng granitoids in western Hebei," *ACTA Petrologica et Mineralogica*, Vol. 27, No. 2, 113–120, Mar. 2008.

# Propogation of an Electromagnetic Beam at the Interface of Isotropic Medium and Gyroelectric Medium

**Qi Liu, Hui Huang, and Yinde Zhang**

School of Electrical Engineering, Beijing Jiaotong University, Beijing 100044, China

**Abstract**— A detailed study on the reflection and transmission characteristics of an electromagnetic beam propogating at the interface of an isotropic medium and a gyroelectric medium in Voigt configuration is presented, for both TM and TE waves. We derived the reflection coefficient and transmission coefficient, respectively. Using the stationary phase approach, analytic expressions for lateral displacements of the reflected and transmitted waves from a gyroelectric medium are obtained, and we also give examples for both cases. It is found that the lateral displacements for TM and TE waves have different characteristics. Only the TM mode is affected by the gyrotropy.

## 1. INTRODUCTION

Gyroelectric medium is an electron plasma with an applied magnetic field. The characteristics of electromagnetic waves propagation in gyrotropic plasmas have been theoretically investigated in many literatures. The magnetoplasma modes in Voigt, perpendicular, and Faraday configurations have been studied by Kushwaha and Halevi [1–3], Gillies and Hlawiczka have done some researches on gyrotropic waveguide in detail [4–8], and dyadic Green's functions for gyrotropic medium have been investigated by Eroglu as well as Li [9–11]. There are also some studies focusing upon the effects of magnetic field on semiconducting plasma slab and negatively refracting surfaces [12, 13]. Furthermore, propagation and scattering characteristics in gyrotropic systems [9, 14–18] and surface modes at the interface of a special gyrotropic medium [19] have been investigated extensively.

In this paper, we focus on the reflection and transmission characteristics of an electromagnetic beam propogating at the interface of an isotropic medium and a gyroelectric medium in Voigt configuration. We consider two cases: incident wave is TM or TE polarized. We present the analytic expressions for the reflection and transmission coefficients and mathematical result for the lateral displacement which is obtained by the stationary phase approach. After we get the result for a specific case, we discuss the different propogation characteristics between TE and TM waves.
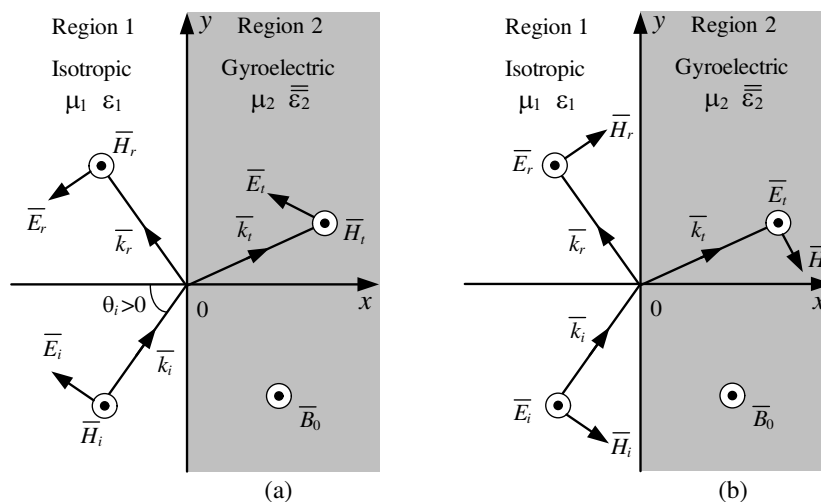


Figure 1: Reflection and transmission of waves on an interface between a semi-infinite isotropic medium (Region 1) and a gyroelectric medium in the Voigt configuration (Region 2). In Region 2, an applied magnetic field $\bar{B}_0$ is in $+z$ direction. (a) TM wave, (b) TE wave.

## 2. REFLECTION AND TRANSMISSION

We consider the configuration in Fig. 1, where a plane wave is incident from an semi-infinite isotropic medium into a gyroelectric medium at an oblique angle $\theta_i$ with respect to the normal of the interface. Region 1 is isotropic medium, with permeability. $\mu_1$ and permittivity $\varepsilon_1$. In Region 2, an external magnetic field $\bar{B}_0$ is applied in $+z$ direction, parallel to the interfaces and perpendicular to the direction of the wave propagation (gyroelectric medium in Voigt configuration). Its permeability is $\mu_2$, while permittivity $\bar{\bar{\varepsilon}}_2$ is a tensor, which takes the following form:

$$\bar{\bar{\varepsilon}}_2 = \begin{bmatrix} \varepsilon_{xx} & i\varepsilon_g & 0 \\ -i\varepsilon_g & \varepsilon_{yy} & 0 \\ 0 & 0 & \varepsilon_{zz} \end{bmatrix}, \tag{1}$$

where elements are given by

$$\varepsilon_{xx} = \varepsilon_{yy} = \varepsilon_\infty \left( 1 - \frac{\omega_p^2}{\omega^2 - \omega_c^2} \right), \quad \varepsilon_{zz} = \varepsilon_\infty \left( 1 - \frac{\omega_p^2}{\omega^2} \right), \quad \varepsilon_g = \varepsilon_\infty \left[ -\frac{\omega_p^2 \omega_c}{\omega(\omega^2 - \omega_c^2)} \right]. \tag{2}$$

Here, $\omega_p = \sqrt{Nq_e^2/m_{eff}\varepsilon_\infty}$ and $\bar{\omega}_c = q_e \bar{B}_0/m_{eff}$ are the plasma and cyclotron frequencies respectively, $\varepsilon_\infty$ is the background permittivity, $N$ is the electron density, $m_{eff}$ is the effective mass, and $q_e$ is the electron charge.

It is known that in gyroelectric medium in the Voigt configuration, waves can be decoupled into TE and TM modes and with different dispersion relations [13, 20]. So we calculate the two modes respectively.

### 2.1. Case 1: TM Incident Waves

We focus on TM waves first. For Fig. 1(a), with wave vectors $\bar{k}_i^{\text{TM}} = \hat{y}k_y^{\text{TM}} + \hat{x}k_{1x}^{\text{TM}}$ (incident) and $\bar{k}_r^{\text{TM}} = \hat{y}k_y^{\text{TM}} - \hat{x}k_{1x}^{\text{TM}}$ (reflection) in the isotropic medium, and $\bar{k}_t^{\text{TM}} = \hat{y}k_y^{\text{TM}} + \hat{x}k_{2x}^{\text{TM}}$ (transmission) in the gyroelectric medium, the dispersion relations can be expressed as

$$\left(k_y^{\text{TM}}\right)^2 + \left(k_{1x}^{\text{TM}}\right)^2 = \omega^2 \mu_1 \varepsilon_1, \tag{3}$$

$$\left(k_y^{\text{TM}}\right)^2 + \left(k_{2x}^{\text{TM}}\right)^2 = \omega^2 \mu_2 \varepsilon_V. \tag{4}$$

Here $\varepsilon_V = (\varepsilon_{xx}^2 - \varepsilon_g^2)/\varepsilon_{xx}$, is the equivalent permittivity of the gyroelectric medium in the Voigt configuration for TM waves.

According to the Maxwell equations, matching the boundary conditions gives the transmission and reflection coefficients for TM waves

$$R^{\text{TM}} = \frac{\sigma k_{1x}^{\text{TM}} - k_{2x}^{\text{TM}} + i\tau k_y^{\text{TM}}}{\sigma k_{1x}^{\text{TM}} + k_{2x}^{TM} - i\tau k_y^{\text{TM}}}, \tag{5}$$

$$T^{\text{TM}} = \frac{2\sigma k_{1x}^{\text{TM}}}{\sigma k_{1x}^{\text{TM}} + k_{2x}^{\text{TM}} - i\tau k_y^{\text{TM}}}, \tag{6}$$

where the parameters $\sigma$ and $\tau$ are dimensionless, defined as

$$\sigma = \frac{\varepsilon_V}{\varepsilon_1}, \quad \text{and} \quad \tau = \frac{\varepsilon_g}{\varepsilon_{xx}}. \tag{7}$$

Here $\tau$ is a direct manifestation of the applied magnetic field $\bar{B}_0$, arising from the off-diagonal element $\varepsilon_g$ in the permittivity tensor. Without an external magnetic field, $\varepsilon_g$ and $\tau$ are zero.

### 2.2. Case 2: TE Incident Waves

Now we turn to TE modes, shown in Fig. 1(b). For TE waves, since the electric field is in $\pm z$ direction, only $\varepsilon_{zz}$, element in $z$ direction of the whole permittivity tensor, works. So TE waves in the gyroelectric medium behaves the same as it does in the isotropic medium with the permittivity $\varepsilon_{zz}$.

With wave vectors $\bar{k}_i^{\text{TE}} = \hat{y}k_y^{\text{TE}} + \hat{x}k_{1x}^{\text{TE}}$ (incident) and $\bar{k}_r^{\text{TE}} = \hat{y}k_y^{\text{TE}} - \hat{x}k_{1x}^{\text{TE}}$ (reflection) in the isotropic medium, and $\bar{k}_t^{\text{TE}} = \hat{y}k_y^{\text{TE}} + \hat{x}k_{2x}^{\text{TE}}$ (transmission) in the gyroelectric medium, it is easy to

get the transmission and reflection coefficients for TE waves, written as

$$R^{\mathrm{TE}} = \frac{1 - p_{12}^{\mathrm{TE}}}{1 + p_{12}^{\mathrm{TE}}}, \qquad T^{\mathrm{TE}} = \frac{2}{1 + p_{12}^{\mathrm{TE}}}, \tag{8}$$

where

$$p_{12}^{\mathrm{TE}} = \frac{\mu_1 k_{2x}^{\mathrm{TE}}}{\mu_2 k_{1x}^{\mathrm{TE}}}. \tag{9}$$

## 3. LATERAL DISPLACEMENTS OF THE REFLECTED AND TRANSMITTED WAVES

The Goos-Hänchen (GH) effect [21, 22] has been studied for many years. GH lateral displacement refers to the spatial displacement of a reflected wave from the position expected by geometrical reflection. Traditionally, GH shift is always a phenomenon during total reflection, when an electromagnetic beam is reflected at the interface between media with different reflective indexes. In fact, when reflection or transmission coefficient is not real, GH shift $\phi$ appears, along with GH lateral displacement.

For TE case, according to Eqs. (8) and (9), we can see that only when the total reflection occurs at the interface, $R^{\mathrm{TE}}$ becomes imaginary, same as the isotropic case. However, for TM waves, from Eqs. (5) and (6), the reflection and transmission coefficient are always imaginary with the introduction of $\tau$, result of the gyrotropy, so there always exists GH shift, no matter total reflection occurs or not. Since this, our attention is only paid to the TM case.

The lateral displacement has the well-known expression $S = -d\phi/dk_y$, which was proposed by Artmann using the stationary phase method [23]. After some algebra manipulations, and by noting that the denominators of both coefficients are the same, the lateral displacements of the reflection and transmission for TM waves can be expressed as

$$
\begin{aligned}
S_t^{\mathrm{TM}} &= -\frac{1}{|T^{\mathrm{TM}}|^2} \left\{ \mathrm{Re}\left[T^{\mathrm{TM}}\right] \frac{\partial \mathrm{Im}\left[T^{\mathrm{TM}}\right]}{\partial k_y} - \mathrm{Im}\left[T^{\mathrm{TM}}\right] \frac{\partial \mathrm{Re}\left[T^{\mathrm{TM}}\right]}{\partial k_y} \right\} \\
&= \frac{-\tau k_y^{\mathrm{TM}}}{(\sigma k_{1x}^{\mathrm{TM}} + k_{2x}^{\mathrm{TM}})^2 + (\tau k_y^{\mathrm{TM}})^2} \left( \frac{\sigma k_{1x}^{\mathrm{TM}} + k_{2x}^{\mathrm{TM}}}{k_y^{\mathrm{TM}}} + \frac{\sigma k_y^{\mathrm{TM}}}{k_{1x}^{\mathrm{TM}}} + \frac{k_y^{\mathrm{TM}}}{k_{2x}^{\mathrm{TM}}} \right)
\end{aligned} \tag{10}
$$

$$
S_r^{\mathrm{TM}} = -\frac{1}{|R^{\mathrm{TM}}|^2} \left\{ \mathrm{Re}\left[R^{\mathrm{TM}}\right] \frac{\partial \mathrm{Im}\left[R^{\mathrm{TM}}\right]}{\partial k_y} - \mathrm{Im}\left[R^{\mathrm{TM}}\right] \frac{\partial \mathrm{Re}\left[R^{\mathrm{TM}}\right]}{\partial k_y} \right\} = S_t^{\mathrm{TM}} + \Delta S_{rt}^{\mathrm{TM}}, \tag{11}
$$

where

$$
\Delta S_{rt}^{\mathrm{TM}} = \frac{-\tau k_y^{\mathrm{TM}}}{\left(\sigma k_{1x}^{\mathrm{TM}} - k_{2x}^{\mathrm{TM}}\right)^2 + \left(\tau k_y^{\mathrm{TM}}\right)^2} \left( \frac{\sigma k_{1x}^{\mathrm{TM}} - k_{2x}^{\mathrm{TM}}}{k_y^{\mathrm{TM}}} + \frac{\sigma k_y^{\mathrm{TM}}}{k_{1x}^{\mathrm{TM}}} - \frac{k_y^{\mathrm{TM}}}{k_{2x}^{\mathrm{TM}}} \right). \tag{12}
$$

## 4. RESULT AND DISCUSSION

Here, we consider an indium antimony (InSb) with an exteral magnetic field as the gyrotropic medium. And the isotropic medium is vacuum. The material parameters used in the computation are: $\mu_1 = \mu_2 = \mu_0$, $\varepsilon_1 = \varepsilon_0$, $\varepsilon_\infty = 15\varepsilon_0$, $N = 10^{22}\,\mathrm{m}^{-3}$, and $m_{\mathit{eff}} = 0.015m_0 = 0.13664 \times 10^{-31}\,\mathrm{kg}$. Hence, $\omega_p = 1.19 \times 10^{13}\,\mathrm{rad/s}$ and $\omega_c/\omega_p = 0.98B_0$. We plot the lateral displacements in the $(\omega, \theta_i)$ plane with a color scale proportional to the magnitude, shown in Fig. 2. Fig. 2(a) is for the TE incident waves, and Fig. 2(b) and Fig. 2(c) are for TM waves. The frequencies are normalized to the plasma frequency $\omega_p$, and the displacements are normalized to $\lambda_0 = 2\pi c/\omega$, the incident wavelength in vacuum.

It is interesting to compare the TE and TM cases.

For TE case, similar to isotropic cases, GH shift appears only during total reflection. And in this situation, transmitted wave is evanescent in the $x$ direction, so what we considered is only GH lateral displacement of the reflected waves, not including that of transmitted waves. From Fig. 2(a), we can see that, corresponding to the change of $\varepsilon_{zz}$ with frequency, there are two regions (A and B) separated by $\omega_p$. In Region A, total reflection occurs on the interface so GH lateral displacement appears; while in Region B there is no total reflection and no GH lateral displacement. Moreover, TE modes is independent of the external magnetic field.
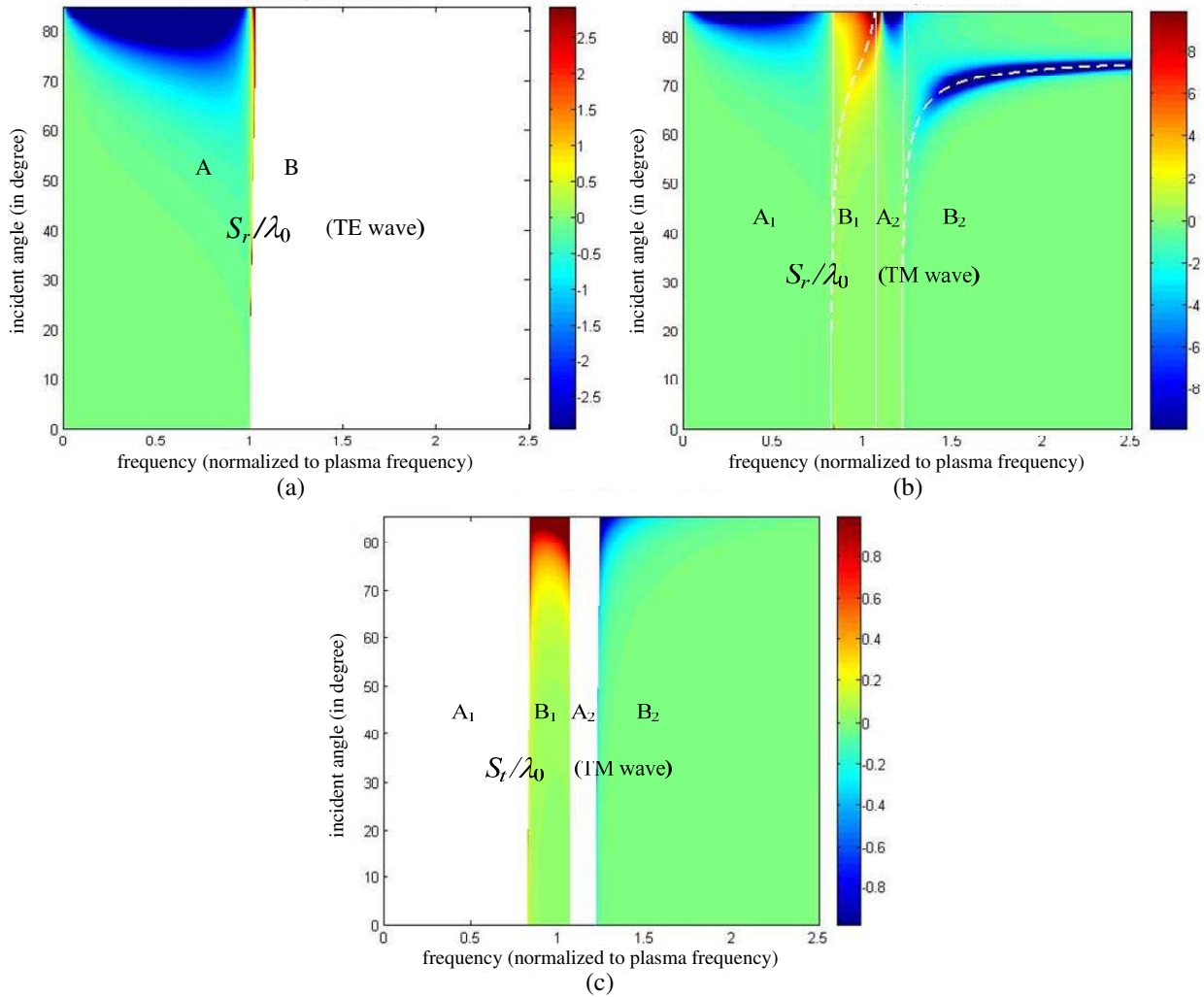
Figure 2: Lateral displacements of TE or TM waves transmitted and reflected from the interface of vacuum and gyroelectric medium, the Brewster angle is also shown for TM cases(in white dashed line). The frequencies are normalized to $\omega_p$, and the displacements are normalized to $\lambda_0 = 2\pi c/\omega$, the incident wavelength. (a) The lateral displacement of reflected TE waves $S_r$, (b) $S_r$ for TM waves with an applied magnetic field $\bar{B}_0 = +\hat{z}0.4\,\mathrm{T}$, (c) $S_t$ for TM waves with the same applied magnetic field as (b).

For TM waves, corresponding to the change of equivalent permittivity $\varepsilon_V$, the existence of the applied magnetic field splits each region up into two, marked with subscript 1 and 2. In Regions $B_1$ and $B_2$, there is no total reflection at the interface, while both reflection and transmission coefficients are imaginary, $S_r$ and $S_t$ exist. However, in Regions $A_1$ and $A_2$, total reflection occurs at the interface, and the transmitted wave is evanescent, making GH lateral displacement for transmitted waves meaningless, shown blank in Fig. 2(c).

It is also of interest to note that in regions $B_1$ and $B_2$ of Fig. 2(b), there is a large displacement of reflected TM waves. It is due to the Brewster angle, shown in the white dashed line in Fig. 2(b). For TM waves, there is an abrupt phase change near the Brewster angle [24–26] which causes a large lateral shift for the reflected beam. Nevertheless, there is no abrupt change for the phase of the transmission coefficient at the Brewster angle. Therefore, we expect a large lateral shift of the reflected beam near the Brewster angle but no such phenomenon for the transmitted beam.

## 5. CONCLUSION

This paper investigates the reflection and transmission characteristics of an electromagnetic beam propogating at the interface of an isotropic medium and a gyroelectric medium in Voigt configuration, for both TE and TM modes. Both reflection and transmission coefficients are derived,

along with analytic expressions for lateral GH displacements for each. Meanwhile, several cases for lateral shift are shown. The results here may have potential applications in magnetic modulations and Terherz researches.

**ACKNOWLEDGMENT**

**REFERENCES**

1. Kushwaha, M. S. and P. Halevi, "Magnetoplasmons in thin films in the Voigt configuration," *Physical Review B*, Vol. 36, 5960–5967, 1987.

2. Kushwaha, M. S. and P. Halevi, "Magnetoplasma modes in thin films in the Faraday configuration," *Physical Review B*, Vol. 35, 3879–3889, 1987.

3. Kushwaha, M. S. and P. Halevi, "Magnetoplasmons in thin films in the perpendicular configuration," *Physical Review B*, Vol. 38, 12428–12435, 1988.

4. Gillies, J. R. and P. Hlawiczka, "TE and TM modes in gyrotropic waveguides," *J. Phys. D: Appl. Phys.*, Vol. 9, 1315, 1976.

5. Gillies, J. R. and P. Hlawiczka, "Elliptically polarized modes in gyrotropic waveguides. II. An alternative treatment of the longitudinally magnetized case," *J. Phys. D: Appl. Phys.*, Vol. 10, 1891, 1977.

6. Hlawiczka, P., "Elliptically polarized modes in gyrotropic waveguides," *J. Phys. D: Appl. Phys.*, Vol. 9, 1957, 1976.

7. Hlawiczka, P., "A gyrotropic waveguide with dielectric boundaries: The longitudinally magnetised case," *J. Phys. D: Appl. Phys.*, Vol. 11, 1157, 1978.

8. Hlawiczka, P., "The gyrotropic waveguide with a normal applied DC field," *J. Phys. D: Appl. Phys.*, Vol. 11, 1941, 1978.

9. Eroglu, A. and J. K. Lee, "Wave propagation and dispersion characteristics for a nonreciprocal electrically gyrotropic medium," *Progress In Electromagnetics Research*, Vol. 62, 237–260, 2006.

10. Li, L. W., N. H. Lim, and J. A. Kong, "Cylindrical vector wave function representation of Green's dyadic in gyrotropic bianisotropic media — Abstract," *Journal of Electromagnetic Waves and Applications*, Vol. 17, No. 11, 1589–1591, 2003.

11. Li, L. W., N. H. Lim, W. Y. Yin, and J. A. Kong, "Eigenfunctional expansion of dyadic Green's functions in gyrotropic media using cylindrical vector wave functions — Abstract," *Journal of Electromagnetic Waves and Applications*, Vol. 17, No. 12, 1731–1733, 2003.

12. Ivanov, S. T. and N. I. Nikolaev, "Magnetic-field effect on wave dispersion in a free semiconductor plasma slab," *J. Phys. D: Appl. Phys.*, Vol. 32, 430, 1999.

13. Boardman, A., N. King, Y. Rapoport, and L. Velasco, "Gyrotropic impact upon negatively refracting surfaces," *New J. Phys.*, Vol. 7, 1–24, 2005.

14. Zhang, M., L. W. Li, T. S. Yeo, and M. S. Leong, "Scattering by a gyrotropic bianisotropic cylinder of arbitrary cross section: An analysis using generalized multipole technique — Abstract," *Journal of Electromagnetic Waves and Applications*, Vol. 17, No. 7, 1049–1051, 2003.

15. Yin, W. Y., L. W. Li, and M. S. Leong, "Scattering from multiple bianisotropic cylinders and their modeling of cylindrical objects of arbitrary cross-section — Abstract," *Journal of Electromagnetic Waves and Applications*, Vol. 14, No. 5, 611–612, 2000.

16. Tan, E. L. and S. Y. Tan, "Cylindrical vector wave function representations of electromagnetic fields in gyrotropic bianisotropic media," *Journal of Electromagnetic Waves and Applications*, Vol. 13, No. 11, 1461–1476, 1999.

17. Bass, F. and L. Resnick, "Spatial and temporal rotation of the polarization plane of electromagnetic waves reflected from and transmitted through a gyrotropic plate," *Journal of Electromagnetic Waves and Applications*, Vol. 17, No. 8, 1131–1137, 2003.

18. Censor, D. and M. D. Fox, "Polarimetry in the presence of various external reflection and retrodirection mirroring mechanisms, for chiral and gyrotropic media," *Journal of Electromagnetic Waves and Applications*, Vol. 11, No. 3, 297–313, 1997.

19. Huang, H., Y. Fan, B. I. Wu, F. Kong, and J. A. Kong, "Surface modes at the interfaces between isotropic media and uniaxial plasma," *Progress In Electromagnetics Research*, Vol. 76, 1–14, 2007.

20. Huang, H., Y. Fan, F. Kong, B.-I. Wu, and J. A. Kong, "Influence of external magnetic field on a symmetrical gyrotropic slab in terms of Goos-Hänchen shifts," *Progress In Electromagnetics Research*, Vol. 82, 137–150, 2008.

21. Goos, F. and H. Hänchen, "Ein neuer und fundamentaler versuch zur totalreflexion," *Annals of Physics*, Vol. 1, 333–334, 1947.

22. Goos, F. and H. Hänchen, "Neumessung des strahlversetzungseffeketes bei totalreflexion," *Annals of Physics*, Vol. 5, 251–252, 1949.

23. Artmann, K., "Berechnung der seitenversetzung des totalreflektierten strahles," *Annals of Physics*, Vol. 2, 87–102, 1948.

24. Lai, H. M. and S. W. Chan, "Large and negative Goos-Hänchen shift near the Brewster dip on reflection from weakly absorbing media," *Optics Letters*, Vol. 27, 680–682, 2002.

25. Lai, H. M., S. W. Chan, and W. H. Wong, "Nonspecular effects on reflection from absorbing media at and around Brewster's dip," *Journal of the Optical Society of America A*, Vol. 23, 3208–3216, 2006.

26. Wang, L. G. and S. Y. Zhu, "Large positive and negative Goos-Hänchen shifts from a weakly absorbing left-handed slab," *Journal of Applied Physics*, Vol. 98, 043522, 2005.

# On the Vision of Depth

**S. L. Vesely[1] and A. A. Vesely[2]**

[1]I.T.B. — C.N.R., Italy
[2]Via L. Anelli 13, Milano, Italy

**Abstract**— Most techniques introduced so far by instrument-makers to minimize chromatic aberrations avail themselves of (monochromatic) point sources and are devised for correcting flat images. However, when reproducing spatial scenes, the color combination does contribute to depth perception. The purpose of this paper is to briefly account for the dependence of depth decoding upon the illumination conditions. We consider decoding by the eyes in the two extreme cases of LASER and natural lighting.

## 1. INTRODUCTION

The visual channel ranks among the highest capacity information carriers. Hence, it is of paramount importance in medicine and in science to provide easily interpretable visual representations. In this paper, we address pictorial representations specifically devised to convey topographic information about regions that are uneasy to reach or inaccessible by other means than optical ones. In order to faithfully reproduce the scene, reconstruction algorithms have been developed, which usually take sampling rates into account, but disregard illumination conditions. The data used for rendering of a 3-D region may or may not embed explicit depth information [1]. In case it does not, algorithms may assume a 3-D model for reckoning a depth estimate. However, the depth sensed during data acquisition is subject to much the same restrictions as that reckoned after; namely, the lighting conditions.

Before dealing with the perception of depth proper in next section, one remark on the *physical space* is in order. Besides requesting confirmation by experience, classical physics has the intent to state natural phenomena objectively, which means independently on any specific observer. Nonetheless, spatial experiences rest on the senses of touch, balance, sight, etc. as well as on proprioception and psychological traits, whereas hypothetic-deductive accounts of the geometric space are drawn from logical and epistemological presuppositions, and are assumed to fully apply only to empty space. In addition, historically, with the creation of non-euclidean geometries the geometric figures started to be distinguished from the idealizations of real objects. Since then, mathematics and physics can be told apart. On the one hand, the mathematical concepts of length, width, and height have been ascribed to our world to distinguish it from others, that we can only form a mental picture of, such as either the two-dimensional "Flatland", or worlds with extra dimensions, whose models can be calculated and shown on computer screens. On the other hand, physical sciences have continued to base the distinction between deceptive and genuine things on substantiated experience, i.e., on the sensorial perception of the environment.

Among the modern physical theories, Einstein's general relativity maintains the classical assumption that the experimenter is an indiscerptible entity easily distinguished from the environment. On the opposite, in the quantum mechanical theories the outcome of an event is assumed to depend to a varying degree on the observer. When the information to be retrieved relies entirely on the visual channel, without being supported by any of the other usually coincidental sensorial experiences, telecommunications could adopt a position intermediate between these two extremes, consisting of separating as much as possible the inferred part of the perception from the signal actually received. In the following, we shall be concerned with some effects of narrow-band illumination and with analyzing the sensation of depth under natural lighting conditions.

## 2. DEPTH DECODINGS

Except for quantum mechanics, where the limitations inherent in the measurement process are accounted for by the uncertainty principle, the optical instruments are assumed to display objects' *shapes* independently of any accompanying condition. Therefore, many computer-graphics techniques devise to create the illusion of space for pictures specified spatially, but already projected on a screen, and set out to elicit depth perception by taking recourse to the psychological experience of natural illumination. Looking at an image on the display, except for color and brightness, the light rebounded from the subjects situated towards the front of the scene is qualitatively exactly

the same as that coming from the visible things in its furthest parts. Although both psychological and anatomic-physiologic traits are involved in the perception of space, it is known that sometimes their contributions can be separated. For example, there is one distinct effect of depth, the parallax, known to depend just on binocular disparity. A simple way to appreciate parallax is to look at one small, nearby thing while keeping only one eye open at a time, and to observe its apparent displacement against the background by alternating which eye is used for observing. Surveying avail itself of geometric methods based on parallax to obtain objective and accurate mappings. Besides, parallax can be exploited, together with binocular perspective, to create the illusion of depth. There are many methods based on binocular disparity to convey 3-D stereoscopic vision. Among them, the holographic techniques are distinctive in that they manage to encode the parallax in the pictures. This means that there is at least one feature of depth, which can be encoded. That trait can be picked up by healthy unaided eyes from a rainbow hologram. Moreover, it is not the only depth effect which can be encoded: The need to adjust the depth-of-field range when shooting photographs evidences another decodable effect, resting in a complicated way on the relative aperture of camera lenses. Owing to the distance between the portrayed subjects and the objective lens, the passively diffused sunlight changes its angular spread, and becomes the more bundled the farther apart from the camera the targets lay. On account of this, diacaustic patterns form instead of light points in the back focal plane of a converging lens. Although the effect is similar, the blurred regions on the film plane of a modern objective lens, instead originate from diffraction.

Computer graphics techniques manage to model a *unique* 3-D shape at a glance by blending the images from a number of stacked focal planes. Instead, the perception of depth is usually achieved by ways of eyes accommodation together with their vergence so as to allow the parts aimed at within the whole scene to fuse in a sequel of matched stigmatic shapes. In daylight, by purpose, both methods result in shapes tied to the same perceptual pattern. However, if the prevailing lighting conditions differ markedly from those normally experienced, the viewed shapes can quite differ from one another. As we shall try and show, there are indeed instances, where that happens.

## 3. RELATION BETWEEN DEPTH AND ANGLE OF SIGHT

Objects are commonly perceived as shapes that span an inner volume. However, the perceived shape of tiny things changes when they are observed through a lens of large magnifying power, or a microscope. In facts, magnification allows to notice a greater number of details, widens the visual angles, and alters lighting. Opaque surfaces, despite enlargement, reveal no structure other than the surface itself, and perceived depths vary mainly because of angular widening. A smaller shape distortion of the same kind ensues if, instead, we come closer to the thing with our naked eyes. For surfaces that look gauzy when enlarged, the perceived depths vary also because of the refraction index w.r.t. the air. This holds true even for invisible rays going trough regions concealed behind surfaces that are opaque under sunlight. This time, however, the topographic interpretation of signals detected after transmission trough the surface, must be redone from scratch. For X-rays, either the restored pictures are taken to conform to known anatomical sections, as in medicine, or the structure models have to rely on signal interpretation, as in X-ray crystallography. In medicine, radiographs are obtained by casting a *shadow* of a body on a flat screen. The developed silhouette shows regions of different darkness, delineating the contour of structures whose topological relationships are known. However, as we are unaware of materials endowed with a refraction index for X-rays bigger than 1, with which to forge magnifying lenses, radiographs don't resemble photographs. That is to say, enlarged structures become more recognizable without angular magnification. Yet, projection reconstruction algorithms, which collect several perpendicularly projected shadows from a body in angular steps, do provide a means to reconstruct images, as they do increase the angular views under which the details appear [2]. Therefore, the number of details shown on CT radiographic images might be increased, even if they fail to reproduce true localizations owing to both, the "unintuitive" refraction index of materials with respect to the air for X radiation, and the new depths.

## 4. ON THE X-RAY CRYSTAL STRUCTURE DETERMINATION

By tradition, the investigations on the crystals' structure have never been tied to angular enlargements. Firstly, the Wigner-Seitz cell texture has been attributed to the optically homogeneous regions in the crystal volume. Secondly, the scattering of X-rays might not be called a passive one, as the impairment in the quality of many irradiated materials seems to point to their involvement in some resonance reactions. In past times, when crystals worth their name used to belong to one of 14

Bravais' geometric symmetry classes, cleavage breaks along specific planes were thought to express their structures. Hence, in the 19th century, to determine the Miller indices, the researchers looked after some clearly noticeable crystal facet, to which to attach the crystallographic axes. Later on, Sohncke showed that the crystals' directional properties could comply with 3-D point-group symmetries. Owing to the smallness of the supposed atomic constituents, whose dimensions amount to about $10^{-8}$ m, i.e., well below the magnifying possibilities of an optical microscope, no image in the usual meaning can be obtained. Thence, Von Laue suggested to test the discreteness of the internal structure using X-rays. According to physical optics, diffractograms lend themselves to determine an atomic space-lattice if the wavelength of the impinging radiation has the same order of magnitude as the grating pitch(s). Especially for X-rays, as $\lambda \to 0$, the Fresnel's approximation for propagation brings about only a small correction to geometric optics. Therefore, according to the energetic theory of Helmholtz-Kirchhoff, the X wave-fronts propagating between the secondary source-points and the image-points join them one to one. Classically the determination of the crystal structure by X-rays is handled as an inverse scattering problem, and is solved in the *reciprocal space*[1]. Nowadays the task of leaning on macroscopic surface traits is avoided. As the crystal shapes are supposed to be extrinsic to their microscopic structures, the latter are solved by analyzing ab initio data pertaining to very many diffraction patterns of crystalline powders. In recent years even the structure of *non periodic* macromolecules has successfully been tackled with powerful computers. In telecommunications, the closely related problem of reproducing 3-D (optical) images encoded in holographic gratings has been solved by resorting to Fourier transforms. Owing to historical grounds, the phase encoded variables are again defined in a Fourier domain, that is different from the "true space", where the image is assumed to form. Keeping in mind that, unlike holograms, the phase of X-diffractograms cannot be fixed, we will try and show that, with a narrow passband, as many images interlaced with diffractograms as desired can be obtained from a grating. However, the commonly experienced image-to-space relationships are missing.

## 5. SPATIAL EXTENSION OF IMAGES OBTAINED WITH COLLIMATED LIGHTING

Consider a collimated light pencil aligned to the optical axis of a system, and falling onto a perpendicularly placed screen. If a narrow-mesh grating is placed in front of the screen, the "geometric" shadow cast on it shows slight fringes, and fades with increasing distance. As gratings are dispersive optical elements, to sharpen the fringes very narrow-banded beams are requested. According to diffraction theory, a Fraunhofer diffraction pattern of the grating forms without lenses, and it becomes large enough to be clearly distinguishable with the naked eyes when the screen is far apart from the grating. The pattern can be enlarged by putting the grating and a converging lens one right behind the other. In the latter case, a grating's virtual image forms against the lens, in the plane geometrically conjugate to the object plane, while the pattern migrates from a far apart distance to the lens' back focal plane, superposing on the frequency response of the lens' brim. The focal plane is so called, because a far away source appears in-focus on it. If the lens' brim is circular, its frequency response is called an Airy disk, and is constituted of the slightly modulated source image. Again, Talbot [3] has found that, if the grating is *periodic*, no lens is needed to obtain many sharp images of it. Even if those images of both the source and the grating form at the finite, they are *delocalized*. To explain this concept better, let's suppose that a passive, perfectly flat grating has an exactly prescribed pitch and, "by way of the uncertainty relation", also an indefinite extension. Its images form inasmuch as the beams, that belong to different diffraction orders of the far apart distant pattern, come to a focus one after another along the optical axis. As this feature is common to multifocal lenses, for each focus there has to arise an image slice. In the assumed ideal case, each image bears the same features of the original periodic grating. Hence, the whole of the frequency spectrum, i.e., the ordered disposition of the source's Airy disks, forms already on each focal plane. That means that a faded shadow projected by a periodic grating under natural lighting, turns into an infinity of packed slices under monochromatic lighting. As images are on a

---

[1] In a few words, every point object in real space $\mathbb{R}^3$ is supposed to scatter the light impinging upon it as a spherical wave front. The waves scattered from the lattice planes superpose, interfering with one another according to the experimental Bragg's law. Bragg's law also entails the conservation of the impulse $\Delta \mathbf{k} = \mathbf{G}$, where $\Delta \mathbf{k}$ is the variation of the wave vector $\mathbf{k}$ upon scattering into the $\mathbf{k}'$ direction. $\mathbf{G}$ is the linear momentum exchanged with the lattice by way of conservation. $\mathbf{G}$ is defined in the reciprocal space $(\mathbb{R}^3)^{-1}$ and to its unit cell, called first Brillouin zone, is associated a 3-bein. Thanks to quantum mechanics, this picture was accepted as dual of Heisenberg's $\gamma$-rays microscope thought experiment. Geometrically the Wigner-Seitz cell is obtained by the Ewald construction. In the telecommunications' praxis the H-K equation is solved in the Fourier space and then transformed back to the geometric space. If there is no need of transforming from momentum to proper space, elliptical functions allow describing doubly periodic images.

par with diffractograms, in sheer intensity patterns they can be accidentally blended together. In practice, as neither the beams are infinitely narrow, nor the gratings are indefinitely extended, the piled up images progressively fade.

## 6. THE SPACE VIEWED TROUGH A BEE'S EYES

In the previous section we have explained that a narrow gaussian beam gives rise to a lot of echoes of the illuminated objects, especially if they are symmetric. If those echoes are not properly filtered, the images can greatly differ from those that the same objects form in the sunlight. Images can be filtered much like transmitted signals [4, 5]. In particular, if the phase shifts from the carrier can be tracked, the parallax can be phase encoded. A typical method for visible light parallax encoding consists in registering an interferential pattern on a flat film. The developed film results in a non periodic grating, called hologram, characterized by spectral parameters: frequency, amplitude, and phase shift. If the hologram is illuminated again by the same carrier to which it was originally exposed, its first order *diffraction pattern* can be made to render 3-D images, either virtual or real pseudoscopic ones. In Fourier optics, 3-D images and non-periodic patterns are the dual of one another.

For photographs editing purposes, the *spatial frequency concept* introduced for encoded narrow-band signals is extended to sunlight by analogy. The Fourier transform of a flat picture is assumed to represent its frequencies, the highest of which are usually taken towards the edges. Spatial frequency filtering has been exploited to modify contrast, but 3-D rendering as in holograms doesn't work. One problem of encoding depth by defining suitable frequencies arises because in sunlight depth is perceived at most *once*. Pinhole-cameras never capture it; they project sharp and dull pictures of the whole scene on *every* flat screen by letting through only paraxial light. Mammals' eyes, that depend upon refraction for forming images, perceive depth in a way that also involves chromatic dispersion [6]. For example, nearby objects exhibit more intense red hues and their brightness is more contrasted than the background. Apparently, the tints that contribute to aerial perspectives of a scene arise from progressive collimation of the light received, that increases with depth, as well as from the visual angle subtended by the passively diffusing things, that decreases with depth. As colors are associated with wavelengths, it makes sense to wonder whether a dispersion relation holds for sunlight. However, human perception encodes as colors different stimuli, besides distance. Whether depth encoding is the only means for perceiving it depends on whether a single healthy eye projects images onto the surface of the retina even if they are out of focus, like the field lens in a modern objective lens does: If it does not, then the whole of a scene gets transformed into a spatial image extended in the vitreous humour, and the transformed depth could be read; otherwise, a flat image gets projected on the surface of the retina and encoding remains the only means to perceive depth. Be that as it may, the dioptric visual organs usually do not deploy any duality between aperiodic stigmatic images and spatial frequency patterns for seeing. Therefore, especially for the purpose of encoding depth, we propose a concept alternative to spatial frequency, which we describe as follows. Unlike mammals, the insects which see their surrounding illuminated in the same way as we do, and apparently use the light alike to orient themselves in space, do not focus. Their composed eyes presumably sense the angle spreads and the directions of the scattered light directly. Nevertheless, their ommatidia produce very many telescopic images of the whole scene, as viewed from different directions from two hemispherical convex surfaces, and use the same multiplicative properties, witch telecommunications attribute to the narrow-band spatial frequency spectrum [7]. Since the discovery of random dot stereograms, it is known that by looking at flat quasi-periodic tessellations even our concave retinas are apt to sense depth, the foreground being encoded with shorter repetition rates than the background. Hence, there is a way of encoding in a picture format how the angular light spreads about various directions, that apparently works even for focalizing systems. As we have to accommodate for far distance to view depth in this case[2], we call "sunlight diffraction pattern" the scene image as formed by bees' eyes. The use of such quasi-periodic patterns might lead to methods of decoding depth in "white" light that are simpler than simulation of vergence and accommodation mechanisms.

## 7. CONCLUSION

The perception of space extension is compelled from the whole of human experience, and deploys complex neurological processes, which differ from bare signal reception. Nevertheless, if all other

---

[2]In random dot stereograms the represented *non-periodic* subject is concealed as such in the plane of the quasi-periodic pattern.

accompanying sensations are lacking, the eyes are able on their own to decode depth from daylight scenes as well as from amplitude, frequency, and phase encoded signals. However, the sensed depth relies on the lighting conditions. We have discussed steady illumination conditions in the two extreme cases of a narrow-banded source and the sun. We conclude that, in the absence of any auxiliary clue, it is generally neither allowed to locate perceived objects in customary space, nor to represent the received signals by having recourse to the usual wave characteristics. In our opinion, though, a sort of spatial frequencies can be attributed even to solar diffused lighting, so as to allow electromagnetism to be extended to comply with the images received.

## ACKNOWLEDGMENT

## REFERENCES

1. Remondino, F. and S. El-Hakim, "Image-based 3D modelling: A review," *Photogrammetric Record*, Vol. 21, No. 115, 269–91, 2006.
2. Glover, P. and P. Mansfield, "Limits to magnetic resonance microscopy," *Rep. Prog. Phys.*, Vol. 65, 1489–1511, 2002.
3. Maripov, A. and Y. Ismanov, "The Talbot effect (a self-imaging phenomenon) in holography," *J. Optics (Paris)*, Vol. 25, No. 1, 3–8, 1994.
4. Ives, H. E., "Parallax panoramagrams made with a large diameter lens," *J.O.S.A.*, Vol. 20, No. 6, 332–342, 1930.
5. Leith, E. N. and J. Upatnieks, "Reconstructed wavefronts and communication Theory," *J.O.S.A.*, Vol. 52, No. 10, 1123–1130, 1961.
6. Wald, G. and D. R. Griffin, "The change in refractive power of the human eye in dim and bright light," *J.O.S.A.*, Vol. 37, No. 5, 321–336, 1947.
7. Lippmann, G., "Épreuves réversibles donnant la sensation du relief," *J. de Phys., 4e série*, Vol. 7, 821–825, 1908.

# Analysis of Coupled Nonuniform Transmission Lines as an Initial Value Problem

**Mohammad Khalaj-Amirhosseini**

College of Electrical Engineering, Iran University of Science and Technology, Tehran, Iran

**Abstract**— Coupled Nonuniform Transmission Lines (CNTLs) are widely used in RF and microwave circuits. The analysis of CNTLs is a Boundary Value Problem (BVP) naturally, which need an optimization process in some methods. To overcome needing optimization process, we propose an approach to analyze CNTLs as several Initial Value Problems (IVPs), in this paper. First, the necessary IVPs are defined. Then the solution of the main BVP is obtained as the linear summation of the solutions obtained from IVPs. Finally, the validity of the introduced approach is studied using an example.

## 1. INTRODUCTION

Coupled Nonuniform Transmission Lines (CNTLs) are widely used in RF and microwave circuits [1, 2]. The differential equations describing CNTLs have non-constant matrices, so except for a few special cases no analytical solution exists for them. Some methods such as decoupling [3], cascading many short sections [4, 5], finite difference [6], Taylor's series expansion [7], Fourier series expansion [8], the equivalent sources method [9] and the method of moments [10] have been introduced to analyze CNTLs. In some of these methods such as finite difference and Taylor's series expansion, it is necessary to use an optimization process to satisfy terminal conditions. This is due to the nature of terminal conditions in CNTLs, which are two-point type. In the other word, the analysis of CNTLs is a Boundary Value Problem (BVP) naturally. To overcome needing optimization process, we propose an approach to analyze CNTLs as several Initial Value Problems (IVPs), in this paper. First, the necessary IVPs are defined. Then the solution of the main BVP is obtained as the linear summation of the solutions obtained from IVPs. Finally, the validity of the introduced approach is studied using an example.

## 2. CNTLS AS BVP

In this section, analysis of CNTLs are presented as a boundary value problem (BVP). Figure 1 shows a typical CNTL consisting of $N$ lines with length $d$ and with arbitrary terminal loads of $Z_{S,n}(\omega)$ and $Z_{L,n}(\omega)$, in which $n = 1, 2, \ldots, N$.

The differential equations describing CNTLs in the frequency domain are given by

$$\frac{d\mathbf{V}(z)}{dz} = -\mathbf{Z}(z)\mathbf{I}(z) \tag{1}$$

$$\frac{d\mathbf{I}(z)}{dz} = -\mathbf{Y}(z)\mathbf{V}(z) \tag{2}$$

in which $\mathbf{V}$ and $\mathbf{I}$ are $N \times 1$ voltage and current vectors, respectively. Also we have

$$\mathbf{Z}(z) = \mathbf{R}(z) + j\omega\mathbf{L}(z) \tag{3}$$
$$\mathbf{Y}(z) = \mathbf{G}(z) + j\omega\mathbf{C}(z) \tag{4}$$

In (3), (4), $\mathbf{R}$, $\mathbf{L}$, $\mathbf{G}$ and $\mathbf{C}$ are the per-unit-length matrices of the CNTLs, whose dimension is $N \times N$. Furthermore, the terminal conditions for loaded CNTLs are as follows

$$\mathbf{V}(0) + \mathbf{Z}_S\mathbf{I}(0) = \mathbf{V}_S \tag{5}$$
$$\mathbf{V}(d) - \mathbf{Z}_L\mathbf{I}(d) = \mathbf{0} \tag{6}$$

where $\mathbf{Z}_S$ and $\mathbf{Z}_L$ are diagonal source and load matrices, respectively. One sees from (1)–(6) that the analysis of loaded CNTLs is a boundary value problem (BVP).
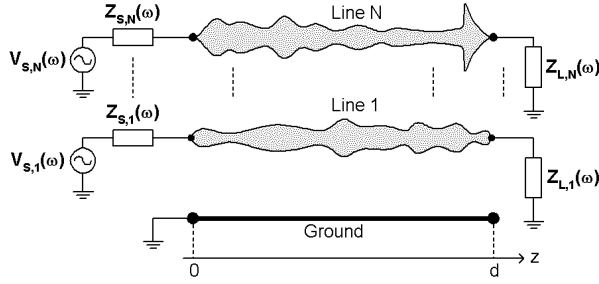
Figure 1: A typical coupled nonuniform transmission line.
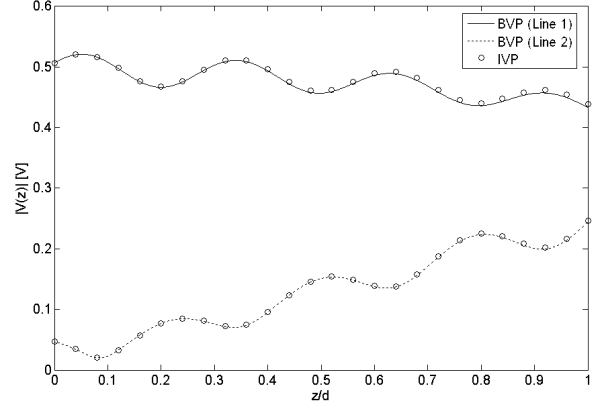


Figure 2: The amplitude of voltages of two lines for $k = 0$.

## 3. SOLVING CNTLS AS IVP

In this section, the CNTLs, which are BVP, are analyzed as an Initial Value Problem (IVP). For this purpose, we define the following $2N$ boundary conditions instead of (5), (6).

$$\begin{cases} \mathbf{I}(0) = 0 \\ \mathbf{V}(0) = [\ 0 \quad 0 \quad \cdots \quad V_n(0) = 1 \quad \cdots \quad 0\ ] \end{cases} \tag{7}$$

$$\begin{cases} \mathbf{V}(0) = 0 \\ \mathbf{I}(0) = [\ 0 \quad 0 \quad \cdots \quad I_n(0) = 1/Z_0 \quad \cdots \quad 0\ ] \end{cases} \tag{8}$$

where $n = 1, 2, \ldots, N$ and $Z_0$ is an arbitrary impedance value. The voltage and currents determined from the IVPs (7) and (8) are denoted by $\left\{ \mathbf{V}_V^{(n)}(z), \mathbf{I}_V^{(n)}(z) \right\}$ and $\left\{ \mathbf{V}_I^{(n)}(z), \mathbf{I}_I^{(n)}(z) \right\}$, respectively. Because of the linearity of differential Equations (1), (2), we can use the superposition principal to write the voltage and current of CNTLs as follows

$$\mathbf{V}(z) = \sum_{n=1}^{N} \alpha_V^{(n)} \mathbf{V}_V^{(n)}(z) + \sum_{n=1}^{N} \alpha_I^{(n)} \mathbf{V}_I^{(n)}(z) \tag{9}$$

$$\mathbf{I}(z) = \sum_{n=1}^{N} \alpha_V^{(n)} \mathbf{I}_V^{(n)}(z) + \sum_{n=1}^{N} \alpha_I^{(n)} \mathbf{I}_I^{(n)}(z) \tag{10}$$

The relations (9), (10) can be write in a matrix form as follows

$$\begin{bmatrix} \mathbf{V}(z) \\ \mathbf{I}(z) \end{bmatrix} = \begin{bmatrix} \mathbf{T}_{VV}(z) & \mathbf{T}_{VI}(z) \\ \mathbf{T}_{IV}(z) & \mathbf{T}_{II}(z) \end{bmatrix} \begin{bmatrix} \alpha_V \\ \alpha_I \end{bmatrix} \tag{11}$$

where $\alpha_V = [\ \alpha_V^{(1)} \quad \cdots \quad \alpha_V^{(N)}\ ]^T$ and $\alpha_I = [\ \alpha_I^{(1)} \quad \cdots \quad \alpha_I^{(N)}\ ]^T$ are the vectors of coefficients and the dimension of four submatrices is $N \times N$. The vectors of coefficients can be obtained using (11) in the boundary conditions (5), (6) as follows

$$\begin{bmatrix} \mathbf{T}_{VV}(0) + \mathbf{Z}_S \mathbf{T}_{IV}(0) & \mathbf{T}_{VI}(0) + \mathbf{Z}_S \mathbf{T}_{II}(0) \\ \mathbf{T}_{VV}(d) - \mathbf{Z}_L \mathbf{T}_{IV}(d) & \mathbf{T}_{VI}(d) - \mathbf{Z}_L \mathbf{T}_{II}(d) \end{bmatrix} \begin{bmatrix} \alpha_V \\ \alpha_I \end{bmatrix} = \begin{bmatrix} \mathbf{V}_S \\ \mathbf{0} \end{bmatrix} \tag{12}$$

Also, the $ABCD$ matrix that relates the voltage and current vectors at $z = 0$ to those at $z = d$, can be obtained as follows

$$\begin{bmatrix} \mathbf{A} & \mathbf{B} \\ \mathbf{C} & \mathbf{D} \end{bmatrix} = \begin{bmatrix} \mathbf{T}_{VV}(0) & \mathbf{T}_{VI}(0) \\ \mathbf{T}_{IV}(0) & \mathbf{T}_{II}(0) \end{bmatrix} \begin{bmatrix} \mathbf{T}_{VV}(d) & \mathbf{T}_{VI}(d) \\ \mathbf{T}_{IV}(d) & \mathbf{T}_{II}(d) \end{bmatrix}^{-1} \tag{13}$$

## 4. EXAMPLE AND RESULTS

In this section, an example is presented to study the validity of the introduced approach. Consider a lossless microstrip CNTL with $N = 2$ strips. The substrate permittivity is $\varepsilon_r = 10$, the width of strips as well as the gap between them are equal to the thickness of the substrate. This inhomogeneous structure has the following the per-unit-length matrices.

$$\mathbf{L}(z) = \mathbf{L}_0 \exp(kz/d) \tag{14}$$

$$\mathbf{C}(z) = \mathbf{C}_0 \exp(-kz/d) \tag{15}$$

$$\mathbf{R}(z) = \mathbf{G}(z) = 0 \tag{16}$$

where

$$\mathbf{L}_0 = \begin{bmatrix} 425.6 & 74.83 \\ 74.83 & 425.6 \end{bmatrix} \text{nH/m} \tag{17}$$

$$\mathbf{C}_0 = \begin{bmatrix} 174.9 & -14.25 \\ -14.25 & 174.9 \end{bmatrix} \text{pF/m} \tag{18}$$

Assume that $d = 20\,\text{cm}$, $f = 1.0\,\text{GHz}$, $Z_{S,1} = Z_{S,2} = 50\,\Omega$, $Z_{L,1} = Z_{L,2} = 50\,\Omega$, $V_{S,1} = 1\,\text{V}$ and $V_{S,2} = 0$. Figures 2–5, compare the amplitude and the phase of voltages and currents of two lines, obtained from the cascading $N = 5000$ uniform transmission lines (BVP) and from the proposed method (IVP) considering $N = 5000$ finite difference steps for $k = 0$. One sees an excellent agreement between the results of two approaches. Figures 6–8, depict the element functions of the matrices defined in (11) for $k = 0$ and $k = 0.5$. It is seen that $\mathbf{T}_{vv}(z) = \mathbf{T}_{ii}(z)$ are real functions and $\mathbf{T}_{vi}(z)$ and $\mathbf{T}_{iv}(z)$ are imaginary functions. Also, as the variation of the line parameters versus
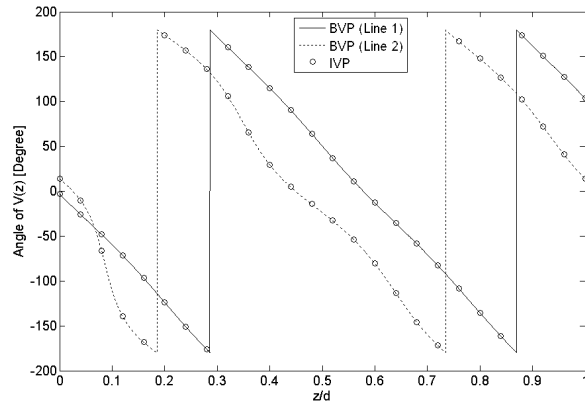


Figure 3: The phase of voltages of two lines for $k = 0$.
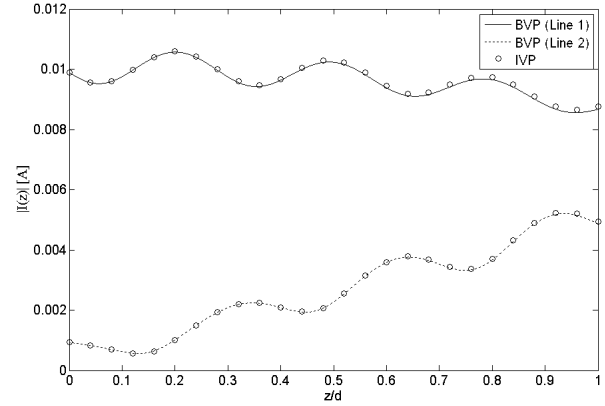


Figure 4: The amplitude of currents of two lines for $k = 0$.
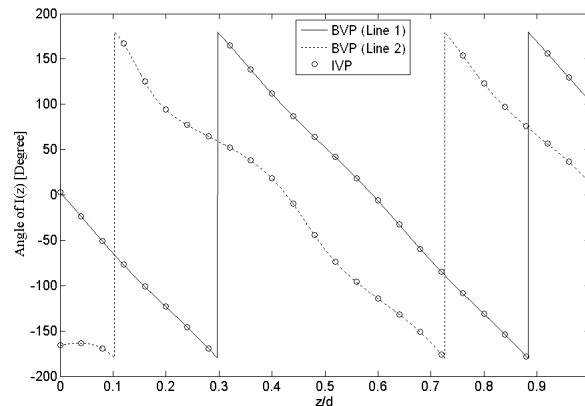


Figure 5: The phase of currents of two lines for $k = 0$.
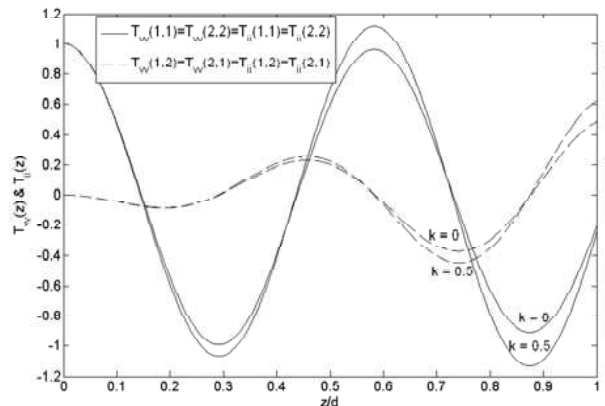


Figure 6: The element functions of the matrices $\mathbf{T}_{vv}(z)$ and $\mathbf{T}_{ii}(z)$.
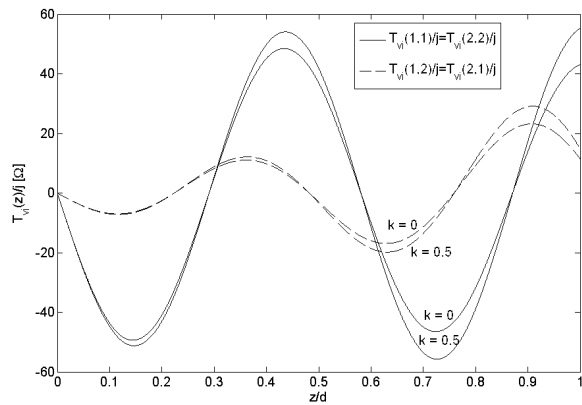
Figure 7: The element functions of the matrix $\mathbf{T}_{vi}(z)$.
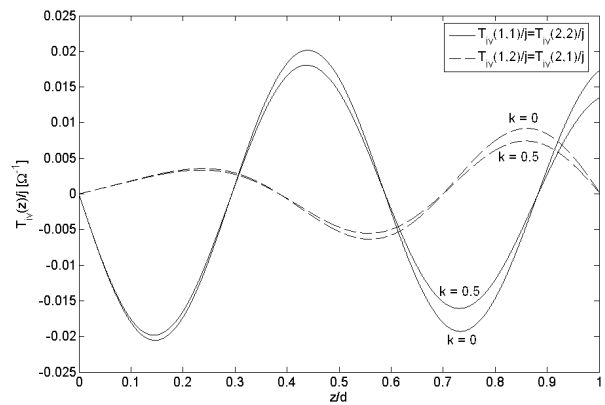
Figure 8: The element functions of the matrix $\mathbf{T}_{iv}(z)$.

$z$ ($k$ in this example) increases, the amplitude of alteration of $\mathbf{T}_{vv}(z)$, $\mathbf{T}_{ii}(z)$ and $\mathbf{T}_{vi}(z)$ increases and that of $\mathbf{T}_{iv}(z)$ decreases.

## 5. CONCLUSIONS

The analysis of CNTLs is a Boundary Value Problem (BVP) naturally, which need an optimization process in some methods. To overcome needing optimization process, an approach to analyze CNTLs as several Initial Value Problems (IVPs) was proposed. First, the necessary IVPs are defined. Then the solution of the main BVP is obtained as the linear summation of the solutions obtained from IVPs. Finally, the validity of the introduced approach is studied using an example. An excellent agreement between the results of two approaches was seen.

## REFERENCES

1. Hayden, L. A. and V. K. Tripathi, "Nonuniform coupled microstrip transversal filters for analog signal processing," *IEEE Trans. Microw. Theory and Tech.*, 47–53, Jan. 1991.
2. Dhaene, T., L. Martens, and D. D. Zutter, "Transient simulation of arbitrary nonuniform interconnection structures characterized by scattering parameters," *IEEE Trans. Circuits and Sys.-I*, 928–937, Nov. 1992.
3. Khalaj-Amirhosseini, M., "Analysis of coupled nonuniform transmission lines through analysis of uncoupled ones," *Int. Symp. On Antennas and Prop. (ISAP'06)*, Singapore, Nov. 1–4, 2006.
4. Paul, C. R., *Analysis of Multiconductor Transmission Lines*, John Wiley and Sons Inc., 1994.
5. Khalaj-Amirhosseini, M., "Using linear sections instead of uniform ones to analyze the coupled nonuniform transmission lines," *Int. J. RF and Microwave Computer-aided Eng.*, Vol. 19, No. 1, 75–79, Jan. 2009.
6. Khalaj-Amirhosseini, M., "Analysis of coupled or single nonuniform transmission lines using step-by-step numerical integration," *Progress In Electromagnetics Research*, PIER 58, 187–198, 2006.
7. Khalaj-Amirhosseini, M., "Analysis of coupled nonuniform transmission lines using Taylor's series expansion," *IEEE Trans. Electromagn. Compat.*, 594–600, Aug. 2006.
8. Khalaj-Amirhossein, M., "Analysis of periodic and aperiodic coupled nonuniform transmission lines using the Fourier series expansion," *Progress In Electromagnetics Research*, PIER 65, 15–26, 2006.
9. Khalaj-Amirhosseini, M., "Analysis of coupled or single nonuniform transmission lines using the equivalent sources method," *IEEE Symp. Microw. Ant. Prop. EMC (MAPE 2007)*, Hangzhou, China, Aug. 14–17, 2007.
10. Khalaj-Amirhosseini, M., "Analysis of coupled or single nonuniform transmission lines using the method of Moments," *Int. J. RF and Microwave Computer-aided Eng.*, Vol. 18, No. 4, 376–382, Jul. 2008.

# Synthesis about Analytical Approaches for Calculating the Magnetic Field Produced by Permanent Magnets of Various Topologies

**R. Ravaud and G. Lemarquand**

Laboratoire d'Acoustique de l'Universite du Maine, UMR CNRS 6613, Le Mans, France

**Abstract**— This paper discusses the way of choosing an analytical model for calculating the magnetic field produced by permanent magnets of various topologies and magnetization directions. Many studies have led authors to calculate the magnetic field produced by permanent magnets by using 1D, 2D or 3D analytical models by using the well known Maxwell's equations. In this paper, we discuss the interest of using such approaches for several topologies of permanent magnets. In particular, we study the case of parallelepipedic, ring and tile permanent magnets. It is emphasized that the main goal of such studies is to obtain a fully analytical expression of the three magnetic field components.

## 1. INTRODUCTION

Many authors are interested in calculating the magnetic field produced by permanent magnets or coils. Strictly speaking, authors generally use the coulombian model [1–3] for calculating the magnetic field produced by permanent magnets and the amperian current model [4] for calculating the magnetic field created by coils. On the other hand, some authors have used the Maxwell tensor [5] or elliptic formulations [6–8] and serial expressions [9, 10] for calculating the magnetic field produced by magnetic charge sources.

For parallelepipedic magnets with uniform polarizations, the magnetic field can be determined analytically by using the coulombian model, the amperian current model, the magnetic scalar and vector potentials. All these methods lead authors to determine the three magnetic field components in fully analytical forms. Indeed, the analytical expression of the magnetic field produced by parallelepipedic magnets does not require any special functions. For parallelepipedic coils, by using the analogy between the coulombian model and the amperian current model, the magnetic field can also be determined in a fully analytical form. However, the loops are replaced by fictitious current density layers.

For ring permanent magnets, the choice of the model used depends on the magnetisation direction. Indeed, for radially magnetized ring permanent magnets, the amperian current model is more suitable than the coulombian mode as the last one requires 3 integrals though the amperian current model requires only two integrals for calculating the three magnetic field components.

For arc-shaped permanent magnets, it is more difficult to guess what model to use for calculating the three magnetic field components. For example, the amperian current model of a magnet is more suitable than the coulombian model for calculating the magnetic field created by radially magnetized arc-shaped permanent magnets. Conversely, the coulombian model is more suitable than the amperian current model for calculating the magnetic field produced by arc-shaped permanent magnets with orthoradial polarizations. The radial currents flowing in massive disks generate a magnetic field that is often modeled with the Biot-Savart Law. Such an approach allows us to use both elliptic integrals and a numerical term for calculating the three magnetic field components. However, by using the analogy between the Maxwell 's equations, it can be more interesting to use the coulombian model in specific configurations.

In short, all these studies lead us to conclude that some simple rules allow us to guess what model is the most appropriate for calculating the magnetic field produced either by permanent magnets or by currents. This paper makes a review of the main configurations of permanent magnets studied in the literature and gives indications about how to use an analytical model for calculating the magnetic field created by charge or current distributions.

## 2. MAGNETIC FIELD PRODUCED BY PARALLELEPIPEDIC MAGNETS OF VARIOUS MAGNETIZATION DIRECTIONS

The uniformly magnetized parallelepiped magnets seem to be the only topology that can be studied by using either the coulombian model or the amperian current model. Indeed, the modeling of such topologies requires analytical expressions that do not need any special functions. As a consequence, by using the coulombian model of a magnet, each face can be replaced by a uniform
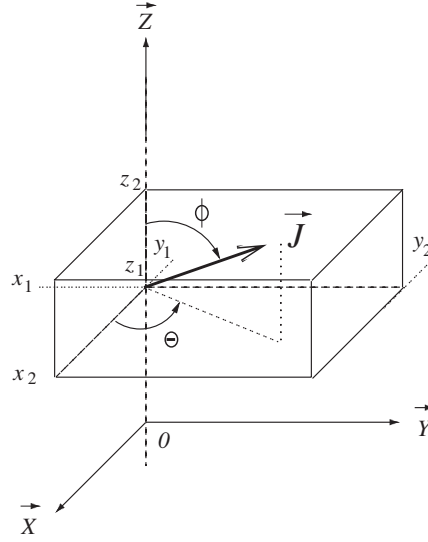
Figure 1: Representation of a parallelepipedic magnet of various polarization direction.

charge distribution. Let us consider the Figure 1 in which we have represented a parallelepipedic magnet of various and uniform direction, denoted $\vec{J}$.

The magnetic polarization is expressed as follows:

$$\vec{J} = J\cos(\theta)\sin(\phi)\vec{u}_x + J\sin(\theta)\sin(\phi)\vec{u}_y + J\cos(\phi)\vec{u}_z \tag{1}$$

By using the coulombian model of a magnet [11], the magnetic field $\vec{H}(x,y,z)$ created by this parallelepipedic magnet can be expresed as follows:

$$\vec{H}(x,y,z) = H_x(x,y,z)\vec{u}_x + H_y(x,y,z)\vec{u}_y + H_z(x,y,z)\vec{u}_z \tag{2}$$

with

$$
\begin{aligned}
H_x(x,y,z) =& \frac{J\sin(\phi)\cos(\theta)}{4\pi\mu_0}\vartheta^{(ijk)}\left\{\arctan\left[\frac{(y-y_j)(z-z_k)}{(x-x_i)\xi_{ijk}}\right]\right\} + \frac{J\sin(\phi)\sin(\theta)}{4\pi\mu_0}\vartheta^{(ijk)} \\
& \left\{-\log\left[z-z_k+\xi_{ijk}\right]\right\} + \frac{J\cos(\phi)}{4\pi\mu_0}\vartheta^{(ijk)}\left\{-\log\left[y-y_j+\xi_{ijk}\right]\right\} \\
H_y(x,y,z) =& \frac{J\sin(\phi)\cos(\theta)}{4\pi\mu_0}\vartheta^{(ijk)}\left\{-\log\left[z-z_k+\xi_{ijk}\right]\right\} + \frac{J\sin(\phi)\sin(\theta)}{4\pi\mu_0}\vartheta^{(ijk)} \\
& \left\{\arctan\left[\frac{(x-x_i)(z-z_k)}{(y-y_j)\xi_{ijk}}\right]\right\} + \frac{J\cos(\phi)}{4\pi\mu_0}\vartheta^{(ijk)}\left\{-\log\left[x-x_i+\xi_{ijk}\right]\right\} \\
H_z(x,y,z) =& \frac{J\sin(\phi)\cos(\theta)}{4\pi\mu_0}\vartheta^{(ijk)}\left\{-\log\left[y-y_j+\xi_{ijk}\right]\right\} + \frac{J\sin(\phi)\sin(\theta)}{4\pi\mu_0}\vartheta^{(ijk)} \\
& \left\{-\log\left[x-x_i+\xi_{ijk}\right]\right\} + \frac{J\cos(\phi)}{4\pi\mu_0}\vartheta^{(ijk)}\left\{\arctan\left[\frac{(x-x_i)(y-y_j)}{(z-z_k)\xi_{ijk}}\right]\right\}
\end{aligned} \tag{3}
$$

$$\vartheta^{(ijk)}\{\bullet\} = \sum_{i=1}^{2}\sum_{j=1}^{2}\sum_{k=1}^{2}(-1)^{i+j+k}(\bullet)$$

$$\xi_{ijk} = \sqrt{(x-x_i)^2+(y-y_j)^2+(z-z_k)^2}$$

The previous relations can be illustrated in Figure 2 in which we have represented the magnetic field iso-lines in the three observation planes ($xy$, $xy$, $yz$).
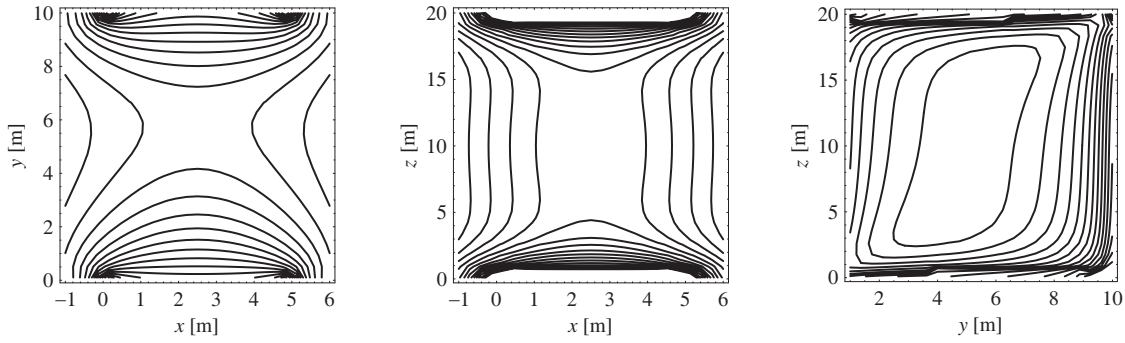
Figure 2: 2D representation of the magnetic field iso-lines created by a parallelepipedic magnet whose polarization is $\vec{J} = \frac{J}{\sqrt{2}}\vec{u}_y + \frac{J}{\sqrt{2}}\vec{u}_z$; $(x\text{-}y)$-plane: $z = 19.9\,\text{mm}$, $(x\text{-}z)$-plane: $y = 5\,\text{mm}$, $(y\text{-}z)$-plane: $x = 4.5\,\text{mm}$.
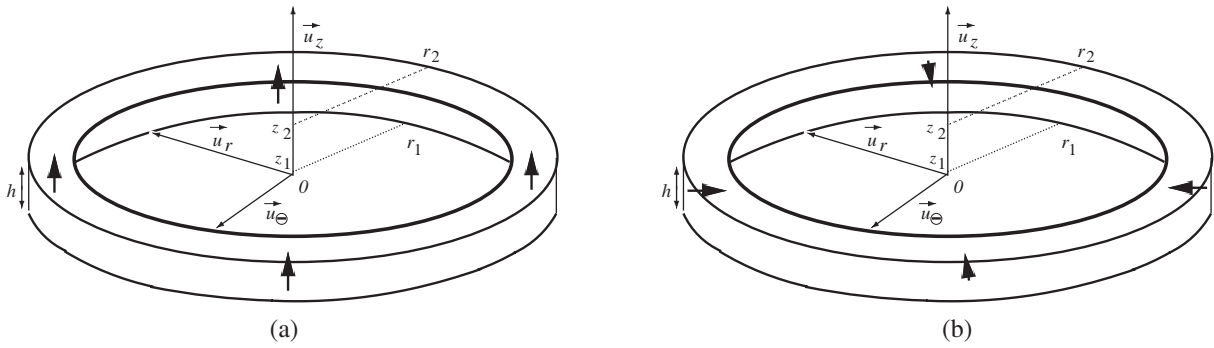


Figure 3: (a) Ring permanent magnet whose polarization is axial. (b) Ring permanent magnet whose polarization is radial.

## 3. MAGNETIC FIELD PRODUCED BY RING MAGNETS OF VARIOUS MAGNETIZATION DIRECTIONS

Let us now consider the case of ring permanent magnets of radial and axial polarization directions, as shown in Figure 3. These two configurations have the same topology but not the same polarization direction. For the ring permanent magnet whose polarization is axial, the coulombian or the amperian current models lead to an analytical formulation of the two magnetic field components $H_r(r, z)$ and $H_z(r, z)$. These two approaches require the analytical calculation of two surface integrals leading to expressions based on elliptic functions.

For the ring permanent magnet whose polarization is radial, the amperian current model is more suitable than the coulombian model for calculating the magnetic field outside it [12]. Indeed, in the coulombian approach, the radial component of the magnetic field requires one numerical integration [13]. In the amperian current approach, the same component is based only on elliptic integrals whose calculations are directly performed in $Mathematica$. We can say that it is easier to use the amperian current model in such a configuration because it requires the calculation of two integrals though the coulombian model requires the calculation of three integrals. We illustrate it in the following expression of the radial component which is based only on elliptic integrals.

$$H_r(r, z) = \frac{J}{4\pi\mu_0} \sum_{i=1}^{2} \sum_{k=1}^{2} (-1)^{i+k} \left( g(i, k, 2\pi) - g(i, k, 0) \right) \tag{4}$$

with

$$g(i, k, \tilde{\theta}) = 2(z - z_k) f\left( r^2 + (z - z_k)^2,\ r^2 + r_i^2 + (z - z_k)^2,\ rr_i,\ -r^2 - 2(z - z_k)^2,\ \tilde{\theta} \right)$$

$$f\left( a, b, e, c, x, \tilde{\theta} \right) = \eta \left( 2\xi_1 \left( 2ce^2 + \xi_2 \right) \right) \mathbf{F}^* [\phi_2, \phi_3]$$

$$+ \eta \left( -e^2(c - x)(bx\sqrt{2} + 2\xi_1) \right) \mathbf{\Pi}^* \left[ \phi_1^+, \phi_2, \phi_3 \right]$$

$$+\eta \left(e^2(c-x)(bx\sqrt{2}-2\xi_1)\right)\mathbf{\Pi}^*\left[\phi_1^-,\phi_2,\phi_3\right]$$

$$-2\eta ax\left(xe^2-ce^2\sqrt{2}+b\xi_1\right)\mathbf{\Pi}^*\left[\phi_1^+,\phi_2,\phi_3\right]$$

$$-2\eta ax\left(-xe^2+ce^2\sqrt{2}+b\xi_1\right)\mathbf{\Pi}^*\left[\phi_1^-,\phi_2,\phi_3\right] \tag{5}$$

where $\mathbf{F}^*[\mathbf{x},\mathbf{y}]$ and $\mathbf{\Pi}^*[\mathbf{x},\mathbf{y},\mathbf{z}]$ are the elliptic integrals of the second and third kind and

$$\xi_1 = \sqrt{e^2 x(x-c)}$$
$$\xi_2 = x\left(b^2-2e^2\right)$$
$$\eta = \frac{i\sqrt{\dfrac{-e^2\sin\left(\tilde{\theta}\right)^2}{(b-2e)^2}}\csc\left(\tilde{\theta}\right)}{2\sqrt{\dfrac{-1}{b+2e}}x\xi_1\left(2ce^2+\xi_2\right)} \tag{6}$$

The reader can see the research paper [12] for more details about the definitions of the parameters used. It is emphasized here that it was the first time in the literature that the radial component expression of the magnetic field created by a ring permanent magnet whose polarization is radial is obtained with only elliptic integrals. Such a magnetic field component is an important element of information for the design of loudspeakers or electric machines in which the radial field allows the movement of translating or rotating parts.

## 4. MAGNETIC FIELD PRODUCED BY TILE MAGNETS OF VARIOUSMAGNETIZATION DIRECTIONS

Tile permanent magnets of various magnetization directions can also be modeled by using the coulombian model or the amperian current model. However, the magnetization direction has an influence on the choice of model used. We have represented in Figure 4 a tile permanent magnet whose polarization is radial and a tile permanent magnet whose polarization is axial. As explained in [12], a tile permanent magnet whose polarization is radial should be modeled by using the amperian current model. Indeed, this last approach allows us to obtain analytical expressions of the magnetic field radial component and a simple semi-analytical expression of the axial component. In the coulombian approach, the radial and axial field components are expressed in relatively tedious semi-analytical expressions based on one numerical integration. Consequently, for this topology and this magnetization direction, it is more interesting to use the amperian current model rather than the coulombian approach.



(a)                                                     (b)
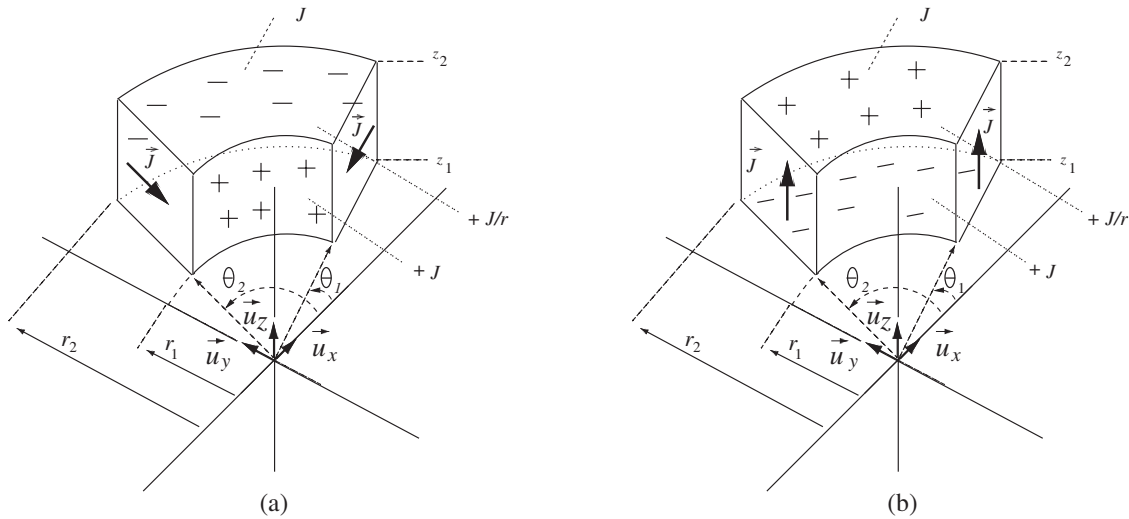
Figure 4: (a) Tile permanent magnet whose polarization is axial. (b) Tile permanent magnet whose polarization is radial.

For tile permanent magnets axially magnetized, the coulombian approach requires the calculation of two surface integrals. Such a way of modeling this problem leads to analytical expressions for three magnetic field components. The amperian current model leads also to analytical expressions for the three magnetic field components. However, the amperian current model requires four times two surface integrals, which is more complicated that only two times two surface integrals. Consequently, it is more interesting to use the coulombian model rather than the amperian current model for calculating the magnetic field produced by a tile permanent magnet whose polarization is axial.

## 5. CONCLUSION

This paper has presented a synthesis about the analytical models used for calculating the magnetic field created by permanent magnets of various topologies and magnetization directions. The parallelepipedic magnets can be modeled with the coulombian and amperian current models as these two approaches lead to a fully analytical formulation. The ring and tile permanent magnets require more care. The radially magnetized arc-shaped permanent magnets should be studied with the amperian current model thouch axially magnetized arc-shaped permanent magnets should be modeled with the coulombian model. Such results are interesting for the study of complex structures made of arc-shaped permanent magnets of various magnetization directions.

**REFERENCES**

1. Ravaud, R., G. Lemarquand, V. Lemarquand, and C. Depollier, "Discussion about the analytical calculation of the magnetic field created by permanent magnets," *Progress In Electromagnetics Research B*, Vol. 11, 281–297, 2009.
2. Marble, A. E., "Strong, stray static magnetic fields," *IEEE Trans. Magn.*, Vol. 44, No. 5, 576–580, 2008.
3. Lemarquand, G. and V. Lemarquand, "Annular magnet position sensor," *IEEE. Trans. Magn.*, Vol. 26, No. 5, 2041–2043, 1990.
4. Akyel, C., S. I. Babic, and M. M. Mahmoudi, "Mutual inductance calculation for non-coaxial circular air coils with parallel axes," *Progress In Electromagnetics Research*, PIER 91, 287–301, 2009.
5. Varga, E. and A. Beyer, "Magnetic field of a uniformly magnetized hollow cylinder," *IEEE Trans. Magn.*, Vol. 34, No. 3, 613–618, 1998.
6. Azzerboni, B., E. Cardelli, M. Raugi, A. Tellini, and G. Tina, "Analytic expressions for magnetic field from finite curved conductors," *IEEE Trans. Magn.*, Vol. 27, No. 2, 750–757, 1991.
7. Babic, S. I. and C. Akyel, "Improvement in the analytical calculation of the magnetic field produced by permanent magnet rings," *Progress In Electromagnetics Research C*, Vol. 5, 71–82, 2008.
8. Ravaud, R., G. Lemarquand, and V. Lemarquand, "Magnetic field created by tile permanent magnets," *IEEE Trans. Magn.*, Vol. 45, No. 7, 2920–2926, 2009.
9. Selvaggi, J. P., S. Salon, O. M. Kwon, and M. V. K. Chari, "Computation of the three-dimensional magnetic field from solid permanent-magnet bipolar cylinders by employing toroidal harmonics," *IEEE Trans. Magn.*, Vol. 43, No. 10, 3833–3839, 2007.
10. Jian, L. and K. T. Chau, "Analytical calculation of magnetic field distribution in coaxial magnetic gears," *Progress In Electromagnetics Research*, PIER 92, 1–16, 2009.
11. Ravaud, R. and G. Lemarquand, "Magnetic field produced by a parallelepipedic magnet of various and uniform polarization," *Progress In Electromagnetics Research*, PIER 98, 207–219, 2009.
12. Ravaud, R. and G. Lemarquand, "Comparison of the coulombian and amperian current models for calculating the magnetic field produced by arc-shaped permanent magnets radially magnetized," *Progress In Electromagnetics Research*, PIER 95, 309–327, 2009.
13. Ravaud, R., G. Lemarquand, V. Lemarquand, and C. Depollier, "The three exact components of the magnetic field created by a radially magnetized tile permanent magnet.," *Progress In Electromagnetics Research*, PIER 88, 307–319, 2008.

# Film's Forming Materials for THz Spectral Range Purposes

**E. N. Kotlikov[1], V. A. Ivanov[2], and A. N. Tropin[2]**

[1]St. Petersburg's State University of Aerospace Instrumentation, Russia
[2]Scientific Research Institute "Giricond", St. Petersburg, Russia

**Abstract**— At the presented work, we report the results of research of optical properties PbTe, ZnSe, ZnS, $BaF_2$ and $PbF_2$ thin films in a wide infrared spectral range. These materials are used for manufacturing thin film multilayer interference systems working in the mid-infrared and probably be applied in far infrared to submillimeter. Optical properties in our understanding are spectral dependences of refractive index and extinction coefficient of layers. Films with thicknesses 3–7 microns were received by thermal vacuum deposition on single-crystal silicon substrates. Refractive index and extinction coefficient dispersion in 1.5–150 microns spectral range (2–200 THz) were determined by method based on analysis of the transmission and reflection interference spectra. Films of PbTe under consideration do not possess appreciable absorption bands in the investigated spectral range. While, other investigated films have intensive absorption bands in the 25–100 microns region. With using of the investigated materials the "solar blind" filter for 1.0–50 microns spectral range on the single-crystal silicon substrate was designed and made.

## 1. INTRODUCTION

Thin film optical coatings find application in various areas of a science and engineering. Now great efforts are being made in the far infrared and terahertz spectral ranges technology. THz spectral range development will allow improving a various control and diagnostics methods. Use of submillimeters radiation represents the great interest in such application as safety control, check of packing, semiconductor characterization, analysis of a chemical compound, biochemical researches, with promising output in spectroscopy and construction of the image in defensive systems [1]. It is obvious, that corresponding transformation of spectral and phase characteristics of optical elements working in appropriate spectral range is necessary. This transformation can be carried out with using of multilayer thin-film systems layered on refracting sides of optical elements.

The aim of this study was investigation of optical films of some materials applied in middle infrared and which can be used in far infrared. As a film's forming materials under investigation we considered PbTe, $BaF_2$, $PbF_2$, ZnSe and ZnS which are extensively used for producing multilayer coatings in 4–20 microns spectral range [2].

## 2. THE METHOD USED FOR DETERMINING THE OPTICAL PARAMETERS OF THE FILMS

Optical parameters of thin films we determined by spectrophotometric method [3]. This kind of procedure consists of the measurements of transmittance and reflectance spectra of absorbing film on low absorbing substrate with known optical properties.

As substrates we used single-crystal silicon wafers. For the determining of substrate optical constants the transmittance and reflectance of the clean silicon wafer were measured. The measured spectra include the effects associated with the multireflection in the wafer. The interference-free transmittance and reflectance of the clean silicon wafer with considering the back side effects are given by the well known equations:

$$T_S = \frac{(1 - R_f)^2 e^{-\gamma}}{1 - R_f^2 e^{-2\gamma}}, \quad R_S = R_f \frac{1 + (1 - 2R_f)e^{-2\gamma}}{1 - R_f^2 e^{-2\gamma}}, \tag{1}$$

where $R_f = \frac{(n_S-1)^2+k_S^2}{(n_S+1)^2+k_S^2}$ — Fresnel reflectance for the air — substrate interface, $n_S$ and $k_S$ — refractive index and extinction coefficient of the substrate, alternately, $\gamma = (4\pi/\lambda)k_S d_S$, where $d_S$ is substrate thickness.

The optical constants of a substrate were obtained by solving of the following system of equations for each wavelength:

$$\begin{cases} T_S - T_{\exp}^S = 0 \\ R_S - R_{\exp}^S = 0 \end{cases} \tag{2}$$

where $T_{\exp}^S$ and $R_{\exp}^S$ — measured values of transmittance and reflectance of the clean wafer.

In this study, correction for back surface reflection has been made by a method of intensity addition. In this case, the transmission $T$ and reflection $R$ of filmed substrate with considering the back side effects are given by the following equations:

$$T = \frac{T_0(1 - R_f)e^{-\gamma}}{1 - R_f R'e^{-2\gamma}}, \quad R = R_0 + R_f \frac{T_0^2 e^{-2\gamma}}{1 - R_f R'e^{-2\gamma}}, \tag{3}$$

where $T_0$ and $R_0$ — transmittance and reflectance of a film on semi-infinite substrate, alternately, $R'$ — reflectance of a system similar $R_0$, but at illumination from a substrate.

The optical constants of a film were defined by the solving of the following equations system:

$$\begin{cases} T - T_{\exp} = 0 \\ R - R_{\exp} = 0 \end{cases} \tag{4}$$

where $T_{\exp}$ and $R_{\exp}$ — measured values of transmittance and reflectance of the filmed wafer, $T$ and $R$ are received by the expression (3), at that $T_0$ and $R_0$ in (3) were calculated on corresponding expressions for a film on semi-infinite substrate [4]. The roots of the system (4) at every wavelength were calculated by Newton's iterative method.

The thicknesses of films were defined on extrema in transmission spectra in those spectral areas where absorption in the film is absent (or insignificant) and dispersion of a refractive index is small.

## 3. EXPERIMENTAL SETUP AND RESULTS

The films were deposited in the vacuum system VU-2M (USSR) by thermal evaporation. During the evaporation process the pressure in vacuum chamber was not worse than $3 \times 10^{-3}$ Pa. Initial substances were evaporated from molybdenum boat with direct heating. The temperature of the silicon substrate for all deposition was $100°$C with the temperature accuracy no worse than $\pm 2°$C.

During the deposition the film thickness was controlled by monitoring the changes in transmittance from the monitor piece at reference wavelength 2.5 mkm.

The optical measurements were done at room temperature with Fourier-transform infrared spectrometers. Reflectance and transmittance between near infrared and 20 microns were taken with FT-IR spectrometers FSM — 1201 (JSC Monitoring, Russia). Measurements from 20 to 150 microns were made with Bruker VERTEX 70 FT-IR Spectrometer.

The index of refraction and the extinction coefficient of the films were computed by the step-wise procedure previously described. Calculated dispersion characteristics of optical constants of investigated materials are shown in Figs. 1(a)–1(e). In Figs. 1(c)–1(e) dark circles correspond to the data received for BaF$_2$, ZnSe and ZnS bulk materials in the works [5–7], alternately.

In the region to 20 microns refractive indices of all investigated films have normal dispersion and decrease with increasing wavelength. Comparison with the results received for solid structures [5–7] shows that take place usual for films decrease in a refraction index and substantial growth of absorption losses. This is primary due to the fact that the optical properties of vacuum-deposited films can vary appreciable depending on the evaporation conditions during film preparation. Immediate cause of that is presence in films the impurity caused by interaction of evaporated substance with a material of the evaporator and residual gases in the chamber, a deviation from stoichiometry at deposition, and also film's porosity.

## 4. "SOLAR BLIND" FILTER

With using of the investigated materials the "solar blind" filter for 1.0–50 microns spectral range on the single-crystal silicon substrate was designed and made. According to requirements this filter blocks radiation in short wavelength up to 4.5 microns and has the maximum possible transmittance from 5 to 50 microns. The long pass coating was deposited on one side of a substrate. Another side of the substrate was coated by the diamond like carbon (DLC) film with thickness optimized for interval from 9 to 12 microns. The following Fig. 2 illustrates calculated and measured transmittance for the produced filter.

The presented characteristics are in close agreement. It means that optical parameters of films were defined truly and there were no serious errors at filter manufacturing process.
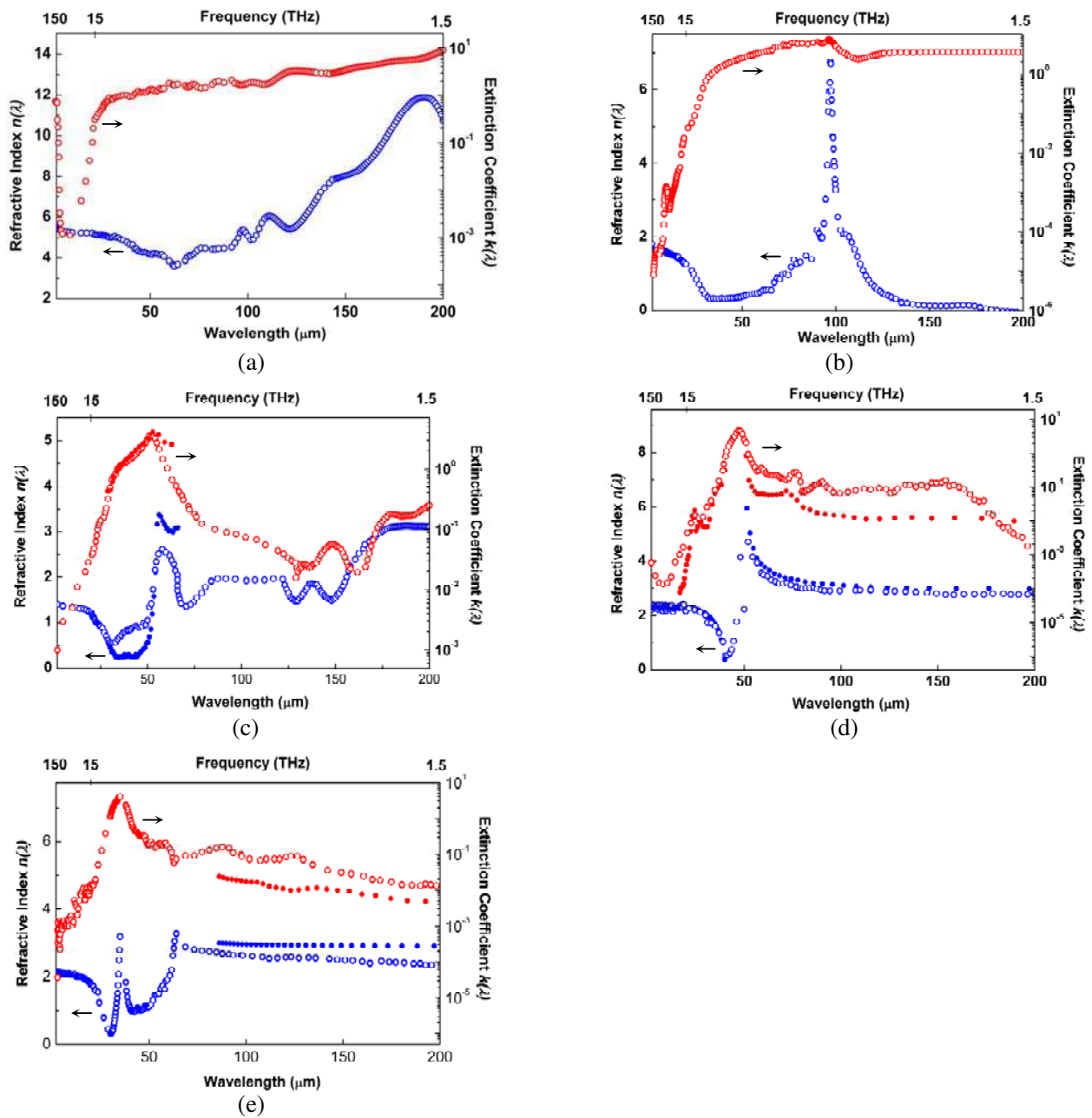
Figure 1: Calculated optical constants (open circles) of (a) PbTe, (b) PbF$_2$, (c) BaF$_2$, (d) ZnSe and (e) ZnS films. Dark circles in Fig. (c) are the data of Ref. 5; in Fig. (d) of Ref. 6; in Fig. (e) of Ref. 7.
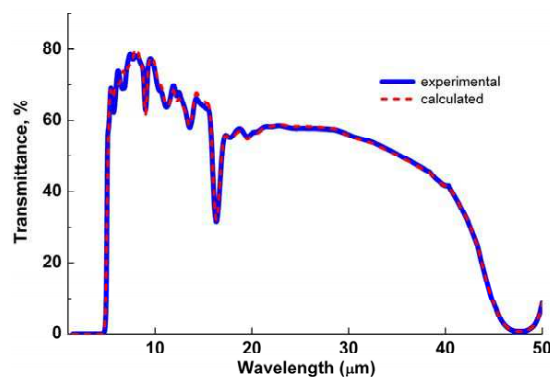


Figure 2: Spectral responses of "solar blind" filter.

## 5. CONCLUSIONS

On the basis of measured transmittance and reflectance of films on silicon substrates, we investigated optical properties of PbTe, ZnSe, ZnS, $BaF_2$ and $PbF_2$ thin films in a wide infrared spectral range. Layers of PbTe under consideration do not possess appreciable absorption bands in the investigated spectral range. Extinction coefficient of the lead telluride film in the region beyond 20 microns monotonously increases up to $k = 3$ at $150\,\mu m$ and caused by free carrier absorption. Other investigated materials have intensive absorption bands in infrared. $BaF_2$ film has the absorption band from 30 to $65\,\mu m$ with a maximum at 54 microns. ZnS and ZnSe films have strong absorption bands centering at $35\,\mu m$ and $47\,\mu m$,respectively, caused by lattice vibration. Lead fluoride film has strong absorption beyond 20 micron and cannot be used in this spectral region.

The experimental results indicate that films of PbTe and $PbF_2$ can be applied in near and mid-infrared. But films of ZnS, ZnSe and $BaF_2$ have small absorption in the region with wavelength more than 70-80 $\mu m$ and can be used for manufacturing of broadband antireflection, beam splitter and another kind of multilayer optical coatings for far infrared and THz range purposes.

## ACKNOWLEDGMENT

## REFERENCES

1. Ferguson, B. and X.-C. Zhang, "Materials for terahertz science and technology," *Nat. Mater.*, Vol. 1, Sept. 26–33, 2002.
2. Willey, R. R., *Practical Design and Production of Optical Thin Films*, CRC Press, New York, 2002.
3. Heavens, O. S., "Optical constants of thin films," *Physics of Thin Films*, Academic Press, New York, 1964.
4. Born, M. and E. Wolf, *Principles of Optics*, The MacMillan Company, New York, 1964.
5. Nakagava, I., "Far-infrared reflection spectra, optical and dielectric constants, and lattice vibration of some fluoride crystals," *Bulletin of the Chemical Society of Japan*, Vol. 44, 3014–3020, 1971.
6. Deneuville, A., D. Tanner, and P. H. Holloway, "Optical constants of ZnSe in the far infrared," *Rhys. Rev. B*, Vol. 43, No. 8, 6544–6550, 1991.
7. Thamizhmani, L., A. K. Azad, J. M. Dai, and W. Zhang, "Far infrared optical and dielectric response of ZnS measured by terahertz time-domain spectroscopy," *Appl. Phys. Lett.*, Vol. 86, 131111, 1–3, 2005.

# Wave Propagation in Corrugated Circular Grating

**F. Emami**

Optoelectronic Research Center
Electronic Department, Shiraz University of Technology, Shiraz, Iran

**Abstract**— Wave propagation in a hollow circular media is discussed, when the outer layer of the structure has a corrugated refractive index. Using the coupled mode theory for this periodic structure, we could find the field distribution through the different layers of this structure. The field coupling parameter was calculated. It is shown that there is a forward relation between the coupling and the gratings height such as in a slab corrugated waveguide. It is found that there is a small decrease in the amount of the coupling strength in the internal layer due to the external structure excitation. Such a structure can be used in distributed feedback semiconductor lasers.

## 1. INTRODUCTION

Corrugated structures have many applications in single mode lasers [1]. If we have a slab waveguide with periodic variations of the refractive indices at the interface of the active and the guide layers, a distributed feedback (DFB) laser is generated [1, 2]. There are two contacts at the top and the bottom of this slab and by using the carrier injection into the structure a laser output light is formed. Laser feedback mechanism is made by the energy or power exchange between two components of the optical fields, forward and backward waves, which is due to the grating structure [1]. Mathematically, there is a theory called coupled mode theory (CMT), or may be its revised form, which can be expressed this energy exchange between two components [1–3]. The amount of the energy transfer, which can be expressed by the coupling coefficient, is function of the structure properties [4]. There are lots of works on this coefficient in the literature for the slab waveguides [5, 6]. Here the CMT is applied for the structures with a circular cross section and the related results are derived.

## 2. DESCRIPTION OF THE COUPLING COEFFICIENT

Consider a hollow circular dielectric waveguide (HCDW) which can be used in DFB laser diode with a corrugated outer layer of the cladding as shown in Fig. 1. Outer contact is not shown in the figure.

The governing equation of the wave propagation in this structure is the Helmholtz equation. Define the refractive index of the HCDW structure as:

$$\varepsilon_r(r, \varphi, z) = \bar{\varepsilon}_r(r, \varphi) + \Delta\varepsilon_r(r, \varphi, z) \tag{1}$$
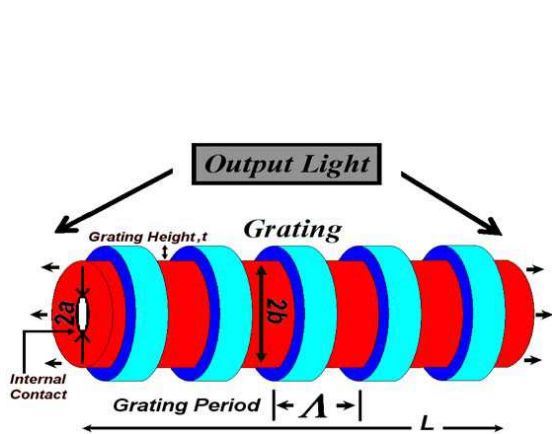


Figure 1: Schematic structure of a hollow circular dielectric waveguide.
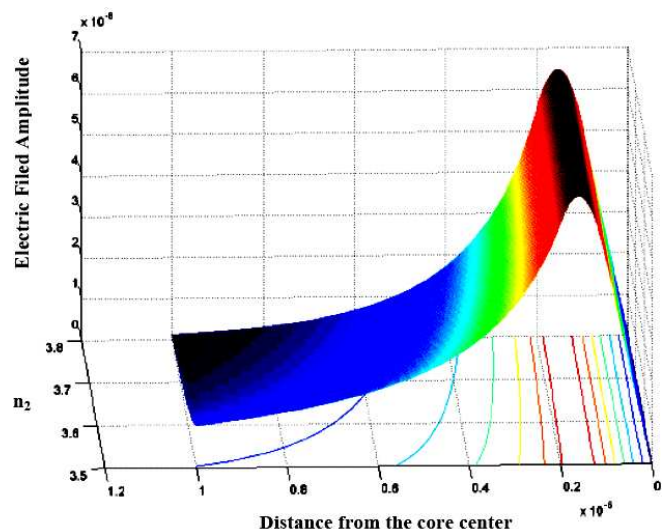


Figure 2: Electric field distribution in a hollow circular dielectric waveguide for variable core indices, $n_2$.

where $\bar{\varepsilon}_r(r, \varphi)$ is the average index and the perturbing term $\Delta\varepsilon_r(r, \varphi, z)$ is nonzero only in the corrugation region. In (1), there is a symmetric form for index and the $\varphi$ dependency can be ignored, so:

$$\varepsilon_r(r, \varphi, z) = \varepsilon_r(r, z) = n^2(r, z) = \sum_{-\infty}^{+\infty} \left[ A_m(r) e^{j\frac{2m\pi z}{\Lambda}} \right] \tag{2}$$

where $A_m(r)$ is the Fourier coefficient of the $m$-th term, $n$ is the refractive index and $\Lambda$ is shown in Fig. 1. The value of these Fourier coefficients are depends on the grating shape and layer indices. Usual structures of the corrugated layer are trapezoidal (containing the rectangular, triangular and saw tooth) and sinusoidal forms [1, 4, 6]. Consider the phase matching condition in the CMT [1] it is possible to define the coupling coefficient for this structure as:

$$\kappa = \frac{k_0^2}{2\beta} \frac{\int_0^\infty \Delta\varepsilon_r(r, z) \psi^2(r) \, dr}{\int_0^\infty \psi^2(r) \, dr} \tag{3}$$

where $\beta$ is the propagation constant, $k_0$ is the vacuum wave number and $\psi(r)$ is the $r$ variations of the optical field.

## 3. NUMERICAL RESULTS

Consider a practical HCDW with an active layer in the region $a < r < b$ as shown in Fig. 1. The field distribution through the core and cladding were calculated and plotted in Fig. 2 versus the core refractive index.

As shown, for a dense active layer the field power is more and there is a large field confinement factor and generally, outside the core the field amplitude decreases. Indeed, the coupling coefficient is a function of the core index and it is possible to calculate this dependency numerically. The results are plotted in Fig. 3.

As seen, for the higher indices there is a larger coupling between the forward and backward fields and hence the laser threshold occurs for lower injection current.

In the planar slab waveguides, the coupling amount is an increasing function of the grating height [4, 6]. In our simulation this behavior is seen too. Increasing the grating height, $t$ in Fig. 1, can causes more powerful engage of two fields and it means there is higher coupling values. Such a prediction is calculated and the results are drawn in Fig. 4.

Other parameters which have important effect on the coupling coefficient are the input and output clad indices. This effect was calculated too and the results are plotted in Fig. 5.

This behavior can be interpreted physically. For lower values of the inner or outer indices, the difference between the active layer index and the cladding layer index increases so there is more field confinement; it is shown in Fig. 5.
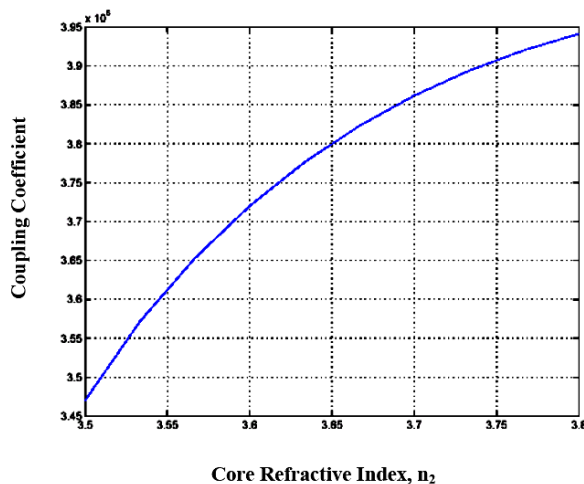


Figure 3: Coupling coefficient of a hollow circular dielectric waveguide versus core indices, $n_2$.
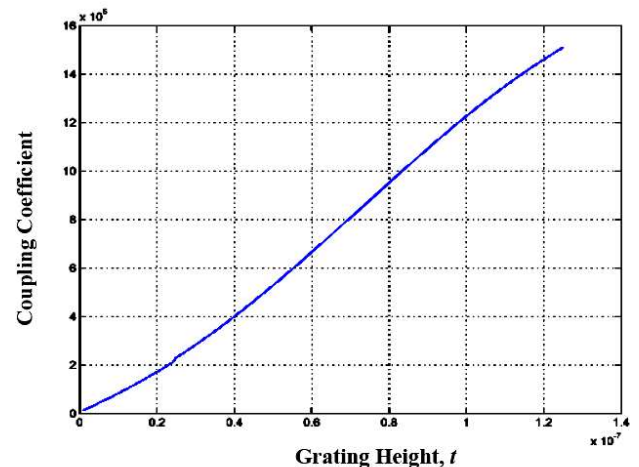


Figure 4: Coupling coefficient of a hollow circular dielectric waveguide versus the corrugation height, $t$.
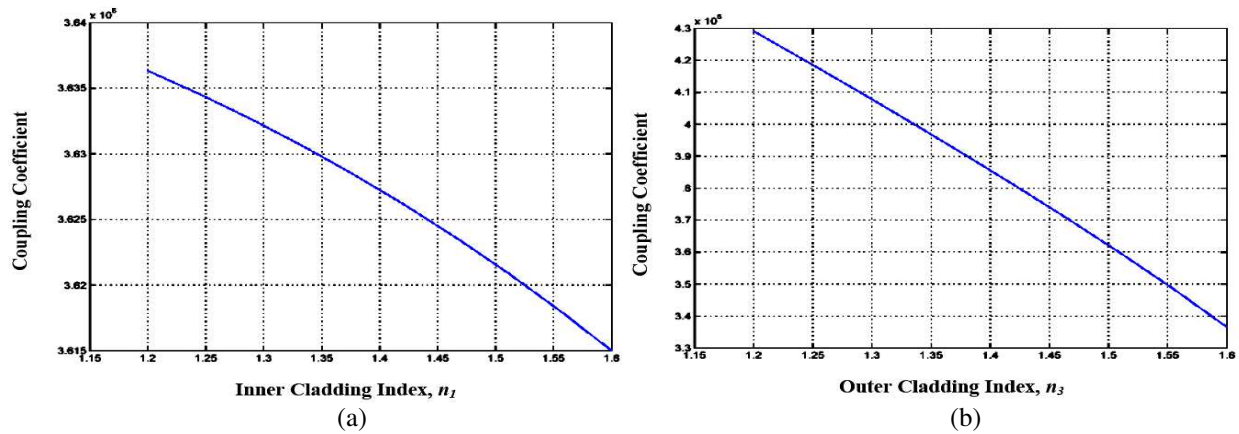
Figure 5: Coupling coefficient of a hollow circular dielectric waveguide versus, (a) the inner clad index and (b) the outer clad index.

## 4. CONCLUSION

The wave propagation and the amount of the coupling coefficient in HCDW structures are simulated in this article. The general behavior is the same as reported in the slab guides. Higher coupling is derived for the active layers with large indices and the gratings with higher height. These calculations were done for the dominant mode and when the perturbing conditions are satisfied. For the cladding layers with lower indices there is more confinement, so the coupling strength increases and there is lasing action in lower injecting currents.

## REFERENCES

1. Agrawal, G. P. and N. K. Dutta, *Semiconductor Lasers*, 2nd Edition, Van Nostrand Reinhold, New York, 1993.
2. Morthier, G. and P. Vankvikelberge, *Handbook of Distributed Feedback Laser Diodes*, Artech House, Boston, 1997.
3. Wang, J. Y. and M. Cada, "Analysis of optimum design of distributed feedback lasers using coupled power theory," *IEEE Journal of Quantum Electronics*, Vol. 36, 52–58, 2000.
4. Emami, F., "Effect of parameter variations of a corrugated periodic waveguide," *Proceedings of International Multi-conference of Engineers and Computer Scientists*, 1696–1700, Hong-Kong, March 2007.
5. Yang, C. S., Y. C. Chiang, and H. C. Chang, "Analysis of non-uniform non-linear distributed feedback structure using a simple numerical approach," *IEEE Journal of Quantum Electronics*, Vol. 40, 1337–1340, 2004.
6. Ghafouri-Shiraz, H., *Distributed Feedback Laser Diodes*, Wiley, New York, 1995.

# Frequency Selective Surfaces with Thin Triangular Conducting Elements

**A. Pekmezci and T. Ege**

Faculty of Engineering, Department of Electrical and Electronics Engineering, University of Gaziantep
Gaziantep 27310, Turkey

**Abstract**— In this paper, scattering characteristics of a planar Frequency Selective Surface (FSS) comprising of thin triangular-shaped conductors printed on dielectric substrate is investigated for both TM and TE incidence. Verification of the algorithm has been carried out by comparing the results obtained using this algorithm (simply by removing the appropriate sides of the triangle) with the results of other researchers using strips or L-shaped conductors. Variations of the reflection and transmission coefficients with frequency for some parameters of interest are presented.

## 1. INTRODUCTION

Frequency Selective Surface (FSS) is a surface which is usually constructed from periodically arranged metallic patches of arbitrary geometries or their complementary geometry having aperture elements similar to patches within a metallic screen. As the metallic patches are arranged periodically in air or a dielectric substrate, FSS shows total reflection properties (reflects nearly all energy) at some specific frequency whereas in the complementary structures where the metallic screen is perforated, transmits all energy (total transmission) at the resonance frequency [1]. For this reason, different shape and configuration of the geometries for FSS has been the subject of investigation by many researchers in order to present the reflection and transmission characteristics of that structure [2, 3].

Although theoretical investigations dealing with several different types of FSS can be found in the literature, no study has been done on FSSs comprising of triangular-shaped conductors. That is why, in this paper, we present the reflection and transmission characteristics of FSS formed by a two dimensional array of triangular-shaped conductors printed on a dielectric substrate.

## 2. FORMULATION OF THE FSS SCATTERING PROBLEM

Since the triangular conducting elements are printed periodically on an infinite planar surface as shown in Figure 1, the scattered fields inside the dielectric slab and in the air on either side are expanded into Floquet modes of the form

$$\vec{\Psi}_{mpq}(x, y) = \frac{1}{\sqrt{A}} e^{-j\vec{K}_{Tpq} \cdot \vec{\rho}} \vec{u}_{mpq} \tag{1}$$

where

$A = d_x d_y$ (area of rectangular unit cell)

$\vec{K}_{Tpq} = \left( k_x + \frac{2\pi p}{d_x} \right) \vec{a}_x + \left( k_y + \frac{2\pi q}{d_y} \right) \vec{a}_y = k_{xpq}\vec{a}_x + k_{ypq}\vec{a}_y$

$\vec{\rho} = x\vec{a}_x + y\vec{a}_y$

$\vec{u}_{1pq} = \dfrac{\vec{K}_{Tpq}}{\left| \vec{K}_{Tpq} \right|}, \; m = 1$ for TM mode

$\vec{u}_{2pq} = a_z \times \vec{u}_{1pq}, \; m = 2$ for TE mode

and $\; p = q = 0, \pm 1, \pm 2, \ldots$

In the absence of the metallic scatterers on the dielectric slab, the scattered fields contain zero order Floquet modes whereas the scattered fields produced by the currents induced on the conducting elements contains higher order Floquet modes. Hence, the electromagnetic fields in air on either side and inside the dielectric slab were expanded into Floquet modes. These modes must also satisfy the following boundary conditions:

  I) The tangential components of the scattered electric fields must be continuous at $z = 0$.

 II) At $z = 0$, the tangential component of the scattered magnetic fields are discontinuous by an amount equal to the induced current density on the metallic scatterers.

III) The tangential components of the scattered electric and magnetic fields are continuous at $z = t$.

Using these boundary conditions, an expression is obtained for the scattered fields in terms of the current density induced on a triangular conducting element. Finally, forcing the total electric field (incident + scattered) to vanish on the conducting elements yields an integral equation for the unknown induced current density. This resulting integral equation is then converted to a linear matrix equation by using the Moment Method (MM). For this induced current on the conducting elements are expressed in terms of piecewise triangular basis function [4, 5]. That is, for any current $J_{n,k}$ flowing from the segment $h_{k-1}$ to $h_{k+1}$ along the $\eta$-axis on a conducting arm, we can write the basis function in the form of

$$
J_{n,k}(\eta, \tau) = \begin{cases} \dfrac{I_k}{\Delta_n}(\eta - h_{k-1}) & h_{k-1} \leq \eta \leq h_k \\[2mm] \dfrac{I_k}{\Delta_n}(h_{k+1} - \eta) & h_k \leq \eta \leq h_{k+1} \end{cases} \tag{2}
$$

where $\Delta_n$ is the segment size and the subscripts $n$ (1, 2, 3) indicates the $n$th arm of the triangle and $k$ indicates the segment number which supports the current $I_k$, respectively.

    Solution of the matrix equation yields the unknown current coefficients which are then used to obtain the reflection and transmission coefficients [6].

## 3. NUMERICAL RESULTS

In this section, reflection and transmission coefficients for TM and TE incident plane waves are plotted versus frequency. The effect of changes in dielectric constant on the frequency response of the structure over a specific frequency range is also emphasized. In the analysis of triangular shaped FSS, we present the length and the width of the triangular conducting element by $L$ and $w$, respectively as shown in Figure 2. The angle of $\alpha$ is also used to determine the type of the triangular conducting elements printed on a dielectric substrate with a thickness $t$ and relative permittivity $\varepsilon_r$. In all our numerical computations, the following parameters are considered all over the paper for a dielectric backed FSS: $L_1 = L_2 = L_3 = 0.94\,\text{cm}$, $w = 0.047\,\text{cm}$, $d_x = d_y = 1\,\text{cm}$, $t = 0.5\,\text{cm}$ and $\alpha = 60°$. Furthermore, total number of induced currents on the conductor is taken to be 30 and 161 Floquet modes are used. Over the range of frequencies considered, the only propagating mode is the zero order Floquet mode and the other higher order modes are evanescent or decaying.

    In Figure 3, magnitudes of reflection and transmission coefficients are plotted versus frequency. TM incident waves are fully reflected at 13 GHz for a freestanding triangular-shaped FSS and 10.1 GHz for a dielectric backed triangular-shaped FSS at normal incidence. When the incident plane wave is TE polarized, the resonance frequency shifts to 13.6 GHz and 10.5 GHz for a freestanding and for a dielectric backed triangular-shaped FSS, respectively.
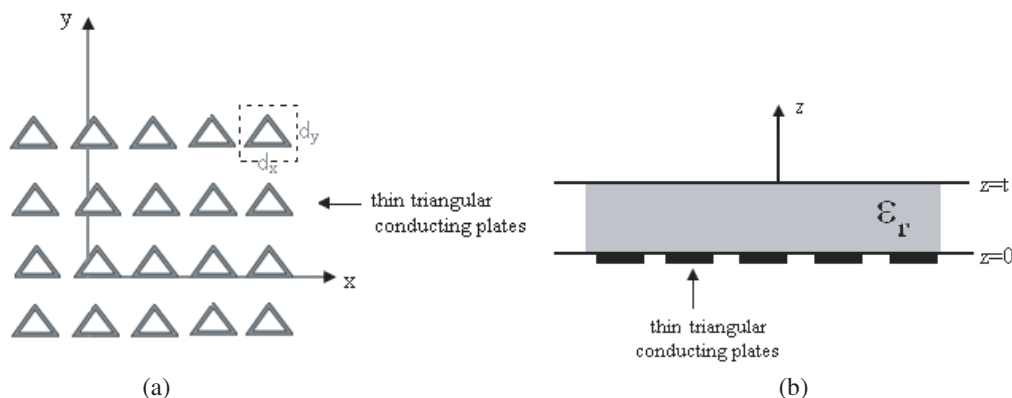


Figure 1: Triangular conducting elements printed periodically on a dielectric slab. (a) Top view. (b) Side view.

Figure 4 shows the variation of the reflection coefficient with dielectric constant for both TM and TE polarized normally incident plane waves as a function of frequency. So, when we increase the value of $\varepsilon_r$, the resonant frequency decreases with a value of $f_o/\sqrt{(\varepsilon_r + 1)/2}$ where $f_o$ is the freestanding resonance frequency [3].
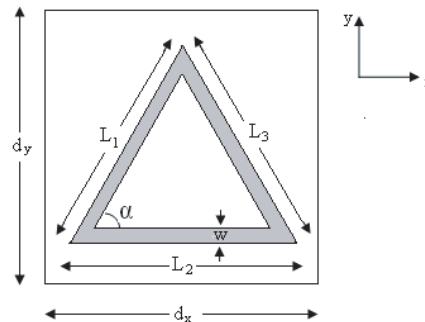


Figure 2: Geometry of triangular conducting element in a rectangular unit cell.
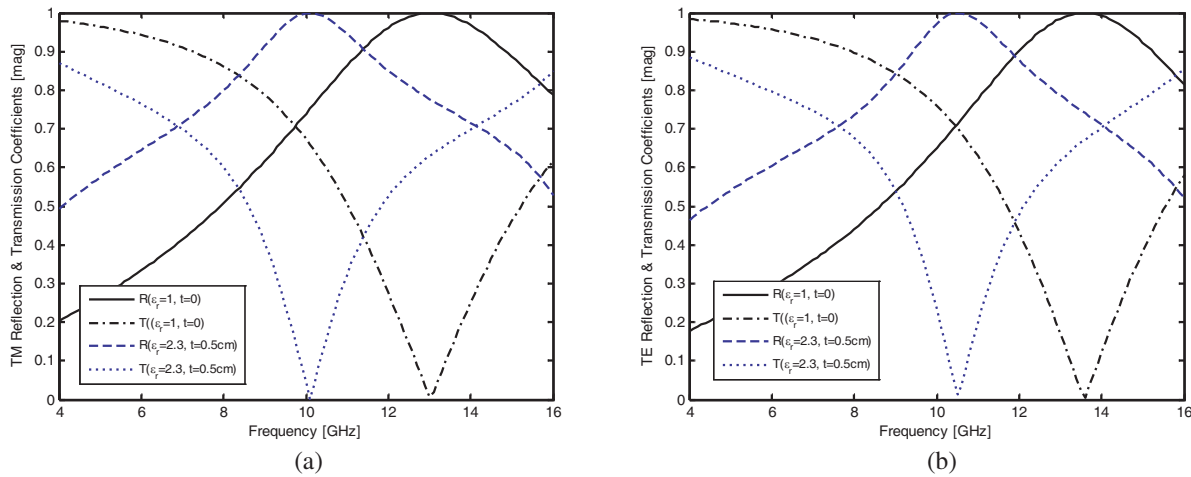


Figure 3: (a) TM and (b) TE reflection and transmission coefficients for the freestanding and dielectric backed triangular-shaped FSS.
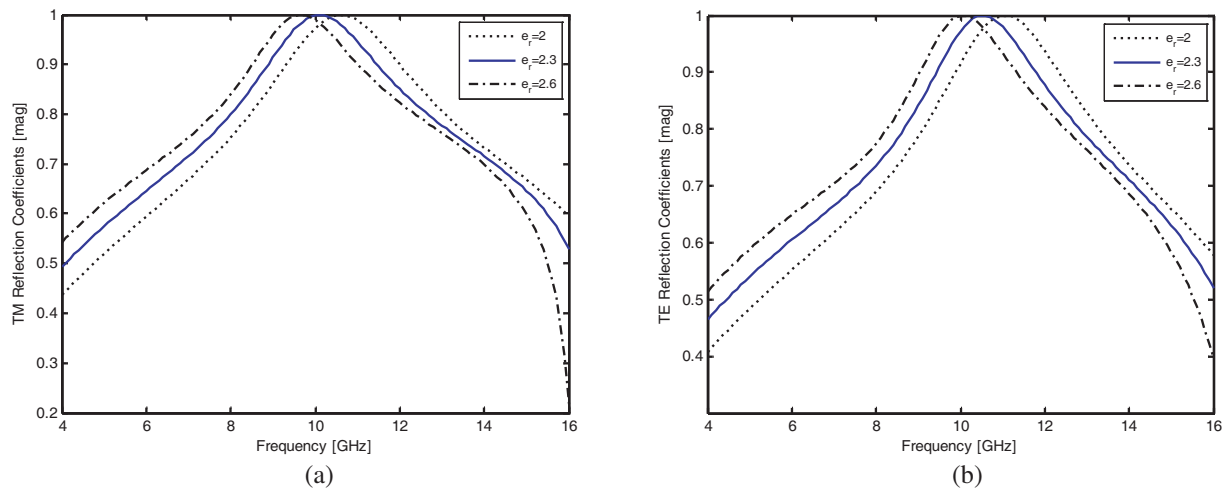


Figure 4: (a) TM and (b) TE reflection coefficients versus frequency for triangular-shaped FSS at different values of $\varepsilon_r$.

## 4. CONCLUSION

A generalized formulation of the scattering by a two dimensional array of periodically arranged thin triangular conducting elements printed on a dielectric substrate was developed and used to calculate the reflection and transmission coefficients of such a surface. Numerical results show that full reflection and transmission is possible for a FSS comprising of thin triangular conducting elements at normal incidence. Hence, such a surface can exhibit band-stop filter characteristics and the resonant frequency shifts downward as the dielectric constant increases. Only single resonance is observed in the frequency range of 4–16 GHz.

**REFERENCES**

1. Balanis, C. A., *Modern Antenna Handbook*, John Wiley & Sons, Inc., 2008.
2. Mittra, R., C. H. Chan, and T. Cwik, "Techniques for analyzing frequency selective surfaces — A review," *IEEE Proceedings*, Vol. 76, No. 12, 1593–1615, 1988.
3. Munk, B. A., *Frequency Selective Surfaces: Theory and Design*, John Wiley & Sons, Inc., 2000.
4. Bhattachharyya, A. K., *Phased Array Antennas*, John Wiley & Sons, Inc., 2006.
5. Amitay, N., V. Galindo, and C. P. Wu, *Theory And Analysis of Phased Array Antennas*, John Wiley & Sons, Inc., 1972.
6. Harrington, R. F., "Matrix methods for field problems," *IEEE Proceedings*, Vol. 55, No. 2, 136–149, 1967.

# A New Phase Measurement Technique for RF Power Amplifier Only Measuring Magnitudes

**A. H. Yuzer[1, 2] and S. Demir[1]**

[1]Electrical and Electronics Engineering, Middle East Technical University, Ankara, Turkey
[2]Electrical and Electronics Engineering, Zonguldak Karaelmas University, Zonguldak, Turkey

**Abstract**— In this study, a new phase measurement setup to measure magnitudes and phases of the fundamental components and intermodulation created by an amplifier under two tone excitation is reported. There are three signal generators, one digital attenuator and one spectrum analyzer in the measurement setup. There is no need to any other special electronic circuits (e.g., mixer, filter, etc.). Phase is found/measured mathematically based on magnitude measurements. Also absolute phase difference between the frequency components can be measured. Measured phase error is better than 1° for repetitive measurements.

## 1. INTRODUCTION

Amplifier characterization is an important issue especially in the design of amplifiers and systems involving amplifiers such as linearizers and wireless communication systems. Behavioral modeling is one of the characterization techniques where a mathematical relation between input and output is constructed. There are a number of behavioral modeling techniques. First step of modeling is measurement of the magnitudes and phases of the signals at the input/output of the amplifier. When an amplifier is excited with a one-tone signal, AM/AM and AM/PM distortion appears at the output. When an amplifier is excited with a two-tone signal, inter-modulation distortion (IMD) components are observed at the output. Magnitudes and phases of these signals are needed to construct an accurate model. Several measurement setups [1–5] are proposed these quantities.

In this study, a new measurement technique is proposed to measure both the magnitudes and the phases of signals generated by the amplifier. The measurement setup given in Figure 1 is prepared to measure AM/AM, AM/PM distortion, magnitudes and phases of intermodulation (IMD) and fundamental (FUND) components created by the amplifier. Phase measurement setup is constructed based on complex number addition.

## 2. MEASUREMENT SETUP

Signal generators ("SGA" and "SGB") as shown in Figure 1 are used to create a two-tone signal. Another signal generator named as "SGC" is used as reference signal source to measure the phase. A sample amplifier whose gain is greater than 33 dB around working frequency and P1 dB is 33 dBm is examined in this study.

It is assumed that there are two complex numbers named the first complex number and the second complex number; in phasor domain representation $m_{SG1}\angle\phi_1$ and $m_{SG2}\angle\phi_2$ respectively. Another number, $m_{tot}\angle\phi_{tot}$ is defined as in (1). Phase difference between the first and the second complex number can be found mathematically as given in (2).

$$m_{SG1}\angle\phi_1 \text{ and } m_{SG2}\angle\phi_2 = m_{tot}\angle\phi_{tot} \tag{1}$$

$$|\phi_1 - \phi_2| = \cos^{-1}\frac{m_{tot}^2 - m_{SG1}^2 - m_{SG2}^2}{2 * m_{SG1} * m_{SG2}} \tag{2}$$

$m_{SG1}$ represents the magnitude of the signal created at the output of the amplifier and $\omega_1$ represents the phase of that signal. $m_{SG2}$ represents the magnitude of the signal created at the output of the digital attenuator. $m_{tot}$ represents the value read at the spectrum analyzer (SA). If we know/measure $m_{SG1}$, $m_{SG2}$ and $m_{tot}$ we can find "$|\phi_1 - \phi_2|$" by using (2). Although only the relative phase difference can be found by using (2), absolute phase difference between IMD and FUND can also be measured by using this measurement setup.

## 3. PHASE MEASUREMENT

First step of phase measurement is extraction of the lookup table (LUT) which includes digital attenuator attenuation levels for all levels of SGA and SGB.

Then, to measure phase of IMD, $m_{SG1}$ value measured using spectrum analyzer (SA) while two-tone signal is applied to the amplifier by using "SGA" and "SGB". After taking this output in "SGA"-on, and "SGB"-on, and "SGC"-off state, "SGC" output is enabled only and using LUT, digital attenuator is adjusted such that $m_{SG2}$ is equal to $m_{SG1}$. If $m_{SG1}$ and $m_{SG2}$ has equal and "$|\phi_1 - \phi_2| = 120°$", $m_{tot}$ magnitude will be equal to that of $m_{SG1}$. The reason of this condition is to diminish error due to power level difference while measuring the signal levels using SA. Afterwards, in addition to "SGC", signal generators "SGA" and "SGB" are enabled to measure $m_{tot}$ value. Phase difference between reference signal and IMD signal created by amplifier is calculated mathematically using (2).

An initial procedure is needed to measure absolute phase. 4 single tone signals having zero phase shift between each other and frequencies 1 Hz, 2 Hz, 3 Hz and 4 Hz is created mathematically in MATLAB and loaded to the arbitrary wave shape generator (AWSG). AWSG repetition frequency is set as equal to the input excitation tone spacing namely $\Delta_f$. The signal created at the output of AWSG is given as in (3). DSB-SC signal is created by "SGC" taking AWSG as message signal and local oscillator as carrier signal as given in (4). Upper 4-tone of the 8-tone signal at the output of "SGC" is used as the reference signal. There is no phase difference among this 4-tone as given in (4).
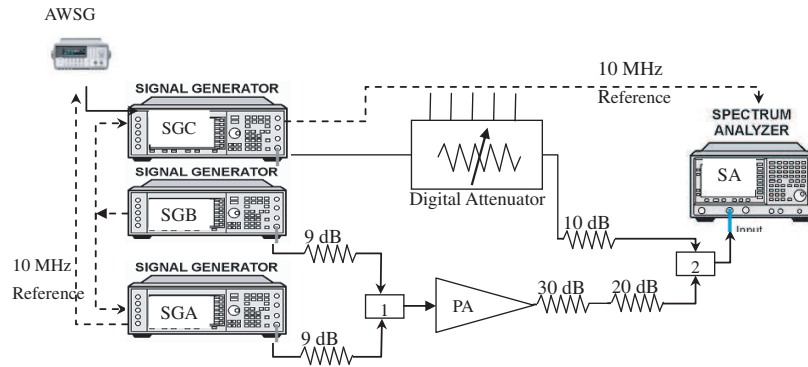


Figure 1: Measurement setup.

Some initial procedure needed to measure absolute phase. 4 tone signal having zero phase shift between each other and frequencies 1 Hz, 2 Hz, 3 Hz and 4 Hz is created mathematically in MATLAB and loaded to the arbitrary wave shape generator (AWSG). AWSG repetition frequency is set as equal to the input excitation tone spacing namely $\Delta_f$. The signal created at the output of AWSG is given as in (3). DSB-SC signal is created by SGC taking AWSG as message signal and local oscillator as carrier signal as given in (4). Upper 4 tone of signal includes 8 tone signal at the output of "SGC" is used as reference signal. There is no phase difference between upper 4 tone as given in (4).

$$V_{AWSG}(t) = \cos(2\pi * \Delta_f * t + \phi_m) + \cos(2\pi * 2 * \Delta_f * t + \phi_m) + \cos(2\pi * 3 * \Delta_f * t + \phi_m) + \cos(2\pi * 4 * \Delta_f * t + \phi_m) \quad (3)$$

$$V_{SGC}(t) = \sum_{k=1}^{4} [\cos((\omega_c - 2 * \pi * k * \Delta_f) * t + \phi_m - \phi_c)] + \sum_{k=1}^{4} [\cos((\omega_c + 2 * \pi * k * \Delta_f) * t + \phi_m + \phi_c)] \quad (4)$$

where "$\omega_c$ represents the "SGC" frequency and $\phi_m$ represents the local oscillator phase of SGC. "$\omega_c$" adjusted such that upper 4 tone gives same frequency spectra with the signal created at the amplifier considering IMD and FUND frequencies. 10 MHz reference signal created by SGB is transferred to the SGA and SGC with shortest possible cable connection for phase locking. Magnitude and phase of lower band Fundamental component (FUNDL) is measured 4 times while power level swept from $-22.7$ dBm to $-2.7$ dBm to investigate phase measurement setup accuracy and repeatability.

Both magnitudes and phases of lower and upper band IMD & FUND components are measured under two tone 30 MHz & 31 MHz excitation by using this measurement setup. Measurement results are given in Figure 3.
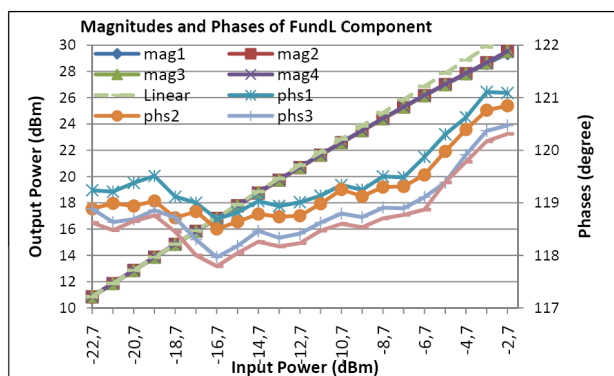
Figure 2: Repeated phase measurement.
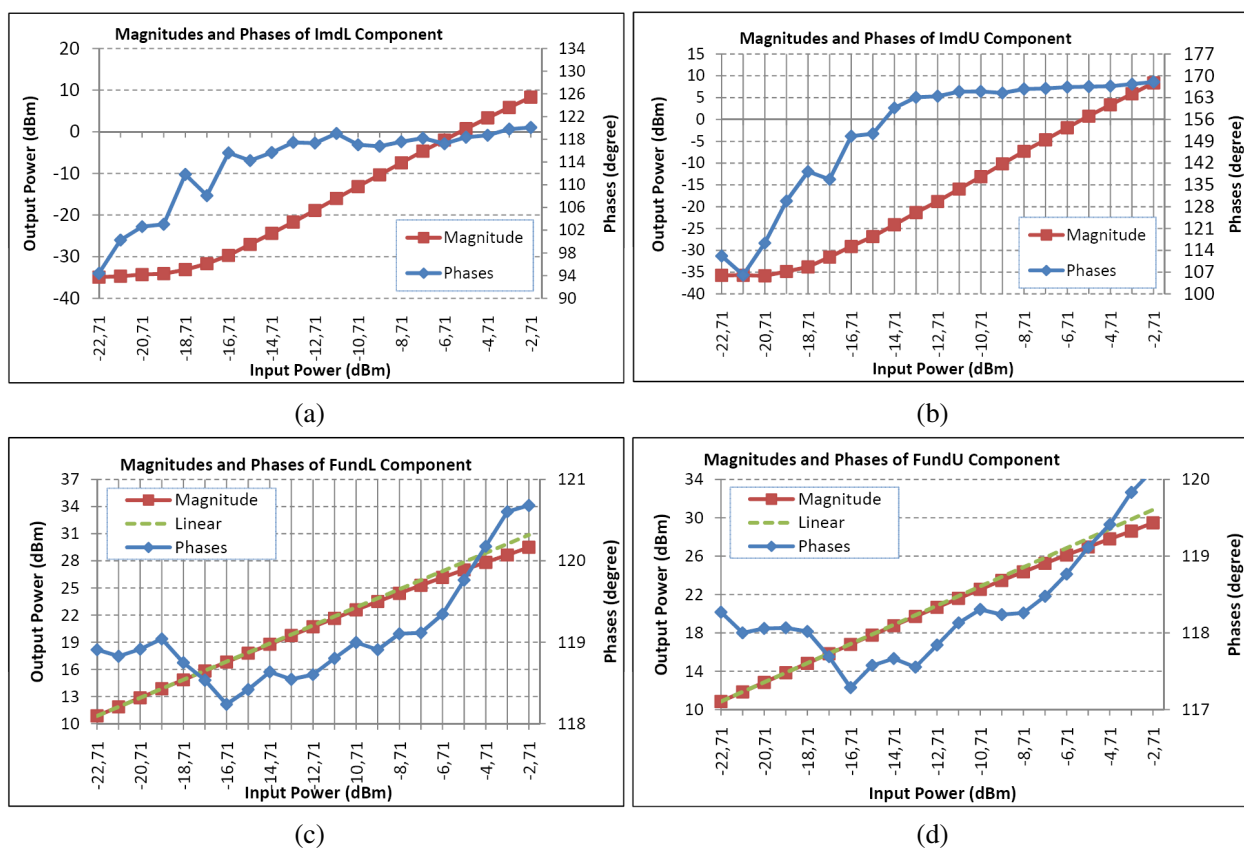


Figure 3: Magnitude and phase measurement result for (a) ImdL (b) ImdU (c) FundL and (d) FundU components.

## 4. CONCLUSION

In this study a phase measurement setup is proposed. In this model phase of signal is mathematically calculated based on magnitude measurements. This algorithm decreases the time needed to measure phase. Absolute phase difference between IMDL and IMDU created under two tone excitation is measured after adding AWSG to the setup to create 4 tone signal having zero phase shift between each other. Repetitive phase measurement error is lower than $0.5°$ as given in Figure 2. Then both magnitude and phase of IMDL, IMDU, FUNDL and FUNDU components created by amplifier under two tone 30 MHz & 31 MHz excitations are measured and given in Figure 3.

## REFERENCES

1. Crespo-Cadenas, C., J. Reina-Tosina, and M. J. Madero-Ayora, "Phase characterization of two-tone intermodulation distortion," *2005 IEEE MTT-S International Microwave Symposium*

*Digest*, 4, June 12–17, 2005.

2. Martins, J. P. and N. B. Carvalho, "Multitone phase and amplitude measurement for nonlinear device characterization," *IEEE Transactions on Microwave Theory and Techniques*, Vol. 53, No. 6, 1982–1989, June 2005.

3. Lee, S.-Y., Y.-S.b Lee, and Y.-H. Jeong, "A novel phase measurement technique for IM3 components in RF power amplifiers," *IEEE Transactions on Microwave Theory and Techniques*, Vol. 54, No. 1, 451–457, Jan. 2006.

4. Walker, A., M. Steer, and K. G. Gard, "A vector intermodulation analyzer applied to behavioral modeling of nonlinear amplifiers with memory," *IEEE Transactions on Microwave Theory and Techniques*, Vol. 54, No. 5, 1991–1999, May 2006.

5. Futatsumori, S., M. Furuno, T. Hikage, T. Nojima, A. Akasegawa, T. Nakanishi, and K. Yamanaka, "Precise measurement of IMD behavior in 5-GHz HTS resonators and evaluation of nonlinear microwave characteristics," *IEEE Transactions on Applied Superconductivity*, Vol. 19, No. 3, 3595–3599, June 2009.

# Structure Improvement for Suppressing High Mode of Folded Waveguide Traveling Wave Tube

**Tianyu Fang, Jin Xu, Huarong Gong, Hairong Yin, Zhigang Lu, and Tao Tang**

School of Physical Electronic, University of Electronic Science and Technology of China
Chengdu 610054, China

**Abstract**— The Folded Waveguide Traveling-Wave Tube (FWTWT) is known as a slow wave structure that has advantages of high power capability, high thermal capacity and robust structure comparing to the conventional Helix-TWT and Coupled-Cavity TWT. Though it has these advantages, the interaction between microwave and electron beam is usually disturbed by high modes. Thereby it affects the performance of FWTWT. There are already a lot of studies about "loss button" on the coupled-cavity TWT since this additional component has a great ability to restrain its upper band-edge. So, theoretically, by attaching oscillators filled with loss medium to the regular structure, high modes in FWTWT can be restrained distinctly as well.

The improvement is based on a regular folded waveguide traveling wave tube operating from 24 GHz to 65 GHz. The main mode and high modes of the FWTWT are operating at 24–44 GHz and on the frequency higher than 45 GHz respectively. The loss oscillators are designed for operating at certain frequency and restraining high mode greatly. Based on resonant conditions in this paper, main parameters of the oscillators such as the dimensions and loss medium are considered and analyzed. Detailed theoretical analysis of this new structure will be presented in this paper.

## 1. INTRODUCTION

As a kind of the most potential traveling wave tube, some particular designs of folded waveguide traveling wave tube (FWTWT) still have problems. It is possible that FWTWT operates on high modes. The theoretical analyses will be presented in this paper. To solve this problem, introducing an oscillator to the traveling wave tube (TWT) is a simple and effective solution. This approach is derived from improvement on coupled-cavity [1]. To figure out the performance of this improvement, we have coordinated the use of two computational tools: Ansoft HFSS [2] and CST Microwave Studio [3]. The effects of this improvement for suppressing high mode of folded waveguide traveling wave tube will also be discussed here.

## 2. HIGH MODES OF FWTWT

The traveling electromagnetic wave in slow wave structure interacts with the electron beam in the electron-path. While the group velocity of electrons is slightly more than the phase velocity of the electromagnetic field, the extra energy of the electron beam would transfer to the electromagnetic wave effectively.

A schematic of the FWTWT structure is shown in Figure 1, while the dimensions of our model are shown in Table 1. Dispersion and interaction impedance are obtained using a 3-D electromagnetic code, Ansoft HFSS. Dispersion diagram shown in Figure 2 is the simulation results based on our model.

Moreover, interaction impedance, as one of the most important parameters, is used to measure the efficiency the interaction between the traveling electromagnetic field and electron beam. If the impedance is high enough, electron beam would be coupled with the corresponding electromagnetic wave. Additional, if the group velocity of electron is close to the phase velocity of high mode electromagnetic wave, the tube would easily be operated at high mode. The on-axis interaction impedance is shown in Figure 3. The variation of the dispersion curve of the first high mode is relatively flat while normalized phase variety per period is about $2\pi$, which means the variation of phase velocity is little too. When the group velocity of electrons slows down to the first high mode, and the interaction impedance is large enough at $2\pi$, which is about 10 Ohm in this model, high mode would be stimulated at this time.

## 3. LOSS BUTTON ON COUPLED-CAVITY TWT AND THE REGULAR FWTWT

In coupled-cavity TWT, it is easy to generate self-excited oscillation at upper band edge of the main mode. After introducing the oscillators which are called loss button, the self-excited oscillation is restrained well [4].

Figure 1: Schematic of the basic FWTWT.

| $a$ | 5.50 mm |
|-----|---------|
| $b$ | 1.00 mm |
| $R_2$ | 0.50 mm |
| $R_0$ | 0.56 mm |
| $S$ | 1.26 mm |
| $p$ | 2.00 mm |
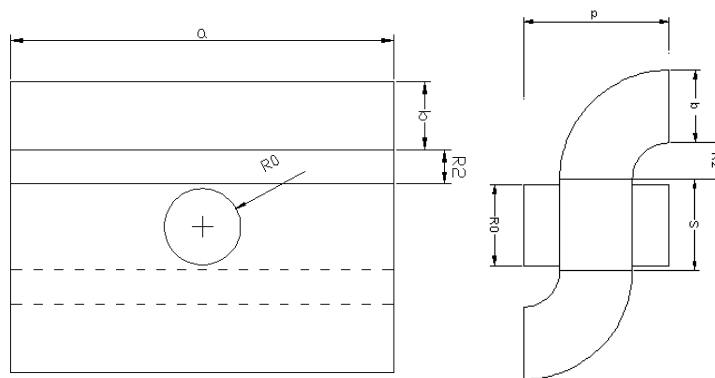
Table 1: Dimensions of the basic FWTWT.
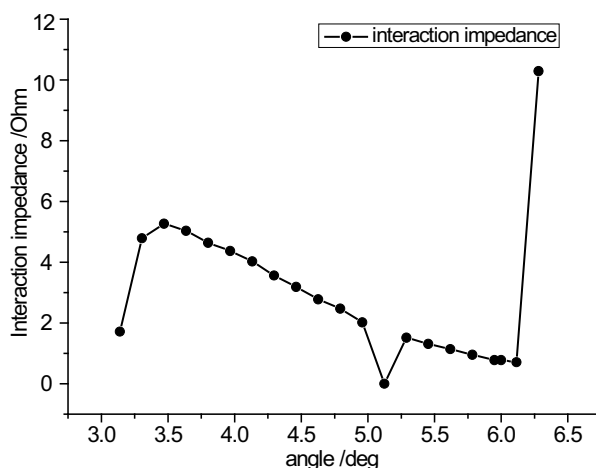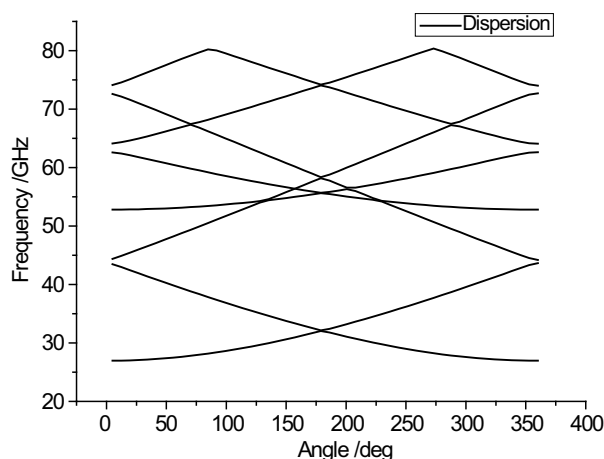


Figure 2: Dispersion diagram of regular FWTWT.



Figure 3: Interaction impedance of regular FWTWT.

Even the mode we want to suppress in FWTWT is not caused by the same way in the coupled-cavity TWT, this approach still work. Due to the role of loss button is restraining the field of target frequency oscillate in this lossy oscillator. Therefore, we attach oscillators to folded waveguide, and call them loss button as well.

Usually, there are two kinds of oscillator which can be attached to the TWT, cylindrical and cuboids oscillator. In order to couple the wave traveling into waveguide, loss button should be chosen based on the position where loss button is located and which field we want to couple. It is easy to realize that the field in the guide is the strongest at the inner-corner. Therefore, the best choice for a loss button is to locate at the corner. According to the electric and magnetic field at this corner shown in Figures 4 and 5, while the oscillator designed cylindrical with $l > 2.1R$, the main mode in loss button should be $TE_{111}$ mode which can fitly coupled with electromagnetic field in TWT. The final view of the new structure is shown in Figure 6, which is a model restructured in CST Microwave Studio. In this model, the length of loss button is 5.6 mm. The radius of loss button is 0.25 mm. The material filled in loss button is alumina 96%. Its relative permittivity is 9.38 and loss tangent is about 0.006. There is 0.01 mm overlapped between loss buttons and slow wave structure.

## 4. FREQUENCY CHARACTERISTIC OF NEW STRUCTURE WITH LOSS BUTTON

After applying the suit of model mentioned above in CST Microwave Studio, we have reran the simulations on computer. The simulation results about dispersion characteristics are shown in Figure 7. It shows that many new dispersion curves appear after loading loss buttons with the TWT. Mode 1 of new structure comes very closely to the mode 1 of original structure. Mode 2
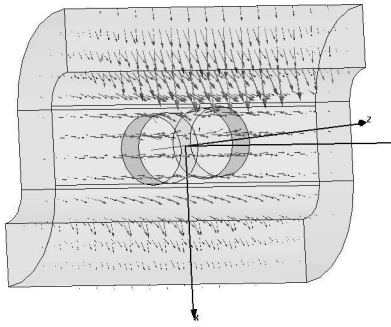
Figure 4: E-field in TWT.
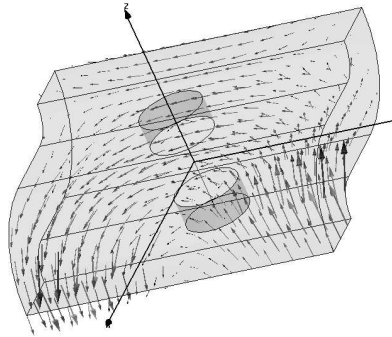


Figure 5: M-field in TWT.
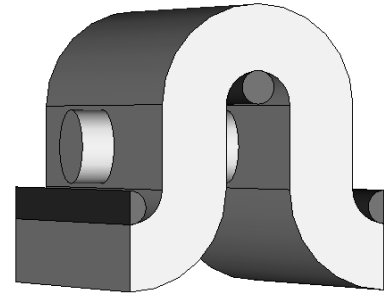


Figure 6: A period model of FWTWT loading with loss button in CST.
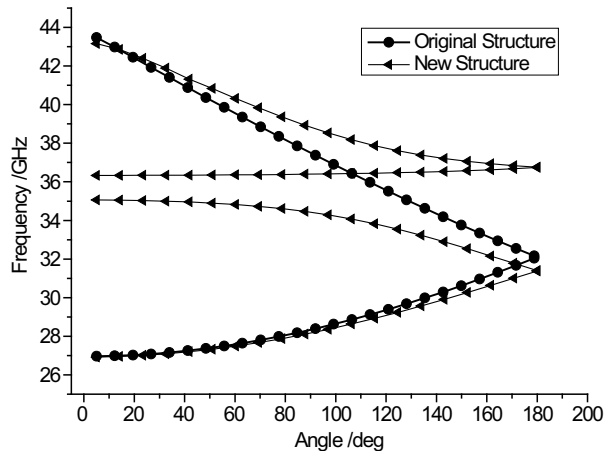


Figure 7: Dispersion of regular structure and new structure.
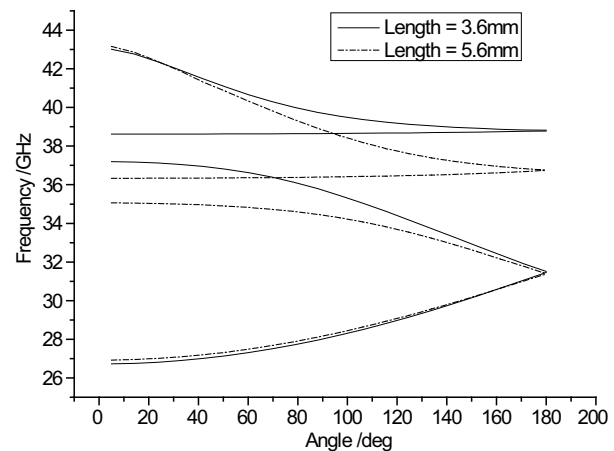


Figure 8: Dispersion diagrams of two structures.

of original structure, operating from about 32 GHz to 44 GHz, is split into three curves in the new structure. Apparently, the middle one among these three curves is almost a constant at 36.5 GHz that is the frequency where loss button oscillate. Group velocity is obviously suppressed around the frequency of 36.5 GHz. This effect to the dispersion of TWT means that the gain of target frequency is also inhibited.

However, it is necessary to do more study to analysis this phenomenon and the causes.

## 5. EFFECTS OF CHANGES OF LOSS BUTTON

Performance of this renewed structure is affected by certain parameters. The radius, length and material of oscillator are main effective parameters to the loss button design. However, normally, the choice of materials is not haphazard. It's always based on the current material. Once the material is decided, dimensions of loss button are the most effective parameters. Simulations and discussions below, based on the material mentioned above, will show the effects of every single parameter of them. All of following simulations are based on a model of folded waveguide traveling wave tube loading with loss buttons in 3-D electromagnetic code CST Microwave Studio.

Figure 8 shows the dispersions of two structures. Solid curves indicate the dispersion characteristic when the length of loss button is 3.6 mm. The dash curves show the dispersion characteristic when the length of loss button is 5.6 mm. It is easy to see those modes 3 of these two structures are the main reasons which cause their dispersions difference. Just as discussed above, mode 3 of TWT with loss button as a new dispersion curve comes with the loss button. The frequency of this mode is the resonant frequency of the loss button. The curves just above and below it are split from original mode 2. Upper band-edge and lower band-edge are almost unchanged. Also, the middle oscillation curve means where the group velocity is suppressed and the gain of which target frequency is inhibited. After simulating structures of other lengths, their dispersion curves are all split by mode 3.

So, simply we just compare the resonant frequency curves. By extracting data of mode 3 of

all simulations results on different lengths of the loss button, we synthesized them into Figure 9. It is intuitive to figure out the relationship between the length of loss button and the oscillation frequency. The resonant frequency of the loss button is going down while the length of loss button is going up. Once the radius of loss button is decided, the best way to suppress a target frequency is to change the length of loss button since the length of loss button is easy to process.

As simple as we discussed above, the relationship between the length of loss button and resonant frequency is shown in Figure 10. It is obvious that the resonant frequency is inversely proportional to the radius of loss button.
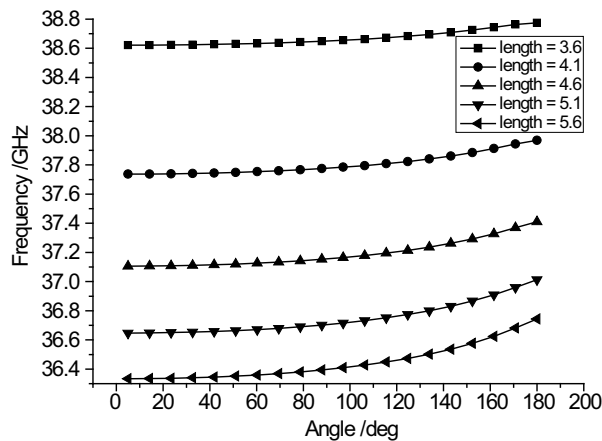


Figure 9: Synthesized simulations results about the effects of different lengths.
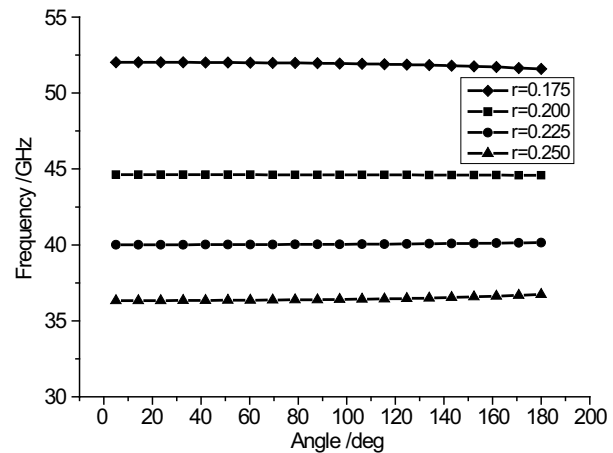
Figure 10: The effects caused by changing the radius of loss button.

## 6. CONCLUSIONS

In this paper, we presented a new way, by loading oscillators attach to TWT, to suppress high-mode oscillation. This paper also systematically analyzed where and how to add which kind of oscillator to the waveguide.

This paper presented the comparison of dispersions between regular FWTWT and improved FWTWT by using simulation tools. At the meantime, we went deep into simulations about the effects brought by the changes of loss button.

It is necessary to point out that above quantitative result are all based on particular structure. The interaction impedance of basic structure or the dispersion characteristics of FWTWT loading with loss button may different if the structure changes. However, simulation results of the relationships between resonant frequency and dimensions of loss button are stated. The theoretical analysis and computational simulation results in this paper could be reference for future research.

## ACKNOWLEDGMENT

## REFERENCES

1. Allen, et al., "Traveling wave tube with thermally-insensitive loss button structure," United States Patent, Patent Number 5,391,963.
2. "High frequency structure simulator user's guide," Ansoft Co., 2005.
3. CST Microwave Studio, Computer Simulation Technology. [Online]. Available: http://www.cst-america.com.
4. Liu, S. and X. Zhang, "The resonant loss technique for Suppressing spurious oscillation in CCTWTS," *Vacuum Electronics*, Vol. 34, No. 10, 1064–1076, 1986.

# Size Reduction and Harmonic Suppression of Narrow Bandpass Waveguide Filters Using Nonuniform Waveguides

**M. Yazdani**, **M. Khalaj-Amirhosseini**, and **F. Hosseini**

Department of Electrical Engineering, Iran University of Science and Technology, Tehran, Iran

**Abstract**— In this paper potential use of nonuniform transmission line theory to design compact waveguide filters is demonstrated. This theory helps us to design compact nonuniform waveguide structures such as waveguide narroband bandpass or bandreject filters. The normalized width function of the nonuniform waveguide, which is expanded in a truncated Fourier series, is designed by optimization. As an example the optimization process of a second order chebyshev narrowband waveguide bandpass filter at 4.135 GHz is presented. By doing optimization and replacing optimized nonuniform waveguides instead of uniform ones, a 68% size reduction is approached.

## 1. INTRODUCTION

Recent advancements in wireless communications in conjunction with the ever increasing demand for size reduction of various wireless systems and devices have led us to numerous constraints on the size, weight, and power consumption of modern communication systems and devices. RF/Microwave filters, which are integral parts of any wireless communication system, are not exceptions to this rule. Besides size reduction, low insertion losses and large stopband without spurious response are other points which are important in microwave filters. Combining all these features with a good return loss constitutes a great challenge. In recent years, many efforts have been made to miniaturize waveguide filters. In [1], a compact waveguide bandpass filter using both inductive and capacitive circular posts is introduced. In another research narrow bandpass waveguide filter using frequency selective surfaces loaded with surface mount capacitors is achieved [2]. In [3], a proper admittance inverter is designed such that electric length of waveguide sections are very smaller than the conventional ones and a compact band pass waveguide filter utilizing Complementary Split Ring Resonators (CSRRs) with size reduction about 66% is approached.

In this paper, we use Nonuniform Transmission Line (NTL) theory [4] to compact narrowband waveguide BandPass Filters (BPFs). The basic idea comes from replacing the hallow Uniform WaveGuides (UWGs) with optimized Nonuniform WaveGuides (NWGs). By using NWG instead of UWG, the distance between shunt inductive irises is reduced. As an example a second order chebyshev shunt inductive irises waveguide BPF at center frequency 4.135 GHz having is compacted and its spurious response is completely suppressed.

## 2. COMPACT BPF WITH NWG

As we know waveguide band-pass filters are widely used in communication systems. Fig. 1(a) shows the structure of a conventional shunt inductive irises waveguide BPF of order $n$. As it is seen the filter is composed of several uniform waveguides with different lengths which are located between the irises. Due to using lengthy waveguides, this filter is lengthy at low frequencies so the size reduction becomes an attractive point in designing of this kind of filters. This purpose can be achieved by using nonuniform waveguides instead of uniform ones. Therefore, we have to design nonuniform waveguides so that they act as lengthy uniform waveguides. Fig. 1(b) depicts the nonuniform waveguide BPF.

At first, we consider a typical Uniform Waveguide (UWG) with length $L_0$ and power-voltage impedance $Z_0$ of dominant mode at frequency $f_0$, as shown in Fig. 2(a). Then we consider a typical Nonuniform Waveguide (NWG), whose characteristic impedance at frequency $f_0$ is $Z(z)$ and its length is $L$ which is smaller than $L_0$, as shown in Fig. 2(b). Also, Fig. 3 shows the longitudinal view of the NWG, whose side is varied as $b(z)$. The aim is to design the NWG so that its $ABCD$ parameters at frequency $f_0$ are equal to those of UWG.

## 3. ANALYSIS OF NWGS

In this section, a general method is proposed to analyse NWGs. There are some ways to analyse the nonuniform transmission lines such as finite difference [5], Taylor's series expansion [6] and Fourier series expansion [7]. Of course, the most straightforward method is subdividing NTLs into
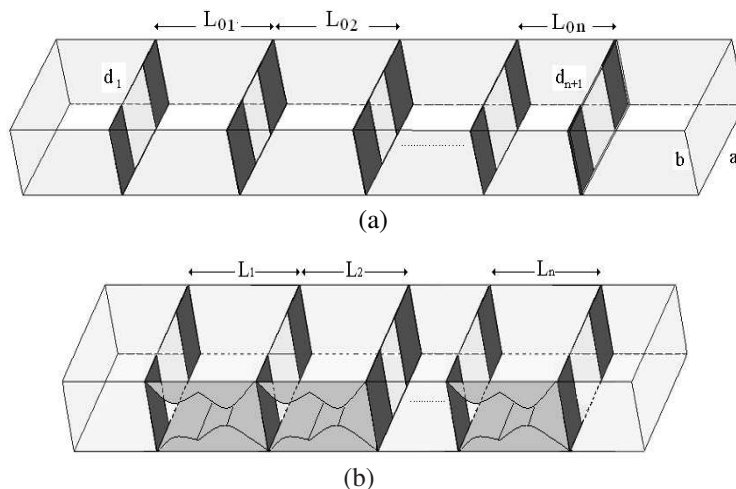
Figure 1: (a) A conventional waveguide BPF using uniform waveguides. (b) The compacted BPF using nonuniform waveguides.
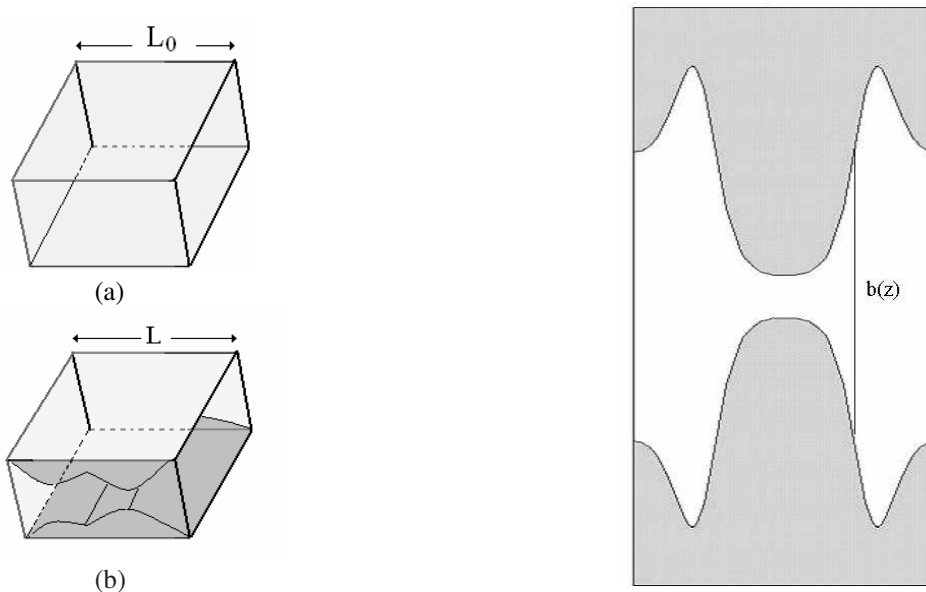


Figure 2: (a) A UWG with length $L_0$. (b) A NWG with length $L < L_0$.

Figure 3: The longitudinal view of a NWG.

$K$ uniform electrically short segments of length $\Delta z$. The $ABCD$ parameters of the whole NWG are obtained from those of the segments as follows:

$$\begin{bmatrix} A & B \\ C & D \end{bmatrix} = \begin{bmatrix} A_1 & B_1 \\ C_1 & D_1 \end{bmatrix} \cdots \begin{bmatrix} A_k & B_k \\ C_k & D_k \end{bmatrix} \cdots \begin{bmatrix} A_K & B_K \\ C_K & D_K \end{bmatrix} \tag{1}$$

where $A_k, B_k, C_k$ and $D_k$ are the $ABCD$ parameters of the $k$-th uniform segment. The impedance of waveguide at each segment is considered as the following form [8]:

$$Z(z) = 754 \frac{b(z)}{a} \sqrt{\frac{\mu_0}{\varepsilon_0}} \left( 1 - \left( \frac{f_c}{f_0} \right)^2 \right)^{-0.5} \tag{2}$$

Also, the electrical length of each segment can be found using:

$$\Delta \theta = 2\pi \frac{\Delta z}{\lambda_0} \left( 1 - \left( \frac{f_c}{f_0} \right)^2 \right)^{-0.5} \tag{3}$$

In (2) and (3), $f_c$ is the cutoff frequency of the uniform waveguide.

Table 1: The dimensions of designed conventional waveguide BPF (all in mm).

| $a$ | $b$ | $L_{01}$ | $L_{02}$ | $d_1$ | $d_2$ | $d_3$ |
|------|------|-------|-------|-------|-------|-------|
| 58.2 | 29.1 | 43.62 | 43.62 | 20.05 | 10.77 | 20.05 |

## 4. DESIGN OF NWGS

In order to design optimally compact nonuniform waveguide, the following Fourier series expansion is considered for the normalized side width of the waveguide:

$$\ln\left(b(z)\right) = \sum_{n=0}^{N} C_n \cos\left(\frac{2\pi n z}{L}\right) \tag{4}$$

which is a symmetric function.

An optimum designed NWG of length $L$ should have the $ABCD$ parameters as close as possible to the $ABCD$ parameters of UWG with length $L_0$. Therefore, the optimum values of the coefficients $C_n$ will be obtained through minimizing the following error function [9].

$$\text{Error} = \sqrt{\frac{1}{4}\left(|A - A_0|^2 + Z_0^{-2}|B - B_0|^2 + Z_0^2|C - C_0|^2 + |D - D_0|^2\right)} \tag{5}$$

where $A$, $B$, $C$, $D$ are the $ABCD$ parameters of compact NWGs obtained from (1) and also $A_0$,



(a)                                                    (b)
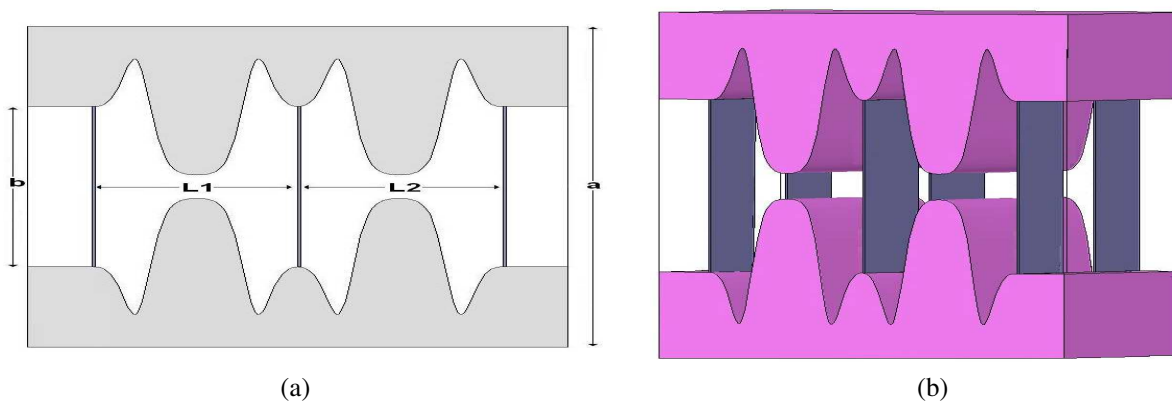
Figure 4: The optimized compacted waveguide BPF, (a) Longitudinal view, (b) 3D view.
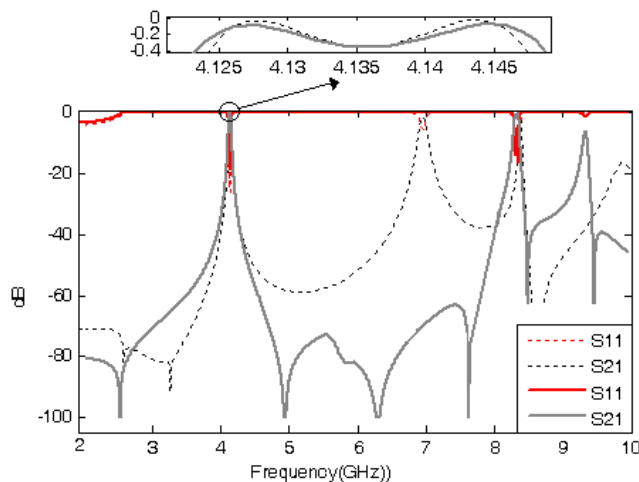


Figure 5: The simulation results of the conventional and compacted waveguide BPFs. Dashed lines: Conventional filter, Solid lines: Compacted filter

$B_0$, $C_0$, $D_0$ are the *ABCD* parameters of UWGs as follows:

$$\begin{bmatrix} A_0 & B_0 \\ C_0 & D_0 \end{bmatrix} = \left\{ \begin{array}{cc} \cos(\beta_0 L_0) & jZ_0 \sin(\beta_0 L_0) \\ jZ_0^{-1} \sin(\beta_0 L_0) & \cos(\beta_0 L_0) \end{array} \right\} \tag{6}$$

in which $\beta_0$ is the phase constant of the UWG. Moreover, defined error function (5) should be restricted by some constraints such as easy fabrication or the following matching at two ends of NWG:

$$Z(L) = Z(0) = Z_0 \tag{7}$$

## 5. DESIGN AND SIMULATION

According to the above explanation, a compact narrowband BPF can be achieved by using NWGs. As an example, a second order chebyshev waveguide BPF is considered. The specifications of the proposed filter are as follows: center frequency ($f_0$) = 4.135 GHz, fractional bandwidth (BW) = 0.5% and Ripple = 0.38 dB. First we design conventional waveguide BPF by using design formula in [10–12]. Table 1 tabulates the dimensions of designed BPF.

We do optimization for a UWG with length $L_1 = L_2 = 13.82$ mm instead of $L_{01} = L_{02} = 43.62$ mm, at frequency $f_0$. Fig. 4 depicts the optimized NWG. The compacted BPF has 27.64 mm length compared with 87.24 mm in the conventional one, whose mean is 68% size reduction. Fig. 5 shows the simulation results of the conventional and compacted waveguide BPFs (simulation was done by HFSS software). In addition to the good agreement between the responses of two filters at center frequency, the spurious response of the conventional BPF at 7 GHz has been suppressed in compacted BPF. Moreover, the attenuation of the compacted filter is very more than that of conventional one at stopband frequencies. These advantages besides size reduction are the attractive points of using NWGs instead of using UWGs.

## 6. CONCLUSION

The nonuniform transmission line theory was used to design compact waveguide narrowband filters. The normalized width function of the nonuniform waveguide, which is expanded in a truncated Fourier series, is designed by optimization. As an example the optimization process of a second order chebyshev narrowband waveguide bandpass filter at 4.135 GHz was presented. By doing optimization and replacing optimized nonuniform waveguides instead of uniform ones, a 68% size reduction is approached.

### REFERENCES

1. Li, H., Q. Wang, R. Liu, and X. Zhang, "Economical compact waveguide band-pass filter with circular posts," *Microwave and Millimeter Wave Technology, 2008, ICMMT2008*, Vol. 1, No. 21–24, 318–319, Apr. 2008.
2. Amjadi, S. M. and M. Soleimani, "Narrow band-pass waveguide filter using frequency selective surfaces loaded with surface mount capacitors," *Electromagnetics in Advanced Applications, 2007, ICEAA 2007*, 173–176, Sept. 2007.
3. Bahrami, H., M. Hakkak, and A. Pirhadi, "Analysis and design of highly compact band-pass waveguide filter utilizing complementary split ring resonators," *Progress In Electromagnetics Research*, PIER 80, 107–122, 2008.
4. Khalaj-Amirhosseini, M., "Nonuniform transmission lines as compact uniform transmission lines," *progress In Electromagnetics Research C*, Vol. 4, 205–211, 2008.
5. Khalaj-Amirhosseini, M., "Analysis of coupled or single nonuniform transmission lines using step-by-step numerical integration," *Progress In Electromagnetics Research*, PIER 58, No. 58, 187–198, 2006.
6. Khalaj-Amirhosseini, M., "Analysis of nonuniform transmission lines using Taylor's series expansion," *Int. J. RF and Microwave Computer-Aided Engineering*, Vol. 16, No. 5, 536–544, Sep. 2006.
7. Khalaj-Amirhosseini, M., "Analysis of nonuniform transmission lines using Fourier series expansion," *Int. J. of RF and Microwave Computer-Aided Engineering*, Vol. 17, No. 3, 345–352, May 2007.
8. Rizzi, P. A., *Microwave Engineering, Passive Circuits*, 2nd Edition, Prentice Hall, 1988.
9. Khalaj-Amirhosseini, M., "Microstrip nonuniform impedance resonators," *Progress In Electromagnetic Research*, PIER 67, 329–339, 2007.

10. Matthaei, G. L., *Microwave Filters, Impedance Matching Networks, and Coupling Structures*, 2nd Edition, Artech House, Dedham, Mass., 1980.

11. Pozar, D. M., *Microwave Engineering*, 2nd Edition, Addison-Wesley, 1990.

12. Collin, R. E., *Foundation for Microwave Engineering*, 2nd Edition, McGraw-Hill, New York, 1996.

# An Asymmetric Dual-band HTS Band-pass Filter for American Mobile Phone System

**A. M. Abu Hudrouss**[1,2], **A. B. Jayyousi**[1,3], **and M. J. Lancaster**[4]

[1]Electrical Engineering Department, Birmingham University, UK
[2]Electrical Engineering Department, IUG-Gaza, P. O. Box 108, Gaza, Palestine
[3]Electrical Engineering Department, University of Amman, Jordan
[4]Electrical and Comp. Department, Birmingham University, Edgbaston, Birmingham, B15 2TT, UK

**Abstract**— The American Mobile Phone System (AMPS) has a very complex frequency allocation which is divided between two operators A and B. Therefore, high performance multiple-band system components are desired in both the downlink and uplink. High Temperature Superconducting (HTS) filter and amplifier can be used in the reverse link reception where high sensitivity is desired and the power is within the range that HTS can handle. In this paper, we introduce a nine-pole bandpass filter to be used in operator B for reverse link reception. The filter is an example of dual-band filter with asymmetric response.

## 1. INTRODUCTION

Modern mobile communication systems require improved sensitivity and selectivity to support the growth in multimedia services, increased coverage, longer talk time and large number of subscribers. This in turn leads to demands for highly selective RF filters. This also forces the operators to seek more efficient sharing of the limited frequency spectrum. This initiates the need for HTS single and multiple bandpass filters to be used in the base stations in order to efficiently utilize the limited space [1–3].

The American Mobile Phone System (AMPS) uses the frequency band from 824 to 849 MHz for communication from the handset to their base stations (the uplink) and 896.0 to 894.0 MHz for the communication from the base stations to the handset (the downlink). This enables full duplex conversation. Historically, a band A and a band B were allocated first, then further allocations of A' and B' were given by the Federal Communications Commission (FCC) to mobile radio. The allocated spectrum gives 416 channels with a bandwidth of 30 kHz for each of the operator [4].

Figure 1 shows these allocations in more detail. In every region, two providers (denoted A and B) share this spectrum in non-contiguous segments. This complex allocation leads to potential operational problems. Cross-talk at the band edges between the two operators can lead to interference problems, with the consequence of unusable channels [4]. Limiting interference with the non-contiguous frequency allocations often requires highly selective filters that can easily be realized using HTS technology.

This gives rise to the need for four distinguishable filters for the whole system. Each one is a dual-band with (A, A') or (B, B') bandwidths for both uplink and downlink. It is worth noting that the only difference between the uplink filter and the downlink filter is in the centre frequency, as the bandwidth of each band does not change.

Each filter must have a very rapid roll off (within each 30 kHz channel) and provide high adjacent channel attenuation at the operators' band edges. This has been previously attained by cavity filters where a surrounding cylinder is coated with thick film HTS material and has an internal HTS thick-film split ring resonator [4]. For example, 16 and 10 pole filters have been used for the lower and upper bands respectively for operator A. The filters have been also designed using HTS thin-film but again two distinctive filters have been used to achieve the dual-band performance [5].

In this paper, a nine-pole planar bandpass HTS filter is presented. The filter can be used on the used for reception on the masthead for B operator. A symmetrical triple band HTS filter has been previously designed using an optimization algorithm introduced in [3]. The same algorithm has been used to design the desired asymmetric dual-band filter.

## 2. FILTER SPECIFICATIONS

A filter is designed for the base station receiver for band B and B'.
    **Centre frequency** = 842 MHz, **Stop-band bandwidth** = 1.5 MHz,
    **1st passband bandwidth** = 10 MHz, and **2nd passband bandwidth** = 2.5 MHz.
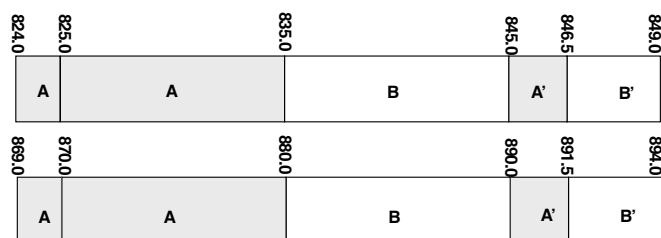
Figure 1: Channel allocations for mobile radio in the USA for base station and mobile handsets. Frequencies are given in MHz [4]; The top is the mobile transmission spectrum allocation and the bottom is the base transmission spectrum allocation.
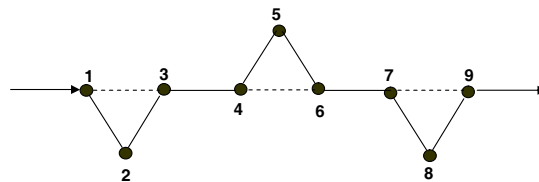


Figure 2: Trisection cascaded topology for the nine-pole dual-band asymmetric HTS filter for mobile communication.

Table 1: Coupling Matrix for the 9th Order Asymmetrical Dual Pass-band Filter.

|   | 2 | 3 | 4 | 5 | 6 | 7 | 8 | 9 | 10 |
|---|---|---|---|---|---|---|---|---|----|
| 1 | −.0732 | .0863 | 0.7575 | 0 | 0 | 0 | 0 | 0 | 0 |
| 2 | .0863 | .5504 | 0.2239 | 0 | 0 | 0 | 0 | 0 | 0 |
| 3 | .7575 | .2239 | −.0477 | .4977 | 0 | 0 | 0 | 0 | 0 |
| 4 |  |  | .4977 | −.087 | .1714 | .4986 | 0 | 0 | 0 |
| 5 |  |  |  | .1714 | .5841 | .1722 | 0 | 0 | 0 |
| 6 |  |  |  | .4986 | 0.1722 | −.0868 | 0.4977 | 0 | 0 |
| 7 |  |  |  |  |  | .4977 | −.0482 | .2236 | .7574 |
| 8 |  |  |  |  |  |  | .2236 | 0.5509 | .087 |
| 9 |  |  |  |  |  |  | .7574 | .087 | −.0732 |

## 3. FUNCTION OPTIMIZATION

To achieve the specified response, a nine-resonator trisection filter has been chosen. The topology filter is depicted in Fig. 2, where the solid line indicates the direct couplings and the dashed lines indicate cross couplings. The filter consists of three-cascaded trisections, each of these has one cross coupling that enable the production of a single attenuation pole at finite frequency. This topology has been chosen as it allows an asymmetrical response. The other advantage of this topology is that it minimizes the spurious coupling by allowing a good separation between non-adjacent and non-coupled resonators compared to cascaded quadruplets or canonical topologies.

Another merit is that each transmission zero is controlled by one cross coupling from the related tri-section which enables relatively easy tuning on both simulation and manufacturing levels. However, the total number of transmission zeros to be realised is less compared to the canonical topology.

To realize these specifications, the full coupling matrix is constructed using the synthesis method developed by Cameron [6]. The coupling matrix has been synthesized to the desired topology using optimization method developed by Jayyousi [7]. Table 1 gives the resultant matrix and the response is depicted in Fig. 3.

## 4. FILTER FABRICATION

The filter layout is shown in Fig. 4 where the main resonator is the highly miniaturized interdigital dual-spiral resonators developed by Zhou [8]. The resonators have a very low sensitivity to the substrate thickness variation and a small far-field radiation which makes them suitable for a small fractional bandwidth. The resonator dimensions have been found to be $4.25\,\text{mm} \times 1.95\,\text{mm}$ and the resonator line-width is $50\,\mu\text{m}$.

The filter design was carried out according to the coupled-resonators design methodology, which is covered in [9]. The substrate is MgO with a thickness of $0.5\,\text{mm}$ and the chip size is $32\,\text{mm} \times 12\,\text{mm}$, using YBCO thin film on both sides of the substrate. The filter has been simulated and optimized using Sonnet software [10] with a resolution of $50\,\mu\text{m} \times 50\,\mu\text{m}$. The simulation results are depicted in Fig. 5.
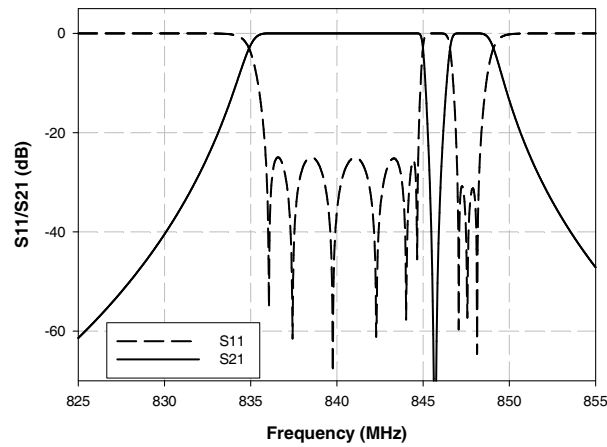
Figure 3: Reflection and insertion losses for the 9-pole asymmetrical dual-passband filter (theoretical).
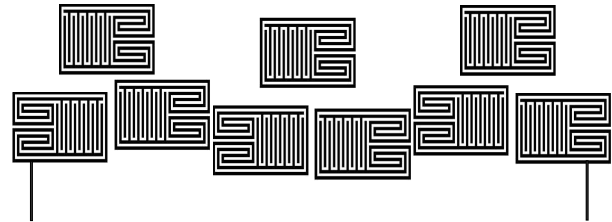


Figure 4: The nine-pole dual-band asymmetric HTS filter layout for downlink in American mobile communication (Figure is not to scale).
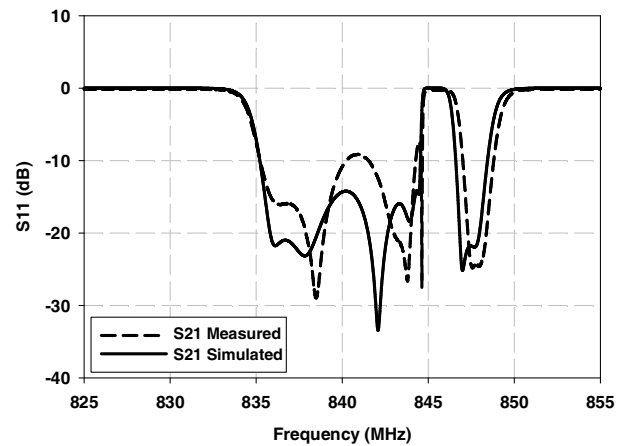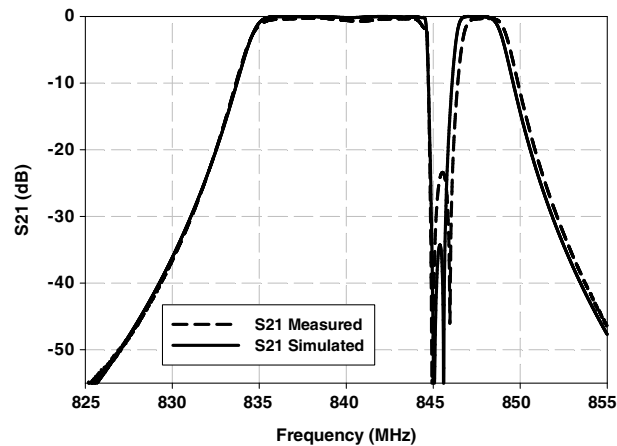




Figure 5: Measured and simulated reflection and insertion losses for the 9-pole asymmetrical dual-passband filter.

## 5. MEASUREMENT RESULTS

The experimental result is depicted in Fig. 5. The centre frequency is shifted down by 4.85 MHz from the simulated response.

Without any tuning, the resultant total bandwidth is 14.3672 MHz with a discrepancy of 0.3672 MHz compared to the designed one; the passbands are 9.9727 MHz, and 2.1953 MHz. The maximum rejection is $-7.743$ dB for the first passband and $-24.05$ dB for the second passband. The maximum insertion losses in the passbands are $-0.23$ dB and $-0.279$ dB.

## ACKNOWLEDGMENT

## REFERENCES

1. Hong, J.-S., M. J. Lancaster, D. Jedamzik, and R. B. Greed, "On the development of superconducting microstrip filters for mobile communications applications," *IEEE Trans. on Microwave Theory and Tech.*, Vol. 47, No. 9, 1656–1663, Sep. 1999.

2. Li, H., A. He, S. Li, X. Zhang, C. Li, L. Sun, Q. Zhang, F. Li, Q Luo, C. Gu, and Y. He, "Development of HTS filters for applications in mobile communications, satellite receiver and metrological radar," *International Journal of Modern Physics B*, Vol. 21, No. 18-19, 3266–3269, 2007.

3. Abu Hudrouss, A. M., A. B. Jayyousi, and M. J. Lancaster, "Triple-band HTS Filter using

dual spiral resonators with capacitive-loading," *IEEE on Applied Superconductivity*, Vol. 1, No. 3, 1728–1732, Sep. 2008.

4. Lancaster, M. J., *Passive Microwave Device Applications of High-temperature Superconductors*, 1st Edition, 295–297, Cambridge University Press, UK, 1997.

5. Spares, E. R., K. F. Raihn, A. A. Davis, R. L. Alvarez, P. J. Marozick, and G. L. Hey-Shipton, "HTS AMPS-A and AMPS-B filters for cellular receive base stations," *IEEE on Applied Superconductivity*, Vol. 2, No. 3, 4018–4021, Sep. 1999.

6. Cameron, J. C., "Advanced coupling matrix synthesis techniques for microwave filters," *IEEE Trans. on Microwave Theory Tech.*, Vol. 51, 1–10, Jan. 2003.

7. Jayyousi, A. B. and M. J. Lancaster, "A gradient-based optimization technique employing determinants for the synthesis of microwave coupled filters," *IEEE MTT-S International Microwave Symposium Digest*, 1369–1372, Jun. 2004.

8. Zhou, J., M. J. Lancaster, and F. Huang, "Superconducting microstrip filters using compact resonators with double-spiral inductors and interdigital capacitors," *IEEE MTT-S International Microwave Symposium Digest*, Vol. 3, 1889–1892, Jun. 2003.

9. Hong, J.-S. and M. J. Lancaster, *Microstrip Filters for RF/microwave Applications*, Ch. 8, John Wiley & Sons, Inc., 2001.

10. *EM User's Manual*, Sonnet Software Inc., Version 12, 2009.

# A New Algorithm about Extrapolating Near Distance Field to Far-field of Large Size Antenna

**Yongxin Zhao[1], Jianjun Wei[2], Nan-Jing Li[3], and Chu Feng Hu[3]**

[1]The 46th Middle School of Xi'an, Shaanxi, China
[2]Shaanxi Qiangde Technology Co., Ltd., Shaanxi, China
[3]National Key Laboratory of UAV Specialty Technique, Northwestern Polytechnic University
Xi'an, China

**Abstract**— In order to meet the approximate plane-wave irradiation condition, adequate large field or compact range system is needed for antenna pattern measurement, especially for large size antenna, but an outside testing field site or a compact range system is very expensive. Near-field planar scanning system is another method, however it is time-consuming and only suited for directional antenna. In this paper, a new extrapolating technique by connecting near-distance field with far-field of large-size antenna is set up. If a large size antenna is short in vertical plane, its irradiating field in horizontal plane can be respected as cylinder wave distribution, an ideal aperture as a reference irradiating source is utilized; its width is the maximum size of the tested antenna. In term of the ideal aperture a phase-correction coefficient $g(x)$ connected with spherical and plane wave can be deduced, and used to calculate the far-field of the tested antenna. In fact the convolution calculation between $g(x)$ and near-field can be replaced by Fast Fourier Transform, thus the calculating procedure could be completed simply and quickly. By theoretical simulation for a simple long antenna, the pattern extrapolated can be obtained correctly. Experimental results of complex antenna show that this new technique makes experiment agree to theory precisely, moreover, it permits the measurement distance to be reduced by 15 percent of the minimum distance of far-field. Also, there is no serious limitation of measurement for antenna in dimension of aperture and depth.

## 1. INTRODUCTION

Generally the measurement of antenna pattern needs a huge testing field or complex expensive compact range system [1, 2]. For large size antenna of high frequency, an outside test field site or a compact range system is very expensive. On the other hand, near-field scanning is very time-consuming [3]. In order to solve this problem, a new near-distance test method to extrapolate pattern of antenna with little height is set up in this paper.

Near-distance is defined as the Fresnel zone of the DUT [4].The near-distance antenna measurement system is identical to far-field, but the distance is much shorter, so the testing distance can easily be met and the pattern of antenna is obtained by extrapolating technique. In this paper, the extrapolating technique is described in detail, and the precision, effect and advantages of the technique are discussed.

## 2. THE ARITHMETIC OF EXTRAPOLATING TECHNIQUE

As we know, the electric field can be expressed by vector magnetic potential as following expression:

$$\vec{E} = j\omega \left( \hat{k} \times \hat{k} \times \vec{A} \right) \tag{1}$$

When time dependence is harmonic, the vector magnetic potential $\vec{A}$ at the observation point caused by the surfaced current $\vec{J}$ can be gained in following expression:

$$\vec{A} = \frac{\mu}{4\pi} \int \vec{J} \cdot \frac{e^{-jkR}}{R} dl \tag{2}$$

Equation (2) can be coordinated to the format including Green Function of 2-D free space:

$$A_s^N(k, R_0) = \frac{\mu}{4\pi} \int\limits_V \frac{\sqrt{k} \cdot J(r')}{\sqrt{|R_0 - r'|}} \cdot \frac{e^{-jk|R_0 - r'|}}{\sqrt{k|R_0 - r'|}} dr'$$

$$\approx \frac{\mu}{4\pi} \int\limits_V \frac{\sqrt{k} \cdot g(r')}{|R_0 - r'|^{1/2}} \cdot \sqrt{\pi/2} \cdot e^{-j\pi/4} \cdot H_0^{(2)}(k|R_0 - r'|) dr' \tag{3}$$

In Equation (4), the error can be analyzed by assuming $Ratio = \mathrm{e}^{-\mathrm{j}(kR+\pi/4)}/(\sqrt{\pi kR/2}\mathrm{H}_0^{(2)}(kR))$, let $k = 20$ (when frequency is $1\,\mathrm{GHz}$), distance $R$ varies from $1\,\mathrm{m}$ to $8\,\mathrm{m}$, the result is listed in Table 1.

Table 1: Font sizes for papers approximation error in Equation (3).

| $R$ /m | **2** | **4** | **8** |
|---|---|---|---|
| $kR$ | 40 | 80 | 160 |
| $|Ratio|$ | 1.002 | 1.001 | 1.001 |
| $\arg(Ratio)$/degree | $-0.18$ | $-0.09$ | $-0.05$ |

The relative error of amplitude is lower than $0.02\%$ and the error of phase is lower than $0.5°$. So results from Equation (3) has an excellent precision.

If $R_0 \gg r'_{\max}$, the denominator $|R_0 - r'|^{1/2}$ in Equation (3) can be approximated as $|R_0|^{1/2}$, also named $R_0^{1/2}$. According to the Hankel addition theory:

$$\mathrm{H}_0^{(2)}(k|R_0 - r'|) = \sum_{n=-\infty}^{\infty} \mathrm{H}_0^{(2)}(kR_0)\mathrm{j}_n(kr')\mathrm{e}^{\mathrm{j}n(\varphi_0 - \varphi')} \tag{4}$$

$\mathrm{j}_n(kr')$ is the first Bessel function. Replacing Equation (4) to Equation (3), a series is derived by the following expression:

$$A_s^N(k, R_0) \approx \frac{k}{R_0^{1/2}} \sum_{n=-\infty}^{\infty} \mathrm{H}_0^{(2)}(kR_0)\mathrm{e}^{\mathrm{j}n\varphi_0} \int_V J(r')\mathrm{Besselj}_n(kr')\mathrm{e}^{-\mathrm{j}n\varphi'}\mathrm{d}r' \tag{5}$$

Note $\int_V J(r')\mathrm{j}_n(kr')\mathrm{e}^{-\mathrm{j}n\varphi'}\mathrm{d}r' = S_n^k$, this is the generalized Fourier series of target image, which belongs to inherence scattering characteristic, and it is irrelative to measurement distance. So Equation (5) can be reformatted into Equation (6):

$$A_s^N(k, R_0) \approx \frac{k}{R_0^{1/2}} \sum_{n=-\infty}^{\infty} S_n^k \mathrm{H}_0^{(2)}(kR_0)\mathrm{e}^{\mathrm{j}n\varphi_0} \tag{6}$$

According to the large argument approximation theory in Hankel function, Equation (6) is turned into Equation (7):

$$E_s^F(k, R) \approx \frac{1}{R^{1/2}}\sqrt{\frac{2k}{\pi}}\mathrm{e}^{\mathrm{j}(kR + \frac{\pi}{4})} \sum_{n=-\infty}^{\infty} S_n^k \mathrm{e}^{\mathrm{j}n(\varphi_0 + \frac{\pi}{2})} \tag{7}$$

Connect Equation (6) with Equation (7), the following will be derived:

$$A_s^F(k, R) \approx \int A_s^N(k, R_0) \sum_{n=-\infty}^{\infty} \frac{\mathrm{j}^n \mathrm{e}^{\mathrm{j}n(\varphi - \varphi_0)}}{\mathrm{H}_0^{(2)}(kR_0)}\mathrm{d}\varphi_0 = A_s^N(k, \varphi_0) * \sum_{n=-\infty}^{\infty} \frac{\mathrm{j}^n \mathrm{e}^{\mathrm{j}n(\varphi_0)}}{\mathrm{H}_0^{(2)}(kR_0)} \tag{8}$$

In fact, the series in Equation (8) must be truncated, generally $|n| \leq N_0, N_0 \geq \mathrm{int}(2kD)$, where $D$ is the minimum radius enclosing the DUT.

## 3. SIMULATION AND EXPERIMENTS

A linear antenna with length of 1m works at $10\,\mathrm{GHz}$. Amplitude and phase is constant along the surface of antenna. Its near-distance pattern ($R = 10\,\mathrm{m}$) and extrapolated pattern (far-field) are shown in Fig. 1. As we know, its extrapolated pattern is coincidence with ideal far-field pattern which is a sinc function.

In the experiment, A navigation antenna as DUT, $fr = 1224\,\mathrm{MHz}$, its length is $2.4\,\mathrm{m}$; the testing distance is $17\,\mathrm{m}$, as Fig. 2. The near-distance pattern ($R = 17\,\mathrm{m}$), extrapolated pattern (far-field) and the simulated pattern are shown in Fig. 3, we can find, after extrapolation, the elevation angle becomes lower, and the extrapolated pattern is more slippery than near-distance pattern, and the main lobe becomes narrower, the extrapolated pattern is more coincidence with simulated pattern.

After gain calibration by a standard antenna, the absolute gain of DUT can be calculated. As shown in Fig. 4, the extrapolated gain is $0.56\,\mathrm{dB}$ higher than the near-distance gain.
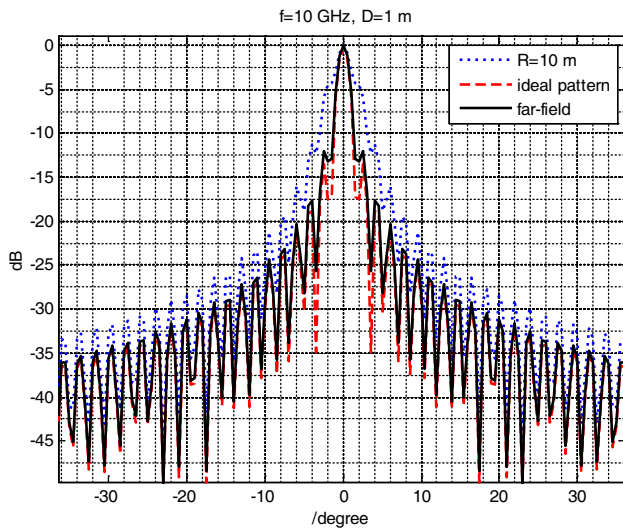
Figure 1: Normalized pattern of a linear antenna.
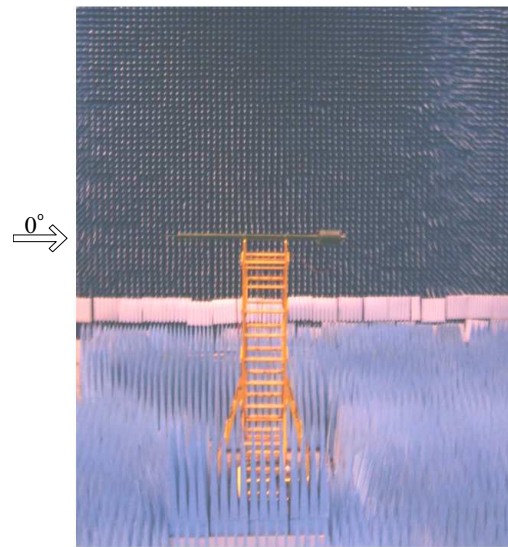


Figure 2: DUT is a navigation antenna.
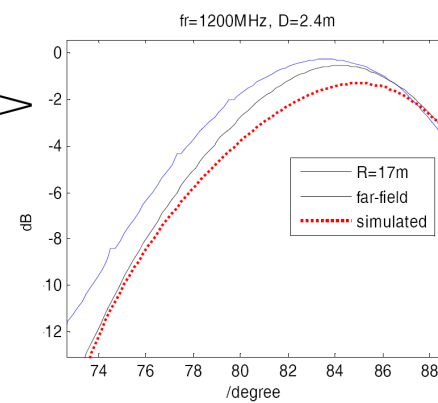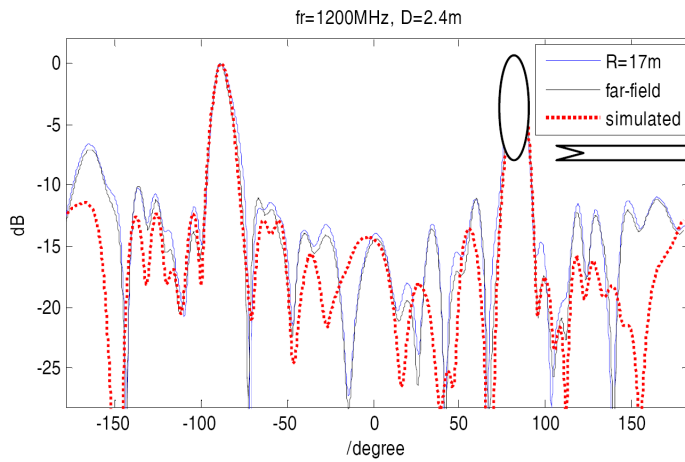


Figure 3: The normalized pattern of DUT.
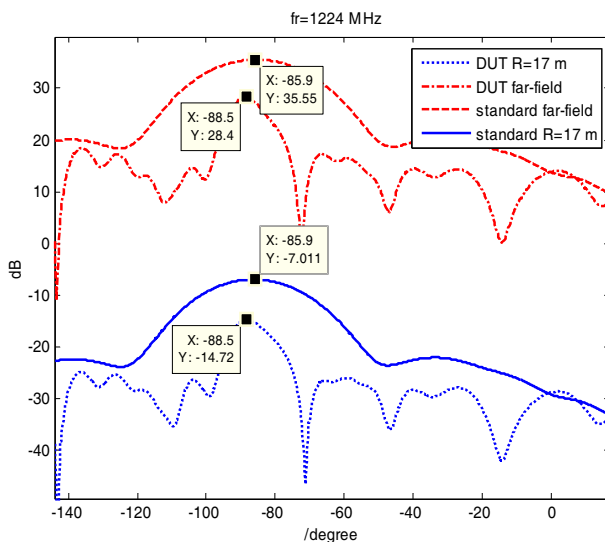


The ideal gain of standard antenna is 15 dBi
Far-field: Gain_DUT=
28.40-35.55+15.00 =**7.85dBi**
Near-diatance: Gain_DUT=
-14.72-(-7.01)+15.00=**7.29 dBi**
△**Gain=0.56 dB**

Figure 4: Gain data from near-distance and far-field.

## 4. CONCLUSION

By simulation validation, the arithmetic of extrapolating technique is accurate enough. By experimental validation, some advantages of extrapolating technique can be found: extrapolated pattern is more slippery, the gain calculation is more accurate.

For low height antenna, extrapolating technique in this paper will be widely useful.

## REFERENCES

1. Johnson, R. C., "Compact range techniques and measurements," *IEEE Trans. on Antenna and Propagation*, Vol. 17, No. 5, 568–576, 1969.
2. Odendaal, J. W., "Radar cross section measurements using near-field radar imaging," *IEEE Trans. on Instrumention and Measurement*, Vol. 45, No. 6, 948–954, 1996.
3. La Haie, I. J., "Overview of an image-based technique for predicting far field radar cross-section from near field measurements," *IEEE Antennas and Propagation Magazine*, Vol. 45, No. 6, 159–169, 2003.
4. La Haie, I. J., "An improved version of the circular near field-to-far field transformation (CNFFFT)," *Proceedings of the 27th Annual Meeting of the Antenna Measurement Techniques Association (AMTA '05)*, 196–201, Newport, RI, 2005.
5. Rice, S. A. and I. J. LaHale, "A partial rotation formulation of the circular near-field-to-far-field transformation (CNFFFT)," *IEEE Antennas and Propagation Magazine*, Vol. 49, No. 3, 209–214, 2007.

# Design of Multi-band Antenna Using Sperrtopf

**Tsutomu Yokoyama[1], T. Hoashi[2], and T. Nakamiya[3]**

[1]Department of General Education, Sojo University, 4-22-1 Ikeda, Kumamoto 860-0082, Japan
[2]Department of Electronics, Computer and Network, Sojo University
4-22-1 Ikeda, Kumamoto 860-0082, Japan
[3]Department of Electronics and Intelligent Systems Engineering, Tokai University
9-1-1 Toroku, Kumamoto 862-8652, Japan

**Abstract**— In this paper, a novel design method for two band antenna using monopole antenna with Sperrtopf for mobile communication and Digital communications System is presented. We made a trial two-band antenna, with operating frequencies of 800 MHz and 2.04 GHz, and examined the design method by the comparing measured VSWR of the antenna with the simulation results using simulation soft WIPL-D Microwave and Nec-2.

The simulation results of the VSWR were in good agreement with the experimental results.

## 1. INTRODUCTION

Multi-functionality and the mass transmission of both still and animated images have become indispensable attributes of telecommunication technology during recent years. In particular, there have been remarkable improvements in mobile phone technology. However, there have been on-going difficulties in making compact antenna with multi band functions.

Up to now, an analysis of linear antenna has been performed using transmission line approximation [1] and integral equations [2, 3]. Egashira et al. showed that current distribution of different radius antenna was represented equivalently by current distribution of the impedance loadings antenna and the characteristics of antennas with wires of different radii could be analyzed using equivalent loaded antennae.

In earlier paper, we proposed a design method for multi-band antenna using wires of different radii [4].

In this paper, we propose a novel design method for two-band antenna using monopole antenna with Sperrtopf. This design method is simple, easy to make and cheap. Firstly, using antenna analysis software Nec-2, we estimated the length and radius of monopole antenna and the position of Sperrtopf necessary for the two operating frequencies of 800 MHz and 2.04 GHz.available on a mobile phone antenna. This frequency band can be applied to a mobile phone antenna. Secondly, the current distribution of this antenna was measured using a shield loop [5] (current probe). Thirdly, we measured the VSWR of the antenna with the network analyzer and compared it with the results obtained using Nec-2. Finally, the radiation pattern of the antenna was obtained using antenna analysis software Microwave.

## 2. DESIGN OF A TWO-BAND ANTENNA

We designed a two-band antenna using a monopole with Sperrtopf for the higher operating frequency bands. Here, we choose the length of Sperrtopf as 1/4 the wave length of the higher band frequency and the parameters of each part of the antenna were chosen as shown in Fig. 1, so as to be smaller than 2.0 for the VSWR of the two band antenna.

Figure 1 shows the structure of the trial two-band antenna constructed using a monopole antenna with Sperrtopf mounted on the horizontal conductive plane. Where $\lambda_1 = 147$ mm and $\lambda_2 = 375$ mm, they represent wavelengths of 2.04 GHz and 800 MHz, respectively. Parameters of this antenna are shown in Fig. 1. These values were selected as the VSWR of the antenna became smaller than 1.5 at operating frequencies. We were approximated to the Sperrtopf as a transmission line of the terminal short-circuits.

Figure 2 shows the VSWR of two band antenna from 700 MHz to 2010 MHz using antenna analysis software Nec-2. The VSWR value at 800 MHz and 2.04 MHz are smaller than 1.5. In this simulation ground plane is infinity.
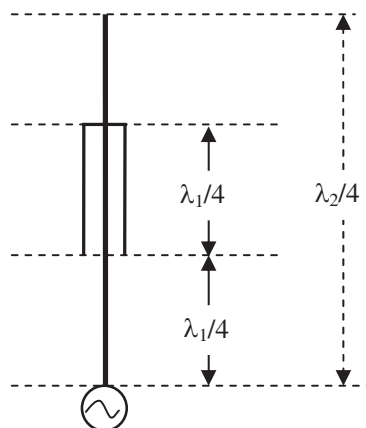
Figure 1: Structure of two band antenna with Sperrtopf.
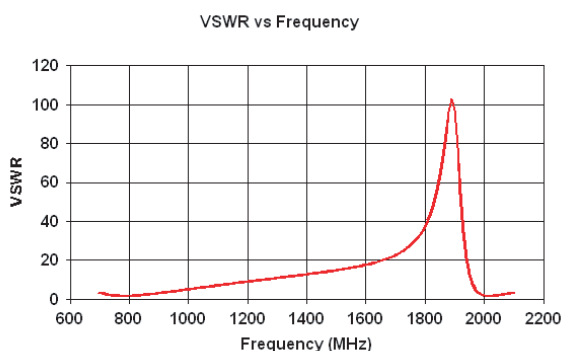


Figure 2: The VSWR of two band antenna of the operating frequencies at 800 MHz and 2.04 GHz.
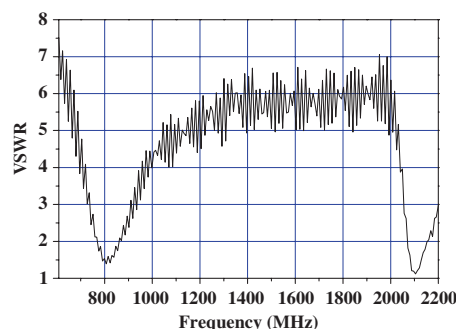


Figure 3: Measurement of VSWR.

## 3. MEASUREMENT RESULTS

### 3.1. Current Distribution Measurement

Figure 4 shows the measurement system of current distribution of the antenna. We measured the current distribution of the test antenna when the operating frequency was 800 MHz.

Signals from the generator were fed in to the antenna, while the same was fed into one channel of the vector voltmeter, as shown in Fig. 4. The other channel of the vector voltmeter was fed by the voltage induced on the shield loop [5–7].

We measured the relative amplitude and the phase of the current distribution on the antenna using the electromotive force induced on the shield loop by moving the shielded loop 5.0 mm along the antenna.

Figure 5 shows the measured relative amplitude of current distribution on the trial antenna. Each marked point represents the measured value of the relative amplitude and phase of the current on the antenna at a distance of a point 4.0 mm from the test antenna center.

### 3.2. VSWR

We measured the VSWR of the trial antenna using a Network Analyzer to examine the characteristics of the antenna and to compare them with the simulation results of the antenna.

Figure 3 shows the measured VSWR of the antenna against the frequency. This antenna has good characteristics at both 800 MHz and 2.05 GHz. It seems that this antenna is suitable for two-band antenna. These operating frequencies agreed well with the frequencies in Fig. 1 estimated using Nec-2 simulation software.

## 4. RADIATION PATTERN

Figure 6 shows the radiation pattern of the test antenna. Here, the feeding point is at the starting point and the antenna is in the direction of the $Z$ axis and the ground is in the $X$-$Y$ plane. We simulated the antenna as shown in Fig. 1, mounting it on an infinite conductive plane.
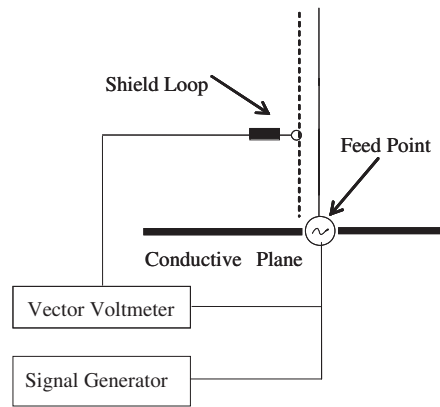
Figure 4: Measurement system of current distribution.
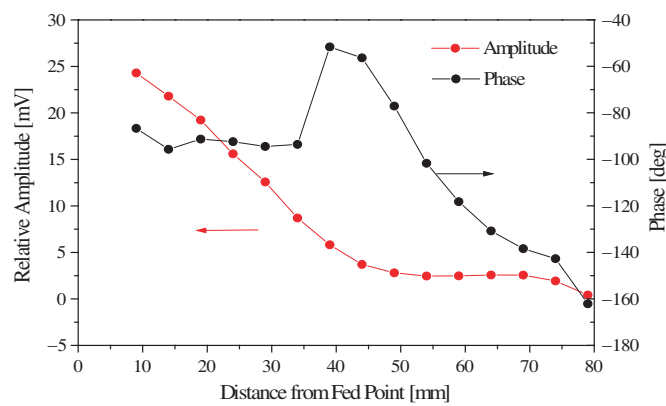


Figure 5: Measurement and simulation of current distribution of test antenna at 800 MHz.
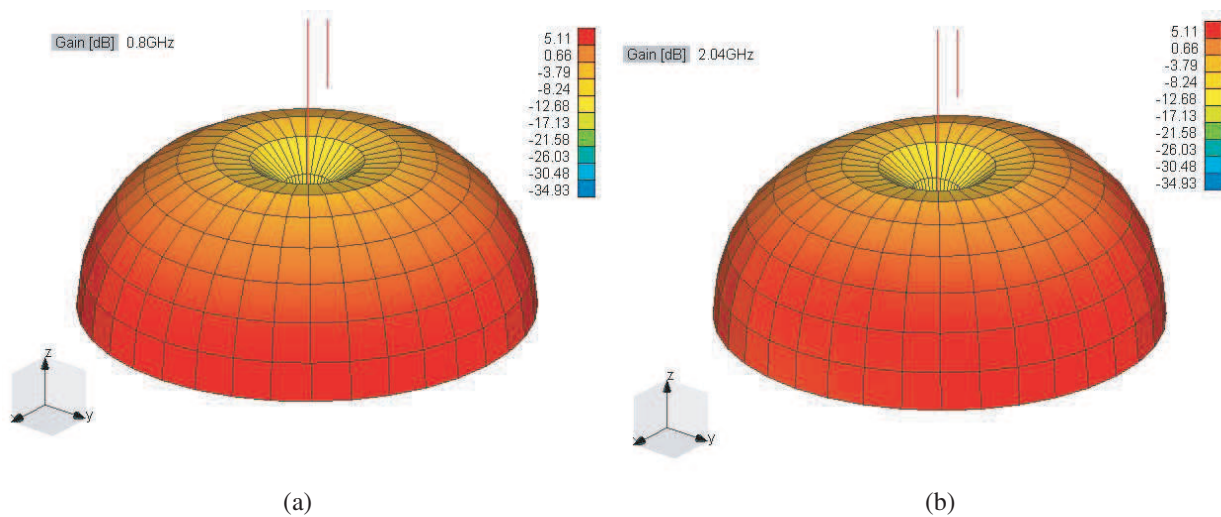


Figure 6: Radiation Patterns of the test antenna at (a) 800 MHz and (b) 2.04 GHz.

## 5. CONCLUSION

A novel design method for two band antennas using monopole antenna with Sperrtopf, operating at 800 MHz and 2.04 GHz suitable for mobile handsets has been proposed. The simulated results for the two operating frequency bands agreed well with measurement results of VSWR and current distribution. These results show that the antennas designed using a monopole with Sperrtopf is good candidates for multi-band antenna applications.

**REFERENCES**

1. Schelkunoff, S. A., *Electromagnetic Wave*, D. Von Nostrand Co. lnc., Chap. 11, 1952.
2. Hallen, E., "Theoretical investigation into the transmitting and receiving qualities of antennas," *Nova Acta Upssala*, Vol. 11, No. 4, 1938.
3. Egashira, S., M. Yaguchi, and A. Sakitani, "Consideration on the measurement of current distribution on bent wire antenna," *IEEE Trans. Antennas Propagat.*, Vol. 6, No. 7, 918–926, July 1988.
4. Yokoyama, T., T. Hoashi, K. Murata, S. Egashira, K. Egashira, and T. Nakamiya, "Design of multi-band antenna using different radius wires," *PIERS Proceedings*, 1273–1276, Beijing, China, March 23–27, 2009.
5. Edwardes, H. N., "The measurement of current distribution in aerials at VHF," *Proceedings of the I.R.E.*, 351–354, Australia, April 1963.
6. Yokoyama. T., K. Koga, and S. Egashira, "Estimation of radiation pattern by near field measurement of linear antenna," *International Conference on Microwave and Millimeter Wave and Millimeter Wave Technology*, 357–360, 2002.
7. Nakamura, T., S. Yamaguchi, T. Yokoyama, and S. Egashira, "Ladder antenna," *3rd International Conference on Microwave and Millimeter Wave Technology*, 396–372, Beijing, August 2002.

# Radiation Patterns of Circumferential-spherical Arrays of Circular Patches

**D. B. Ferreira**, **A. F. Tinoco S.**, and **J. C. da S. Lacava**

Instituto Tecnológico de Aeronáutica, Brazil

**Abstract**— This paper presents an efficient approach for the calculation of the radiation patterns of circumferential-spherical arrays of circular patches. Using the global coordinate system technique and *Mathematica*'s powerful algorithms for calculating spherical harmonic functions, a computationally- efficient CAD was implemented to evaluate the array radiation patterns and its results were compared with those from *HFSS* software.

## 1. INTRODUCTION

Microstrip antennas are customary components in modern communication systems, since they are low-profile, low-weight, low-cost, and well suited for integration with microwave circuits [1]. Antennas printed on planar surfaces or conformed onto cylindrical bodies have been discussed in many publications [1, 2]. However, such is not the case of spherical microstrip antenna arrays, a canonical configuration of great practical interest because of their potential of 360° coverage in any radial direction. Rigorous analysis of such arrays was carried out using the method of moments (MoM) [3, 4]. Nevertheless, the application of the MoM involves high complexity and time-consuming calculations even if only for the far-field evaluation. But, differently from planar and cylindrical geometries, where truncated grounds and diffraction at the edges of the conducting surfaces affect the radiation patterns, thin spherical arrays can be accurately analyzed with the electric surface current model. When associated with the cavity model the radiation patterns can be evaluated, thus avoiding the application of the MoM. As an example of this technique, a two-element array is analyzed for a wide range of patch spacing values and a four-element array is studied in this paper. The arrays results have been validated by comparison with those from *HFSS* version 11.1 package [5].

## 2. SPHERICAL-CIRCULAR CIRCUMFERENTIAL ARRAY

The array geometry under consideration is shown in Fig. 1. It is conformed onto a dielectric layer (of relative permittivity $\varepsilon_r$, magnetic permeability $\mu_0$ and thickness $h$) that covers a ground sphere of radius $a$. The $n$-th circular patch (Fig. 2) whose center is located at $(\alpha, \beta_n)$ is fed by a coaxial probe at $(\theta_{pn}, \phi_{pn})$. The array is embedded in free space of electromagnetic characteristics $\varepsilon_0$ and $\mu_0$. Using the vector-Legendre transformation and a circuit model to evaluate the spectral Green's
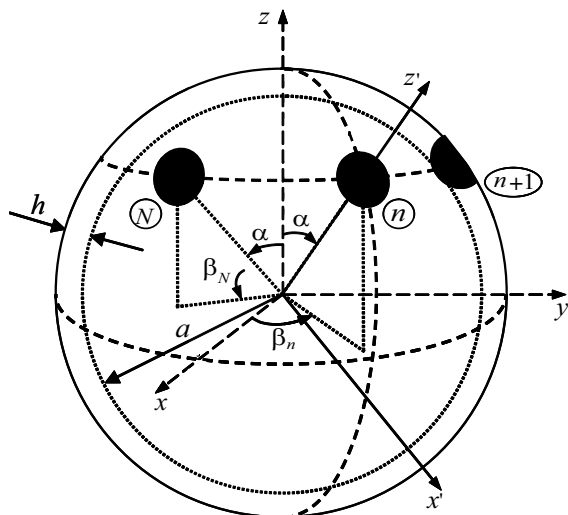


Figure 1: Circumferential-spherical array geometry.
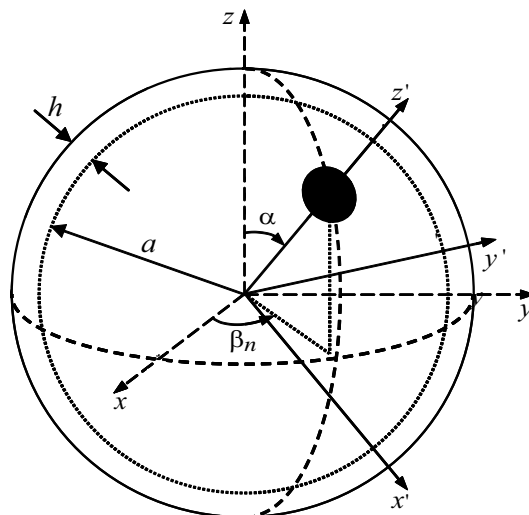


Figure 2: Geometry of the $n$-th spherical-circular array element.

functions, the far-field radiated by each array element can be calculated according to the electric surface current model. In this work, the electric surface current density located on the patch is estimated from the cavity model. However, if this model is applied to the patch geometry of Fig. 2, which is not simmetric with respect to the $z$-axis, the complexity of the numerical calculations increases because, in this case, the associated Legendre functions of the first and the second kinds are both required for characterizing the electric surface current density. To overcome this limitation, the pattern rotation technique is used. Starting from the expressions for $E_{\theta'}(.)$ and $E_{\phi'}(.)$ obtained for a patch located symmetrically in relation to the $z'$-axis (in which case only the function of the first kind is involved) and using the global coordinate system [6], the following expressions for the components of the far electric field radiated by the $n$-th array element are obtained:

$$E_{rot\theta}(\theta, \phi) = A_n E'_\theta(\theta', \phi') - B_n E'_\phi(\theta', \phi'), \tag{1}$$

$$E_{rot\phi}(\theta, \phi) = B_n E'_\theta(\theta', \phi') + A_n E'_\phi(\theta', \phi'), \tag{2}$$

where

$$A_n = [-\cos\theta \sin\alpha \cos(\phi - \beta_n) + \sin\theta \cos\alpha]/\sin\theta', \tag{3}$$

$$B_n = [\sin\alpha \sin(\phi - \beta_n)]/\sin\theta', \tag{4}$$

and $E_{\theta'}(.)$ and $E_{\phi'}(.)$ are given in [7].

To illustrate this approach, a spherical-circular antenna (Fig. 2) is designed to operate at 3.1 GHz (TM$_{11}$ mode), for $h = 0.762$ mm, $\varepsilon_r = 2.5$, $\tan\delta = 0.0022$, $a = 100$ mm, fed at $\theta_{pn} = 27.1°$ and $\phi_{pn} = 0°$, and whose center is positioned at $\alpha = 30°$ and $\beta_n = 0°$. Figs. 3 and 4 show the results obtained with our special-purpose CAD for the radiation patterns in the $xz$- and $yz$-planes compared to those simulated in *HFSS*. As observed, they are in excellent agreement. Having thus validated the radiation pattern rotation procedure, applications for circumferential-spherical arrays are discussed next.

## 3. APPLICATION

The geometry of the spherical-circular circumferential array, whose patches are centered along a $\theta$-constant cone, is shown in Fig. 1. Since for such array there is no diffraction at the edges of the conducting surfaces, and coupling among the array elements can be neglected for radiation pattern purposes, the following expressions for the components of the total radiated far electric field are determined:

$$E_{R\theta}(\theta, \phi) = \sum_{i=1}^{N} A_i E_{\theta_i}(\theta_i, \phi_i) - B_i E_{\phi_i}(\theta_i, \phi_i), \tag{5}$$

$$E_{R\phi}(\theta, \phi) = \sum_{i=1}^{N} B_i E_{\theta_i}(\theta_i, \phi_i) + A_i E_{\phi_i}(\theta_i, \phi_i), \tag{6}$$
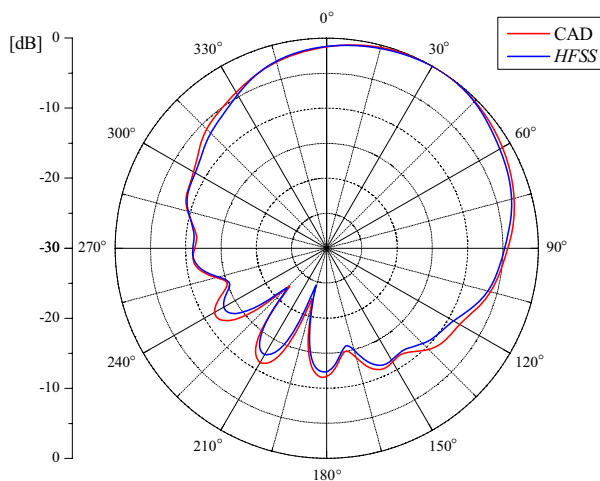


Figure 3: $E_{rot\theta}$ radiation pattern: $xz$ plane.
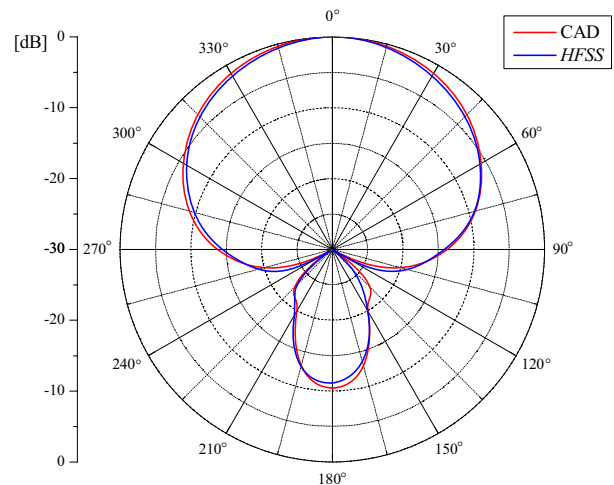


Figure 4: $E_{rot\phi}$ radiation pattern: $yz$ plane.

where the expressions for $A_i$ and $B_i$ are derived from (3) and (4) by replacing $n$ with $i$ and $\theta'$ with $\theta_i$.

As a first application, an array consisting of two spherical-circular elements, as shown in Fig. 5, was designed to operate at 3.1 GHz (TM$_{11}$ mode, $h = 0.762$ mm, $\varepsilon_r = 2.5$, $\tan\delta = 0.0022$ and $a = 100$ mm).

In this case, the elements are fed by identical currents, $\beta_1 = 0°$, $\beta_2 = 180°$ and three values (15°, 45° and 90°) of the angle $\alpha$ were used in order to validate the developed approach over a wide range of patch spacing values. Figs. 6–11 show the results obtained with the special-purpose CAD for the radiation patterns in the $xz$- and $yz$-planes compared to those simulated in *HFSS*. As seen, they are in excellent agreement, even in the case when the patches are closer together ($\alpha = 15°$).

As a second application, the four-element array shown in Fig. 12 is also considered. For this array, $\alpha = 35°$. Results for the radiation patterns are presented in Figs. 13–15. Once again, the radiation patterns generated by the special-purpose CAD and *HFSS* are in excellent agreement. Therefore, the preceding results support the validation of the superposition procedure presented here for the determination of the radiated far field of a spherical circumferential array. Also, the accuracy of these results confirms the assumption made about the mutual coupling among the elements of circumferential arrays being insignificant for the computation of the radiation pattern.
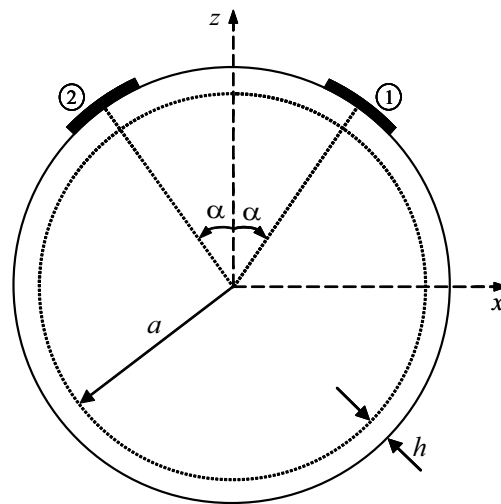


Figure 5: Two-element array: $xz$ plane cut.
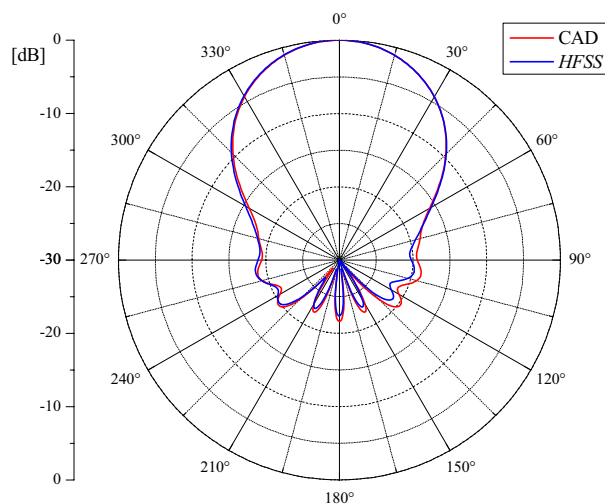


Figure 6: $E_{R\theta}$ radiation pattern: $xz$ plane — $\alpha = 15°$.
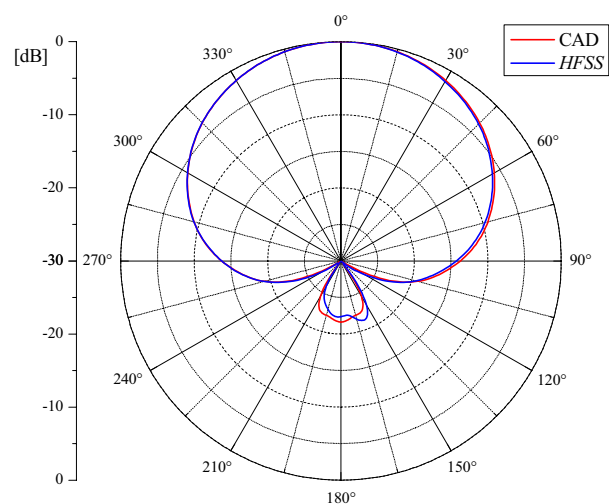
Figure 7: $E_{R\phi}$ radiation pattern: $yz$ plane — $\alpha = 15°$.
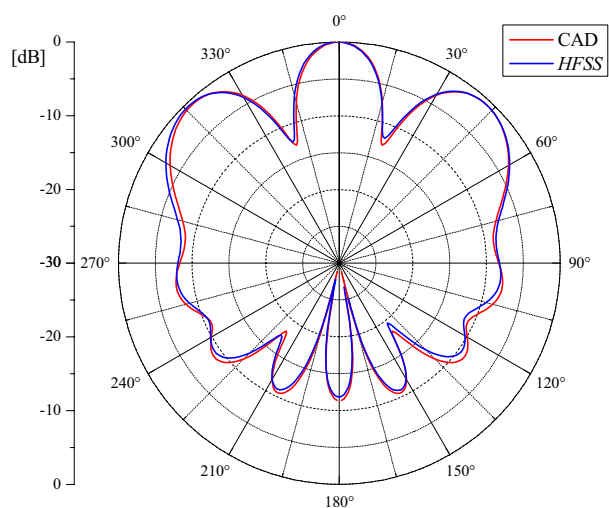
Figure 8: $E_{R\theta}$ radiation pattern: $xz$ plane — $\alpha = 45°$.
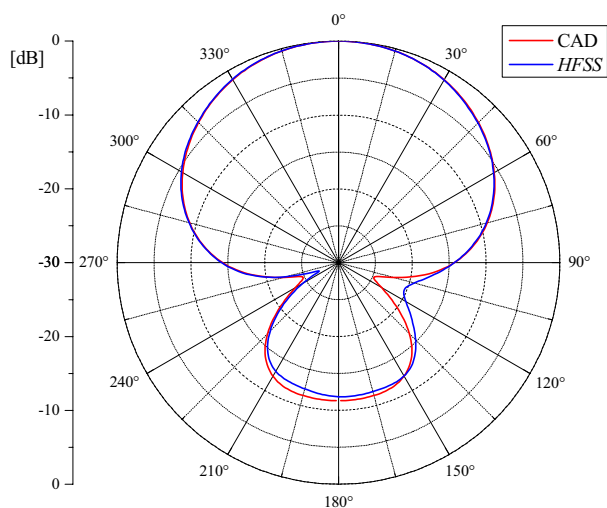


Figure 9: $E_{R\phi}$ radiation pattern: $yz$ plane — $\alpha = 45°$.
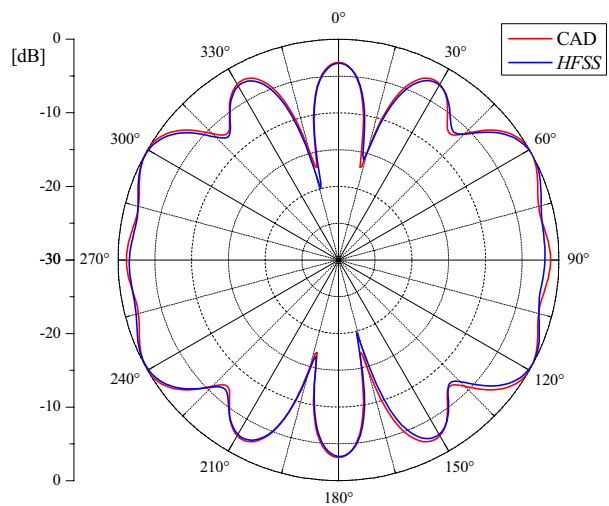


Figure 10: $E_{R\theta}$ radiation pattern: $xz$ plane — $\alpha = 90°$.
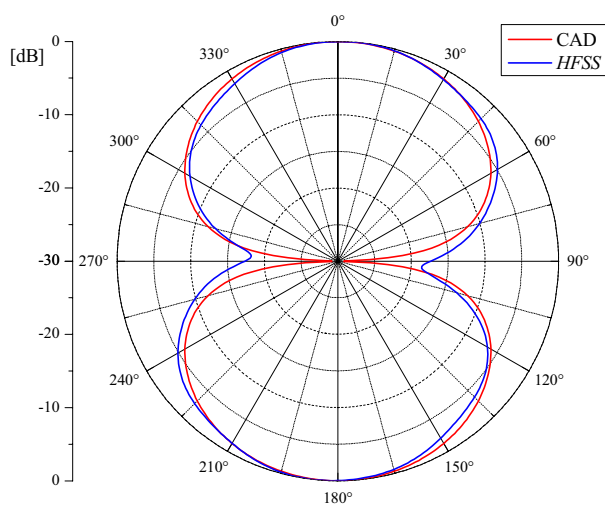


Figure 11: $E_{R\phi}$ radiation pattern: $yz$ plane — $\alpha = 90°$.
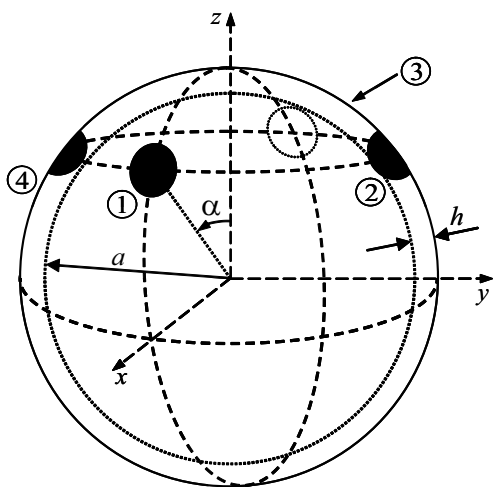


Figure 12: Four-element array.
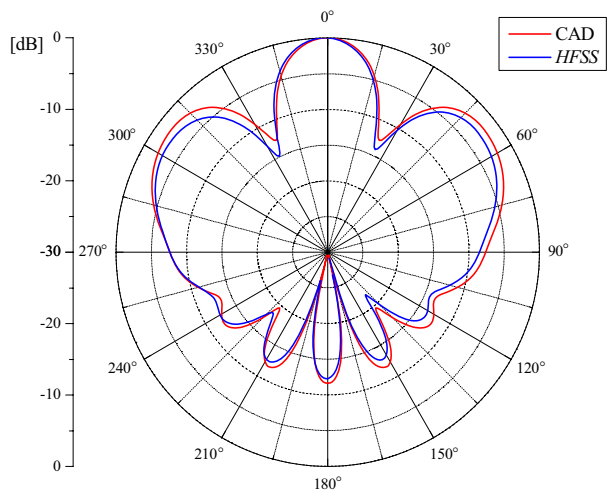


Figure 13: $E_{R\theta}$ radiation pattern: $yz$ plane.
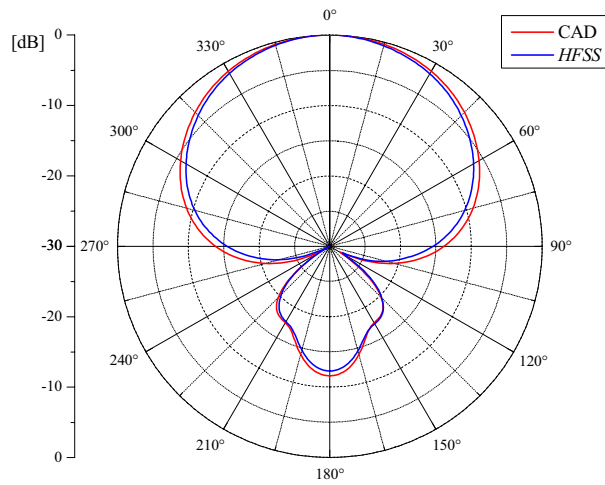
Figure 14: $E_{R\phi}$ radiation pattern: $xz$ plane.
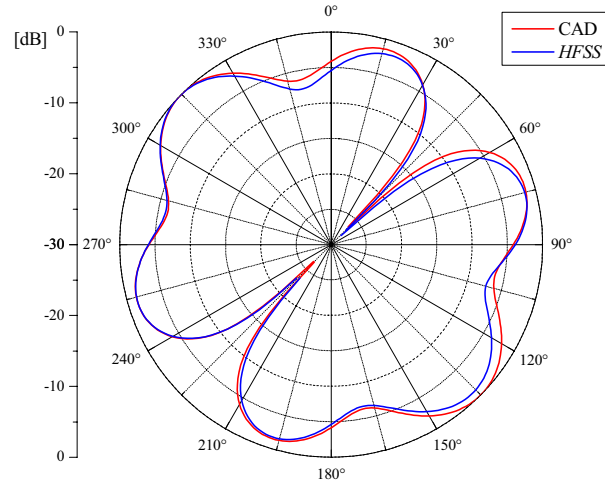


Figure 15: $E_{R\theta}$ radiation pattern: $xy$ plane.

## 4. CONCLUSIONS

An effective procedure to determine the radiation patterns of thin spherical-circular circumferential arrays is presented in this paper. Their computation using a special-purpose CAD software implemented in *Mathematica* proved accurate and numerically efficient when compared to other techniques, such as the finite element method employed by *HFSS*. These advantageous features support the use of the CAD for quick and precise prototyping, hence saving valuable computational time during further optimization with high-performance software such as *HFSS*. In addition, since it requires no powerful computers to run, the CAD is particularly suitable for educational purposes.

### REFERENCES

1. Garg, R., P. Bhartia, I. Bahl, and A. Ittipiboon, *Microstrip Antenna Design Handbook*, Artech House Inc., Norwood, MA, 2001.
2. Wong, K.-L., *Design of Nonplanar Microstrip Antennas and Transmission Lines*, Wiley, New York, 1999.
3. Sipus, Z., N. Burum, S. Skokic, and P.-S. Kildal, "Analysis of spherical arrays of microstrip antennas using moment method in spectral domain," *IEE Proc. — Microw. Antennas Propag.*, Vol. 153, 533–543, 2006.
4. Costa, L. A., "Antenas de microfita esférico-retangulares," M. S. thesis, Universidade Federal de Minas Gerais, Belo Horizonte, Brasil, 2006 (in Portuguese).
5. HFSS, Ansoft Corporation, <www.ansoft.com/products/hf/ansoft_hfss/>.
6. Sengupta, D. L., T. M. Smith, and R. W. Larson, "Radiation characteristics of spherical array of circularly polarized elements," *IEEE Trans. Antennas Propagat.*, Vol. 16, No. 1, 2–7, 1968.
7. Ferreira, D. B. and J. C. S. Lacava, "An efficient approach to the analysis and synthesis of spherical-circular thin microstrip antennas," *Antennas and Propagat. Society Int. Symp.*, Toronto, Canada, July 2010.

# Design of Low-cost Antennas for Globalstar Applications

**Daniel C. Nascimento, R. Schildberg, and J. C. da S. Lacava**

Laboratório de Antenas e Propagação, Instituto Tecnológico de Aeronáutica, Brazil

**Abstract**— A new efficient approach for designing low-cost probe-fed circularly-polarized microstrip antennas for Globastar user terminals is presented in this paper. Instead of the conventional truncated-corner square patch topology, two rectangular patches with truncated corners are utilized here as the receiver and transmitter radiators. Comparisons between experimental and simulated results for axial ratio, input impedance and radiation patterns are presented. Good radiation efficiency is obtained using even the FR4 laminate.

## 1. INTRODUCTION

The last generation of communication satellites supports mobile communication applications, enabling mobile phone operators like Globalstar, among others, to offer global coverage services. This system provides voice and data connections by means of satellite phones, as well as solutions for asset tracking, remote sensing, environmental and geographic monitoring and control of in-field operations by means of the integrated satellite modem. Subscribers have access to the system through LEO (Low Earth Orbit) satellites, operating in a Walter delta constellation [1, 2]. Manufacturing of the second-generation Globalstar satellites proceeds and the constellation deployment is expected to begin in the summer of 2010 [3]. Due to the wide application of this system and the recent expansion of its ground structure, the user terminal antenna is an important development topic. Helical structures can be used as antennas on mobile terminals [4], particularly on cars or trucks, but they tend to be bulky. On the other hand, microstrip antennas are widely used in mobile communication systems, radar systems, and aerospace applications due to their low weight, low profile and easy manufacturing. Thus, a microstrip antenna specifically designed for Globalstar applications, printed on a low-cost FR4 substrate and convenient for series production, is reported in this paper. To improve the radiation efficiency over the uplink ($Tx$: 1.61073 to 1.62549 GHz) and the downlink ($Rx$: 2.48439 to 2.49915 GHz) bandwidths simultaneously, electrically thick substrates ($h = 6.2$ mm) must be used [5]. Consequently the antenna input impedance becomes strongly inductive if the standard design of probe-fed truncated-corner square microstrip patches is followed. To overcome this limitation, two rectangular truncated corner patches are used instead of a square one.

## 2. ANTENNA DESIGN

The antenna design starts from a truncated-corner square microstrip patch, whose initial dimensions can be obtained from the *Estimate* option of *Ansoft Designer* [6]. Then, the geometry shown in Fig. 1, where the transmitting and receiving antennas are both positioned on the same substrate, is created in the *HFSS* [7] environment. In the present case, each antenna is fed by a 50-Ω SMA connector. After that, the patch dimensions are modified following a new approach [5] in order
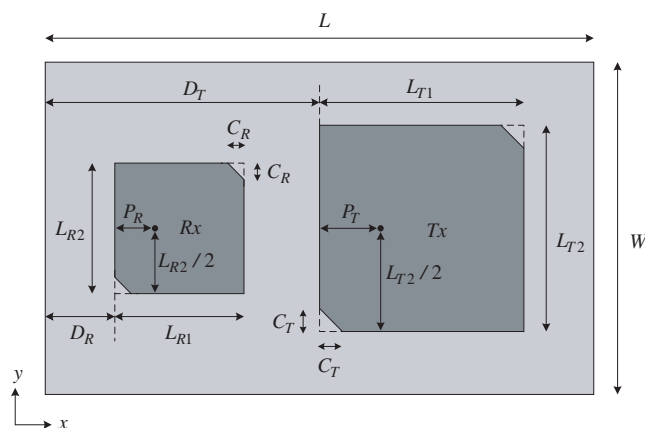


Figure 1: Geometry of the Globalstar antenna.



Figure 2: Globalstar antenna prototype.

Table 1: Optimized antennas dimensions.

| Rx antenna dimensions and probe position. | | Tx antenna dimensions and probe position. | | Ground plane and dielectric dimension. | |
|---|---|---|---|---|---|
| $L_{R1}$ | 27.80 mm | $L_{T1}$ | 43.00 mm | $L$ | 70.00 mm |
| $L_{R2}$ | 24.80 mm | $L_{T2}$ | 41.05 mm | $W$ | 165.00 mm |
| $C_R$ | 6.50 mm | $C_T$ | 7.55 mm | $D_R$ | 18.60 mm |
| $P_R$ | 4.70 mm | $P_T$ | 34.25 mm | $D_T$ | 98.50 mm |
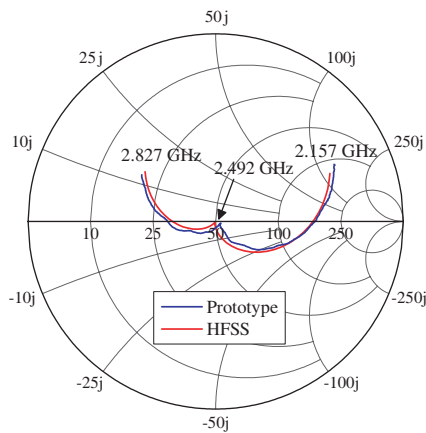


Figure 3: $Rx$ antenna input impedance.
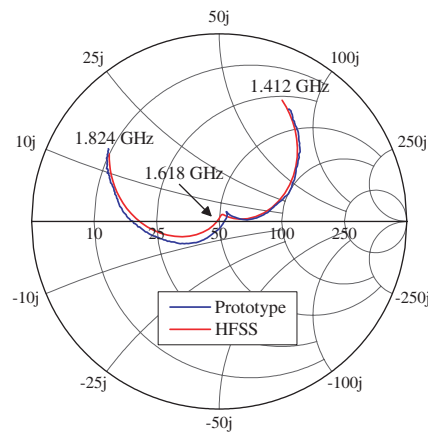


Figure 4: $Tx$ antenna input impedance.
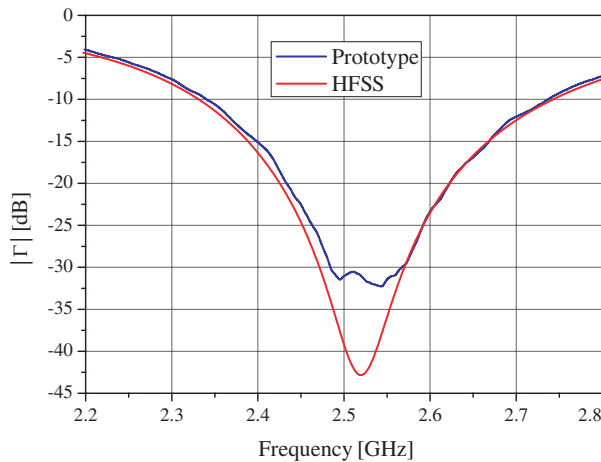


Figure 5: $Rx$ antenna reflection coefficient magnitude.
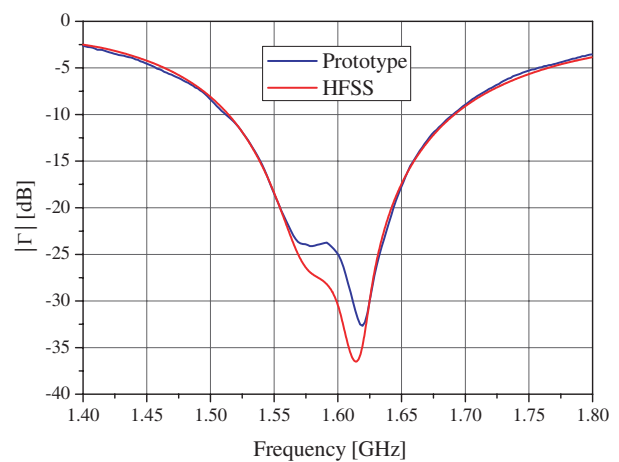


Figure 6: $Tx$ antenna reflection coefficient magnitude.

to optimize the broadside axial ratio (BAR) and the return loss at the operating frequency. Such procedure is described next.

With a 50-Ω load connected to the $Rx$ feeder, the $Tx$ patch is first optimized for the best broadside axial ratio. After that, the 50-Ω load is connected to the $Tx$ feeder and now the $Rx$ patch is optimized. This procedure must be repeated until both antennas reach the desired axial ratio level. At the end, although both antennas exhibit an excellent BAR, their input impedances are highly inductive and can not be perfectly matched to a 50-Ω SMA connector without an external network. To overcome this limitation, the procedure presented in [5] to design a rectangular patch from a square one is applied here in order to obtain the desired BAR and return loss both at the same frequency. The antenna dimensions after such optimization are presented in the Table 1.

## 3. ANTENNA PROTOTYPE AND MEASUREMENTS

A prototype antenna with the optimized dimensions (Table 1) was manufactured (Fig. 2) on FR4 substrate ($\varepsilon_r = 4.465$, thickness = 6.2 mm, and loss tangent = 0.02). Measurements of the input impedances of the receiving ($Rx$) and the transmitting ($Tx$) antennas are shown in Figs. 3 and 4 in comparison with *HFSS* simulations, showing very good agreement.

The reflection coefficient magnitude ($|\Gamma|$) of each antenna is shown in Figs. 5 and 6. It can be seen that the best matching points occur right at the center frequencies of the receiving and the transmitting bands, and that the antennas are properly matched to 50-$\Omega$ SMA connectors. To complete the analysis, the broadside axial ratio and the radiation pattern are analyzed next.

The radiation pattern and the broadside axial ratio were measured in an anechoic chamber: the prototype and the transmitter setup are shown in Figs. 7 and 8. The Globalstar antenna axial ratio measurement assumes its $z$-axis to coincide with the direction of the anechoic chamber transmitter antenna (a linearly-polarized horn antenna). Therefore, rotating the horn antenna around the $z$-axis, the axial ratio value can be obtained from the difference between the maximum and the minimum intensity of the received field. Experimental and simulated results for the $Rx$ antenna are in good agreement, as shown in Fig. 9. As observed, BAR is less than 3 dB over the $Rx$ operating band. The spinning-dipole (SD) radiation pattern is another important parameter related to circularly-polarized antennas. Fig. 10 shows the $Rx$ antenna pattern measured at 2.492 GHz: the antenna under test rotates on the $yz$ plane while the horn antenna rotates around the $z$-axis, at a rate that is 90 times faster than the Globalstar antenna; thus for every 4 degrees of rotation of the Globalstar antenna (on the $yz$ plane) the horn antenna completes a full rotation. For all these measurements, a 50-$\Omega$ load was connected to the feeder of the $Tx$ antenna.

As the *HFSS* software does not generate a SD radiation pattern, a special procedure was de-
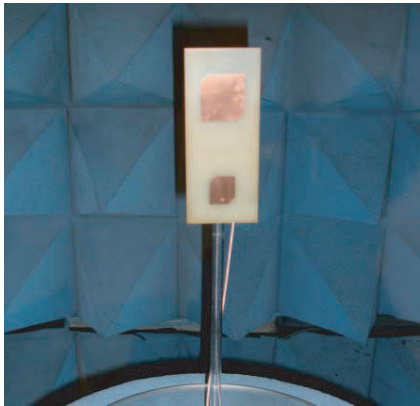


Figure 7: Globalstar antenna in the anechoic chamber.
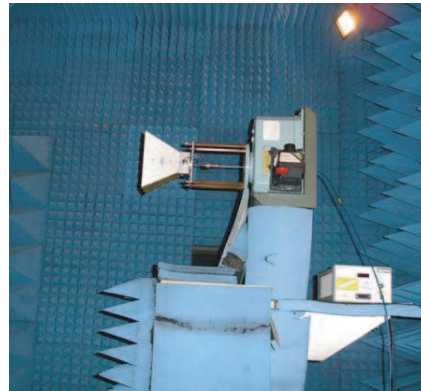


Figure 8: Anechoic chamber: Transmitter setup.
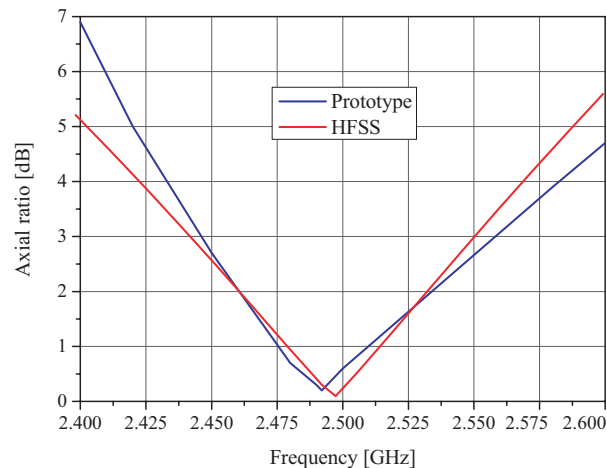


Figure 9: Broadside axial ratio versus frequency for $Rx$ antenna.
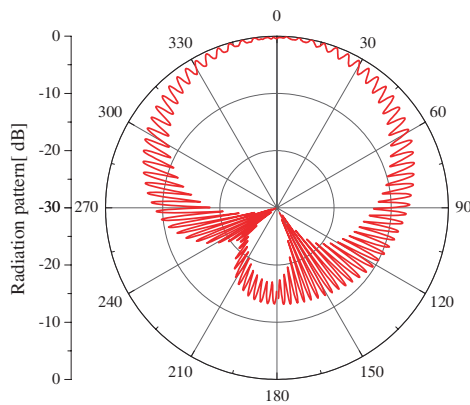
Figure 10: Experimental spinning-dipole radiation pattern: $Rx$ antenna — $yz$ plane.
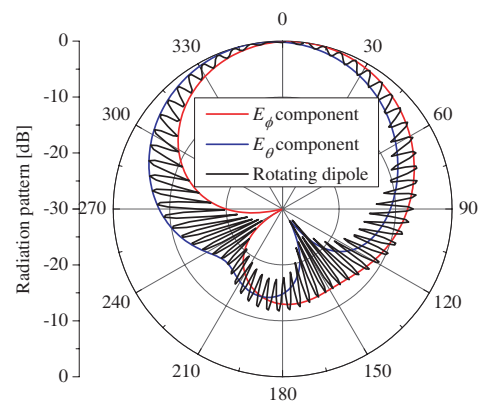


Figure 11: Simulated spinning-dipole radiation pattern: $Rx$ antenna — $yz$ plane.

vised to produce an equivalent pattern. First the magnitude and phase angle of the $E_\theta$ and $E_\phi$ components were extracted from the *HFSS* simulation and then, using the expressions determined in [8] and the *OriginLab* [9] software, the radiation pattern (on the $yz$ plane) shown in Fig. 11 was created. Comparing the patterns so obtained from *HFSS* data to those measured in the anechoic chamber, very good agreement is observed, indicating the beam width is approximated 100 degrees for an axial ratio better than 3 dB. The dissimilarity between the back sides of the patterns is caused by the coaxial cable that runs to the Globalstar antenna feed system. Also, the components $E_\theta$ and $E_\phi$ in Fig. 11 are asymmetrical due to the radiator position over the ground plane and to the substrate thickness. Similar behaviors were equally observed for the $Tx$ antenna. Procedures to overcome these limitations will be presented in future works.

## 4. CONCLUSION

The focus of this paper is on the design of low-cost probe-fed truncated-corner rectangular microstrip antennas for Globalstar user terminals. Using the FR4 laminate for its low cost, acceptable radiation efficiency (close to 70%) and adequate 10-dB return loss and 3-dB BAR bandwidths can be obtained, even for a thick substrate. The adoption of the rectangular truncated-corner geometry, instead of a square one, made it possible to simultaneously obtain the best values of BAR and return loss at the operating frequencies. As the design procedures do not make use of external matching networks, the antenna construction process gets simplified. Experimental and simulated results validate the proposed approach.

## ACKNOWLEDGMENT

## REFERENCES

1. Hui, L. and X. Gu, "Study of termination-concerned routing performance in LEO and MEO satellite communication networks," *ISSCAA*, China, Jan. 2006.
2. Campos, D., L. G. G. Ojeda, V. A. Aquino, and D. B. Lopez, "Satellite indoor mobile communications path propagation losses," *Proceedings of 16th IEEE ICECC*, Mexico, Feb. 2006.
3. GLOBALSTAR, http://www.globalstarusa.com, last access in Jan. 2010.
4. Ho, H. Y. P., "A helical antenna array design for mobile satellite communication system," *Proceedings of the Asia Pacific Microwave Conference*, Hong Kong, China, Dec. 1997.
5. Nascimento, D. C., R. Schildberg, and J. C. S. Lacava, "Design of low-cost microstrip antennas for Glonass applications," *PIERS Online*, Vol. 4, No. 7, 767–770, 2008.
6. Ansoft Designer, Ansys. http://www.ansoft.com/products/hf/ansoft_designer/, last access in Jan. 2010.
7. HFSS, Ansys. Available in http://www.ansoft.com/products/hf/hfss, last access in Jan. 2010.
8. Maciel, D. C. M., "Redes de antenas de microfita circularmente polarizadas com apontamento de feixe e controle de nível de lóbulos secundários," M. Sc. Thesis, ITA, 2005 (in Portuguese).
9. Origin, OriginLab. Available in http://www.originlab.com/, last access in Jan. 2010.

# Miniaturization of a Ultra Wide Band Antenna

**Hyung Kuk Yoon**, **Jin A. Park**, **Yohan Lim**, **Young Joong Yoon**, **and Cheon-Hee Lee**
Yonsei University, South Korea

**Abstract**— In this paper, a research on the miniaturization of UWB antenna is presented. The main concept is to secure current paths to support additional resonance mode over wide bandwidth using tapering, modified sleeve and truncated ground plane. It is designed in the frequency band of 2.9–9.1 GHz to support UWB services. The proposed antenna has a dimension of $10 \times 8 \times 0.652\,\text{mm}^3$ and the ground size of $30 \times 30\,\text{mm}^3$. Since the proposed antenna has printed structure and very compact size, it can be easily integrated with the other RF circuit.

## 1. INTRODUCTION

These days, short-range high data-rate wireless communications is applied in multimedia device. UWB radio technology can meet these requirements and has been studied since 2000 [1]. The good performances of the antenna such as gain, radiation pattern and impedance matching are required to be almost consistent along the whole operating band [2]. Because of the demands for small devices, small and compact UWB antenna is needed. In the UWB systems, accordingly, the dimension of the antennas is important part [2, 3].

Recently, demanding for small devices such as mobile device application is promising, antenna size should be miniaturized to apply various applications in spite of the degrading some performances [4, 5]. So, the researches on very compact UWB antenna are investigated and most of the results has compact dimension by using high dielectric constant material, but also has additional matching circuit, parasitic patch or unstable antenna performance such as gain, radiation pattern [5].

As shown in the previous researches, reducing the size of the antenna causes bad effect on the antenna performances such as impedance matching, impedance bandwidth, stable gain, and radiation efficiency [6, 7]. So, when the antenna is designed, the trade of between antenna size and performance should be considered [2].

In this paper, a miniaturized ultra wide band antenna with enhanced performances is proposed. The main concept of the proposed antenna is to secure current paths to support additional resonance mode over wide bandwidth using tapering, modified sleeve and truncated ground plain. It is designed in the frequency band of 2.9–9.1 GHz to support UWB services. The proposed antenna has a very compact dimension of $10 \times 8 \times 0.652\,\text{mm}^3$. Also, no additional impedance-matching circuit is required so that the occupied length of the antenna on PCB is very small. Measurements of the return loss and antenna patterns of the antenna mounted on PCB have been performed, which show good agreements with the CST microwave studio simulations. The bandwidth of the antenna for $-10\,\text{dB}$ return loss is approximately 6 GHz (3 GHz–9 GHz), which can be applied in the UWB communication system.

## 2. ANTENNA DESIGN

Figure 1 shows the geometry of the antenna which is fed by microstrip line. Empirically the effect of tapering angle denoted on the return loss is studied and this simulation results are shown in Fig. 2. As the tapered angle is wider the matching condition in the low frequency band is better [8, 10].

Figure 3 shows the geometry of the antenna fed by tapered microstrip. Numerically the effect of feeding tapering angle (denoted $W_t$) on the return loss is studied and the simulation results are shown in Fig. 4. As the angle is rapid, the matching condition in the low frequency band is better [8, 9].

Truncated ground plane is also used to broaden the bandwidth. The truncated ground plane is playing an important role in the broadband characteristics of this antenna, because it helps matching the patch with the feed line in a wide range of frequencies. This is because the truncation creates a capacitive load that neutralizes the inductive nature of the patch to produce nearly-pure resistive input impedance [1].

It can be seen that the length $G_t$ slightly affects the impedance matching especially at higher frequencies. However, the effect on the impedance bandwidth is negligible if the length $G_t$ is more
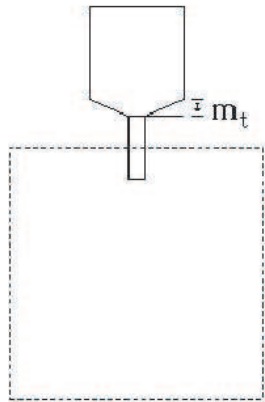
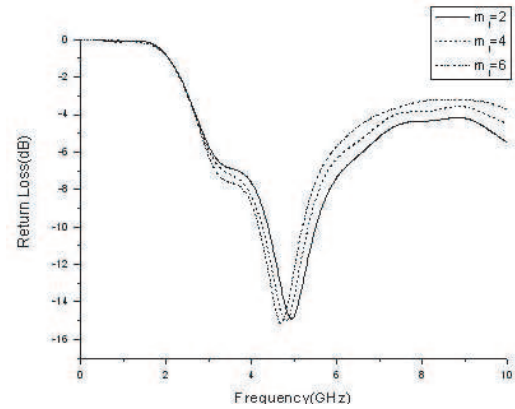Figure 1: The tapered monopole antenna.



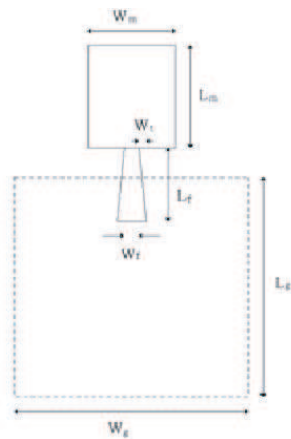Figure 2: Return loss characteristic with respect to the antenna tapering angle.



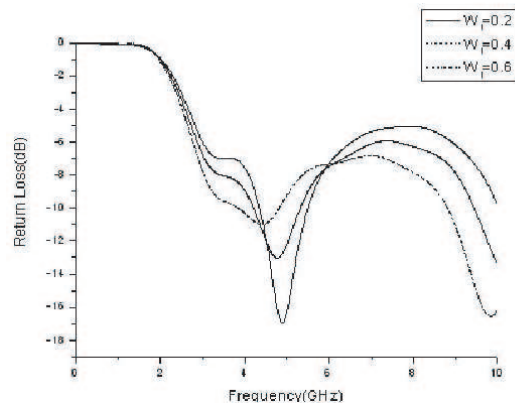Figure 3: The monopole antenna with tapered feed line.



Figure 4: Return loss characteristic with respect to the feed tapering angle.
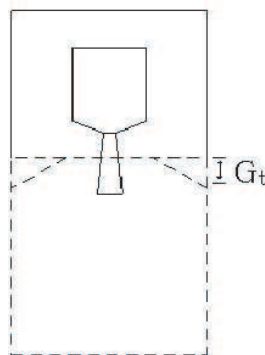


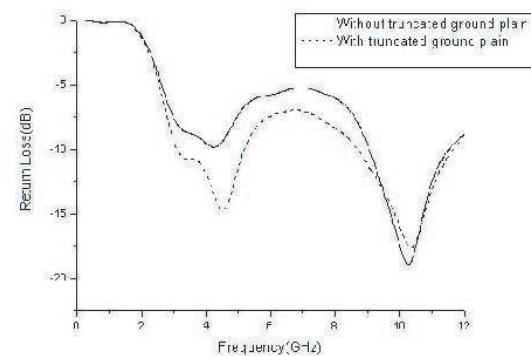Figure 5: The monopole antenna with truncated ground.



Figure 6: Return loss characteristic via angle of the truncated angle ($G_t = 4$).

than 5 mm. The features of small size and independence of the impedance bandwidth on the length of the ground plane make it easy to integrate with other RF circuits [2].

Generally, the sleeve can be treated as an extension of the ground plane. It is equivalent to place a "virtual source" located on the top of the sleeve, and thus an additionally resonant mode is excited above the fundamental mode when the sleeves are added to the tapering monopole antenna. With a proper selection of the sleeves, two resonant modes can be introduced at the close frequencies with the good impedance matching, and results in a wide-band performance [11, 12]. From the CST microwave studio simulation, it is observed that the broadest impedance bandwidth is achieved by using sleeves of 1.8 mm height as shown in Fig. 7. A quite wide bandwidth (more than 4 GHz) can

be realized while $S_w$ is 1 mm. Therefore, the optimum $S_l$ and $S_w$ are both chosen as 1 mm.

Figure 9 shows the geometry of proposed antenna. As shown in Fig. 9, the radiating element is a slotted patch with a bevel and fed by a half coplanar waveguide. Four slots are inserted into the radiator to obtain broadband impedance matching adjusting current paths. The radiating element is printed on the surface of a high dielectric substrate, Rogers RO3010, whose thickness is 0.635 mm and dielectric constant is 10.2, and the ground plane, and the signal line are printed FR4 with thickness 1 mm, dielectric constant of 4.6.
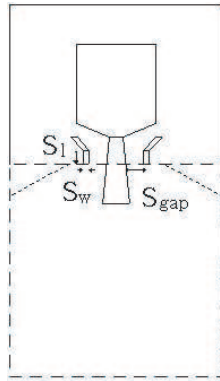


Figure 7: The monopole antenna with modified sleeve.
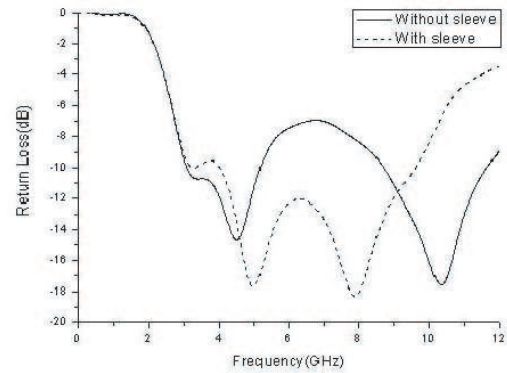


Figure 8: Return loss characteristic with respect to sleeve.
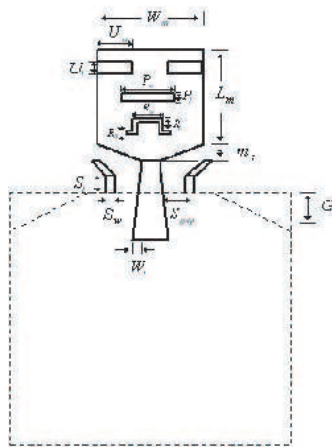


Figure 9: Proposed antenna.
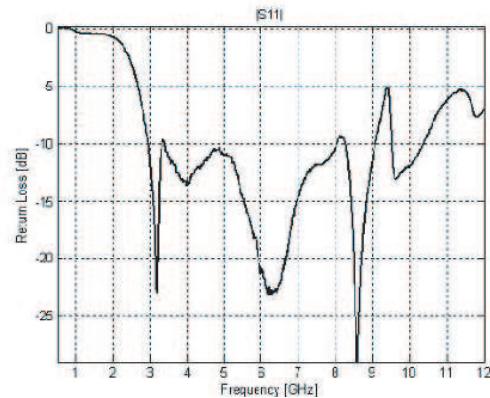


Figure 10: Return loss characteristics of the proposed antenna (measured).

## 3. CONCLUSION

In this paper, a research on the miniaturization of UWB antenna is presented. To miniaturize UWB antenna, tapering, modified sleeve and truncated ground plain are used. Also, some slots are inserted into the monopole. The proposed antenna has a dimension of $10 \times 8 \times 0.652$ and the ground size of $30 \times 30 \, \text{mm}^3$. From the measurement, the impedance bandwidth with respect to return loss less than $-10 \, \text{dB}$ is 2.9–9.1 GHz. The measured radiation pattern of the proposed antenna is in a good agreement with the simulated one. The maximum gain of the monopole prototype is 2.4 dBi. It is expected to be used in various applications of UWB systems. It can enhance the antenna performance for applications that be operated in different frequency band.

**REFERENCES**

1. Wu, C. Y., C. L. Tang, and A. C. Chen, "Compact surface-mount UWB monopole antenna for mobile applications," *PIERS Online*, Vol. 2, No. 2, 150–152, 2006.
2. Radiom, S., H. Aliakbarian, G. Vandenbosch, and G. Gielen, "Miniaturization of UWB antennas and its influence on antenna-transceiver performance," *Proceedings of IWAT2008*, Chiba, Japan, 2008.
3. Park, J. A., H. K. Yoon, Y. J. Yoon, and C.-H. Lee, "A compact polarization diversity antenna for UWB systems," *Asia-Pacific Microwave Conference Proceedings*, Vol. 12, No. 18, 2008.
4. Lee, J. N. and J. K. Park, "Compact UWB chip antenna design using the coupling concept," *Progress In Electromagnetics Research Symposium*, 341–351, 2009.
5. Jung, J., Y. Kim, H. Lee, and Y. Lim, "Analysis and design of stacked helix chip antenna," *Inst. Electron. Eng. Korea 43-TC*, 216–220, 2006.
6. Kwon, D.-H. and Y.-J. Kim, "GA small ceramic chip antenna for ultra-wideband systems," *2004 UWBST & IWUWBS Proceedings*, 2004.
7. Jung, J., Y. Kim, H. Lee, and Y. Lim, "Analysis and design of stacked helix chip antenna," *Inst. Electron. Eng. Korea 43-TC*, 216–220, 2006.
8. Go, H.-C. and Y.-W. Jang, "Multi-band modified fork shaped microstrip monopole antenna with ground plane including dual-triangle portion," *Electronic Letters*, Vol. 40, No. 10, May 2004.
9. Hammoud, P. P. and F. Colomel, "Matching the input impedance of a broadband disc monopole," *Electronics Letters*, Vol. 29, 406–407, Feb. 1993.
10. Agarwall, N. P., G. Kumar, and K. P. Ray, "Wide-band planar monopole antennas," *IEEE Trans. Antennas Propagation*, Vol. 46, No. 2, 294–295, 1998.
11. Moon, J. I., S. O. Park, and K. Y. Park, "Broadband sleeve monopole type antenna for dual-band PCS/IMT-2000," *Electronics Letters*, Vol. 36, 1829–1830, 2000.
12. Ali, M., S. S. Stuchly, and K. Caputa, "A wideband dual meander sleeve antenna," *Antennas and Propagation Society International Symposium*, 1124–1127, 1995.

# Bandwidth Estimating Strategy for a 2-Layer Rectangular Suspended Microstrip Antenna

**Laila F. Marzall[1] and J. C. da S. Lacava[2]**

[1]TSM Antennas, Brazil
[2]Laboratório de Antenas e Propagação, Instituto Tecnológico de Aeronáutica, Brazil

**Abstract**— This paper presents a strategy for estimating the impedance bandwidth of linearly-polarized suspended microstrip antennas. Based on the cavity model and conformal mapping method (used for calculating the effective permittivity of a two-layer microstrip line), an iterative algorithm was implemented in *Mathematica* for estimating the air gap thickness. Results are compared with *HFSS* simulations in order to validate the proposed procedure.

## 1. INTRODUCTION

Suspended microstrip antennas are an effective design option when features like a wide impedance bandwidth (BW), high input power and low cost are required altogether for the same structure [1]. Its design consists of introducing between the ground and the suspended substrate an air gap, whose thickness defines the antenna's impedance behavior and, consequently, determines its BW. Nowadays, although antenna designers may be aided by commercial software like the *HFSS* package [2], the procedure for determining the air gap thickness to achieve a specified BW can become a tedious iterative process, as full-wave simulators are used to evaluate the antenna's current distribution and from there its input impedance and BW. Consequently, a simplified model to assist designers in establishing the initial substrate and air gap thickness can be instrumental for attaining the desired BW faster. Therefore, this paper presents a strategy for estimating the impedance bandwidth of a probe-fed linearly-polarized (LP) rectangular suspended microstrip patch based on cavity model and the conformal mapping method (in order to calculate the effective permittivity of a two-layer microstrip line [3]). With this intent, an algorithm has been implemented in *Mathematica* [4] for estimating the 10-dB return loss BW. For validation purposes, a set of rectangular patches printed on a thin substrate is analyzed.

## 2. THEORY

The geometry of a typical probe-fed LP suspended microstrip antenna is shown in Fig. 1. The rectangular patch, whose dimensions are designated by $L$ (patch length) and $W$ (radiating edge width), is printed on a suspended dielectric substrate of thickness $h_{s1}$. An air-gap of thickness $h_{gap}$ separates the substrate from the ground plane. According to [5], the antenna impedance bandwidth can be expressed in terms of its quality factor ($Q$) and the maximum allowable standing wave ratio ($\rho$) as follows,

$$BW = \frac{1}{Q} \frac{\rho - 1}{\sqrt{\rho}}.$$

In general, the $Q$-factor can be calculated from

$$Q = \frac{2\omega_0 W_E}{P_d + P_c + P_r},$$

where $P_d$ denotes the power absorbed by the dielectric, $P_c$ the metallic losses, $P_r$ the radiated power, $W_E$ the time-average electric energy, $\omega_0 = 2\pi f_0$ and $f_0$ is the operating frequency.

For single-layer thin microstrip antennas, simple analytical expressions for $P_d$, $P_c$ and $W_E$, derived from the cavity model, are well known [6]. Unfortunately, equivalent expressions for two-layer structures are not straightforward. However, using conformal mapping to calculate the effective permittivity of a two-layer microstrip line and the cavity model technique, the expressions for $P_d$, $P_c$, $P_r$ and $W_E$ can be obtained. Table 1 shows the normalized functions evaluated for the suspended geometry presented in Fig. 1, where $R_s$ is the surface resistance, $h = h_{s1} + h_{gap}$, Si(.) denotes the sine integral function, $\varepsilon_0$, $\mu_0$, $\eta_0$ and $k_0$ are the free space electric permittivity, magnetic permeability, intrinsic impedance and wave number, $\delta_d$ and $\varepsilon_r$ are the dielectric loss tangent and relative permittivity, respectively.
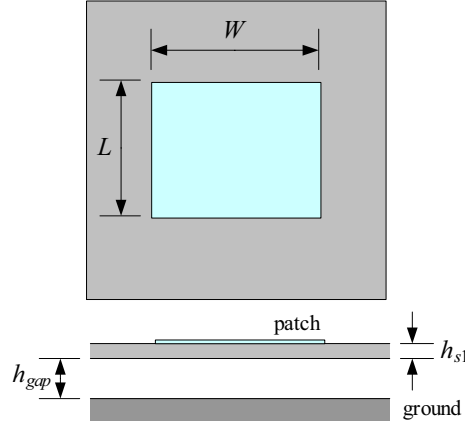
Figure 1: Suspended microstrip antenna geometry.

Table 1: Normalized expressions for $P_d$, $P_c$, $P_r$ and $W_E$ in case of suspended antennas.

| | |
|---|---|
| $P_d = \frac{\omega_0 \varepsilon_0 \varepsilon_r \delta_d}{4} \left( W_{ef} h_{s1} L \right)$ | $P_c = \frac{R_s}{2} \left( \frac{\pi}{2L\omega_0\mu_0} \right)^2 W \left( L + h \right)$ |
| $P_r = \frac{k_0 W}{\pi \eta_0} h^2 \left( \frac{\cos\ (k_0 W) - 1}{k_0 W} + Si\ (k_0 W) - \frac{1}{k_0 W} \left( 1 - \frac{sin(k_0 W)}{k_0 W} \right) \right)$ | $W_E = \frac{\varepsilon_0 \varepsilon_{ref}}{8} \left( W_{ef} h L \right)$ |
| $W_{ef} = W + \frac{2h}{\pi} \ell n \left[ 17.08 \left( \frac{W}{2h} + 0.92 \right) \right]$ | $\varepsilon_{ref} = 1 - q_1 - q_2 + \varepsilon_r \frac{(q_1 + q_2)^2}{q_2 + \varepsilon_r q_1}$ |
| $q_1 = \frac{1}{2} \frac{h_1}{h} \left( 1 + \frac{\pi}{4} - \frac{h}{W_{ef}} \ell n \left[ \frac{\pi}{h} W_{ef} \frac{sin\left( \frac{\pi}{2} \frac{h_1}{h} \right)}{\frac{\pi}{2} \frac{h_1}{h}} + \cos\ \left( \frac{\pi}{2} \frac{h_1}{h} \right) \right] \right)$ | $q_2 = 1 - q_1 - \frac{1}{2} \left( \frac{\ell n \left[ \frac{\pi}{h} W_{ef} - 1 \right]}{\frac{W_{ef}}{h}} \right)$ |

It is worth mentioning that, to further simplify this approach, the two-slot model customarily used for describing the standard rectangular microstrip antenna radiation mechanism [7] was utilized for calculating the radiated power, under the assumption of uncoupled slots (i.e., two isolated slots).

## 3. VALIDATION PROCEDURE

Using the expressions presented in Table 1, an iterative algorithm was implemented in *Mathematica* for estimating the 10-dB return loss bandwidth of suspended microstrip antennas. For validation purposes, a set of rectangular patches printed on a thin substrate ($h_{s1} = 1.524\,\text{mm}$) was designed in *HFSS* package to operate at 2.45 GHz. The thickness of the air-gap layer ($h_{gap}$) was swept between 1 and 9 mm. Table 2 shows the substrate characteristics. The patch dimensions ($w_p$, $l_p$, and, $y_p$) were defined under the zero-input-reactance ($X_{in} = 0$) design criteria. The *HFSS* simulations and the estimated results are compared in Figs. 2–4. As seen, they are in good agreement.

Table 2: Suspended substrate characteristics.

| | Suspended substrate | $\varepsilon_r$ | $\delta_d$ | $h_{s1}$ (mm) | $h_{gap}$ (mm) |
|---|---|---|---|---|---|
| 1 | Arlon CuClad 250GX | 2.5 | 0.0022 | | |
| 2 | Arlon AR450 | 4.5 | 0.0026 | 1.524 | 1 to 9 |
| 3 | Rogers RT Duroid 6010 | 10.2 | 0.0023 | | |

## 4. APPLICATION

Based on IEEE 802.11b (2.4–2.4835 GHz) protocol and ETSI EN 301 525 V1.1.1 (2000-06) standard, the project of a suspended antenna is presented here as an application of the proposed strategy. The element so designed can also be used in a low-cross-polarization LP array [1]. Fig. 5 shows the multilayer structure under consideration, which utilizes three types of PCB laminates: Arlon CuClad 250GX ($h_{s1} = 1.524\,\text{mm}$) for the patch ($w_p = 58.7$, $\lambda_p = 46.1$ and $y_p = 15.8\,\text{mm}$, based on the zero-input-reactance condition), Arlon AR450 ($h_{s2} = 1.1938\,\text{mm}$) for the array beam-forming feed network (BF), and FR-4 for the reflector ($w_r = 100\,\text{mm}$, $\lambda_r = 100\,\text{mm}$ and $h_r = 1.6\,\text{mm}$). In this particular configuration, the patch is directly fed by a 50-$\Omega$ coaxial probe at $x = 0$ and $y = -(\ell_p/2 - y_p)$. Moreover, the element must operate at 2.45 GHz and cover the aforementioned
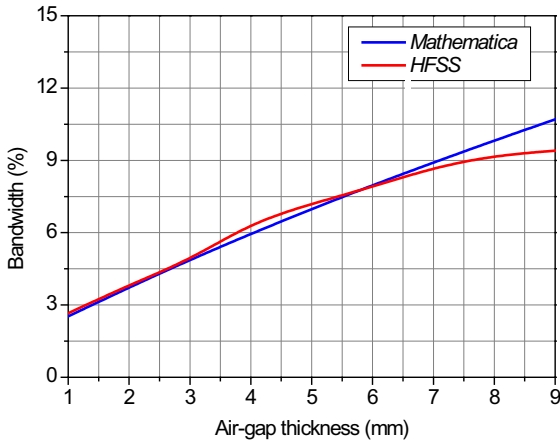
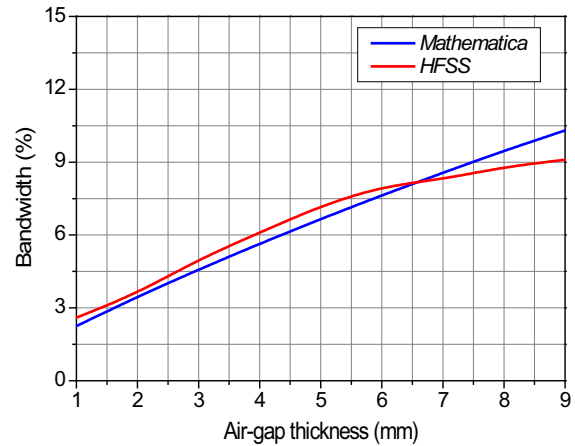Figure 2: Suspended antenna bandwidth versus air gap thickness: $\varepsilon_r = 2.5$ e $h_{s1} = 1.524\,\mathrm{mm}$.



Figure 3: Suspended antenna bandwidth versus air gap thickness: $\varepsilon_r = 4.5$ e $h_{s1} = 1.524\,\mathrm{mm}$.
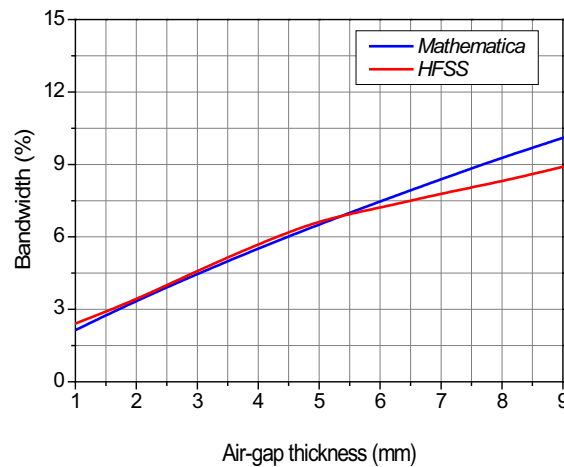


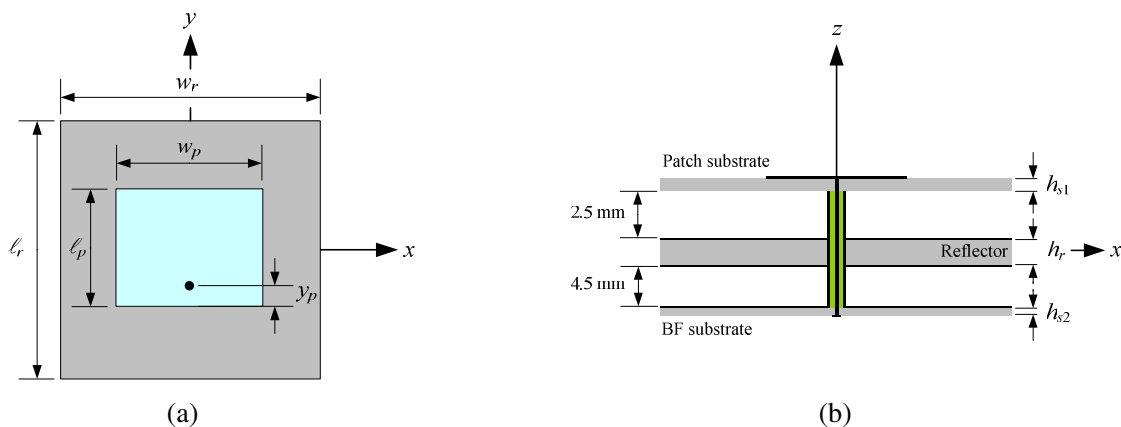Figure 4: Suspended antenna bandwidth versus air gap thickness: $\varepsilon_r = 10.2$ e $h_{s1} = 1.524\,\mathrm{mm}$.



Figure 5: Suspended microstrip antenna geometry: (a) top view, (b) side view.

bandwidth. To comply with the ETSI standard requirements, the air gap thickness for a 4.4-% BW design criterion was estimated, with the iterative *Mathematica*-based algorithm, to be $h_{gap} = 2.5\,\mathrm{mm}$. The resulting multilayer structure was then analyzed with the *HFSS* package. Results for the reflection coefficient magnitude (assuming a 50-$\Omega$ SMA connector feeding the array) are shown in Fig. 6. As seen, a 2.5-mm air gap results in 4.8-% BW under 10-dB return loss condition, close to the starting value of 4.4% used for estimating the air gap thickness.
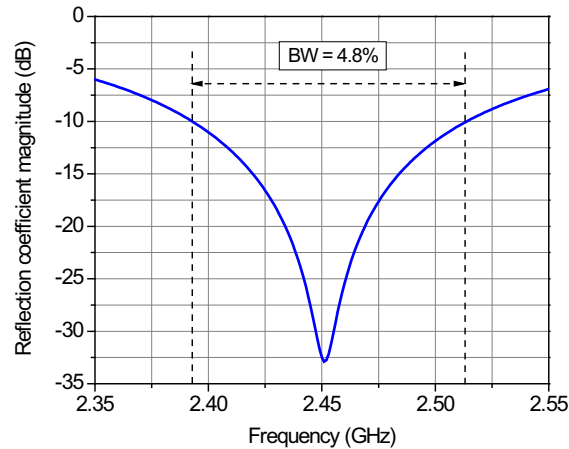
Figure 6: Reflection coefficient magnitude: note the bandwidth symmetry with respect to the operating frequency.

## 5. CONCLUSIONS

An effective model for estimating the impedance bandwidth of a probe-fed linearly-polarized rectangular suspended microstrip antenna is proposed. It utilizes the cavity model and conformal mapping for calculating the effective permittivity of a two-layer microstrip line, and manages to reduce the computational time taken in determining the air gap thickness for a specified bandwidth. Results obtained with a special-purpose numerical tool that was developed to validate the new approach agree very well with simulated results (via *HFSS*). Finally, the design of a suspended radiator is presented as an application of the proposed strategy.

## ACKNOWLEDGMENT

## REFERENCES

1. Marzall, L. F., R. Schildberg, and J. C. da S. Lacava, "High-performance, low-cross-polarization suspended patch array for WLAN applications," *Proceedings of IEEE International Conference on Antennas and Propagation*, Charleston, USA, June 2009.
2. HFSS, Ansoft Corporation, www.ansoft.com/products/hf/ansoft_hfss/.
3. Svacina, J., "Analysis of multilayer microstrip lines by conformal method," *IEEE Trans. Microw. Theory Tech.*, Vol. 40, No. 4, 769–772, 1992.
4. Mathematica, Wolfram Research, http://www.wolfram.com/products/ mathematica/.
5. Derneryd, A. G. and A. G. Lind, "Extended analysis of rectangular microstrip antennas," *IEEE Trans. Antennas Propagat.*, Vol. 27, No. 6, 846–849, 1979.
6. Ramesh, G, P. Bhartia, I. Bahl, and A. Ittipiboon, *Microstrip Antenna Design Handbook*, Artech House, Norwood, 2001.
7. Derneryd, A. G., "A theoretical investigation of the rectangular microstrip antenna element," *IEEE Trans. Antennas Propagat.*, Vol. 26, No. 4, 532–535, 1978.

# An Effective Strategy for Designing Probe-fed Linearly-polarized Thick Microstrip Arrays with Symmetrical Return Loss Bandwidth

**Laila F. Marzall[1], Daniel C. Nascimento[2], R. Schildberg[2], and J. C. da S. Lacava[2]**

[1]TSM Antennas, Brazil

[2]Laboratório de Antenas e Propagação, Instituto Tecnológico de Aeronáutica, Brazil

**Abstract**— A new strategy for designing probe-fed linearly-polarized thick microstrip antennas is proposed in this work. Symmetrical return loss bandwidth is obtained by designing the patch to operate at the zero input reactance condition ($X_{in} = 0$). Applications for a single microstrip element and a linear array of suspended ones are presented. Experimental and simulated results validate the proposed strategy.

## 1. INTRODUCTION

When the standard design procedure is applied to probe-fed linearly-polarized (LP) microstrip radiator with a thick substrate — which is a practical way to increase bandwidth — the antenna exhibits an inductive input reactance that is difficult to match to the feeder network, and affects significantly its bandwidth symmetry [1, 2]. Many techniques are available for compensating the probe's inductance, but their use depends largely on the expertise of the antenna designer. Series capacitors, which can be implemented in several ways, are a possibility [3]. Other techniques, like changing the probe's geometry, can be utilized [4]. However, if such modified elements are used in a linear array, the complexities of its feeder network will likely increase, and, consequently, the difficulty in designing it. To overcome this limitation, a new strategy for designing probe-fed LP thick microstrip antennas is presented. The main outcome of this new proposal is the development of arrays with symmetrical bandwidth, resulting therefore in simpler feeder network designs. First, the new strategy is applied to the design of a single element. Subsequently, it is used for designing a WLAN array of suspended microstrip antennas to comply with the IEEE 802.11b (2.4–2.4835 GHz) protocol and the ETSI EN 301 525 V1.1.1 (2000-06) standard [5]. Experimental results validate the proposed strategy.

## 2. SINGLE ELEMENT: COMPARISON BETWEEN THE STANDARD AND THE NEW DESIGN

The typical geometry of a probe-fed LP rectangular patch microstrip antenna is presented in Fig. 1, where $\ell_p$ denotes the patch length, $w_p$ the radiating width, $y_p$ the probe position along the $y$-axis, and $h$ the substrate thickness. In this case, the antenna is directly fed by a 50-$\Omega$ SMA connector. According to the standard procedure for designing a LP patch in the fundamental mode $TM_{10}$, the operating frequency is set up at the maximum input resistance point.

Following this procedure and using the commercial software *HFSS* [6] for optimizing the radiator dimensions, a rectangular antenna consisting of a $h = 6$ mm thick, air ($\varepsilon_r = 1$) substrate, fed by a 1.3-mm diameter coaxial probe, was designed to operate at 2.45 GHz. Using a rectangular ground plane (125 mm×100 mm), the following optimized dimensions were obtained: $\ell_p = 50.4$ mm, $w_p = 65.5$ mm and $y_p = 15.75$ mm. Results for the input impedance and the reflection coefficient magnitude ($|\Gamma|$) are presented in Fig. 2(a). As shown, the maximum input resistance occurs at the operating frequency (2.45 GHz). As a result, the antenna input impedance is highly inductive ($Z_{in} = 50 + j66\,\Omega$, at 2.45 GHz) and can not be perfectly matched to a 50-$\Omega$ SMA connector ($|\Gamma| = -5.5$ dB) without an external network. Hence, the radiator bandwidth is asymmetrical in relation to the operating frequency. Thus, a new approach for designing probe-fed thick microstrip antennas is proposed next. Differently from the first approach, it consists of designing the patch to operate at the zero input reactance condition ($X_{in} = 0$). Using this new criterion, the antenna is redesigned to operate at 2.45 GHz for the same air-layer thickness, ground plane dimensions and probe diameter used in the standard design. The new optimized dimensions are: $\ell_p = 55.0$ mm, $w_p = 71.5$ mm, and $y_p = 2.0$ mm. Results for the input impedance and the reflection coefficient magnitude of the new antenna are shown in Fig. 2(b). Now, the antenna matches perfectly the 50-$\Omega$ SMA connector and presents a symmetrical bandwidth in relation to the operating frequency
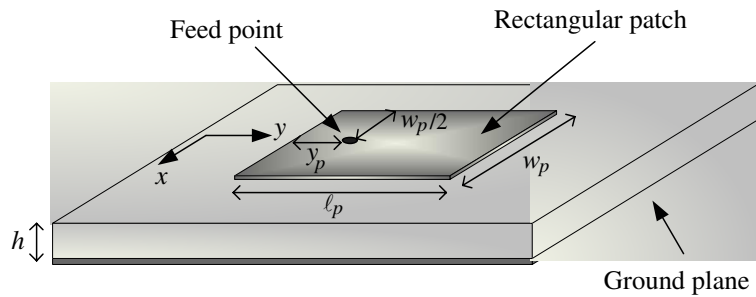
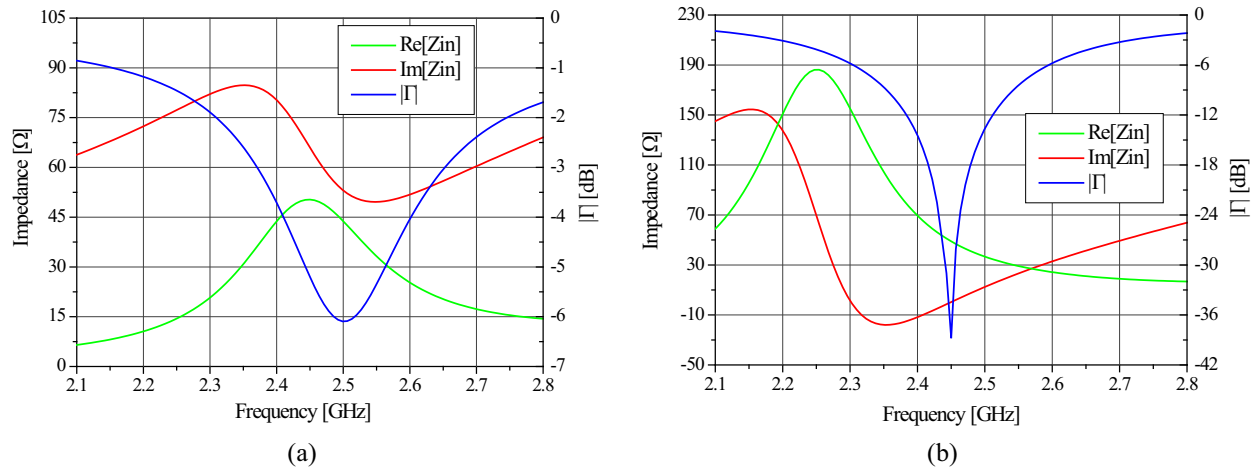Figure 1: Linearly polarized probe-fed microstrip antenna.



Figure 2: Input impedance and reflection coefficient magnitude: (a) standard design, (b) new design.
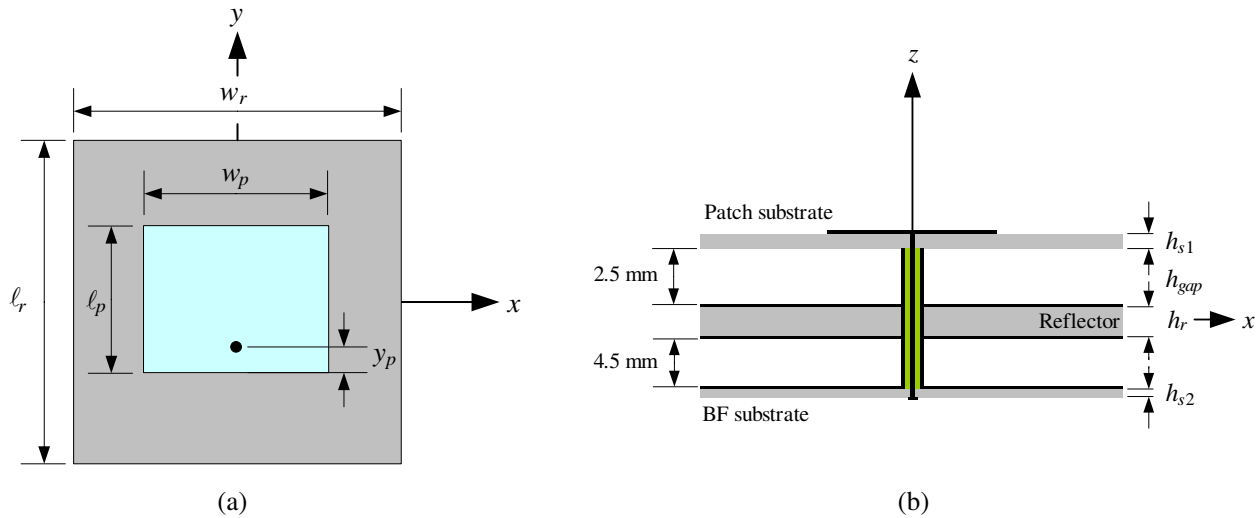


Figure 3: Suspended microstrip antenna geometry: (a) top view, (b) side view.

(2.45 GHz). In addition, as observed in Fig. 2(b), the maximum resistance is greater than $50\,\Omega$ and occurs at a frequency below 2.45 GHz.

## 3. SUSPENDED MICROSTRIP ANTENNA DESIGN

The project of a suspended microstrip radiator, based on IEEE 802.11b (2.4–2.4835 GHz) protocol and ETSI EN 301 525 V1.1.1 (2000-06) standard, is discussed next as another application of the proposed strategy.

The typical multilayer structure is shown in Fig. 3: the rectangular patch is printed on a dielectric substrate of thickness $h_{s1}$ and an air gap of thickness $h_{gap}$ separates it from the ground plane.

In this particular configuration, the patch is directly fed by a 50-$\Omega$ coaxial probe at $x = 0$ and $y = -(\ell_p/2 - y_p)$. The multilayer structure under consideration utilizes three types of PCB laminates: Arlon CuCLad 250GX ($h_{s1} = 1.524$ mm) for the patch ($w_p = 58.7$, $\ell_p = 46.1$ and $y_p = 15.8$ mm, based on the zero input reactance criterion), Arlon AR450 ($h_{s2} = 1.1938$ mm) for the array beam forming (BF) network, and FR-4 for the reflector ($w_r = 100$ mm, $\ell_r = 100$ mm and $h_r = 1.6$ mm). Furthermore, the element must operate at 2.45 GHz and cover the aforementioned bandwidth. For optimizing the element BW, the air gap spacing was set at 2.5 mm, resulting in a bandwidth of 4.8% at 10-dB return loss condition (Fig. 4).

## 4. LOW-CROSS-POLARIZATION SUSPENDED PATCH LINEAR ARRAY

Using the suspended microstrip element previously designed, a low-cross-polarization WLAN array that meets the ETSI standard minimum gain of 14 dBi is proposed [7]. To comply with the gain and cross-polarization requirements, an eight-element array, divided in two subgroups with 180° phase shift excitation, was designed. To control the side lobe level (SLL), the Dolph-Chebyshev method was used to determine the excitation coefficients for a $-20$ dB SLL. The array topology is presented in Fig. 5 ($w_r = 200$ mm, $\ell_r = 800$ mm, $w_s = 100$ mm, $\ell_s = 720$ mm, and $d = 0.75\lambda_0$) and its impedance matrix is given in Table 1. As seen, there is low mutual coupling between the array elements, thus simplifying the feeder network design.

Hence, the individual reflection coefficient magnitudes of the eight elements of the array present a similar behavior, as shown in Fig. 6.

Based on this fact, the feeder network topology could be implemented in a simple way, as shown in Fig. 7. Just four T-junction power dividers were required: two on the first level (1N1 and 1N2), one on the second level (2N) and the last on the third level (3N), where a microstrip line was used to implement the 180° phase shift between the two array subgroups. The elements' input
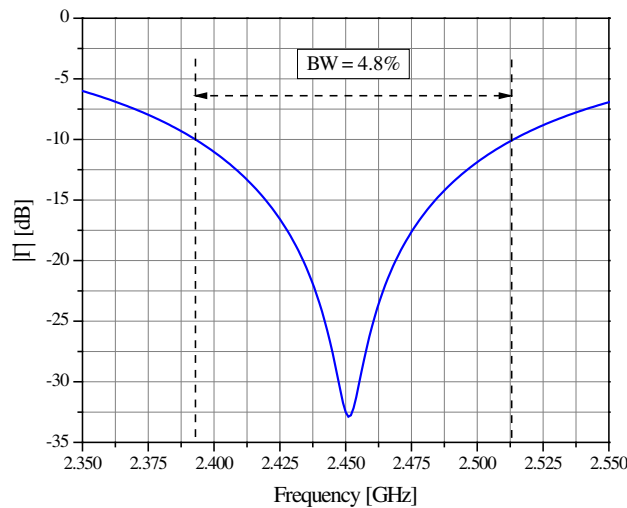


Figure 4: Reflection coefficient magnitude: Note the symmetry of the bandwidth in relation to the operating frequency.

Table 1: Impedance matrix ($\Omega$) of the array elements simulated by *HFSS*.

| N | $Z_{4N}$ | $Z_{3N}$ | $Z_{2N}$ | $Z_{1N}$ | $Z_{5N}$ | $Z_{6N}$ | $Z_{7N}$ | $Z_{8N}$ |
|---|---|---|---|---|---|---|---|---|
| 4 | $53.3 + 7.4i$ | $-4.8 - 5.8i$ | $2.2 + 0.1i$ | $-0.4 + 0.4i$ | $8.9 + 5.4i$ | $-2.9 + 0.8i$ | $0.4 - 0.7i$ | $0.1 + 0.2i$ |
| 3 | $-4.8 - 5.8i$ | $52.7 + 6.2i$ | $-4.2 - 5.7i$ | $2.1 + 0.1i$ | $-3.0 + 0.9i$ | $0.4 - 0.7i$ | $0$ | $0$ |
| 2 | $2.2 + 0.1i$ | $-4.2 - 5.7i$ | $51.8 + 5.8i$ | $-4.3 - 5.7i$ | $0.4 - 0.7i$ | $0$ | $0$ | $0$ |
| 1 | $-0.4 + 0.4i$ | $2.1 + 0.1i$ | $-4.3 - 5.7i$ | $52.7 + 5.9i$ | $0$ | $0$ | $0$ | $0$ |
| 5 | $8.9 + 5.4i$ | $-3.0 + 0.9i$ | $0.4 - 0.7i$ | $0$ | $54.1 + 7.6i$ | $-4.8 - 5.8i$ | $2.2$ | $-0.4 + 0.4i$ |
| 6 | $-2.9 + 0.8i$ | $0.4 - 0.7i$ | $0$ | $0$ | $-4.8 - 5.8i$ | $52.4 + 6.1i$ | $-4.2 - 5.7i$ | $2.1 + 0.1i$ |
| 7 | $0.4 - 0.7i$ | $0$ | $0$ | $0$ | $2.2$ | $-4.2 - 5.7i$ | $52.2 + 6.0i$ | $-4.3 - 5.7i$ |
| 8 | $0.1 + 0.2i$ | $0$ | $0$ | $0$ | $-0.4 + 0.4i$ | $2.1 + 0.1i$ | $-4.3 - 5.7i$ | $52.7 + 5.9i$ |

impedance and respective Dolph-Chebyshev excitation coefficients for the required SLL level are shown in Table 2. The feed network was placed behind the reflector to avoid spurious radiation. The final array geometry is depicted in Fig. 8.

Experimental and simulated results for the reflection coefficient magnitude are shown in Fig. 9. As expected, symmetrical return loss BW was established.
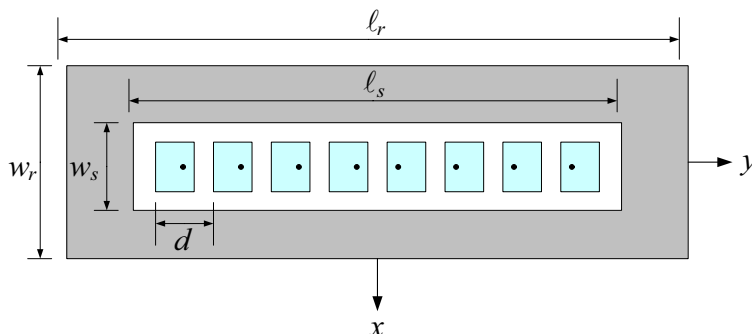


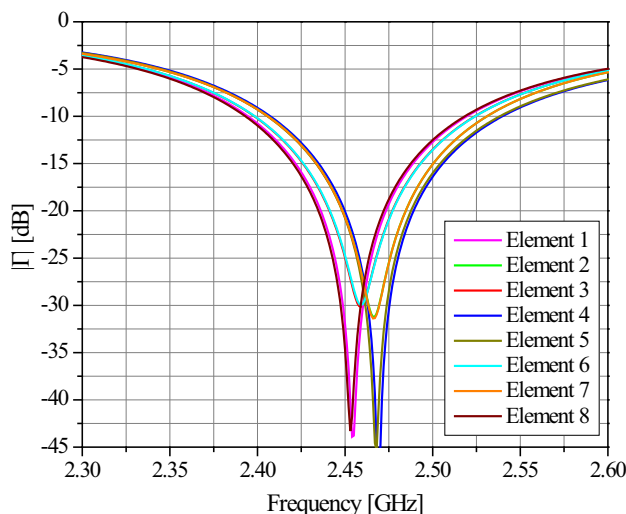Figure 5: Array topology: two subgroups with 180° phase shift excitation.



Figure 6: Individual reflection coefficient magnitude behavior.
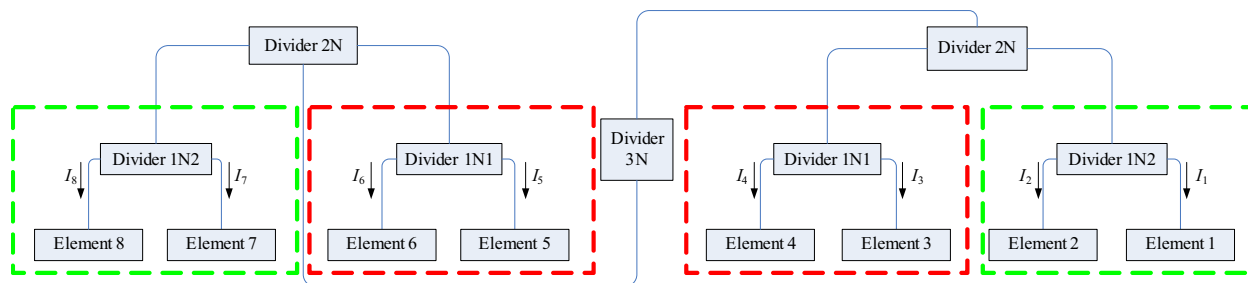


Figure 7: Array BF network topology: composed by simple T-junction power dividers.

Table 2: Input impedance ($\Omega$) and Dolph-Chebyshev excitation coefficient of the array elements.

| $N$ | 1 | 2 | 3 | 4 | 5 | 6 | 7 | 8 |
|---|---|---|---|---|---|---|---|---|
| $Z_N$ | $50.3 + 0.6i$ | $45.1 - 7.0i$ | $48.8 - 4.6i$ | $43.5 - 3.8i$ | $44.3 - 3.2i$ | $48.3 - 4.5i$ | $45.4 - 6.2i$ | $50.0 + 0.3i$ |
| $I_N$ | 0.58 | 0.66 | 0.88 | 1.00 | 1.00 | 0.88 | 0.66 | 0.58 |
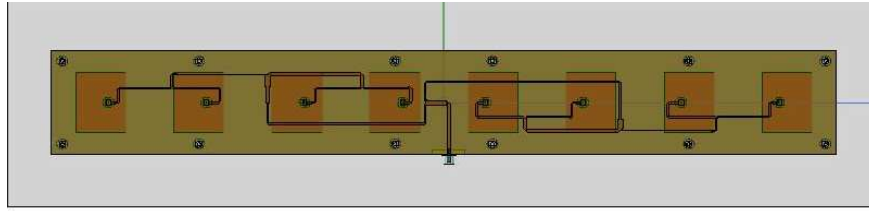
Figure 8: Final array geometry: backside view.
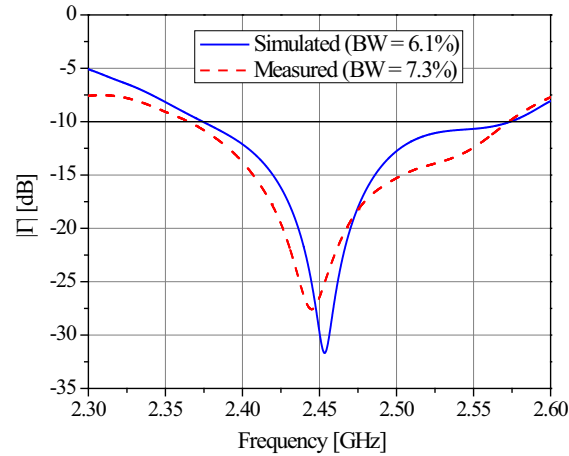


Figure 9: Array reflection coefficient magnitude.

## 5. CONCLUSION

This paper presents a new effective strategy for designing probe-fed LP thick microstrip antennas. It consists in designing the patch to operate at the zero input reactance condition ($X_{in} = 0$), which results in a symmetrical return loss bandwidth. As external matching networks are no longer required, the antenna construction process is simplified. Besides, the new approach can be applied to the design of microstrip radiators of arbitrary patch shapes regardless of the substrate thickness. Experimental results for a linear array of suspended microstrip elements validate the design strategy.

## ACKNOWLEDGMENT

## REFERENCES

1. Garg, P., P. Bhartia, I. Bahl, and A. Ittipiboon, *Microstrip Antenna Design Handbook*, Artech House, Boston, 2001.
2. Volakis, J. L., *Antenna Engineering Handbook*, 4th Edition, McGraw-Hill, New York, 2007.
3. Hall, P. S., "Probe compensation in thick microstrip patches," *Electron. Lett.*, Vol. 23, No. 11, 606–607, 1987.
4. Chang, F. A. and K. L. Wong, "A broadband probe-fed patch antenna with a thickened probe pin," *Proc. Asia-Pacific Microwave Conf.*, 1247–1250, Dec. 2001.
5. Marzall, L. F., "Antenna arrays with suspended microstrip radiators," M.Sc. Thesis, Technological Institute of Aeronautics, São José dos Campos, Brazil, 2009 (in Portuguese).
6. HFSS, Ansoft Corporation, www.ansoft.com/products/hf/ansoft_hfss/.
7. Marzall, L. F., R. Schildberg, and J. C. S. Lacava, "High-performance, low-cross-polarization suspended patch array for WLAN applications," *Proceedings of IEEE International Conference on Antennas and Propagation*, Charleston, USA, June 2009.

# Structural Analysis of the Microstrip Sample Holder

**M. R. F. Gontijo[1], E. Y. S. Lutif[1], A. J. F. Orlando[1], and A. C. C. Migliano[1, 2]**

[1]Aerospace Technological Institute (ITA), CTA, Brazil
[2]Advanced Study Institute (IEAv), CTA, Brazil

**Abstract**— The challenge in the characterization thin films is the low sensibility of the sample holder and a mode of the observation of the sensibility of the sample holder is the study of the reflection coefficient and transmission of the electromagnetic waves. However, the reflection parameters and transmission are dependents of the physical property and geometric parameters, this approach can be analyzed through computerized simulation XFDTD. In this paper we have analyzed the electromagnetic sensibility, the largest work area, input impedance and output impedance, distribution of the magnitude of the electromagnetic vectors, density of electric current and average electric potency. The largest work area went to $w/h = 5$, in which possess a broad band between $0.326\,\text{GHz}$ until $4.12\,\text{GHz}$.

## 1. INTRODUCTION

The innovation of the techniques in the characterization of thin films was motivated by the nanotechnology progress. The exact knowledge of material permittivity $\varepsilon^*$ and permeability $\mu^*$ is essential in the study of physical phenomena which govern interactions between electromagnetic waves and matter [1, 2]. The different techniques have been developed for measuring the intrinsic properties of materials are: microstrip, stripline and coplanar.

The difficult in the characterization of thin films is low sensibility of the sample holder and a mode for the observation of the sensibility of the sample holder is the study of the reflection coefficient and transmission of the electromagnetic waves.

Since, the reflection parameters and transmission are dependents of the physical property and geometric parameters. This approach can be analyzed through computerized simulation XFDTD. XFDTD is a computer simulation technique with which an arbitrary space is meshed with small cells ($\Delta x \Delta y \Delta z$: $\Delta x$, $\Delta y$, $\Delta z < \lambda/10$) and the electromagnetic field and current are calculated in the space by solving Maxwell's equations in each cell at each time step of $\Delta t(< \lambda/10c)$ [3].

In this work it is analyzed a holder sample of the type microstrip, where the results of the simulations are presented using software XFDTD version 6.4, such as geometric characteristics are discussed, input impedance and output impedance, the dominant mode of propagation of the electromagnetic fields and to validate the simulation use the Newton's Complex Iterative Method to determine the real permittivity and imaginary of the sample holder.

## 2. STRUCTURAL ANALYSIS

The critical dimensions for the microstrip sample holder are as follows: the housing is perfect electrical metal with inside dimensions of $(12 \times 10 \times 0.64)\,\text{mm}$, the permittivity relative of the air equal 1.0 and perfect dielectric with dimensions $(11 \times 7 \times 0.64)\,\text{mm}$. For each simulation the width of the conductor perfect center varied of $(2.6, 2.8, 3.0, 3.2, 3.4, 3.6, 3.8$ and $4.0)$ mm. The sample holder show Figure 1 was meshed with cells, each of which are $(0.01 \times 0.01 \times 0.01)\,\text{mm}$ in size for the FDTD simulation and center conductor was excited for a source of radio frequency of 1 Volt operating in scale from $300\,\text{MHz}$ to $10\,\text{GHz}$. The objective of this work is analyze the
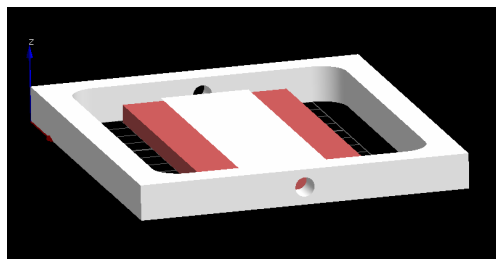


Figure 1: Sample holder simulation.

electromagnetic sensibility, input impedance and output impedance, determining the largest work area where $w$ width of the electrical strip and $h$ the thickness of the dielectric layer, distribution of the magnitude of the vectors electromagnetic, density of electric current and average electric potency.

## 3. RESULTS AND DISCUSSION

Figure 2 presents the behavior of the magnitude $S_{11}$ in function of the applied frequency and Figure 3 shows the behavior of magnitude $S_{21}$ in function of the applied frequency.

Work area correspond the graph that it possesses the largest frequency and better electromagnetic sensibility. The electromagnetic sensibility is related with low reflection smaller than $-30$ dB and transmission near than $0$ dB. $w = 3.2$ mm was what show the largest area of work of $0.326$ GHz until $4.12$ GHz and better electromagnetic sensibility and making the ratio of the conductor width with the thickness of the dielectric has $w/h = 5$. Figure 4 and 5 show the analysis of the input impedance and of output impedance in function of frequency.

Analyzing with $w/h = 5$ in the way of electromagnetic transmission to identify of as the magnitude electromagnetic field. Figure 6 and 7 show the magnitude of the vector electric field and the magnitude of the vector magnetic in the middle of the sample holder with $w/h = 5$.

Figure 8 shows the magnitude of the density of electric current and in this analysis was noticed that the density of the electric current condenses between the conductor and the dielectric air.

In Table 1 shows the dependences of the electromagnetic fields in function of the conductor width and as the magnitudes of the electromagnetic fields, magnitude of the electric current density and
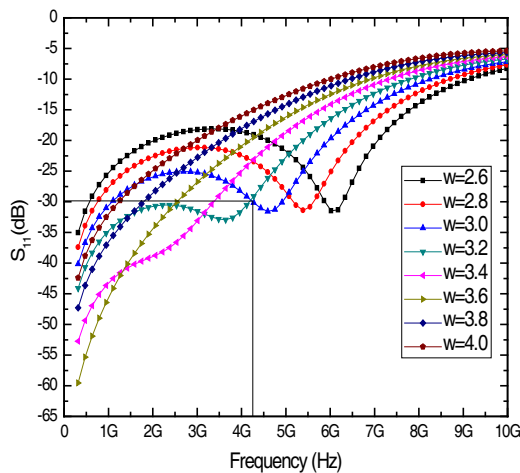


Figure 2: Magnitude $S_{11}$ in function of the frequency.
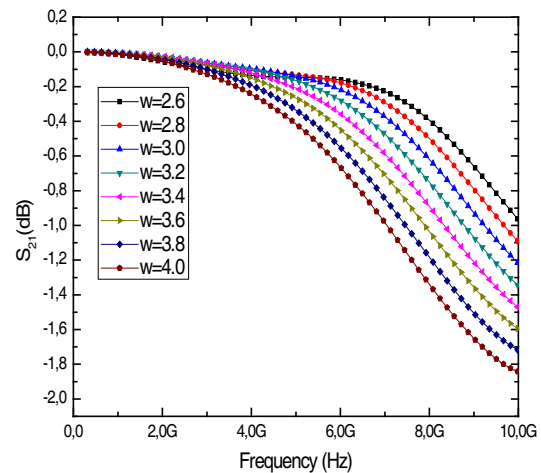


Figure 3: Magnitude $S_{21}$ in function of the frequency.
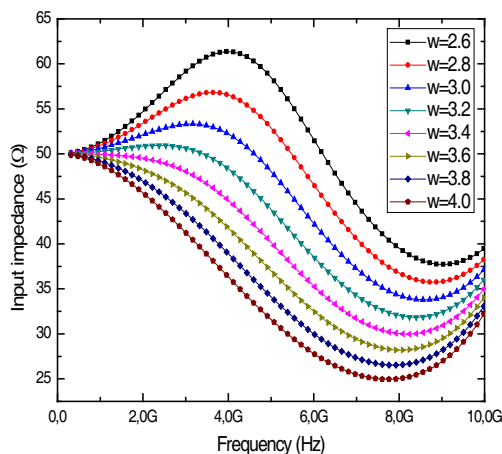


Figure 4: Input impedance in function of the frequency.
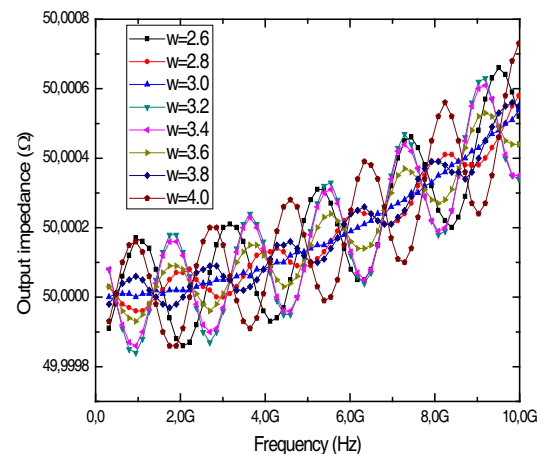


Figure 5: Output impedance in function of the frequency.
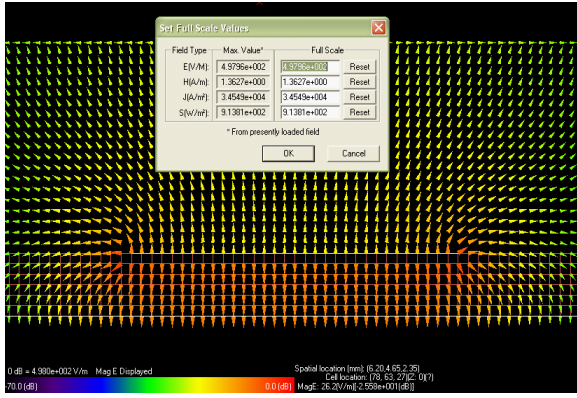
Figure 6: Distribution of the magnitude of the vector electric field in the middle of the holder sample.
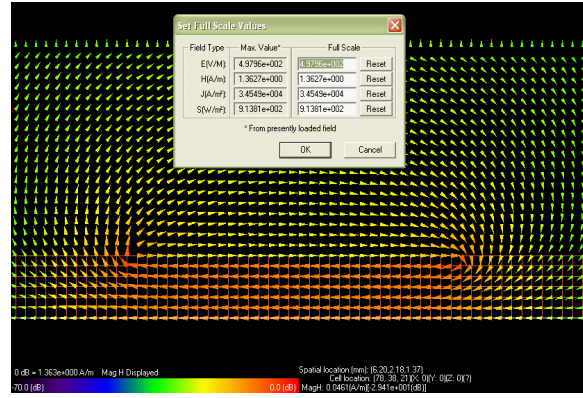


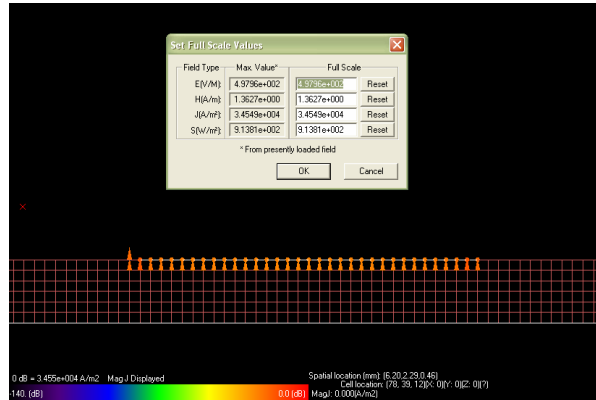Figure 7: Distribution of the magnitude of the vector magnetic field in the middle of the holder sample.



Figure 8: Magnitude of the density of electric current.

average electric potency.

To validate the simulation Newton's interactive complex method it was used with the Method of Transmission/Reflection to measure the real permittivity and imaginary permittivity.

For the application of the Iterative Method, an initial estimation is necessary for $\alpha_s$ and $\beta_s$. It is used when the holder sample obtained by doing $\Gamma = 0$ as:

$$\alpha_s = -\frac{\ln |S_{21}|}{d} \tag{1}$$

and

$$\beta_s = -\frac{\varphi + 2n\pi + \beta_0 d}{d} \tag{2}$$

where $\varphi$ is the phase of $S_{21}$, $\beta_0 = \omega\sqrt{\varepsilon_0 \mu_0}$, $d = 12\,\mathrm{mm}$, due to simulation the best value of $n$ was 1. Therefore, the expression for $\varepsilon'$ and $\varepsilon''$:

$$\varepsilon' = \left(\frac{c}{\omega}\right)^2 \left(\beta_s^2 - \alpha_s^2\right) \tag{3}$$

and

$$\varepsilon'' = 2\alpha_s\beta_s \left(\frac{c}{\omega}\right)^2 \tag{4}$$

where, $c$ is the speed of light in free space and is the $\omega$ angular speed. The Figure 8 shows the frequency responses of $\varepsilon'$ and $\varepsilon''$.

Table 1: Magnitude of the electric field, of the magnetic field, of the electric current density and the average of the electric potency as a function of conductor width.

| Conductor width | Magnitude electric field (V/m) | Magnitude magnetic field (A/m) | Magnitude of the electric current density (A/m$^2$) | Average electric potency (W/m$^2$) |
|---|---|---|---|---|
| 2.6 | $6.46431 \times 10^2$ | 1.7133 | $4.3396 \times 10^4$ | $1.4934 \times 10^3$ |
| 2.8 | $5.9371 \times 10^2$ | 1.5839 | $4.0159 \times 10^4$ | $1.2675 \times 10^3$ |
| 3.0 | $5.4253 \times 10^2$ | 1.4638 | $3.7128 \times 10^4$ | $1.0700 \times 10^3$ |
| 3.2 | $4.9796 \times 10^2$ | 1.3627 | $3.4549 \times 10^4$ | $9.1381 \times 10^2$ |
| 3.4 | $4.6337 \times 10^2$ | 1.2860 | $3.2562 \times 10^4$ | $8.0202 \times 10^2$ |
| 3.6 | $4.3997 \times 10^2$ | 1.2344 | $3.1194 \times 10^4$ | $7.3050 \times 10^2$ |
| 3.8 | $4.2705 \times 10^2$ | 1.2047 | $3.0381 \times 10^4$ | $6.9168 \times 10^2$ |
| 4.0 | $4.2265 \times 10^2$ | 1.1920 | $3.0002 \times 10^4$ | $6.7714 \times 10^2$ |
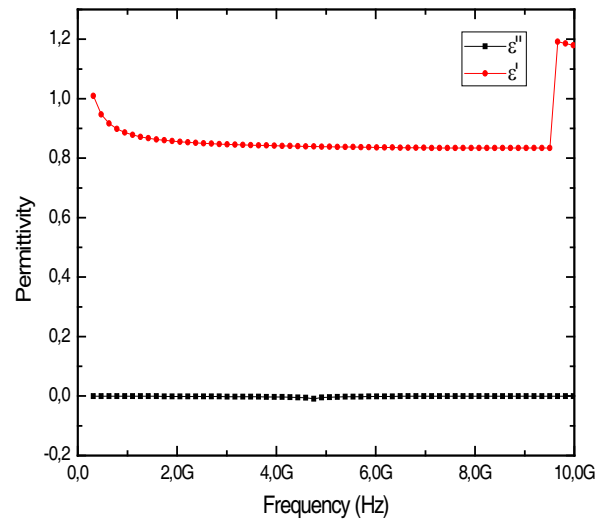


Figure 9: Frequency response of the real permittivity and imaginary permittivity for holder sample. Was observed a pick in the real permittivity near frequency at 9.5 GHz, this is due to phase inversion.

## 4. CONCLUSIONS

The sample hold with this dimensions of the housing and ratio $w/h = 5$ it showed to be a good option to do characterization of nanoscale films due to excellent electromagnetic sensibility in the band 0.326 GHz until 4.12 GHz. Mathematical result using Newton's interactive complex method coincides with the complex electric permittivity than was generated in the simulation.

**REFERENCES**

1. Yoshihiro, K., *Microwave Integrated Circuits*, Marcel Dekker, New York, 1991.
2. Chen, L. F., C. K. Ong, C. P. Neo, V. V. Varadan, and V. K. Varandan, *Microwave Electronics: Measurement and Materials Characterization*, John Wiley, New York, 2004.
3. Kim, Y. K., "FDTD analysis on the current and electric field distribution in a PCB stripline structure," *IEEE International Symposium on Electromagnetic Compatibility*, 691–694, Washington, USA, August 2000.
4. Taflove, A., *Computational Electrodynamics*, Arteck House, Boston, 1995.
5. De Oliveira, A. J. B., M. T. de Melo, L. L. D. Cabral, S. R. O. de Souza, "Plaster glue complex permittivity response in microwave range," *Materils Reseach*, Vol. 7, No. 4, 565–568, 2004.

# Novel Application of CPW in Antenna Design for Dual-frequency Operation

**Guo-Chao Wang and Jia-Dong Xu**

School of Electronics and Information, Northwestern Polytechnical University
Xi'an 710072, China

**Abstract**— In this paper, we propose a novel application of coplanar waveguide (CPW) in antenna design: by appropriate adjusting its impedance, CPW can act as both a transmission line and radiator at the same time. That is, unlike the traditional way, an extra independent frequency can be obtained without adding new component or increasing the complexity. So the new design and the original one are almost the same in geometry however completely different incapability. Through this method, antenna design could be more simple and flexible. To do this, the impedance of CPW should be carefully designed and most of all, avoid of being $50\,\Omega$, otherwise the CPW will turn out to be merely transmission line (the traditional and most common usage of CPW). Here, we choose a classical single frequency planar antenna as an example to prove that by incorporating the advanced CPW, the former single frequency antenna could resonates at two different frequencies independently — the original one and the one comes from CPW. In addition, two frequencies share a very similar pattern. Since each resonant point relates to one parameter exclusively, we only need to modify one parameter at one time to place the two frequencies at the anticipate points to meet different requirements. However, impedance of CPW should be changed correspondingly to ensure sufficient gain at each frequency. In order to determine the performance of CPW's impedance as well as other two geometry parameters on frequency, parametric study is carried out using simulation software HFSS and experimental results. At last, by careful adjustment of these three parameters, we merge the two frequencies so as to acquire a wide-band operation which covers $4\,\text{GHz}$ and more than 50% relative band-width. Simulated and measured results show excellent agreement; hence proves the validity of the new capability of CPW.

## 1. INTRODUCTION

With rapid development, modern wireless communication system calls for dual-band operations such as wireless local area network (WLAN) and intelligent transportation system (ITS). Planar antennas have been found wide spread application due to their attractive advantages like ease of fabrication, low cost, low profile. Compare to other transmission line structure, CPW offers merits including simple configuration of a single metallic layer, easy integration with circuit, low elimination of via and solder pads, etc. There are comprehensive study focus on CPW-fed planar antennas for dual band operation, including monopole antenna with two branches [1], two annual ring strip antenna [2], two annual slot ring antenna [3], circuit slot antenna with back slit back patch [4], circuit slot antenna with back strip [5] and so on. Most CPW-fed planar antenna reported in literature achieves dual band operation by adding components to original single design. Though extra frequency can be obtained, the whole design becomes more complex and more sensitive. However, the use and geometry of CPW is so rigors that in most cases it is rectangular transmission line with $50\,\Omega$ impedance exclusively. Other applications of CPW have received scant attention. Circular CPW-fed (CCPW) by a disk radiator through a CPW line [6], tapered CPW whose impedance changes gradually [7], meandered CPW which is able to excite two modes [8] are reported. However, they still act as transmission line only and is responsible to no radiation themselves. This paper provides a novel function of CPW — radiator. By changing the CPW's impedance away from $50\,\Omega$, it can act as radiator and transmission line at the same time. Such hybrid application of CPW can provide dual band operation without adding extra component. To test feasibility of this novel function of CPW, we propose a typical single band planar slot antenna as example. In the following sections, we will prove that by incorporating new CPW, it can produce two independent resonant frequencies.

## 2. ANTENNA DESIGN

The geometry of the proposed antenna is shown in Figure 1. The antenna was constructed by printing it on an FR4 substrate with dielectric constant 4.4 and substrate thickness $0.8\,\text{mm}$ and its size is $W\,(35\,\text{mm}) \times L\,(40\,\text{mm})$. The radius of outer and inner ring slot's rim are $R_{out}$ and $R_{in}$

respectively. CPW strip has a width of $W_c$, length $L_c$ and gap $g$. In this paper, $W_c$ is fixed at 3 mm. The central circular patch has a notch for matching with width $W_n$ and length $L_n$. Shape of it will be similar to that in [3] or [5] if add second ring slot, or back strip (responsible for secondary band in [3] and [5] respectively). Although proposed antenna looks almost the same to traditional single band one, its CPW's impedance is no longer 50 Ω. By accurately modifying the impedance of the CPW, it can achieve dual band operation while introducing no element. Furthermore, the two resonant frequencies of the proposed antennas are decided by the circumferences of the outer and inner annular-ring slots rim respectively so as to be independent.

## 3. EXPERIMENTAL RESULT AND DISCUSSION

To illustrate the new CPW's function, we select randomly a series of parameters. For operating first resonant frequency (4 GHz), we choose $R_{in} = 7.5$ mm. Furthermore, for obtaining the second resonant frequency (about 5 GHz), we choose $R_{out} = 13.5$ mm, $W_c = 3$ mm, $L_c = 15.04$ mm, $g = 0.9$ mm.

Figure 2 demonstrates its simulation return loss and we can clearly see two resonant frequencies. To prove that the secondary (lower) resonant frequency is due to the CPW, the effect of the impedance of CPW on return loss is shown in Figure 3. It is easy to find that as impedance approaching to 50 Ω, the secondary resonant frequency diminish gradually.

If ever the CPW's impedance becomes 50 Ω (gap's width becomes 0.25 mm), the antenna degrades to conventional one with single band and CPW is merely a transmission line. Hence the
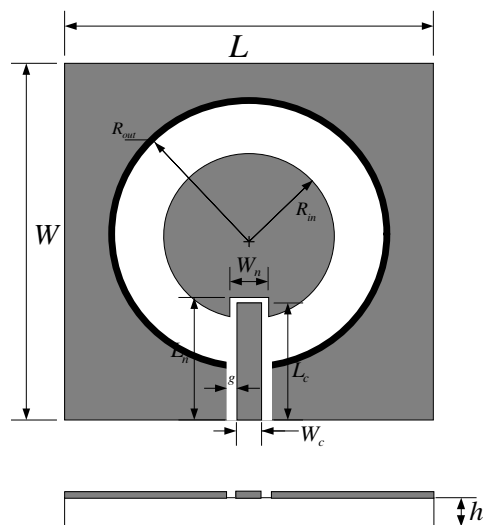


Figure 1: Geometry of CPW-fed annular slot antenna.
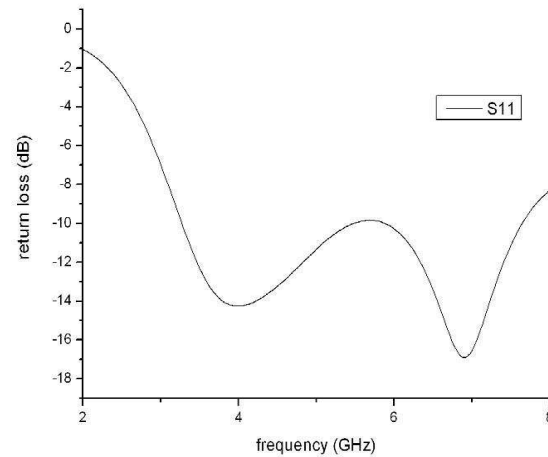


Figure 2: A dual band operation.
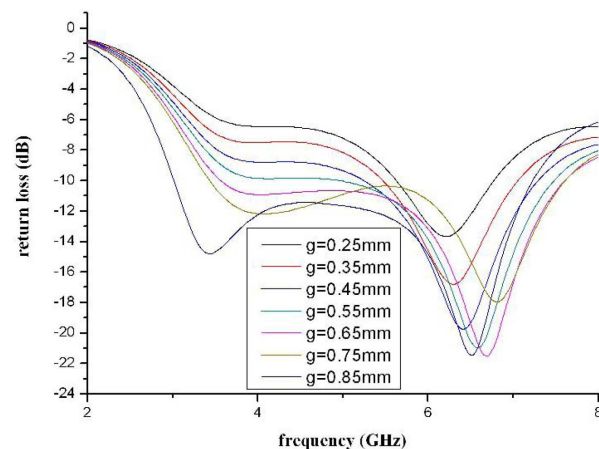


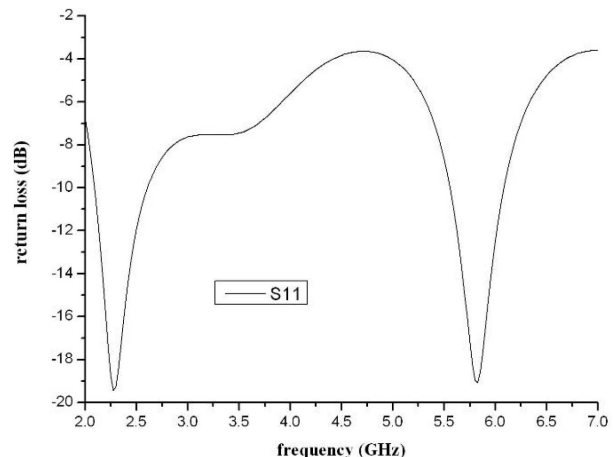Figure 3: CPW impedance's effect on return loss.



Figure 4: Dual operation for WLAN.

extra resonant frequency is due to the "mismatching" CPW. Because the key point lies in the impedance of the CPW and the impedance is decided by width of CPW's slot, the whole design seems almost the same with the original one but completely different in capability.

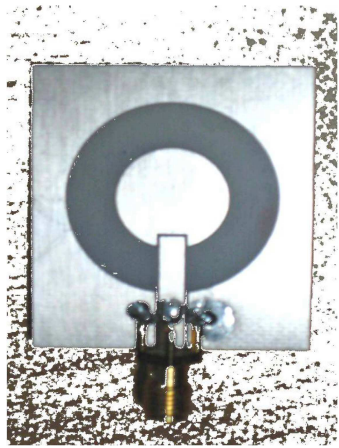The higher, original resonant point comes from the circumference of the outer rim of slot. The
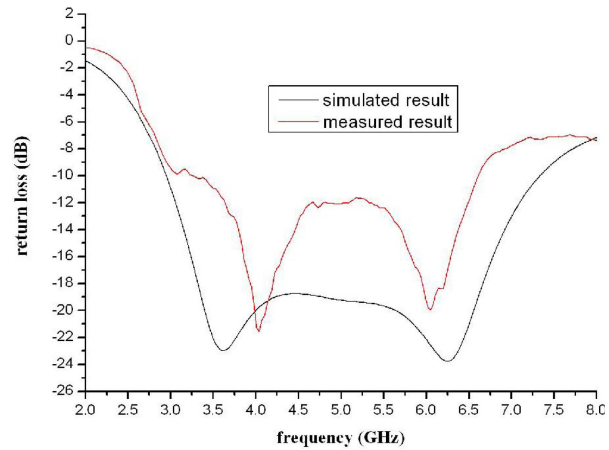


Figure 5: Antenna prototype.



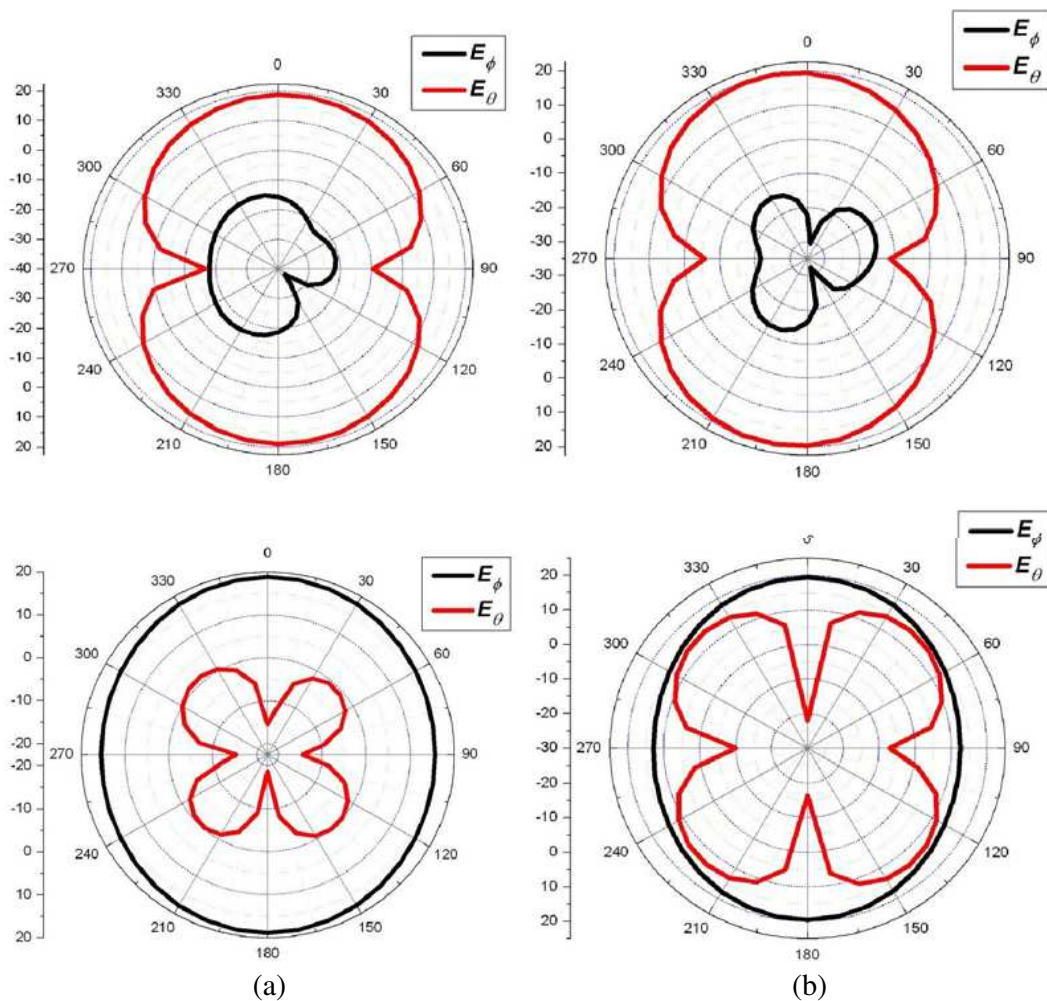Figure 6: Simulated and measured return loss *versus* frequency for wide band operation.



(a)



(b)

Figure 7: Radiation pattern at both resonant frequencies (a) 4 GHz, (b) 6 GHz (upper: $\theta = 0°$, lower: $\theta = 90°$).

Table 1: Parameters for proposed wide band antenna.

| $R_{in}$ | $R_{out}$ | $L_c$ | $W_c$ | $g$ |
|---|---|---|---|---|
| 7.5 mm | 14 mm | 16.02 mm | 1.5 mm | 0.67 mm |

lower, extra frequency is related to the perimeter of inner slot rim. We find both frequencies are inversely ratio to perimeters. Further more, there is little mutual influence between two frequencies. That is, only one parameter needs being modified at one time to place these two resonant frequencies at the anticipate points to actualize various applications. However, different impedance of CPW is required to obtain different dual band operations with sufficient gain at both resonant points. Take WLAN for example, we just need to make the $R_{in} = 12.7$ mm, $R_{out} = 14.1$ mm to place two band cover 2.4 GHz and 5.8 GHz. And $W_c = 3.0$ mm, $L_c = 15.3$ mm, $g = 1.2$ mm to ensure sufficient gain at each resonant point. Its return loss shown in Figure 4 demonstrates it perfectly meet the WLAN requirement.

Radiation characteristics at lower and higher operating frequencies are presented in Figure 7. Same polarization planes and omni-directional radiation patterns are observed. Hence, when two band merge together, wide-band operation can be realized in both impedance and pattern means. After careful parametric study, values of parameters are obtained to achieve wide band operation and are shown in Table 1. Real object fabricated based on these parameters is depicted in Figure 5. The measured as well as simulation result are plotted in Figure 6 and show good agreement.

Though relative big differences exist in center part of band, it clearly proves that dual band operation can be achieved by changing impedance of CPW. This design achieves a band covers range of 3.6 GHz below $-10$ dB (over 70% relative band width).

## 4. CONCLUSION

The novel application of CPW is proposed and investigated. It is demonstrated numerically and experimentally that non $50\,\Omega$ CPW can act transmission line and another radiator at the same time. This hybrid design can simplify the dual band antenna design. Moreover, resonant frequency from CPW has little influence on the original one and vise versa. Agreement between experiment and simulation prove the feasibility of new capability of CPW. Differences may come from SMA connector and solder on central conduct line and ground which will change the impedance of the CPW.

## REFERENCES

1. Chen, H.-D. and H.-T. Chen, "A CPW-fed dual-frequency monopole antenna," *IEEE Transactions on Antennas and Propagation*, Vol. 52, No. 4, April 2004.
2. Ren, Y.-J. and K. Chang, "Broadband dual-frequency CPW-fed annual-ring antenna," *IEEE Antennas and Propagation Society International Symposium 2006*, 9–14, July 2006.
3. Sze, J.-Y., C. I. G. Hsu, and J. J. Jiao, "CPW-fed circular slot antenna with slit back-patch for 2.4 = 5 GHz dual-band operation," *Electronics Letters*, Vol. 42, No. 10, May 11, 2006.
4. Chen, J.-S., "Dual-frequency annular-ring slot antennas fed by CPW feed and microstrip line feed," *IEEE Transactions on Antennas and Propagation*, Vol. 53, No. 1, January 2005.
5. Chen, J.-S. and H.-W. Chien, "Studies of wideband slot antennas with back-strip," *Asia-Pacific Microwave Conference, APMC 2008*, 1–4, December 16–20, 2008.
6. Lee, C.-M., T. C. Yo, C. H. Luo, C.-H. Tu, and Y.-Z. Juang, "Broadband disk monopole antenna with a circular CPW-feeding line," *IEEE Antennas and Propagation International Symposium*, 773–776, June 9–15, 2007.
7. Wu, Q., R. Jin, J. Geng, and M. Ding, "Compact CPW-fed quasi-circular monopole with very wide bandwidth," *Electronics Letters*, Vol. 43, No. 2, January 18, 2007.
8. Liu, W. C., "Broadband dual-frequency meandered CPW-fed monopole antenna," *Electronics Letters*, Vol. 40, No. 21, October 14, 2004.

# Ground Slotted Landa Shape Single Feed UWB Circular Polarized Antenna for 2.4 GHz RFID Reader

**E. A. F. Abdallah**[1], **T. G. Abo-Elnaga**[1], **and H. El-Hennawy**[2]

[1]Electronics Research Institute, Egypt
[2]Faculty of Engineering, Ain Shams University, Egypt

**Abstract**— Supper High Frequency (SHF) $2.4 \sim 2.483$ GHz Ultra Wide Band (UWB) circularly polarized antenna is proposed for the Radio Frequency Identification (RFID) applications. The antenna is composed of FR4 substrate where a microstrip patch antenna is placed on the top and no ground plane beneath it. The patch antenna excited through microstrip line matched to the antenna through one fourth microstrip line transformer with stub. The ground plane lies beneath the feeding scheme where a landa shape slot is etched in the ground plane. The proposed antenna achieves measured $-10$ dB bandwidth of 1.77 GHz from 2.34–4.11 GHz which agrees with the computed results. The proposed antenna has 3 dB axial ratio bandwidth of 89.1089 MHz (2.39934 MHz–2.48845 MHz) which covers the required band. The antenna scheme occupies an area of $29 \times 32$ mm². The proposed antenna is simple, cheap and offers an acceptable other antenna parameters on the 2.4 GHz RFID readers bandwidth.

## 1. INTRODUCTION

The first RFID application was the "Identification Friend or Foe" system (IFF) and it was used by the British in the Second World War. Transponders were placed into fighter planes and tanks, and reading units could query them to decide whether to attack. Successors of this technology are still used in armies around the world. The first commercial RFID application was the "Electronic Article Surveillance" (EAS). It was developed in the seventies as a theft prevention system. In the eighties RFID technology got a boost when Norway and several US states decided to use RFID for toll collection on roads. In recent years, RFID technology has been rapidly developed and applied to many service industries, distribution logistics, manufacturing companies, and goods flow systems. In RFID system, the role of antennas (for reader and tag) is very important. The reader antenna should have circular polarization (CP) characteristic since the tag antenna can be arbitrarily positioned on the target. Most RFID systems operate at ISM frequencies, such as 13.56 MHz, 2.45 GHz and 5.8 GHz, some work at UHF frequencies such as $840 \sim 845$ MHz, $920 \sim 925$ MHz (China), $952 \sim 954$ MHz (Japan), $868 \sim 870$ MHz (Europe) and $902 \sim 928$ MHz (USA), etc [1]. Printed monopole antennas have many attractive features such as light weight, low profile, simple structure, wide impedance-bandwidth, omnidirectional radiation patterns and in general, are linearly polarized (LP) [2]. Typically, the planar CP antenna is achieved through using patch antenna and slot antenna [3]. In this paper, Ultra Wide Band (UWB) circularly polarized antenna is proposed for the supper high frequency (SHF) $2.4 \sim 2.483$ GHz Radio Frequency Identification (RFID) applications where circular polarization can be enhanced through slotting the ground plane of a printed monopole antenna with landa shape. The antenna is composed of FR4 layer with dielectric constant of 4.65 and height of 1.5 mm. Microstrip patch antenna is placed on the top of the substrate and no ground plane beneath it. The patch antenna is excited through microstrip line matched to the antenna through quarter-wavelength microstrip line transformer with stub and their dimensions are optimized to enhance the matching between the antenna and the microstrip line. The ground plane lies beneath the feeding scheme. Landa shape slot is etched in the ground plane and its dimensions are optimized to enhance the circular polarization. The proposed antenna achieves measured $-10$ dB bandwidth of 1.77 GHz from 2.34–4.11 GHz which agrees with the computed results. The proposed antenna has 3 dB axial ratio bandwidth of 89.1089 MHz (2.39934 MHz–2.48845 MHz) which cover the required band (2.400 MHz–2.483 MHz). The antenna scheme occupies an area of $29 \times 32$ mm². The proposed antenna is simple, cheap and offers an acceptable other antenna parameters on the 2.4 GHz RFID readers bandwidth.

## 2. ANTENNA DESIGN

The schematic diagram of the proposed Ultra Wide Band (UWB) circularly polarized antenna is illustrated in Figure 1(a) and Figure 1(b) where top and bottom view of the proposed antenna are shown, respectively, where the antenna was etched on FR4 substrate with relative permittivity $\varepsilon_r =$

4.65, loss tangent $\tan \delta = 0.02$ and thickness $h = 1.5\,\text{mm}$. The antenna length $L_a$ is calculated using Equations (1) and (2) [4] where $\lambda_g$, $\lambda_r$ and $\varepsilon_{re}$ are the guided wavelength, resonance wavelength and effective dielectric constant, respectively. The matching between the radiator element and the 50 ohm microstrip line with length $L_{1f}$ and width $W_{1f}$ is done through quarter-wavelength transformer with width $W_f$ and length $L_f$. Microstrip stub with width $W_s$, length $L_s$ and offset length $L_o = 4.85\,\text{mm}$ is added to the quarter-wavelength transformer as shown in Figure 1(a). Landa shape slot with curvature radius $R$ and vertical upper length $L_2$, upper width $W_2$, horizontal upper length $L_3$, horizontal upper width $W_2$, Lower vertical length $L_4$ and lower vertical width $W_3$ is etched in rectangular ground plane with length $L_g$ and width $W_g$ as shown in Figure 1(b). The whole structure as shown in Figure 2 is optimized using IE3D Zeland based on the method of moment. All dimensions are given in Table 1.

$$L_a \approx \frac{\lambda_g}{4} = \frac{\lambda_r}{4\sqrt{\varepsilon_{re}}} \tag{1}$$

$$\varepsilon_{re} = \frac{\varepsilon_r + 1}{2} \tag{2}$$
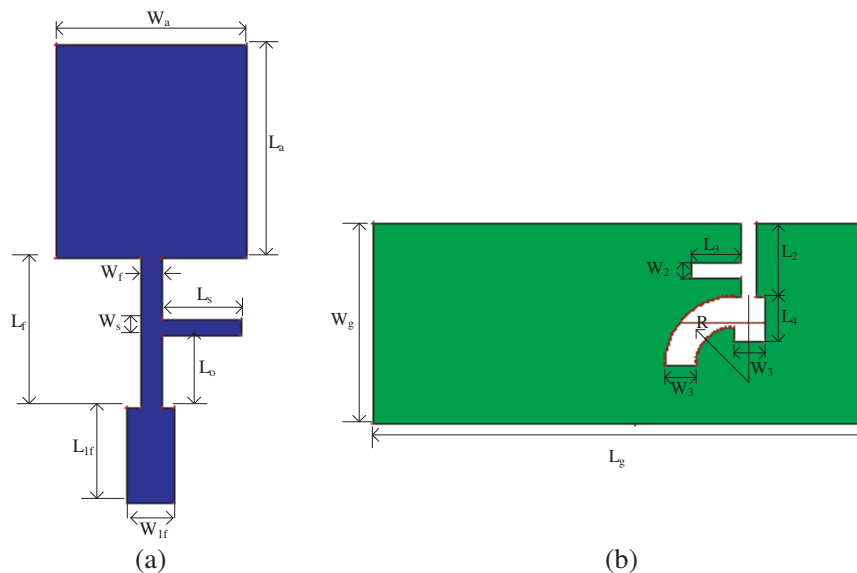


Figure 1: (a) The antenna upper view. (b) The antenna bottom view.
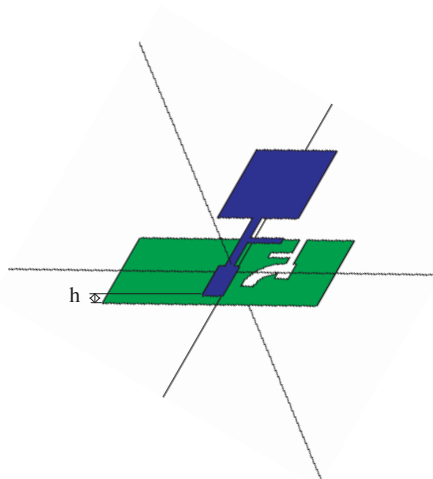


Figure 2: Proposed antenna whole structure.

Table 1: The proposed antenna optimized dimensions.

| Dimension | $L_a$ | $W_a$ | $L_{1f}$ | $W_{1f}$ |
|---|---|---|---|---|
| Dimension (mm) | 13.5 | 12 | 6 | 3 |
| Dimension | $W_f$ | $L_f$ | $W_s$ | $L_s$ |
| Dimension (mm) | 1.4 | 9.5 | 1 | 4.987 |
| Dimension | $R$ | $L_2$ | $W_2$ | $L_3$ |
| Dimension (mm) | 4.5 | 4.737 | 1 | 3.254 |
| Dimension | $L_4$ | $W_3$ | $L_g$ | $W_g$ |
| Dimension (mm) | 2.97 | 2 | 32 | 13 |



(a)                                        (b)
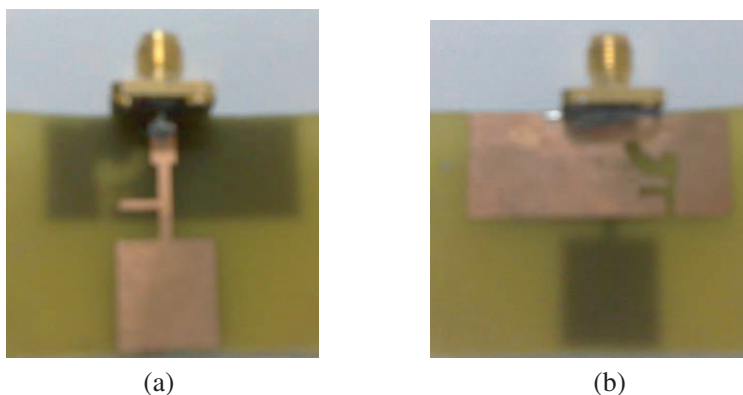
Figure 3: (a) Fabricated antenna (upper view). (b) Fabricated antenna (bottom view).
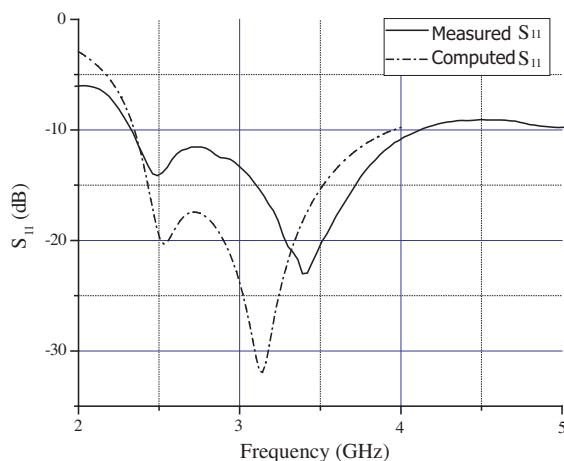


Figure 4: Simulated and measured return loss against frequency.

## 3. SIMULATED AND MEASURED RESULTS

The proposed antenna was fabricated as shown in Figure 3 where upper and bottom views are shown in Figures 3(a) and 3(b), respectively. The proposed antenna achieves measured $-10$ dB bandwidth of 1.77 GHz from 2.34–4.11 GHz which is slightly better than the computed results. The proposed antenna has 3 dB axial ratio bandwidth of 89.1089 MHz (2.39934 MHz–2.48845 MHz) as shown in Figure 5 which covers the required band (2.400 MHz–2.483 MHz). Figure 6 and Figure 7 show antenna gain and directivity, respectively. It should be noted that the antenna is not directive and that the value of directivity D (dBi) is less than 2.3 at frequency $f = 2.4$ GHz. This causes reduction in antenna gain in addition to low radiation efficiency. Figure 8 shows the proposed antenna polar radiation pattern from which, the proposed antenna introduces Right Hand Circular Polarization performance. it is clear that, Figure 8, that the back radiation is very large due to

removing the ground plane under antenna and the existence of the slot. The discrepancies are mainly because of the fabrication difficulty in precise alignment between the patch antenna and the landa shape slotted ground plane.
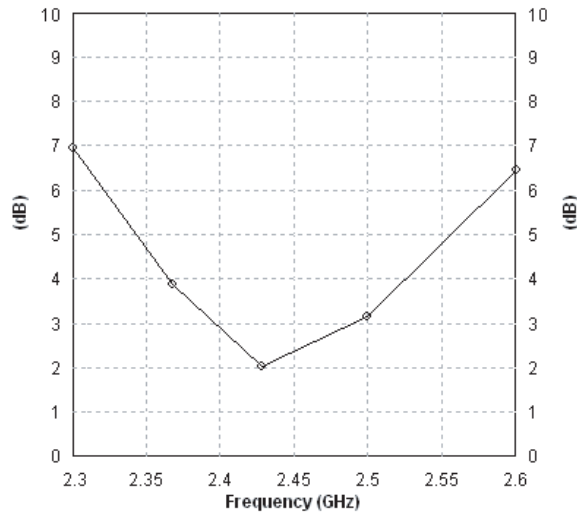


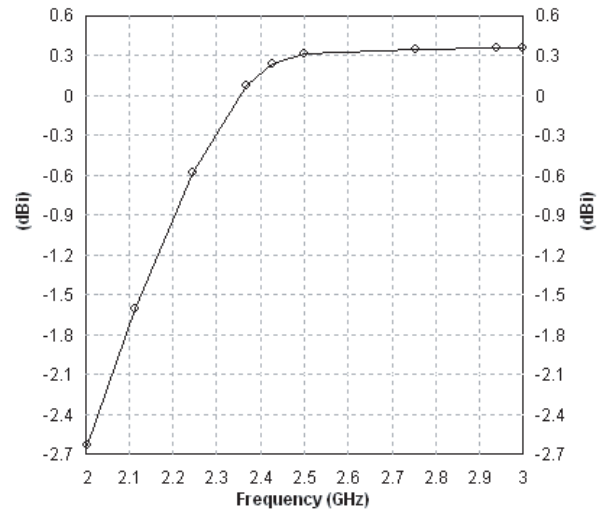Figure 5: Antenna axial ratio versus frequency.
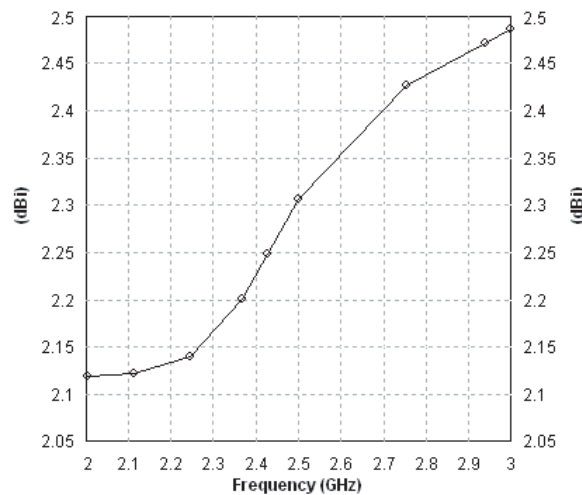


Figure 6: Antenna gain versus frequency.



Figure 7: Proposed antenna directivity versus frequency and the SMA soldering process before measurement.
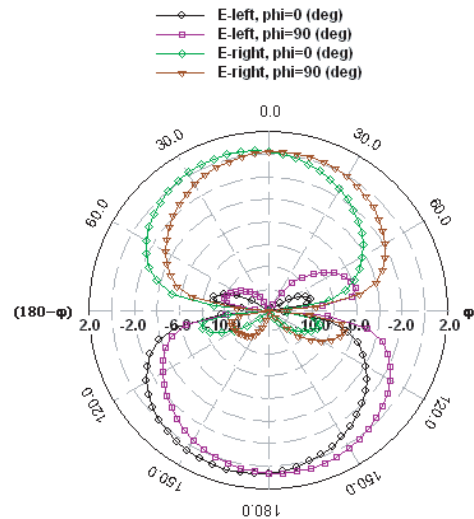


Figure 8: Proposed antenna polar radiation pattern.

## 4. CONCLUSION

Ultra Wide Band UWB circular polarized antenna with right circular polarization has been investigated and fabricated. In the proposed antenna design, matching is done through quarter wavelength microstrip transformer with stub. Landa shape is slotted in the ground plane which can not only be used to enhance the impedance bandwidth, but also to excite circularly polarized radiation waves. IE3D Zeland software has been used in the optimization process. The proposed fabricated antenna achieves measured $-10$ dB bandwidth of 1.77 GHz from 2.34–4.11 GHz which agrees with the computed results and the 3 dB axial ratio bandwidth of 89.1089 MHz (2.39934 MHz–2.48845 MHz) which covers the required band (2.400 MHz–2.483 MHz).

## REFERENCES

1. Barthel, H., "Regulatory status for RFID in the UHF spectrum," EPC Global, Brussels, Belgium, March 2009.

2. Jou, C. F., J.-W. Wu, and C.-J. Wang, "Novel broadband monopole antennas with dual-band circular polarization," *IEEE Transactions on Antennas and Propagation*, Vol. 57, No. 4, 1027–1034, 2009.

3. Sze, J.-Y., C.-I. G. Hsu, M.-H. Ho, Y.-H. Ou, and M.-T. Wu, "Design of circularly polarized annular-ring slot antennas fed by a double-bent microstrip line," *IEEE Transactions on Antennas and Propagation*, Vol. 55, No. 11, 3134–3139, 2007.

4. Ma, G. T. and J. S. Wu, "Ultrawideband band-notched folded strip monopole antenna," *IEEE Transactions on Antennas and Propagation*, Vol. 55, No. 9, 2473–2479, 2007.

# Ground Slotted Phi Shape UWB Stacked Circular Polarized Antenna for 5.8 GHz RFID Reader

**E. A. F. Abdallah**[1], **T. G. Abo-Elnaga**[1], **and H. El-Hennawy**[2]

[1]Electronics Research Institute, Egypt
[2]Faculty of Engineering, Ain Shams University, Egypt

**Abstract**— The design of Ultra Wide Band (UWB) circularly polarized antenna is proposed for 5.8 GHz band (5.725 GHz–5.875 GHz) Radio Frequency Identification (RFID) applications. The antenna is composed of three layers, upper FR4 layer where a well aligned two stacked Cross-slotted circular patch antennas placed upper and beneath it, middle foam layer, bottom FR4 layer with stepped L shape microstrip line on the top and almost phi shape slot etched in the ground plane beneath the L shape microstrip line. The proposed antenna achieves $-10$ dB measured bandwidth of 690 MHz (5.48 GHz–6.17 GHz) which agrees with the simulated results. It also achieves 3 dB axial ratio bandwidth of 207.921 MHz (5.6732 GHz–5.88119 GHz). The proposed antenna occupies a volume of $25 \times 25 \times 4.6$ mm$^3$ and offers an acceptable other antenna parameters within the 5.8 GHz RFID readers bandwidth.

## 1. INTRODUCTION

Radio Frequency Identification (RFID) is the technology that uses radio frequency (RF) signals for automatic identification of objects and items. RFID has become very popular in many services industry, distribution logistics, manufacturing companies and goods flow systems. In these application systems data are transferred to a local reader from a remote transponder(tag) including an antenna and an application specific integrated circuit (ASIC). RFID systems use frequency ranges that have been reserved specifically for industrial, scientific or medical applications, known as the ISM frequencies, such as 13.56 MHz, 2.45 GHz and 5.8 GHz, some work at UHF frequencies such as $840 \sim 845$ MHz, $920 \sim 925$ MHz (China), $952 \sim 954$ MHz (Japan), $868 \sim 870$ MHz (Europe) and $902 \sim 928$ MHz (USA), etc. [1]. The 5.8 GHz band (5.725 GHz–5.875 GHz) gains very high data rates and almost used by movement sensor systems such as those in shops or department stores. For more flexible orientation between reader and tag, circularly polarized (CP) reader antennas have been used in RFID systems. In this paper an Ultra Wide Band (UWB) circularly polarized antenna is proposed for 5.8 GHz band (5.725 GHz–5.875 GHz) Radio Frequency Identification (RFID) applications. The antenna is composed of three layers, upper FR4 layer with two stacked cross-slotted circular patch antennas separated by the thickness of this layer and well aligned with each other, middle foam layer, bottom FR4 layer with stepped L shape microstrip line on the top and almost phi shape slot etched in the ground plane beneath L shaped microstrip line. Feeding scheme dimensions optimized to guarantee the circular polarization operation of the proposed antenna. The proposed antenna achieves $-10$ dB measured bandwidth of 690 MHz (5.48 GHz–6.17 GHz) which agrees with the simulated results. The proposed antenna achieves 3 dB axial ratio bandwidth of 207.921 MHz (5.6732 GHz–5.88119 GHz) which covers the required band. The cross slotted circular patch occupies an area of radius 6.7 mm and square of 25 mm length for the ground plane. The proposed antenna is simple, cheap and offers an acceptable other antenna parameters on the 5.8 GHz RFID readers bandwidth.

## 2. ANTENNA DESIGN

The use of the aperture-coupled feed can provide more freedom parameters in impedance-matching design without the need of soldering contact between radiating elements and feeding circuit. Circular polarization CP radiation for the aperture-coupled microstrip antennas is produced by designing the aperture as a centered cross slot to excite two orthogonal resonant modes with 90° phase difference. By carefully adjusting the slot lengths of the cross slot to be different and with an adequate length ratio, the CP performance with lower axial ratio can be achieved. In addition, the current paths of the two orthogonal resonant modes would be lengthened due to the existence of the cross slot in the ground plane, and consequently the CP operating frequency of the cross-slot-coupled microstrip antenna is lower than that of the probe-feed microstrip antenna with the same patch size [2]. In this paper, the CP design of two stacked cross slotted circular microstrip antennas fed

through the coupling of a phi shape slot in the ground plane of stepped L shape microstrip line is proposed. The proposed antenna is single feed and the required two orthogonal resonant modes are excited by a series feed configuration [3] through the coupling of the phi slot. The two cross slotted stacked circular patches radii is chosen to be equal. Based on Equation (1) and Equation (2) [4], the cross slotted circular patch radius $R$ was calculated and it is found to be 6.7 mm with resonance frequency $f_r = 5.8$ GHz with slot length $L_s$ and width $W_s$ optimized to be 8 mm and 1 mm, respectively. FR4 material substrate with dielectric constant $\varepsilon_r = 4.65$ and thickness $h = 1.5$ mm was chosen to place both cross slotted stacked circular patches on both sides as shown in Figure 1. Figure 2 shows the feeding scheme where phi shape slot in the ground plane with inner radius $R_2$, outer radius $R_1$, arm length $L_{sf}$ and arm width $W_{sf}$ are optimized using IE3D Zeland electromagnetic simulator based on the method of moments and found to be 3.1 mm, 4.1 mm, 4.9 mm and 1.5 mm, respectively. The ground plane is chosen to be square with length $L_g = 25$ mm. The geometric dimensions of the stepped L shape microstrip line shown in Figure 2 was optimized using IE3D and found to be $W_{1f} = 0.75$ mm, $W_{2f} = 2.72$ mm, $L_{3f} = 9.87$ mm, $L_{2f} = 5.37$ mm, $L_{1f} = 9.2332$ mm. A foam layer with dielectric constant $\varepsilon_r = 1.05$ and thickness $h_1 = 1.6$ mm is inserted between the two FR4 substrates where the upper substrate contains the two stacked slotted circular patches
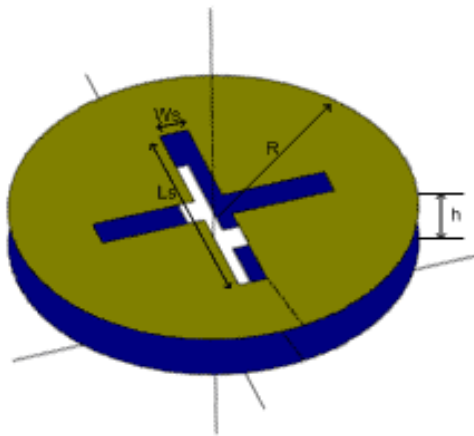


Figure 1: Two cross slotted stacked circular patches antenna deposited on two sides of upper FR4 substrate.
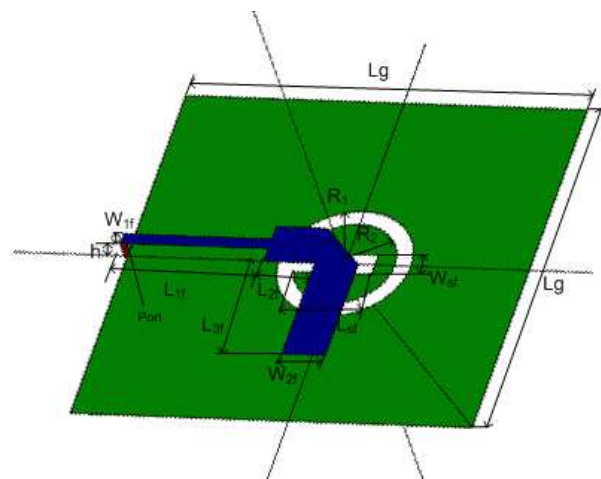


Figure 2: Feeding scheme of the proposed antenna deposited on two sides of lower FR4 substrate.
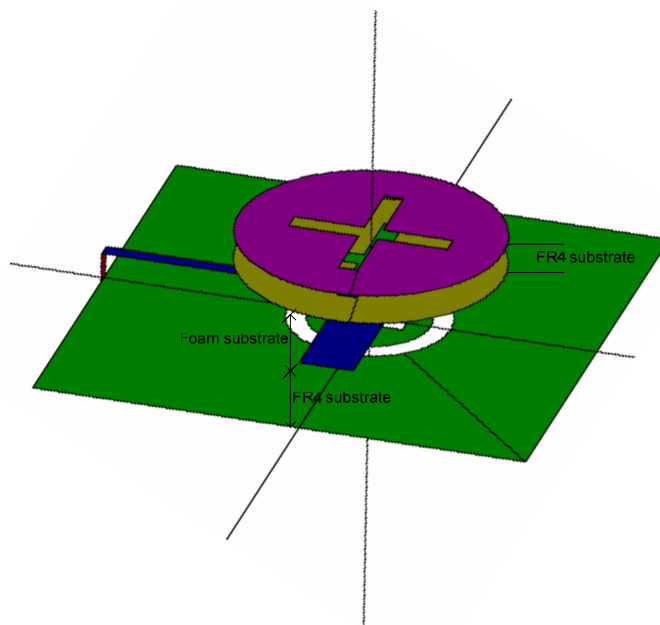


Figure 3: Complete proposed antenna structure.

and the lower containing the feeding system as shown in Figure 3.

$$R = \frac{A}{\left\{1 + \frac{2h_1}{\pi \varepsilon_r A}\left[\ln\left(\frac{\pi A}{2h_1}\right)\right] + 1.7726\right\}^{1/2}} \tag{1}$$

where

$$A = \frac{8.791 \times 10^9}{f_r \sqrt{\varepsilon_r}} \tag{2}$$

## 3. SIMULATED AND MEASURED RESULTS

The circular polarized two cross slotted circular patches with phi shape slot in its ground plane whole structure is simulated using IE3D simulator and its optimum dimensions were found as stated previously. The proposed antenna was fabricated as shown in Figure 4 where upper, bottom and side view are shown in Figures 4(a), 4(b) and 4(c), respectively. The measured and simulated reflection coefficient $S_{11}$ are shown in Figure 5. The proposed antenna achieves $-10$ dB measured bandwidth of 690 MHz (5.48 GHz–6.17 GHz) compared with 960 MHz (5.08 GHz–6.04 GHz) computed bandwidth. The discrepancies are mainly because of the fabrication difficulty in precise alignment between the phi shape slotted ground plane, L shape stepped microstrip line and the two well aligned cross slotted circular patches and the SMA soldering process before measurement. The proposed antenna achieves 3 dB axial ratio bandwidth of 207.92 MHz (5.6732 GHz–5.88119 GHz) as shown in Figure 6 which cover the required band. Figure 7 and Figure 8 show both proposed antenna gain and directivity respectively. Figure 9 and Figure 10 show the proposed antenna polar and cartesian radiation pattern, respectively from which, the proposed antenna introduces a Left Hand Circular Polarization performance.
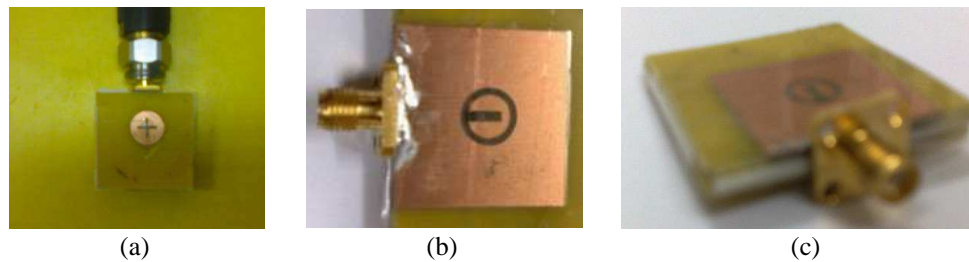


(a)　　　　　　　　　(b)　　　　　　　　　(c)

Figure 4: (a) Fabricated antenna upper view. (b) Fabricated antenna bottom view. (c) Fabricated antenna side view.
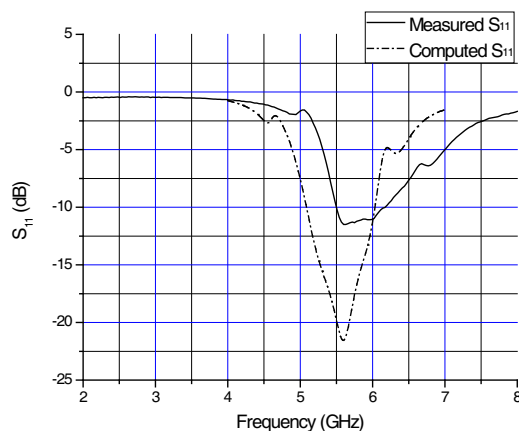


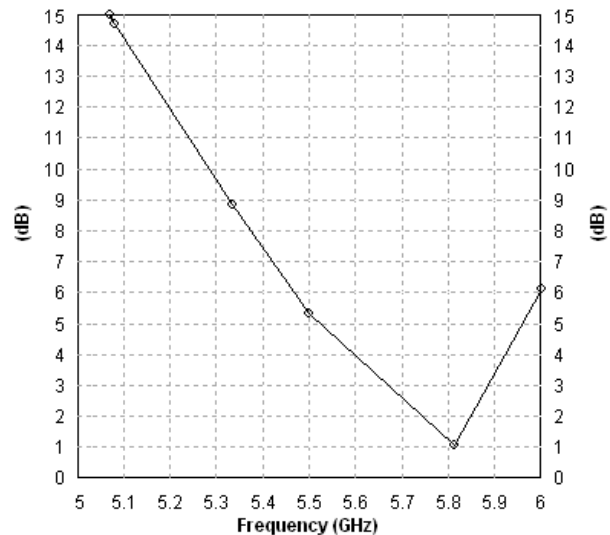Figure 5: Proposed antenna $S_{11}$ versus frequency.

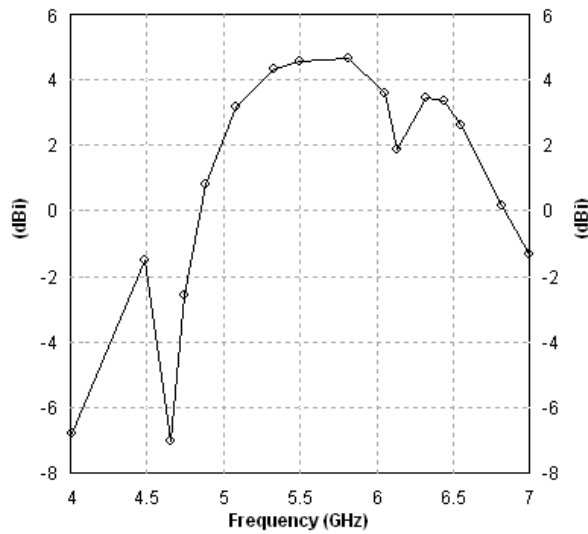Figure 6: Proposed antenna axial ratio versus frequency.

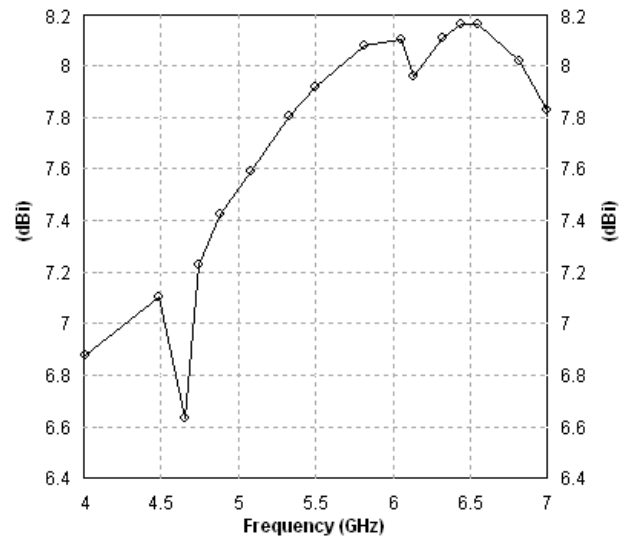Figure 7: Proposed antenna gain versus frequency.



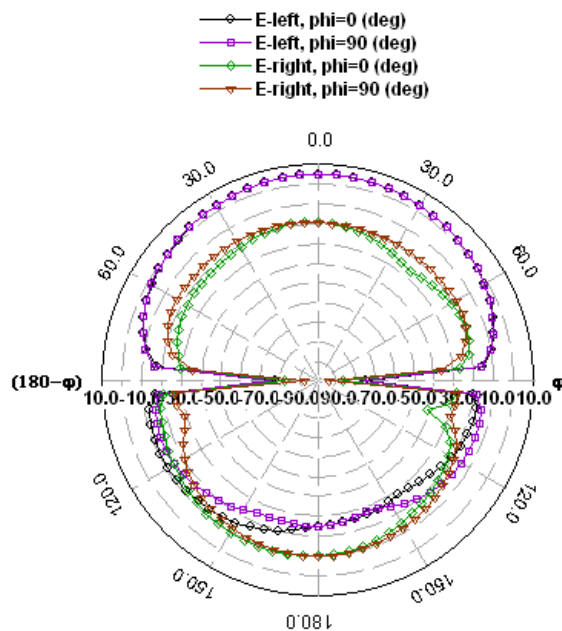Figure 8: Proposed antenna directivity versus frequency.

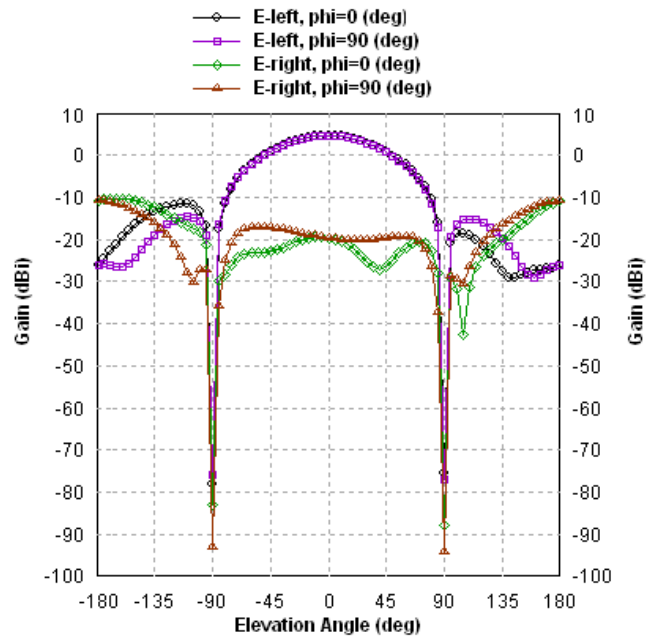

Figure 9: Proposed antenna polar radiation pattern.



Figure 10: Proposed antenna cartesian radiation pattern.

## 4. CONCLUSIONS

Circular Polarized two stacked cross slotted circular patches fed by L shape stepped microstrip line with phi shape slot in its ground plane was investigated and fabricated for 5.8 GHz RFID reader antenna. Both stacking and slotting methodologies were used for bandwidth enhancement. Circular polarization was enhanced through the feeding system where stepped microstrip line placed over a phi shape slotted ground plane. The proposed antenna achieves −10 dB measured bandwidth of 690 MHz (5.48 GHz–6.17 GHz) compared with 960 MHz (5.08 GHz–6.04 GHz) computed bandwidth with 3 dB axial ratio bandwidth of 207.921 MHz (5.6732 GHz–5.88119 GHz) which covers the required band. The proposed fabricated antenna is cheap, compact and suitable for 5.8 GHz RFID reader applications.

### REFERENCES

1. Barthel, H., *Regulatory Status for RFID in the UHF Spectrum*, EPC Global, Brussels, Belgium, March 2009.

2. Row, S. J., " Design of aperture-coupled annular-ring microstrip antennas for circular polarization," *IEEE Trans. Antennas Propag.*, Vol. 53, No. 5, 1779–1784, 2005.

3. Targonski, D. S. and M. D. Pozar, "Design of wideband circularly polarized aperture-coupled microstrip antennas," *IEEE Trans. Antennas Propag.*, Vol. 41, No. 2, 214–220, 1993.

4. Shen, L., S. Long, M. Allerding, and M. Walton, "Resonant frequency of a circular disc, printed-circuit antenna," *IEEE Trans. Antennas Propag.*, Vol. 25, No. 4, 595–596, July 1977.

# An Electromagnetic Target Classification Method for the Target Sets with Alien Target: Application to Small-scale Aircraft Targets

**M. Secmen[1] and G. Turhan-Sayan[2]**

[1]Department of Electrical and Electronics Engineering, Izmir Institution of Technology, Izmir, Turkey
[2]Department of Electrical and Electronics Engineering, Middle East Technical University, Ankara, Turkey

**Abstract**— The electromagnetic target classification is a challenging problem since the scattered field from a target is highly dependent on operating frequency, polarization and aspect angle. In order to minimize adverse effects of these dependencies an intelligent classifier containing some distinguishable target features is needed. In addition, in order to be suitable for real target applications, the properties of operating with moderate frequency bandwidth and discriminating an alien target from a target set containing friend targets are important. In this study, an electromagnetic target classification method for isolated targets using noisy data in the classifier design to obtain high accuracy performance in a wider SNR range and having the ability of discrimination of an alien target without any priori information is introduced. The proposed method is mainly based on a late-time resonance region target classification technique, which was reported recently to use the multiple signal classification (MUSIC) algorithm and natural-resonance mechanism modeled by singularity expansion method (SEM) for target feature extraction, and modified for target sets containing alien target(s). The proposed classifier design method is demonstrated and tested for a target set of five friend and one alien small-scale aircraft targets. According to the test result, the proposed method gives high accuracy rates for this target set.

## 1. INTRODUCTION

The scattering from an electromagnetic target is a complex mechanism due to the fact that the scattered fields are strongly dependent on operation frequency, polarization (both transmitter and receiver) and aspect angle (azimuth and elevation). Besides, the additional environmental noise makes the electromagnetic target classification problem more complicated. Therefore, in order to diminish the dependencies of all these mentioned facts an intelligent classifier distinguishing test targets with some specially designed features is needed. Besides, the criteria of the accuracy, satisfactory noise performance, high decision speed in real time, small memory requirements and simplicity should be satisfied. In addition, in order to be suitable for real target applications, the properties of operating with moderate frequency bandwidth and discriminating alien targets from friend targets are important.

A finite size electromagnetic target has three different scattering regions with respect to operating frequency: Rayleigh region, resonance region and optical region. The resonance region of a target (target dimensions are comparable to $\lambda$) in which the proposed method in this paper also works has stronger operation frequency but slighter aspect angle dependency with respect to radar cross section change that about 15–20 degrees changes in aspect angle is needed to observe moderate changes in scattered fields for most of the targets in this region.

The resonance region methods mainly base on the Singularity Expansion Method (SEM) formulated by C. E. Baum [1]. According to this method, the scattered frequency response of an electromagnetic target is represented as a sum of an entire function and a meromorphic function resulting in a time limited function plus superposition of damped sinusoidals in the time response such that

$$H(s,\Omega) = G(s,\Omega) + \sum_{n=1}^{\infty} \frac{R_n(s,\Omega)}{(s-s_n)(s-s_n^*)}, \quad h(t,\Omega) = g(t,\Omega) + \sum_{n=1}^{\infty} b_n(\Omega)e^{\alpha_n t}\cos(w_n t + \theta_n) \quad (1)$$

Here, time limited function $g(t,\Omega)$ is defined as forced response due to the interaction of the incident wave with the target and it continues until the wave fully passes the target. Afterwards, only the infinite summation part exists (the late-time response). This time limited function has no standard form as the summation part and its magnitude is stronger as compared to the summation part. Therefore, the resonance region methods try to stay away from early-time response containing

forced response and want to study in the late-time region. In the same equation the complex valued $s_n = \alpha_n + j\omega_n$ parameters are called as target poles (complex natural resonance frequencies). The most important property of these parameters is to be independent from aspect angle and polarization leading to an aspect and polarization invariant target classification. Therefore, the initial resonance region methods attempt to make the classification by calculating the target pole values directly [2, 3]. However, the estimation of pole values is so sensitive to the random additive noise that while these methods give good results for noiseless signals, the estimated values become to deviate significantly even for moderate noisy data. Therefore, the following improved methods have used the pole information in an indirect manner supported with signal processing tools or algorithms.

The Multiple Signal Classification (MUSIC) algorithm, which is the signal processing tool used in the proposed method, is a line spectra method trying to estimate the parameters of the un-damped/damped sinusoidal signals as the summation part of the above equation (late-time response) under additive Gaussian noise.

In the proposed method, by help of MUSIC algorithm, MUSIC spectrum matrices (MSMs) are constructed for each reference aspect angle of each friend target, which will be briefly explained in the following part; but, was given in detail in [4]. In the next step, the optimal late-time interval and fused MSMs for each friend target are extracted. Finally, the classification is done by comparing fused MSMs of friend targets with MSM of test target [4]. In this study, the proposed method is also modified in order to discriminate alien target(s) from friend targets. In order to demonstrate the proposed method, a target set containing five friend and one alien small-scale aircraft targets is selected and the application of the method to this set and test results are given in the final part.

## 2. THE THEORY OF THE METHOD

The natural response of a scattered field from a target at a certain aspect angle with additional Gaussian noise in the late-time interval can be expressed in discrete time domain as

$$y(n) = x(n) + w(n) = \sum_{i=1}^{L} b_i e^{s_i n \Delta t} + w(n), \quad n = 1, 2, \ldots, N \tag{2}$$

where $s_i = \alpha_i + j\omega_i$ is the $i$th target pole, $L$ is the number of dominant poles over the frequency bandwidth, $w(n)$ is the Gaussian noise and $\Delta t$ is the sampling interval. As the first step to construct MSM belonging to this signal, the sampled correlation matrix is formed as [5]

$$IR = \frac{1}{N} \sum_{n=m}^{N} \overline{y(n)} \, \overline{y(n)}^H, \quad \overline{y(n)} = [y(n)y(n-1)\ldots y(n-L+1)]^T \tag{3}$$

Then, by using the singular value decomposition (SVD) method, G matrix is constructed as G $= [e_{L+1} \ldots e_m]$ in terms of a subset of eigenvectors of the correlation matrix for $i = L+1, \ldots, m$ belonging to eigenvalues $\lambda_i = \sigma^2$ with $\sigma^2$ being the variance of Gaussian noise. Then, the MUSIC Spectrum Matrix (MSM) is computed in the complex frequency domain as a matrix $P(u, v)$:

$$P(u, v) = \frac{1}{a^H(u, v) \, GG^H a(u, v)} \, , \ \ a(u, v) = \begin{bmatrix} 1 & e^{-(\alpha_u + j\omega_v)} & \ldots & e^{-(\alpha_u + j\omega_v)(m-1)} \end{bmatrix}^T \tag{4}$$

According to MUSIC algorithm, the matrix gives peak values at $s_i = \alpha_u + j\omega_v$ revealing the target pole values. However, as the other direct pole extraction methods although the algorithm gives accurate results for noiseless or low noisy signals, the pole values may shift with the increasing noise. Therefore, the proposed method uses the whole matrix containing the distribution of target's natural resonance related power at the associated aspect angle instead of target pole values directly.

At the phase of selection of optimal late-time interval and construction of feature database, assume that there exist $K$ friend targets with $M$ reference aspect angle/polarization conditions for each target resulting in a total number of $K \times M$ scattered signals. Each signal is divided into $p = 1, \ldots, P$ certain subintervals in order to determine the optimal late-time interval. Here, the aim is to find a suitable time interval where the scattered signal fits the expression given in (2). This interval should not be in the early-time interval where the forced response is dominant; but, also not be in further late-time intervals where noise is dominant over natural-resonance response. For this purpose, MSMs of all scattered signals for all selected subintervals are constructed with

MUSIC algorithm described above. Then, the MSMs belonging $M$ different reference aspect angles are normalized and superposed and fused MSM (FMSM) is obtained for a subinterval of a friend target. This procedure is repeated for all subinterval/friend targets. If a subinterval is a candidate of optimal late-time interval fitting the expression in (2), the MSMs of a friend target should have roughly same peak locations (pole values) on the matrices; therefore, the FMSM as the superposition of these MSMs should have same peak locations. Accordingly, the MSMs of a target should be highly correlated with FMSM of same target in the optimal late-time interval. On the other hand, the MSMs of a target should be highly uncorrelated with FMSM of another target since their peak locations are different. As a result, the optimal late-time interval is determined after a detailed investigation that the parameter $r_{total}$ given in (5) gives maximum value in selected time interval.

$$r_{total}(p) = \frac{1}{KM} \sum_{i=1}^{K} r_{i,match} - \frac{1}{K(K-1)M} \sum_{i=1}^{K} r_{i,mismatch},$$

$$r_{i,match} = \sum_{j=1}^{M} \sum_{v=1}^{k_2} \sum_{u=1}^{k_1} FMSM_i(u,v) P_{i,j}(u,v) \tag{5}$$

$$r_{i,mismatch} = \sum_{\substack{k=1 \\ k \neq i}}^{K} \sum_{j=1}^{M} \sum_{v=1}^{k_2} \sum_{u=1}^{k_1} FMSM_i(u,v) P_{k,j}(u,v)$$

Here, $FMSM_i$ refers to the FMSM of the $i$th friend target and $P_{i,j}$ refers to the MSM of friend target $i$ at the reference aspect angle $j$. After the selection of the optimal late-time interval, FMSMs belonging to this interval are obtained and stored as feature database for $K$ friend targets. In addition, as being different from the original method in [4], $r_{i,match}$ values (also mean $(\mu_i)$ and standard deviation $(\sigma_i)$ values) are stored for friend targets in order to be used for alien target discrimination. At the test phase, the scattered field of a test target (friend or alien) at an unknown aspect angle are obtained. Then, the MSM belonging to the selected optimal late-time interval for this target is extracted. Finally, the correlation values between FMSMs of friend targets and this MSM are obtained with according to (6). By using maximum of these correlation values and the following algorithm, test target is classified as $i^*$th friend target or an alien target.

$$r(i) = \sum_{v=1}^{k_2} \sum_{u=1}^{k_1} FMSM_i(u,v) P_{test}(u,v), \quad r(i^*) = \max(r(i)) \quad \forall i = 1, \ldots, K \tag{6}$$

• Test target = target $i^*$ if $(\mu_{i^*} - 3\sigma_{i^*}) \leq r(i^*)$; otherwise, Test target = alien target.

The main idea in this decision criterion is that if test target is indeed $i^*$th friend target, the correlation between MSM of test target and FMSM of $i^*$th target should be high and also close enough to $r_{i^*,match}$ values or mean value $(\mu_{i^*})$. However, if test target is an alien target, the correlations should be sufficiently low with each of friend target including $i^*$th target having maximum correlation with MSM of test target. Here, the value $(\mu_{i^*} - 3\sigma_{i^*})$ is selected due to giving best results in most applications tested including the following application.

## 3. THE APPLICATION TO SMALL-SCALE AIRCRAFT TARGETS

The performance of the proposed classifier design method is demonstrated for a target set of five small-scale aircraft targets (Airbus, Boeing 747, Caravelle, P-7 and Tu 154) and an alien aircraft target (DC-10) The aim of this simulation is to classify all five aircraft in target set and discriminate DC-10 from this target set. All six aircraft targets, whose dimensions are scaled by 1/100, are modeled by perfectly conducting, straight, thin wires. The wire lengths for body, wing and tail of each target are given in Table 1.

Geometrically, the aircraft models lie in $xy$ plane with nose pointing $+y$ direction as described in Figure 1(a). The backscattered responses of targets are numerically (MoM) generated at the aspects of $\phi = 5, 10, 15, 22.5, 30, 37.5, 45, 52.5, 60, 67.5, 75$ and $82.5$ degrees and fixed $\theta = 60$ degrees for 0–1024 MHz frequency band with $\Delta f = 4$ MHz. For the noise analysis, time-domain are synthesized at the SNR values of 20, 15, 10, 5 and 0 dB with time span 250 nanoseconds and 512 time samples ($\Delta t \cong 500$ psec). For example, the backscattered time domain signal for Airbus at 5 degrees aspect angle with 10 dB SNR level is plotted in Figure 1(b).

The feature database of the classifier is constructed at 10 dB SNR level for the friend aircraft targets at five aspects ($\phi = 5, 15, 30, 45$ and $75$ degrees) out of 12 different aspects. In the step

Table 1: The dimensions of all aircraft targets.

| Substructures | Target (Airbus) | Target 2 (Boeing 747) | Target 3 (Caravelle) | Target 4 (P-7) | Target 5 (Tu 154) | Target 6 (Alien target) (DC-10) |
|---|---|---|---|---|---|---|
| Body length (m) | 0.5408 | 0.7066 | 0.3200 | 0.3435 | 0.4790 | 0.6342 |
| Wing length (m) | 0.4484 | 0.5964 | 0.3440 | 0.3250 | 0.3755 | 0.5348 |
| Tail length (m) | 0.1626 | 0.2217 | 0.1092 | 0.1573 | 0.1340 | 0.2437 |
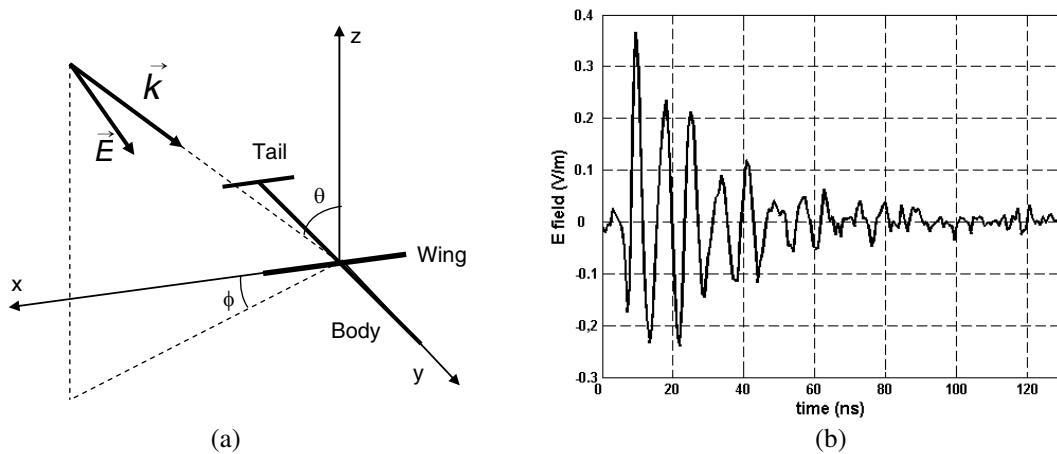


Figure 1: (a) Geometry for small-scale aircraft targets. (b) Time-domain signal backscattered from Airbus at $\phi = 5$ degrees aspect angle with 10 dB SNR level.
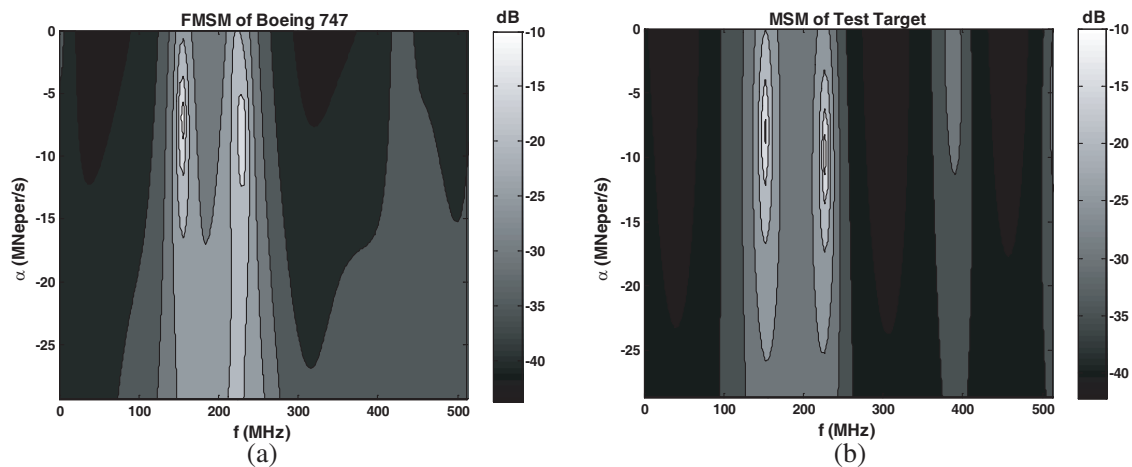


Figure 2: (a) FMSM of Boeing 747. (b) MSM belonging to test target (Boeing 747 at $\phi = 82.5$ degree aspect angle with 10 dB SNR level).

of choosing the optimal late-time interval, the subintervals are constructed with a total length of $N = 64$ and the MUSIC parameters are chosen as $L = 16$ and $m = 32$. The optimal late-time interval is found to be the interval 16–48 nsec for this target set. Accordingly, FMSM features are obtained belonging to this subinterval, where a sample for Boeing 747 is shown in Figure 2(a) (others in [4]), and the criterion $(\mu_i - 3\sigma_i)$ values are also stored (0.2607 for Boeing 747).

After completing the classifier design, in decision stage all aspect angles are used for testing purposes making a total number of (6 targets) × (12 aspects) = 72 signals at each SNR level and trial. As an example, the MSM for Boeing 747 at $\phi = 82.5$ degrees with SNR = 10 dB computed over the optimal latetime interval is shown in Figure 2(b). The matched correlation coefficient for this test target/aspect is computed as 0.6231 (between spectra in Figures 2(a) and (b)) while the mismatched correlation coefficients are computed as 0.0373, 0.0239, 0.0278 and 0.1875 for

Progress In Electromagnetics Research Symposium Proceedings, Cambridge, USA, July 5–8, 2010Airbus, Boeing 747, Caravelle and P-7, respectively. The maximum correlation coefficient (0.6231) is sufficiently above the criterion value (0.2607) that test target is correctly classified as Boeing 747. In other test example belonging to DC-10 (alien target) at $\phi$=10 degrees with SNR = 10 dB, the maximum coefficient is found from correlation with FMSM of Boeing 747 as 0.1471 which is lower than 0.2607; therefore, test target is correctly classified as an alien target. According to overall test result, the proposed method gives almost 100 percent accuracy for SNR = 20 and 15 dB and this rate gradually drops to 99, 94 and 89 percent for SNR = 10, 5 and 0 dB, respectively that the capability of classification of friend targets and discrimination of an alien target from the friend targets is said to be successful for the proposed method. Thus, the proposed method gives satisfactory results with moderate frequency bandwidth even at low SNR values for this target set although the classifier design approach need a few reference aspects and small memory storage.

REFERENCES

1. Baum, C. E., E. J. Rothwell, K. M. Chen, et al., "The singularity expansion method and its application to target identification," *Proc. IEEE*, Vol. 79, No. 10, 1481–1492, 1991.

2. Van Blaricum, M. L. and R. Mittra, "A technique for extracting the poles and residues of a system directly from its transient response," *IEEE Trans. Ant. Propag.*, Vol. 23, No. 6, 777–781, 1975.

3. Chuang, C. W. and D. L. Moffatt, "Natural resonances of radar targets via Prony's method and target discrimination," *IEEE Trans. Aero. and Elect. Sys.*, Vol. 12, No. 5, 583–589, 1976.

4. Secmen, M. and G. Turhan-Sayan, "Radar target classification method with reduced aspect dependency and improved noise performance using multiple signal classification algorithm," *IET Radar, Sonar and Navig.*, Vol. 3, No. 6, 583–595, 2009.

5. Stoica, P. and R. Moses, *Introduction to Spectral Analysis,* Prentice Hall, New Jersey, 1997.

# Unsupervised Electromagnetic Target Classification by Self-organizing Map Type Clustering

**T. T. Katilmis**, **E. Ekmekci**, and **G. Turhan-Sayan**

Department of Electrical and Electronics Engineering, Middle East Technical University, Ankara, Turkey

**Abstract**— In this study, design of a completely unsupervised electromagnetic target classifier will be described based on the use of Self-Organizing Map (SOM) type artificial neural network training and Wigner distribution (WD) based target feature extraction technique. The suggested classification method will be demonstrated for a target library of four dielectric spheres which have exactly the same size but slightly different permittivity values.

## 1. INTRODUCTION

Electromagnetic target recognition is a challenging problem due to the aspect and polarization dependent nature of system response. Various target classification methods have been suggested in resonance region based on the use of aspect and polarization invariant target poles either directly or indirectly [1–3]. As most of these methods perform successfully to discriminate targets under the ideal noise-free case, only a few of those are demonstrated to be satisfactory in recognizing targets using noisy electromagnetic scattered data. Feature extraction is known to be a very important problem in target classifier design. Electromagnetic system modeling and signal processing techniques used to extract target features should be selected appropriately to provide robustness against noise while minimizing the sensitivity of classifier to varying conditions of excitation and/or detection regarding aspect and polarization. To satisfy these critical requirements in the present design work, target features are extracted from the available late-time natural response waveforms using a well known time-frequency representation technique, the Wigner-Ville distribution, as described in [4].

Most of the methods reported in electromagnetic target recognition literature have used the conventional supervised classifier design technique that makes use of a reference signal database composed of scattered signals each labeled by the type and properties of the associated library target. The classifier design method suggested here, however, does not need to have any sort of *a priori* information about the number or types of library targets or about the origin (i.e., the target label and aspect/polarization conditions) of reference signals used in classifier design. Instead, a set of transient response waveforms collected from an unknown number of targets at unknown aspect/polarization conditions are processed first to extract useful features from the natural response part of each signal. Then, these features are grouped into non-overlapping clusters of a self-organizing map (SOM) constructed by the well known unsupervised learning algorithm of Kohonen [5]. Signals scattered by the same target at different aspects and/or polarizations must be represented within the same cluster if the classifier is trained successfully.

The classifier design technique outlined above will be demonstrated for a set of four perfect dielectric spheres of the same size but having slightly different permittivity values.

## 2. SOM TRAINING METHOD

The SOM network is originally defined by Kohonen [5] as a two-dimensional layer of neurons and the associated unsupervised training algorithm creates a mapping from a high dimensional input vector space onto a two dimensional output lattice called the SOM output map. The weight vectors $(\bar{w}_{ij})$ belonging to neurons $(n_{ij})$ (for $i = 1, \ldots, I$ and $j = 1, \ldots, J$) are randomly initialized. These weight vectors have the same length $(K)$ as the training and testing feature vectors. In a given iteration $(t)$ of the training procedure, one of the training feature vectors is randomly selected and compared to the weight vectors of the SOM lattice to determine the winning neuron $(n_{i^*j^*})$ whose weight vector is closest to the training target feature input $\bar{u}(t)$ in the $L_2$ norm sense:

$$\left\{ \sum_{k=1}^{K} [u_k(t) - w_{i^*j^*k}(t)]^2 \right\}^{1/2} \leq \left\{ \sum_{k=1}^{K} [u_k(t) - w_{ijk}(t)]^2 \right\}^{1/2} \quad \text{for all } i, j \qquad (1)$$

and the weight vectors are updated as

$$\bar{w}_{ij}(t+1) = \bar{w}_{ij}(t) + N_{i^*j^*}(t)\,\eta(t)\,\lfloor \bar{u}(t) - \bar{w}_{ij}(t) \rfloor \tag{2}$$

where $\eta(t)$ is the learning rate and $N_{i^*j^*}(t)$ is a neighborhood function centered at the winning neuron $n_{i^*j^*}$ of that particular iteration. Both the learning rate and the width of the neighborhood function are decreased as the iteration index $(t)$ increases for fine-tuning.

## 3. APPLICATIONS AND RESULTS

SOM type electromagnetic target classification was demonstrated for perfect conductors earlier [6]. In this paper, this approach is applied to dielectric targets with more complicated resonance mechanisms. A SOM type electromagnetic target classifier is designed for four dielectric spheres $S_1$, $S_2$, $S_3$ and $S_4$ which have the same radii of 10 cm and relative permittivity ($\varepsilon_r$) values of 3, 4, 5 and 6, respectively. Although having a simple geometry, these spheres are challenging targets as electromagnetic waves can penetrate into such objects to create complicated interior resonance mechanisms with a large number of closely located poles [3]. Also, the classifier problem studied here is a difficult one since the spherical targets of this classifier design problem are only slightly different from each other having very similar and overlapping pole patterns.

In this design exercise, the SOM classifier is trained and tested by partitioned energy type feature vectors [4] extracted from the natural response related scattered signals of these spheres over the late-time interval of [16.8–20.1] nanosecond. Problem geometry used to synthesize such electromagnetic data is shown in Figure 1(a). Scattered transient response of the sphere $S_2$ for the bi-static aspect angle $\theta_b = 180 - \theta = 105$ degrees at 20 dB signal to noise ratio (SNR) is shown in Figure 1(b) and the feature vector extracted from this signal is plotted in Figure 1(c),
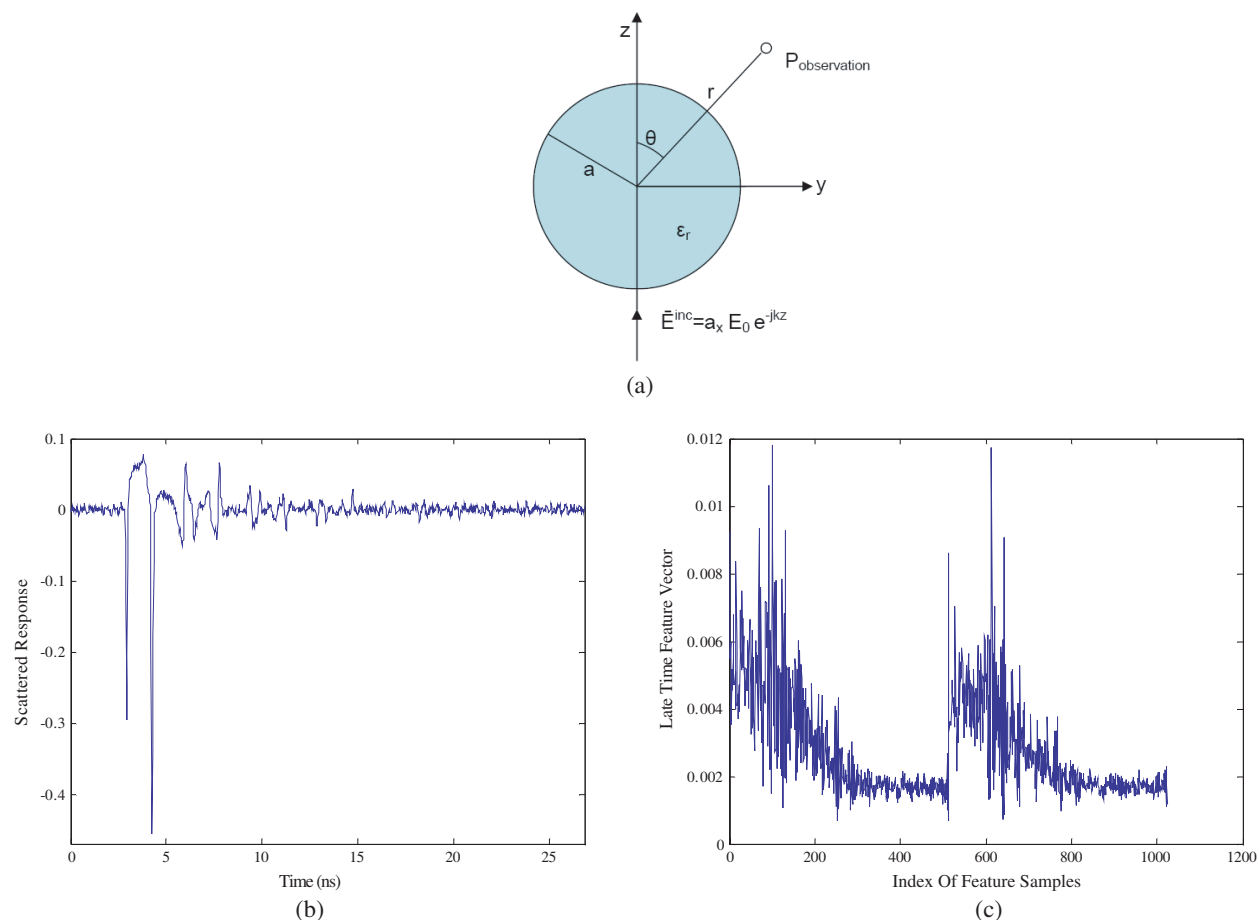


(a)



(b)

(c)

Figure 1: (a) Problem geometry used to synthesize electromagnetic signals scattered from dielectric spheres. (b) Scattered response of the sphere $S_2$ at $\theta = 75$ degrees aspect angle at 20 dB SNR level. (c) Feature vector extracted from the signal in part (b).

as an example. The frequency bandwidth used to synthesize such data extends from 37.3 MHz to 19.1 GHz and the overall time span of the resulting scattered signals (sampled at 1024 points) is 26.8 nanoseconds. Similar far field scattered responses are computed at the aspects defined by $\varphi = \pi/2$ and $\theta = 5, 15, 30, 45, 60, 75, 90, 105, 120, 135, 165$ and 179 degrees for each sphere. Only six of those aspects ($\theta = 5, 30, 75, 105, 135$ and 179 degrees) are used to train the SOM classifiers in this paper.

Regarding the SOM learning algorithm, the maximum number of iterations is taken to be 500 epochs (using each and every training feature vector only once at each iteration but in a random order) with initial learning rate of 0.5 and using a Gaussian type neighborhood function.

First, a SOM classifier is designed by noise-free data (i.e., at infinite SNR level) and it is tested at SNR levels of infinity, 20 dB, 15 dB and 10 dB with accuracy rates of 100, 100, 81 and 47 percent levels, respectively. The SOM map showing the winning neurons of training data and the resulting
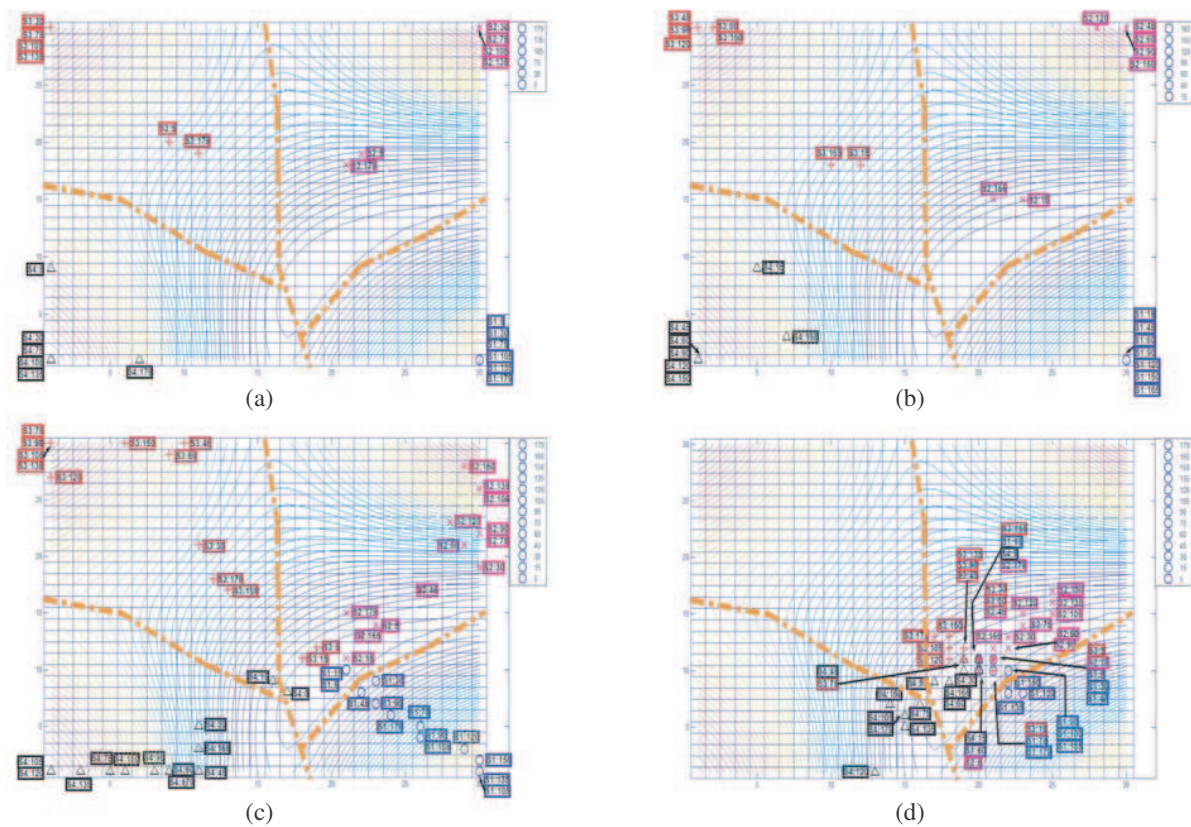


Figure 2: Cluster boundaries and winning neuron locations for (a) noise-free training features, (b) noise-free test features, (c) test features at 20 dB SNR and (d) test features at 10 dB SNR on the SOM classifier output trained by noise-free data. (Markers: $S_1$-blue circles, $S_2$-magenta cross signs, $S_3$-red plus signs and $S_4$-black triangles).
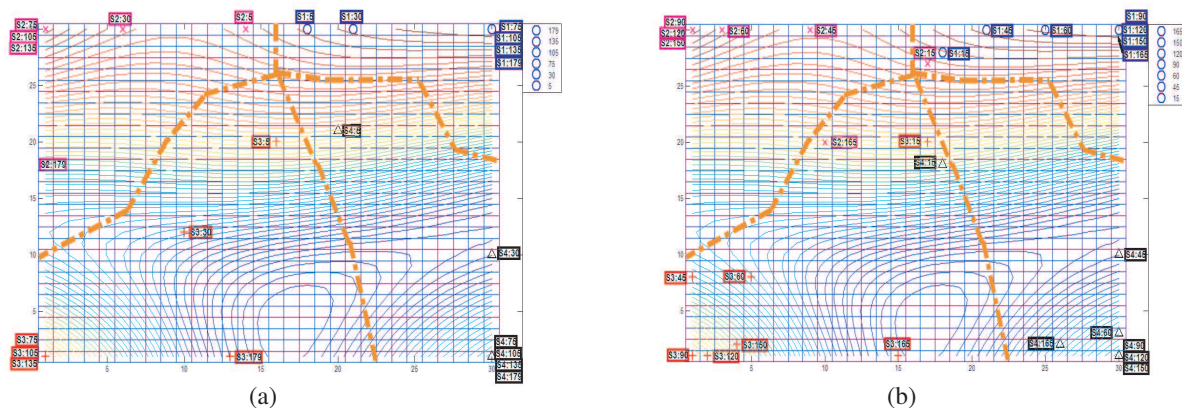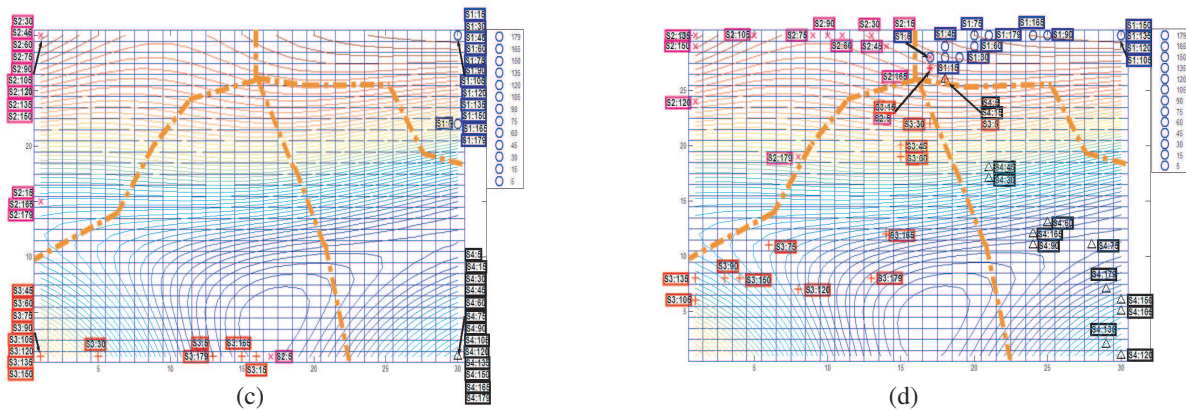
Figure 3: Cluster boundaries and winning neuron locations for (a) training features at 20 dB SNR, (b) test features at 20 dB SNR, (c) noise-free test features and (d) test features at 10 dB SNR on the SOM classifier output trained by slightly noisy data at 20 dB SNR. (Markers: $S_1$-blue circles, $S_2$-magenta cross signs, $S_3$-red plus signs and $S_4$-black triangles).

clusters for each sphere is given in Figure 2(a). Winning test neurons at noise-free, 20 dB and 10 dB SNR levels are shown on the SOM outputs given in Figures 2(b) through 2(d).

Next, the classifier design is repeated by using slightly noisy data at 20 dB SNR with the resulting cluster map shown in Figure 3(a). This SOM classifier is tested at 20 dB, infinite and 10 dB SNR levels as shown in Figures 3(b), 3(c) and 3 (d) with accuracy rates of 100, 100, 100 and 75 percent, respectively. It is observed that the classification accuracy is significantly increased at lower SNR levels by designing the classifier with slightly noisy data.

## 4. CONCLUSION

In this paper, two SOM classifiers are designed to classify four very similar dielectric spheres in a completely unsupervised manner using first noise-free then slightly noisy reference scattered data. Both classifiers attained 100 percent accuracy rates at 20 dB SNR and above. The SOM classifier designed at 20 dB SNR not only performed much better to discriminate targets at higher noise levels but also has a much better clustering behavior at all noise levels, in general.

## REFERENCES

1. Moffatt, D. L., J. D. Young, A. A. Ksienski, H. Lin, and C. M. Fhoads, "Transient response characteristics in identification and imaging," *IEEE Trans. Antennas and Propagation*, Vol. 29, 192–205, 1981.
2. Nyquist, D. P., K. M. Chen, E. Rothwell, and B. Drachman, "Radar target discrimination using the extinction-pulse technique," *IEEE Trans. Antennas and Propagation*, Vol. 33, 929–937, Sep. 1985.
3. Turhan-Sayan, G. and M. Kuzuoglu, "Pole estimation for arbitrarily-shaped dielectric targets by a genetic algorithm-based resonance annihilation technique," *IEE Electronics Letters*, Vol. 37, No. 6, 380–381, Mar. 2001.
4. Turhan-Sayan, G., "Real time electromagnetic target classification using a novel feature extraction technique with PCA-based fusion," *IEEE Trans. Antennas and Propagation*, Vol. 53, No. 2, 766–776, Feb. 2005.
5. Kohonen, T., *Self-organisation and Associative Memory*, Springer-Verlag, 1989.
6. Turhan-Sayan, G., K. Leblebicioglu, and T. Ince, "Electromagnetic target classification using time frequency analysis and neural networks," *Microw. Opt. Technol. Lett.*, Vol. 21, No. 1, 63–69, 1999.

# Computing the Magnetic Induction Field Due to a Radially-magnetized Finite Cylindrical Permanent Magnet by Employing Toroidal Harmonics

**J. P. Selvaggi**, **S. J. Salon**, and **M. V. K. Chari**

Rensselaer Polytechnic Institute, Troy, NY 12180-3590, USA

**Abstract**— The authors present a method for computing the external magnetic induction field from a radially-magnetized cylindrical permanent magnet. The method relies on the application of the cylindrical free-space Green's function. The cylindrical free-space Green's function can be expanded in terms of zeroth-order toroidal functions, and this leads to a toroidal harmonic expansion for the inverse distance function between a source point and an observation point. The toroidal harmonic representation allows the cylindrical azimuthal variable to be uncoupled from its axial and radial variables. The uncoupling of the cylindrical azimuthal variable leads to some useful simplifications in the analysis of cylindrical permanent magnets.

## 1. INTRODUCTION

There are a number of methods that can be employed for computing the magnetic induction field from a radially-magnetized permanent magnet [1–7]. For example, Furlani et al. [4] has developed a method for computing the field from a radially magnetized multi-pole cylinder made up of multiple sectors whose radial magnetization changes polarity with each successive sector. Mayergoyz et al. [5] has developed a method for computing the magnetic induction field from a cylindrical magnet with arbitrary magnetization vectors within the magnet. Peng et al. [6] develops the on-axis equations for the magnetic induction field from radially-magnetized permanent-magnet rings. These are just a few of the many methods one will find in the literature. The authors will employ an alternate method using the cylindrical free-space Green's function [8] which leads to a toroidal harmonic expansion. This was first introduced for computing the magnetic induction field from permanent-magnet bipolar cylinders [7]. One advantage of this method is that the azimuthal variable, $\phi$, within the toroidal harmonic expansion, is directly uncoupled from the radial variable, $\rho$, and the axial variable, $z$. If one needs to integrate over a volume or a surface, the azimuthal integration is usually trivial when the toroidal harmonic expansion is used to represent the inverse distance between a source point and an observation point. The azimuthal integration leads to a closed form expression in terms of elementary functions. Whether the magnetic system exhibits azimuthal symmetry (axi-symmetric) or not makes no difference-the azimuthal integration can usually be done in closed form.

The magnetic induction field from a radially-magnetized cylindrical permanent magnet is axi-symmetric, and therefore only the radial and axial components of the magnetic induction field will exist. One can view a radially-magnetized permanent magnet as an axi-symmetric Halbach array [9] composed of multiple radially-magnetized cylindrical sectors as illustrated in Figure 1.

If each sector were uniformly and radially magnetized but alternating in polarity, then the system would not be axi-symmetric. In other words, an azimuthal dependence would exist. However, the analysis presented in this paper can easily be adapted to handle the non-axisymmetric case. No real limitation exists for modeling cylindrical permanent magnets with the cylindrical Green's function approach. If the permanent magnet exhibits a high coercivity, its magnetization is for all practical purposes independent of an externally applied field. This allows one to model the permanent magnet as if it had a fixed magnetization. If this is not the case then the magnetization vector may be extremely difficult to model. A very clear and concise description of the various properties of magnetic materials is given by Furlani [10].

## 2. BASIC THEORY AND FORMULATION

Figure 2 represents a simplified model of a radially-magnetized finite cylindrical permanent magnet.

The parameter $a$ is the inner radius, and the parameter $b$ is the outer radius. Also, $\delta = b - a$ is the thickness, and $R = \frac{b+a}{2}$ is the mid-radius. The magnetization vector, $\mathbf{M}$, is assumed to be uniform and radially directed as illustrated in Figure 2. The authors will employ the equivalent current model [8, 10] in order to solve for the external magnetic induction field. The equivalent
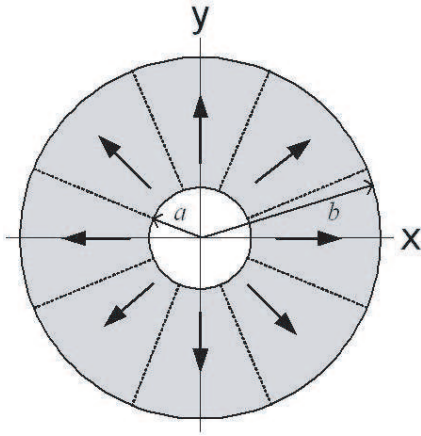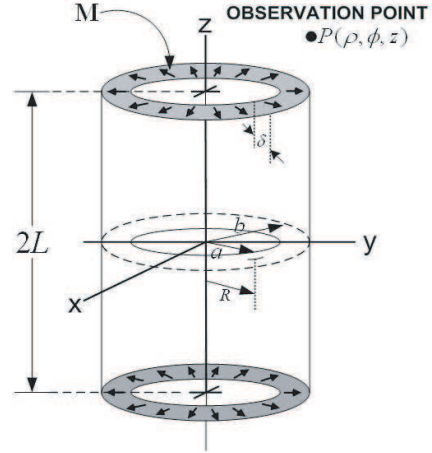
Figure 1: Radially-magnetized Halbach array.



Figure 2: Radially magnetized permanent magnet.

current model employs the magnetic vector potential function. The magnetic vector potential, valid for some arbitrary point, $P(\rho, \phi, z)$, external to the magnetic material can be written as

$$\mathbf{A} = \frac{\mu_0}{4\pi} \int_{V'} \frac{\mathbf{J}_M}{|\mathbf{r} - \mathbf{r}'|} dV' + \frac{\mu_0}{4\pi} \oint_{S'} \frac{\mathbf{j}_M}{|\mathbf{r} - \mathbf{r}'|} dS', \tag{1}$$

where the equivalent magnetic volume current density and the equivalent magnetic surface current density, respectively, are given by

$$\mathbf{J}_M = \boldsymbol{\nabla}' \times \mathbf{M} \left( \rho', \phi', z' \right) \frac{A}{m^2}, \tag{2}$$

$$\mathbf{j}_M = \mathbf{M} \left( \rho', \phi', z' \right) \times \hat{n}' \frac{A}{m}, \tag{3}$$

and where the unit-normal vector, $\hat{n}'$, represents the outward unit-normal vector from the closed surface of the permanent magnet. For a uniform radial-magnetization vector, $\mathbf{M} = M_0 \hat{\rho}$ the volume current density, $\mathbf{J}_M$, and the surface charge density, $\mathbf{j}_M$, are given by

$$\mathbf{J}_M = 0, \tag{4}$$

and

$$\mathbf{j}_M = \begin{cases} M_0 \hat{\rho}' \times \hat{z}'|_{z=L} = -M_0 \hat{\phi}' \\ M_0 \hat{\rho}' \times \hat{z}'|_{z=-L} = +M_0 \hat{\phi}' \\ M_0 \hat{\rho}' \times \hat{\rho}'|_{\rho=b} = 0 \\ M_0 \hat{\rho}' \times \hat{\rho}'|_{\rho=a} = 0 \end{cases}. \tag{5}$$

We have defined $\hat{\rho}'|_{\rho=b} = +\hat{\rho}'$, $\hat{\rho}'|_{\rho=a} = -\hat{\rho}'$, $\hat{z}'|_{z=L} = +\hat{z}'$ and $\hat{z}'|_{z=-L} = -\hat{z}'$.

The distance between some source point $P'(\rho', \phi', z')$ within the magnet or on its surface, and some arbitrary external observation point, $P(\rho, \phi, z)$, expressed in cylindrical coordinates is given by

$$|\mathbf{r} - \mathbf{r}'| = \sqrt{\rho^2 + \rho'^2 + (z - z')^2 - 2\rho\rho' \cos (\phi - \phi')}. \tag{6}$$

The free-space Green's function in cylindrical coordinates [8, 11] leads to the following toroidal harmonic expansion for $|\mathbf{r} - \mathbf{r}'|^{-1}$ [12–20]:

$$\frac{1}{|\mathbf{r} - \mathbf{r}'|} = \frac{1}{\pi \sqrt{\rho \rho'}} \sum_{m=0}^{\infty} \varepsilon_m Q_{m-\frac{1}{2}} (\xi) \cos \left[ m \left( \phi - \phi' \right) \right], \tag{7}$$

where $Q_{m-\frac{1}{2}}(\xi)$ is called a Legendre function of the second kind and half-integral degree [21]. It is also called a zeroth-order toroidal function or Ring function [22]. It has an infinite series

representation [19] given by

$$Q_{m-\frac{1}{2}}(\xi) = \pi \sum_{n=0}^{\infty} \frac{(4n+2m-1)!!}{2^{2n+m}(n+m)!n!} \frac{1}{(2\xi)^{2n+m+\frac{1}{2}}}, \tag{8}$$

where the argument of the toroidal function is defined as follows:

$$\xi = \frac{\rho^2 + \rho'^2 + (z-z')^2}{2\rho\rho'} > 1. \tag{9}$$

The symbol $\varepsilon_m$ called the Neumann factor [23] where $\varepsilon_0 = 1$ and $\varepsilon_0 = 2$ for all $m \geq 1$. Also, $(4n+2m-1)!! = 1 \cdot 3 \cdot 5 \cdot 7 \ldots (4n+2m-1)$ for all $m, n \geq 0$. Employing Eqs. (4), (5), and (7) allows Eq. (1) to be written as

$$\mathbf{A} = \frac{\mu_0 M_0}{4\pi^2 \sqrt{\rho}} \sum_{m=0}^{\infty} \varepsilon_m \int_0^{2\pi} \int_{R-\frac{\delta}{2}}^{R+\frac{\delta}{2}} \left[ Q_{m-\frac{1}{2}}(\xi_2) - Q_{m-\frac{1}{2}}(\xi_1) \right] \sqrt{\rho'} \cos\left[ m\left(\phi - \phi'\right) \right] \hat{\phi}' d\rho' d\phi', \tag{10}$$

where

$$\xi_1 = \frac{\rho^2 + \rho'^2 + (z-L)^2}{2\rho\rho'}, \tag{11}$$

$$\xi_2 = \frac{\rho^2 + \rho'^2 + (z+L)^2}{2\rho\rho'}, \tag{12}$$

$$\hat{\phi}' = -\sin\left(\phi'\right)\hat{x} + \cos\left(\phi'\right)\hat{y}. \tag{13}$$

One can easily integrate on the $\phi'$ variable and immediately notice that only the $m = 1$ term survives the azimuthal integration in Eq. (10). After the azimuthal integration, Eq. (10) becomes

$$\mathbf{A} = \frac{\mu_0 M_0}{2\pi\sqrt{\rho}} \hat{\phi} \int_{R-\frac{\delta}{2}}^{R+\frac{\delta}{2}} \left[ Q_{\frac{1}{2}}(\xi_2) - Q_{\frac{1}{2}}(\xi_1) \right] \sqrt{\rho'} d\rho'. \tag{14}$$

The magnetic vector potential has only an azimuthal component. In other words, the physical problem is completely axi-symmetric.

One can now employ the toroidal harmonic expansion given by Eq. (8). With $m = 1$ in Eq. (8), one can rewrite Eq. (14) as follows:

$$A_\phi = \frac{\mu_0 M_0}{4} \sum_{n=0}^{\infty} \frac{(4n+1)!!\rho^{2n+1}}{2^{2n}(n+1)!n!} \int_{R-\frac{\delta}{2}}^{R+\frac{\delta}{2}} \left[ \frac{(\rho')^{2n+2}}{\left[ \rho'^2 + \rho^2 + (z+L)^2 \right]^{2n+\frac{3}{2}}} - \frac{(\rho')^{2n+2}}{\left[ \rho'^2 + \rho^2 + (z-L)^2 \right]^{2n+\frac{3}{2}}} \right] d\rho'. \tag{15}$$

The integral in Eq. (15) can be integrated and expressed in a number of ways. We will choose to employ a Gauss hypergeometric function [24] representation. This representation has been employed by Labinac et al. [25], Agashe et al. [26, 27] and Selvaggi et al. [7] with much success. More will be said later about the use of hypergeometric functions. The magnetic vector potential is given in its final form as

$$A_\phi = \frac{\mu_0 M_0}{4} \sum_{n=0}^{\infty} \frac{(4n+1)!!\rho^{2n+1}}{2^{2n}(2n+3)(n+1)!n!} (F_n - G_n), \tag{16}$$

where

$$
F_n = \frac{1}{\rho^2 + (z+L)^2} \left\{ \left( R + \frac{\delta}{2} \right)^{2n+3} \frac{\mathbf{F}\left(1, 1-n; n+\frac{5}{2}; -\frac{\left(R+\frac{\delta}{2}\right)^2}{\rho^2+(z+L)^2}\right)}{\left[\rho^2 + \left(R+\frac{\delta}{2}\right)^2 + (z+L)^2\right]^{2n+\frac{1}{2}}} \right.
$$
$$
\left. - \left( R - \frac{\delta}{2} \right)^{2n+3} \frac{\mathbf{F}\left(1, 1-n; n+\frac{5}{2}; -\frac{\left(R-\frac{\delta}{2}\right)^2}{\rho^2+(z+L)^2}\right)}{\left[\rho^2 + \left(R-\frac{\delta}{2}\right)^2 + (z+L)^2\right]^{2n+\frac{1}{2}}} \right\}, \tag{17}
$$

and

$$
G_n = \frac{1}{\rho^2 + (z-L)^2} \left\{ \left( R + \frac{\delta}{2} \right)^{2n+3} \frac{\mathbf{F}\left(1, 1-n; n+\frac{5}{2}; -\frac{\left(R+\frac{\delta}{2}\right)^2}{\rho^2+(z-L)^2}\right)}{\left[\rho^2 + \left(R+\frac{\delta}{2}\right)^2 + (z-L)^2\right]^{2n+\frac{1}{2}}} \right.
$$
$$
\left. - \left( R - \frac{\delta}{2} \right)^{2n+3} \frac{\mathbf{F}\left(1, 1-n; n+\frac{5}{2}; -\frac{\left(R-\frac{\delta}{2}\right)^2}{\rho^2+(z-L)^2}\right)}{\left[\rho^2 + \left(R-\frac{\delta}{2}\right)^2 + (z-L)^2\right]^{2n+\frac{1}{2}}} \right\}. \tag{18}
$$

The advantage of employing hypergeometric functions to represent the magnetic vector potential is that for each $n$ in Eq. (16) one can immediately expand the series in terms of elementary functions. This becomes a very useful feature when one is interested in performing a parametric study. Also, as discussed in Agashe et al. [26], the hypergeometric representation converges fairly quickly and this allows one to make quick modifications during the modeling process. Another advantage is that powerful symbolic mathematical packages such as Mathematica [28] and Maple [29] are well equipped to deal with almost all the various forms of hypergeometric functions. This allows one to take advantage of their extensive mathematical subroutines in order to avoid much of the algebraic complexity associated with manipulating the more complex mathematical functions that one encounters in the solution of many real-world engineering problems.

One can now find the vector components of magnetic induction field due to the radially-magnetized permanent magnet cylinder as follows:

$$
B_\rho = -\frac{\partial}{\partial z}\left(A_\phi\right), \tag{19}
$$

$$
B_z = \frac{1}{\rho}\frac{\partial}{\partial \rho}\left(\rho A_\phi\right). \tag{20}
$$

In order to compute the components of the magnetic induction field components for finite $n$, one only needs to employ the following:

$$
B_\rho^{(N)} = -\sum_{n=0}^{N} \frac{\partial}{\partial z}\left(A_\phi^{(n)}\right), \tag{21}
$$

$$
B_z^{(N)} = \frac{1}{\rho}\sum_{n=0}^{N} \frac{\partial}{\partial \rho}\left(\rho A_\phi^{(n)}\right), \tag{22}
$$

where $N$ is large enough to obtain an accurate representation of the magnetic induction field. Fortunately $N$ may not have to be too large to get an accurate solution [26]. However, if one needs to compute the magnetic induction field components close to the cylindrical boundary of the magnet, one will, in general, need more terms in the expansion given by Eqs. (21) and (22). Fortunately, Mathematica and Maple can make the necessary computations very quickly. The series expansion for the vector potential converges fast enough that it can also be used for performing a purely numerical computation. We will illustrate this point in Section 3 of this article.

A simple check of Eq. (16) can be performed by finding expressions for the magnetic induction field anywhere along the $z$ axis. The only term which survives in the two summations given by Eqs. (21) and (22) when $\rho \to 0$ is the $N = 0$ term of the axial component of the magnetic induction field. The radial component of the magnetic induction field on the $z$ axis is identically equal to zero. The axial component of the magnetic induction field for $\rho = 0$ is given by

$$
\begin{aligned}
B_z^{(N=0)}\big|_{\rho=0} = \frac{\mu_0 M_0}{2} \Bigg\{ &\left[ \frac{\left(R+\frac{\delta}{2}\right)}{\sqrt{\left(R+\frac{\delta}{2}\right)^2 + (z-L)^2}} - \frac{\left(R-\frac{\delta}{2}\right)}{\sqrt{\left(R-\frac{\delta}{2}\right)^2 + (z-L)^2}} \right] \\
&- \left[ \frac{\left(R+\frac{\delta}{2}\right)}{\sqrt{\left(R+\frac{\delta}{2}\right)^2 + (z+L)^2}} - \frac{\left(R-\frac{\delta}{2}\right)}{\sqrt{\left(R-\frac{\delta}{2}\right)^2 + (z+L)^2}} \right] \\
&+ Ln\left[ \frac{\left(R+\frac{\delta}{2}\right)+\sqrt{\left(R+\frac{\delta}{2}\right)^2+(z+L)^2}}{\left(R+\frac{\delta}{2}\right)+\sqrt{\left(R+\frac{\delta}{2}\right)^2+(z-L)^2}} \right] - Ln\left[ \frac{\left(R-\frac{\delta}{2}\right)+\sqrt{\left(R-\frac{\delta}{2}\right)^2+(z+L)^2}}{\left(R-\frac{\delta}{2}\right)+\sqrt{\left(R-\frac{\delta}{2}\right)^2+(z-L)^2}} \right] \Bigg\}.
\end{aligned}
\tag{23}
$$

Equation (23) is exactly what one obtains by doing a direct integration of Eq. (15) with $n = 0$ and then employing Eq. (20) or (22) while letting $\rho \to 0$. The hypergeometric formulation allows one to obtain expressions for the magnetic induction field in terms of elementary functions which are usually in the same form as those found in most textbooks, and this allows for a relatively simple way to check ones solution.

In formulating the problem discussed in this paper, one could have used an Elliptic integral approach. In fact, a relationship exists between the toroidal function $Q_{\frac{1}{2}}(\xi)$ and the complete Elliptic integral of the first and second kind [22]. This is given by

$$
Q_{\frac{1}{2}}(\xi) = \xi \sqrt{\frac{2}{\xi+1}} K\left(\sqrt{\frac{2}{\xi+1}}\right) - \sqrt{2(\xi+1)} E\left(\sqrt{\frac{2}{\xi+1}}\right).
\tag{24}
$$

One could use Eq. (24) in order to transform Eq. (14) into an Elliptic integral formulation especially if one is feels more comfortable with this approach.

## 3. ILLUSTRATIVE EXAMPLE

Consider the following example taken from pages 245–247 of Furlani [10] or Furlani et al. [4]. The model used for this example is illustrated in Figure 2 and has the following data: $2L = 0.04\,\text{m}$, $a = 0.02\,\text{m}$, $b = 0.04\,\text{m}$, $M_0 = 4.3 \times 10^5\,\frac{A}{m}$, $\delta = 0.02\,\text{m}$ and $R = 0.03\,\text{m}$. Employing Eqs. (16), (21)
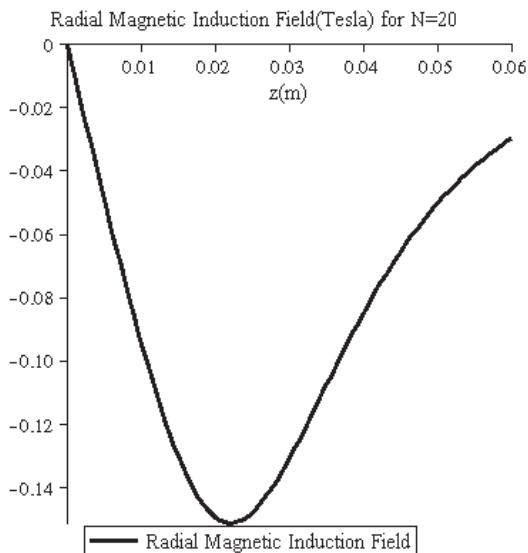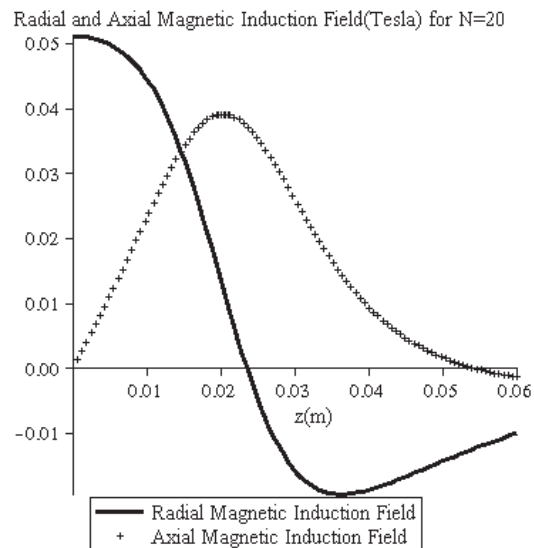


Figure 3: $B_z$ on the $z$ axis.



Figure 4: $B_\rho$ and $B_z$ at $\rho = 0.05\,\text{m}$.

and (22), one can develop a number of useful plots for the radial and axial magnetic induction field. We chose $N = 20$ in Eqs. (21) and (22). For larger values of $N$, the plots change only slightly.

Figures 3, 4 and 5 are identical to the plots that Furlani et al. [4] develops for the radially-magnetized axi-symmetric cylinder except for a minor issue [30]. Two of Furlani's plots have the wrong captions and axis labels. The captions and axis labels which describe Figures 5 and 7 in Furlani et al. [4] should be reversed. In other words, the caption and axis label for Figure 5 of Furlani et al. [4] actually describes his Figure 7 and vice-versa. One can easily see that in Figure 4 of this article, the radial component of the magnetic induction field should be at its largest value at $z = 0$. However, in Figure 5 of Furlani et al. [4], the radial component of the magnetic induction field is zero at $z = 0$. However, only $B_z$ can be zero on the $x$-$y$ plane. In fact, one will see that our plot in Figure 4 actually corresponds to the plot given in Figure 7 of Furlani et al. [4]. Unfortunately, the same plots given on page 247 of Furlani [10] are also mislabeled.

Consider Figure 4 with $-0.06 \le z \le 0.06$ m as illustrated in Figure 6 below.

One should notice that the radial component of the magnetic induction field in Figure 6 must reach its largest value on the $x$-$y$ plane based upon the chosen model illustrated in Figure 2. Also, Figure 7 illustrates why we chose $N = 20$.

In Figure 7, the radial and axial components of the magnetic induction field change little for
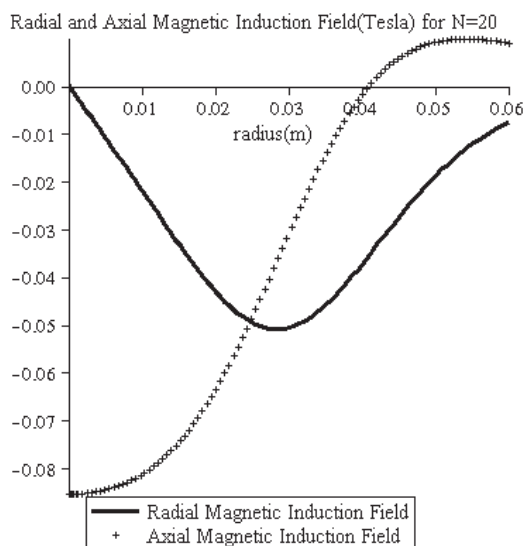


Figure 5: $B_\rho$ and $B_z$ at $z = 0.04$ m.
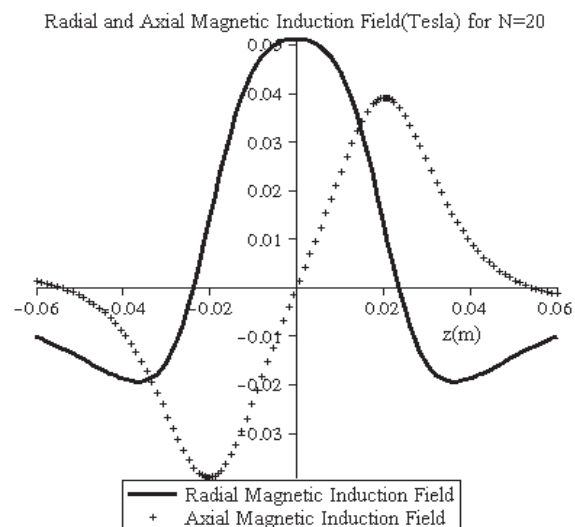


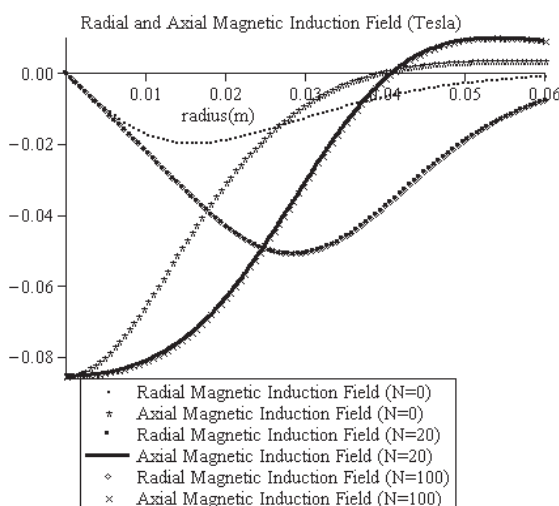Figure 6: $B_\rho$ and $B_z$ at $\rho = 0.05$ m.

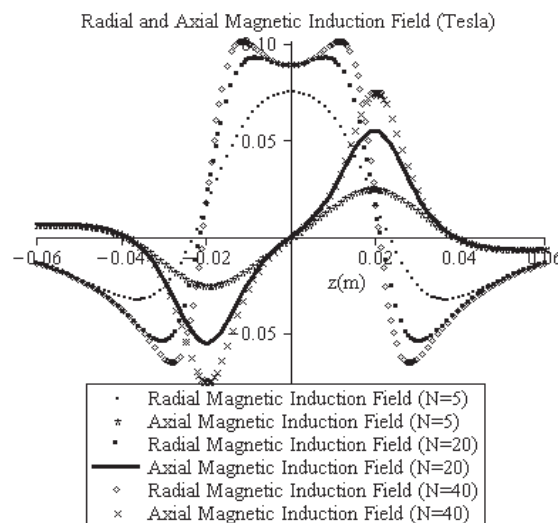

Figure 7: $B_\rho$ and $B_z$ at $z = 0.04$ m.



Figure 8: $B_\rho$ and $B_z$ at $\rho = 0.04005$ m.

$N = 20$ or $N = 100$. In fact, the $N = 20$ plot and the $N = 100$ plot almost overlap. What do the axial and radial magnetic induction field components look like at $\rho = 0.04005\,\text{m}$? This is fairly close to the outer radius of the cylinder. Figure 8 shows the plot.

One can see from Figure 8 that a larger value of $N$ will be required to accurately represent the magnetic induction field close to the cylindrical surface. In fact, extremely good accuracy is achieved in Figure 8 if $N$ is chosen to be 50 or larger.

Furlani et al. [4] and Furlani [10] used a semi-analytical approach to solve this same problem and then checked his results using finite element analysis. We, on the other hand, have used a completely analytical approach and were able to match the results with those given by Furlani. We chose $N$ to be as large as 300 without any difficulty since Eq. (16) converges rather quickly. We created all plots within the Maple environment.

## 4. DISCUSSION AND CONCLUSION

The authors have developed a method of solution for solving for the external magnetic induction field produced by a radially-magnetized permanent magnet cylinder. We employed the cylindrical free-space Green's function which produced a toroidal harmonic expansion. An equivalent current model was used to formulate a magnetic vector potential function which was then used as an ancillary step in the computation of the radial and axial external magnetic induction field. In order to find a closed form expression, in terms of special functions, we chose to develop an infinite series expansion which employed hypergeometric functions. Alternative methods using Elliptic integrals or Bessel functions could have been employed. However, the use of hypergeometric functions offered an interesting alternative. This approach leads rather quickly to recognizable limiting cases as well as being numerically very stable. We were able to check our results with those given by Furlani et al. [4] and Furlani [10] and our results completely agreed.

The method introduced in this article can easily be modified to handle the non-axisymmetric case discussed by Furlani et al. [4] and Furlani [10]. In fact, one may recognize that the azimuthal integration in Eq. (10) went from 0 to $2\pi$. In the non-axisymmetric case, the azimuthal integration would be from, let's say, $\phi_1$ to $\phi_2$. Depending on one's choice of $\phi_1$ and $\phi_2$, this would lead to a solution for the magnetic induction field which may include the complete set of zeroth-order toroidal functions, $Q_{m-\frac{1}{2}}(\xi)$, valid for all $m \geq 1$ and not just the restricted axi-symmetric set which employed only the $Q_{\frac{1}{2}}(\xi)$ toroidal function derived for the $m = 1$ case. We must exclude the $m = 0$ term when using the equivalent current model since this implies a monopole contribution. In fact, the $m = 0$ term will mathematically be zero. A much more general approach introduced by Selvaggi et al. [31, 32] has been developed for solving problems with integral kernels of the form $\frac{e^{-k|r-r'|}}{|r-r'|}$ and $\frac{e^{\pm ik|r-r'|}}{|r-r'|}$. The first represents the Yukawa potential kernel and the second represents the radiation kernel. Both have been studied for circular cylindrical geometries.

### REFERENCES

1. Ravaud, R. and G. Lemarquand, "Analytical expressions of the magnetic field created by tile permanent magnets of various magnetization directions," *PIERS Proceedings*, 511–515, Moscow, Russia, August 18–21, 2009.

2. Ravaud, R. and G. Lemarquand, "Discussion about the magnetic field produces by cylindrical halbach structures," *Progress In Electromagnetics Research B*, Vol. 13, 275–308, 2009.

3. Babic, S. I., "Improvement in the analytical calculation of the magnetic field produced by permanent magnet rings," *Progress In Electromagnetics Research C*, Vol. 5, 71–82, 2008.

4. Furlani, E. P., S. Reznik, and A. Kroll, "A three-dimensional field solution for radially polarized cylinders," *IEEE Trans. Magn.*, Vol. 31, No. 1, 844–851, January 1995.

5. Mayergoyz, I. D., E. P. Furlani, and S. Reznik, "The computation of magnetic fields of permanent magnet cylinders used in the electrophotographic process," *J. Appl. Phys.*, Vol. 73, No. 10, 5440–5442, May 15, 1993.

6. Peng, Q. L., S. M. McMurry, and J. M. D. Coey, "Axial magnetic field produced by axially and radially magnetized permanent rings," *J. Magn. Magn. Mater.*, Vol. 268, 165–169, 2004.

7. Selvaggi, J., S. Salon, O. Kwon, and M. V. K. Chari, "Computation of the three-dimensional magnetic field from solid permanent-magnet bipolar cylinders employing toroidal harmonics," *IEEE Trans. Magn.*, Vol. 43, No. 10, 3833–3839, October 2007.

8. Jackson, J. D., *Classical Electrodynamics*, 3rd Edition, 197, John Wiley and Sons, New York, 1999.

9. Halbach, K., "Design of permanent multipole magnets with oriented rare earth cobalt material," *Nucl. Instr. Meth.*, 169, 1–10, 1980.

10. Furlani, E. P., *Permanent Magnet and Electromechanical Devices*, 224–247, Academic Press, San Diego, CA, 2001.

11. Smythe, W. R., *Static and Dynamic Electricity*, 3rd Edition, 204, McGraw-Hill, New York, 1968.

12. Bouwkamp, C. J. and N. G. de Bruijn, "The electrical field of a point charge inside a cylinder, in connection with wave guide theory," *J. Appl. Phys.*, 18, 562–577, 1947.

13. Snow, C., "Magnetic fields of cylindrical coils and annular coils," *Natl. Bur. Stand., Applied Mathematics Series*, Vol. 38, 1–3, 1953.

14. Snow, C., "Formulas for computing capacitance and inductance," *Natl. Bur. Stand. Circular*, Vol. 544, 13–17, 1954.

15. Snow, C., "Hypergeometric and legendre functions with applications to integral equations of potential theory," *Natl. Bur. Stand. Applied Mathematics Series*, Vol. 19, 228–277, 1952.

16. Cohl, H. S., J. E. Tohline, and A. R. P. Rau, "Developments in determining the gravitational potential using toroidal functions," *Astron. Nachr.*, Vol. 321, 363–372, 2000.

17. Cohl, H. S. and J. E. Tohline, "A compact cylindrical Green's function expansion for the solution of potential problems," *The Astrophysical Journal*, 527, 86–101, 1999.

18. Cohl, H. S., A. R. P. Rau, J. E. Tohline, D. A. Browne, J. E. Cazes, and E. I. Barnes, "Useful alternative to the multipole expansion of 1/r potentials," *Phys. Rev. A*, Vol. 64, 052509-5, 2001.

19. Selvaggi, J., S. Salon, O. Kwon, and M. V. K. Chari, "Calculating the external magnetic field from permanent magnets in permanent-magnet motors-an alternative method," *IEEE Trans. Magn.*, Vol. 40, No. 5, 3278–3285, 2004.

20. Selvaggi, J., S. Salon, and M. V. K. Chari, "An application of toroidal functions in electrostatics," *Am. J. Phys.*, Vol. 75, No. 8, 724–727, 2007.

21. Lebedev, N. N., *Special Functions and Their Applications*, 186–188, Prentice-Hall, New Jersey, 1965.

22. Abramowitz, M. and I. Stegun, *Handbook of Mathematical Functions*, 336–337, Dover Publications Inc., New York, 1972.

23. Morse, P. M. and H. Feshbach, *Methods of Theoretical Physics Part I*, Vol. 744, McGraw Hill, New York, 1953.

24. Whittaker, E. T. and G. N. Watson, *A Course of Modern Analysis*, 4th Edition, 281–301, Cambridge at University Press, 1952.

25. Labinac, V., N. Erceg, and D. Kotnik-Karuza, "Magnetic field of a cylindrical coil," *Am. J. Phys.*, Vol. 74, No. 7, 621–627, 2006.

26. Agashe, J. S. and D. P. Arnold, "A study of scaling and geometry effects on the forces between cuboidal and cylindrical magnets using analytical force solutions," *J. Phys. D: Appl. Phys.*, 105001-9, 2008.

27. Agashe, J. S. and D. P. Arnold, "Corrigendum — A study of scaling and geometry effects on the forces between cuboidal and cylindrical magnets using analytical force solutions," *J. Phys. D: Appl. Phys.* Vol. 42, 099801, 2009.

28. Wolfram Research Inc., *Mathematica*, Version 7.0.1, 61820–7237, Champaign, IL, 100 Trade Center Drive, USA, 2008.

29. Waterloo Maple Inc., *Maple*, Version 13.01, Waterloo, Ontario, Canada N2L 6C2, 2009.

30. Furlani, E. P., *The Institute for Lasers Photonics and Biophotonics*, University at Buffalo, 458 Natural Sciences Complex, North Campus, Buffalo, NY 14260, email communication: The author discussed this issue with Dr. Furlani and he agreed that his plots have the incorrect captions and labels, however, his data and computations are all correct, September 28, 2009.

31. Selvaggi, J. P., S. J. Salon, and M. V. K. Chari, "A toroidal harmonic representation of the Yukawa- potential kernel for a circular cylindrical source," *PIERS Proceedings*, 46–51, Cambridge, USA, July 2–6, 2008.

32. Selvaggi, J. P., S. J. Salon, and M. V. K. Chari, "The vector potential of a circular cylindrical antenna in terms of a toroidal harmonic expansion," *J. Appl. Phys.*, Vol. 104, 033913-7, 2008.

# Ultra Wide Band Communication through Plasma Generated by Corona Effect around High Voltage Line

**M. Johnny and S. A. Hassani Gangaraj**

Iran University of Science and Technology, Iran

**Abstract**— The transfer of information plays an important role in communications systems. There is an ongoing increase in the extension of the lines of information transfer and communications antenna. However, what is very important is this, to forward the greatest amount of information with the least waste of energy. Among these, the communication channel have noticeable share of transferring information. In earth communication applications transmission lines and wave guides act more efficiently than antennas, and with the less power have the best signal to noise ratio. In this paper, we explain the transmission lines created by ionization of gasses surrounding the lines and at the same time we explain the guides parameters this environment and it's taking effect in proportion to the foreign factors such as wind and existing electromagnetic waves of the air. And we'll see that it can be as a channel of transferring information with an ultra wide band.

## 1. INTRODUCTION

At first we explain the subject we are dealing with. If a long conductor with a radius $r$ has the charge of $\lambda$; there will be an electrostatic field around it. Its electric field intensity at the distance of $x$ from the center of the wire is equal to $\frac{\lambda}{2\pi\epsilon x}$.

This field gives rise to inserting a force to the charged particles. If the intensity of this field is big enough, it can break the air and produce positive ions and electrons, as well. Consequently these particles due to being exposed to this field, gain more momentum so they get farther from or closer to the wire (positive peak of the voltage of the conductor, absorbing the electrons and repelling ions and vice versa). And if these particles upon hitting the surrounding molecules, have enough energy, they'll produce more ions and consequently more charged particles. Thus this gradually increases the conductivity of the air. In fact corona is the increase of charged particles in adjacent to the surface of the conductor as the result of increase of voltage gradient so that voltage gradient can reach to an amount more than resistance breaking point of the surrounding air. It is clear that corona results in the waste of energy in the forms of light and heat. It is the same phenomena that is seen around the power lines as a violet corona at night. Now we calculate the electric field (voltage gradient) in a line with two conductors and we assume that the plane perpendicular to the surface of the conductors in the middle of the distance between them is neutral.

$$V' = \int_{r}^{d/2} \left( \frac{q}{x} + \frac{q}{d-x} \right) \frac{1}{2\pi\varepsilon} \cdot dx = \frac{q}{2\pi\varepsilon} \cdot \ln \frac{d-r}{r} \tag{1}$$

Therefore, the potential in the distance $x$ from the surface of the conductor in proportion to neutral plane is:

$$V'x = \int_{x}^{\frac{d}{2}} \left( \frac{q}{x} + \frac{q}{d-x} \right) \frac{1}{2\pi\varepsilon} \cdot dx = \frac{q}{2\pi\varepsilon} \cdot \ln \frac{d-x}{x} \tag{2}$$

$$|-\nabla V'x| = \frac{q}{2\pi\epsilon} \cdot \frac{d}{x(d-x)} \rightarrow q = \frac{V'}{\ln \frac{d-r}{r}} 2\pi\epsilon. \tag{3}$$

This voltage gradient $x = r$ will be maximized on the surface of the conductor and is calculated by using following formula:

$$\frac{dV'x}{dx} = \frac{V' \cdot d}{x(d-x) \ln \frac{d-r}{r}} \tag{4}$$

Since $d$ in comparison to $r$ is much bigger we can approximated this formula with negligible error:

$$\frac{dV'x}{dx} = \frac{V'}{r} \frac{1}{\ln \frac{d}{r}} \tag{5}$$
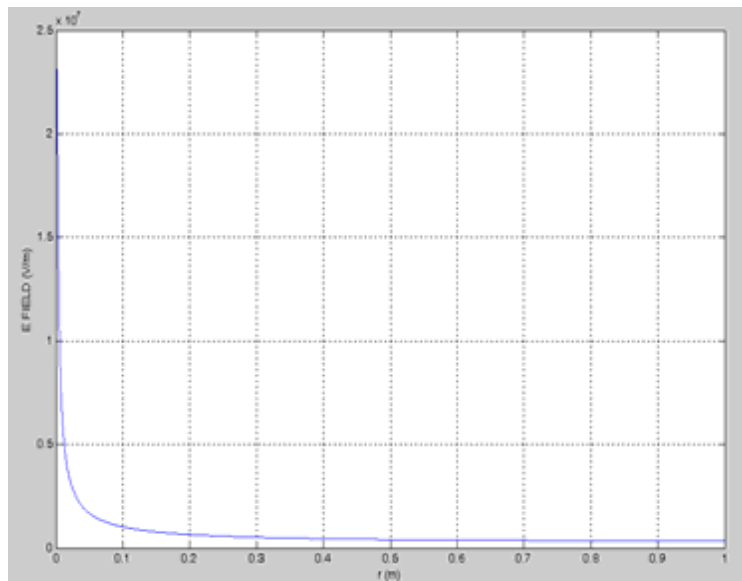
Figure 1. Electric field around wire.

In addition, its graph shown in Figure 1. For the air with no impurities an ordinary condition ($p = 760\,\text{mmHg}$) and the temperature of 25°C the voltage gradient will be ($g_0 = 3000\,\frac{\text{V}}{\text{mm}}$). In which the amount of critical voltage affected by coefficient air density, pressure, and temperature will be as follows ($\delta$ is the air density coefficient):

$$g = \delta g_0 \tag{6}$$

$$\delta = \frac{(273 + 25)}{(273 + t)} \frac{P}{760\,\text{mmHg}} = \frac{3.92P}{273 + t} \tag{7}$$

Now it is necessary to study the motions of ions and free electrons existing around the high voltage wire.

As we know, a molecule after colliding with another molecule travels through a free path until it collides with another molecule. The length of the free path is completely coincidental but we can consider its average. When there is an electric field in an ionized gas, it can give rise to acceleration of charge particles. These charge particles continue their accelerating movement before they collide with other particles. The longer the path is, the particles get more and more energy. And this kinetic energy may get to the extent that after colliding with another molecule produces other ions. The thermal agitation of molecules by collisions can be considered as constant and even velocity, whereas the motion of charged particles in the presence of electric field is an accelerating motion.

The motion of charged particle is an irregular and zigzag but the resultant of all these movements is in the direction of electric field and generally charged particles travel with average velocity that we call it repulsing velocity. And it can be calculated by the relation bellow.

$$V_e = bE \tag{8}$$

where $V_e$ the average velocity and $b$ is called particle motion that is the function of the dimension of the particles and molecules that they move through and the number of molecules in the unit of volume, pressure, and temperature if we pinpoint the problem we can show it in this way. Particle ($A$) with radius $r_A$ moves through a gas with molecule ($B$) with radius $r_B$. The path of particle $A$ is shown in Figure 2 the collision of $A$ and $B$ occurs in area $(r_A + r_B)^2$ that appears when the particles collide with each other, they centers of mass are situated in an area that is called the area of collision and it is shown in the hachured area in Figure 2. In the path shown, the probability of collision of two particles is:

$$a_s dp = ds n_B \tag{9}$$

where $n_B$ is the volume density. On other hand, if we can consider $\lambda_m$ as average free path the probability of the collision in the length of $ds$ is:

$$dp = \frac{ds}{\lambda_m} \tag{10}$$

Therefore, the average free path is given as:

$$\lambda_m = \frac{1}{n_B a_s} \tag{11}$$

$$n = \frac{P}{KT} \tag{12}$$

$$\lambda_m = \frac{1}{a_s} \frac{KT}{P} \tag{13}$$

As we know, area of collision for small particles such as electrons is approximated $\pi r_B^2$ and for ions $4\pi r_B^2$.

$$\lambda_{me} \approx \frac{1}{\pi r_B^2} \frac{KT}{P} \tag{14}$$

$$\lambda_{mi} \approx \frac{1}{4\pi r_B^2} \frac{KT}{P} \tag{15}$$

But it can prove that $\frac{1}{\sqrt{2}}$ should be added in the Equation (15):

$$\lambda_{mi} \approx \frac{1}{4\sqrt{2}\pi r_B^2} \frac{KT}{P} \tag{16}$$

Here is the table average of the lengths of the free paths of some gasses at the 0°C and the pressure of 1 bar.

Table 1.

| $\lambda_m$ for electron [µm] | $\lambda_m$ for molecule [µm] | gas |
|---|---|---|
| 0.063 | 0.11 | $H_2$ |
| 0.33 | 0.058 | $N_2$ |
| 0.36 | 0.064 | $O_2$ |
| 0.23 | 0.041 | $H_2O$ |
| 0.22 | 0.039 | $CO_2$ |

In addition, the average time between two collisions is:

$$t_m = \frac{\lambda_m}{v_m} \tag{17}$$

For a particle with is accelerating under the influence of a foreign force the distance paved by this particle is calculated in the equation of:

$$S = \frac{1}{2}at^2 = \frac{eE}{2m}t_m^2 \rightarrow V_e = \frac{eE}{2m}\tau_m \rightarrow= \left(\frac{e\lambda_m}{2mV_m}\right) \tag{18}$$

where $V_e$ in the abovementioned equation is the average velocity of the collision of two particles.

Average velocity of electrons in the ordinary condition is $150\,\text{km/s}$ and for positive ions are $0.5\,\text{km/s}$.
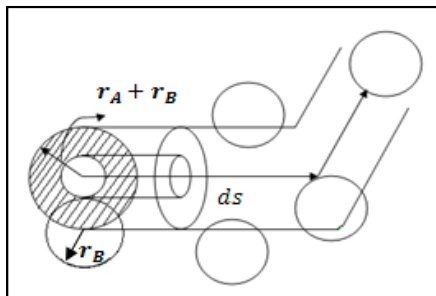


Figure 2.
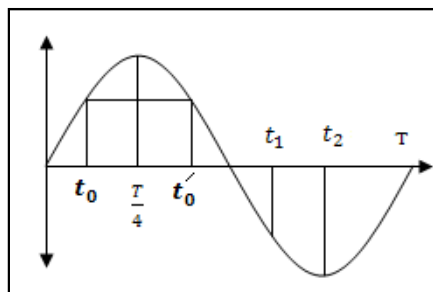


Figure 3.
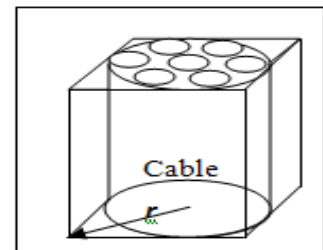


Figure 4.  Optimum radius of shield.

Table 2.

| Ionization energy [ev] | Excitation energy [ev] | Gas |
|:---:|:---:|:---:|
| 13.6 | 10.2 | H |
| 15.9 | 10.8 | $H_2$ |
| 24 | 19 | He |
| 15.6 | 6.3 | $N_2$ |
| 12.1 | 7.9 | $O_2$ |
| 14.4 | 6.8 | $CO_2$ |
| 12.7 | 7.6 | Evaporated water |
| 15.6 | 6.8 | $SF_6$ |

## 2. THE STUDY OF THE IONIZATION OF GAS MOLECULE RESULTING FROM THE COLLISION OF ELECTRONS WITH IT

The energy that a charge particle gets from foreign electric field can be calculated from this equation:

$$\Delta W = eE\lambda_e \tag{19}$$

If the energy is big enough it can provide adequate energy to ionized. The collided molecule and there for another free electron can be produce positive ions, because of their high mass, exchange less energy, in fact they play no role in ionization; however, if this energy is less than ionization and bigger than the agitation limit, it will give rise to the production and propagation of photon. But if their energy is less than agitation limit, a little percentage of electron's energy is transferred to atom and therefore leads to the increase of heat in environment.

Now we analyze the motion of an electron in an electrical field equal to $3000\,\frac{V}{mm}$. Suppose that electron travel the distance $\lambda_m$ with the zero initial velocity in an electric field like the above-mentioned one. Therefore the increase of energy in this electron upon the first collision for $N_2$ is:

$$E = 3 \times 10^6\,\frac{V}{m}\ \text{and}\ \lambda_e = 0.33 \times 10^{-6}\,\text{m} \rightarrow \Delta W_1 = 0.99\,\text{ev}$$

Imaging that there will be no waste of energy from the first to the seventh collision, the amount of this energy is big enough to produce another electron:

$$7 \times 0.99\,\text{ev} = 6.93\,\text{ev} \rightarrow 6.93\,\text{ev} > 6.3\,\text{ev} \rightarrow 6.93\,\text{ev} - 6.3\,\text{ev} = 0.63\,\text{ev: remained energy}$$

$$h\vartheta = 6.3\,\text{ev} \rightarrow \vartheta = \frac{6.3}{h} \rightarrow \vartheta = 1.52 \times 10^{15}\,\text{Hz} \rightarrow \lambda = 1973A^{\cdot} \tag{20}$$

This wavelength is in the domain of blue and ultra violet that causes the high voltage lines to be seen as bright and blue at night. As we saw in the case of uniform distribution of energy the energy of electron before it reaches the point to ionize the air molecule $N_2$ causes the emission of blue photon and agitation of air.

In fact, because of no uniform distribution of energy called Einstein distribution, some of the electrons have enough energy to ionize air molecules $N_2$. Nevertheless, the number of these electrons is much smaller than the number of electrons in the unit of volume .Therefore, the main cause of ionization of air is the critical voltage gradient.

## 3. THE STUDY OF IONIZATION OF THE AIR AROUND THE HIGH VOLTAGE LINE IN COMPLETED SINUSOIDAL CYCLE

As it is seen, the voltage on the high voltage line begins to increase till the voltage gradient on the surface of the conductor reaches a critical point and the air in the boundary of line begin to ionize. The following relation [3, 5], can calculate this time delay:

$$(5) \rightarrow \frac{V}{a}\frac{\sin\left(\frac{2\pi t}{T}\right)}{\ln\left(\frac{d}{a}\right)} = g \tag{21}$$

From the above relation the amount of $t_0$ is calculated (see Figure 3). At this time the air in the boundary of the wire is broken and after this time travels till the moment of $\frac{T}{4}$ the boundary

of breaking from wire till the rate of $r_{\max}$, and then from $\frac{T}{4}$ to $t_0'$ boundary of breaking returns to the surface of wire. At this period of time the positive ions get farther away from the surface of wire and the electrons get closer to the wire. From the moment of $\frac{T}{4}$ to $t_0'$ is called time interval. We can come to conclusion that from the moment of $t_0'$ till $t_1$ since the voltage gradient does not reach critical limit on the surface of line the air does not get ionized and keeps its natural form. When we get to the time $t_1 = \frac{T}{2} + t_0$, the voltage gradient on the surface of the wire returns to its own critical point and the air around the cable's surface starts to ionize and with the elapse of time this boundary advances beyond the wire. In this case, positives ions travel to the wire (at the speed of $0.5\,\text{km/s}$) and the electrons get distance from the wire and at this interval the existing electrons simultaneously travel to the surface of the wire and the effect of electric field resulting from the accumulation of positive ions emerging on the surface of wire become neutralize therefore they don't affect on instantaneous electric field and this field only depends on the instantaneous voltage and the distance from the surface of wire. In this case we notice that the electrons getting distance from the wire have a velocity much more than the velocity of field critical boundary that is obtained from this relation:

The boundary of ionized air

$$(5) \rightarrow \frac{V'(t)}{r} \frac{1}{\ln\left(\frac{d}{r}\right)} = g \rightarrow \frac{dr}{dt} = \frac{dr}{d(V'(t))} \frac{dV(t)}{dt} = \frac{1}{g \ln\left(\frac{d}{r} - 1\right)} \frac{d(V(t))}{dt} \tag{22}$$

The average velocity between the times $t_1$ and $t_2 = \frac{3T}{4}$ is obtained through the following equation:

$$\bar{V} = \frac{r_{\max} - a}{t_2 - t_1} \tag{23}$$

In which $r_{\max}$ is obtained by substituting max voltage in the Equation (5) later, it will be shown that $\bar{V}$ is much smaller than the electron escape velocity from the surface of the conductor. Therefore the environment that is in verge of ionization includes only the positive ions. Moreover, the only existing electrons are the same electrons on ionization boundary. In other words, by getting distance from the surface of the wire the maximum density of electrons is observed which is located on the boundary of ionization. The density of these ions and electrons are equal to the number of air molecules in the unit of volume that is given by the following equation:

$$N_{e^-} = N_{p^+} = \frac{1000\,\text{lit}}{22.4\,\text{lit}} \times N_a = 2.688 \times 10^{25} \tag{24}$$

Now take the following typical values [3]:

$$d = 2.5\,\text{m} \rightarrow r_{\max} = 11.8\,\text{mm} \quad f = 50\,\text{Hz} \quad t_1 = 1.65\,\text{ms} + \frac{T}{2}(2k+1)$$

$$t_2 = 5\,\text{ms} + \frac{T}{2}(2k+1) \quad V_m = 330\,\text{kv} \quad a = 5.08\,\text{mm} \quad \bar{V} = 2\,\text{m/s} \quad \alpha = \frac{t_2 - t_1}{T} \tag{25}$$

$\alpha$ is the band wide coefficient that is defined in the above equation.

## 4. PLASMA [2, 7]

Plasma is a gas that contains approximately equal numbers of positive and negative charges and is present in the sun and most stars.

As we mentioned before particles of over environment consist of ions with mass much more than electrons approximately $1837 \times Z$ ($Z$ is the mass number) therefore, we can conclude that in sinusoidal field only electrons can change place because of their light mass. Let's consider an electron with $m_e = 9.109 \times 10^{-31}\,\text{kg}$ and $e = 1.6 \times 10^{-19}$ on the $x$-axis. Now we exert a sinusoidal electric field on the direction of $x$-axis.

In this condition, the equations governing the motion are as follows:

$$-e\bar{E} = m\frac{d^2x}{dt^2} = -m\omega^2\bar{x} \tag{26}$$

$$x = \frac{e\bar{E}}{m\omega^2} \tag{27}$$

If we imaging that the number of electrons in the unit of volume is equal to $N$, we will have a polarization and displacement vector:

$$P = \frac{-Ne^2E}{m\omega^2} \text{ and } D = \varepsilon \cdot E + P = \varepsilon \cdot \left(1 - \frac{Ne^2}{m\omega^2\varepsilon}\right) \cdot E \tag{28}$$

$$\omega_p = \sqrt{\frac{Ne^2}{m\omega}} \left(\frac{\text{rad}}{\text{s}}\right) \tag{29}$$

$$\rightarrow D = \varepsilon \cdot \left(1 - \frac{\omega_p^2}{\omega^2}\right) E \tag{30}$$

Therefore, plasma cutoff frequency is:

$$f_p = \frac{\omega_p}{2\pi} = \frac{1}{2\pi}\sqrt{\frac{Ne^2}{m\omega}} \text{ (Hz)} = \varepsilon \cdot \left(1 - \frac{f_p^2}{f^2}\right) \tag{31}$$

$$\gamma = j\omega\sqrt{\mu\varepsilon} \cdot \sqrt{1 - \frac{f_p^2}{f^2}} \text{ and } n_c = \frac{n_0}{\sqrt{1 - \frac{f_p^2}{f^2}}} \tag{32}$$

For electron with known parameter:

$$f_p = 9\sqrt{N} \tag{33}$$

According to the above mentioned statements, since in positive half-cycle, the density of electrons decreases with the distance from the wire (because of their absorption to the wire) there will be no shield to transfer a wave like a wave channel through it. But in a negative half-cycle $[t_1, t_2]$ in Figure 5 the existing are only advancing in the ionization boundary. Therefore, the electrons enclose the wire like the shield and exactly like a coaxial cable that can carry the wave through itself and in addition keep the inner environment immune from penetrating waves outside. In addition to corona noise effect created by the movement of electrons out of the shield they do not have the ability to enter the electron shield and corona noise cannot the wave channel.

## 5. THE OPTIMUM WAVE CHANNEL RADIUS

In order that consecutive collision of waves and their reflection take place one after the other on the surface of the wire and the inner surface of the shield (to decrease distortion), we consider optimum radius less than maximum $r$ (fig and base on this radius we calculate $t_2$. The appropriate time to transfer wave through this environment is between $t_1$ and $t_1 + 2.3$ ms.
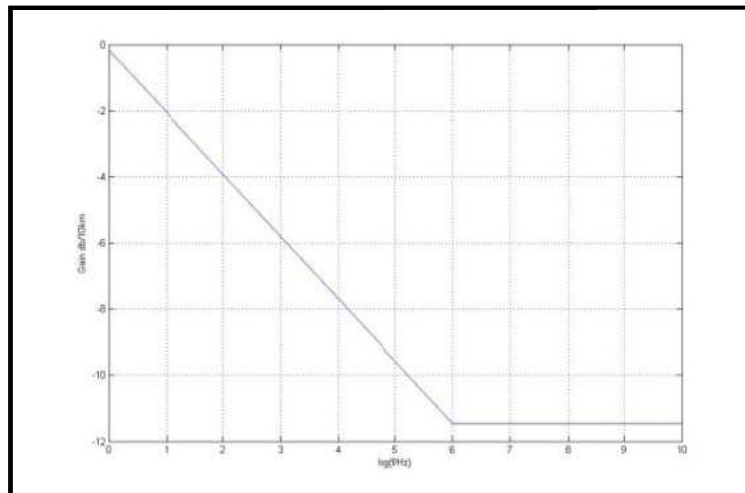


Figure 5. Attenuation in terms of $\log(f)$.

## 6. THE STUDY OF FREQUENCY CHARACTERISTIC AROUND WIRE (POSITIVE IONS) [7]

Since the environment formed around the wire is very similar to the ionosphere in terms of materials and components, the two environments are a kind of plasma and their differences have to do with their ions density, pressure, and heat. The analysis of this environment of transmission is exactly similar to the analysis made for the environment of ionosphere and only parameters such as pressure, heat, and density of positive ions change.

## 7. THE ATTENUATION COEFFICIENT FOR THE PROPAGATION OF WAVES IN IONOSPHERE

Conductivity coefficient and electric permeability of ionosphere based on ionosphere parameters such as ion density and collision frequency are defined as follows:

$$\alpha = \omega \sqrt{\frac{\mu\epsilon.}{2}\left(\sqrt{1 + \frac{\sigma^2}{\omega^2\varepsilon^2}} - 1\right)} \tag{34}$$

$$\varepsilon = \varepsilon_r \varepsilon_v = \varepsilon_v\left(1 - \frac{Ne^2}{\varepsilon_v m(v^2 + \omega^2)}\right) \tag{35}$$

$$\mu = \mu_v \rightarrow \sigma = \frac{Ne^2 v}{m(v^2 + \omega^2)} \tag{36}$$

$$a = \omega\sqrt{\frac{\epsilon_r}{2}\left(\sqrt{1 + \frac{\sigma^2}{\omega^2\varepsilon^2}} - 1\right)} = \frac{\omega}{c}\sqrt{\frac{1}{2}\left(\sqrt{\varepsilon_r^2 + \left[(1 - \varepsilon_r)\frac{v}{\omega}\right]^2}\right) - \frac{\varepsilon_r}{2}} \tag{37}$$

Collision frequency indicates the number of effective collisions among the molecules which form *"positive ions"* of the environment. The rate of collision frequency in the ionosphere approximately at the altitude of 90 km from the surface of the sea is equal to $10^6\,\text{sec}^{-1}$ and the altitude of 300 km of the sea is $10^3\,\text{sec}^{-1}$. But in the environment of transmission around the wire considering the following equation we have:

$$v = N_A \sigma_{AB}\sqrt{\frac{8K_B T}{\pi\mu_{AB}}} \qquad N_A = 2.688 \times 10^{25} \tag{38}$$

$r_A$ and $r_B$ have been considered for molecule of nitrogen:

$$\sigma_{AB} = \pi(r_A + r_B)^2 = \pi(2 \times 1.7 \times 10^{-10})^2 = 2.463 \times 10^{25}\,\text{m}^2$$

$$K_B = 1.38 \times 10^{-23} \text{ and } T = 300K \quad \mu_{AB} = \frac{m_A m_B}{m_A + m_B} \cong \frac{m_N}{2} = \frac{28 \times 1837 \times 9.109 \times 10^{-31}}{2}$$

Considering the above-mentioned values collision frequency for this environment is as follows:

$$v = 1.04\,\text{GHz}$$

And the attenuation graph in terms of dB in every 1000 meters has been drawn based on various frequencies that from $10^6\,\text{Hz}$ onward we get attenuation equal to 81 dB per 10 km (see Figure 5).

## 8. CONCLUSION

Based on the aforementioned materials the environment, which was defined for transmission of information, has unique features as follows:

1) Extensive wide band can be considered as a turning point in communication through power lines.

2) Because of high cut-off frequency of environment around the wave channel this environment is completely immune from the noise of outside the environment as well as electromagnetic waves.

3) Since the corona noise is made due to the motion of electrons and the boundary layer is closer to the wire in comparison to outside electrons as well, it can decrease the effect of corona noise to great extent.

4) Since the wave channel environment around the wire has a short radius, it is affected less by the weather conditions such as wind, rain and so on.

**ACKNOWLEDGMENT**

**REFERENCES**

1. Gurnett, D. A. and A. Bhattacharjee, *Introduction to Plasma Physics: With Space and Laboratory Applications*, 2005.
2. Cheng, D. K., *Field and Wave Electromagnetics*, 1992.
3. Mohseni, M., *High Voltage Engineering*, Tehran University.
4. Hughes, T. P., *Networks of Power: Electrification in Western Society*, 1880–1930, The Johns Hopkins University Press, Baltimore, Maryland, 1983.
5. Naidu, M. S., *High Voltage Engineering*, Technology, 1999.
6. Skilling, H. H., *Electric Transmission Lines: Distributed Constants, Theory, and Applications*, 1951.
7. Jordan, E. C. and K. G. Balmain, *Electromagnetic Waves and Radiating Systems*, Technology, 1968.

# Novel GLLH EM Cloak with Front Branching and without Exceed Light Speed Violation

**Ganquan Xie**, **Jianhua Li**, **Lee Xie**, and **Feng Xie**

GL Geophysical Laboratory, USA

**Abstract**— In this paper, we propose new Global and Local (GL) electromagnetic (EM) cloaks with distinctive class material $a_{\alpha\beta} \log^{\alpha}(b_{\alpha\beta}/h)h^{\beta}$ (GLLH Cloak) without exceed light speed violation. The refractive index of the GLLH cloak material, $n(r)$, is large than one or equal to one. Our GLLH cloak is created by GLLH EM modeling and GLLH EM cloak inversion with searching class $a_{\alpha\beta} \log^{\alpha}(b_{\alpha\beta}/h)h^{\beta}$. The GLLH cloaks in this paper have finite speed and have no exceed light speed? Physical violations and have more advantages. The GLLH EM cloaks can be practicable by using normal materials and are available for all broad frequency band. The GLLH EM cloak inversion and electromagnetic integral equation for cloak are presented in this paper. The novel EM wave propagation and front branching in the GLLH cloak by GLLH EM modeling are presented in this paper. The EM wave front propagation in GLLH cloak is behind of the front in free space. At time steps $118dt$, in the GLLH cloak, the wave front is curved as a crescent like and propagates slower than the light in free space. At the time step $119dt$, the EM wave inside of the GLLH cloak propagates slower than light speed, moreover, its two crescent front peaks intersect at a front branching point. At the front branching point, the front is split to two fronts. The novel front branching and crescent like wave propagation are displayed in the following Figures 1, 2 and 4–6 in this paper. The GLLH class cloak and GL inner cloak can be gravityles cloak. All copyright and patent of the GLLH EM cloaks and GL modeling and inversion methods are reserved by authors in GL Geophysical Laboratory.

## 1. INTRODUCTION

We discovered the GILD double layer cloth phenomena in Figure 3 in [1] to prevent detection from the exterior EM wave in 2001. The creating motivation of our GLLH invisible cloak without exceed light speed is from our double layer cloth observation in our paper [1] in 2001. The Figure 3 shows the double layer cloths in [1]. The wave front in our double layer cloth is similar with the wave front in our new GLLH cloak in Figures 1 and 2. Using **GL** EM Inversion, we propose a GLLH EM cloak with distinctive class material $a_{\alpha\beta} \log^{\alpha}(b_{\alpha\beta}/h)h^{\beta}$ without exceed light speed violation in Section 2 of our paper [2]. GLLH means that GL is GL method, L is log, H is $h = r - R_i$.

The description order of our paper is as follows. Novel EM propagations in GLLH cloak without exceed light speed are presented in Section 2. We propose the invisible properties of the GLLH
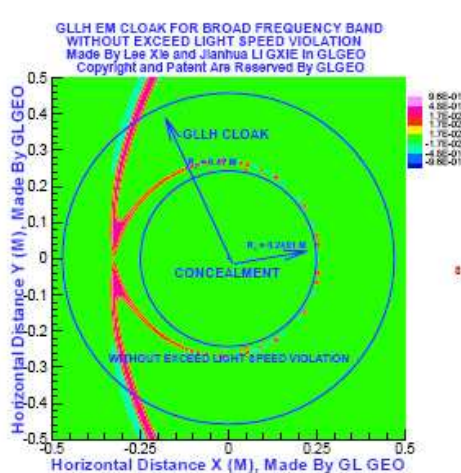


Figure 1: Electric wave propagation at time step $118dt$, the wave front is curved as the crescent like, red S in right is source location.
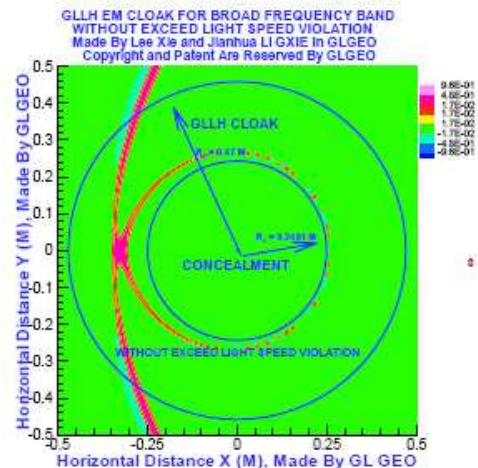
Figure 2: Electric wave propagation at time step $119dt$, the two peaks of the crescent like wave front intersects at a branching point, red S in right is source location.
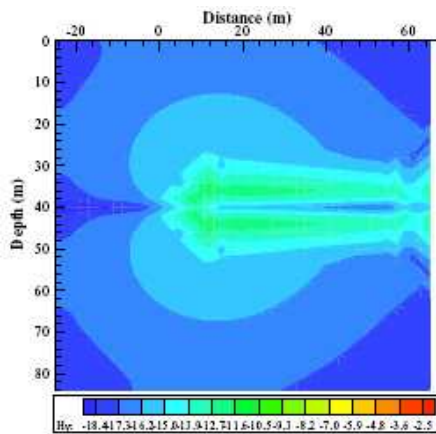
Figure 3: We discovered the double cloth phenomenon in 2001 in our paper [1]. The front in our double cloth is simlar with front in Figure 1.
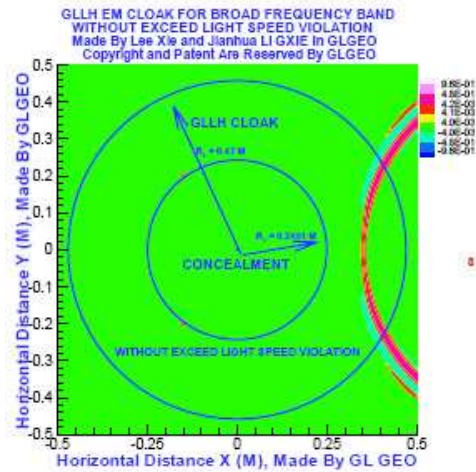
Figure 4: At time step $50dt$, front of *Electric wave*, $E_{xx}$ inside of the GLLH EM cloak $R_1 \leq r \leq R_2$ propagates slower than light speed.

EM cloak in Section 3. The GLLH EM double layer cloak is proposed in Section 4. We propose the EM wave field decay to zero inverse radial in Section 5. The history and discuss are presented in Section 6. Reader please refer my detailed paper in 2010arXiv10053999X in the arXiv, in http://arxiv.org/abs/1005.3999.

## 2. NOVEL EM PROPAGATION IN GLLH EM CLOAK WITHOUT EXCEED LIGHT SPEED

In this section, we present a novel EM propagation in the GLLH EM cloak without exceed light speed. The EM wave proagation pattern completely is new, and never be shown in other authors' papers.

### 2.1. Novel Electric Wave Propagation

The electric intensity wave is excited by the point source $S$, which is denoted by red S in the figures in this paper. In Figures, the source by red S is located in free space, in the right side outside of the whole GLLH EM cloak, at $(0.83m, 0.0, 0.0)$. In Figure 1, at time step $118dt$, *electric wave*, $E_{xx}$ inside of the GLEM cloak $R_1 \leq r \leq R_2$ propagates slower than light speed. Its front inside of GLLH EM cloak is behind of the electric wave front in free space. The Figure 2 shows that at time step $119dt$, *electric wave*, $E_{xx}$ inside of the GLEM cloak $R_1 \leq r \leq R_2$ propagates slower than light speed. The upside and downside parts of curved CRESCENT electric wave front are intersected at a branching point. These branching points form a 2D subsurface which depends on the source location. In this Figure and Figure 2, the red S denotes the source which is located in the right of the cloak. The front branching point is located in left of the concealment. The Figure 4 shows that at time step $50dt$, *electric wave*, $E_{xx}$ inside of the GLLH EM cloak $R_1 \leq r \leq R_2$ propagates slower than light speed. The Figure 5 shows that at time step $110dt$, *electric wave*, $E_{xx}$ inside of the GLLH EM cloak $R_1 \leq r \leq R_2$ propagates slower than light speed. The Figure 6 shows that at time step $120dt$, *electric wave*, $E_{xx}$ inside of the GLEM cloak $R_1 \leq r \leq R_2$ propagates slower than light. The front has been split to two wave fronts, The outgoing front propagates forward to left and going to outer boundary $r = R_2$. The attractive front propagates and shrinks to the inner boundary. The speed of the attractive wave front is going to zero. Its amptulide is rapidly decay to zero. The red S denotes the source which is located in the right of the cloak. The front branching point is located in left of the concealment. At time step $130dt$, *electric wave*, $E_{xx}$ inside of the GLEM cloak $R_1 \leq r \leq R_2$ propagates slower than light speed. Its outgoing wave front inside of GLLH EM cloak is behind of the electric wave front in free space. Other attracting wave front propagates much slow than the light speed. Its speed is going to zero. The more figures in 2010arXiv10053999X (GLLH paper) show that the novel propagation and front branching and crescent curved front of EM wave through the GLLH EM invisible cloak. The front branching point is located in right of the concealment in the simulation.The front branching point is moveable and
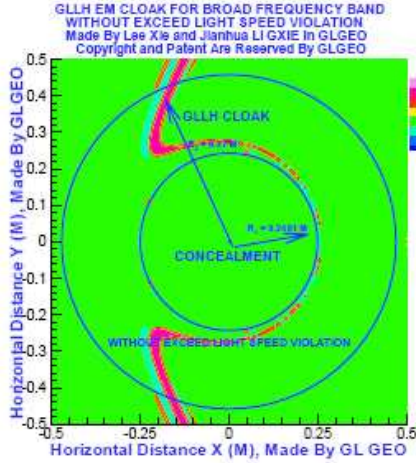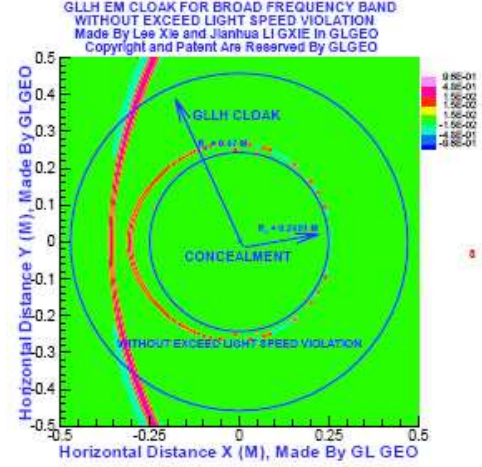
Figure 5: At time step $110dt$, front of *Electric wave*, $E_{xx}$ inside of the GLLH EM cloak $R_1 \leq r \leq R_2$ propagates slower than light speed.

Figure 6: At time step $120dt$, front of *Electric wave*, $E_{xx}$ inside of the GLLH EM cloak $R_1 \leq r \leq R_2$ propagates slower than light speed. The curved front is split to two branching fronts.

depends on the source location.

## 3. INVISIBLE PROPERTIES OF GLLH EM CLOAK

By using the GL EM Metro Carlo inversion method in GLLH paper Ref. [3], we solve the GL EM cloak inversion (11), (12), (13), (14) and (15) of GLLH paper Ref., and obtain the GLLH EM invisible cloak. The invisible properties of the GLLH EM cloak are verified in this section.

### 3.1. The Invisibility of the GLEM Cloak

**Statement 1** The exterior EM field is not scattering interfered by the cloak Because our GLLH EM exterior cloak inversion, by substituting the GLLH EM cloak in (2)–(5) of GLLH paper Ref. and EM wave field by GL modeling [2] into (11) and (12) of GLLH paper Ref., such that the integral Equations (11) and (12) were held, we have identity (6) GLLH paper Ref. for any exterior source and frequency. therefore, any exterior EM wave field must not be scattering interfered by the cloak. By the 3D GL EM modeling [2] GLLH paper Ref. simulations, electric wave propagations in the Figures 1–6 verify that there is no any reflction and no any scattering from the cloak to interfer the exterior EM field in free space. By calculations, when $R_i = 0.2491$ meter and $R_o = 0.47$ meter, we can prove that on the outer boundary of the cloak $r = R_o$, $\bar{\varepsilon}$ and $\bar{\mu}$ in (2)–(5) of GLLH paper Ref. satisfy

$$\begin{aligned} \varepsilon_r = \varepsilon_\theta = \varepsilon_\phi = 1, & \ \ r \in R_o, \\ \mu_r = \mu_\theta = \mu_\phi = 1, & \ \ r \in R_o. \end{aligned} \tag{1}$$

This is necessary condition for the invisibility of the cloak. From the GLLH EM cloak exterior inversion (11) and (12), we can prove that the condition (17) of GLLH paper Ref. is necessary.

**Statement 2** Any exterior EM wave field can not penetrate into the concealment. From the GLLH EM inner cloak inversion (13) and (14) of [2], and EM integral Equations (8) and (9) of [2], the Statement 2 is proved. Also, because on the inner boundary $r = R_i$, the refractive index $\sqrt{\varepsilon_r \mu_\theta}$ or $\sqrt{\varepsilon_\theta \mu_r}$ in (4)–(5) of [2] is infinite, from the convergence of integral (11)–(14) of [2], the EM wave field must be vanished on the inner boundary $r = R_i$. We obtain the condition

$$\begin{aligned} E_\theta = E_\phi = 0, & \ \ r \in R_i \\ H_\theta = H_\phi = 0, & \ \ r \in R_i \end{aligned} \tag{2}$$

Inversely, the conditions (17) and (18) of [2] are sufficient condition for the invisibility of the GLLH EM cloak in (2)–(5) of [2].

### 3.2. Without Exceed Light Speed Violation

**Statement 3** The refractive index in the GLLH EM cloak configration in this paper is large than one, the group speed in the cloak is finite and less than one.

From (4) of [2], the $\varepsilon_r$ and $\mu_r$ are finite positive and monotone increase function on variable $r$ in the $R_i \leq r \leq R_o$. Moreover, their minimum on the inner boundary of the cloak are

$$\varepsilon_r(R_i) = \mu_r(R_i) = \frac{2R_o^2(R_o - R_i)}{R_i^2(1 + 4R_o + 2R_o^2)} > 0, \tag{3}$$

their maximum value on the outer boundary $R_o = 0.47$ of the cloak are one. From (5), the $\varepsilon_\theta$ and $\mu_\theta$ are monotone decrease function on variable $r$ in the $R_i \leq r \leq R_o$, moreover, their maximum value on the inner boundary of the cloak are infinite, their minimum value on the outer boundary, $R_o = 0.47$ meter of the cloak are one. The refractive index of the GLLH EM cloak in (2)–(5) of [2] is,

$$n(r) = \sqrt{\varepsilon_r \mu_\theta} = \sqrt{\varepsilon_\theta \mu_r} \geq 1. \tag{4}$$

The group speed is finite and $V_g \leq 1$. Therefore, in the annular configuration $R_i \leq r \leq R_o$, with $R_i = 0.24$ and $R_o = 0.47$. The GLLH EM invisible cloak material in (2)–(5) of [2] has no violation of exceeding light speed. The novel electric intensity wave propagations, which are shown in Figures 1–6, in the GLLH EM cloak in (2)–(4) of [2] verify that the GLLH EM cloak is invisible cloak without exceed light speed violation.

### 3.3. Wave Front Branching

The EM wave propagation in the GLLH EM cloak is completely novel that are displaying in Figures 1–6. In particular, in Figure 1, EM wave front is curved around the concealment to form a Crescent like and its upside and downside two parts intersect at a moveable branching point, which form a 2D subsurface. The Figure 6 shows that the two wave fronts are separately propagation from the branching point. The first wave front is forward propagating outgoing. The attracting wave front is shrinking propagating and approaching to the inner boundary $r = R_i$. The speed of two wave front propagation are shower then the light speed. The attracting wave front propagating is very shower. Its amplitude is rapidly decay to zero. Its propagation speed is going to zero. The front branching points form a moveable 2D subsurface which depend on the source location. The front branching point and source point are separately located on two sides of the concealment room. In Figures, the source is located in the right side of the cloak which is denoted by red S, the front branching point is located at the left side of the concealment. These novel EM wave propagations in our GLLH EM cloak and wave front branching phnomena only display in our paper. They never appear in other cloaks and never appear in other materials. The GLLH EM cloak, novel wave propagations and wave front branching are patent and copyright by authors in GL Geophysical Laboratory.

### 4. GLLH EM DOUBLE LAYER CLOAK

We propose new GLLH EM double layer cloak in this section.

**Statement 4** When the concealment room of the single layer cloak is fill in the basic EM materials $\varepsilon_0$ and $\mu_0$ or normal material with refractive index $n \geq 1$, and the cloak materials are finite, then there is no EM field can be excited by source inside of the concealment.

We have proved the statement in [10, 15] of Ref. in [2]. The Statement 4 theoreticaly confirms that our double layer cloth phenomena in 2001 in [1] is a credible physical discovering. We propose GL double layer cloak in [9, 11–13, 16] of Ref. of [2] and new GLLH EM double cloak here without exceed light speed violation in this paper and [2]. Our GLLH EM double layer cloak has advantages to overcome the three physical violations.

### 5. EM WAVE FIELD DECAY TO ZERO INVERSE RADIAL

**Statement 5** When source is located outside of the GLLH invisible cloak in (2)–(5), the observer $r$ is located inside of the cloak and is going to the inner boundary $r = R_i$, the EM wave field delay to zero inverse radial. We have

$$\begin{aligned} E_r(r,\theta,\phi) = E_\theta(r,\theta,\phi) = E_\phi = 0, \ \text{when } r = R_i, \\ H_r(r,\theta,\phi) = H_\theta(r,\theta,\phi) = H_\phi = 0, \ \text{when } r = R_i, \end{aligned} \tag{5}$$

where $r = R_i$ is the inner boundary of the GLLH cloak, on the inner boundary $r = R_i$, the radial electric wave field $E_r(r, \theta, \phi) = 0$ and the radial magnetic wave field $H_r(r, \theta, \phi) = 0$ are distictive property of the GLLH invisible cloak. On the inner boundary of other transformed cloak, the radial wave EM field are not zero.

## 6. HISTORY AND DISCUSSION

We discovered the GILD double layer cloth phenomena [1] to prevent detection from the exterior EM wave in 2001. The double layer cloth was appeared in residual magnetic field $H_y$ in the GILD EM modeling and inversion [1]. The creating motivation of our GLLH invisible cloak without exceed light speed is from our double layer cloth observation in our paper [1] in 2001. The Figure 3 shows the double layer cloths in [1]. The wave front in our double layer cloth is similar with the wave front in our new GLLH cloak in Figures 1 and 2. Our GILD double layer cloth phenomena and our GLLH cloak are patented and copyrighted by authors in GL Geophysical Laboratory. Many times repeat GILD simulations show that the GILD double layer cloth is a mathematical physical phenomenon. We develop complete new GL EM modeling [2] of Ref. in [2] and GL EM inversion [3] of Ref. in [2] in 2003 to investigate the strange phenomena. We did find mirage [5] of Ref. in [2] and double layer cloaks [9–13] of Ref. in [2]. Our GLLH EM cloaks in this paper and in previous papers are based on the GL EM modeling and inversion and number theory. We deeply investigate the relationship between the field and material interactive scattering and non scattering and propose the GLLH EM cloak inversion. Our GL methods do not need artificial boundary condition to truncate the infinite domain. The GL method does not need to solve big matrix equation. The GL method combines the analytical method and numerical method. It can perform analytical and numerical or mixed field simulation and material generation. Front branching is complete novel propagation. Attracting front has benefit for detect the exterior field information in invisible cloaked concealment.

The GLLH EM cloak materials (4)–(5) in [2] is similar with the form $N^\alpha / \log^\beta N$ in number theory [20–22] of Ref. in [2] and $h^\alpha \log^\beta(1/h)$ in superconvergent estimation [5, 23] of Ref. in [2]. That is consistent with our double layer cloth phenomena discovered in the residual field in [1]. By paper [20] of Ref. in [2] and [21] of Ref. in [2], GOLDBACH's conjecture proof will have a big step forwarding and will be resolved completely. The electromagnetic physics is governed by Maxwell equation. The equation is main tool for physics that relative both of geometry and number theory. Our GL EM full wave field modeling and inversion are based on the Maxwell equation The form $N^\alpha / \log^\beta N$ and $h^\alpha \log^\beta(1/h)$ are important mathematical form in the number theory and numerical estimation A good luck thing is that we chose these form and their appreciate combination and GL EM inversion to discover the invisible cloak material in without exceed light speed. Other
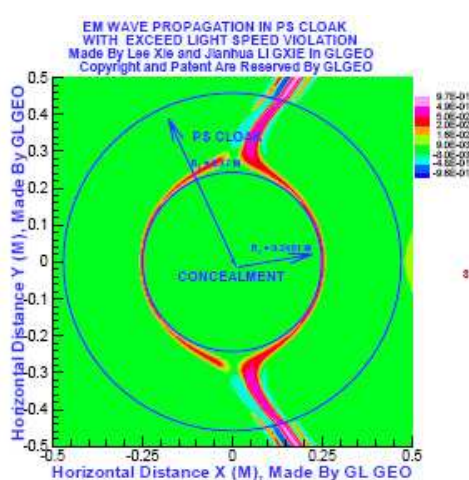


Figure 7: At time step $84dt$, front of *Electric wave*, $E_{xx}$ inside of the PS cloak $R_1 \leq r \leq R_2$ propagation is split two phase around the concealment, the front phase exceed light speed. It shows Ps cloak has infinite speed violation. The red S in right is source.
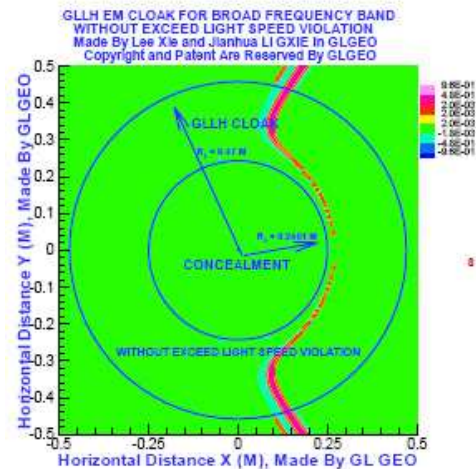
Figure 8: At time step $84dt$, front of *Electric wave*, $E_{xx}$ inside of the GLLH EM cloak $R_1 \leq r \leq R_2$ propagates slower than light speed. The red S in right is source.
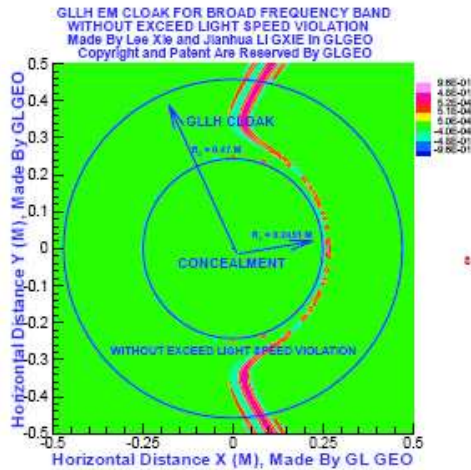
Figure 9: At time step 90$dt$, front of *Electric wave*, $E_{xx}$ inside of the GLLH EM cloak $R_1 \leq r \leq R_2$ propagates slower than light speed.
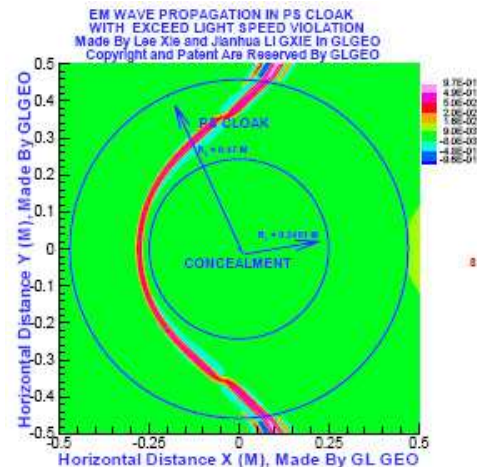
Figure 10: At time step 90$dt$, front of *Electric wave*, $E_{xx}$ inside of the PS cloak $R_1 \leq r \leq R_2$ propagation is much more exceed light speed. The red S in right is source.

cloaks based on the coordinate geometry transformation have exceed light speed and infinite speed physical violations.

To compare with Ps cloak, which is based on the coordinate transformation, we simulate EM full wave propagation through the Ps cloak material using our GL EM modeling with same source, frequency band and domain geometry as our GLLH EM cloak simulation. In Figure 7, at 84 time steps, the EM wave propagates through Ps cloak, its front is split to two phases, its front phase much more exceeds the light speed. In the same time, 84 timestep the Ps cloak front distributes around the inner boundary anular that shows Ps cloak's speed is infinite violation on the inner boundary spherical annular. In Figure 8, at 84 time step, the EM wave propagates in the GLLH EM cloak and slower than the light speed. Its front inside the GLLH EM cloak is behind of the front in the free space. At 90 time steps, the Figure 10 shows that the speed of EM wave inside Ps cloak much more exceed the light speed. At 90 time step, the EM propagation in GLLH EM cloak is presented in Figure 9, it is obvious that the EM wave front inside GLLH EM cloak is behind of its front in the free space which shows that the speed of EM wave inside GLLH EM cloak is not exceeding light speed. We propose GLLH EM cloak without exceed light speed in ellipsoid, 2 polar geometry domain and other geometry domain. For overcoming the infinite speed in [14] of Ref. in [2]. Ulf Leonhardt et al. proposed a new cloak with finite speed based, on a Euclid and non Euclid joint transform [17] of Ref. in [2]. The ULF cloak overcomes the "infinite speed" physical violation, even though its refractive index less than one in some subdomain, for example, $n(\sigma, \sigma', \tau) = n(0.75\pi, \pi, \tau) < 1$. Our GLLH EM cloak without exceed light speed in the 2 poplars geometry domain and in the ellipsoid domain will be published. The GLLH cloak is patented and copyrighted by authors in GL Geophysical Laboratory. The detailed references is presented in our paper in 2010arXiv10053999X.

## ACKNOWLEDGMENT

## REFERENCES

1. Li, J., G. Xie, C. Lin, and J. Liu, "2.5 dimensional GILD electromagnetic modeling and application," *SEG, Expanded Abstracts,* Vol. 21, No. 1, 692–695, 2002, http://www.segdl.org/journals/doc/SEGLIBhome/dci /searchDCI.jsp.
2. Xie, G., J. Li, L. Xie, and F. Xie, "GLLH EM invisible cloak with novel front branching and without exceed light speed violations?" *Physics, Optics*, May 21, 2010, 2010arXiv10053999X.

# Three Dimensional Imaging and Focusing of Ground Penetrating Radar Data

**Said I. Elkhetali**

The Higher Institute of Electronics Bani Walid, Libya

**Abstract**— This paper presents three dimensional modelling of electromagnetic wave propagation into the ground to obtain images as seen by ground penetrating radar and the focusing of these images. The proposed application is detection of groundwater buried valley aquifers in the desert. It takes into consideration the rough surface scattering by subterranean interfaces.

Two approaches for modelling scattering from rough surfaces have been tried, namely facet modelling and the continuous rough surface. Measurements were performed to determine scattering patterns of facets that are smaller than the wavelength since no published data was found in the literature even after searching for scattering by single hydrometeors. The measured scattering patterns are fitted to cosine functions having different powers to compare them to the point scatterer model. The results of simulation by facets are compared to reflection by using geometrical optics. Spatial averaging to reduce the effect of rough surface scattering is investigated. Flat rough interfaces and a buried valley are simulated. Spatial averaging is used for mitigation of the effect of rough surface scattering and Synthetic aperture radar technique is used for focusing the image of a buried valley.

## 1. INTRODUCTION

This paper is result of work in attempting in using ground penetrating radar for detection groundwater in the Sahara desert. Groundwater is relatively deep, deeper than 50 m, generally and the upper layers are dry. Groundwater could be found in acquifers called buried valleys and have a cross section having a "V" or "U" shape [1]. The proposed radar uses frequencies in the HF band.

Interfaces between earth layers may be rough, causing clutter to the ground penetrating radar receiver. The interfaces could have boulders, surface irregularities and grooves that could be smaller than the wavelength since the wavelength is relatively long. The antenna beam, being broad, causes the radar to receive scattering from such objects even when they are positioned far from it. The main objective of this paper is to investigate, by simulation, the effects of rough surface scattering on the radar signals and image and then how to alleviate them by spatial averaging and by migration.

Two approaches for rough surface modelling are used; facet modelling is one way and another is the continuous rough surface [2].

## 2. MODELLING

To model rough surface scattering, we must establish how the antenna pattern spreads, then use two models to assess the reflection from subterranean surfaces.

### 2.1. Antenna Radiation Pattern

Figure 1 in presents the radiation patterns of a dipole antenna in the $H$-plane and the $E$-planes. The patterns are derived from equations given by Engheta et al. [3].

It is evident, whatever the antenna orientation may be, that there is the possibility of receiving clutter due to the pattern of the antenna being broad in either direction. It can also be observed that for a ground having low permittivity the antenna beam becomes broader in either direction which is the case in for the desert environment.

### 2.2. The Continuous Rough Surface Model

This is obtained by calculating the radar cross section per unit area according to Equation (1) given by Qureshi [2] for a ground having a surface roughness expressed by Gaussian function and using the radar equation to obtain the shape of the reflected signal summing the contribution of all the surface area.

$$
\sigma°(x,y) = \frac{4 \cdot \pi \cdot F_1(x,y) \cdot 2T^2}{\lambda^2} \cdot e^{-1 \cdot \Psi(x)^2} \cdot \sum_{m=1}^{\infty} \frac{\Psi(x)^{2 \cdot m}}{m! \cdot m} \cdot e^{\frac{-1 \cdot \Psi(x)^2 \cdot T^2}{4 \cdot m \cdot \sigma^2} \cdot \left( \frac{u(x,y)^2 + v(x,y)^2}{w(x)^2} \right)}
$$

$$
+ \frac{4 \cdot \pi \cdot F_1(x,y)^2 \cdot A}{\lambda^2} \cdot e^{-1 \cdot \Psi(x)^2} \cdot \text{sinc}(k \cdot u(x,y) \cdot x)^2 \cdot \text{sinc}(k \cdot v(x,y) \cdot y)^2 \qquad (1)
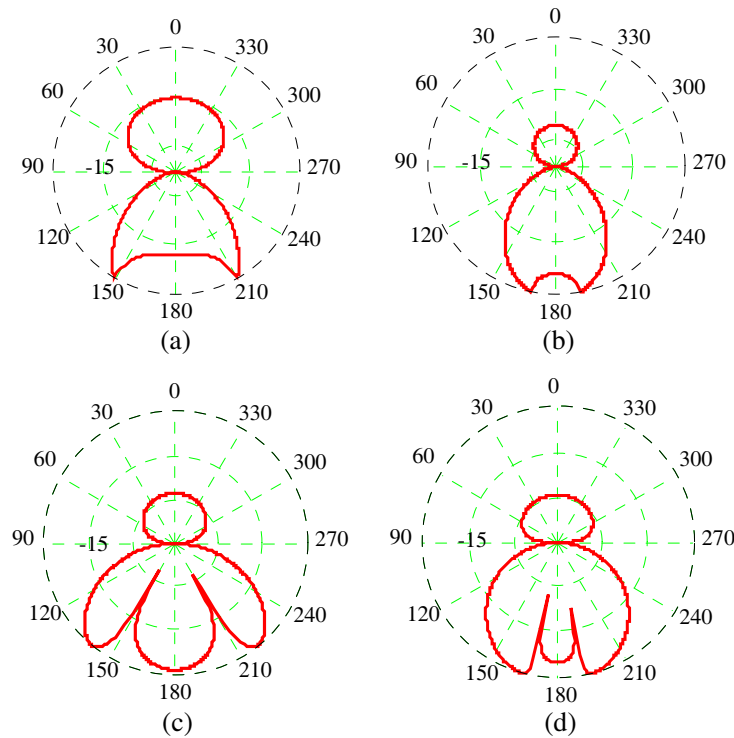$$

Figure 1: The shape of the radiation pattern of a dipole antenna (in dB) in the $H$-plane. Permittivity is (a) 4 and (b) 25 and pattern in the $E$-plane for permittivity of (c) 4 and (d) 25 respectively.

where the embedded functions are

$$F_1(x,y) = \frac{1 + \cos(\theta_1(x)) \cdot \cos(\theta_2(x)) - \sin(\theta_1(x)) \cdot \sin(\theta_2(x)) \cdot \cos(\theta_3(x,y))}{\cos(\theta_1(x) + \cos(\theta_2(x))}$$

$$u(x,y) = \sin(\theta_1(x)) - \sin(\theta_2(x)) \cdot \cos(\theta_3(x,y)),$$

$$v(x,y) = -(\sin(\theta_2(x)) \cdot \sin(\theta_3(x,y)))$$

$$w(x) = -(\cos(\theta_1(x)) + \cos(\theta_2(x))), \quad \Psi(x,f) = k(f) \cdot \sigma \cdot w(x)$$

and the variables, $T$ is the correlation distance, $\sigma^\circ$ is the scattering cross section per unit area and $\sigma$ is standard deviation of the surface height. Figure 2 parts (a) and (b) present the normalized reflected signal and the reflecting zone, respectively, assuming a surface statistics being $k\sigma = 0.25$ for $f = 20\,\text{MHz}$ and $T = 5\lambda$.

Figure 2 showed that scattering comes from a zone rather than a point. However, it does not cater for scattering by individual rocks. Most importantly it would not be appropriate to simulate geologic structures such as aquifers because it is based on the statistics of the surface only.
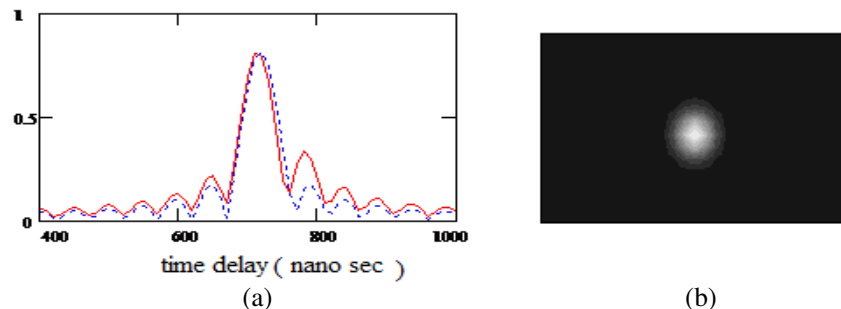


Figure 2: A normalised reflected radar signal and the scattering zone. (In part (a) the dotted line is obtained by ray tracing and the solid is by facet modelling).

**2.3. Scatter Cross Section of Individual Scatterers**

Measurements were performed to determine scattering patterns of facets that are smaller than the wavelength since no published data was found in the literature even after searching for scattering by single hydrometeors.

It is observed that as the size of a object is made smaller with respect to the wavelength its scattering pattern becomes less directive. The mean lobe becomes broader and will have less sidelobes.

**2.4. Simulation Using Facet Model**

A patch of ground modelled by facets will scatter energy with a radiation pattern similar to an antenna array composed of elementary antennas. Mathematically, the pattern of each facet resembles a cosine function with different power depending on the ratio of the facet to wavelength. The facets are tilted randomly to simulate a rough surface.

In this section simulated images of buried valleys with facet modelling are presented. The roughness of the surface is varied to see how the image looks. The effect of scattering from targets off-line between the antennas is included.

**3. MITIGATION OF CORRUPTIONS**

Two techniques are tried; special averaging and focusing (migration).

**3.1. Spatial Averaging**

One possible cure of the effect of rough surface scattering is to perform spatial averaging over a limited area. This is similar to stacking of adjacent traces in the seismic survey. The next example shows that averaging can reduce the effect of rough surface scattering. The surface is composed of large tilted facets. The specular component arrives first, the rest are reduced in magnitude as spatial averaging is performed.
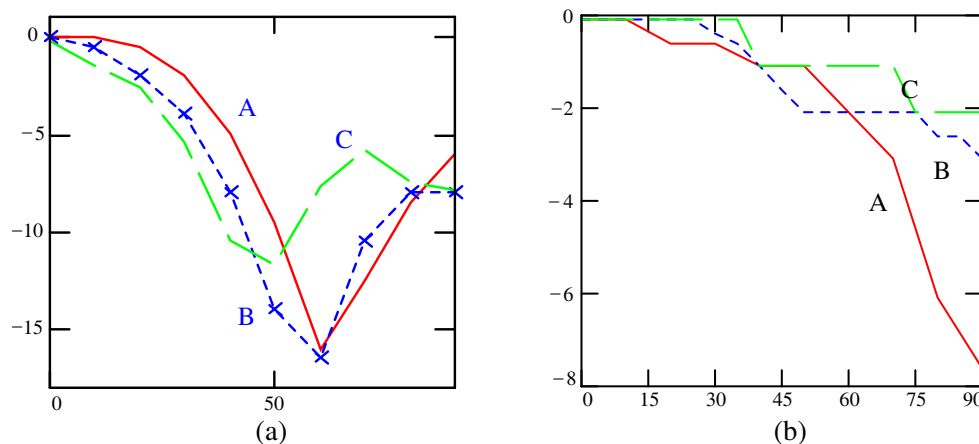


Figure 3: Facet side to wavelength ratio is (a) 0.5 and (b) 0.25. The curves are (A) for 5 GHz, (B) for 6 and (C) for 10 GHz.
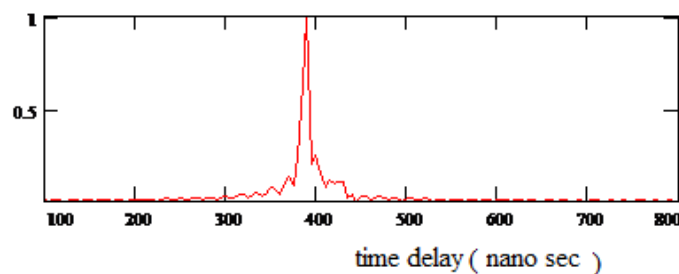


Figure 4: The echo from a surface modelled by relatively small facets having random tilting.

### 3.2. Focusing

Three dimensional imaging requires the collection of data over an area, i.e., a set of parallel lines that are close enough to avoid aliasing. The image appears defocuses because signals are reflected from areas that are not directly below the antenna. The purpose of focussing, or migration which is a term used in geophysics, is to restore the defocused image to its true shape [4].

Migration is performed by summing over an apex of a hyperboloid in three dimensions. Summation at the apex is done coherently by correcting for the phase differences due to variation of range to the point being focused at each frequency component. The values at points along $x$ and $y$ extensions are summed at the point $(x_0, y_0)$, Figure 7. This is the virtual apex of a hyperboloid. The virtual apex is moved throughout the imaged volume. When the virtual apex coincides with a scattering point the energy will be accumulated coherently but if it does not then only noise will accumulate, incoherently, resulting in a small value. The value at any point will be added to the apex after correcting for the phase difference between it and the apex at each frequency. The shape of the migrating hyperboloid depends on the assumed velocity; if it is equal to the ground velocity the result would be good migration, otherwise it would not be.



|      (a)      |      (b)      |      (c)      |
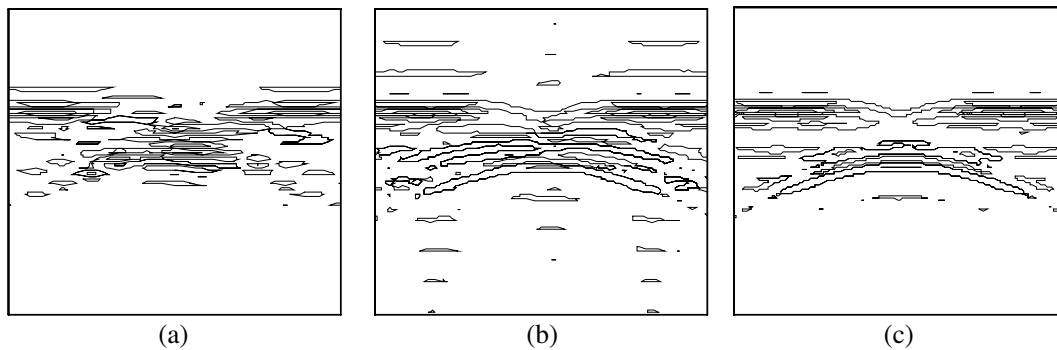
Figure 5: A simulated image of a buried valley using facets. (a) A rough surface, the facet side is 10 m, (b) a smoother surface, the facet side is 5 m and (c) still smoother surface, the facet side is 2 m.
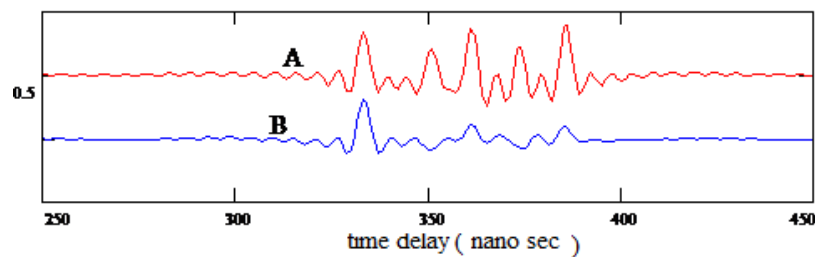


Figure 6: A scattered signal from a rough surface (A) and the signal after the application of spatial averaging.
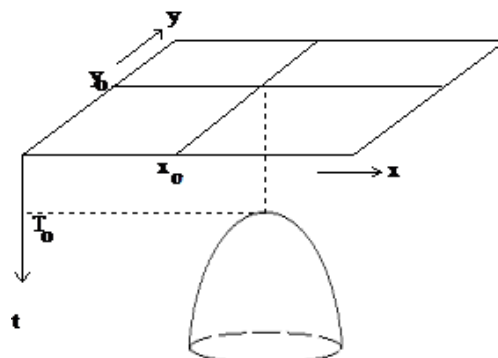


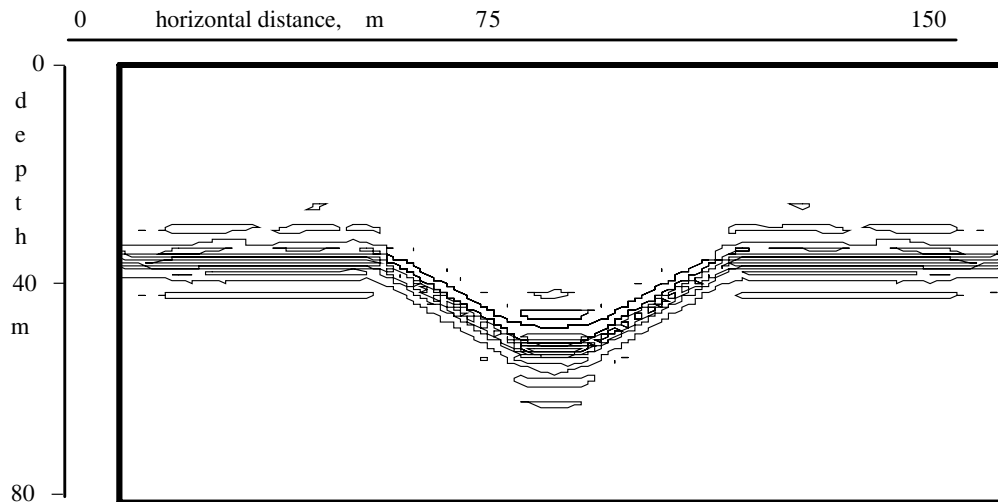Figure 7: The time delay from a point scatterer in 3-D.

Figure 8: Image of the model in Figure 5 after migration.

Figure 8 presents the image of the buried valley a) if there is no sideways scattering (only front and backward). With scattering from all directions being considered. b) A rough surface and c) A smoother surface. It is observed that sideways scattering alters the valley image when the valley has a bearing angle with respect to the survey line.

## 4. CONCLUSION

As a surface becomes rougher other areas around the specular reflection point begin to scatter energy making the beam broader and also the received radar pulse becomes broader because reflections arriving from points outside the specular point arrive later that the specular reflection causing the broadening of the pulse. This type of scattering brings scattered energy that is coming off the line connecting the transmitter and receiver antenna.

Scattering by individual relatively large facets resembles a sinc function but as the facet becomes smaller compared with the wavelength the scattering pattern becomes broader, looking like a radiation pattern of element antennas. The smoothness depends also on the frequency and bandwidth, if the frequency is lower and band is narrower, the surface appears smoother.

The radar image becomes cluttered due to scattering from rough interfaces. Spatial averaging and migration could reduce the effect of clutter.

Investigation of 3-D imaging of ground particularly when certain geologic structures exist is useful to gain insight into how they would look in a real GPR survey and to appraise the GPR's capability of providing a tool to investigate subterranean aquifers.

**REFERENCES**

1. Elkhetali, S. I., "Application of ground probing radar for detection of groundwater in arid regions," Ph.D. Thesis, School of Electronic and Electrical Engineering, University of Birmingham, UK, 1998.
2. Qureshi, M. A., "Sideways scattering of electromagnetic waves from rough surfaces," Ph.D. Thesis, School of Electronic and Electrical Engineering, University of Birmingham, 1968.
3. Engheta, N., C. H. Papas, and C. Elachi, "Radiation patterns of interfacial dipole antennas," *Radio Science*, Vol. 17, No. 6, 1557–1566, 1982.
4. Yilmaz, O., *Seismic Data Processing*, Society for Exploration Geophysicists, Tulsa, OK, 1987.
5. Ulaby, F. T., R. K. Moore, and A. K. Fung, *Microwave Remote Sensing; Active and Passive*, Addison-Wesley, Reading Mass., USA, 1981.
6. Goodman, D., "Ground penetrating radar simulation in engineering and archaeology," *Geophysics*, Vol. 59, No. 2, 224, 1994.
7. Jol, H. M., "A comparison of the 25, 50, 100, and 200 MHz with 400 and 1000 V transmitters: A ground penetrating radar field study," *54th Meeting of the E.A.E.G. and Technical Exhibition*, Paris, June 1–5, 1992.

# A Variable Step Size Algorithm for Blind Equalization of QAM Signals

**Wei Xue[1, 2], Xiaoniu Yang[1], and Zhaoyang Zhang[2]**

[1]National Laboratory of Information Control Technology for Communication System
Jiaxing, Zhejiang 314033, China
[2]Department of Information Science and Electronic Engineering
Zhejiang Uinversity, Hangzhou, Zhejiang 310027, China

**Abstract**— The constant modulus algorithm (CMA) is one widely used algorithm for blind equalization of QAM signals. The algorithm exhibits slow convergence rate and large steady state mean square error and the phase-blind nature in comparison with the algorithms used in conventional data-aided equalization schemes. In this paper, a variable step size modified constant modulus algorithm is proposed. The proposed algorithm can speed up convergence rate and decrease steady state mean square error and correct phase error and frequency offset at the same time. The simulation results demonstrate the effectiveness of the proposed algorithm in improving convergence rate and reducing steady state mean square error.

## 1. INTRODUCTION

Quadrature amplitude Modulation (QAM) schemes have been used widely in modern communication systems due to high bandwidth and power efficiency [1]. QAM signals are sensitive to intersymbol interference (ISI) caused by multi-path propagation and the fading of the channel [2], so it is necessary to use equalization technique to mitigate the effect of ISI. Conventional adaptive equalizers employ a training sequence which is known both at the transmitter and the receiver to update their filter coefficients. However, when sending a training sequence is impractical or impossible, it is desirable to equalize a channel without the training sequence. Such equalizers are known as blind equalizers because they blindly deconvolve the transmitted data sequence from the unknown channel.

The constant modulus algorithm (CMA) [3] is one widely used blind equalization algorithm for QAM signals. CMA has the disadvantages of the slow convergence rate and large steady state mean square error (MSE) and phase-blind nature. Several new algorithms [4–10] have been introduced to overcome the disadvantages of CMA. Modified constant modulus algorithm (MCMA) [4] shows the performance improvement in convergence behavior and can correct the phase error and frequency offset at the same time.

In this paper, a variable step size modified constant modulus algorithm is proposed. In the algorithm the step size in stochastic gradient descent methods is changed to obtain faster convergence rate and lower steady state MSE. The simulation results show the effectiveness of the proposed algorithm in performance improvement.

## 2. PRINCIPLE OF BLIND EQUALIZATION

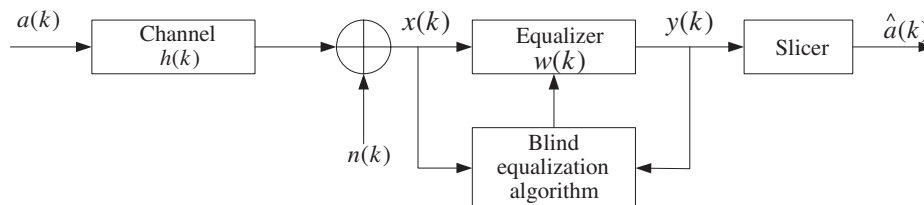The equivalent baseband model of blind equalization system is shown in Fig. 1.



Figure 1: Equivalent baseband model of blind equalization system.

The received signal $x(k)$ can be written as

$$x(k) = \sum_{i=0}^{L-1} h(i)a(k-i) + n(k) \qquad (1)$$

where $h(k)$ is the overall complex baseband equivalent impulse response of the transmitter filter, unknown channel and receiver filter. The length of $h(k)$ is $L$. The input data sequence $a(k)$ is assumed to be independent and identically distributed. $n(k)$ is the additive white Gaussian noise.

The output of equalizer can be written as

$$y(k) = X^T(k)W(k) \tag{2}$$

where

$$W(k) = [w_0(k), w_1(k), \ldots, w_{N-1}(k)]^T \tag{3}$$
$$X(k) = [x(k), x(k-1), \ldots, x(k-N+1)]^T \tag{4}$$

$W(k)$ is the equalizer tap weights vector, $X(k)$ is the input vector of equalizer. The length of equalizer tap weights is $N$.

## 3. CONSTANT MODULUS ALGORITHM (CMA) AND MODIFIED CMA

The CMA proposed by Godard [3] is the most popular algorithm for blind equalization of QAM signals, the cost function of CMA is given by

$$J(k) = E\left[\left(|y(k)|^2 - R_2\right)^2\right] \tag{5}$$

where $E[\cdot]$ indicates the statistical expectation, $y(k)$ is the output of equalizer and $R_2$ is a constant that depends on transmitted data statistics, it is given by

$$R_2 = \frac{E\left[|a(k)|^4\right]}{E\left[|a(k)|^2\right]} \tag{6}$$

The error signal is given by

$$e(k) = y(k)\left(|y(k)|^2 - R_2\right) \tag{7}$$

The update of tap weights vector can be written as

$$W(k+1) = W(k) - \mu \cdot e(k) \cdot X^*(k) \tag{8}$$

where $\mu$ is the step size parameter.

Modified CMA [4] modifies the cost function of CMA to the form of real and imaginary parts, the modified cost function can be written as

$$J(k) = J_R(k) + J_I(k) \tag{9}$$

where $J_R(k)$ and $J_I(k)$ are the cost function for real and imaginary parts of the equalizer output $y(k) = y_R(k) + jy_I(k)$ respectively, they are defined as

$$J_R(k) = E\left[\left(|y_R(k)|^2 - R_{2,R}\right)^2\right] \tag{10}$$

$$J_I(k) = E\left[\left(|y_I(k)|^2 - R_{2,I}\right)^2\right] \tag{11}$$

where $R_{2,R}$ and $R_{2,I}$ are the real constants determined by the real and imaginary parts of transmitted data sequence respectively, they are defined as

$$R_{2,R} = \frac{E\left[|a_R(k)|^4\right]}{E\left[|a_R(k)|^2\right]} \tag{12}$$

$$R_{2,I} = \frac{E\left[|a_I(k)|^4\right]}{E\left[|a_I(k)|^2\right]} \tag{13}$$

where the error signal $e(k) = e_R(k) + e_I(k)$ is given by

$$e_R(k) = y_R(k)\left(|y_R(k)|^2 - R_{2,R}\right) \tag{14}$$

$$e_I(k) = y_I(k)\left(|y_I(k)|^2 - R_{2,I}\right) \tag{15}$$

The cost function of CMA is only based on a single modulus, so the minimum of cost function is not zero even in the absence of noise. For some practical digital systems the state steady MSE is not sufficiently low for proper decision. The cost function is also phase-blind and CMA can converge even in the presence of the phase error, the performance of CMA can be severely degraded by phase error and carrier frequency offset.

In contrast, the cost function of MCMA separates the output of equalizer to real and imaginary parts and estimates the error signal for real and imaginary parts respectively. The cost functions of MCMA use both modulus and phase of the equalizer output, so MCMA can correct the phase rotation and spinning phase error.

## 4. VARIABLE STEP SIZE MCMA

The choice of $\mu$ in the update of tap weights vector is very critical for MCMA. A small $\mu$ will ensure lower steady state MSE, but the algorithm will converge slowly; a large $\mu$ can provide faster convergence rate at the cost of higher steady state MSE. Any selection must be a compromise between convergence rate and steady state MSE.

Here a variable step size MCMA is proposed in which the step size is adjusted according to the region where the received signal lies in the constellation plane. During the transient stages the output of equalizer will be scattered around a large area of the transmitted data symbols. However, in the steady state the output of equalizer will lie in a close neighborhood of the transmitted data symbols. Therefore, a larger step size could be used in the transient stages and a smaller step size could be used in the steady state to obtain faster convergence rate in the transient stages and lower MSE in the steady state.

In the variable step size scheme, $M$ regions $D_1$, $D_2$,..., $D_M$ are chosen in the constellation for M-QAM signals. The region $D_i (i = 1, 2, \ldots, M)$ represents a small circular area around the point of the transmitted data symbol constellation with the radius $d$. Fig. 2 shows the regions for a 16-QAM data constellation.

In Fig. 2, when the output of equalizer lies out of the region $D_i$ a larger step size is chosen and when the output of equalizer lies in the region $D_i$ a smaller step size is chosen. Then the variable step size scheme can be written as

$$\mu = \begin{cases} \mu_0 \text{ if } y(k) \notin \cup D_i \\ \mu_1 \text{ if } y(k) \in D_i \end{cases} \tag{16}$$
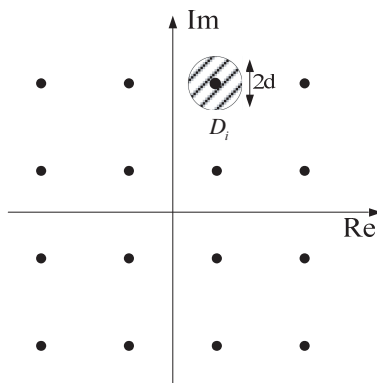
where $\mu_0 > \mu_1$.



Figure 2: The region $D_i$ of variable step size for 16-QAM signals.

## 5. SIMULATION RESULTS

In the simulations the variable step size MCMA (VSS-MCMA) is compared with CMA and MCMA with 16-QAM signals. The equivalent impulse response of channel [11] used in simulations is $[-0.005 - 0.004j \ 0.009 + 0.03j \ -0.024 - 0.104j \ 0.854 + 0.520j \ -0.218 + 0.273j \ 0.049 + 0.074j \ - 0.016 + 0.020j]$. Here a 7-tap complex equalizer is used with the initialization of center tap set to 1 and other taps set to 0. The SNR at the input of equalizer is 30 dB. The parameters for VSS-MCMA are $\mu_0 = 0.0003$, $\mu_1 = \mu_0/5$ and $d = 0.6$, the step sizes of CMA and MCMA are both 0.0001.

Figure 3 shows the constellations after convergence without a carrier frequency offset ($\Delta f/R = 0$). Fig. 4 shows the constellations after convergence with a carrier frequency offset ($\Delta f/R = 0.00005$). It can be seen that the output of CMA in Fig. 3 has a phase rotation due to the channel and the output of CMA in Fig. 4 is spinning due to the carrier frequency offset; MCMA corrects phase rotation and frequency offset effectively and VSS-MCMA achieves the phase recovery with the output lying in smaller areas around the points of the transmitted data symbol constellation than those of MCMA.
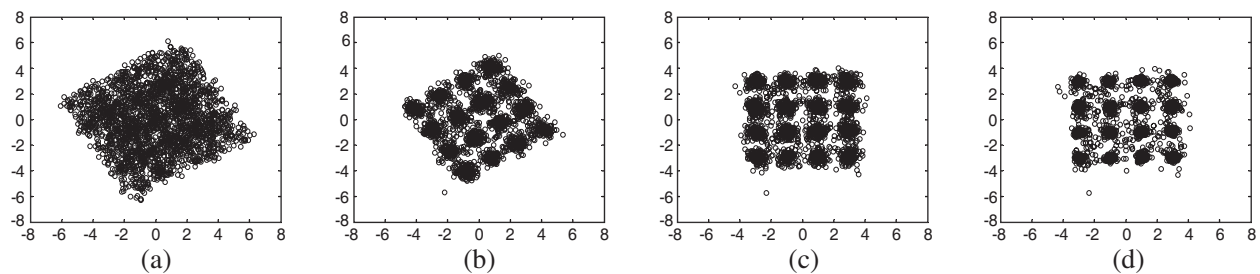


Figure 3: Constellations of 16-QAM signals without a carrier frequency offset. (a) No equalization, (b) CMA, (c) MCMA and (d) VSS-MCMA.
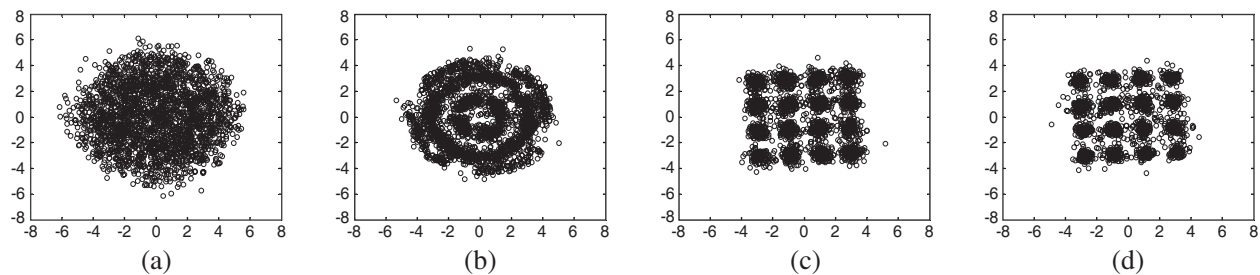


Figure 4: Constellations of 16-QAM signals with a carrier frequency offset. (a) No equalization, (b) CMA, (c) MCMA and (d) VSS-MCMA.
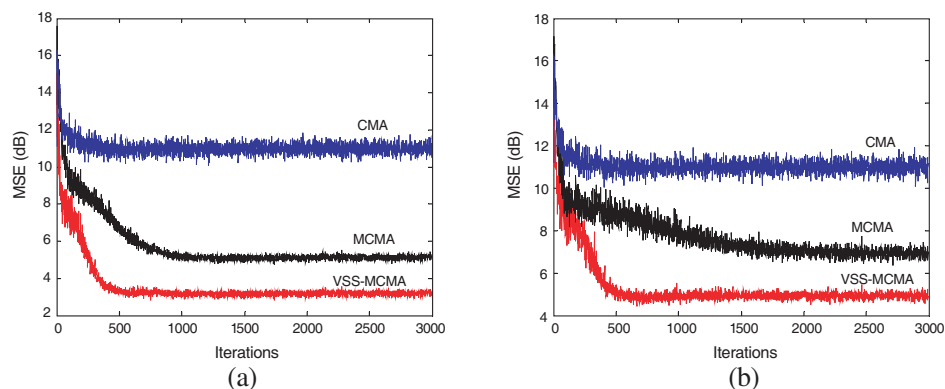


Figure 5: Comparison of MSE for CMA, MCMA and VSS-MCMA. (a) Without a carrier frequency offset and (b) with a carrier frequency offset.

Figure 5 shows the MSE curves that represent the ensemble averaged MSE values over 500 independent runs for the three algorithms. It can be seen that CMA has large steady state MSE due to the phase error; MCMA decreases the steady state MSE greatly but converges slowly in the presence of carrier frequency offset; VSS-MCMA achieves lowest steady state MSE and the fastest convergence rate despite of the carrier frequency offset and has better equalization performance than that of MCMA.

## 6. CONCLUSION

In this paper, a variable step size modified constant modulus algorithm (VSS-MCMA) is proposed. The step size of the algorithm is adjusted according to the region where the received signal lies in the constellation plane. The VSS-MCMA can obtain fast convergence rate, small steady state MSE and the recovery of the phase rotation and frequency offset. The simulation results for 16-QAM signals demonstrate the effectiveness of the VSS-MCMA in the equalization performance enhancement.

### REFERENCES

1. Xiong, F. Q., *Digital Modulation Techniques*, Artech House, London, 2000.
2. Proakis, J. G., *Digital Communications*, 4th Edition, McGraw-Hill, New York, NY, 2001.
3. Godard, D. N., "Self-recovering equalization and carrier tracking in two-dimensional data communication systems," *IEEE Transactions on Communications*, Vol. 28, 1867–1875, 1980.
4. Oh, K. N. and Y. O. Chin, "Modified constant modulus algorithm: Blind equalization and carrier phase recovery algorithm," *1995 IEEE International Conference on Communications*, Vol. 1, 498–502, June 1995.
5. Yang, J., J. J. Werner, and G. Dumont, "The multimodulus blind equalization and its generalized algorithms," *IEEE Journal on Selected Areas in Communications*, Vo1. 20, No. 5, 997–1015, June 2002.
6. Weerackody, V., S. A. Kassam, and K. R. Laker, "A simple hard-limited adaptive algorithm for blind equalization," *IEEE Transactions on Communications*, Vol. 39, No. 7, 482–487, 1992.
7. Thakallapalli, S. R., S. R. Nelatury, and S. S. Rao, "A new error function for fast phase recovery of QAM signals in CMA blind equalizers," *IEEE Workshop on Statistical Signal Processing*, 70–73, 2003.
8. Chen, S., T. B. Cook, and L. C. Anderson, "Blind FIR equalization for high-order QAM signaling," *Proceedings of IEEE ICSP'2*, 2002.
9. Ready, M. J. and R. P. Gooch, "Blind equalization based on radius directed adaptation," *Proceedings of ICASSP'90*, 1699–1702, 1990.
10. Weerackody, V. and S. A. Kassam, "Dual-mode type algorithms for blind equalization," *IEEE Transactions on Communications*, Vol. 42, No. 1, 22–28, 1994.
11. Li, X. L. and X. D. Zhang, "A family of generalized constant modulus algorithms for blind equalization," *IEEE Transactions on Communications*, Vol. 54, No. 11, 1913–1917, 2006.

# Metamaterial Hat

**Soheil Hashemi[1], Ali Mohtadi[1], Ali Abdolali[2], and Homayoon Oraizi[2]**

[1]Department of Electrical and Computer Engineering, Tehran University
Tehran 14395515, Iran
[2]Department of Electrical Engineering, Iran University of Science and Technology
Tehran 1684613114, Iran

**Abstract**— Due to the fact that the electromagnetic fields have an effect on different body organs and their functions and that there should be a specific range for these fields, in this paper the attempt is to decrease the transmission of waves to the interior body organs by means of utilizing an appropriate covering on the body. So the main goal of this paper is acquiring the optimal characteristics of that covering and comparing the conventional materials with Metamaterial.

## 1. INTRODUCTION

Since the time that the idea of Metamaterials has been brought up, numerous utilizations have been found for them. The primary idea of the negative value of permeability and permittivity was put forward by Veslago [1]. A metamaterial is a material that gains its properties from its structure rather than directly from its composition. To distinguish metamaterials from other composite materials, the metamaterial label is usually used for a material that has unusual properties. Such unusual properties could be a negative refractive index or infinite inertia (which are not found in naturally occurring materials). It gains these extraordinary properties from it's negative real part of permeability and permittivity:

$$\begin{cases} \varepsilon_l = \varepsilon_l' - j\varepsilon_l'' \\ \mu_l = \mu_l' - j\mu_l'' \end{cases} \Rightarrow \begin{cases} k_l = \omega\sqrt{\mu_0\varepsilon_0\mu_l\varepsilon_l} = \pm k' \pm jk'' \\ \eta = \sqrt{\dfrac{\mu_0\mu_l}{\varepsilon_0\varepsilon_l}} = \pm\eta' \pm j\eta'' \end{cases}$$

Metamaterials usually consist of periodic structures and its physical accomplishment was first implemented through an array of thin wires (TWs) and split ring resonators (SRRs) [2–4]. Various applications for MTMs has been done. However, here we are concerned with the macroscopic properties of metamaterials, where the values of permittivity and permeability are described by the appropriate Drude, Lorentz and resonance models, Among metamaterial's applications are shielding and reducing radar cross section [5, 6].There are abundant methods for analyzing the transmission of electromagnetic fields in such environment [7–9] .some examples of these exact analytic methods are as followings: recursive method, matrix method, computational electrodynamics modelling techniques and physical optics approximation. Although various numerical and computational methods are available like FDTD, MOM and TLM in this paper we make use of finite difference time domain (FDTD) numerical method, which is an efficient method for computation fields. The FDTF method is described in many references [10, 11].

## 2. PROBLEM DESCRIPTION AND SOLUTION

According to the researches conducted by the world health organization, electromagnetic fields affect the body organs in several ways, which probably the most severe effect concerns the human brain and particularly their impact on Pineal gland which secrets Melatonin.

Therefore, the need is intensely felt to find a solution for abating the harmful effects of electromagnetic fields on the brain. We propose to devise a hat which reduces penetration of waves into the brain to a great extent. Based on what has been posed in the introduction, the properties of novel meta materials, prompted us to think of them as a suitable substance that can be used in the hats in comparison with their old counterparts namely conventional materials.

As a result, for achieving this objective we simulated the human head with a cell phone antenna with and without the hat and examined the situation with FDTD method [10, 11]. We chose the cell phone antenna for this simulation due to the great usage of this device by people. By means of this simulation we computed the fields radiated by the cell phone antenna and penetrating into the brain and attempted to decrease them through optimizing the variables of permeability ($\varepsilon$), permittivity ($\mu$) and conductivity ($\sigma$).

## 3. NUMERICAL COMPUTATION

The structure taken into consideration for this problem is close to reality. As it is shown in Fig. 1, this model consists of human head and a cellphone or the human head with an incident plane wave.

The human head includes an interior part with the following electromagnetic characteristics: ($\varepsilon = 42$, $\mu = 1$, $\sigma = 0.99$ s/m), and an exterior cortex with electromagnetic characteristics: ($\varepsilon = 5 - j0.25$, $\mu = 1$) which are caught from Specific Anthropomorphic Mannequin.

1) As an example a cell phone is consists of a frame and a helix antenna with the following characteristics:

Antenna:
- Length $= 23$ mm
- Number of circles $= 10$
- Radius $= 1$ mm
- Frequency $= 1.1$ GHz
- Power $= 1$ W

Frame:
- Length $= 40$ mm
- Wide $= 18$ mm
- Height $= 10$ mm

2) In the structure being explored in this paper, the incident plane wave is radiated to the head and is calculated with a propagation normal of $(1, -1, 1)$, and electric field vector of $(0.798, 0.548, -0.249)$.

A hat with thickness 6 mm covers this model as shown in Fig. 1.
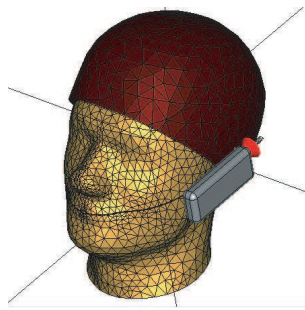


Figure 1: Photo of structure.
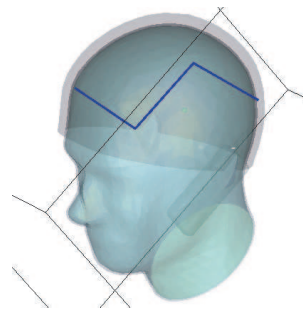


Figure 2: A selected path in the brain for calculation of the field power.
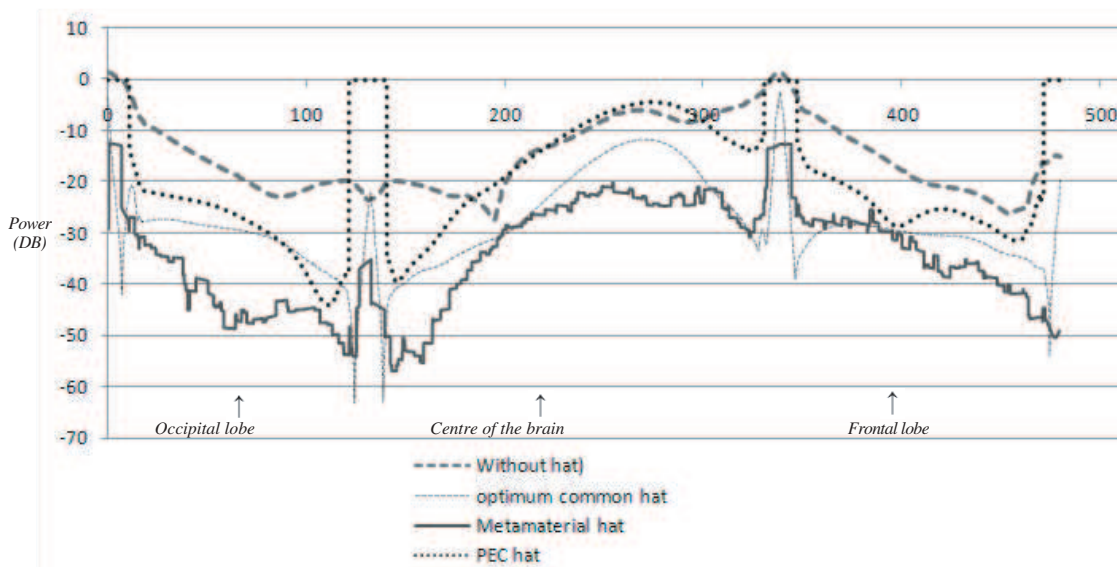


Figure 3: Conventional hat ($\varepsilon = 3$, $\mu = 20$, $\sigma = 5$ s/m), metamaterial hat ($\varepsilon = -1$, $\mu = -30$, $\sigma = 4$ s/m), power of radiation by cellphone antenna in selected path 3.
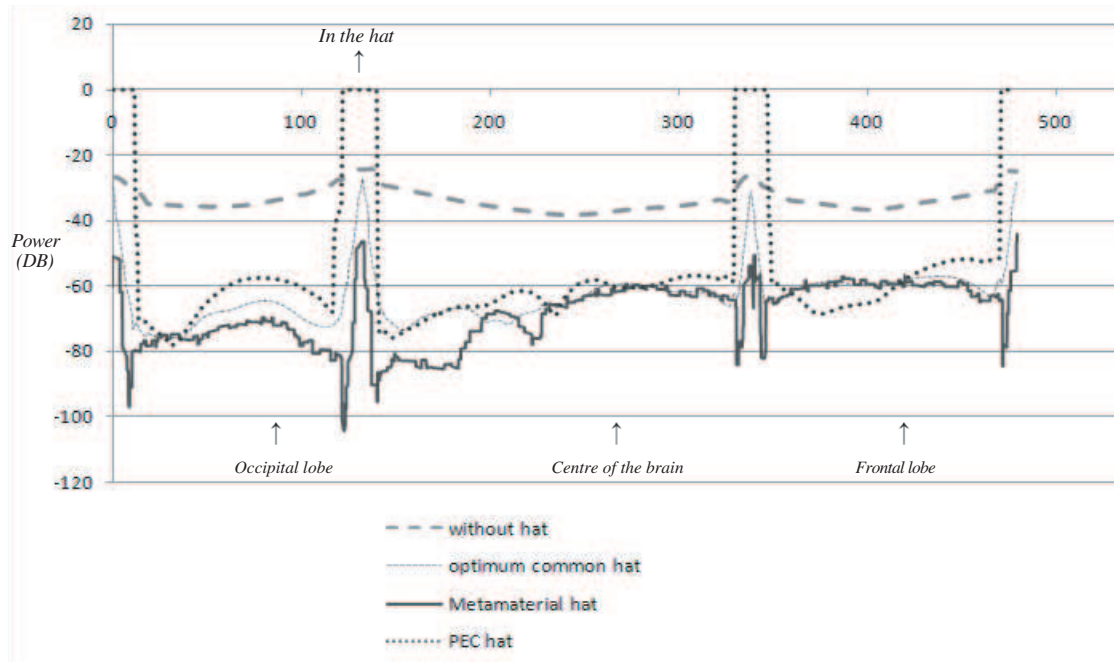
Figure 4: Conventional hat ($\varepsilon = 3$, $\mu = 20$, $\sigma = 5\,\text{s/m}$), metamaterial hat ($\varepsilon = -1$, $\mu = -30$, $\sigma = 4\,\text{s/m}$), transfer power of incident plane wave in selected path.

## 4. RESULT

In the Fig. 3 and Fig. 4, we observe the results in both radiating types, include the cellphone antenna and the incident plane wave as shown in Fig. 1. The fields computations are shown in the frontal lobe, occipital lobe, and the centre of the brain. The curves in Fig. 3 and Fig. 4 compare the electromagnetic power in different states of a head:

Without a hat, with a pec hat, with an optimized common material hat, and an optimum Metamaterial hat.

## 5. CONCLUSION

Recently numerous utilizations have been found for metamaterials. We have optimized magnitude of permeability ($\varepsilon$), permittivity ($\mu$) and conductivity ($\sigma$) to reduce penetration of waves into the brain to a great extent in practical frequencies. After the optimization and comparison of the hat in three states of being made from Metamaterials, common materials, and PEC we come to this conclusion that the optimization of the conventional material made hat cease to improve when it gets to $\mu/\varepsilon \approx 6$ and specially when $\varepsilon \approx 3$ and $\mu \approx 20$. However, the optimization of the Metamaterial made hat not only bears better results, but also improves by increasing the absolute value of $\mu$ when both permeability ($\varepsilon$), permittivity ($\mu$) are negative. predominancy of Metamaterials indicates potential usage of this material in antipenetration material. Besides, the optimum value for $\sigma$ of hat in both cases is about 5 s/m.

**REFERENCES**

1. Veselago, V. G., "The electrodynamics of substances with simultaneously negative values of $\varepsilon$ and $\mu$," *Soviet Physics Uspekhi*, Vol. 10, No. 4, 509–514, Jan.-Feb. 1968.
2. Smith, D. R., S. C. Nemat-Nasser, and S. Schultz, "Microwave transmission through a two-dimensional, isotropic, left-handed metamaterial," *Appl. Phys. Lett.*, Vol. 78, No. 4, 489–491, 2001.
3. Marques, R., F. Martin, and M. Sorolla, *Metamaterials with Negative Parameters Theory, Design, and Microwave Applications*, 1st Edition, Wiley, 2008,
4. Ziolkowski, R. W. and E. Heyman, "Wave propagation in media having negative permittivity and permeability," *Phys. Rev. E, Stat. Phys. Plasmas Fluids Relat.*, Vol. 64, No. 5, 056 625, 2001.

5. Oraizi, H. and A. Abdolali, "Mathematical formulation for zero reflection from multilayer metamaterial structures and their notable applications," *IET Microwaves, Antennas & Propagation Journal*, Vol. 3, No. 6, 987–996, Sep. 2009.

6. Oraizi, H. and A. Abdolali, "Ultra wide band RCS optimization of multilayerd cylindrical structures for arbitrarily polarized incident plane waves," *Progress In Electromagnetics Research*, PIER 78, 129–157, 2008.

7. Kong, J. A., "Electromagnetic wave interaction with stratified negative isotropic media," *Progress In Electromagnetics Research*, PIER 35, 1–52, 2002.

8. Oraizi, H. and A. Abdolali, "Design and optimization of planar multilayer antireflection metamaterial coatings at Ku band under circularly polarized oblique plane wave incidence," *Progress In Electromagnetics Research C*, Vol. 3, 1–18, 2008.

9. Cory, H. and C. Zach, "Wave Propagation in Metamaterial Multilayered Structures," *Microwave and Optical Technology Letters*, Vol. 40, No. 6, 460–465, Mar. 2004.

10. Wang, M. Y., J. Xu, J. Wu, B. Wei, H.-L. Li, T. Xu, and D.-B. Ge, "FDTD study on wave propagation in layered structures with biaxial anisotropic metamaterials," *Progress In Electromagnetics Research*, PIER 81, 253–265, 2008.

11. Sevgi, L. and S. Paker, "FDTD based RCS calculations and antenna simulation," *AEU, International J. of Electronics*, Vol. 52, No. 2, 65–75, 1986.

# The Influence of Electric Field on Magnetic Vortices in Confined Magnetic Structures

**A. P. Pyatakov[1, 2] and G. A. Meshkov[1]**

[1]Physics Department, M. V. Lomonosov Moscow State University, Russia
[2]A. M. Prokhorov General Physics Institute, Russian Academy of Science, Russia

**Abstract**— The existence of inhomogeneous magnetoelectric interaction in magnetic dielectrics provides with the possibility to stabilize by gradient electric field the vortex or antivortex state in magnetic nanoparticle. This system can be considered as electrically switchable 2-state logic magnetic element.

## 1. INTRODUCTION

Nowadays the magnetic dots that stabilize the magnetic vortex state are considered as promising elements of recording media and microwave signal-processing devices [1, 2]. The control of vortices characteristics such as chirality, polarity or winding number (the topological charge) remains a challenging problem. Several means of magnetic vortex state control such as remagnetizing with pulses of magnetic field [3–5] or spin currents [6] have been proposed. However all this techniques imply high current density and, as a consequence, the energy loses.

The alternative way of magnetic state switching based on the electric field induced micromagnetic structure transformation in magnetoelectric media was recently demonstrated in the series of work [7–11]. There is an additional interaction that should be taken into account when we consider micromagnetic structure under influence of electric field or the structures in magnetic ferroelectrics (multiferroics). It is proportional to spatial derivatives of magnetic order parameter vector $P_i M_j \nabla_k M_n$, where $\nabla$ is differential operator, and $P$, $M$ are electric and magnetic order parameters, respectively. This type of interaction is responsible for electric field driven magnetic domain wall motion in ferrimagnetic iron garnet films [11], local junction of electric and magnetic properties in the Tellegen particles of magnetoelectric metamaterial [12], and magnetically induced electric polarization in spiral multiferroics [13].

In this report, we will show that the gradient electric field produced by point electrode (e.g., cantilever tip of atomic force microscope) can stabilize in magnetic dielectric nanoparticle either vortex or antivortex state depending on the electric polarity of the tip.

## 2. THE KEY INTERACTIONS IN MAGNETIC DIELECTRIC NANOPARTICLES

Magnetoelectric materials, mostly being ferrimagnets or weak ferromagnets, have rather moderate value of spontaneous magnetization. This results in large exchange length $l_{exch} = \sqrt{2A/M_s^2}$, where $A$ is the exchange stiffness, $M_S$ is saturation magnetization, and large magnetostatic lengths $l_{MS} = 2\sqrt{AK}/M_s^2$ (the maximum size of single domain particle, where $K$ is anisotropy constant) compared to conventional ferromagnets. The typical values for room temperature magnetoelectric iron garnet films are: $l_{exch} = 0.5\,\mu m$, $l_{MS} = 5\,\mu m$ and room temperature multiferroic bismuth ferrite: $l_{exch} = 1.5\,\mu m$, $l_{MS} = 240\,\mu m$. Thus the magnetic dielectric particles of nanometric size should be in homogeneous magnetic state since exchange interaction is the predominant one.

The only thing that can compete against the exchange interaction in magnetic dielectrics on this nanometer scale is the spin flexoelectricity that for isotropic media can be represented in the form [14, 15]:

$$F_{ME} = \gamma \cdot \vec{P} \cdot (\vec{m} \cdot (\nabla \cdot \vec{m}) - (\vec{m} \cdot \nabla)\,\vec{m}) \tag{1}$$

where $\gamma$ is magnetoelectric constant, $\vec{P}$ is electric polarization, $\vec{m}$ is unit vector of magnetic order parameter.

## 3. THE CRITICAL VOLTAGE OF VORTEX/ANTIVORTEX NUCLEATION

Let us consider the magnetic vortex with the magnetization distribution in the area distant from the vortex core that can be represented in the simple form:

$$M = M\left[\vec{n} \times \frac{\vec{r}}{r}\right] \tag{2}$$

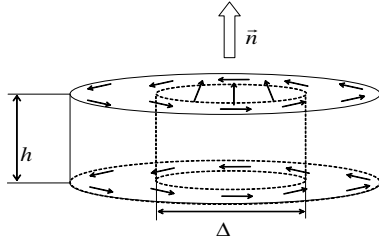(a)                                     (b)

Figure 1: The magnetization distribution of the magnetic particle in vortex state. The dashed line shows the vortex core region.
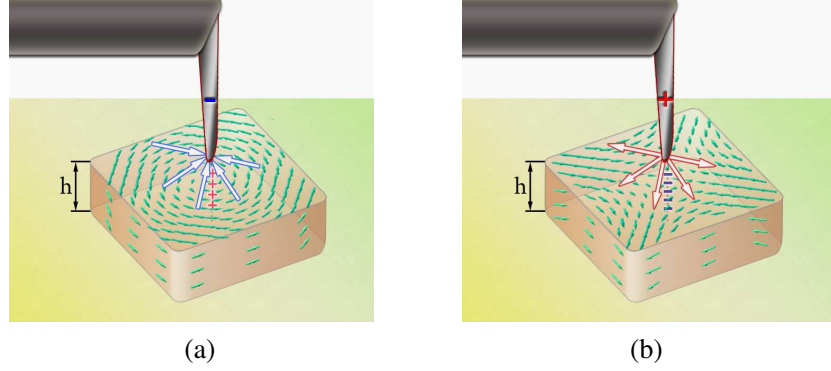
Figure 2: Magnetic dielectric nanoparticle subjected to the electric field from the cantilever tip (the electric polarity depends on the sign of magnetoelectric constant in (1). (a) Electrically induced magnetic vortex state, (b) electrically induced magnetic antivortex state.

where $\vec{n}$ is the normal to the plane of magnetic vortex, $\vec{r}$ is radius vector (Fig. 1).

Due to the inhomogeneous magnetoelectric interaction (1) the micromagnetic distribution in the vortex is associated with the radial distribution of electric polarization [15, 16]. This polarization distribution corresponds to the electric charge that can be found as an integral over the surface of the cylinder wrapping the vortex core (shown with dashed line in Fig. 1):

$$Q = \int_V -\mathrm{div}\, P dV = -\oint_S P dS = \pm 2\pi\gamma\chi_e h \qquad (3)$$

where $\chi_e$ is electric susceptibility of the medium, $h$ is the height of the particle, the signs "$\pm$" correspond to the vortex and antivortex state, respectively.

The magnetoelectric energy thus can be represented in the form of electrostatic energy of the charge (3) in the electric potential $\varphi$ of the point electrode:

$$W_{ME} = q\varphi = 2\pi\gamma \cdot h \cdot \varphi, \qquad (4)$$

where $q$ is the integral charge, $h$ is the height of the particle.

The exchange energy can be estimated as

$$W_{Exch} = A\left(\frac{2\pi}{\Delta}\right)^2 h\Delta^2 = A\left(2\pi\right)^2 h, \qquad (5)$$

where $\Delta$ is the size of the vortex core (Fig. 1).

The electric field can stabilize the vortex state for one sign of the charge and antivortex state for another (see Fig. 2) when the condition of the phase transition into the vortex state is fulfilled:

$$W_{Exch} + W_{ME} < 0, \qquad (6)$$

Thus the critical potential of the electrode tip in which the nucleation of the vortex (antivortex) occurs can be found from (6):

$$|\varphi_C| = \frac{2\pi A}{\gamma} \qquad (7)$$

For $\gamma \sim 10^{-6}$ (typical values for BiFeO$_3$ and iron garnet) it gives us $\varphi_c = \pm 150\,\mathrm{V}$ for $A \sim 10^{-7}\,\mathrm{erg/cm}$ (exchange stiffness typical for room temperature magnets). Although this voltage is too high to be considered in magnetic electronics applications the application multiferroic materials with larger values of parameter $\gamma$ is possible.

## 4. CONCLUSIONS

We have shown that the electric field can stabilize the vortex state for one sign of the electric charge of the electrode and antivortex state for another. This possibility besides fundamental interest can be considered as a prototypical example of electrically switchable magnetic system with two logic states. The use of ferroelectric media as a material of the tip electrode will make it possible to implement the memory cell based on this principle.

**REFERENCES**

1. Pribiag, V. S., I. N. Krivorotov, G. D. Fuchs, et al., *Nature Physics*, Vol. 3, 498–503, 2007.
2. Guslienko, K. Y., *J. Nanosc. Nanotechn.*, Vol. 8, 2745–2760, 2008.
3. Van Waeyenberge, B., et al., *Nature (London)*, Vol. 444, 461, 2006.
4. Tanase, M., A. K. Petford-Long, O. Heinonen, et al., *Phys. Rev. B*, Vol. 79, 014436, 2009.
5. Prosandeev, S., I. Ponomareva, I. Kornev, and L. Bellaiche, *Phys. Rev. Lett.*, Vol. 100, 047201, 2008.
6. Yamada, K., et al., *Nat. Mater.*, Vol. 6, 269, 2007.
7. Chu, Y.-H., L. W. Martin, M. B. Holcomb, et al., *Nat. Mater.*, Vol. 7, 478, 2008.
8. Zavaliche, F., H. Zheng, L. Mohaddes-Ardabili, et al., *Nano Lett.*, Vol. 5, 1793, 2005.
9. Chung, T. K., G. P. Carman, and K. P. Mohanchandra, *Appl. Phys. Lett.*, Vol. 92, 112509, 2008.
10. Palkar, V. R. and K. Prashanthi, *Appl. Phys. Lett.*, Vol. 93, 132906, 2008.
11. Logginov, A. S., G. A. Meshkov, A. V. Nikolaev, et al., *Appl. Phys. Lett.*, Vol. 93, 182510, 2008.
12. Kamenetskii, E. O., M. Sigalov, and R. Shavit, *J. Appl. Phys.*, Vol. 105, 013537, 2009.
13. Cheong, S.-W. and M. Mostovoy, *Nat. Mater.*, Vol. 6, 13, 2007.
14. Sparavigna, A., A. Strigazzi, and A. Zvezdin, *Phys. Rev. B*, Vol. 50, 2953, 1994.
15. Mostovoy, M., *Phys. Rev. Lett.*, Vol. 96, 067601, 2006.
16. Delaney, K. T., M. Mostovoy, and N. A. Spaldin, "Superexchange-driven magnetoelectricity in magnetic vortices," *Phys. Rev. Lett.*, Vol. 102, 157203, 2009.

# A Novel and Reliable Method for Bandwidth Expansion in Microstrip Array Antenna

**Mohsen Fallah**, **F. H. Kashani**, and **S. H. Mohseni**

Department of Electrical Engineering, Iran University of Science and Technology (IUST), Tehran, Iran

**Abstract**— In this paper a new and simple method for increasing the bandwidth of microstrip array antenna is presented. In this method, which we may call it low match method, all elements of array antenna are matched in a frequency band very closed to the resonant frequency of each elements of antenna. This method is implemented in an array of $8 \times 8$ elements and an increased bandwidth of 4% in the frequency rang of 10.2–10.6 GHz with 23.42 dBi Gain, and 58% efficiency is obtained. There is a good agreement between the simulation and the experimental results.

## 1. INTRODUCTION

Over the past many years, microstrip patch antennas have been investigated extensively because of its low profile, light weight, and low cost in fabrication. These low profile antennas are useful in aircraft, satellite and missile applications, where size, weight, cost, performance, ease of installation, and aerodynamic profile are strict constraints. Microstrip array antenna used in array configuration to synthesize a required pattern that cannot be achieved with a single element. In addition, they are used to scan the beam of antenna in an antenna system, increase the directivity, and perform various other functions which would be difficult with any one single element. The elements can be fed by a single line or by multiple lines in a feed network arrangement. The first is referred to as a series-feed network while the second is referred to as a corporate-feed network. In this paper the uniform corporate-feed network is worked.

Microstrip array are limited from disadvantages such as low efficiency, low power, and low polarization purity, spurious feed radiation and very narrow bandwidth [1–4]. There has been considerable effort from researchers toward increasing its bandwidth. A conventional way to increase the bandwidth is to either increase the height of the dielectric or decrease the dielectric constant. However, the first approach would make it unsuitable for low profile structures and increase unwanted surface wave which result strong mutual coupling between array elements, while the later approach make matching circuit to the patch difficult. For microstrip antenna, the dielectric constants are usually in the range of $2.2 \leq \varepsilon_r \leq 12$. Dielectric constants in the lower end of the range can give us better efficiency and better bandwidth, but at the expense of a large element size. High dielectric constants have greater losses so they are less efficient and have relatively small bandwidth. In this work the Aleron Cuclad (Gtx) dielectric with $\varepsilon_r = 2.33$ with height $h = 1.588$ mm is used.

## 2. MICROSTRIP ARRAY ANTENNA WITH CORPORATED FEED NETWORK

The corporate-feed network is used to provide power splits of $2^n$ ($n = 2, 4, 8, 16, 32, \ldots$) [2]. This feed line network is realized by using tapered lines or quarter wavelength impedance transformers. In this method, the designer has more control on phase and amplitude of each element and it is ideal for scanning phased arrays, multi-beam arrays, or shaped-beam arrays [2–4]. The radiated $E$-field formula for single element patch can be given as [4]:

$$E = jk_0 W V_0 e^{-jkr} \Big/ \pi r \left\{ \sin\left(\frac{k_0 h}{2}\cos\phi\right) \Big/ \frac{k_0 h}{2}\cos\phi \right\} \cos\left(\frac{k_0 L_e}{2}\cos\phi\right) \tag{1}$$

where $W$ is the width of patch antenna, $L_e$ is the extended length, $V_0 = hE_0$ is voltage across radiating slot, $h$ is substrate height, $K_0 = {2\pi}/{\lambda}$ and $r$ is the far field distance from the antenna. Also the array factor can be written as [4]:

$$FA = \sin^2(N\pi(d_x/\lambda)\sin\theta)/N^2 \sin^2(\pi(d_x/\lambda)\sin\theta) \tag{2}$$

where $N$ is the number of elements and $d_x$ is spacing between them.

With combining element pattern and array factor, we obtain the normalized radiation pattern. Our fabricated antenna has dielectric permittivity of $\varepsilon_r = 2.33$, height of 1.58 mm, and resonance frequency of 10.4 GHz. Measured return loss shown return loss less than $-10$ dB in frequency

rang from 10.2 GHz to 10.6 GHz (4% bandwidth). Because of uniform distribution of amplitude in all elements, we predicate $-13$ dB sidelobe levels, more over, the measured result validate this prediction. Measured radiation efficiency is also 23.42 dBi. Fig. 1 shows fabricated antenna and Fig. 2 shows measured return loss.

Figure 3 is shown simulated $E$ and $H$-planes patterns of antenna and Figs. 4 and 5 are shown the $E$-plane and $H$-plane patterns, respectively.
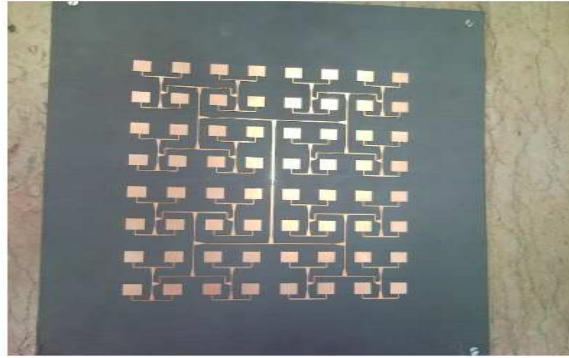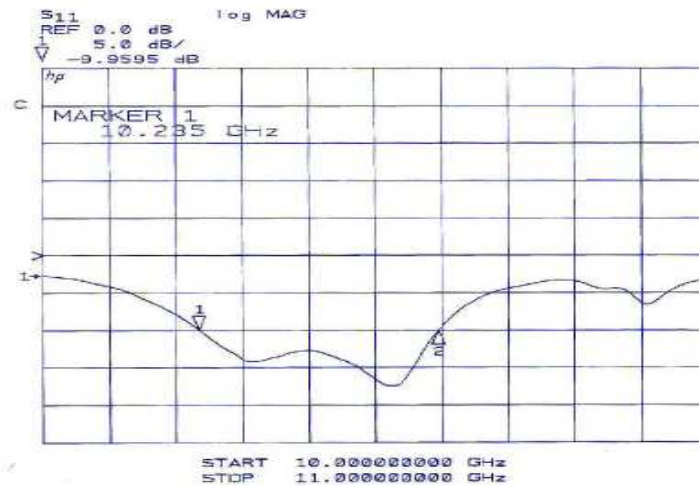


Figure 1: Fabricated antenna.



Figure 2: Measured return loss of antenna.
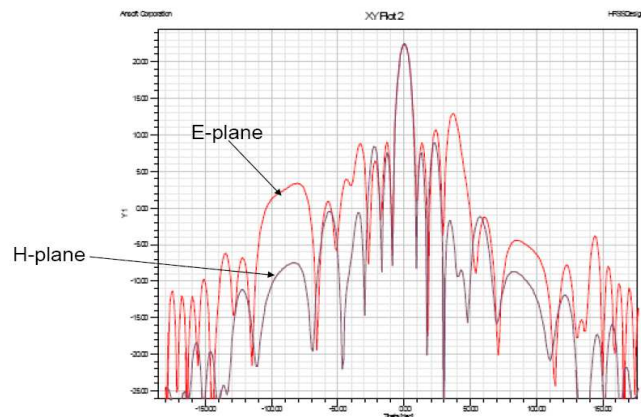


Figure 3: Simulated pattern of $E$ and $H$-plane patterns of antenna.

## 3. DESIGN PROCEDURE

The aim of this work is to design and fabricate a microstrip antenna array with these parameters: Bandwidth: 10.2 GHz–10.6 GHz (4% bandwidth), gain grater than 23 dBi, radiation efficiency grater than 50%. Our dielectric is Aleron CuClad GTx 233 with permittivity 2.33 and height 1.58 mm with loss tangent 0.01. Simulation results shows that we need at least 64 elements to achieve this gain. But achieving this bandwidth using conventional methods is not possible. For achieving this bandwidth, we divide array to four 16 elements cluster, each cluster with 4 × 4 elements. One cluster matches at 10.2 GHz, the second at 10.3 GHz, the third at 10.5 GHz, and the last at 10.6 GHz. But, all elements are designed such that they resonate at 10.4 GHz. Using this novel, and simple method we have achieved required bandwidth with adequate radiation efficiency. For reducing adverse effects of feed lines discontinuities, we have used tapered lines and tapered bends.
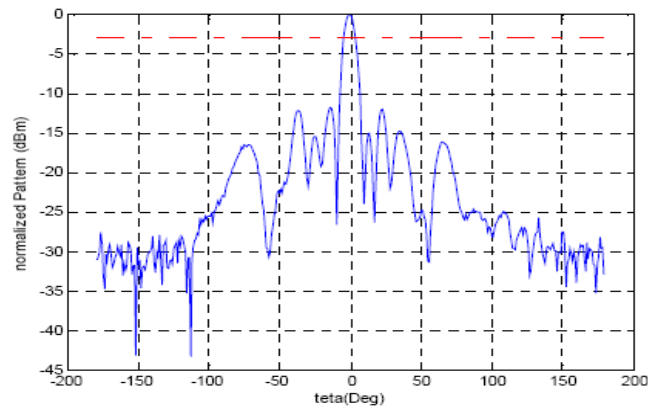


(a) measured *E*-plane pattern
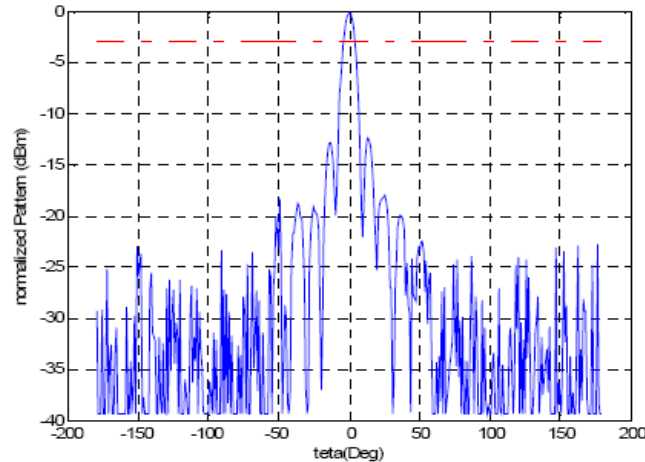


(b) measured *H*-plane pattern

Figure 4: Measured pattern of (a) *E*-plane, and (b) *H*-plane.

## 4. CONCLUSION

In this paper, a novel and reliable method for bandwidth enhancement in microstrip patch antenna is presented. In this method, bandwidth of an array antenna expands to 4%. This work is used matching of the array antenna elements near the resonating frequency.

### REFERENCES

1. Mailloux, R. J., F. Mcllvenna, and N. P. Kernweis, "Microstrip array technology," *IEEE Trans. Antenna Propagation*, Vol. 29, No. 1, January 1981.
2. Alam, M. M., M. M. R. Sonchoy, and M. O. Goni, "Design and performance analysis of microstrip array antenna," *PIERS Proceedings*, 1837–1842, Moscow, Russia, August 18–21, 2009.

3. Garg, R., P. Baharati, I. Bahl, and A. Ittipiboon, *Microstrip Antenna Design Handbook*, Artech House, Inc, 2001.
4. Balanis, C. A., *Antenna Engineering*, 2nd Edition, Wielly.
5. Visser, H. J., *Array and Phased Array Antenna Basics*, John Wiely & Sons, Ltd., 2005.

# A Highly Efficient Doherty Power Amplifier with Impedance Transform

**Guorui Yang, Quanyuan Feng, and Wen Pan**

Institute of Microelectronics, Southwest Jiaotong University, ChengDu 610031, China

**Abstract**— This paper analyses the efficiency influence factors for the Doherty amplifier output network with finite device output impedance. It presents an impedance transform method which changes the proportion of impedance to enhance efficiency, and reduces the load impedance of Doherty from $25\,\Omega$ to $12.5\,\Omega$ for decrease loss. So an enhanced Doherty amplifier is implemented at $2.14\,\text{GHz}$ using freescale devices. It achieves a linear power gain of $14.4\,\text{dB}$ with 1-dB output compression at $53.6\,\text{dBm}$ while PAE is $58.4\%$, and the PAE is $39.5\%$ at $46\,\text{dBm}$ which is improved about $5.2\%$ comparison with the classical structure.

## 1. INTRODUCTION

In modern wireless communication system, power amplifier is the import module of transmit, it transforms DC power into RF power, and supplies the antenna with RF signal, So the Amplifier is the most power consume cell of the communication system. At the same time, it requires that the RF signals should be amplified with no distortion for better communication quality. So enhance efficiency and satisfy the linearity requirements are critical for the power amplifier. In recent years, several PA performance enhancement techniques including Kahn envelope elimination and restoration (EER), envelop tracking (ET), linear amplification using nonlinear component (LINC), and Doherty techniques and so on [1, 2] are being actively reported. In those techniques, the Doherty amplifier is the most promising choice with simple structure and high efficiency, as Fig. 1 shows.

The Doherty technique was developed in the 1930s by W. H. Doherty [3], and the basic operation principles has been well described in [4, 5]. The classical Doherty amplifier consists of two cell with the main amplifier cell and the auxiliary amplifier cell. The clou is enhances efficiency by load modulate. At low output power levels, the main amplifier cell operates as a linear current source and the auxiliary amplifier is cut off, and at high output power, the main amplifier cell acts as a invariable voltage source, and the auxiliary amplifier operates as a linear current source. Each cell load's impedance changes with its output current, and insures the high efficiency of amplifier keep a wide power range, as Fig. 2 shows.

For realizes the main cell operate and the auxiliary cell cut off at low power levels, the main amplifier is biased at class AB or class B mode, and the auxiliary amplifier is biased at class C mode. However, each amplifier cell is the source with infinite device output impedance in fact, the output current of each cell will mutual feed-in and lead the terminal load current decrease, the output power loss and the efficiency fall. For solves this problem, one advanced method is apply the uneven power drive structure to improve the linearity and enhance the efficiency at suitable
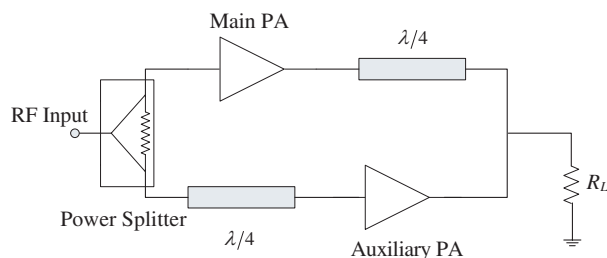


Figure 1: Schematic diagram of the classical Doherty amplifier.
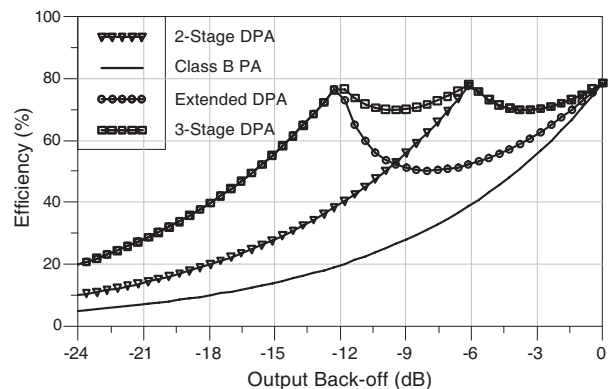


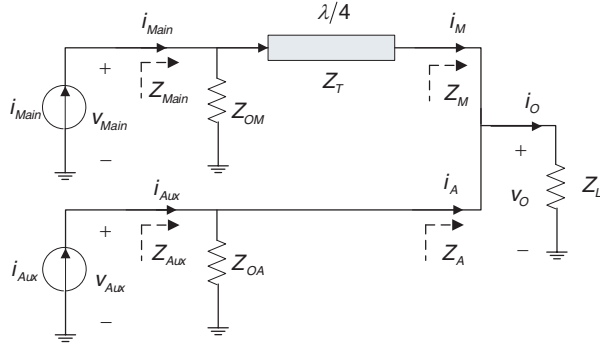Figure 2: Efficiency of the multiple Doherty PA using ideal class B power amplifier.

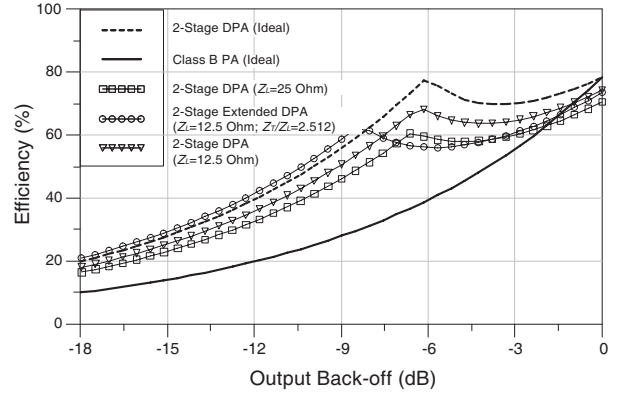Figure 3: Doherty output network with finite device output impedance.



Figure 4: Efficiency of the multiple Doherty PA with finite device output impedance.

proportion [6]. Other is apply the extended structure to choose a suitable proportion of current at peak power levels and enhance efficiency [7]. This paper analyses the operation principles of Doherty PA output network with infinite device output impedance, and attempt to enhance the efficiency by impedance transform.

## 2. ANALYSIS OF DOHERTY STRUCTURE WITH FINITE DEVICE OUTPUT IMPEDANCE

The Doherty output network with finite device output impedance as Fig. 3 shows. $i_{\mathrm{Main}}$ and $i_{\mathrm{Aux}}$ are the mean output current of the main cell and the auxiliary cell, which is controlled by the input port of each cell, respectively. $Z_{OM}$ and $Z_{OA}$ are the finite device output impedance, $Z_L$ is the load impedance, and $Z_T$ is the quarter-wave microstrip characteristic impedance. Moreover, assume that the microstrip is lossless and the main cell and the auxiliary cell are using ideal Class B power amplifiers.

Base the superposition principle, the current source $i_{\mathrm{Main}}$ and $i_{\mathrm{Aux}}$ independently operates, $i_O^m$ and $i_O^a$ are the current of each cell feed-in the load terminal, respectively. So $i_O$ adds up to:

$$i_O = i_O^m + i_O^a = \frac{i_{\mathrm{Main}} \cdot Z_T + \dfrac{i_{\mathrm{Aux}} \cdot Z_T^2}{Z_{OM}}}{Z_L + \dfrac{Z_T^2}{Z_{OM}} + \dfrac{Z_T^2 \cdot Z_L}{Z_{OM} \cdot Z_{OA}}} \xrightarrow[Z_{OA} \to \infty]{Z_{OM} \to \infty} \frac{i_{\mathrm{Main}} \cdot Z_T}{Z_L} = i_M + i_A \qquad (1)$$

the load current $i_O$ is decreased on account of the finite impedance $Z_{OM}$ and $Z_{OA}$, Thereby more output power loss and the efficient fall. The efficiency of the Doherty amplifier is calculated by:

$$\eta = \begin{cases} \dfrac{\pi}{2} \cdot \dfrac{1}{\dfrac{Z_L}{Z_T} + \dfrac{Z_T}{Z_{OM}} + \dfrac{Z_T \cdot Z_L}{Z_{OM} \cdot Z_{OA}}} \cdot \dfrac{v_O}{VDD} \cdot 100\% & \left( 0 \le v_O \le \dfrac{VDD}{\dfrac{Z_T}{Z_L} \cdot \left(1 + \dfrac{Z_L}{Z_{OA}}\right)} \right) \\[4ex] \dfrac{2}{\pi} \cdot \dfrac{1}{v_O \cdot \left(1 + \dfrac{Z_L}{Z_{OA}} + \dfrac{Z_L}{Z_T}\right) + VDD \cdot \left(\dfrac{Z_L}{Z_{OM}} - \dfrac{Z_L}{Z_T}\right)} \cdot \dfrac{v_O^2}{VDD} \cdot 100\% & \left( \dfrac{VDD}{\dfrac{Z_T}{Z_L} \cdot \left(1 + \dfrac{Z_L}{Z_{OA}}\right)} \le v_O \le VDD \right) \end{cases} \qquad (2)$$

In (2), $\eta$ is the drain efficiency, $VDD$ is the drain DC voltage, and $v_O$ is the mean voltage of load terminal in Fig. 3. From (2), the power back-off point is equated with the milestone of $v_O$ which can being express:

$$v_O = \frac{VDD}{\dfrac{Z_T}{Z_L} \cdot \left(1 + \dfrac{Z_L}{Z_{OA}}\right)} \qquad (3)$$

So the power back-off point has relationship with the value of $Z_T/Z_L$ when premise $Z_{OA}$ is infinite. When the proportion become bigger, the main cell is saturated early and the auxiliary cell

Table 1: Relationship of $Z_T/Z_L$ to power back-off point.

| Power Back-off Point | 3 dB | 4 dB | 5 dB | 6 dB | 7 dB | 8 dB | 9 dB | 10 dB | 11 dB | 12 dB |
|---|---|---|---|---|---|---|---|---|---|---|
| $Z_L/Z_T$ | 0.708 | 0.603 | 0.562 | 0.501 | 0.447 | 0.398 | 0.355 | 0.316 | 0.282 | 0.251 |
| $Z_T/Z_L$ | 1.413 | 1.585 | 1.778 | 1.995 | 2.239 | 2.512 | 2.818 | 3.162 | 3.548 | 3.981 |

feed more current in the load terminal, the extended power range of high efficiency become wide. The relationship of $Z_T/Z_L$ to power back-off point as the Table 1 shows.

At the same time, the drain efficiency reduces in all power range because of the finite impedance $Z_{OM}$ and $Z_{OA}$ in (2). If play down the load impedance $Z_L$ when $Z_T/Z_L$ is ensured, the load current $i_O$ will increase and more power feed-in the terminal, and the efficiency is improved. Fig. 4 indicates the efficiency of the Doherty amplifier with finite device output impedance which can enhances efficiency by transform impedance properly.

## 3. AMPLIFIER IMPLEMENTATION AND RESULTS

To validate anterior analysis, a 2.14 GHz Doherty power amplifier using Freescale MRF6S21140H devices with impedance transform is implemented. Fig. 5 shows the measured power-added efficiency (PAE) of an extended Doherty amplifier with different $Z_T/Z_L$, the efficiency is enhanced in low power level with the proportion rise, but its linearity decline in high power level of because of impedance mismatching. Fig. 6 shows the measured PAE of an extended Doherty amplifier with different load impedance ($Z_L = 12.5\,\Omega$, $25\,\Omega$) for an single-tone signal, the PAE with lower load impedance is improved by 1.0% at output power of 46 dBm (40 W).
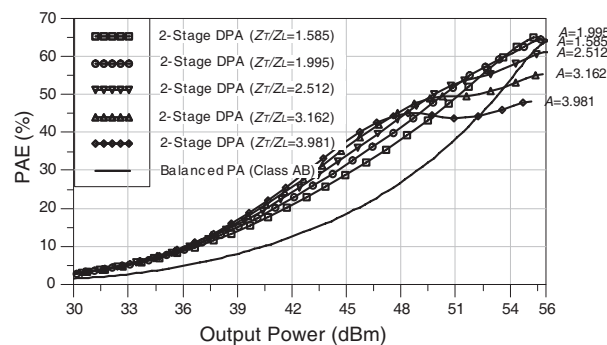


Figure 5: Efficiency of the Doherty amplifier with different proportion of $Z_L$ to $Z_T$.
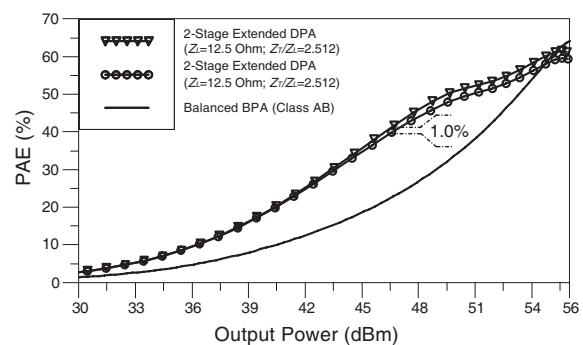
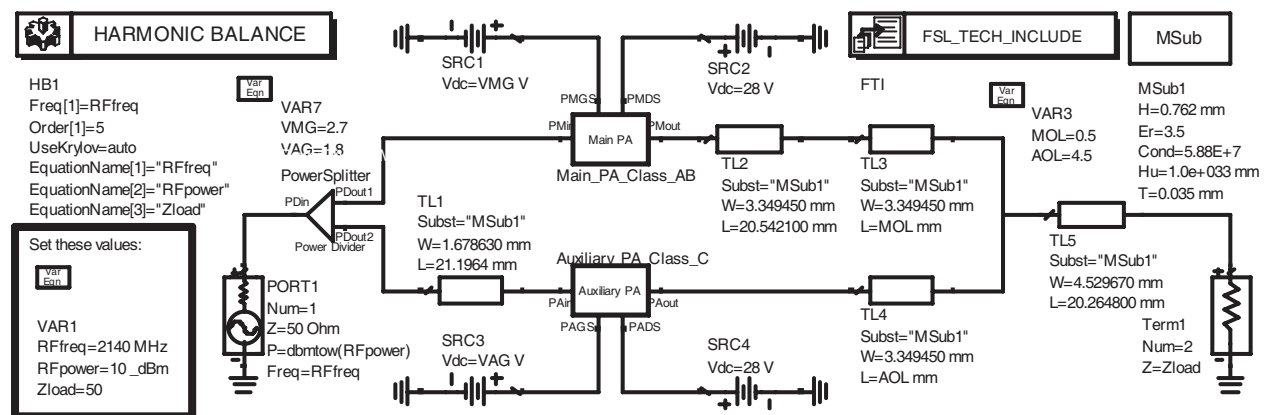Figure 6: Efficiency of the extended Doherty amplifier with different load impedance.



Figure 7: Schematic diagram of the highly efficiency Doherty power amplifier with impedance transform.

Form the foregoing simulate results, an enhanced Doherty power amplifier with $Z_L = 12.5\,\Omega$ and $Z_T/Z_L = 2.512$ is designed with Freescale MRF6S21140H devices and the Taconic RF-35 laminates ($\varepsilon_r \sim 3.5$, $0.030''$) for high efficiency, as Fig. 7 shows. The input signal is divided equally
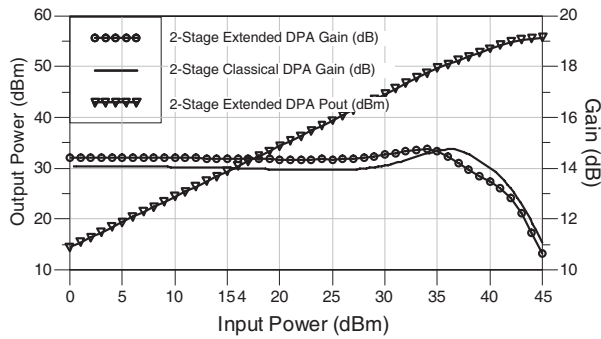
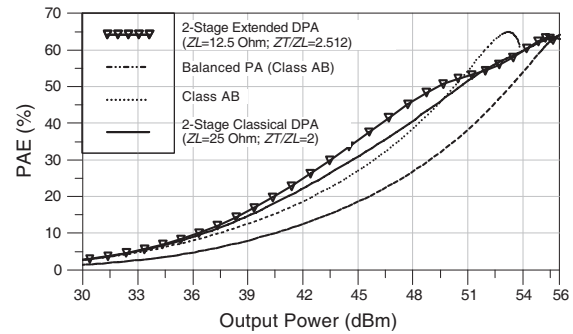Figure 8: Output power and gain of the enhanced Doherty power amplifier.

Figure 9: PAE of the enhanced DPA and the classical DPA.

by a microstrip Wilkinson power divider cell before feeding to the input matching network. The main amplifier is biased at Class AB ($VGS_{\text{Main}} = 2.7\,\text{V}$) and the auxiliary amplifier is biased at Class C ($VGS_{\text{Aux}} = 1.8\,\text{V}$), both drain voltage are set to $VDD = 28\,\text{V}$. At the same time, two cell are further optimized to achieve high efficiency and power, which source impedance and load impedance are matching to $50\,\Omega$ and $25\,\Omega$, respectively. The impedance transformation from the terminal load ($Z_{Load} = 50\,\Omega$) to $Z_L = 12.5\,\Omega$ is done using a quarter-wave microstrip line TL5 ($Z_0 = 25\,\Omega$) and the quarter-wave transformation from $Z_L$ to the output of the main cell is done using microstrip TL2 ($Z_0 = 2.512 \cdot Z_L = 31.4\,\Omega$), the microstrip TL3 and TL4 are the offset lines for reduce the mutual feed-in current. The design is tested with a single-tone signal at $2.14\,\text{GHz}$, the results as Figs. 8 and 9 shows.

Figure 8 depicts the gain and the output power of the enhanced Doherty amplifier, it achieves a linear power gain of $14.4\,\text{dB}$ with 1-dB output compression at $53.6\,\text{dBm}$, the gain is improved by $0.4\,\text{dB}$ comparison with classical DPA. Fig. 9 depicts the measured PAE of the enhanced DPA and the classical DPA, the PAE of the enhanced Doherty amplifier with impedance transformation is measured to be $58.4\%$ at 1-dB compression point, and $39.5\%$ at $8\,\text{dB}$ back-off which output power achieves $46\,\text{dBm}$. In comparison with the 2-stage classical DPA ($Z_L = 25\,\Omega$, $Z_T/Z_L = 2$) and the balanced PA (Class AB), the measured PAE is improved about $5.2\%$ and $18.4\%$ with the output power $46\,\text{dBm}$. Though the linearity of the enhanced Doherty amplifier deteriorated because the class C cell feed-in more power at high power levels, it can achieves more high efficiency and gain.

## 4. CONCLUSION

This paper present the extended structure and reduce the load impedance method to enhance efficiency, and an enhanced Doherty power amplifier with impedance transform ($Z_L = 12.5\,\Omega$, $Z_T/Z_L = 2.512$) is designed. In comparison with the classical structure and the balanced structure, the PAE is improved about $5.2\%$ and $18.4\%$ with the output power $46\,\text{dBm}$, and achieves a linear power gain of $14.4\,\text{dB}$ with 1-dB output compression at $53.6\,\text{dBm}$ which PAE is $58.4\%$. The experimental result shows that the impedance transform method is feasibility in Doherty amplifiers.

## REFERENCES

1. Yang, Y., J. Cha, B. Shin, and B. Kim, "A fully matched N-way Doherty amplifier with optimized linearity," *IEEE Transactions on Microwave Theory and Techniques*, Vol. 51, No. 3, 986–993, 2003.
2. Pelk, M. J., W. C. E. Neo, J. R. Gajadharsing, R. S. Pengelly, and De Vreede, L. C. N., "A high-efficiency 100-W GaN three-way Doherty for base-station applications," *IEEE Transactions on Microwave Theory and Techniques*, 1–10, 2008.
3. Doherty, W. H., "A new high efficiency power amplifier for modulate waves," *Proceedings of the IRE*, Vol. 24, No. 9, 1163–1182, 1936.
4. Raab, F. H., "Efficiency of Doherty RF power-amplifiers," *IEEE Trans. Broadcast*, Vol. 33, No. 3, 77–83, 1987.

5. McMorrow, R. J., D. M. Upton, and P. R. Maloney, "Microwave Doherty amplifier," *IEEE MTT-S Int. Microwave Symp. Dig.*, Vol. 3, 1653–1656, 1994.

6. Chen, X., Y. Guo, and X. Shi, "A high linearity and efficiency Doherty power amplifier for retrodirective communication," *Progress In Electromagnetics Research Symposium*, 151–156, Hangzhou, China, March 24–28, 2008.

7. Iwamoto, M., A. Williamsm, P.-F. Chen, A. G. Metzger, L. E. Larson, and P. M. Asbeck, "An extended Doherty amplifier with high efficiency over a wide power range," *IEEE Transactions on Microwave Theory and Techniques*, Vol. 49, No. 12, 2472–2479, 2001.

# Comparison of Bit Error Rate for Propagation Mechanisms of Millimeter Waves in a Practical Communication Systems Employing PSK and FSK

**Preethi Kumar and M. Jayakumar**

Applied Electromagnetics Research Group, Department of Electronics and Communication Engineering
Amrita Vishwa Vidyapeetham (Amrita University), Coimbatore, India

**Abstract**— Millimeter waves have opened a new door to next generation communication systems. These high-frequency signals are advantageous due to the high bandwidths, and hence, the high data rates they present. However, their main drawback is the presence of attenuation factors that adversely affect the quality of the received signal. We have described the various propagation mechanisms that lead to the attenuation of radio waves in the frequency range of 40 GHz for different modulation techniques such as m-PSK and m-FSK. The comparison shows that, as the number of signals needed to represent the digital information increases, the Bit Error Rate (BER) of the PSK system increases, while the BER of an FSK system decreases. We have concluded that BPSK, QPSK or 8FSK are the most advantageous modulation schemes in a practical communication system, under worst case climatic conditions.

## 1. INTRODUCTION

Consider a practical communication system transmitting and receiving millimeter waves. In the transmitter side, the antenna technology for millimeter wave signal propagation shows a lot of challenges in the wide band design [2]. Khaddaj Mallat et al. [3] have shown the variation of the BER at the receiving end, with Signal to Noise Ratio (SNR), with operating frequency and with local oscillator power for the six port receiver architecture, which shows superior performance when compared with the conventional homodyne receiver architecture for the QPSK modulation scheme. A number of propagation mechanisms exist between the transmitter and the receiver. The extensive study on millimeter wave propagation under various propagation parameters that has been published by Federal Communication Commission [4] gives the insight into the attenuation in this frequency band.

The channel between the transmitter and the receiver consists of atmospheric gases, dry air, water vapor, buildings and vegetation, each of which act as an attenuation factor, thus increasing the BER of the communication system. Underwater micro wave propagation is affected by sea water attenuation. The main cause of dispersion of energy of a transmitted millimeter wave is the free space path loss modeled by the Friis formula [1]. In addition, atmospheric attenuation occurs due to absorption caused by different gases present in the atmosphere. The so caused attenuation does not follow a monotonic pattern. It has peak attenuation at frequencies corresponding to the absorption frequency of specific gases present in the atmosphere. For example, oxygen absorption occurs at 60 GHz. Thus, the BER is extremely high at this frequency. However, the BER at 70 GHz is much lower since no absorption spectrum is present at that frequency. A graph of the frequency vs. attenuation caused due to atmosphere has been plotted in [5]. The loss due to atmosphere is further increased by the presence of water vapor, which cause refractive dispersion losses. The attenuation due to atmosphere has been modeled as a function of temperature, pressure, humidity and frequency in [6]. Another major factor causing the attenuation of millimeter waves is the scattering and reflection due to buildings [7, 8], which has been modeled as functions of their geometry and the material out of which they are constructed. Another natural cause of attenuation is vegetation. The height of the vegetation and the frequency are the major parameters that decide the loss due to vegetation [7].

## 2. MODELLING THE RECEIVED SIGNAL

Let the transmitted signal have a power $P_t$. Let the received power be $P_r$. The frequency of the millimeter waves is denoted by $f$. The distance between the transmitter and receiver is $D$. Let $c$ be the speed of light. Let $G_t$ and $G_r$ represent the transmitter and receiver antenna gains respectively. The upper limit of the power received, when power $P_t$ is transmitted is given by the Friis formula, which accounts for the free space path loss [1]:

$$P_r = P_t G_t G_r \left( \frac{c}{4\pi D f} \right)^2 \tag{1}$$

Loss due to atmospheric gases has been measured accurately and its variation with frequency has been plotted in [5]. We have taken the value of attenuation at $40\,\text{GHz}$ from this report, in order to calculate the BER. Let the values of loss obtained from this graph be denoted by $L_{atm}$. Apart from atmospheric gases, a typical component present in the atmosphere is water vapor. The attenuation due to water vapor is due to refractive dispersion denoted by $R'(f)$ and refractive absorption denoted by $R''(f)$ [6]. The frequency independent refractivity is denoted by $R_0$. All three refractions are in parts per million (ppm). The following empirical results are stated for refraction due to water vapor

$$R_e''(f) = \left[ b_f p + b_e e \theta^3 \right] f e \theta^{2.5} \tag{2}$$

$$R_e'(f) = b_0 e \theta^{2.4} f^{2.05} \tag{3}$$

where $b_0 = 6.47 \times 10^{-6}$, $b_f = 1.40 \times 10^{-6}$, $b_e = 5.4 \times 10^{-5}$.

The attenuation is given by:

$$L_{wv} = \int_0^d \alpha(x) dx \tag{4}$$

$$\alpha(x) = 0.1820 f R''(f) \tag{5}$$

Loss due to buildings is modeled based on their physical geometry and the characteristics of materials out of which they are constructed. The expression for loss is given as [7]:

$$L_b = S_G S_R \mu_p \tag{6}$$

where $S_G$: Scattering coefficient based on the geometry of the building, $S_R$: Reflection coefficient based on the material of the building and $\mu_p$ is the polarization coefficient. The reflection coefficient $S_R$ is material specific and is calculated as a function of the surface roughness which in turn is defined by the Rayleigh roughness criterion. The polarization coefficient $\mu_p$ is defined in terms of incident and reflected azimuthal and elevation angles. The expression for loss due to vegetation has been empirically derived [7] as:

$$L_{veg} = 0.39 f^{0.39} d^{0.25} \; \text{— Trees with leaves} \tag{7}$$

$$L_{veg} = 0.37 f^{0.18} d^{0.59} \; \text{— Trees without leaves} \tag{8}$$

where, $L$: Loss in dB, $f$: Frequency in MHz, $d$: Height of the vegetation in meters.

For a channel consisting of buildings made of wood and having vegetation of height $0.5\,\text{m}$, we define the received power $P_r$ as:

$$P_r = 10 \log P_t + 20 \log c - 20 \log 4\pi D - 20 \log f - 10 \log L_{atm} - 10 \log L_{wv} - 10 \log L_b - 10 \log L_{veg} \tag{9}$$

## 3. MODELLING THE BER FOR THE RECEIVED POWER

Expressions for the BER in an m-PSK and an m-FSK system are presented below. They have been calculated with the help of the mathematical formulae given in [9].

## 4. SIMULATION RESULTS OF BER

Under free-space, clear sky, Line of Sight (LOS) conditions, the variation of power received with distance of propagation, for various EIRP values at $40\,\text{GHz}$ is shown in Figure 1. For an EIRP of $50\,\text{dB}$, the power received is $-54.48\,\text{dB}$ at a distance of $100\,\text{m}$ and it decreases to $-88.48\,\text{dB}$ at a distance of $5\,\text{km}$. This figure has been taken as a reference for the analysis of propagation mechanisms.

In order to evaluate the Bit Error Rate of a practical communication system employing PSK or FSK, we substitute the values of received power $P_r$ into the BER equations. The simulation parameters are as defined below.

| | |
|---|---|
| Distance between transmitter and receiver: | 1000 m |
| Pressure: | 101325.024 Pa |
| Temperature: | 288 K |
| Relative humidity: | 0.70 |

The simulated values of BER for a PSK and an FSK system are shown in Figures 2 and 3.

Table 1: BER of m-PSK systems.

| Type of modulation | BER expression |
|---|---|
| Binary PSK | $\text{BER} = \dfrac{1}{2} erfc \left( \dfrac{E_b}{N_0} \right)$ |
| Quaternary PSK | $\text{BER} = \dfrac{1}{2} erfc \left( \dfrac{E_b}{N_0} \right)$ |
| 8-PSK | $\text{BER} = \dfrac{1}{3} erfc \left( \sqrt{\dfrac{3E_b}{N_0}} \sin \dfrac{\pi}{8} \right)$ |
| 16-PSK | $\text{BER} = \dfrac{1}{4} erfc \left( \sqrt{\dfrac{4E_b}{N_0}} \sin \left( \dfrac{\pi}{16} \right) \right)$ |

Table 2: BER of m-FSK systems.

| Type of modulation | BER expression |
|---|---|
| Binary FSK | $\text{BER} \leq \dfrac{1}{2} erfc \left( \dfrac{E_b}{2N_0} \right)$ |
| Quaternary FSK | $\text{BER} \leq \dfrac{3}{4} erfc \left( \dfrac{E_b}{N_0} \right)$ |
| 8-FSK | $\text{BER} \leq \dfrac{7}{6} erfc \left( \dfrac{3E_b}{2N_0} \right)$ |
| 16-FSK | $\text{BER} \leq \dfrac{15}{8} erfc \left( \dfrac{2E_b}{N_0} \right)$ |
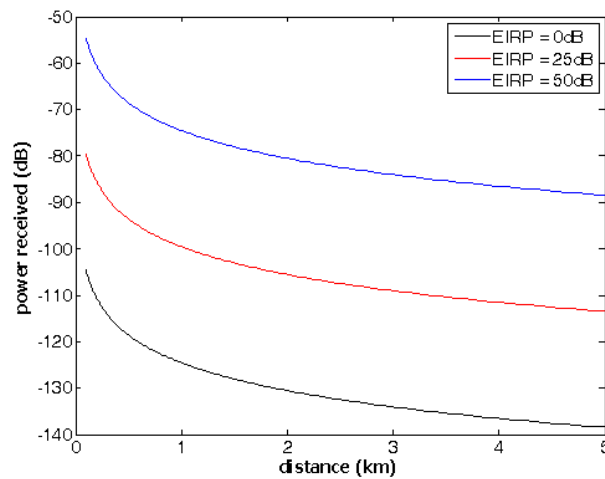


Figure 1: Received power Vs. distance at 40 GHz.

## 5. RESULTS AND DISCUSSION

Figure 2 shows the BER of a PSK system that has been affected by free space path loss, atmospheric attenuation, water vapor dispersion, reflection and scattering due to wooden buildings, and loss due to vegetation. Figure 3 shows the results for a FSK system.

On comparing Figure 2 and Figure 3, we find that the FSK system presents a better BER than the PSK system for the same EIRP values. For smaller values of EIRP (till 41 dB), the BER offered by the FSK and PSK systems are similar. However, as the EIRP increases, the BER of the FSK system drops at a much higher rate than the BER of the PSK system. At an EIRP of 50 dB, the BFSK system's BER is $10^{-6}$, while that of the BPSK system is only $10^{-3}$.

Figure 2 shows that the BERs of a BPSK and a QPSK system are equal. For low values of EIRP, the BERs of BPSK, QPSK, 8PSK and 16PSK systems are almost the same. However, as EIRP increases, the BER of the BPSK and QPSK systems drop in a very fast fashion, leading to a very good BER of $10^{-6}$ at 50 dB. It can be noted that, the BPSK and QPSK systems offer the lowest BER. We note that the BER increases as the value of M increases.

Figure 3 shows that the BER is maximum for a BFSK system. The 16FSK system offers the lowest BER. The QFSK system offers a 10 times lower BER than the BFSK system. The 8FSK system offers a 100 times lower BER at the same EIRP. In contrast to PSK systems, we see that in FSK systems, as M increases, the BER decreases rapidly. However, as M increases the number of carrier signals also increases. This leads to complexity in demodulation. Thus, as a tradeoff between the BER and the complexity, it would be best to use 8FSK signal, which not only offers a sufficiently low BER, but also accounts for lower complexity of system implementation than 16FSK, especially at the receiver side.
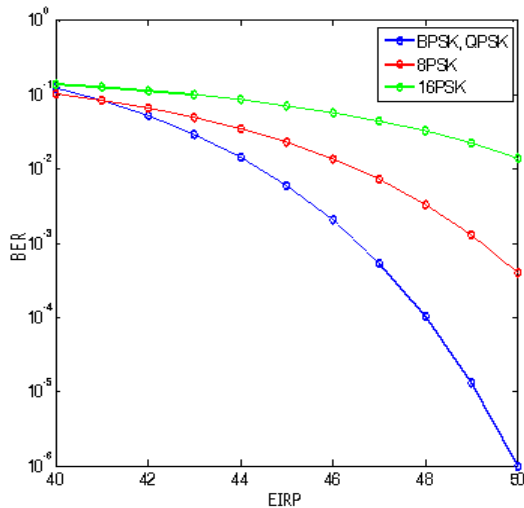
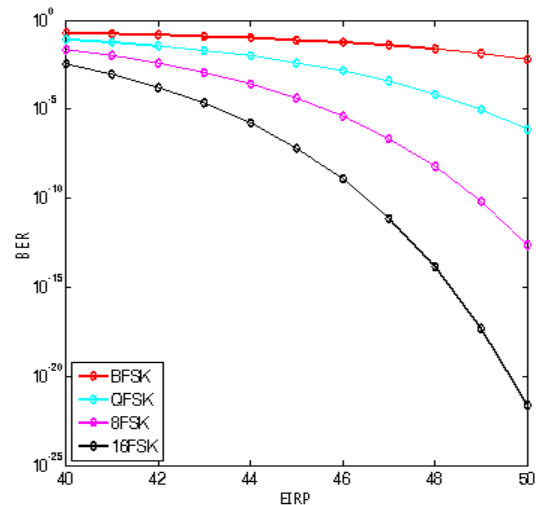Figure 2: BER Vs EIRP for a practical PSK system in the 40 GHz range.



Figure 3: BER Vs EIRP for a practical FSK system in the 40 GHz range.

## 6. CONCLUSION

We have estimated the losses caused due to various natural and man-made obstacles present in the channel of a practical communication system, employing mm wave transmission. A number of modulation schemes such as BPSK, QPSK, BFSK, QFSK, M-PSK and M-FSK have been described. Their BERs have been evaluated at 40 GHz for a range of EIRPs. The comparison shows that, as the value of M increases, the BER of PSK system increases, while the BER of an FSK system decreases. We have concluded that BPSK, QPSK or 8FSK are the most advantageous modulation schemes in a practical communication system, under critical climatic conditions.

## ACKNOWLEDGMENT

## REFERENCES

1. Pozar, D. M., *Microwave Engineering*, Wiley & Sons Publications, 3rd Edition, 2004.
2. Costanzo. S., I. Venneri, G. Di Massa, and G. Amendola, "Hybrid array antenna for broadband millimeter-wave applications," *Progress In Electromagnetics Research*, Vol. 83, 173–183, 2008.
3. Mallat, N. K., E. Moldovan, and S. O. Tatu, "Comparative demodulation results for six-port and conventional 60 GHz direct conversion receivers," *Progress In Electromagnetics Research*, Vol. 84, 437–449, 2008.
4. "Millimeter wave propagation: Spectrum management implications," Federal Communications Commission office of Engineering and Technology, Bulletin No. 70, July 1997.
5. "Technology report — A growing number of applications boosts mm-wave technology," High Frequency Electronics Copyright © 2006 Summit Technical Media, May 2006.
6. Liebe H. J., K. C. Allen, G. R. Hand, R. H. Espeland, and E. J. Violette, "Millimeter-wave propagation in moist air: Model versus path data," US Department of Commerce, March 1985.
7. AI-Nuaimi, M. O., "A generalised site shielding procedure for readio system planning at microwave frequencies," *Proceedings of Fifteenth National Radio Science Conference*, Helwan, Cairo, Egypt, February 24–26, 1998.
8. Alejos, A. V., M. G. Sánchez, and I. Cuiñas, "Measurement and analysis of propagation mechanisms at 40 GHz: Viability of site shielding forced by obstacles," *IEEE Transactions on Vehicular Technology*, Vol. 57, No. 6, November 2008.
9. Haykin, S., *Digital Communications*, Wiley India Edition, 2008.

# Using Parallel Computing for Adaptive Beamforming Applications

**Eman Ahmed[1], K. R. Mahmoud[2], Safwat Hamad[1], and Z. T. Fayed[1]**

[1]Faculty of Computer and Information Sciences, Ain Shams University, Abbassia 11566, Cairo, Egypt
[2]Faculty of Engineering, Helwan University, Helwan, Egypt

**Abstract**— Recently, smart antenna systems have been widely considered to provide interference reduction and improve the capacity, data rates, and performance of wireless mobile communication. Smart antenna arrays with adaptive beamforming capability are very effective in the suppression of interference and multipath signals. The techniques of placing nulls in the antenna patterns to suppress interference and maximizing their gain in the direction of desired signal have received considerable attention in the past and are still of great interest using evolutionary algorithms such as genetic algorithms (GA) and particle swarm optimization (PSO) algorithm. In this paper, for adaptive arrays using space division multiple access (SDMA), the optimal radiation pattern design of smart antennas is developed based on the particle swarm optimization (PSO) technique. The PSO is applied to a 24-element uniform circular array (UCA) to calculate the complex excitations, amplitudes and phases of the adaptive array elements. The antenna elements consist of vertical ($z$-directed) half-wave dipole elements equally spaced in the $x$-$y$ plane along a circular ring, where the distance between adjacent elements is $d_c = 0.5\lambda$. It is found that the resulting beampattern optimized by the PSO required a large processing time which is not acceptable for an on line applications. Hence, the demand for a parallel solution that accelerates these computations is considered. Therefore, a parallel version of PSO is proposed and implemented using Compute Unified Device Architecture (CUDA) then applied on a graphics processing unit (GPU). The comparison is presented to show how the parallel version of the PSO outperforms the sequential one, thus an online procedure is available for time-critical applications of the adaptive beamforming.

## 1. INTRODUCTION

Over the last decade, wireless technology has grown at a formidable rate, thereby creating new and improved services at lower costs. This has resulted in an increase in airtime usage and in the number of subscribers. The most practical solution to this problem is to use spatial processing. Andrew Viterbi, founder of Qualcomm Inc., clearly stated: *"Spatial processing remains as the most promising, if not the last frontier, in the evolution of multiple access systems"*.

Spatial processing is the central idea of adaptive antennas or smart-antenna systems. Although it might seem that adaptive antennas have been recently discovered, they date back to World War II with the conventional Bartlett beamformer. It is only of today's advancement in powerful low-cost digital signal processors, general purpose processors (and ASICs — Application-Specific Integrated Circuits), as well as innovative software-based signal-processing techniques (algorithms), that smart antenna systems have received enormous interest worldwide. In fact, many overviews and tutorials have emerged, and a great deal of research is being done on the adaptive and direction-of-arrival (DOA) algorithms for smart-antenna systems. As the number of users and the demand for wireless services increases at an exponential rate, the need for wider coverage area and higher transmission quality rises. Smart-antenna systems provide a solution to this problem [3].

The increasing interest of researchers in using low cost GPUs for applications requiring intensive parallel computing is due to the ability of these devices to solve parallelizable problems much faster than traditional sequential processors. The first applications of evolutionary algorithms (EAs) on GPUs have been developed to solve specific Adaptive beamforming problems; This paper presents an approach for the implementation of PSO algorithms on GPUs which, using the NVIDIA CUDA environment in the adaptive beamforming applications [1]. For each running swarm a thread block is scheduled with a number of threads equal to the number of particles in the swarm The rest of the paper is structured as follows: Section 2 presents the problem formulation. Section 3 describes the experimental results. Finally, conclusions and remarks are presented in Section 4.

## 2. PROBLEM FORMULATION

The techniques of placing nulls in the antenna patterns to suppress interference and maximizing their gain in the direction of desired signal have received considerable attention in the past and are still of great interest using evolutionary algorithms such as genetic algorithms (GA) or the

sequential quadratic programming (SQP) algorithm. It is recognized that the PSO algorithm is a practical and powerful optimization tool for a variety of electromagnetic and antenna design problems. Compared with other evolutionary algorithms such as the GA and simulated annealing (SA), the PSO algorithm is much easier to understand and implement and requires minimum mathematical processing. In recent years, various versions of the PSO algorithm have been successfully used in linear and circular antenna array synthesis problems. Many of the attempts on antenna array synthesis assume that the elements of the array are represented by isotropic point sensors isolated from each other or the element pattern may be modeled by a cosine function. However, in practice, the elements of antenna arrays have finite physical dimensions and specific radiation characteristics [2].

The particle swarm is used in Adaptive Beamforming application as the following:

The particles are manipulated according to the following equations:

$$v_{id}^{k+1} = \omega^k v_{id}^k + c_1^k rand_1(pbest_{id} - x_{id}^k) + c_2^k rand_2(gbest_d - x_{id}^k) \tag{1}$$
$$x_{id}^{k+1} = x_{id}^k + v_{id}^{k+1}\Delta t \tag{2}$$

where, $w^k$ is the current inertia weight introduced to balance between the global and local search abilities $c_1^k$, $c_2^k$ are the current acceleration constants, which represent the weighting of stochastic acceleration terms that pull each particle towards *pbest, gbest*, positions. $rand_1$, $rand_2$, are two random numbers in the range $[0, 1]$. At each iteration $k$, the current weighting value and acceleration rates can be calculated from the following equation:

$$\omega^k = \omega_{\max} - \frac{\omega_{\max} - \omega_{\min}}{iter'_{\max}} \times k, \quad c_1^k = c_1^{\max} - \frac{c_1^{\max} - c_1^{\min}}{iter_{\max}} \times k, \quad \text{and} \quad c_2^k = c_2^{\min} + \frac{c_2^{\max} - c_2^{\min}}{iter_{\max}} \times k$$

where, $w_{\max}$ is the initial weight (0.9), $w_{\min}$ is the final weight (0.4), $iter'_{\max}$ is 0.75 of the maximum iteration number ($iter_{\max}$). The value of the inertia weight is fixed to $w_{\min}$ after $iter'_{\max}$. $c_1^{\max}$ and $c_1^{\min}$ are the maximum and minimum values of $c_1^k$, $c_2^{\max}$ and $c_2^{\min}$ are the maximum and minimum values of $c_2^k$. An improved optimum solution was observed when changing $c_1^k$ from 2.5 to 0.5, changing $c_2^k$ from 0.5 to 2.5,

$$\text{objective function} = \sum_{i=1}^{N} a_i |E(\varphi_i)| - \sum_{j=1}^{M} b_j |E(\varphi_j)| \tag{3}$$

where $E$ is the electric field intensity and the constants $a_i$ and $b_j$ are the weights that control the contribution from each term to the overall objective function. The constant $N$ represents the number of desired users, and $M$ represents the number of interferers. In our analysis, The weights $a_i$ and $b_j$ are considered are considered to be the same.

The implementation is done using cuda where two independent kernels (functions) were used. One kernel is for updating particles position and velocity and the other for calculating fitness for each particle position. Both kernels run for 40 particles in parallel (one thread for each particle) which succeeded in achieving an outstanding performance as stated in the result section.

The Proposed Algorithm (Frame Work) works as following: First we Initialize Particles with Random Positions ($X$), Velocity ($V$) Vectors, *Initial Values of* $\omega$, $c_1$, $c_2$ (*On CPU*). Then one Kernel calculates fitness function (Array Factor) for each particle in parallel one thread for each particle (On GPU). Next, we Calculate the iteration best and global best metrics On CPU. The loop is then executed for max number of iterations.

## 3. EXPERIMENTAL RESULTS

Here we propose the first version of the adaptive beamforming application with PSO using CUDA and this is sample of the experimental results.

Experiments were run on a PC equipped with an Intel Core$^{(TM)}$2Duo processor running at 2.80 GHz with a NVIDIA GeForce 9600 GT video card from NVIDIA corporation. All of the simulation runs were performed under the following settings:

Number of antenna in antenna array = 24
Number of Particle = 40
Number of Iterations = 150

The sequential execution of the program took 4446 ms while running the proposed algorithm on GPU NVIDA (GeForce 9600) the execution time was only 265 ms. In particular the achieved running speedup was of about 16 times as illustrated in Table 1.

In Table 2, the first column displays images illustrating the optimum normalized radiation pattern resulted from the proposed PSO the second column shows figures that illustrate the optimum normalized radiation pattern measured in dB, and the last column illustrates the change of fitness value with iterations. The results were recorded for five different test cases.

Table 1: Sample runs and the average speed up.

| Desired signal direction | Undesired signal direction | Elapsed CPU time in (msecond) | Elapsed GPU time in (msecond) | Speed up rate |
|---|---|---|---|---|
| 0,90,180 | 30 | 4446 | 265 | 16.7774 |
| 0,60 | 180,30 | 4446 | 265 | 16.7774 |
| 180,60 | 240,30 | 4491.985 | 265 | 16.9509 |
| 180 | 60,240 | 4446 | 280 | 15.8786 |
| 180 | 300,120,30 | 4524 | 280 | 16.1571 |
| | | | **Average** | = 16.50828 |

Table 2: Experimental results.
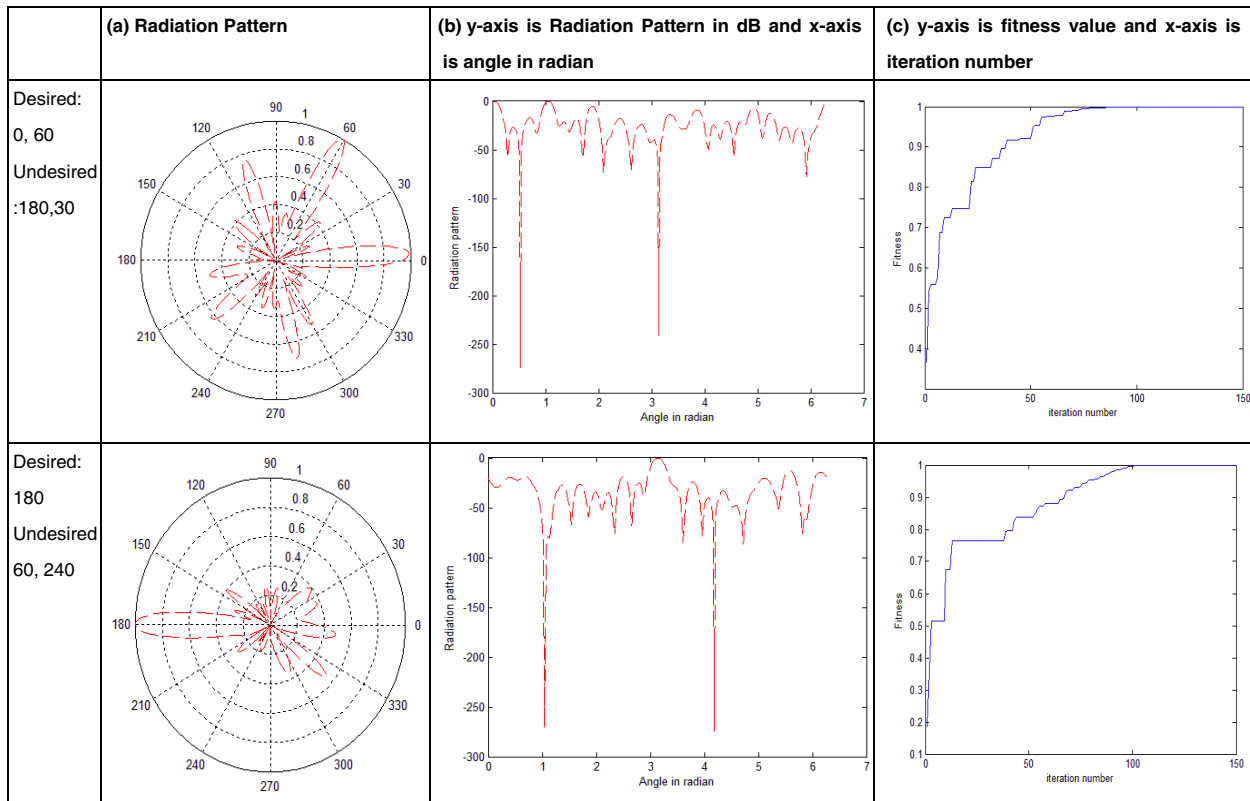


## 4. CONCLUSIONS

In this paper, we have developed a parallel Adaptive Beamforming using PSO on GPU. The experimental results showed that the proposed algorithm is more efficient compared to a well coded serial version in terms of execution time. The possibility to efficiently run many swarms at the same time is another advantage that permits to improve the optimization success rate. Furthermore, the proposed design is modular and versatile: evolutionary steps are split into independent kernels, which makes it easy to adapt them to different variants of the PSO algorithm. For example, the neighborhood topology could be changed by changing the bests Update kernel. More simply, our

CUDAPSO can be adapted to the optimization of other goals by changing the fitness evaluation kernel. The performance still can be improved by using shared memory instead of global memory.

**REFERENCES**

1. Mussi, L. and S. Cagnoni, "Particle swarm optimization within the CUDA architecture," Viale G. Usberti 181a, I-43124 Parma, Italy.
2. Mahmoud, K. R., M. El-Adawy, S. M. M. Ibrahem, R. Bansal, and S. H. Zainud-Deen, "A comparison between circular and hexagonal array geometries for smart antenna systems using particle swarm optimization algorithm," *Progress In Electromagnetics Research*, PIER 72, 75–90, 2007.
3. Balanis, C. A., *Antenna Theory Analysis and Design*, John Wiley & Sons, Inc., Publication, Hoboken, New Jersey, 2005.

# Permanent Magnet Synchronous Motor Decoupling Control Study Based on the Inverse System

**Xiaoning Li[1], Xumei Mao[1], and Weigan Lin[2]**

[1]School of Mechanical Engineering, University of Electronic Science and Technology of China
No. 4, Section 2, North Jianshe Road, Chengdu 610054, China
[2]School of Electronic Engineering, University of Electronic Science and Technology of China
No. 4, Section 2, North Jianshe Road, Chengdu 610054, China

**Abstract**— In this parer, multivariable,nonlinearity inverse system method is applied on the PMSM control system, which is complicated nonlinearity, strong coupled, and we have realized global linearization, at the same time, the motor rator speed and electromagnetic torque have been dynamic decoupled. The validity of this method can be proved by the simulation result.

## 1. INTRODUCTION

The PMSM is a multivariable, nonlinearity, strong, coupled controlled object. It is very hard to control its speed and electromagnetic torque by extra signal. Only can we precisely control it after the speed and torque have been dynamic decoupled. Vector control adopted the coordinate transform to realize decouple based on the motor electromagnetic field theory, but vector controlling just achieve the static decoupling not dynamic doing. Inverse system theory is a new strategy. Its essence is to realize decoupling of multivariable, nonlinearity, strong coupled system by feedback linezation. It can realize linearization in a global range, and then we can decouple the nonlinear system. The inverse system method don't need profound mathematical knowledge, so it is very fit for engineering application. In this paper, multivariable, nonlinearity inverse system method was applied on PMSM control system, by which motor rator speed and electromagnetic torque can be dynamically decoupled. The validity of this method can be proved by the simulation result.

## 2. PMSM DECOUPLING CONTROL INVERSE SYSTEM DESIGN

About PMSM, one effective control tactics is vector control. We can decompose the staror current into the $i_d$ and $i_q$, when we keep $i_d = 0$, the electromagnetic torque of PMSM is directly related to the $i_q$, so we can realize the linear control to PMSM. If we reglect the damping coefficient to simple analyses, the PMSM model can be described by the following equtations based on $d$-$q$ axis:

$d$ axis staror voltage equation

$$u_d = L_d \frac{di_d}{dt} + Ri_d - \omega_r L_q i_q \tag{1}$$

$q$ axis stator voltage equation

$$u_q = L_q \frac{di_q}{dt} + Ri_q + \omega_r L_d i_d + \omega_r \psi_f \tag{2}$$

$q$ axis staror magnetic flux linkage equation

$$\psi_q = L_q i_q \tag{3}$$

$d$ axis staror magnetic flux equation

$$\psi_d = L_d i_d \tag{4}$$

electromagnetic torque equation

$$T_e = P_n[L_{md} i_{fd} i_q + (L_d - L_q) i_d i_q] \tag{5}$$

Here, $u_d$ is $d$ axis stator voltage; $u_q$ is $q$ axis stator voltage; $i_d$ is $d$ axis stator current, $i_q$ is $q$ axis stator current; $\psi_d$ is $d$ axis stator magnetic flux linkage, $\psi_q$ is $q$ axis stator magnetic flux linkage, $\psi_f$ is permanent magnet magnetic flux linkage, $L_d$ is stator winding $d$ axis inductance, $L_q$ is stator winding $q$ axis inductance; $R$ is stator resistance, $\omega_r$ is rator angle speed, $L_{md}$ is $d$ axis

inductance between stator and rotor, $i_{fd}$ is permanent magnet equivalent $d$ axis excitation current, $T_e$ is electromagnetic torque. In order to simplified model, we set two parameter $u_{ind}$ and $u_{inq}$:

$$u_{ind} = \frac{d\psi_d}{dt} + R \cdot i_d \tag{6}$$

$$u_{inq} = \frac{d\psi_q}{dt} + R \cdot i_q \tag{7}$$

Then the PMSM voltage equation can be simplified as:

$$u_d = u_{ind} - \omega_r L_q i_q \tag{8}$$
$$u_q = u_{inq} + \omega_r L_d i_d + \omega_r \psi_f \tag{9}$$

We can prove reversibility by utlizing the Interactor arithmetic. At first, we set up the PMSM state equation:

Select input variable:

$$U = [u_1, u_2]' = [u_{ind}, u_{inq}]' \tag{10}$$

Select Output variable:

$$Y = [y_1, y_2]' = [i_d, \omega_r]' \tag{11}$$

Select State variable:

$$X = [x_1, x_2, x_3]' = [i_d, i_q, \omega_r]' \tag{12}$$

Then the state equation can be expressed:

$$\begin{cases} x_1' = -\frac{R}{L} x_1 + \frac{1}{L} u_1 \\ x_2' = -\frac{R}{L} x_2 + \frac{1}{L} u_2 \\ x_3' = \sigma x_2 - \frac{T_L}{J} \end{cases} \tag{13}$$

In this formula, $\sigma = 3P_n \cdot \psi_f \cdot (2J)^{-1}$, $P_n$ is magnetic poles

Output equation is:

$$y = [i_d, \omega_r]' = [h_1(X), h_2(X)]' = [x_1, x_2] \tag{14}$$

First step we calculate first order deriveate of $y_1$

$$y_1^{(1)} = x_1' = -\frac{R}{L} x_1 + \frac{1}{L} u_1 \tag{15}$$

We set $Y_1 = y_1'$, then

$$t_1 = \text{rank}\left(\frac{\partial Y_1}{\partial U^T}\right) = \text{rank}\left[\frac{1}{L}, 0\right] = 1 \tag{16}$$

Namely Jacobian matrix full rank, so $\alpha_1 = 1$.

Second step we calculate first order deriveate of $y_2$

$$y_2' = \sigma \cdot x_2 - \frac{T_L}{J} \tag{17}$$

Because there is no include $U$, we need to calculate second order deriveate of $y_2$

$$y_2'' = \sigma \cdot \left(-\frac{R}{L} \cdot x_2 + \frac{1}{L} \cdot u_2\right) \tag{18}$$

Obviously, $U$ is included in $y_2''$, so set $Y_2 = [Y_1, y_2'']^T$, then

$$t_2 = \text{rank}\left(\frac{\partial Y_2}{\partial U^T}\right) = \text{rank}\begin{bmatrix} \frac{1}{L} & 0 \\ 0 & \frac{\sigma}{L} \end{bmatrix} = 2 \tag{19}$$

Jacobian matrix full rank, so $\alpha_2 = 2$.

Because

$$\det\left(\frac{\partial Y_2}{\partial U^T}\right) = \text{rank}\begin{bmatrix} \frac{1}{L} & 0 \\ 0 & \frac{\sigma}{L} \end{bmatrix} \neq 0 \tag{20}$$

The system vector relative degree is

$$\alpha = [\alpha_1, \alpha_2]' = [1, 2]' \tag{21}$$

The highest order number of $y_1$ and $y_2$ is separately one and two, so the system nature order is

$$n_e = [1, 2]^T \tag{22}$$

Clearly, the system nature order is equal to vector relative degree. According to Interactor arithmetic, so the system is reversible, PMSM inverse system decoupling control structure diagram is shown in Figure 1.

We embedded the PMSM inverse system before the original system to build a compounded pseudo linear system, then we can convert it to one first order line integration subsystem and one two order line integration subsystem so that it can be better controlled. So for stator current and speed, we can discriminablily design current regulator and speed regulator to build compounded controller together with inverse system in order to realize PMSM decoupling control graph, after we add in a inverse system, complicated PMSM nonlinear system can be reduced to a linear system. Stator current is corresponding to a first-order integrating object, so we adopt generally PI controller, but rotor speed is corresponding to a second order integrating object, and PD controller is used usually.

## 3. SIMULATION ANALYSE OF PMSM VECTOR CONTROL SYSTEM BASED ON THE INVERSE SYSTEM

In this paper, we build PMSM inverse system decoupling control model and proceed simulation test based on MATLAB. By tuning, we set $k_p = 30$, $k_i = 0.1$ as PI controller parameter and $k_p = 1500$, $k_d = 50$ as PD controller parameter. The PMSM motor parameter is:

Stator resistance $R = 2.875\,\Omega$, turning intertia $J = 8 \times 10^{-4}\,\mathrm{kg \cdot m^2}$, magnetic poles $p = 4$, stator inductance $L_d = L_q = L = 8.5\,\mathrm{mH}$. To verify the decoupling characteristics, we set load torque $T_L = 5\,\mathrm{N \cdot m}$ during 0 to 0.2 s, and suddenly load increase $5\,\mathrm{N \cdot m}$ in 0.4 s, simultaneously,
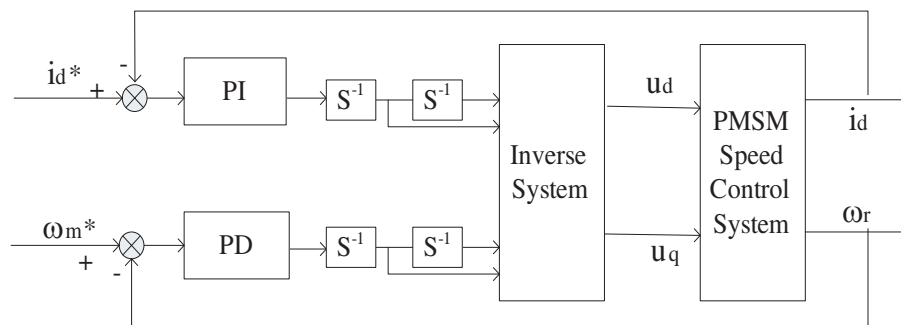


Figure 1: The structure of PMSM based on the inverse system.
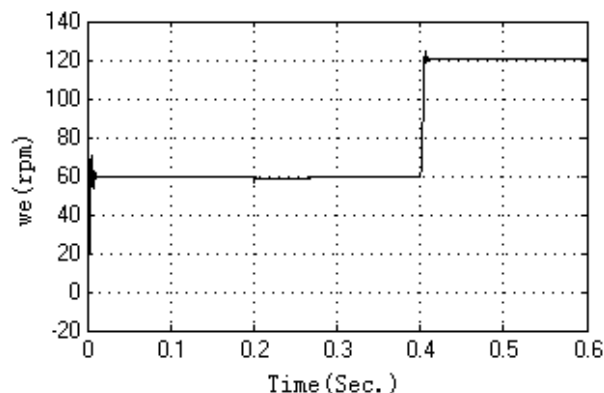


Figure 2: The response of torque when speed mutate.
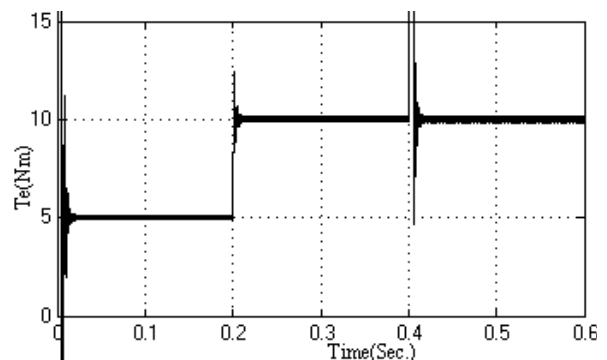
Figure 3: The response of speed when torque mutate.

we set rotor speed $\omega_r = 60\,\text{rad/s}$ during 0 to 0.4 s, and suddenly speed increase 60 rad/s in 0.4 s, from the Figure 2 and Figure 3, we can see that the rator speed keep constant $\omega_r = 60\,\text{rad/s}$ when load torque varied suddenly from $5\,\text{N} \cdot \text{m}$ to $10\,\text{N} \cdot \text{m}$, similarly, the load torque remain uncharged when the rator speed have a sudden charge from 60 rad/s to 120 rad/s from the simulation result, we can see that the PMSM have been depouled by inverse system, we can separately control the speed and torque. So we respectively control speed and torque of PMSM.

## 4. CONCLUSION

In this paper, we adopt inverse system to realize the speed and torque dynamic decoupling control of permanent magnet synchronous motor. We build the inverse system and verified the system by simulation, The validity can be proved by the simulation result.

## REFERENCES

1. Bose, B. K., *Modern Power Electronics and AC Drives*, China Machine Press, Beijing, 2005.
2. Levin, A. U. and K. S. Narendra, "Control of nonlinear dynamical systems using neural networks: Controllability and stabilization," *IEEE Transactions on Neural Networks*, Vol. 2, No. 4, 192–206, 1993.
3. Wang, J., T. Li, K. M. Tsang, et al., "Differential algebraic observer based nonlinear control of permanent magnet synchronous motor," *Proceedings of the CSEE*, Vol. 2, No. 25, 87–92, 2005 (in Chinese).
4. Zhang, C., F. Lin, W. Song, et al., "Nonlinear control of induction motors based on direct feedback linearization," *Proceedings of the CSEE*, Vol. 2, No. 23, 99–107, 2003 (in Chinese).

# Modeling Buck Converter by Using Fourier Analysis

**Mao Zhang[1], Weiping Zhang[2], and Zheng Zhang[2]**

[1]School of Computing, Engineering and Physical Sciences, University of Central Lancashire, UK
[2]North China University of Technology, Shijingshang District, Beijing, China

**Abstract**— By employing theory of PAM (pulse-amplitude-modulation), Buck converter (DC-/DC) have been modeled in this paper. The main contributions are as the followings: (1) A DC transformer model has been proposed to analysis of the voltage gain, efficiency and some steady-state properties; (2) Two a.c. small signal models have been put forward in order to get the transfer functions of input to output and control to output. These a.c. small signal models play an important role on predicting the dynamic behaviors and designing its control system.

## 1. ANALYSIS OF BUCK CONVERTER BY FOURIER TRANSFORMS

Buck converter is one of important traditional converter and applied broadly in the industrial. It is showed in Fig. 1, A Buck converter can be broken into three parts, named as switch network, LPF and the load. The equivalent model is showed in Fig. 2 while we apply the signal process theory to analysis it.

### 1.1. Equivalent Model by PAM

Applying the theory of PAM, a multiplier has been introduced to replace the switch network in Fig. 2, therefore, a new equivalent model, called as PAM-recovery model for converter, can be obtained to shown in Fig. 3.

The driven signal $v_{gs}(t)$, shown in Fig. 3, is a pulse train with a period $T_s$ and width $\tau$. Its exponential form of the Fourier series has been given out by [1]

$$V_{gs}(t) = \sum_{k=-\infty}^{\infty} C_k e^{jk\omega_s t}, \quad C_k = D \sin c(k\omega_s \tau/2), \quad D = \tau/T_S \tag{1}$$

where $\omega_s = 2\pi/T_s$, $\sin c(k\omega_s \tau/2) = \sin(k\omega_s \tau/2)/(k\omega_s \tau/2)$.
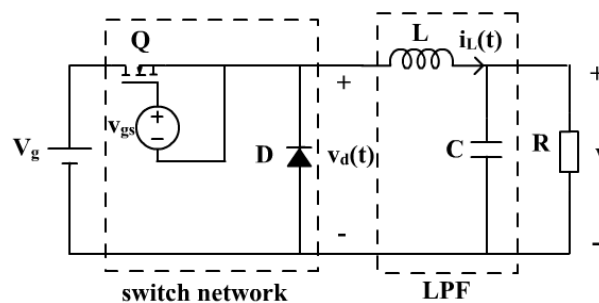


Figure 1: BUCK converter.
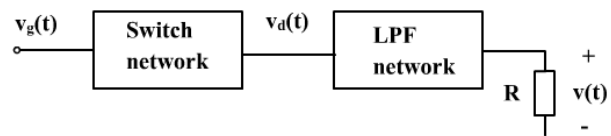


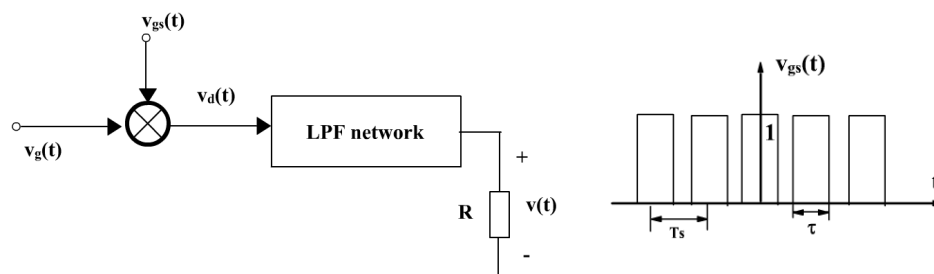Figure 2: The equivalent model of applying signal process.



Figure 3: PAM-recovery model of the converter and the waveform of $v_{gs}(t)$.

Applying the frequency shifting property [1], one can get the frequency response of $v_{gs}(t)$,

$$V_{gs}(\omega) = \sum_{k=-\infty}^{\infty} 2\pi C_k \delta(\omega - k\omega_s), \quad C_k = \frac{\tau}{T_S} \sin c(k\omega_s \tau/2)$$

### 1.2. Analyzing Buck Converter by Employing Fourier Transform

In time domain, the output $v_d(t)$ of multiplier or switch network is that $v_g(t)$ multiplied by $v_{gs}(t)$. Applying the convolution property [1], one can obtain the frequency response of the switch network output,

$$v_d(t) = v_g(t)v_{gs}(t) = \sum_{k=-\infty}^{\infty} C_k e^{jk\omega_s t} v_g(t) \tag{2}$$

$$V_d(\omega) = \frac{1}{2\pi} V_g(\omega)^* V_{gs}(\omega) = \sum_{k=-\infty}^{\infty} C_k V_g(\omega - k\omega_s) \tag{3}$$

In general, the input $V_g$ is a DC voltage source which can be derived from an alternating mains supply through a rectifier and smooth capacitor, so it has DC component and $100\,\text{Hz}$ a.c. ripple. In order to simplify this problem, $V_g(\omega)$ is supposed a band limited signal, shown in Fig. 4(a), $V_g(\omega) = 0$, for $\omega > \omega_M$.

The frequency response $V_d(\omega)$ and $V_g(\omega)$ have been shown in Fig. 4. In Fig. 4, we can find out that $V_d(\omega)$ are one sets of shifting $V_g(\omega)$ in frequency domain. The shifting rule is as the followings: (1) The shifting interval is sampling frequency $\omega_s$, (2) The magnitude is modified by the factor $C_k$.

The transform function of LPF, made of $L$ and $C$ in Fig. 1, is specified by

$$H(\omega) = \frac{1}{LC\omega^2 + \dfrac{L}{R}\omega + 1} \tag{4}$$

Its magnitude frequency response is shown in Fig. 4(d), $\omega_c = 1/\sqrt{LC}$. Therefore, the output $V(\omega)$ can be expressed by

$$V(\omega) = V_d(\omega)H(\omega) = \sum_{k=-\infty}^{\infty} C_k V_g(\omega - k\omega_s)H(\omega) \tag{5}$$

### 2. DC TRANSFORMER MODEL

In this section, a DC transformer model has been investigated to model the basic property of Buck DC/DC converter. If the input $V_g$ is ideal DC voltage source, the $V_g(\omega)$ has only DC component, the Equation (5) can be modified as the follows,

$$V(k\omega_s) = \sum_{k=-\infty}^{\infty} C_k V_g \delta(\omega - k\omega_s)H(\omega) \tag{6}$$

The normalized spectrum has been plotted in Fig. 5. The magnitudes of higher order harmonics are very smaller than DC component, so these components could be neglected when a DC/DC converter are analyzed. (1) In Buck converter, $\omega_s(= 2\pi f_s)$ is the switch frequency and $\omega_c(= 2\pi f_c)$ is a cut-off frequency of LPF. In a practical converter, the switch frequency is much greater than the cutoff frequency, for example, $f_s > 10f_c$, and LPF is second order Butterworth filter. The filter has $-40\,\text{dB}$ attenuation at the switch frequency. (2) The coefficient of Fourier series, shown in Table 1, has be calculated by the formula,

$$C_k = D \sin c(k\omega_s \tau/2), \quad D = \tau/T_S \tag{7}$$

The DC component of output voltage is calculated by formula (6)

$$V(0) = C_0 V_g H(0) = D \cdot V_g \cdot 1 = D V_g \tag{8}$$

If $k = 1$, $V(\omega_s) = C_1 V_g H(\omega_s)$, the normalized magnitude is defined as

$$A_1 = 20\lg\left|\frac{V(\omega_s)}{V(0)}\right| = 20\lg\left|\frac{C_1 H(\omega_s)}{C_0 H(0)}\right| = 20\lg\left|\frac{C_1}{C_0}\right| + 20\lg\left|\frac{H(\omega_s)}{H(0)}\right|$$

If $D = 0.6$, $A_1 = -24.4 - 40 = -64$ dB. Hence, the high order components could be neglected while the DC component of output is calculated. According to Equation (8), the DC equivalent circuit corresponding ideal Buck DC/DC converter can be established. This model, shown in Fig. 6, is called as a DC transformer model for ideal DC/DC converter, and "$-$" means the DC current can pass the transformer. The DC transformer model describes the main function of a DC/DC converter: (1) transformation of DC voltage and current, $V = DV_g$, $I_g = DI$, where $I_g$ is averaging input current. (2) The output voltage can be controlled through changing duty cycle $D$; (3) The model can be modified to account for loss elements such as loss of inductor and power diode and switch to predict the efficiency.
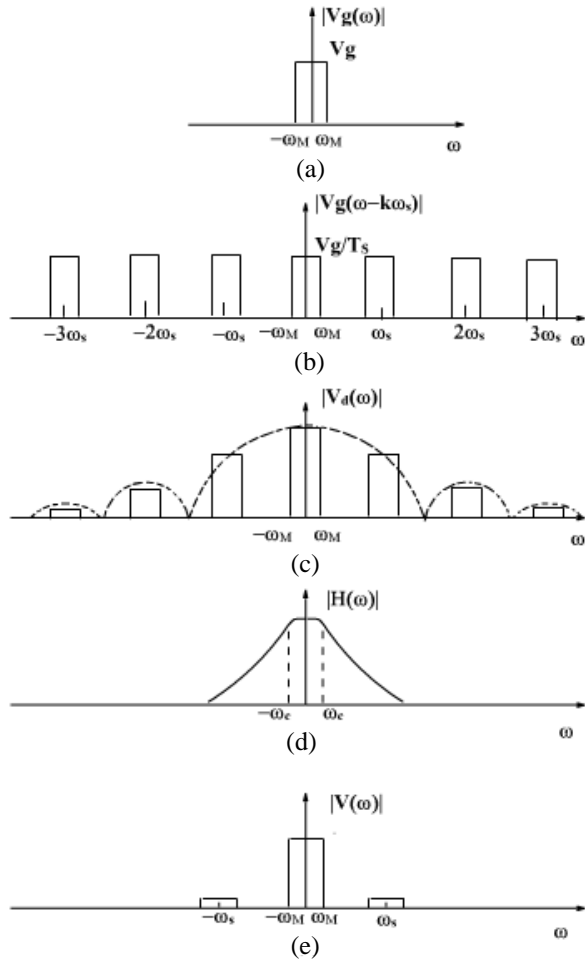


Figure 4: Frequency spectra for PAM.
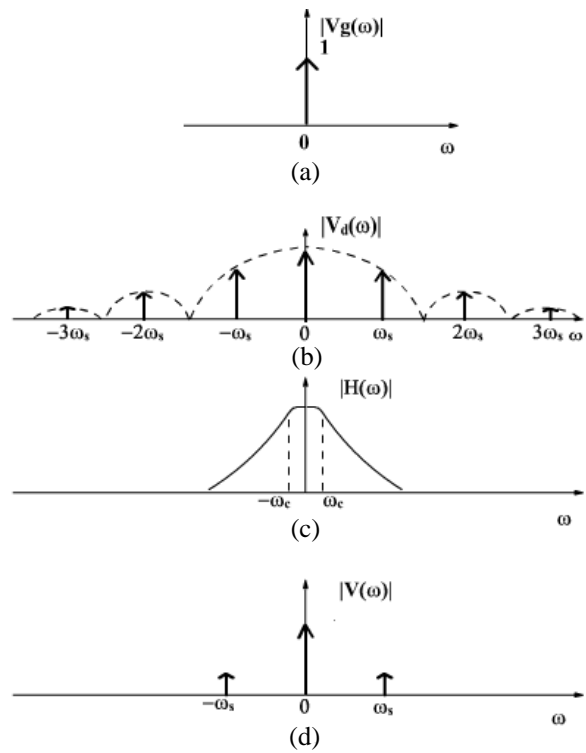


Figure 5: Frequency spectra based on the expression (5).

Table 1: $C_k$ with different $D$ (from $D = 0.4$ to 0.9).

|                    | $k = 0$ | $k = 1$ | $k = 2$ |
|--------------------|---------|---------|---------|
| $C_k$ ($D = 0.4$)  | 0.4     | 0.0730  | 0.0507  |
| $C_k$ ($D = 0.5$)  | 0.5     | 0.0989  | 0.0216  |
| $C_k$ ($D = 0.6$)  | 0.6     | 0.0361  | 0.0338  |
| $C_k$ ($D = 0.7$)  | 0.7     | 0.0591  | 0.048   |
| $C_k$ ($D = 0.8$)  | 0.8     | 0.1013  | 0.0038  |
| $C_k$ ($D = 0.9$)  | 0.9     | 0.0527  | 0.0450  |
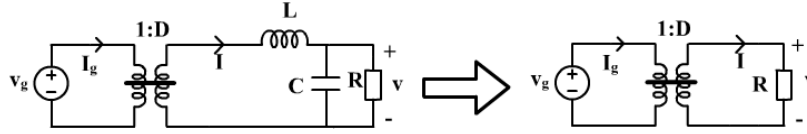
Figure 6: DC transformer model.

## 3. AN a.c. SMALL-SIGNAL MODEL

### 3.1. An a.c. Small-signal Model for Input-output

In this section, two a.c. small-signal models will express the dynamic behaviors of Buck converter. There are the some reasons. (1) In general; the input $V_g$ is a DC voltage source which is derived from an alternating mains supply through a rectifier and smooth capacitor, so it has DC component and about $100 \sim 120\,\text{Hz}$ a.c. ripple, which will lead to the disturbance in the output of the converter. Hence, it is required to find out how to affect the output by the input a.c. ripple; (2) the output current will be changed as the load varies, this will result in the output disturbance.

According to the above discussion, the input voltage can be expressed by

$$v_g(t) = V_g + V_{gm} \cos \omega_{line} t \tag{9}$$

$V_g$ is DC component and $V_{gm} \cos \omega_{line} t$ is the a.c. ripple signal and $f_{line}(= \omega_{line}/2\pi)$ is two time mains frequency. In order to simplify the analysis process and make sense for engineering analysis, the following assumptions have been made, (1). The amplitude of DC signal is greater than that of a.c. signal. $V_g \gg V_{gm}$. (2). The frequency of a.c. signal is much smaller than the switching frequency, $f_{line} \ll f_s$. The above two assumptions imply that the LPF operates in pseudo steady state during a switching period. The net changes of inductor current and capacitor voltage is too small to consider it to affect the behaviors of the converter during one switch period.

Based on above assumptions, $\hat{V}_{gm}(t)(= V_{gm} \cos \omega_{line} t)$ is called as an a.c. low-frequency- small-signal. The Fourier transform of the input voltage is (10), and the frequency spectrum $\hat{V}_g(\omega)$ are shown in Fig. 7(a).

$$V_g(\omega) = V_{gdc}(\omega) + \hat{V}_g(\omega) = 2\pi V_g \delta(\omega) + \pi V_{gm}[\delta(\omega - \omega_{line}) + \delta(\omega + \omega_{line})] \tag{10}$$

The steady state analysis has gotten a useful conclusion which the higher order harmonics can be ignored in analyzing Buck. This conclusion is also suitable for analysis in this section. The output voltage can be expressed

$$V(\omega) = C_0 V_g(\omega) H(\omega) \ \ |\omega| < \omega_s/2 \quad \text{Others is equal to zero} \tag{11}$$

From Equation (10), the a.c. small-signal input is

$$\hat{V}_g(\omega) = V_g(\omega) - V_{gdc}(\omega) = \pi V_{gm}[\delta(\omega - \omega_{line}) + \delta(\omega + \omega_{line})] \tag{12}$$

From Equation (10), the a.c. small-signal output is

$$V(\omega) = V_{dc}(\omega) + \hat{V} = D[V_{gdc}(\omega) + \hat{V}_g(\omega)] \quad |\omega| < \omega_s/2 \tag{13}$$

The a.c. small signal model can be plotted in Fig. 8, from which the transform function of input to output can derived.

$$\left.\frac{\hat{v}(s)}{\hat{v}_g(s)}\right|_{\hat{d}(s)=0} = DH(s) = \frac{D}{LCs^2 + \dfrac{L}{R}s + 1} \quad \text{let } j\omega = s \tag{14}$$

### 3.2. An a.c. Small-signal Model for Control-output

If $v_g(t)$ only have the DC component, and suppose the duty cycle is modulated sinusoidal:

$$d(t) = D + d_m \cos \omega_p t \tag{15}$$

$$v_d(t) = v_g(t)d(t) = V_g(D + d_m \cos \omega_p t) \tag{16}$$
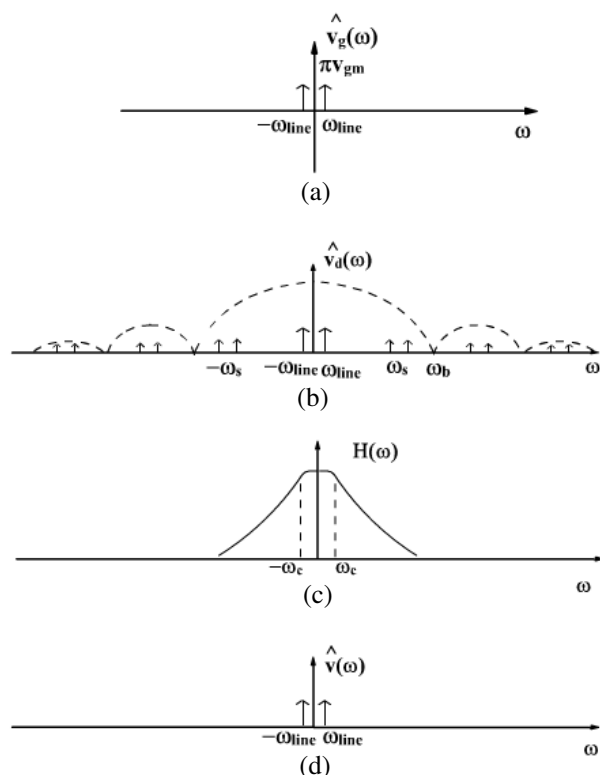
(a)

(b)

(c)

(d)

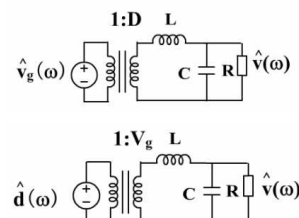Figure 7: The frequency spectrum of $\hat{v}_g(\omega)$, $\hat{v}_d(\omega)$ and $\hat{v}(\omega)$.

Figure 8: a.c. small-signal model of control-to-output and input-output.

The small signal of $\hat{d}(t)$ can be rewritten in (17)

$$\hat{d}(t) = d_m \cos \omega_p t \tag{17}$$

So using Fourier transform, it is obtained (18)

$$\hat{v}(\omega) = DV_g \pi [\delta(\omega - \omega_p) + \delta(\omega + \omega_p)] H(\omega) = V_g \hat{d}(\omega) H(\omega) \tag{18}$$

So when $\hat{v}_g(t) = 0$, the transform function is expressed in (19)

$$\left. \frac{\hat{v}(s)}{\hat{d}(s)} \right|_{\hat{v}_g(s)=0} = \frac{V_g}{LCs^2 + \dfrac{L}{R}s + 1} \tag{19}$$

## 4. CONCLUSIONS

In this paper, it is utilized the PAM theory and approaches to analyze and model Buck converter, and figured out that it (the signal processing theory and approaches) also is a powerful tool in power electronics field. For example, analysis and model of Buck converter is a problem in power electronics and PAM is a problem which belongs to signal processing. However, this paper has shown that both Buck converter and PAM have a same mathematic model. So, a mature theory and method about PAM has been successfully employed to predict the behaviors of Buck converter, extracting the following conclusions,

(1) A DC transformer model, describing the main function of a DC/DC converter, has been proposed to analysis of the voltage gain, average current gain, efficiency and some steady state properties as well as how to controlling the output energy;

(2) An a.c. small-signal model for input-output has been developed. According this model, one can easily get the transfer function of input to output and dynamic input resistance as well as output resistance;

(3) An a.c. small-signal model for control-output and its transform function have been investigated. This model and transform function are necessary for deigning its control system and for analyzing the stability of the closed loop control.

In one word, this paper opened a new window to study DC/DC converter employing the mature theory and approaches in signal process.

**REFERENCES**

1. Phillips, C. L. and J. M. Parr, *Signals Systems and Transforms*, 2nd Edition, 275–277, 1998.
2. Zhang, W. P., *The Control and Modeling of Switch Converter*, 5–15, China Power Publishers, 2006.
3. Erickson, R. W. and D. Masksimovic, *Fundamentals of Power Electronics*, 2nd Edition, Kluwer Academic Publishers, 2001.
4. Ludeman, L. C., *Fundamentals of Digital Signal Processing*, Happer & Row Publishers, Inc., New York, 1986.

# The Comparison of Direct and Indirect Matrix Converters

**P. Chlebis**, **P. Simonik**, **and M. Kabasta**

Department of Electronics, VSB — Technical University of Ostrava, Czech Republic

**Abstract**— In this paper are presented control methods and results of selected types of direct and indirect converters analysis and main output and input characteristic parameters are compared. The criterions for our comparison were the quality of wave forms and the quality and form of output current. By the comparison was also evaluated complexity of the converter circuits, its commutation and control strategy. This contribution summarizes results of some simulations and measurements that refer to conclusion that the special types of matrix converters have characteristics fully comparable with the conventional indirect frequency converters.

## 1. INTRODUCTION

Presently is actual the matrix converter (MC) for energy conversion. Matrix converter has no limit of the output frequency, limitation is only on output amplitude, which is smaller then input amplitude. This limitation can be solved using over modulation technique [1].

Matrix converter replace two energy conversion to only one energy conversion, because within converter is not any energy storage element. The matrix converter requires special semiconductor switches. The matrix converter requires a bidirectional switch, capable of blocking voltage and conducting current in both directions — the energy flow can get from source to load and back. These bidirectional switches, consisting of a pair of devices with turn-off capability, are usually Insulated Gate Bipolar Transistors (IGBTs), are in either a common collector or a common emitter back-to-back arrangement. Usually, each IGBT has an anti-parallel diode. Matrix converters contain an array (Fig. 1(a)) of bidirectional semiconductor switches and this array allows connection of all input lines to all output lines.

If the switches are arranged as shown on Fig. 1(a), then the power flow in converter will be reverse. Thanks to absence of any energy storage element, the instantaneous power on input must be the same as the power on output side. Unfortunately reactive power input does not have to equal the reactive power output. In MC it is possible to control the phase angle between the voltages and current on the input — the output phase angle differs from input phase. Another advantage is that the forms of waveforms at the two sides are independent. So the input could be three-phase AC and output DC, or both could be DC, or both could be AC.

In this case, the MC topology is used for universal power conversion such as: AC/DC, DC/AC, DC/DC, AC/AC without any change of topology [4, 6]. For three phase AC/AC converter is equivalent circuits combining current source rectifier and voltage source inverter connected by DC-link, see Fig. 1(b). Inverter stage has a standard three phases voltage source topology based on six switches $S_7$–$S_{12}$ and rectifier stage based on switches $S_1$–$S_6$ with the same topology. These two converters circuits have provided platform for analyze and derive several extends PWM strategies.
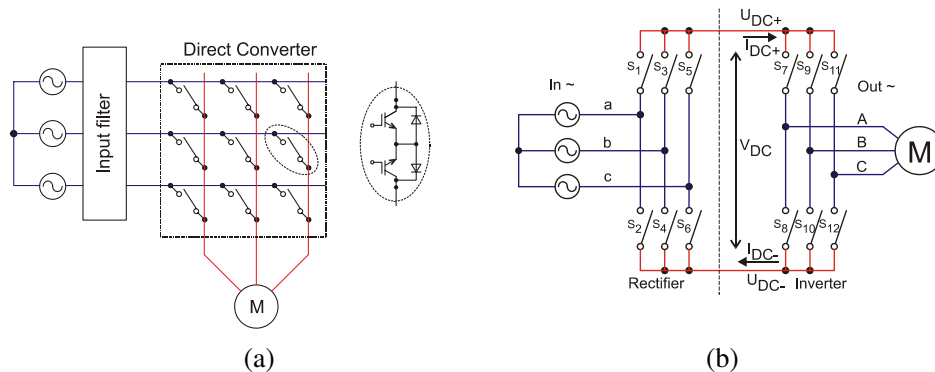


Figure 1: (a) Direct matrix converter and bidirectional switch. (b) Indirect virtual DC-link matrix converter.

## 2. DIRECT CONTROL OF MATRIX CONVERTER

In this case, the output waveforms are made from small pieces of input waveforms. This is done by selecting of the input phases in sequence for defined period of time. The sequence for each phase is the same [3]. The output voltages have inside some segments from three input voltages and input current includes segments from three output currents.

The idea of direct control of MC is based on mathematical expression (1), (2), which describes conditions between output and input side. With help of these equations is defined the duty cycle for each switch.

For output voltage:

$$\begin{bmatrix} v_A(t) \\ v_B(t) \\ v_C(t) \end{bmatrix} = \begin{bmatrix} m_{aA}(t) & m_{bA}(t) & m_{cA}(t) \\ m_{aB}(t) & m_{bB}(t) & m_{cB}(t) \\ m_{aC}(t) & m_{bC}(t) & m_{cC}(t) \end{bmatrix} \begin{bmatrix} v_a(t) \\ v_b(t) \\ v_c(t) \end{bmatrix} \tag{1}$$

For input current:

$$\begin{bmatrix} i_a(t) \\ i_b(t) \\ i_c(t) \end{bmatrix} = \begin{bmatrix} m_{aA}(t) & m_{aB}(t) & m_{aC}(t) \\ m_{bA}(t) & m_{bB}(t) & m_{bC}(t) \\ m_{cA}(t) & m_{cB}(t) & m_{cC}(t) \end{bmatrix} \begin{bmatrix} i_A(t) \\ i_B(t) \\ i_C(t) \end{bmatrix} \tag{2}$$

where $m_{aA}(t) = \frac{t_{aA}}{T_{seq}}$ and $t_{aA}$ are switch connected to the input phase and output phase A. This equation can be represented also in short form:

$$[v_o(t)] = [M(t)][v_I(t)] \quad [i_I(t)] = [M(t)]^T[i_o(t)] \tag{3}$$

where $[M(t)]$ is modulation matrix.

## 3. INDIRECT SPACE VECTOR CONTROL OF MATRIX CONVERTER

A principle of this control strategy is based on virtual DC-link in matrix converter. This DC-link is not physically presented, but the switches are divided to the virtual rectifier and virtual inverter on the Fig. 1(b). The indirect space vector modulation is used as a standard technique in the matrix converter modulation [5].

The basic idea of the indirect modulation technique is to decouple the control of the input current and the control of the output voltage. This is done by splitting the transfer function T for the matrix converter in (4) into the product of a rectifier and an inverter transfer function $\mathbf{T} = \mathbf{I} * \mathbf{R}$,

$$\begin{bmatrix} S_{aA} & S_{bA} & S_{cA} \\ S_{aB} & S_{bB} & S_{cB} \\ S_{aC} & S_{bC} & S_{cC} \end{bmatrix} = \begin{bmatrix} S_7 & S_8 \\ S_9 & S_{10} \\ S_{11} & S_{12} \end{bmatrix} \cdot \begin{bmatrix} S_1 & S_3 & S_5 \\ S_2 & S_4 & S_6 \end{bmatrix} \tag{4}$$

where the matrix $\mathbf{I}$ is the inverter transfer function and the matrix $\mathbf{R}$ is the rectifier transfer function. This way to model the matrix converter provides the basis to regard the matrix converter as a back-to-back PWM converter without any DC-link energy storage.

This means the well know space vector PWM strategies for voltage source inverter (VSI) or PWM rectifier can be applied to the matrix converter.

$$\begin{bmatrix} V_A \\ V_B \\ V_C \end{bmatrix} = \begin{bmatrix} S_7 & S_8 \\ S_9 & S_{10} \\ S_{11} & S_{12} \end{bmatrix} \cdot \begin{bmatrix} S_1 & S_3 & S_5 \\ S_2 & S_4 & S_6 \end{bmatrix} \cdot \begin{bmatrix} V_a \\ V_b \\ V_c \end{bmatrix} \tag{5}$$

The above transfer matrix exhibits that the output phases are compounded by the product and sum of the input phases through inverter switches $S_7$–$S_{12}$ and rectifier switches $S_1$–$S_6$.

If the equivalent circuit is seen from the inverter output phase A, two switches $S_7$ and $S_8$ of phase A from half bridge are directly connected to input phases a, b and c through six rectifiers switches $S_1$–$S_6$. The Fig. 2 shows how the switch set of equivalent circuit is transformed into the relevant switch set of the nine bidirectional switches of matrix converter in phase A. The Fig. 2 also gives a basic idea that the duty cycles of the matrix converter branch can be derived by multiplying the duty cycles of the corresponding rectifier and inverter switches in the equivalent circuit [4].

Therefore, the indirect modulation technique enables well-known space vector PWM to be applied for a rectifier as well as an inverter stage. The switches of inverter can have only eight allowed

combinations, because the output must not be short though three half bridges. These eight combinations can be divided into six active nonzero output voltage vectors $V_1 \sim V_6$ and two zero output voltage vectors $V_0$ show in Fig. 3(a).

The voltage space vector $V_1[100]$ indicates that output phase $V_A$ is connected to positive rail $V_{DC+}$ and the other phases $V_B$, $V_C$ are connected to negative rail $V_{DC-}$.

For virtual rectifier is allowed nine switching combinations to avoid an open circuit in rectifier. These nine combinations are divided into six active nonzero input current vectors $I_1 \sim I_6$ and three zero input current vectors $I_0$ (Fig. 3(a)). Current $I_1$ (ab) indicates that input phase a is connected to the positive rail of the virtual DC-link $V_{DC+}$ and input phase b is connected to the negative rail $V_{DC-}$ (Fig. 3(b)).
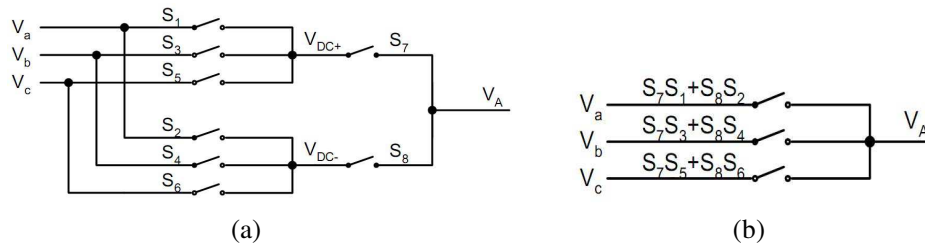


Figure 2: Transformation from equivalent circuit to phase A in matrix converter.
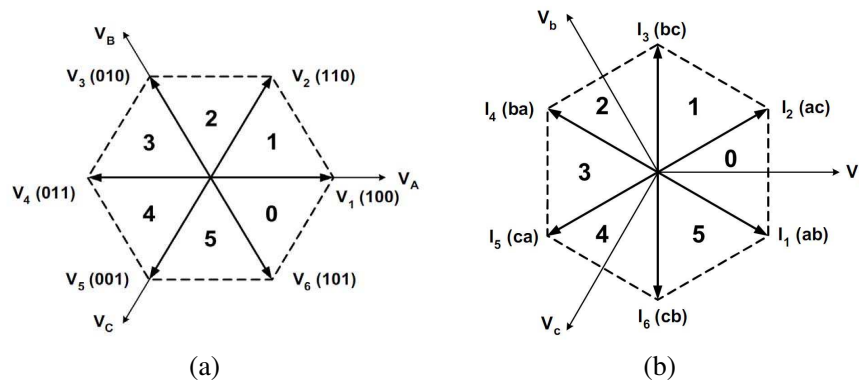


Figure 3: (a) Hexagon of inverter voltage. (b) Hexagon of rectifier current.
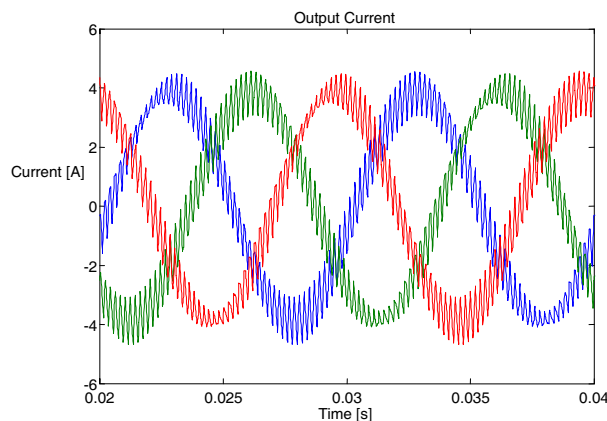


Figure 4: Direct control of matrix converter simulation results.
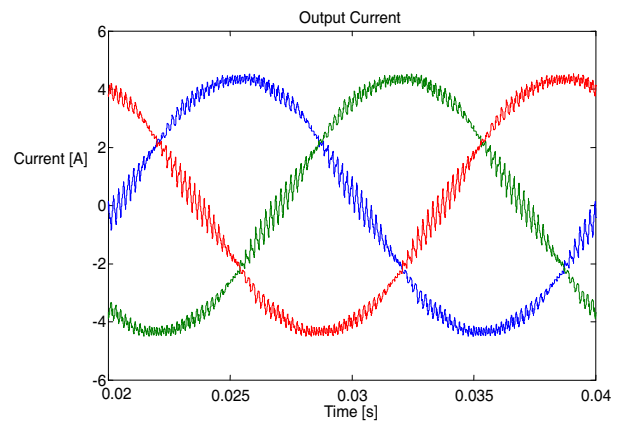
Figure 5: Indirect control of matrix converter simulation results.
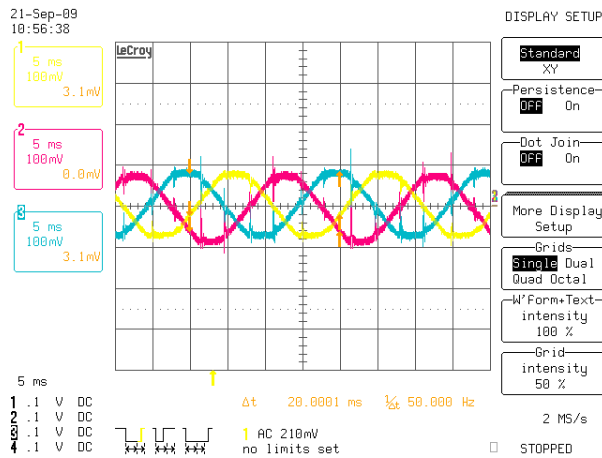
Figure 6: Direct control of matrix converter experimental results.
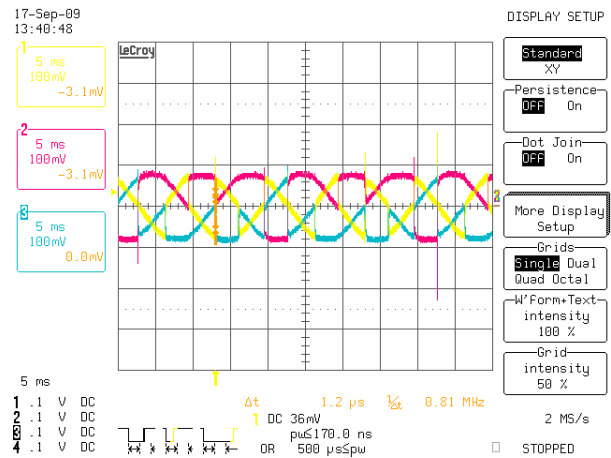


Figure 7: Indirect control of matrix converter experimental results.

## 4. SIMULATION AND EXPERIMENTAL RESULTS

The control of matrix converter is simulated using the Matlab-Simulink package. Difference between direct and indirect control is, that direct control is clearly mathematically based on equation and indirect control is based on predefined rules from table. All simulations were calculated for source voltage 230 V, 50 Hz, load resistance $R = 25\,\Omega$, load inductance $L = 0,005\,$H.

## 5. CONCLUSIONS

Working principle of the matrix converter controlled with the direct transfer function approach and basic from indirect space vector control has been presented. Both control methods were explained and used to get the block diagram for the simulation. The model reproduces a very good waveform on output side. In addition, it can be observed that the matrix converter can generate output frequencies that are not restricted by the source frequency. If is used drive system with MC, then the drive system is capable to operate in all four-quadrant regions. The simulation results agree with the theoretical expectations, that the direct converters are able to create sinusoidal waveforms on output side, which is necessary for good working condition of drive systems.

## ACKNOWLEDGMENT

## REFERENCES

1. Lettl, J., "Matrix converter induction motor drive," *Proceedings of 12th International Power Electronics and Motion Control Conference*, 787–792, Maribor, 2006.
2. Brandstetter, P., T. Krecek, P. Rech, and O. Francik, "Facilities for a digital signals processing of AC drives," *Proceedings of International Conference on Applied Electronics*, 61–64, Pilsen, Czech Republic, 2009.
3. Alesina, A. and M. Venturini, "Analysis and design of optimum-amplitude nine-switch direct AC-AC converters," *IEEE Transactions on Power Electronics*, Vol. 4, No. 1, 1989.
4. Wheeler, P., J. Rodriguez, J. Clare, L. Empringham, and A. Weinstein, "Matrix converters: A technology review," *IEEE Transactions on Power Electronics*, Vol. 49, No. 2, 2002.
5. Wheeler, P., J. C. Clare, and L. Empringham, "A vector controlled MCT matrix converter induction motor drive with minimized commutation times and enhanced waveform quality," *IEEE Industrial Application Society Annual Meeting*, Pittsburgh, 2002.
6. Clare, J. and P. Wheeler, "Introduction to matrix introduction to matrix converter technology," *IEE Seminar*, 2003.

# Design of a High Speed Universal Motor for Organic Agriculture Applications

**Hanzhou Liu[1], David Woodburn[1], Shaohua Lin[1], Thomas X. Wu[1],**
**Jianjian Wei[2], and Keqiang Cao[3]**

[1]School of Electrical Engineering and Computer Science, University of Central Florida
Orlando, FL 32816, USA
[2]Beijing TEPEC Technology Corporation, Beijing 100086, China
[3]Agriculture University of Hebei, Baoding, Hebei 071001, China

**Abstract**— We report on the design of a high-speed and highly efficient universal motor for organic agriculture applications. A motor with the following specifications is designed: 1 kW input power, 220 V input voltage, 20 krpm rotating speed, and 77% efficiency. Firstly, we propose a two pole structure with twenty two slots on the rotor. Secondly, we analyze the structure using magnetic circuit analysis and derive a set of design equations, from which we can obtain initial dimensions. Thirdly, we input our fundamental design into Ansoft RMxprt and then optimize the dimensions to meet the design goals. Finally, we use Ansoft Maxwell to further optimize the design.

## 1. INTRODUCTION

Organic agriculture is an ecological production system that enhances the biodiversity and soil biological activity. It insists on using the minimum off-farm inputs to improve the ecological harmony. In addition, the primary goal is to reduce the pollution to the soil, plants and people. Recently, we find that pests can be effectively controlled by spraying using a high-voltage electrostatic sprayer. Instead of using pesticide, a natural product derived from lignite is used so that this novel pest control is environmental friendly. Therefore, the benefit is that there would be zero pollution to any agricultural products which have been sprayed by this electrostatic sprayer system. The universal motor would be the key part of the sprayer system that pumps liquid out of a container, the liquid will kill the pests without polluting the farm crops. Therefore, the size of this universal motor should be tightly constrained in order to make the motor easy to carry. For the design specifications mentioned above, we propose a systematic methodology for the design of a universal motor. Firstly, we propose a two pole structure with twenty two slots on the rotor. Secondly, we analyze the structure using magnetic circuit analysis and derive a set of design equations, from which we can obtain initial dimensions. Thirdly, we input our fundamental design into Ansoft RMxprt and then optimize the dimensions to meet the design goals. Finally, we use Ansoft Maxwell to further check and optimize the design. Besides an electrical design, we also need to consider thermal issue, which is choosing suitable cooling methods in order to keep the maximum interior temperature under control. For this specific universal motor, the stator is equipped with two main magnetic poles with the excitation winding on each pole to produce the main stator magnetic field [1]. The rotor is equipped with the distributed armature winding connected to a commutator that rotates with the rotor simultaneously. The power source connects to the stator winding, and the current is going through the rotor winding via two carbon brushes [2]. It must be emphasized that a two-pole machine usually has relatively long magnetic field paths through the stator yoke body. Therefore, it is necessary that the stator yoke have sufficient cross-sectional area to allow for a low flux density, and the goal of this design is not to exceed 1.8 T on average.

## 2. KEY STEPS OF THE INITIAL DESIGN

In universal motor design, the multiplication of $D_a^2$ and $L_a$ divided by torque rating is a constant value, $V_T$.

$$\frac{D_a^2 L_a}{T} = V_T \tag{1}$$

where $D_a$ is the diameter of the motor and $L_a$ is the length of the rotor. For example, if we use self-ventilated cooling, then the value of $V_T$ should be approximately $2.9 \, inch^3/(ft \cdot lb)$ [3]. $T$ is the rated torque generated by the induced voltage in the armature.

Torque $T$ in (1) is calculated as

$$T = \frac{V_A I_A}{\omega_m(1 - \beta)} \tag{2}$$

where $V_A$ and $I_A$ represent the induced voltage on the armature and the armature current, respectively. $\beta$ represents the loss, based on our experience, loss is usually selected as 3% [4]. $\omega_m$ represents angular mechanical frequency defined as

$$\omega_m = 2\pi f_m \tag{3}$$

The number of turns per coil $N_c$ can be calculated from

$$N_c = \frac{V_A a}{B_{ag} L_a D_a \omega_m N_r} \tag{4}$$

where $a$ is the number of parallel paths. $B_{ag}$ is the air-gap flux density [5]. $N_r$ is the number of total slots. $V_A$ is about 99% of the terminal voltage, which means the resistances of the field windings and armature windings are fairly small; therefore, we can neglect the voltage drop of these resistances. Then we can decide the number of turns to generate the required induce voltage, $V_A$. Next, the number of field winding turns can be decided as follows:

$$N_f = 2R_{ag}\phi_{sg}/I_f \tag{5}$$

$$R_{ag} = L_a \frac{\pi \left(\frac{Da}{2}\right)}{\mu_0 g_{eff}} em, \tag{6}$$

where $I_f$ is the field winding current, $R_{ag}$ is the air-gap resistance, $g_{eff}$ is the effective air-gap length, which should be a little bit larger than the physical air-gap length. $em$ represents the embrace, which can be any value between 0.7 and 0.8. The DC motor model can be converted to an AC model by a scaling ratio of the DC and AC voltages and a ratio of the electrical and mechanical frequencies [6].
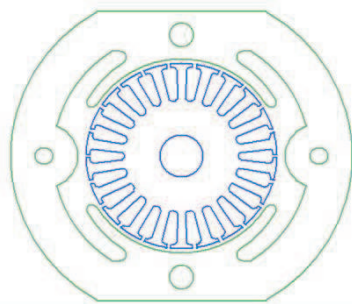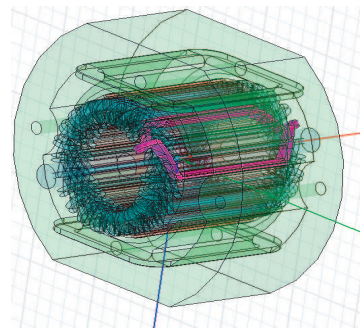


Figure 1: 2D construction.
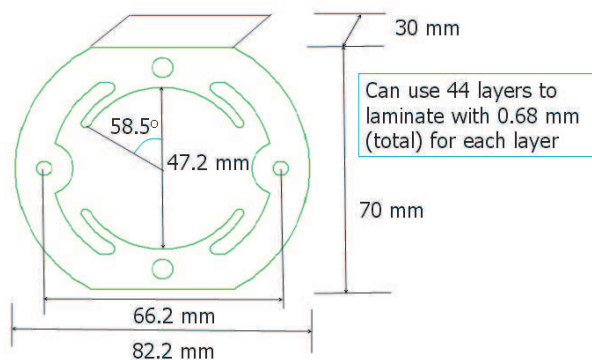


Figure 2: 3D construction.
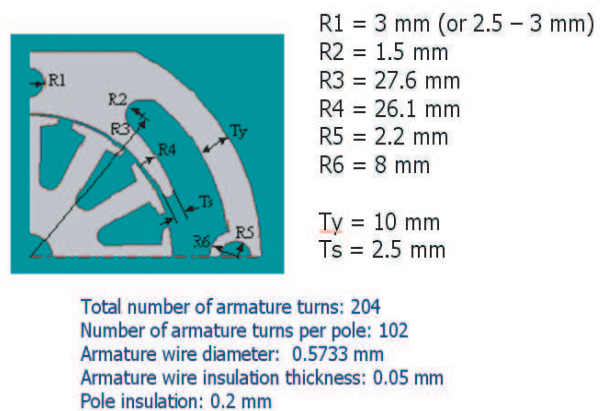


Figure 3: Overall stator dimensions.



Figure 4: Stator pole dimensions.

## 3. RESULTS AND DISCUSSIONS

From the above initial design, we can obtain the geometry of the motor. And then we can input the motor geometry into Ansoft RMxprt, we can obtain the physical construction of the motor. Figure 1 is a 2-dimensional view of the motor designed. It shows the cross-sectional view of the motor, including the stator, rotor with hollow shaft, and all the slots. Figures 2 is a 3-dimensional model. It clearly shows the various internal parts. In the middle, are the rotor windings, which are marked with a dark green color. For clarity, one of the rotor windings is marked with a purple color.

The dimensions are shown in Figure 3, which includes stator inner diameter, outer diameter, length, etc. Because of symmetry, Figure 4 shows only half of a stator pole. Some dimensions of the pole are listed as well. The number of armature turns, turns per pole, wire size, and insulation information come from the RMxprt results data sheet are also shown in Figure 4.

Figure 5 shows the general dimensions of the rotor. Figure 6 shows the dimensions of one slot with the selection of rotor type 4 in RMxprt. Figure 7 shows that the maximum efficiency, approximately 77%, occurs when the rotation speed is around 20 krpm.

Figure 8 shows when the speed gets 20 krpm, the input power value is 1000 watts, which is the exact design requirement. By applying FEA (finite element analysis), a 2D mesh is generated as shown below in Figure 9. With the input power applied, the flux density is simulated as shown in Figure 10. This figure clearly shows that the magnetic flux density's highest magnitude occurs at the stator pole area. And, of course, it will not get saturated.
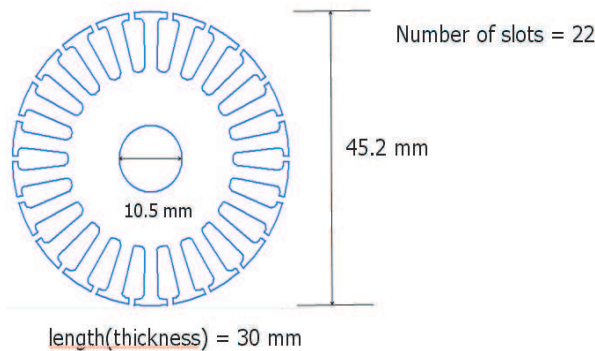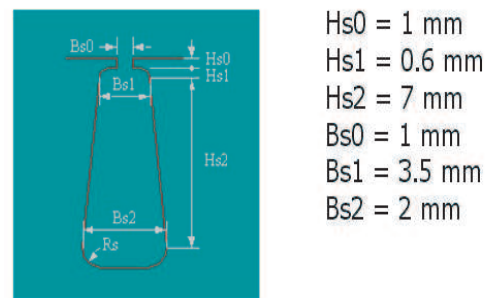


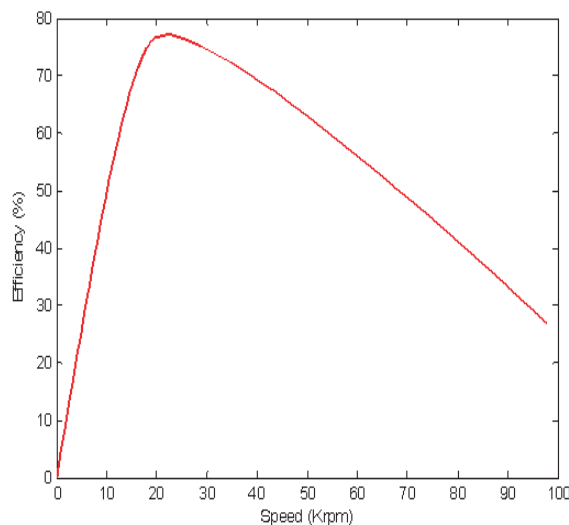Figure 5: Rotor and slots shape.



Figure 6: Slot dimensions.



Figure 7: RMxprt simulation of efficiency vs. speed.
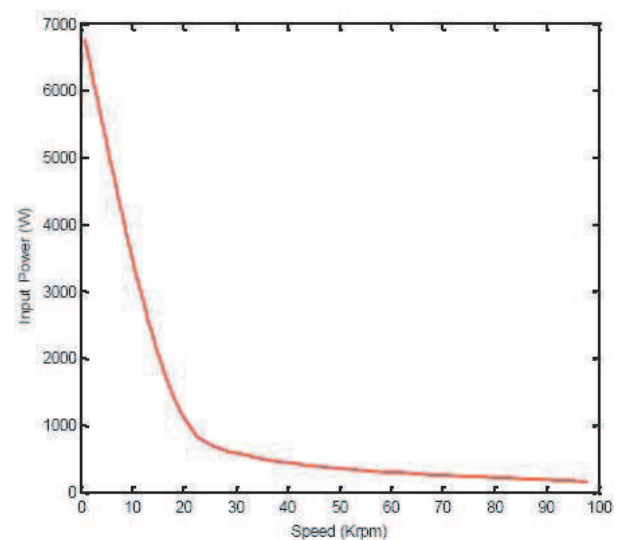


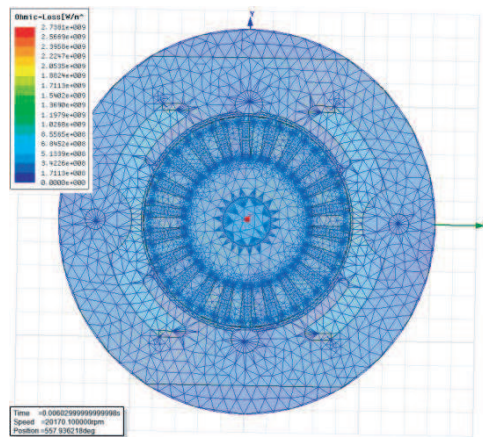Figure 8: RMxprt simulation of input power vs. speed.
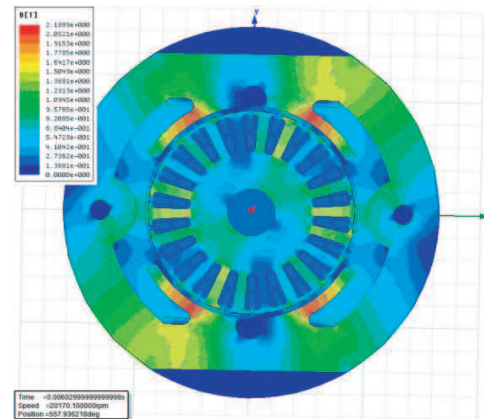
Figure 9: FEA mesh plot.



Figure 10: Flux density magnitude.

## 4. CONCLUSION

In this paper, we have introduced the development of a universal motor and the importance of designing this motor especially for organic agriculture purposes. Furthermore, the basic procedure of designing a universal motor has been summarized. In addition, we provide the simulation results, from which we have a clear view of the whole motor design, with detailed dimensions. We have also shown the results of the transient analysis. The design meets the requirements. Eventually, the universal motor and other components will make up the whole sprayer system for organic agriculture applications.

## REFERENCES

1. Chapman, S. J., *Electric Machinery Fundamentals*, 4th Edition, McGraw-Hill, 2005.
2. Sen, P. C., *Principles of Electric Machinery and Power Electronics*, 2th Edition, John Wiley & Sons, 1997.
3. Cathey, J. J., *Electric Machines Analysis and Design Applying Matlab*, McGraw-Hill, 2001.
4. Chapman, S. J., *Electric Machinery and Power System*, McGraw-Hill, 2002.
5. Hubert, C. L., *Electric Machines*, 2nd Edition, Prentice Hall, 2002.
6. Beaty, H. W. and J. L. Kirtley. Jr., *Electric Motor Handbook*, McGraw-Hill, 1998.

# Shielded and Unshielded Three-conductor Transmission Lines: Modeling and Crosstalk Performance

**Mnaouer Kachout**, **Jamel Bel Hadj Tahar**, and **Fethi Choubani**

Research Unit Systems of Telecommunications (6'Tel) SUP'COM, Tunisia

**Abstract**— In this paper, we study the effect of shielding on the crosstalk between three-conductor transmission lines. The main idea of this work is to demonstrate that shielded lines can be more compact with best performance in terms of crosstalk than unshielded conductors. We demonstrate that by using shielded conductor we can reduce crosstalk with minimum spacing between conductors. We present Π-T hybrid electric equivalent model for three-conductor transmission lines. This model allows us to evaluate near-end crosstalk performance between conductors. Crosstalk obtained by shielded lines separated by distance $d$ is as low as these obtained without shield separated by $20d$.

## 1. INTRODUCTION

In multiconductor transmission lines (MTL) system [1], transient surge in any one of the conductors (generator) causes crosstalk in other adjacent conductors (receptors). It's a common electromagnetic interference (EMI) phenomenon due to electromagnetic coupling between the conductors [2]. Coupling or crosstalk refers to any phenomenon by which a signal transmitted on one circuit or channel of a transmission system creates an undesired effect in another circuit or channel [3]. Crosstalk is usually caused by undesired capacitive, inductive, or conductive coupling from one circuit, part of a circuit, or channel, to another. At present, flat cables for the under-carpet use have a shielded structure to improve crosstalk characteristics [4]. However, unshielded cables are advantageous when a very thin structure is desired [5].

In this paper, we study the crosstalk between three-conductor transmission lines. The objective of this work is to compare crosstalk performance between shielded and unshielded conductors. In other words, we demonstrate that shielded line gives best performance in terms of crosstalk with minimum spacing between wires. We use ribbon cable with circular cylindrical section immersed in a homogeneous medium. Ribbon cables are frequently using to interconnect electronic systems, such as computers.

This paper is organized as follows. First, we present Π-T hybrid electric equivalent model for three conductor transmission lines. At this stage, we are interested in calculating various per-unit-length parameters for unshielded conductors. This model allows us to calculate crosstalk between unshielded conductors. We calculate near-end crosstalk using $S$ parameters. Secondly, we present theoretical foundation to calculate near-end crosstalk between shielded conductors. Finally, to evaluate crosstalk performance, we make same comparisons between shielded and unshielded conductors by varying same parameters, such as, frequency, radius shield and distance between conductors. To do so near-end crosstalk versus frequency and shield radius is evaluated. Then, compared with near-end crosstalk for unshielded conductors with varying distance $d$.

## 2. NEAR-END CROSSTALK FOR THREE-CONDUCTOR TRANSMISSION LINES

A three-conductor transmission lines structure for unshielded and shielded conductor are sketched in Fig. 1(a) and Fig. 1(b). All conductors have the same length $l_w$.

A voltage source $V_S(t)$, with internal resistance $R_S$, is connected to a load $R_L$ via both a generator conductor and reference conductor. A receptor circuit shares the same reference conductor and connects two terminations $R_{NE}$ and $R_{FE}$ by a receptor conductor. We will use this configuration to calculate near-end crosstalk for shield and unshielded conductors.

### 2.1. Near-end Crosstalk for Unshielded Conductors

Π-T hybrid electric equivalent model is depicted in Fig. 2. This model allows us to calculate coupling between unshielded conductors.

In this model, $L_m = l_m * l_w$ represents the mutual inductance between conductors, where $l_m$ is the per-unit length mutual inductance between generator and receptor conductors. $L_g = l_g * l_w$ is the self-inductance of generator conductor, where $l_g$ is the per-unit length inductance of the generator conductor. $L_r = l_r * l_w$ is the self-inductance of the receptor conductor, where $l_r$ is the
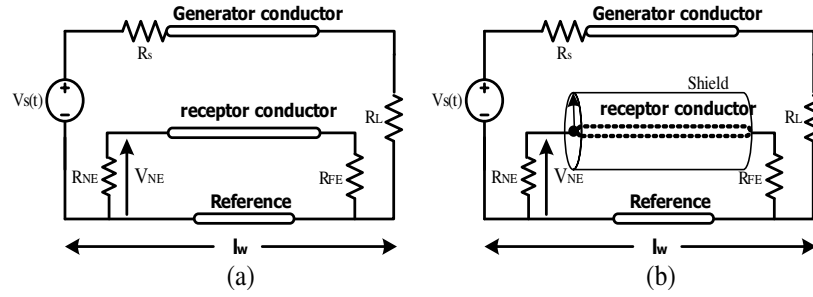
Figure 1: Three-conductor transmission lines illustrating crosstalk, (a) unshielded conductors, (b) receptor conductor is shield.
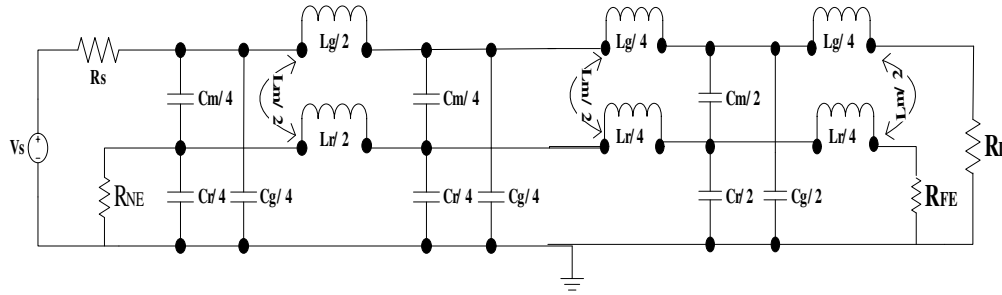


Figure 2: Π-T hybrid electric equivalent model.

per-unit length inductance of the receptor conductor. $C_m = c_m * l_w$ is the mutual capacitance between conductors, where $c_m$ is the per-unit length mutual capacitance between two conductors. $C_r = c_r * l_w$ is the capacitance of receptor conductor, where $c_r$ is the per-unit length capacitance of the receptor conductor. $C_g = c_g * l_w$ is the capacitance of generator conductor, where $c_g$ is the per-unit length capacitance of the generator conductor.

In order to calculate the near-end crosstalk between unshielded conductors depicted in Fig. 1(a), we deal first with various per-unit-length parameters. Conductors having cross sections that are circular cylindrical are referred to as wires. These are some of the few conductor types for which closed-form equations for the per-unit-length parameters can be obtained. The per-unit length inductance parameter matrix [6] is:

$$L = \begin{bmatrix} l_r & l_m \\ l_m & l_g \end{bmatrix} \tag{1}$$

where

$$l_m = \frac{\mu}{2\pi} \ln\left(\frac{d}{r_w}\right) \quad l_r = \frac{\mu}{\pi} \ln\left(\frac{d}{r_w}\right) \quad l_g = \frac{\mu}{\pi} \ln\left(\frac{4d}{r_w}\right) \tag{2}$$

The per-unit length capacitance parameter matrix [7] is:

$$C = \begin{bmatrix} C_g + C_m & -C_m \\ -C_m & C_r + C_m \end{bmatrix} \tag{3}$$

The relation between the per-unit length capacitance and inductance parameters matrix is given in Equation (4).

$$C = \mu \varepsilon L^{-1} \tag{4}$$

The near-end crosstalk can be viewed as a transfer function between the input $V_S(t)$ and the outputs $V_{NE}$ [8]. These transfer functions can be obtained by factoring out $V_S(t)$ and $j\omega$ to give:

$$\frac{\hat{V}_{NE}}{\hat{V}_S} = j\omega\left(\frac{R_{NE}}{R_{NE} + R_{FE}} * \frac{l_m * l_w}{R_S + R_L} + \frac{R_{NE} * R_{FE}}{R_{NE} + R_{FE}} \frac{R_L * c_m * l_w}{R_S + R_L}\right) + \frac{R_{NE}}{R_{NE} + R_{FE}} * \frac{R_0}{R_S + R_L} \tag{5}$$

where

$$\omega = 2\pi f \tag{6}$$

## 2.2. Near-end Crosstalk for Shielded Conductors

In order to illustrate the effect of shielded wire on the crosstalk, we use an infinite ground plane as a reference conductor. The cross-sectional dimension with ground plane reference conductor is presented in Fig. 3. Other choices of reference conductors such as another wire will lead the same conclusions.

The near-end crosstalk is computed as the sum of an inductive coupling due to the mutual inductances and capacitive coupling due to mutual capacitances [9]. The near-end crosstalk is given by:

$$\frac{V_{NE}}{V_S} = jw\left[\left(\frac{R_{NE}}{R_{NE}+R_{FE}}*\frac{C_{RS}C_{GS}}{C_{RS}+C_{GS}}*\frac{R_L}{R_S+R_L}\right)+\left(\frac{R_{NE}}{R_{NE}+R_{FE}}*\frac{L_{GR}}{R_S+R_L}*\frac{R_H}{R_{SH}+jwL_{SH}}\right)\right] \quad (7)$$

In Equation (7), $R_H = l_w * r_h$ is the shield resistance, where $r_h$ is the per-unit length resistance of the shield depends on the construction technique. $L_{GR} = l_w * l_{gr}$ where $l_{gr}$ is the per-unit length mutual inductance parameters between generator and receptor conductors. $L_{SH} = l_w * l_{sh}$ where $l_{sh}$ is the per-unit length inductance parameter of the shield conductor. $C_{RS} = l_w * c_{rs}$ where $c_{rs}$ is the per-unit length mutual inductance parameter between receptor conductor and the shield. $C_{GS} = l_w * c_{gs}$ where $c_{gs}$ is the per-unit length mutual capacitance parameter between generator conductor and the shield. The shield thickness is $t_{sh}$.

The per-unit length inductance parameter matrix is determined by:

$$L = \begin{bmatrix} l_g & l_{gr} \\ l_{gr} & l_{sh} \end{bmatrix} \quad (8)$$

where

$$l_g = \frac{\mu}{2\pi}\ln\left(\frac{2*h}{r_w}\right) \quad l_{gr} = \frac{\mu}{\pi}\ln\left(\frac{2*h}{r_w}\right) \quad l_{sh} = \frac{\mu}{2\pi}\ln\left(\frac{2h}{r_{sh}+t_{sh}}\right) \quad (9)$$

The capacitance matrix specified in Equation (10) can be found using the reciprocal relationship for conductors in a homogeneous medium.

$$C = \begin{bmatrix} c_g + c_{gs} & -c_{gs} \\ -c_{gs} & c_s + c_{gs} \end{bmatrix} = \mu\varepsilon\begin{bmatrix} l_g & l_{gr} \\ l_{gr} & l_{sh} \end{bmatrix}^{-1} \quad (10)$$

The per-unit length mutual inductance parameter between receptor conductor and the shield $c_{rs}$ is set in Equation (11). The dielectric in the interior medium of the shield is $\varepsilon_r$.

$$c_{gr} = \frac{2\pi\varepsilon_r\varepsilon_0}{\ln\left(\frac{r_{sh}}{r_w}\right)} \quad (11)$$

## 3. NEAR-END CROSSTALK PERFORMANCE

In previous section, we calculated the near-end crosstalk for unshielded and shielded conductors. The aim of this study is to show that shielded conductors perform better than unshielded one. In
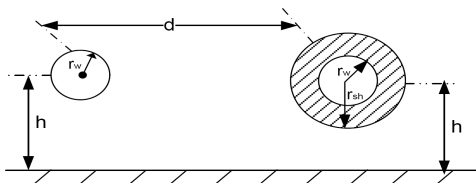


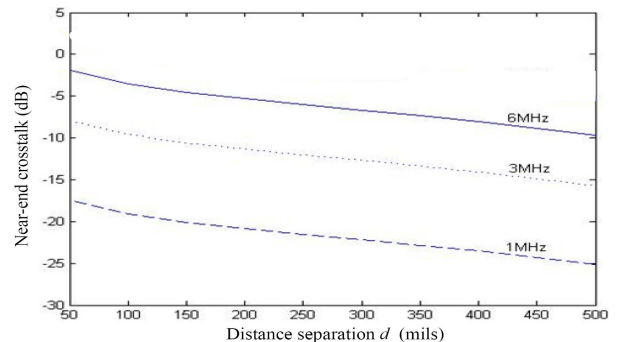Figure 3: Cross-sectional dimension where the reference conductor is a ground plane.



Figure 4: Near-end crosstalk versus distance between unshielded conductors.

order to reach this objective, in this section, we compare near-end crosstalk performance versus shielded and unshielded conductors by varying many parameters, such as, frequency, shield radius $r_{sh}$ and distance $d$. In our case, three conductors, shown in Fig. 1, assumed to be immersed in a homogeneous medium ($\mu = \mu_0$) have same radii $r_w = 15$ mils and same length $l_w = 39370$ mils.

Figure 4 presents the variation of near-end crosstalk versus separation distance between unshielded conductors, shown in Fig. 1(a), for different frequency values.

Near-end crosstalk reduces for more than 5 dB when separation distance increases from 50 mils to 500 mils. Crosstalk reduction is due to a decrease of mutual inductive and capacitive coupling between unshielded conductors. Furthermore, when frequency increases from 1 MHz to 6 MHz, coupling increases too from $-17$ dB to $-3$ dB with distance separation equal to 50 mils. Hence, to reduce crosstalk between conductors we should space them. However, the farther the conductors are, the larger the systems became.

Let's now study the effect of shield radius on crosstalk. Considering the configuration in Fig. 1(b), where we use shield receptor conductor with shield radius $r_{sh}$. Fig. 5 illustrates the near-end crosstalk variation versus frequency for different values of shield radius.

When shield radius increases from $r_{sh} = 45$ mils to $r_{sh} = 360$ mils, near-end crosstalk between conductors increases by more than 5 dB. Therefore, reducing crosstalk using shielded conductors make multi-conductor transmission lines systems more compact. To put side by side the crosstalk performance of two configurations sketched in Fig. 1, we compare in Fig. 6 the near-end crosstalk of shielded conductor to unshielded conductors by changing the distance separation $d$.

Near-end crosstalk for unshielded conductors separated by distance $d = 50$ mils increases from $-20$ dB to $-2$ dB when frequency increases from 1 MHz to 10 MHz. Best near-end crosstalk performance is obtained using shielded receptor conductor with the same distance separation $d = 50$ mils. Moreover, near-end crosstalk performance increases when we space out unshielded conductors. Obtained results presented in Fig. 6 show that unshielded conductors separated by $d = 1000$ mils give the same near-end crosstalk performance as shield conductors separated by $d = 50$ mils.
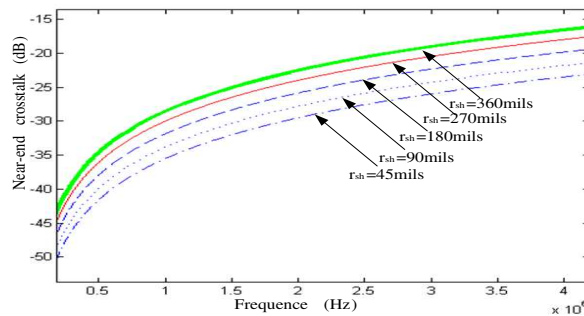


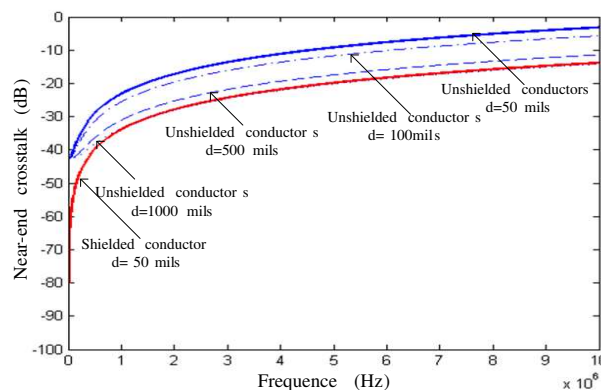Figure 5: Near-end Crosstalk versus frequency for different radius of the shield.



Figure 6: Near-end crosstalk comparison between shield and unshielded conductors.

## 4. CONCLUSION

In this paper, we have studied the effect of shielding on near-end crosstalk performance for three-conductor transmission lines. Π-T hybrid electrical model of three conductor transmission structure has been proposed and used to evaluate near-end crosstalk for unshielded conductors. Also, theoretical foundation to calculate crosstalk for shielded conductors was detailed. Obtained results show that shield reduces near-end crosstalk and improves the compacity by a factor of 20.

**REFERENCES**

1. Paul, C. R., *Analysis of Multiconductor Transmission Lines*, John Wiley, 2007.
2. Roy, A., S. Ghosh, and A. Chakraborty, "Simple crosstalk model of three wires to predict near-end and far-end crosstalk in EMI/EMC environment to facilitate EMI/EMC modeling," *Progress In Electromagnetics Research B*, Vol. 8, 43–58, 2008.
3. Paul, C. R., "A brief history of work in transmission lines for EMC applications," *IEEE Transactions on Electromagnetic Compatibility*, Vol. 49, No. 2, 237–252, 2007.
4. Clements, J. C., "Computation of the capacitance matrix for systems of dielectric-coated cylindrical conductors," *IEEE Transactions on Electromagnetic Compatibility*, Vol. 17, No. 4, 238–248, 1975.
5. Levin, B. M., "Calculation of electrical parameters of two-wire lines in multiconductor cables," *IEEE Transactions on Electromagnetic Compatibility*, Vol. 50, No. 3, 697–703, 2008.
6. Rolfes, L. and B. Schiek, "Methods for the calibrated measurement of the scattering parameters of planar multi-port devices," *Adv. Radio Sci.*, Vol. 5, 439–445, 2007.
7. Servel, G., D. Deschacht, and F. Huret, "Inductance effect in crosstalk prediction," *IEEE Transactions on Advanced Packaging*, Vol. 25, No. 3, 340–347, 2002.
8. McClellan, K. J., T. S. Wailes, Jr., and P. D. Franzon, "Simulation vs calculation of crosstalk," *IEEE 6th Topical Meeting*, Vol. 43, No. 2, 131–134, 2002.
9. Zhang, J. M. and E. G. Friedman, "Effect of shield insertion on reducing crosstalk noise between coupled interconnects," *IEEE International Symposium on Circuits and Systems*, Vol. 5, 529–532, 2004.

# Side Effect Characterization of EBG Structures in Microstrip Patch Antenna

**M. Fallah**, **F. H. Kashani**, and **S. H. Mohseni**

Iran University of Science and Technology (IUST), Tehran, Iran

**Abstract**— The unwanted side effect of EBG structures when integrated with microstrip antenna is investigated in this paper. The main goal of using EBG structures in microstrip antenna is to achieve better gain and efficiency, lower side-lobes and back-lobes levels, and better isolations among array elements, by suppressing surface wave modes. The two dominating side effects may be named as parasitic loading effect and cavity effect. The parasitic loading effect of EBG structure causes the multi resonance antenna resulting in larger bandwidth. Cavity effect on the other hand, is due to reflecting energy from EBG toward antenna and results in a larger Q value and so decreasing the bandwidth. These two side effects are characterized in this work and the EBG structure parameters and number of EBG rows is related to these effects. The design parameters of EBG structures can be managed such that the parasitic effect of EBG structure can be the dominating effect and consequently results in larger bandwidth. This parametric study is implemented in to a microstrip antenna integrated with conventional mushroom-like EBG structure in $E$ plane. According to our results, there is an optimal design for EBG unit cell parameters and number of rows so that in addition to surface wave reduction, a larger bandwidth is achieved.

## 1. INTRODUCTION

With the rapid growth of wireless markets, microstrip antennas became more attractive in antenna community. These antennas are low-profile, low cost and light weight. However, Surface waves are a major drawback for this type of antenna as they lower the antenna efficiency. A narrow impedance bandwidth is another limitation of patch antennas. Two techniques have been used to suppress surface wave propagation, namely micromachining [1, 2] and periodic structures called the electromagnetic band gap (EBG) structures [3–6]. In microstrip antennas, EBG structures surrounding patch element to suppress surface waves to achieve better side lobe and back lobe levels and increased radiation efficiency. It has been shown in article [7] that, placing EBG cells in $E$-plane is sufficient for surface wave reduction and it is not required to have $H$-plane EBG cells. This EBG structures is used in microstrip array antennas between radiating array elements in $E$-plane to reduce mutual coupling between them by suppressing surface waves. However, the effects of EBG structures surrounding the antenna can be considered as two effect, namely parasitic loading effect and cavity effect. The parasitic loading effect increases the bandwidth, whereas the cavity effect decreases the bandwidth. The EBG cells located in close proximity of the radiating edges of the antenna elements provide the parasitic loading and thereby improved bandwidth [8]. On the other hand, the EBG structures also reflect back a part of the energy that propagates along the substrate of the antenna, thus acting as reflecting walls around the antenna and thereby the cavity effect. With few rows of EBG structures, less energy is reflected back and the parasitic effect becomes dominant. This leads to the significant improvement in the bandwidths. As the number of rows is increased, more of the energy propagating along the substrate is reflected back and the cavity effect becomes dominant. This in turn increase the Q-factor of the cavity formed by the EBG structures surrounding the antenna and decreases the bandwidths of the antenna. On the other hand, front to back ratio (FBR) of the antenna increases with the number of EBG rows surrounding the antenna, as expected, due to the suppression of surface waves.

In this paper, in a parametric analysis, it is shown that, there are an optimum number of EBG rows such that in addition to surface wave suppression, an increased bandwidth can be achieved while a minimum size of antenna structure is obtained.

## 2. DESIGN AND PARAMETRIC ANALYSIS OF THE MICROSTRIP PATCH ANTENNA INTEGRATED WITH EBG STRUCTURE

The antenna under investigation is a microstrip patch antenna integrated with one row of conventional mushroom-like EBG patches located half wavelength (15 mm) far from antenna radiating

edges in $E$-plane with resonant frequency at 10 GHz (Fig. 1). EBG structure designed so that, resonant frequency of antenna locates in band gap region of this structure. Fig. 2 showed Dispersion Diagram (DD) of designed EBG structure.

As shown in Fig. 2, resonant frequency of patch antenna (10 GHz) fall in band gap region of this EBG structure and no substrate mode (surface mode) propagate in this frequency. Fig. 3 is shown return loss of antenna with and without EBG structure, and Fig. 4 shown $E$-plane pattern of these two antennas. As shown in Fig. 3, as expected, bandwidth of antenna with one row EBG in $E$-plane is grater than antenna without EBG, due to domination of parasitic effects. Also, surface
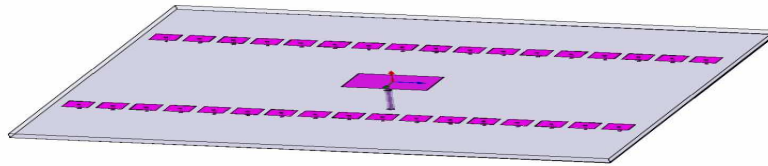


Figure 1: Microstrip patch antenna with resonant frequency at 10 GHz fabricated on $80 \times 80$ mm Aleron CuClad 250 GX(tm) substrate. Substrate parameters are: $\varepsilon_r = 2.5$, dielectric loss tangent = 0.001, dielectric thickness $h = 1.588$ mm. Dimensions of radiating patch element are: patch width $= W = 11.34$ mm, and patch length $= L = 8.3$ mm. This antenna feeds by probe that is feed 1.7 mm far from edge of the patch to achieve impedance matching in resonant frequency. BEG unit cell parameters are: (We (EBG patch width) $= 3.5$ mm, $g$ (gap between adjacent patches) $= 1$ mm, $r$ (radius of via holes) $= 0.2$ mm.
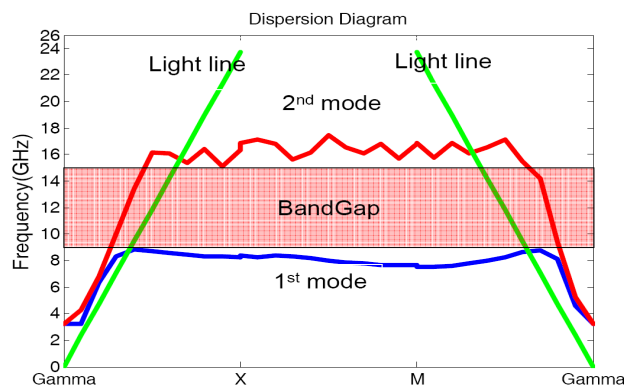


Figure 2: Dispersion diagram of mushroom-like EBG structure showed in Fig. 1. Frequency band-gap parameters are: $f_l =$ lower band-gap frequency $= 8.84$ GHz, $f_u =$ Upper band-gap frequency $= 15.33$ GHz, $f_0 =$ band gap center frequency $= 12.085$ GHz, band gap $= 6.49$ GHz).
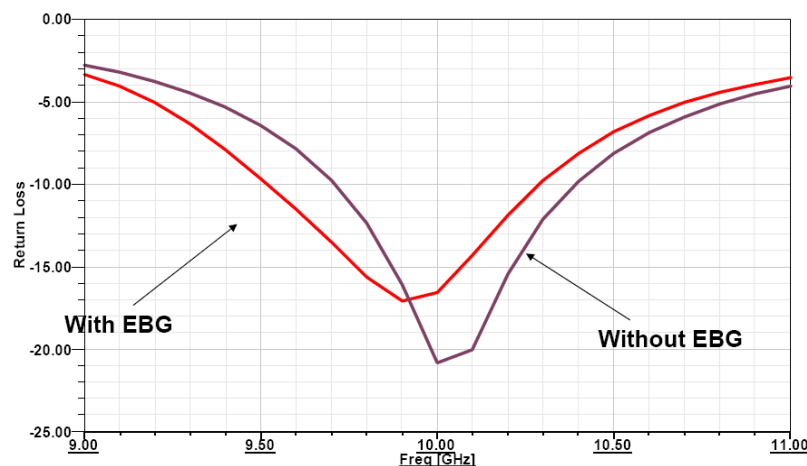


Figure 3: Return loss of patch antenna shown in Fig. 1 with one row EBG and without EBG structures.

wave is reduced in EBG antenna and as a result, the side and back radiations is reduced.

Figure 5 is shown antenna with 5 rows of EBG structures in $E$-plane and Fig. 6 shown return loss and Fig. 7 represented $E$-plane patterns for antenna with one, two, three, four, and five rows, respectively. If number of EBG rows increases up to 4 rows, parasitic effect is dominant. However, with increasing EBG rows from 2 to 4 rows, the bandwidth variation is negligible. With 5 EBG rows, bandwidth suddenly decreases which is the indication of cavity effect domination. Therefore a maximum number of EBG rows exist (i.e., 4 rows), so that, if EBG rows exceeds this number, the bandwidth decreases.
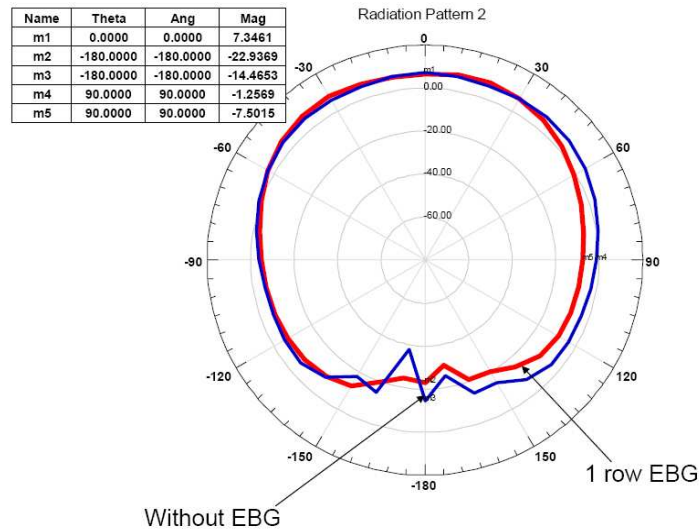


| Name | Theta | Ang | Mag |
|------|-------|-----|-----|
| m1 | 0.0000 | 0.0000 | 7.3461 |
| m2 | -180.0000 | -180.0000 | -22.9369 |
| m3 | -180.0000 | -180.0000 | -14.4653 |
| m4 | 90.0000 | 90.0000 | -1.2569 |
| m5 | 90.0000 | 90.0000 | -7.5015 |

Figure 4: $E$-plane patterns of patch antenna shown in Fig. 1 with one row EBG and without EBG structures.
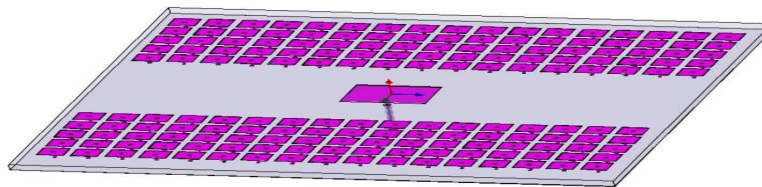


Figure 5: Microstrip patch antenna shown in Fig. 1 with 5 rows of EBG in $E$-plane.
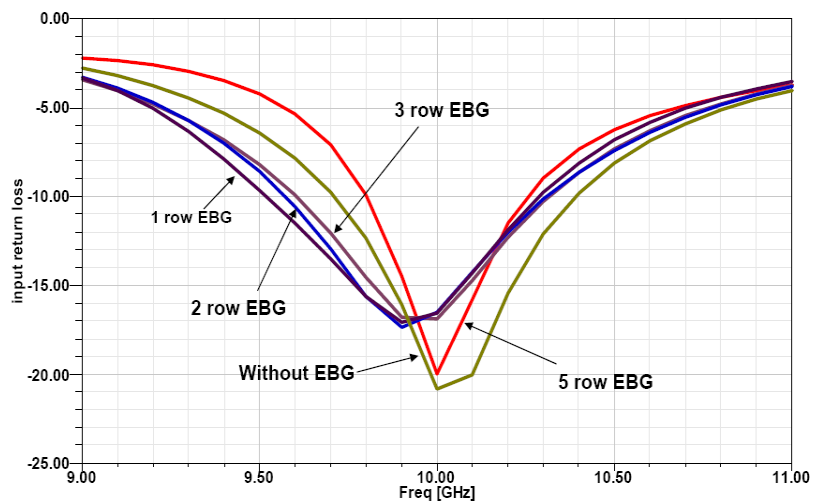


Figure 6: Return loss of patch antenna without and with one, two, three, four, and five rows of EBG structures.
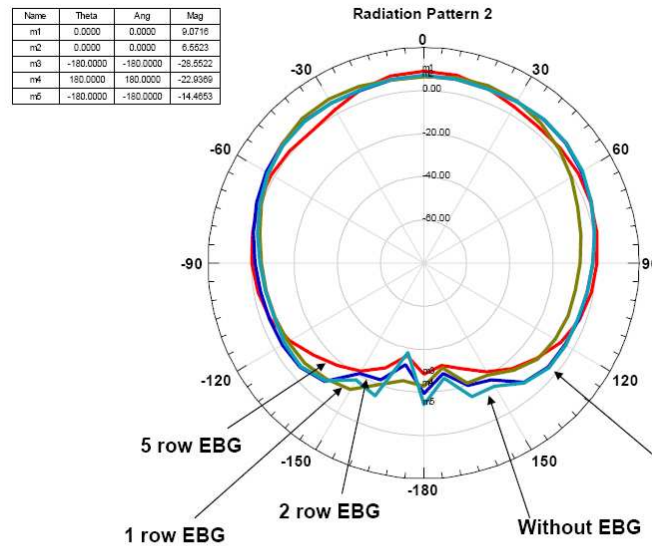
| Name | Theta | Ang | Mag |
|------|-------|-----|-----|
| m1 | 0.0000 | 0.0000 | 9.0716 |
| m2 | 0.0000 | 0.0000 | 6.5523 |
| m3 | -180.0000 | -180.0000 | -26.5522 |
| m4 | 180.0000 | 180.0000 | -22.9369 |
| m5 | -180.0000 | -180.0000 | -14.4653 |

Figure 7: *E*-plane patterns of patch without and with one, two, three, four, and five rows of EBG structures.

## 3. SUMMERY AND CONCLUSION

In this paper, the unwanted side effects of EBG structures which integrated with microstrip antenna is investigated by using parametric analysis. Based on the results obtained in this work, the following can be concluded from the parametric analysis:

1) Increasing the EBG rows results in lower side and back radiation and so better radiation efficiency in the cost of antenna size enhancement.
2) As EBG rows increased from one to four rows, parasitic effect is dominant, but bandwidth improvement is negligible.
3) As EBG rows increases beyond 4 rows, cavity effect becomes dominant and bandwidth suddenly decreases.

From the above discussions, it is obvious that for 2 rows of EBG structures, an acceptable bandwidth is achieved. when 3 or 4 rows of EBG rows are used, bandwidth variations is negligible, but side and back lobe levels decreases in the cost of larger size consumption.

### REFERENCES

1. Gautheir, G. P., A. Courtay, and G. M. Rebiez, "Microstrip antennas on synthesized low dielectric constant substrate," *IEEE Trans. Ant. Propag.*, 1997.
2. Papalymerou, I., R. F. Drayton, and L. P. B. Katehi, "Micromachined patch antennas," *IEEE Trans. Ant. Propag.*, Vol. 46, No. 2, 275–283, 1998.
3. Qian, Y., R. Coccioli, D. Sievenpiper, V. Radisic, E. Yablonovich, and T. Itoh, "Microstrip patch antenna using novel photonic bandgap structures," *Microw. J.*, Vol. 42, No. 1, 66–76, 1999.
4. Coccioli, R., F. R. Yang, K. P. Ma, and T. Itoh, "Aperture coupled patch antenna on UC-PBG substrate," *IEEE Trans. Microw. Theory Tech.*, Vol. 47, No. 11, 2123–2130, 1997.
5. Yang, A. F. and Y. Rahmat-Sami, "A low-profile circularly polarized curl antenna over an electromagnetic band gap (EBG) surface," *Microw. Opt. Technol. Lett.*, Vol. 31, No. 4, 2001.
6. Agi, K., K. J. Maloy, E. Schmiloglu, M. Mojahedi, and E. Niver, "Integration of a microstrip patch antenna with a two-dimentional photonic crystal substrate," *Electromagnetics*, Vol. 19, 277–290, May–Jun. 1999.
7. Yang, F. and Y. Rahmat-Samii, "Microstrip antennas integrated with Electromagnetic Band-Gap (EBG) structures: A low mutual coupling design for array applications," *IEEE Trans. Ant. Propag.*, Vol. 51, No. 10, Oct. 2003.
8. Wood, C., "Improved bandwidth of microstrip antenna using parasitic elements," *IEE Proc. H., Microwave Opt. Antennas*, Vol. 127, 231–234, 1980.